Lecture Notes in Civil Engineering

Ranjith Dissanayake · Priyan Mendis · Kolita Weerasekera · Sudhira De Silva · Shiromal Fernando *Editors*

ICSBE 2020

Proceedings of the 11th International Conference on Sustainable Built Environment

Springer

Lecture Notes in Civil Engineering

Volume 174

Lecture Notes in Civil Engineering (LNCE) publishes the latest developments in Civil Engineering - quickly, informally and in top quality. Though original research reported in proceedings and post-proceedings represents the core of LNCE, edited volumes of exceptionally high quality and interest may also be considered for publication. Volumes published in LNCE embrace all aspects and subfields of, as well as new challenges in, Civil Engineering. Topics in the series include:

- Construction and Structural Mechanics
- Building Materials
- Concrete, Steel and Timber Structures
- Geotechnical Engineering
- Earthquake Engineering
- Coastal Engineering
- Ocean and Offshore Engineering; Ships and Floating Structures
- Hydraulics, Hydrology and Water Resources Engineering
- Environmental Engineering and Sustainability
- Structural Health and Monitoring
- Surveying and Geographical Information Systems
- Indoor Environments
- Transportation and Traffic
- Risk Analysis
- Safety and Security

To submit a proposal or request further information, please contact the appropriate Springer Editor:

– Pierpaolo Riva at pierpaolo.riva@springer.com (Europe and Americas);
– Swati Meherishi at swati.meherishi@springer.com (Asia - except China, and Australia, New Zealand);
– Wayne Hu at wayne.hu@springer.com (China).

All books in the series now indexed by Scopus and EI Compendex database!

More information about this series at http://www.springer.com/series/15087

Ranjith Dissanayake · Priyan Mendis ·
Kolita Weerasekera · Sudhira De Silva ·
Shiromal Fernando
Editors

ICSBE 2020

Proceedings of the 11th International Conference on Sustainable Built Environment

Springer

Editors
Ranjith Dissanayake
Department of Civil Engineering
University of Peradeniya
Kandy, Sri Lanka

Kolita Weerasekera
Department of Civil Engineering
The Open University of Sri Lanka
Nugegoda, Sri Lanka

Shiromal Fernando
Civil and Structural Engineering
Consultants (Pvt) Ltd.
Rajagiriya, Colombo, Sri Lanka

Priyan Mendis
Department of Infrastructure Engineering
University of Melbourne
Parkville, VIC, Australia

Sudhira De Silva
Department of Civil and Environmental
Engineering
University of Ruhuna
Galle, Sri Lanka

ISSN 2366-2557 ISSN 2366-2565 (electronic)
Lecture Notes in Civil Engineering
ISBN 978-981-16-4411-5 ISBN 978-981-16-4412-2 (eBook)
https://doi.org/10.1007/978-981-16-4412-2

Preface

It is with great pleasure that we present the proceedings of the 11th International Conference on Sustainable Built Environment (ICSBE) 2020. This is the eleventh consecutively organized conference following a series of international conference since 2010, keeping its tradition of adhering to engineering excellence.

Taking a step forward from the last ten events, the coverage of specialty areas in this conference has been diversified. This book contains manuscripts of research work from many different sub-specialties. All the manuscripts were presented at parallel sessions on 11th and 12th of December 2020 at the 11th International Conference on Sustainable Built Environment (ICSBE) 2020.

We would like to express our appreciation to all keynote speakers and review and scientific committee members for their invaluable contribution to this conference which strives for a sustainable world through driving innovative research. We are also grateful to the authors for contributing research papers of high quality. The manuscripts in this proceeding book have been reviewed by a panel of academic and professional experts who have vast expertise in their respective fields. The enormous work carried out by these reviewers is gratefully appreciated as well. We are also pleased to acknowledge the advice and assistance provided by the members of the international advisory committee and members of the editorial committee along with many others who volunteered to assist to make this very significant event a success. Furthermore, we acknowledge the financial sponsorship provided by many organizations that have been extremely supportive toward the success of this international conference.

It is the earnest wish of the editors that this proceeding book would be used by the research community and practicing engineers who are directly or indirectly involved in studies related to sustainability.

Editorial Committee
Prof. Ranjith Dissanayake
Prof. Priyan Mendis
Prof. Kolita Weerasekera
Prof. Sudhira De Silva
Eng. Shiromal Fernando
The 11th International Conference on
Sustainable Built Environment (ICSBE) 2020

Kandy, Sri Lanka
Parkville, Australia
Nugegoda, Sri Lanka
Galle, Sri Lanka
Colombo, Sri Lanka
December 2020

Contents

Sustainable Material and Manufacturing

Geotechnical Advances for Sustainable Built Environment

Assessment of Shear Strength Parameters of Marine Dredge Sand

P. G. G. M. Ranbandara, A. M. R. G. Athapaththu, R. U. Thilakarathne, L. C. Kurukulasuriya, and B. P. Gonaduwage

Abstract Cohesion and friction angle represents the shear strength parameters of soils. Linear Mohr–Coulomb envelope is the widely used theoretical concept to describe the shear strength of the soils which are related to the geotechnical analysis and designs. However, sand deviates considerably from linear Mohr–Coulomb envelope due to the effects of factors such as confining pressure, relative density, mineralogy, particle crushing, particle size distribution and fines content. The Colombo port city development project, which is in coastal region, reclaimed dredge sand over 13 m depth. This project was proposed to include low rise and high rise buildings all over the reclaimed land where the type of foundation may vary depending upon the structural loads and subsurface conditions. Therefore, determination of shear strength parameters for different loading condition is of utmost importance to determine the bearing capacity and to select the dimensions of foundations. In this study, basic engineering properties of reclaimed sand collected from Colombo port city project were examined. A series of laboratory direct shear tests were conducted to determine the variation of shear stress over different normal stresses. From the analysis of experimental data, it was revealed that shear stress of dredged sand varies linearly with normal stress up to 100 kPa and showed nonlinear behavior thereafter.

Keywords Land reclamation · Dredge sand · Shear strength · Port city · Relative density · Maximum dry density

1 Introduction

Recently, coastal land reclamation becomes most popular concept in the world due to scarcity of lands for developments. Densely populated areas where space is limited

P. G. G. M. Ranbandara (✉) · A. M. R. G. Athapaththu · R. U. Thilakarathne · L. C. Kurukulasuriya
Department of Civil Engineering, University of Peradeniya, Peradeniya, Sri Lanka
e-mail: gayan_madusanka@eng.pdn.ac.lk

B. P. Gonaduwage
Port City Development Project, Ministry of Urban Development, Colombo, Sri Lanka

R. Dissanayake et al. (eds.), *ICSBE 2020*, Lecture Notes in Civil Engineering 174,
https://doi.org/10.1007/978-981-16-4412-2_1

and expensive, land reclamation can play a major role with most cost effectively and it may be the only way of making lands available for developments. Although land reclamation is very complex process, already this concept had been used for various comprehensive and famous projects such as Hong Kong Disneyland, Changi Airport in Singapore, forest City in Johor, Malaysia and Copacabana Beach in Brazil. Colombo port city is the first and only mega coastal reclamation project in Sri Lanka to date. The extent of the Colombo port city project is 269 ha of reclaimed land from the sea and will be South Asia's premiere residential, retail and business destination considering the smart and green city concepts. This project facilitates various purposes such as commercial, residential, hospitality and recreational etc. Figure 1 shows a conceptual view of Colombo port city project.

Although huge land reclamations project has lot of advantages, various geotechnical issues which associated with these projects are well known. Loose granular sand deposits formed during sand reclamation leads to high risk of liquefaction due to seismic forces. To overcome such failures, reclaimed land needs to be densified to an acceptable level over the depth. Therefore, determination of relative compaction is required to measure the compaction level of the cohesionless soils, in the process of ground improvement. Bo et al. [2] had presented the importance of the deep compaction techniques to overcome the liquefaction issues related to the land reclamation carried out for the Singapore Changi International Airport in term of CPT. Ali et al. [1] had discussed the coastal land reclamation related issues such as ground/fill characteristics, quality control issues, target design performances and construction methodologies etc. Furthermore, causative factors and planning and specification of ground improvements in relations to the calcareous sand also discussed by their study.

Examination of shear strength parameters of dredged sand are utmost important to determine the bearing capacity of foundations for various structures to be built on the reclaimed land. Therefore, shear strength parameters which are required for

Fig. 1 A conceptual view of Colombo port city project

design of foundation also varies with the structural loads. Therefore, assessment of shear strength parameters for dredge sand would be very important for geotechnical analysis and design. Perkins et al. [5] had presented the effect on shallow foundation design criteria under nonlinear shear strength variation. The objectives of this study are to examine the compaction effort and shear behaviour under different normal stresses of dredged sand used in Colombo port city project.

2 Relative Density and Variation of Shear Stress

To obtain the relative density of cohesionless soils, there are some direct methods as well as indirect methods. Sand cone test, rubber balloon method and nuclear density test are the frequently used tests as direct in-situ density tests. Together with the results of minimum, maximum density tests and moisture content test relative density (D_r) can be obtained. Relative density (density index) can be obtained from laboratory tests according to the Eq. (1) which is given in BS 1377-4:1990

$$D_r = \frac{\rho_{d,\max} \times \left(\rho_d - \rho_{d,\min}\right)}{\rho_d \times \left(\rho_{d,max} - \rho_{d,\min}\right)} \tag{1}$$

where D_r is relative density (density index), ρ_d is the dry density, $\rho_{d,min}$ is the dry density at the least dense state and $\rho_{d,max}$ is the dry density at the densest state.

The shear behaviour of dredged sand can be assumed to be elastic perfectly plastic following Mohr–Coulomb failure envelope. According to the Terzaghi et al. [7], sand has considerable deviation from liner Mohr—Coulomb envelope due to effects of confining pressure, relative density, mineralogy, particle crushing, particle size distribution and fines content. As the depth of reclamation is high, the non-linear variation of shear strength of sand can induce considerable effects on the results of a numerical analysis as behaviour of deep foundations, earth dams, soil slopes, and other earth structures in which failure occurs under considerable normal stresses. The secant friction angle concept was the method used to find instantaneous friction angles corresponding to different stress levels. In the case of deep failure surfaces, they are more critical than the shallow failure surfaces when the non-linear shear strength envelope is considered.

According to the explanation by Terzaghi et al. [7], when the granular materials such as sand, rockfill or gravel is subjected to a shearing, particle movements does not occur exclusively on the defined shearing direction. If the particles are in a dense state, the application of low confining pressures tends to move particles out of the way or adjacent particle roll out from the principal direction of shearing known as dilatancy or expansion of granular mass when subjected to the shearing. This out of plane movement of particles leads to develop an additional resistance against shearing which can be attributed to interlocking mechanism near the shearing plane. According to Terzaghi et al. [7] slope of shear strength envelope, which friction angle,

φ' can be explained by sum of two components of interparticle sliding friction, φ'_{μ}, and geometric interference, φ'_{g} as shown in Eq. (2).

$$\varphi' = \varphi'_{\mu} + \varphi'_{g} \tag{2}$$

As confining pressure increases, the up and down movement or pushing adjacent particles out of way become more difficult. It reduces the interlocking between particles and relative particle displacement taken place by crushing or shattering. As a result, particle movement in shearing direction is dominant and grain breakage increased. Consequently, reduction of geometric interference results the lowering of friction angle at higher confining stress levels. Bolton [3] had discussed the effect of normal stress level and relative density which the accepted definition for the state of compaction level of sand to the shear strength parameters with aid of 17 sand types. The bearing capacity of the shallow foundations under nonlinear shear strength variation induced by relative density, effective stress level and scale of the foundation was discussed by Perkins et.al. [5] and a relative density-based approach was proposed.

In the concept of non-linear shear strength of sand, secant friction angle is used as a parameter which is to represent the shear strength under different normal stresses. As states in literatures, double polynomial curve fitting [4] and power curve fitting [3] had been applied by several researchers. Since the normal stress on the soil layers increases with the depth, secant friction angle decreases considerably from these two methods. From the other hand, fitting of linear relation would tend to show a variation in properties, with the angle of friction increases and the cohesion decreases close the zero-stress level [6].

3 Laboratory Experimental Setup

Understanding of the basic engineering properties of dredge sand which has been used for Colombo port city project is always advantages for carrying out analysis, and designs. A series of mechanical analysis, specific gravity tests and compaction tests were conducted according to British standard 1377 (1990). Figure 2 shows the particle size distribution curve. Table 1 summarizes the basic engineering properties. According to the sand compaction test results, maximum and minimum dry densities of dredged sand are 1818 kg/m^3 and 1515 kg/m^3, respectively. Accordingly, maximum and minimum void ratios are identified as 0.77 and 0.47.

4 Shear Strength Variation of Dredged Sand

Although there are several advantages and disadvantages of direct shear test when compared to the triaxial test, for this particular study direct shear test was selected. Since test material is sand, direct shear test is ideally suited for the drained tests and

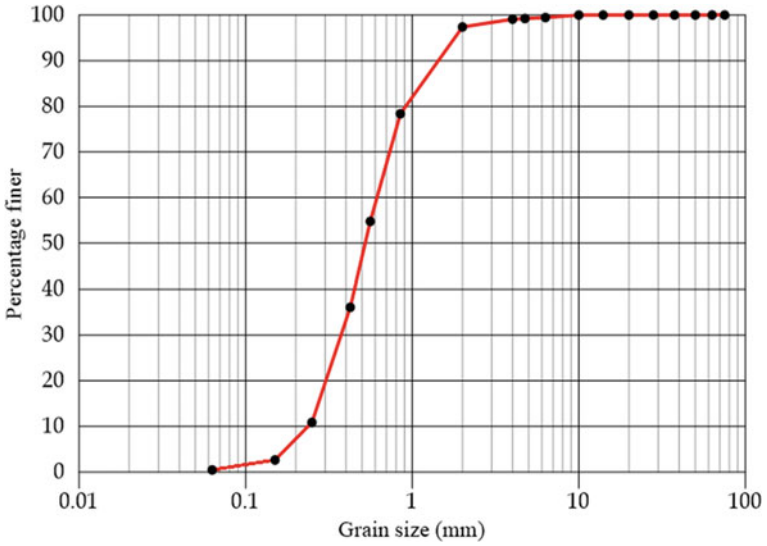

Fig. 2 Particle size distribution (PSD) curve

Table 1 Basic engineering properties of test sand

Property	Value
Fines content, %	0.47
D_{10}, mm	0.24
D_{30}, mm	0.38
D_{50}, mm	0.52
D_{60}, mm	0.62
C_u	2.6
C_c	0.966
Specific gravity	2.68
minimum dry density, kg/m^3	1515
maximum dry density, kg/m^3	1818
e_{max}	0.77
e_{min}	0.47

due to small sample thickness, pore water pressure dissipates rapidly. Also, sample preparation and conducting test is comparatively easier than triaxial test.

Accordingly, to fulfil the main objective of this study, a series of direct shear tests were performed under 6 different normal stresses ranging from 20 to 800 kPa. The normal stresses are 20, 50, 100, 200, 400 and 800 kPa. All direct shear tests were carried out as consolidated drained tests and all samples were prepared with same

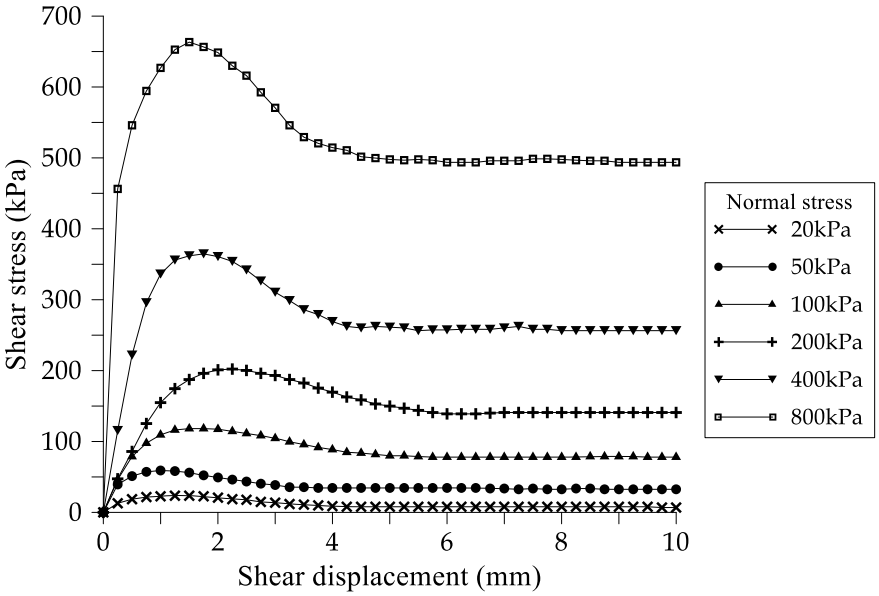

Fig. 3 Variation of shear stress versus shear displacement

95% degree of compaction with a purpose of keeping site conditions when improvements were done before the construction. Figures 3 and 4 show variation of shear stress with shear displacement and failure envelopes of dredged sand, respectively.

Secant friction angle concept with both linear and nonlinear curve fittings method are used for the interpretation of shear strength variation of dredged sand. As Nonlinear curve fitting methods, second order polynomial and power curve fitting were selected. Failure envelopes fitting results were tabulated in Table 2. In these equations, τ and σ_v are shear and normal stresses in kPa, respectively.

Secant friction angle variation under 95% degree of compaction level is tabulated in Table 3 for the comparison purposes. According to the secant friction variation showing in Table 3, for the dredged sand prepared for 95% degree of compaction, secant friction angle decreased by 7° (from 46° to 39°) and 9.5° (from 50.5° to 41°) for both 2nd order polynomial curve fitting and power curve fitting respectively, when normal stress varies from 20 to 800 kPa.

When considered the test materials are completely sandy, intercept of linear envelopes or in other hand cohesion is expected to be approximately zero. However, the cohesion value resulted by linear fitting is 25.5 kPa is too away from the acceptable range since it is too high value for sandy soil. Therefore, it is not suitable to explain the shear strength of sand at the higher normal stresses. According to the failure envelope results in Table 2, second order polynomial curve with zero intercept is fitted well for direct shear test results for test sand when compared with the power curve fitting. However, linear curve fitting is fitted well for the lower normal

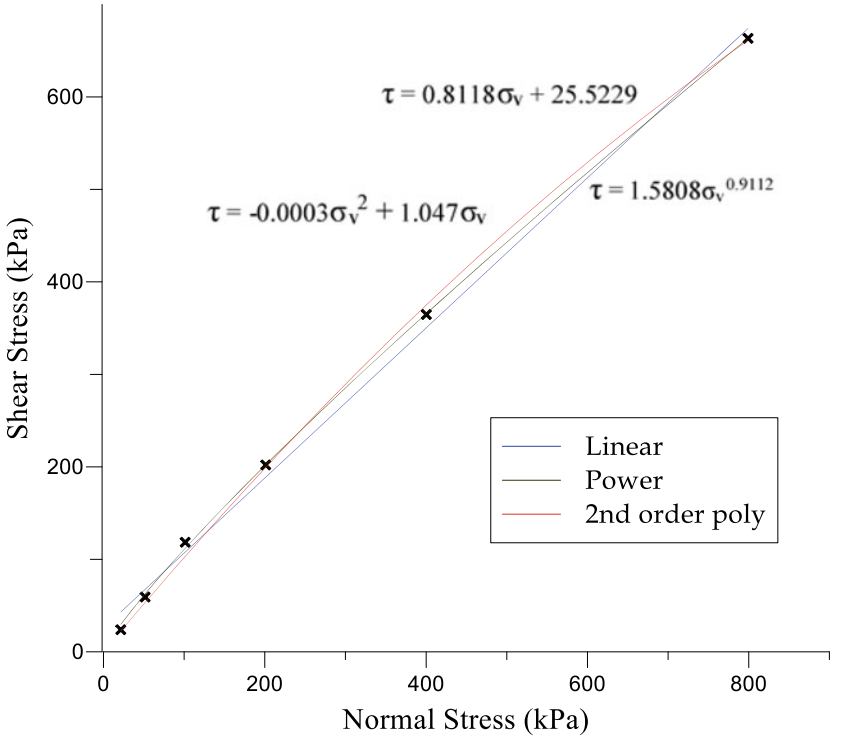

Fig. 4 Linear and nonlinear failure envelopes

Table 2 Failure envelopes

Failure envelope	Equation	R^2 value
Linear	$\tau = 0.8118\sigma_v + 25.5229$	0.9895
2nd order polynomial	$\tau = -0.0003\sigma_v^2 + 1.047\sigma_v$	0.9987
Power curve	$\tau = 1.5808\sigma_v^{0.9112}$	0.9968

Table 3 Secant friction angle variation with normal stress

Normal stress (kPa)	Secant friction angle, (degrees)	
	2nd Order polynomial	Power curve
20	46.0	50.5
50	46.0	48.0
100	45.5	46.5
200	44.5	44.5
400	43.0	43.0
800	39.0	41.0

Table 4 Recommended failure envelopes for normal stress ranges

Normal stress range (kPa)	Failure envelope type	Equation	R^2 value
0–100	Linear	$\tau = 1.1626\sigma_v$	0.9998
100–800	2nd order polynomial	$\tau = -0.0003{\sigma_v}^2 + 1.047\sigma_v$	0.9987

loads and when normal stress increases nonlinear curve fitting is well fitted. Therefore, linear shear behaviour with zero cohesion can recommended for the normal stress range from 0 to 100 kPa while second order polynomial with zero intercept can recommended for the higher loads carrying foundation designs (above 100 kPa) which are rest on the dredged sand. Accordingly, final shear strength variation for two different ranges are tabulated in Table 4.

5 Conclusions

In this study sieve analysis, specific gravity and compaction tests were carried out to determine the basic engineering properties of dredge sand for Colombo Port City project. Also, nonlinear shear strength variation of dredged sand was identified through a series of laboratory direct shear tests conducted under different normal stresses ranging from 20 to 800 kPa prepared for 95% degree of compaction. Following conclusions were drawn based on the direct shear test results.

1. Secant friction angle decreases by 7° (from 46° to 39°) according to the second order polynomial curve fitting.
2. Secant friction angle decreases by 9.5° (from 50.5° to 41°) according to the power curve fitting.
3. Linear behaviour was identified between normal stress and shear stress for the normal stresses range from 0 to100kPa, for dredged marine sand. The friction angle is 49° for zero intercept.
4. Second order polynomial with zero intercept is the most suitable curve fitting to describe the shear strength variation above 100 kPa normal stresses.
5. Due to the particle crushing at higher normal stresses, linear shear strength variation is not applicable for the normal stress ranging over 100 kPa.
6. Nonlinear shear strength variation would be more applicable for the higher structural loads carrying foundations which rest on the sand.

References

1. Ali HE, Damgaard JS (2013) Geotechnical aspects of coastal reclamation projects. In: Proceedings of the 7th international conference on Asian and Pacific Coasts (APAC 2013), Bali, Indonesia
2. Bo MW, Arulrajah A, Horpibulsuk S, Leong M, Disfani MM (2014) Densification of land reclamation sands by deep vibratory compaction techniques. J Mater Civ Eng 26(8):06014016
3. Bolton MD (1986) The strength and dilatancy of sands. Geotechnique 36(1):65–78
4. Hosseini SMR, Jesmani M (2016) Effect of normal stress and relative compaction on secant friction angle of sands. Turk J Eng Environ Sci 38(3):382–391
5. Perkins SW, Madson CR (2000) Bearing capacity of shallow foundations on sand: a relative density approach. J Geotech Geoenviron Eng 126(6):521–530
6. Perry J (1994) A technique for defining non-linear shear strength envelopes, and their incorporation in a slope stability method of analysis. Q J Eng GeolHydrogeol 27(3):231–241
7. Terzaghi K, Peck RB, Mesri G (1996) Soil mechanics in engineering practice. Wiley, London, pp 146–158

Collapsibility Characteristics of a Residual Soil in Matale District, Sri Lanka

C. J. De Zoysa, A. K. T. Dushan, and L. C. Kurukulasuriya

Abstract Collapse is termed as the large volume reduction taken place in partially saturated soils upon wetting under a particular applied pressure, that are otherwise resistant to much larger applied stresses under normal conditions. This phenomenon can be commonly witnessed in Aeolian, alluvial and colluvial type of soils across the globe though not much reported to occur in residual soils. However, a residual soil too can develop into a collapsible soil under certain conditions. In this study, undisturbed soil samples obtained from a construction site in Matale District, Sri Lanka consisting of a residual soil which exhibited unusually low values of dry density was subjected to a series of double oedometer tests to determine the collapse potential and to investigate the variation of collapse potential with the applied normal pressure, relative compaction and degree of saturation. The study revealed that the collapse potential of different locations of the site is directly proportional to the applied normal pressure and inversely proportional to both relative compaction and degree of saturation. Also, it was identified that samples remolded maintaining their in situ dry density can increase the collapse potential of a slightly collapsible soil. A multi-variate regression analysis was performed to develop a relationship for collapse potential in terms of applied normal pressure, relative compaction and degree of saturation.

Keywords Collapse potential · Double oedometer test · Relative compaction · Residual coil · Degree of caturation

1 Introduction

Residual soils are soils subjected to weathering at the same location and the large range of particle size distribution, loose honey comb type structure and large void ratios resulted from the weathering process can induce a collapse potential in these soils where sudden large volume reductions can occur when subjected to wetting.

C. J. De Zoysa · A. K. T. Dushan · L. C. Kurukulasuriya (✉)
Department of Civil Engineering, Faculty of Engineering, University of Peradeniya, Peradeniya, Sri Lanka
e-mail: chank@pdn.ac.lk

R. Dissanayake et al. (eds.), *ICSBE 2020*, Lecture Notes in Civil Engineering 174,
https://doi.org/10.1007/978-981-16-4412-2_2

This significant change of volume and shear strength reduction can lead to severe geotechnical problems such as differential settlements etc. and ultimately structural failures.

Barden et al. [2] stated four conditions that are necessary for collapse to occur.

1. An open, partially unstable, partially saturated fabric
2. A high enough total stress so that the structure is metastable
3. A sufficiently large soil suction or the presence of a bonding or cementing agent that stabilizes the soil in the partially saturated condition
4. The addition of water to the soil in the partially saturated condition

Mainly two types of collapse mechanisms can be identified.

- Hydro Collapse—Cementation bonds break with the addition of water and that causes settling of particles
- Leaching Collapse—Leaching of salts from soil matrix causes increase in void ratio and reduction in volume

Studies about Collapse behavior of soils expands to a vast context where geographical distribution of collapsible soils, means of accurately assessing collapse, laboratory and field measurement techniques of collapse, ground improvement techniques to reduce collapse etc. have been discussed. Researchers have greatly tended to focus on their native soils, their characterization and also classification according to collapse potential.

For characterization, the micro structures of collapsible soils have been observed by different researchers employing Scanning Electron Microscope (SEM) and X-ray Diffraction [7].

Table 1 shows the classification of collapsible soils according to ASTM D5333-03—Standard Test Method for Assessment of Collapse Potential.

Evaluation of collapse potential has been achieved by many researchers [3, 8–10].

Applied Pressure, initial dry density, initial moisture content, degree of compaction, degree of saturation and soil composition are widely considered to be the governing factors of collapsibility. Among them dry unit weight and water content have been identified as the most critical parameters and it has been shown that collapse generally increases with the applied pressure and has inverse relationships with both initial dry unit weight and water content [6]. However, the effect of initial void ratio, bonding, sample disturbance, clay fraction, compaction energy etc. cannot

Table 1 Classification of collapsible soils [1]

C_p%	Severity of the problem
0	None
0.1–2	Slight
2.1–6	Moderate
6.1–10	Moderately severe
> 10	Severe

be neglected easily and hence several researches have been conducted to study the variation of collapse with these factors both qualitatively and quantitatively.

The two main apparatus employed for collapse measurement throughout the history are Oedometer and Triaxial apparatus. Conventional Oedometer has been the most common approach of many researchers from which the variation of collapse potential with changing of different parameters can be observed easily unlike in triaxial apparatus where a very little additional information can be gained. But since oedometer only facilitates one dimensional analysis and some researches focus on directly measuring the change of diameters of the samples and also controlling the stress state and suction, Triaxial apparatus with suction control has been opted by few researchers in the recent past [12]. Suction controlled oedometers have also been used in several cases (Barden et al. 1969). Obtained results from Lawton et al.'s [6] study manifests that both single and double oedometer test approximately produces similar results. Even though some studies [8] show that single oedometer test over-predicts collapse yet double oedometer is considered to be the most effective method of assessing CP because of the possibility of obtaining large amount of data with one test without repeating for different stress levels and easier and quicker assessment of CP at a given stress.

Even though most of the factors have been widely investigated already, the fact that collapse potential values and amount of dependence on these factors can still vary with the site-specific details, inherent factors to these natural deposits and the fact that these studies have been conducted specifically on one type of native soil yet there has been a growing interest in this area of study. And knowing that a relationship of CP with the Pressure, Degree of Saturation and Relative Compaction alone has not been obtained yet though they have been tested non-simultaneously in different other studies, this study focuses on obtaining a relationship for CP in terms of the above mentioned three factors.

The objectives of this paper are,

1. To assess the collapse potential of different samples taken from the location under existing condition.
2. To investigate the relationship of collapsibility with over burden stress, degree of saturation and relative compaction

2 Methods, Results and Discussion

2.1 Sample Collection

Soil samples were collected from three different places of the site as whole area that can be visually identified as consisting of collapsible soil is covered from these main test pits. Locations were named as Location 1, Location 2 and Location 3 and both disturbed and undisturbed samples were collected from each pit according to the pre calculated quantities.

2.2 Experiments, Results and Discussion

Samples were initially subjected to routine tests (Particle size distribution, Atterberg Limits Tests, Specific Gravity Test and Compaction Test [11] and they were classified according to the British Soil Classification System [4]. The obtained soil compositions, Liquid Limits and Soil types are summarized in Tables 2, 3 and 4 respectively.

The Sample 1 was classified as Very silty SAND of intermediate plasticity (SMI) and Samples 2 and 3 were classified as Very silty SAND of low plasticity (SML). Furthermore, Location 1 was predicted to be the least collapsible location before conducting the collapsibility tests according to literature which shows that CP is inversely proportional to particle density and relative compaction. Neither of sample 2 and 3 showed prominent results in favorable to be the most collapsible sample and hence a judgement could not be made merely based on routine test results. (It is also noted that the Sample 2 has the lowest liquid limit and relative compaction but has an intermediate particle density out of the three while Sample 3 has the lowest particle density and intermediate values for liquid limit and relative compaction).

Next, a series of double oedometer tests were conducted on samples obtained from location 1 (the least collapsible soil) and samples from location 3 (the most collapsible soil) changing their relative compactions and degree of saturations. A trial-and-error method was followed in order to prepare the samples with degree of compaction 85, 90 and 100%. Oven dried soil (to maintain the same degree of saturation) was inserted to the oedometer ring itself through a hydraulic jacking

Table 2 Soil Composition

Sample	Clay %	Silt %	Sand %	Gravel %
1	12.23	15.78	64.71	7.28
2	10.23	19.87	63.56	6.34
3	14.2	15.97	64.03	5.8

Table 3 Summary of liquid limits test results

Sample	Liquid limit (%)
1	42
2	33
3	34

Table 4 Results of soil classification

Sample	Soil type
1	Very silty SAND of intermediate plasticity (SMI)
2	Very silty SAND of low plasticity (SML)
3	Very silty SAND of low plasticity (SML)

method where the compaction effort and the number of blows could be changed until the pre-determined weight for the ring containing soil (for the respective degree of compaction, the required weight of the ring with soil was pre calculated) was obtained.

Figure 1 obtained from the collapse measurement tests verifies that Collapse Potential is directly proportional to the applied Pressure which has already been reported in vast amount of literature [3, 6, 10, 12]. However, critical overburden pressure (where maximum collapse will occur and there will be no change afterwards according to the literature [3, 12] was not reached in the experimental series conducted in this study, so that a judgement on that was not possible. The increment pattern is apparent to be similar in both highly collapsible and less collapsible soils when referring to the curves of sample 1 and sample 3. The increment of Collapse Potential with applied pressure is obvious as with greater loading the greater will be the loss of inter-particle bonding.

Figure 2 which shows all the compression curves for different relative compactions manifests that both dry and wet samples show lesser strains for the same stress levels when compacted to a higher degree. No significant change in this behaviour between a highly collapsible and less collapsible soil was visible. This result can be justified through the argument that with densification of soil which leads to decreased void ratios the volume reduction capacity is minimized.

Figure 3 shows that collapse potential is inversely proportional to the relative compaction in a highly or less collapsible soil and it substantiates the previous findings in literature [12]. This behaviour can be explained from the fact that an increase in compaction will lead to a reduced void ratio and hence reduced potential settlement. Also, it is evident that for the highly collapsible soil (Sample 3) a slight increment in relative compaction from its insitu state caused a great reduction of collapse potential

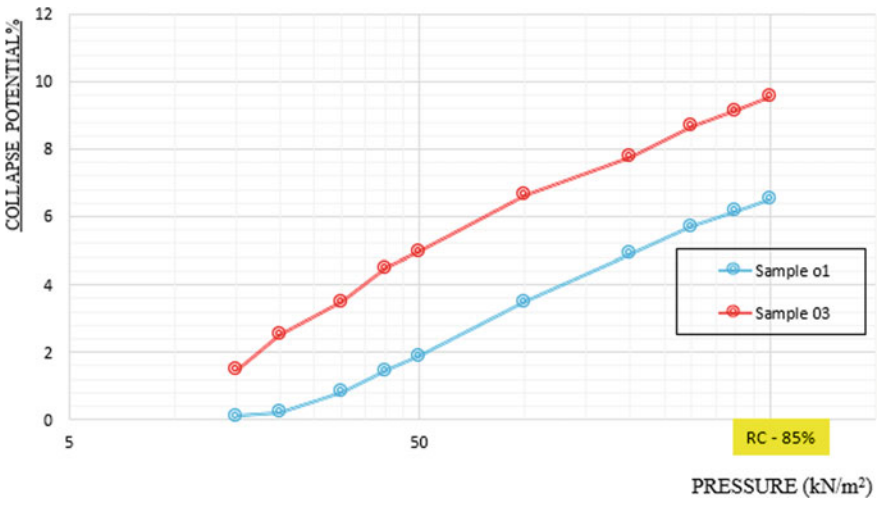

Fig. 1 Variation of Collapse Potential with Pressure for sample 1 and sample 3

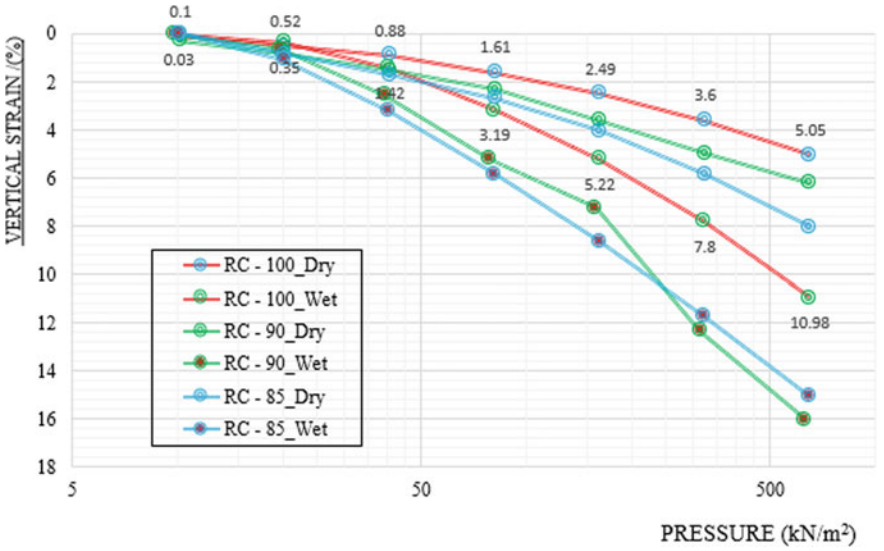

Fig. 2 Variation of strain with Pressure for sample 1

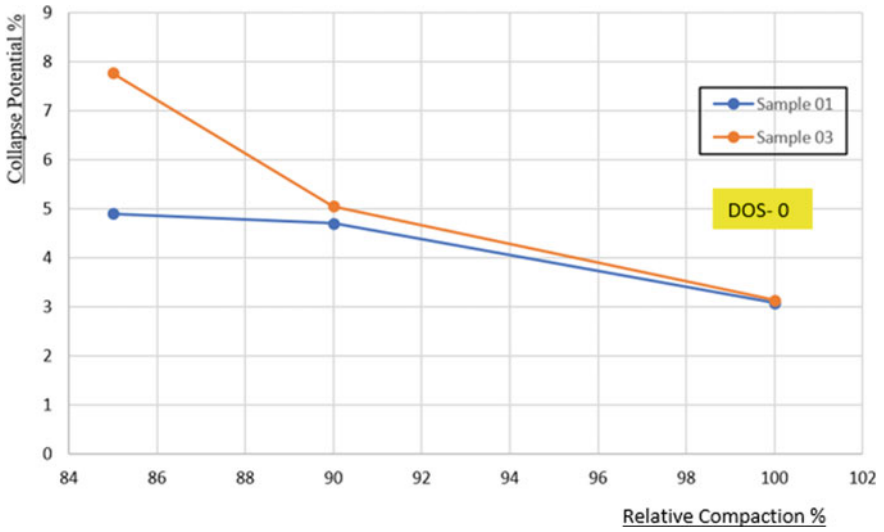

Fig. 3 Variation of collapse potential with relative compaction

whereas such a reduction is evident at a high relative compaction value for the less collapsible soil.

Figure 4 confirms that Collapse Potential is inversely proportional to the Degree of Saturation in a highly or slightly collapsible soil. Also, it is evident that in the slightly collapsible soil this reduction rate is higher than that of the highly collapsible

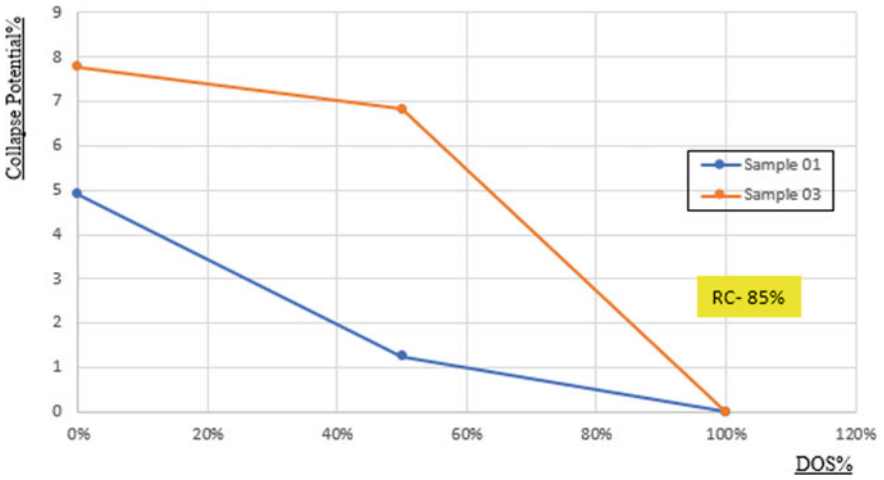

Fig. 4 Variation of collapse potential with degree of saturation

soil at low saturation levels. Also, it can be seen that there is hardly any collapse at the full saturation level of both soils. This inverse relationship can be attributed to the significant compression takes place even with a slight increment of Degree of Saturation and restricted ability for the destruction of cementation bonds with the absence of unfilled voids.

Even though most of the researchers have outlined the effect on initial water content on the collapse potential, correlating collapse potential in terms of Degree of Saturation is not widely found in literature. However recently in one comprehensive research [5] this has been drawn to attention and their conclusions are hardly distinguishable from the observations of this study.

Collapse potential tests performed on the Sample 1 remolded at the same insitu relative compaction of 85% showed that (Fig. 5) remolding a moderately collapsible soil would increase its collapse potential as the binding between the particles would be lost due to remolding. This verifies the claim of Lommler and Bandini [7] that remolding a moderately collapsible sample can increase the collapse potential in it.

2.3 Numerical Relationship

A multi-variate regression analysis was performed to obtain a Numerical Relationship of the dependency of collapse potential on the three selected factors, Pressure, RC and DOS. The following relationship was obtained with an R^2 value of 0.83 through a linear regression analysis of the recorded data.

$$\mathbf{CP = 30.76 + 0.01475\ P - 0.3087\ RC - 0.0210\ S}$$

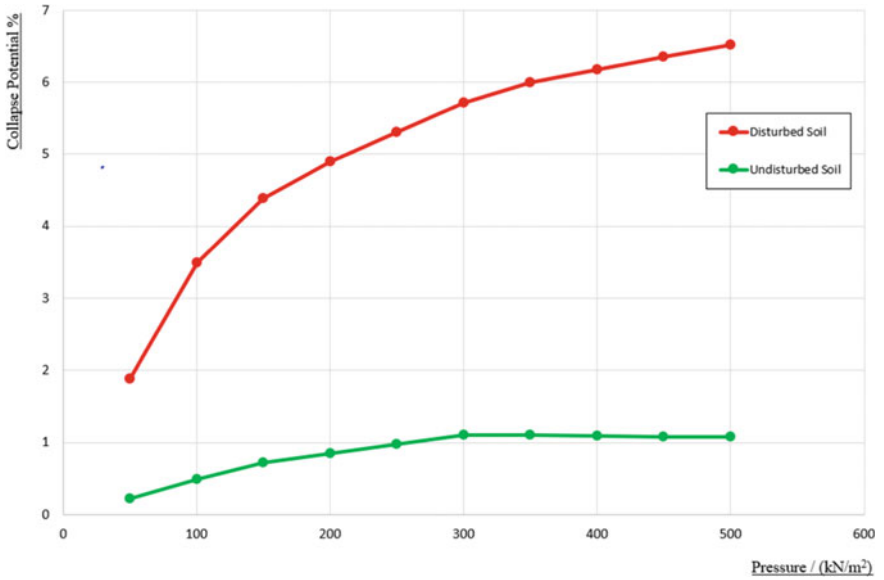

Fig. 5 Variation of collapse potential with pressure for undisturbed and remolded samples

Table 5 *P* values obtained for each parameter from regression analysis

Parameter	*P*
Pressure	0.000
Relative compaction	0.009
Degree of saturation	0.045

where,

CP Collapse Potential
P Pressure
RC Relative Compaction
S Degree of Saturation.

Table 5 shows *P* values obtained for the three parameters and it was evident that the null hypothesis could be rejected and the model can be accepted to fit the data sets of all parameters.

3 Conclusion

This research was aimed at determining the Collapse Potential values of different locations of the site and obtaining the relationship of Collapse Potential with three factors and following conclusions could be reached.

1. Location 3 of the construction site was found to be considerably collapsible compared to other two locations.
2. Collapse Potential is directly proportional to the applied pressure.
3. Collapse Potential is inversely proportional to the Relative Compaction and Degree of Saturation.
4. Using multi-variate analysis, the relationship obtained between Collapse Potential with above three factors ($R^2 = 0.83$) can be expressed as;

$$CP = 30.76 + 0.01475P - 0.3087RC - 0.0210S$$

where,

CP Collapse Potential
P Pressure
RC Relative Compaction
S Degree of Saturation.

All in all, it can be stated that, the above conclusions concur well with the findings in literature and the newly obtained numerical relationship would be supportive in predicting collapse of a similar type of residual soils.

For the use of this collapsible soil in construction, several ground improvement techniques can be suggested as remedial measures such as sand columns, dynamic compaction, prewetting and soil stabilization with chemicals. Incorporating Scanning Electron Micrographs for identifying the nature of soil substructure and its effect on collapsibility and integrating more factors to the relationship such as soil composition and sample disturbance can open up new avenues in this area of research in future.

References

1. ASTM D5333-03 (2003) Standard test method for measurement of collapse potential of soils. Book of ASTM Standards, vol. 04.08. ASTM International, West Conshohocken, PA, pp 1–6
2. Barden L, McGown A, Collins K (1973) The collapse mechanism in partly saturated soil. Eng Geol 7(1):49–60
3. Basma AA, Tuncer ER (1992) Evaluation and control of collapsible soils. J Geotech Eng 118(10):1491–1504
4. Dumbleton MJ (1981) The British soil classification system for engineering purposes: its development and relation to other comparable systems. STIN 83:16577
5. El Howayek A, Huang PT, Bisnett R, Santagata MC (2011) Identification and behavior of collapsible soils
6. Lawton EC, Fragaszy RJ, Hardcastle JH (1989) Collapse of compacted clayey sand. J Geotech Eng 115(9):1252–1267
7. Lommler JC, Bandini P (2015) Characterization of collapsible soils. In: IFCEE 2015, pp 1834–1841
8. Medero GM, Schnaid F, Gehling WY (2009) Oedometer behavior of an artificial cemented highly collapsible soil. J Geotech Geoenviron Eng 135(6):840–843
9. Messad A, Moussai B (2016) Effect of water salinity on Atterberg limits of El-Hodna sabkha soil. Bull Eng Geol Env 75(1):301–309

10. Pereira JH, Fredlund DG (2000) Volume change behavior of collapsible compacted gneiss soil. J Geotech Geoenviron Eng 126(10):907–916
11. British Standard Institution (1990) BS1377: methods of test for soils for civil engineering purposes
12. Sun DA, Sheng DC (2006) Collapse Behavior of Unsaturated Compacted Soils. In: Advances in unsaturated soil, seepage, and environmental geotechnics, pp 102–110
13. Trivedi A, Sud VK (2004) Collapse behavior of coal ash. J Geotech Geoenviron Eng 130(4):403–415

Hydraulic Characteristics of Ballast Subjected to Particle Degradation and Mud Pumping

K. D. K. Rupasinghe, L. A. R. L. Weerarathne, and L. C. Kurukulasuriya

Abstract Ballast is the primary component of a rail track foundation. Ballast aggregates are composed of crushed and coarse grained hard rock. Main functions of ballast are providing adequate permeability for drainage purposes, support the superstructure by distributing the loads from the moving train and provide lateral resistance to tie movement. Similar to shear strength characteristics, drainage capacity is also one of the most important properties of ballast. When it is degraded and aged, broken and foreign particles accumulate within the voids (ballast fouling) and its drainage capacity is decreased. Ballast degradation is mainly due to internal particle breakage and mud pumping. The aim of this research is to study the effect of particle degradation due to particle breakage and mud pumping on hydraulic characteristics of ballast. Rowe cell apparatus was used to conduct permeability tests. Since the ballast particles are large in size, naturally it was impossible to accommodate sufficient amount of sample within the Rowe cell to achieve a better packing of ballast. Therefore, parallel gradation technique was used and a new sample was prepared according to the parallel gradation technique. Series of constant head hydraulic conductivity tests were done for each of the samples with difference fouling percentages and breaking index values. Variation of hydraulic conductivity due to particle degradation in parallel graded ballast was obtained. This investigation revealed that the hydraulic conductivity decreased significantly with the increase in either the fouling percentage or the breakage index.

Keywords Ballast breakage index · Fouling percentage · Hydraulic conductivity · Parallel gradation · Rowe cell

1 Introduction

The rail track network forms an important role of the transportation infrastructure of any country. Due to its ability to be resilient towards the repeated wheel loads,

K. D. K. Rupasinghe · L. A. R. L. Weerarathne · L. C. Kurukulasuriya (✉)
Department of Civil Engineering, Faculty of Engineering, University of Peradeniya, Peradeniya, Sri Lanka
e-mail: chank@pdn.ac.lk

R. Dissanayake et al. (eds.), *ICSBE 2020*, Lecture Notes in Civil Engineering 174,
https://doi.org/10.1007/978-981-16-4412-2_3

low maintenance cost and low construction cost, ballasted rail tracks are the most common tracks in the rail road industry. The major function of ballast layer is to distribute the stresses to the subgrade transferred from the cyclic loading of rolling stock.

Drainage capacity is one of the most important properties of ballast. When it is degraded and aged, fine particles accumulate within the voids (ballast fouling) thus decreasing its drainage capacity. As a result, shear strength of saturated ballasted track is reduced due to development of pore water pressure under cyclic loads transferred from the rolling stock. Ballast degradation is mainly due to internal particle breakage and mud pumping. Internal particle breakage can be defined as abrasion between ballast materials while it is being subjected to cyclic loads. Mud pumping occurs due to the migration of subgrade material into the ballast layer. Due to this ballast fouling, ballast failure may occur and it is a severe problem in railway industry. Therefore, fouled ballast requires a frequent maintenance up to a level. When the internal particle breakage happens due to the abrasion between ballast particles, finer particles will be produced and that will finally fill the voids reducing effective porosity of ballast. Similarly, mud pumping also leads to reduce the voids between the ballast particles.

Degradation of ballast due to particle breakage or mud pumping is known to reduce the shear strength [2]. It can be expected that the hydraulic characteristics of ballast too to be affected by this ballast degradation. Under hydraulic characteristics, hydraulic conductivity is an important parameter to describe how easily water moves through the porous media or how rapid the dissipation of pore water pressure would be. Ballast being a coarse grained material, constant head permeability test can be used to determine the hydraulic conductivity of ballast.

The objectives of this study are to,

1. Investigate the effect of particle breakage on hydraulic conductivity of ballast.
2. Investigate the effect of mud pumping on hydraulic conductivity of ballast.
3. Obtain variation of hydraulic conductivity with particle breakage index and different degrees of fouling due to mud pumping.

2 Literature Review

Parallel gradation technique is a method used to reduce the particle size of ballast used in experiments to suit the equipment used by shifting the gradation curve parallel suitably. Particle size reduction using parallel gradation technique has been carried out with the reduction factor of three considering the size of the Rowe cell apparatus by Shihana et al. [6] and Thanushan et.al. [8].

Su et al. [7] observed that permeability decreased with the increase of fouling ratio for fine and coarse grained sand and permeability corresponding to both low and high water heads approximately followed a linear relationship, high water head having more influence on permeability than low water head and fine sand has more influence on the permeability of ballast than coarse sand. Rahman et al. [5], Danquah et al. [1] and Indraratna et al. [3, 4] also have shown that permeability decreased with

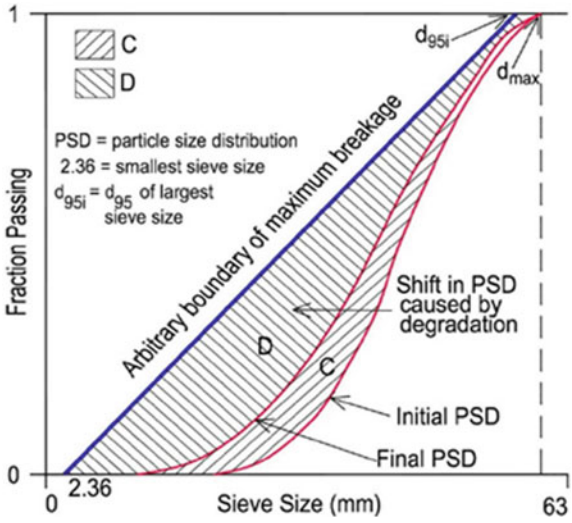

Fig. 1 Ballast breakage index calculation [3]

the increase of fouling ratio for different fouling materials they used. Indraratna et al. [3] introduced an alternative ballast breakage index (BBI) based on particle size distribution (PSD) curves to quantify the degree of ballast breakage. The ballast breakage index (BBI) is calculated on the basis of change in the fraction passing a range of sieves, as shown in Fig. 1.

$$\mathrm{BBI} = \mathrm{C}/(\mathrm{C} + \mathrm{D}) \tag{1}$$

C = Area between initial and final PSD curves
D = Area between the arbitrary boundary of the maximum breakage and final distribution.

3 Materials and Method

3.1 Sample Collection

Ballast and mud are the main two material types that were used in experiments. Ballast samples for conducting hydraulic conductivity tests were collected from a stockpile near Gampola, belonging to the Sri Lanka Railway Department. The mud samples were collected from the pumped up fine grained materials available along the railway track near Gampola railway station. Specific gravity tests were conducted for both ballast and mud samples.

3.2 Parallel Graded Ballast Sample Preparation

In Sri Lanka particle gradation used for railway ballast complies with the Indian standard. Therefore, the targeted particle size distribution curve of ballast for preparing test samples was obtained by using the reduction factor 3 on the lower bound gradation curve of Indian standard considering the size of the Rowe cell apparatus used to conduct the hydraulic conductivity tests. Ballast samples were sieved conforming to dry sieving method described in BS 1377 Part 2:1990. Since sufficient amount of particles were not available, excess larger size particles were crushed using Aggregate Crushing Value (ACV) machine. Then parallel graded ballast sample was prepared to conform to the parallel graded lower bound gradation of Indian Standard.

3.3 Simulation of Ballast Degradation Due to Particle Breakage

The particle breakage was induced on the three similar parallel graded ballast samples which having 27 kg by subjecting each sample to a predetermined number of revolutions of 150, 400 and 600 of Los Angeles Abrasion Value (LAAV) testing machine. In this process, no charges were used to prevent ballast particles from crushing in the rotating drum. Only one-third of the above sample was placed inside the drum at a time considering the safe capacity of the LAAV machine. Ballast Breakage Index was calculated for each sample using Indraratna et al. [3] definition.

3.4 Simulation of Ballast Degradation Due to Mud Pumping

By dividing each of these samples into 3 samples, 9 samples were prepared and calculated amount of mud sample was added in order to define 5, 10 and 15 fouling percentages. With the purpose of simulating the field conditions, calculated amount of mud sample was added to the ballast sample at the bottom of the ballast sample. A constant ballast weight of 8.971 kg was used for each sample. However, weight of the subgrade material added is required to be varied for different Ballast Breakage Indices (BBI) as with the increase in BBI the packing density of ballast too will increase as part of the voids get filled by the broken ballast particles which results in a reduction of void volume. However, the fouling percentage was always expressed as a percentage of the initial void volume corresponding to 0% BBI (i.e. fresh sample). Therefore, the subgrade material added to represent fouling due to mud pumping does not depend on the BBI.

3.5 Constant Head Hydraulic Conductivity Test

A series of constant head hydraulic conductivity tests were conducted to investigate the variation of hydraulic conductivity of ballast subjected to ballast breakage and fouling using Rowe cell apparatus having internal diameter of 254.2 mm and height of 127.20 mm. The initial packing density of the fresh ballast sample was 1691.55 kg/m^3. The variation of the flow rate with the head difference was plotted and hydraulic conductivity was calculated using the Darcy's law using the gradients of the resulting graphs.

4 Results and Discussion

After applying 150, 400 and 600 predetermined number of revolutions on three samples in the LAAV machine, ballast samples were sieved again to determine the particle size distribution curves corresponding to each degree of degradation, as shown in Fig. 2.

For each sample, Ballast Breakage Index (BBI) was evaluated based on the definition proposed by Indraratna et al. [3], corresponding to revolutions of 150, 400 and 600 respectively. The results are summarized in Table 1. Arbitrary boundary of maximum breakage curve for each revolution was plotted matching 3 points; smallest sieve size used, 95% of largest sieve size used and largest sieve size used. Area calculation under each curve was done by calculating the area of each polygon.

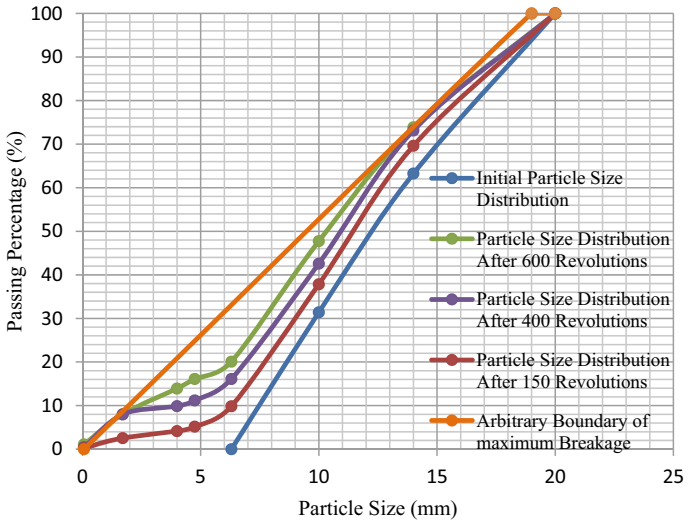

Fig. 2 Particle size distribution curves for initial ballast sample and ballast samples subjected to 150, 400, 600 revolutions in LAAV machine

Table 1 Ballast breakage index (BBI) for each LAAV revolutions

Number of revolutions	Ballast breakage index (%)
150	32
400	58
600	72

Variation of flow rate with hydraulic gradient for fresh ballast sample and 0% fouling percentage ballast samples with 32, 58 and 72% ballast breakage indices are shown in Fig. 3.

Figure 4 shows the variation of flow rate with hydraulic gradient for BBI = 32% ballast samples with 0%, 5%, 10% and 15% fouling.

Figures 5 and 6 refer to the variation of flow rate with hydraulic gradient for ballast samples with 0%, 5%, 10% and 15% fouling for BBI = 58% and BBI = 72% respectively (Table 2).

Figure 7 confirms that hydraulic conductivity is decreased with the increase of the ballast breakage index, as void volume is decreased with the increase of breakage index value due to increase of finer particles (Table 3).

Figure 8 confirms that the hydraulic conductivity is decreased with the increase of fouling percentage for each ballast breakage index, as fines fill up the voids between ballast particles and restrict the flow. The fresh ballast sample (0% fouling and 0% ballast breakage index) has the highest hydraulic conductivity.

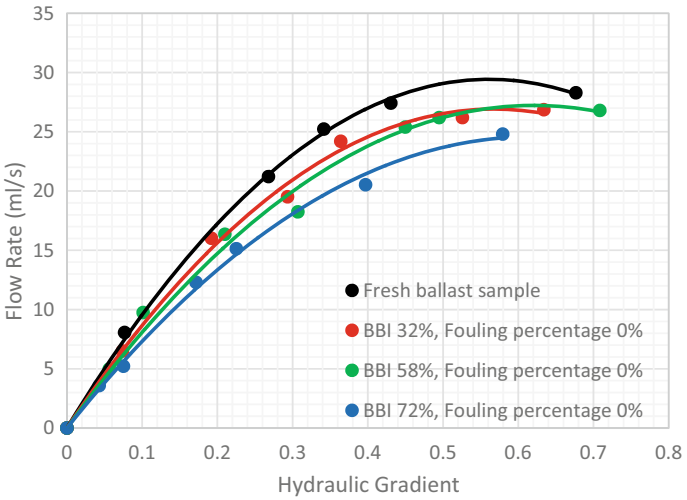

Fig. 3 Variation of flow rate with hydraulic gradient for ballast samples with 0% fouling percentage

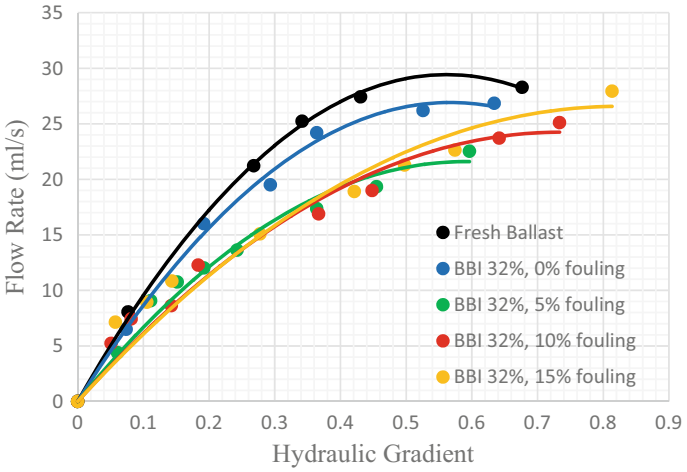

Fig. 4 Variation of flow rate with hydraulic gradient for BBI = 32% ballast samples with different fouling percentages

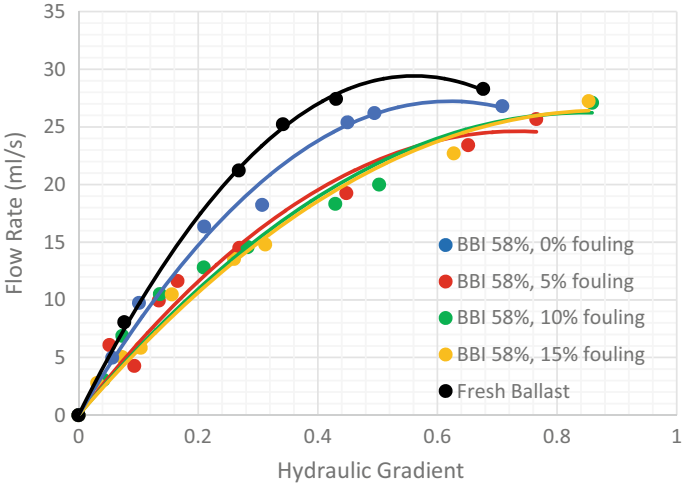

Fig. 5 Variation of flow rate with hydraulic gradient for BBI = 58% ballast samples with different fouling percentages

5 Conclusions

The series of experiments established the variation of the hydraulic conductivity of fresh ballast and degraded ballast due to internal particle breakage and mud pumping. Based on the results, it can be concluded that hydraulic conductivity is decreasing with the fouling percentage for each ballast breakage indices and

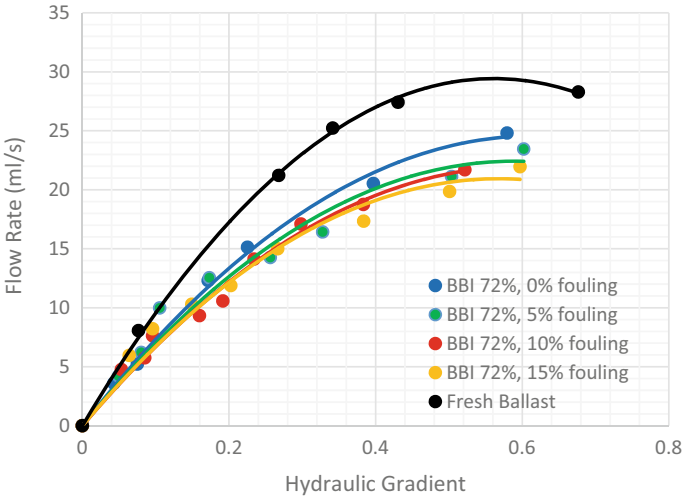

Fig. 6 Variation of flow rate with hydraulic gradient for BBI = 72% ballast samples with different fouling percentages

Table 2 Variation of hydraulic conductivity with breakage index for 0% fouled ballast samples

BBI (%)	Hydraulic Conductivity (cm/s)
0	0.1864
32	0.1705
58	0.1619
72	0.1442

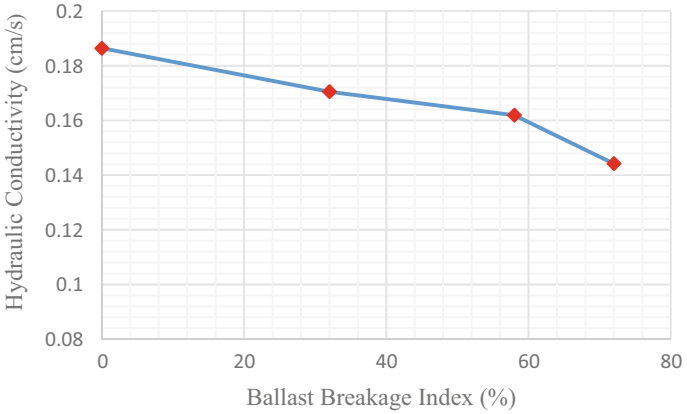

Fig. 7 Variation of hydraulic conductivity with breakage index for 0% fouled ballast samples

Table 3 Variation of hydraulic conductivity with fouling percentage for ballast samples with BBI = 32%, BBI = 58% and BBI = 72%

Fouling percentage (%)	Hydraulic conductivity (cm/s)		
	BBI = 32%	BBI = 58%	BBI = 72%
0	0.1705	0.1619	0.1442
5	0.1317	0.1231	0.1181
10	0.119	0.1149	0.1117
15	0.1176	0.1102	0.1054

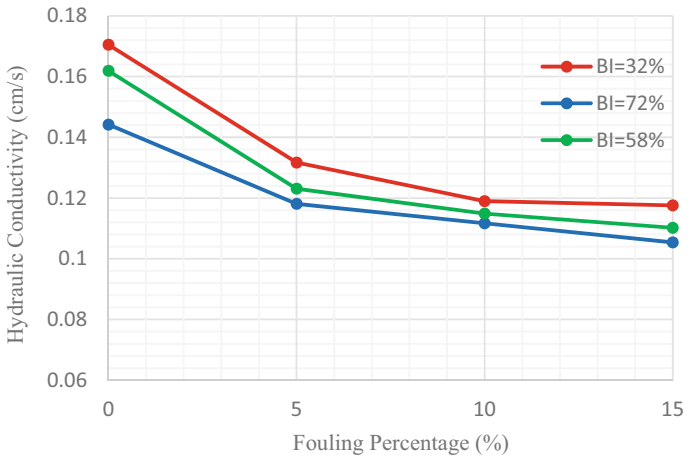

Fig. 8 Variation of hydraulic conductivity with fouling percentage for ballast samples with BI = 32%, BI = 58% and BI = 72%

hydraulic conductivity is decreasing with the ballast breakage index value for each fouling percentages.

References

1. Danquah WO, Ghataora GS, and Burrow MPN (2014) The effect of ballast fouling on the hydraulic conductivity of the rail track substructure. In: XV Danube—European conference on geotechnical engineering, Paper No. 225
2. Dissanayake DMAGB, Kurukulasuriya LC, Dissanayake PBR (2016) Evaluation of shear strength parameters of rail track ballast in Sri Lanka. J Nat Sci Found Sri Lanka 44
3. Indraratna B, Nimbalkar S, Christie D (2009) The performance of rail track incorporating the effects of ballast breakage, confining pressure and geosynthetic reinforcement
4. Indraratna B, Nimbalkar S, Tennakoon N (2010) The behavior of ballasted railway track foundation: track drainage and geosynthetic reinforcement. pp 2378–2387
5. Rahman AJ, Parsons R, Han J (2012) Properties of fouled railroad ballast (Phase 1). Mid-America Transportation Center. Performing Organization Report No. 25-1121-0001-465

6. Shihana AM, Vasan V, Kurukulasuriya LC (2016) Shear strength characteristics of ballast subjected to particle breakage and mud pumping using parallel gradation technique. ICSBE 2016-Submission 173-Ballast degradation
7. Su Z, Huang H, Jing G (2015) Experimental analysis permeability characteristics of fouling railway ballast. No. 9, pp 986–991
8. Thanushan G, Milojan G, Kurukulasuriya LC (2019) Hydraulic characteristics of ballast subjected to particle degradation using parallel gradation technique. In: Proceedings, 10th international conference on structural engineering and construction management (ICSECM), (Oral. 14 December 2019. Earl's Regency Hotel, Kandy, Sri Lanka), ISBN 978-955-589-272-8.

The Effect of Fouling Materials on Permeability Behaviour of Large Size Granular Materials

H. G. S. Mayuranga, S. K. Navaratnarajah, M. M. N. Gimhani, and J. M. M. Y. Karunarathne

Abstract Granular materials are discontinuous, highly heterogeneous materials that are randomly assembled. They are widely used in civil engineering constructions such as in highway pavements, rockfill dams, drainage systems, and rail tracks. In this study, the granular type ballast aggregates were used to analyze its permeability behaviour when it is contaminated with fine particles. The ballast provides rapid drainage and supports the heavy loads apply from the trains. However, the accumulation of fines in the ballast layer which is known as fouling causes disturbance in track drainage which is leading for reduced track performance and frequent track maintenance. Therefore, this study focuses on the determination of permeability behavior of fouled ballast with different levels of fouling experienced in Sri Lankan rail tracks and to propose the stage at which track maintenance should be done. A series of constant head permeability tests were conducted by using large-scale permeability apparatus built in the laboratory. Sandy clay was used as the fouling material and the gradation of ballast currently adopted in Sri Lanka was used. Void contamination index (VCI) was selected to indicate the fouling level and the permeability of ballast was measured at different VCI values. A numerical analysis was carried out to simulate two-dimensional flow under actual track geometry in quantifying the drainage capacity of ballast in different degrees of fouling. By using constant head permeability test results as inputs, drainage capacities at different cases were obtained from the numerical analysis and classified according to the drainage capacity criteria. Based on the research outcomes, a relationship between the hydraulic conductivity of ballast and the VCI% was obtained. Also, the critical fouling levels in different layers of ballast were identified to commence the ballast cleaning work at the rail track site.

Keywords Ballast · Fouling · Large-scale permeability test · Numerical modelling

H. G. S. Mayuranga (✉) · S. K. Navaratnarajah · M. M. N. Gimhani · J. M. M. Y. Karunarathne
Department of Civil Engineering, Faculty of Engineering, University of Peradeniya, Peradeniya, Sri Lanka
e-mail: sushanm@eng.pdn.ac.lk

R. Dissanayake et al. (eds.), *ICSBE 2020*, Lecture Notes in Civil Engineering 174,
https://doi.org/10.1007/978-981-16-4412-2_4

1 Introduction

Large size granular materials are commonly used in civil engineering applications because of their properties such as high strength, permeability, and friction. Ballast is a well-known granular type material used in ballasted railway track which is widely used and traditional track system in most countries including Sri Lanka. The ballast layer supports dynamic stresses transmitted from faster and heavy trains and distributes safely to the underlying layers. Newly placed, uniformly graded, angular shape ballast aggregates with large void spaces ensure the proper drainage of the railway track and thereby keep the track relatively dry to maintain its performance. However, during the operation, ballast aggregates deteriorate due to the breakage of sharp edges and corners of particles [7]. Fines from this particle breakage, fill the void spaces in the ballast layer. Additionally, the infiltration of fines from underlying layers, mud pumping, and sleeper wear results in a fouled ballast layer [4, 9]. Selig and Waters [10] reported that the ballast breakage contributes about 76% for ballast fouling, followed by 3% of infiltration of fines from subgrade, 13% from subballast, 7% from ballast surface, and 1% from sleeper wear. Ballast fouling results in reduced drainage capacity of the ballasted track which is leading to track instability as a result of the creation of excess pore water pressure under repetitive train loading [2, 4, 8]. Further, it makes ballast particles less angular and reduces the shear strength. Therefore, mitigation measures should be taken to reduce ballast fouling and thereby reduce corrective maintenance cost which is comparatively huge. Thus, it is important to accurately predict the stage at which preventive maintenance should be carried out.

In this study, the permeability behaviour of clean and fouled ballast with different fouling levels of sandy clay material was investigated. A large-scale permeability apparatus designed and built at the laboratory was used to conduct a series of constant head permeability tests on clean and fouled ballast. Based on the experimental results, the developed 2-D FEM model was used to predict the drainage capacities of ballast with different fouling levels. Based on the results of numerical simulation, the track drainage was classified under different fouling conditions to identify the stages to conduct ballast cleaning work in ballasted railway tracks. The initial part of this paper explores the methods of quantification of ballast fouling based on the literature survey. Then the experimental investigation, numerical investigation, and the results are presented and discussed.

2 Quantification of Ballast Fouling

Several researchers have introduced various indicators for quantifying ballast fouling. The ‘Fouling Index’ (FI) was introduced by Selig and Waters [10] and it is given by the summation of percentage passing (by weight) 4.75 and 0.075 mm sieves. Further, they defined another index named ‘percentage fouling’ which is given by the ratio of the

dry weight of ballast material passing 9.5 mm sieve to the dry weight of total ballast sample. These methods are based on the mass ratios and cannot capture the difference between various types of fouling materials with different specific gravities [5]. Alternatively, Feldman and Nissen [3] proposed a new index called 'Percentage Void Contamination' (PVC) based on the ratio between the bulk volume of fouling material where particles passing 9.5 mm sieve and the void volume within the total ballast. Although it directly captures the volume of fouling particles, the gradation of fouling material was not considered. In some cases, this will result in an over-estimation of the fouling level. Also, measuring the volume is time-consuming. To overcome these issues, Indraratna et al. [5] introduced the relative ballast fouling ratio based on the solid volumes of fouling and ballast particles. The relative ballast fouling ratio ($R_{b\text{-}f}$) can be expressed as given in Eq. (1) where M_f, M_b, $G_{s\text{-}f}$, and $G_{s\text{-}b}$ are the dry mass of fouling material, dry mass of clean ballast, specific gravity of fouling material, and specific gravity of clean ballast respectively. Since this method is based on the mass of ballast and fouling materials, it reduces the estimation time significantly. After this, Tennakoon [11] described a new parameter called void contamination index (VCI) by applying modifications to PVC to capture the behaviour of different types of fouling material. The VCI can be expressed as given in Eq. (2) where e, G_s, M denotes void ratio, specific gravity, and dry mass respectively, and subscripts f and b denote fouling material and clean ballast respectively. In the current study, VCI is used for representing the level of ballast fouling.

$$R_{b-f} = \frac{M_f\left(\frac{G_{s-b}}{G_{s-f}}\right)}{M_b} \times 100\% \tag{1}$$

$$VCI = \frac{\left(1+e_f\right)}{e_b} \times \frac{G_{sb}}{G_{sf}} \times \frac{M_f}{M_b} \times 100 \tag{2}$$

3 Large-Scale Permeability Test

3.1 Test Materials

The materials used in this study are fresh ballast and fouling material. The fresh ballast was collected from a stockpile at the Nawalapitiya Railway storage yard of Sri Lankan railways. The ballast material was identified as biotite gneiss which is commonly used in Sri Lankan railway lines. The ballast samples were washed and air dried to remove the fine particles attached to ballast aggregates. Test samples were prepared according to the Indian standard gradation which is currently adopted by the Sri Lankan railways. The particle size distribution (PSD) of the test sample and the limits of Indian standard gradation are shown in Fig. 1. The specific gravity

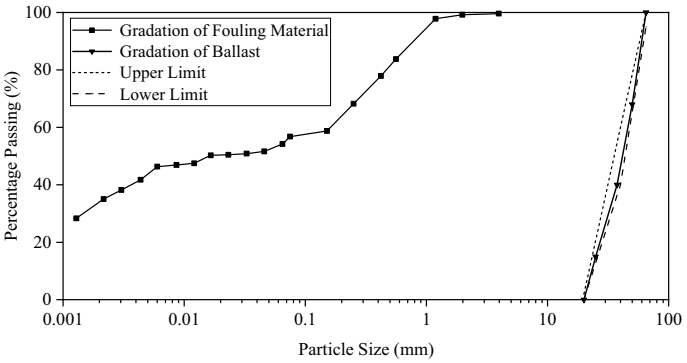

Fig. 1 Particle size distribution of ballast sample and fouling material

and the void ratio of fresh ballast when compacted to the field density were 2.68 and 0.63 respectively [1].

Fouling material collected from Matale area was identified as sandy clay with 48% fines. The gradation of fouling material shown in Fig. 1 was obtained by conducting a hydrometer test at the laboratory. Liquid limit (LL), average plastic limit (PL), and plasticity index (PI) of fouling material obtained from the cone penetration test were 47%, 24%, and 23% respectively. The standard compaction test was used to determine the optimum moisture content (OMC) and the maximum dry density (MDD) of fouling material and reported as 16.5 and 1674 kg/m^3 respectively. The specific gravity and the void ratio of fouling material were found as 2.64 and 0.58 respectively.

3.2 Large-Scale Permeability Apparatus

Large-scale permeability apparatus designed and built at the Geotechnical Engineering Laboratory of the University of Peradeniya was used to study the permeability behaviour of ballast associated with different levels of fouling. The apparatus was designed to observe the permeability behaviour of granular materials under the constant head method. Figure 2a, b shows a photograph and a schematic drawing of the apparatus respectively. The apparatus consists of a cylindrical chamber, water storage, constant head tank, piezometer, and measuring cylinder. The steel cylindrical chamber of 400 mm diameter can accommodate a granular specimen up to a height of 800 mm. The sample size ratio (test specimen diameter to mean diameter of maximum ballast particle size) should be equal to or greater than 6 to avoid the effect from the sample size [6, 11]. The maximum particle size of ballast aggregates used in this study was 63 mm and therefore the sample size ratio was greater than 6. In this study, the ballast specimen height of 400 mm was considered which is greater

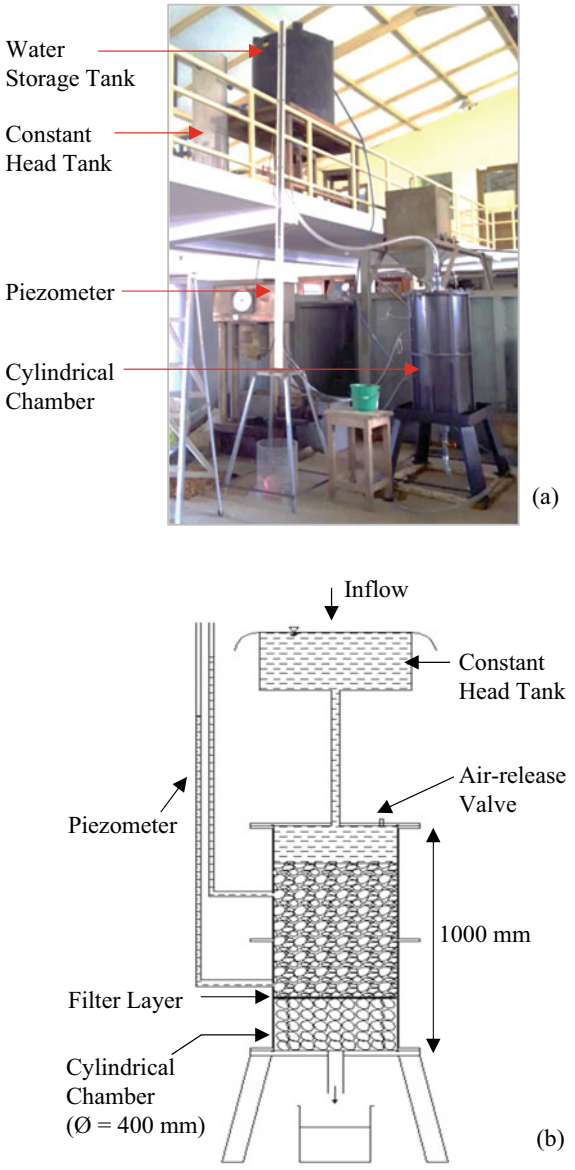

Fig. 2 Large-scale permeability apparatus **a** photograph and **b** schematic drawing

than 5 times the maximum particle size [11]. At the bottom level of the ballast specimen, a filter layer was placed to prevent the washout of fine particles during testing. Under that, a uniformly graded 200 mm thick ballast material layer of size greater than 63 mm was used to maintain a free drainage boundary.

3.3 Testing Procedure

Five different test samples were prepared including one clean ballast sample, and four fouled ballast samples with VCI values of 25, 50, 75, and 100%. Here, the fouling material was mixed with fresh ballast samples according to the required VCI value to obtain uniformly fouled ballast samples. Prepared specimens were placed in the cylindrical chamber in 100 mm thick four equal layers. Each layer was compacted to obtain the field density with a vibratory compactor having a rubber padded base to avoid ballast particle breakage during tamping. After placing the sample, the cylindrical chamber was filled with water and kept for one hour to saturate the sample. Then the constant head tank was filled with water up to the constant level and allowed the water to flow through the specimen. The hydraulic gradient was maintained below 4 to ensure a laminar flow. Head differences were taken from the piezometer for five different flow rate values. Then the variation of head difference against the flow rate was plotted and the gradient was obtained. The equation given in Eq. (3) was derived from Darcy's law and used to calculate the hydraulic conductivity, k of the test sample. Where m is the gradient of the graph, l is the length between piezometers and A is the cross-sectional area of the specimen.

$$k = \frac{ml}{A} \tag{3}$$

3.4 Experimental Results

Figure 3a shows the variation of flow rate with head difference for different VCI values. Based on that the hydraulic conductivity values were calculated using Eq. (3). The obtained values are shown in Table 1. According to that the hydraulic conductivity of clean ballast used in Sri Lankan railway tracks is 0.43 m/s. The variation of hydraulic conductivity of ballast against the VCI value is shown in Fig. 3b. According to that the hydraulic conductivity of ballast reduces with the increase in VCI value. At the 100% VCI value, the hydraulic conductivity is 1.91×10^{-4} m/s which is almost 100% reduction compared to a clean ballast sample. Figure 4 shows the variation of hydraulic conductivity of fouled ballast samples with VCI%. Equation (4) was obtained by considering the exponential variation of data with the correlation coefficient $R^2 = 0.94$. This relationship can be used to predict the hydraulic conductivity of fouled ballast at different VCI%.

$$k = 0.1784e^{-0.074 \times VCI} \tag{4}$$

While unloading the materials from the apparatus at the end of each test, photographs of cross-sections of the samples were taken to observe the distribution of fouling material over the depth of the samples. Figure 5 shows the cross-sections

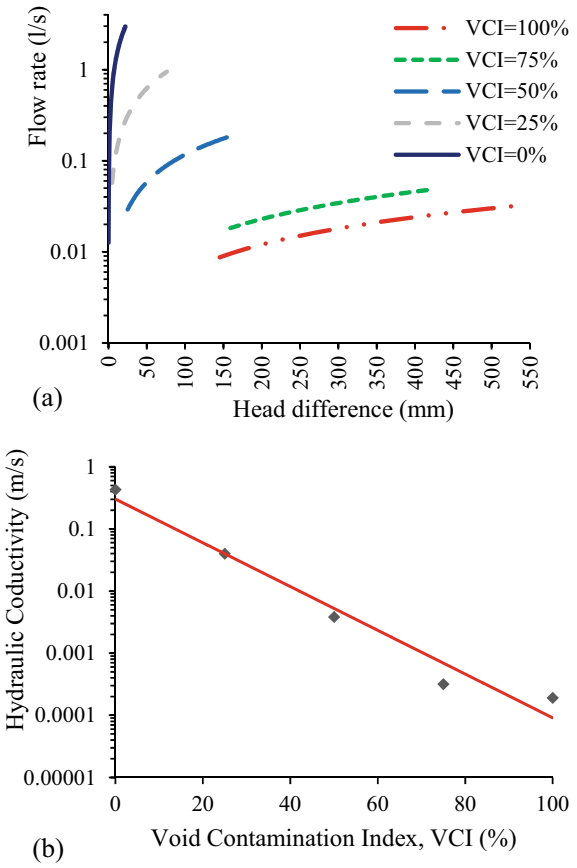

Fig. 3 **a** Variation of flow rate with head difference for different VCI and **b** variation of hydraulic conductivity of ballast with VCI

Table 1 Permeability test results for clean and fouled ballast

Test specimen	VCI (%)	Hydraulic conductivity, k (m/s)	Reduction of k compared to clean ballast (%)
Clean ballast	0	4.30×10^{-1}	–
Fouled ballast	25	3.99×10^{-2}	90.72
	50	3.82×10^{-3}	99.11
	75	3.18×10^{-4}	99.93
	100	1.91×10^{-4}	99.96

of test samples for 25 and 100% VCI at different levels. It can be observed that most of the fines washed out and settled at the bottom layers of the specimen.

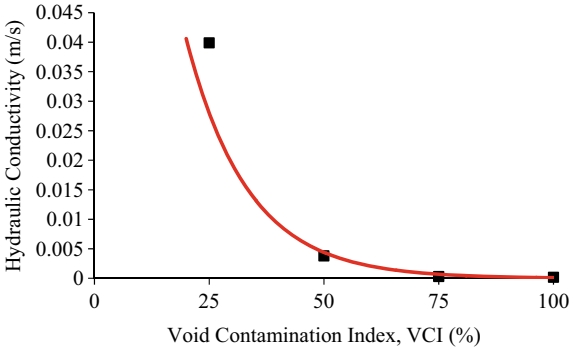

Fig. 4 Variation of hydraulic conductivity of fouled ballast with VCI%

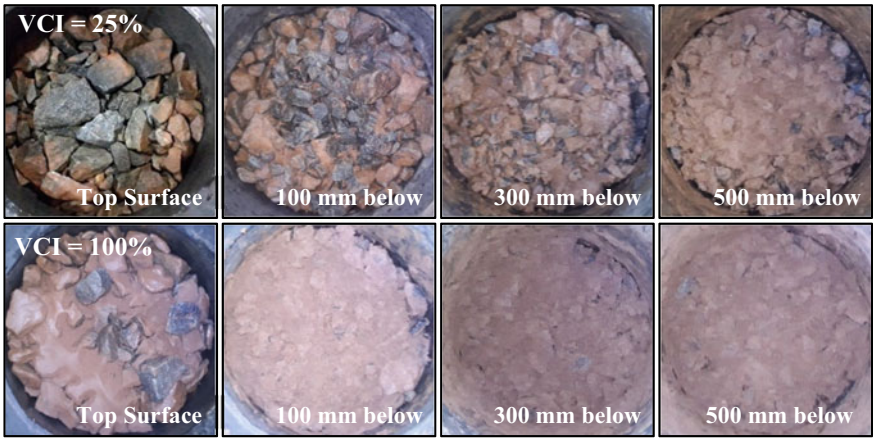

Fig. 5 Cross-sections of test samples for 25 and 100% VCI at different levels

4 Numerical Study

Drainage of water through a ballast layer of a real railway track can happen in vertical as well as horizontal direction. Therefore, a 2-D numerical simulation was conducted using SEEPW (GeoStudio 2012) software to investigate the drainage capacity of ballast under different fouling levels. The hydraulic conductivity values obtained from large-scale permeability tests under different fouling levels were used as input data for the numerical study. Since the pore structure of ballast aggregates in horizontal and vertical directions is random, the horizontal and vertical hydraulic conductivity values (k_h and k_v) were considered as same [11]. A typical railway track cross-section in Sri Lanka is shown in Fig. 6. Since it is symmetric about the middle vertical axis, only a half-track was considered for 2-D seepage analysis.

The boundary conditions used in the 2-D numerical model are; (1) an impermeable layer at the bottom of the ballast layer, (2) free drainage boundary condition on top

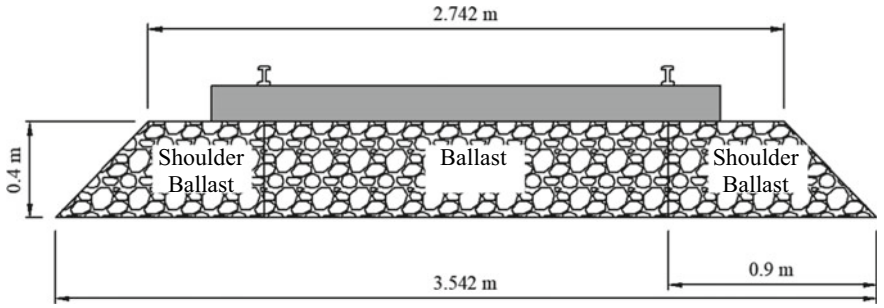

Fig. 6 A typical railway track cross-section (above the subballast layer) in Sri Lanka

of the shoulder ballast, and (3) symmetric boundary condition at the centreline of the rail track. A hydraulic head similar to ballast layer height was assigned at the top surface of the ballast layer. The analysis was carried out under steady-state flow conditions. The 2-D model was analyzed under three possible scenarios as described below.

Scenario 1: A newly constructed ballasted track was divided into 3 equal horizontal layers of 133 mm thick as shown in Fig. 7a. The hydraulic conductivity values at different fouling levels were obtained.

Scenario 2: A track with fouled ballast that is subjected to undercutting was simulated. The track was divided into two horizontal layers where the top layer contained clean ballast and the bottom layer contained fouled ballast of 100% VCI as shown in Fig. 7b. The clean ballast layer thickness was varied and the minimum depth required for acceptable drainage of ballast was determined.

Scenario 3: A track subjected to shoulder cleaning was simulated. The ballasted track was divided into 4 parts as shown in Fig. 7c. The ballast layer was divided into 3 equal horizontal layers with different fouling levels.

For the 2-D numerical analysis, a critical flow rate (Q_c) of 1×10^{-4} m^3/s over the unit length of the ballasted track was adopted by considering the maximum rainfall intensity of Sri Lanka. The maximum drainage capacity (Q) of a ballasted track can be obtained from seepage analysis for different fouling levels. According to [12], the ratio between the computed drainage capacity and the critical flow rate (Q/Q_c) can be used for the classification of track drainage as given in Table 2.

4.1 Numerical Study Results

The maximum drainage capacity (Q) of ballast under different fouling levels were obtained for each scenario. Based on that the drainage of ballast at each condition was classified according to the drainage classification criteria proposed by Terzaghi

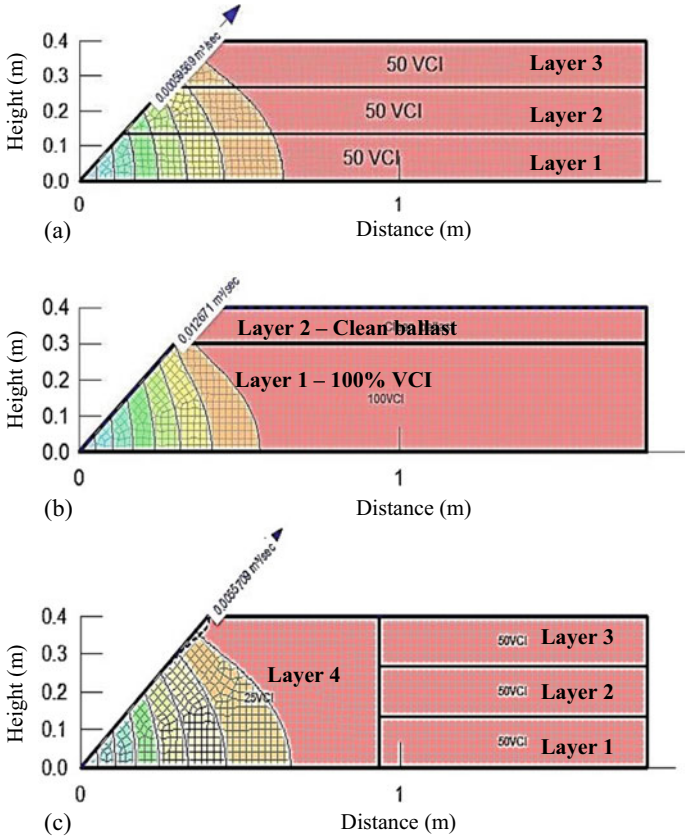

Fig. 7 Developed numerical model for **a** scenario 1, **b** scenario 2, and **b** scenario 3

Table 2 Criteria for drainage classification [12]

Drainage type	Criteria
Free Drainage	$Q/Q_c > 100$
Good Drainage	$10 < Q/Q_c < 100$
Acceptable Drainage	$1 < Q/Q_c < 10$
Poor Drainage	$0.1 < Q/Q_c < 1$
Very Poor Drainage	$0.01 < Q/Q_c < 0.1$
Impervious	$Q/Q_c < 0.001$

and Peck [12]. The results for Scenario 1 are summarized in Table 3. According to that, clean ballast provides good drainage, while completely fouled ballast provides very poor drainage. Still, good drainage is there when the VCI values in the top layers are less than 25% even though the VCI values in the bottom layers are larger. When

Table 3 Results for scenario 1

VCI (%)			Q/Q_c	Classification
Layer 1	Layer 2	Layer 3		
0	0	0	83.819	Good drainage
50	0	0	56.666	
100	0	0	55.421	
0	0	25	41.893	
50	50	0	27.416	
100	50	0	27.164	
100	100	0	26.918	
0	0	50	12.868	
25	25	25	7.778	Acceptable drainage
50	25	25	5.398	
100	25	25	5.154	
100	50	25	2.773	
100	100	25	2.522	
0	0	100	0.966	Poor drainage
50	50	50	0.745	
100	50	50	0.505	
100	100	50	0.265	
100	100	100	0.037	Very poor drainage

the VCI value in Layer 3 (top layer) increases, the drainage capability of the ballast reduces regardless of the fouling levels in the bottom layers.

The results obtained for Scenario 2 are summarized in Table 4. According to the results, when the clean ballast layer thickness decreases, the drainage capability of the ballast also decreases.

Table 5 represents the results obtained in Scenario 3. There is a significant impact on track drainage from the fouling level in the shoulder ballast. When the VCI

Table 4 Results for scenario 2

Fresh ballast layer thickness (mm)	Q/Q_c	Classification
300	62.528	Good drainage
200	41.204	
100	15.839	
50	6.322	Acceptabled
25	4.000	
30	2.858	
20	1.468	
10	1.380	

Table 5 Results for scenario 3

VCI (%)				Q/Q_c	Classification
Layer 1	Layer 2	Layer 3	Layer 4		
0	0	0	0	75.970	Good drainage
50	50	0	0	75.110	
100	100	0	0	75.091	
50	50	50	0	74.871	
100	100	100	0	74.853	
50	50	50	25	69.636	
0	0	0	25	7.138	Acceptable drainage
50	50	0	25	7.011	
100	100	0	25	6.995	
100	100	100	25	6.947	
0	0	0	50	0.685	Poor drainage
50	50	0	50	0.678	
50	50	50	50	0.675	
100	100	0	50	0.671	
100	100	100	50	0.666	
0	0	0	100	0.034	Very poor drainage
50	50	0	100	0.034	
50	50	50	100	0.034	
100	100	0	100	0.034	
100	100	100	100	0.034	

increases in the shoulder layer, the track drainage decreases regardless of the VCI values in Layer 1–3. In the cases where the shoulder ballast is fouled to more than 50% VCI, it is seen that the drainage is classified as 'poor drainage' even if the other ballast layers are relatively clean. Therefore shoulder ballast layer should be cleaned or replaced to maintain an acceptable drainage capacity when it reaches 50% VCI. Still, the good drainage is there when the shoulder ballast is clean even though Layer 1–3 are completely fouled.

According to the drainage classification obtained for major possible ways of contamination of track ballast, the track cleaning work must be done for poor drainage, very poor drainage, and impervious conditions. Further, at the acceptable drainage condition, the decision of ballast cleaning should be taken for the better performance of ballasted tracks and to avoid expensive corrective maintenance costs.

5 Conclusion

The main objective of this research study was to understand the permeability behaviour of rail ballast contaminated with fouling materials and to determine the stage at which the maintenance works should be carried out for proper functioning of the ballast layer. In this study, the Void Contamination Index (VCI) was used to quantify the fouling level of ballast. A large-scale constant head permeability test apparatus was used to obtain the hydraulic conductivity values for clean ballast and ballast contaminated with sandy clay material with 25, 50, 75, and 100% VCI values. The results reflected that the increase in the fouling level dramatically reduces the hydraulic conductivity of the ballast. By considering the exponential variation of obtained hydraulic conductivity values against VCI, a relationship was presented to predict the hydraulic conductivity at any fouling level for track ballast used in Sri Lankan railways. A 2-D numerical model was developed based on the experimental data to classify the track drainage at various fouling conditions. The track drainage classification obtained under three different scenarios exhibited the stages where the ballast cleaning should be carried out. According to the results, the contamination of the top layer of the ballast significantly reduces the drainage capacity even though the bottom layers are clean. Therefore, it is important to maintain a clean ballast layer at the top. Based on the numerical investigation results, it is clear that the undercutting operation can be used to maintain the track drainage at a good or acceptable drainage condition. Further, contaminated shoulder ballast highly reduces the track drainage. Therefore, it is important to maintain a clean shoulder ballast in railway tracks to facilitate better drainage.

Acknowledgements The support provided by the University of Peradeniya Research Grant (Grant No: URG 2017/29/E) and Accelerating Higher Education Expansion and Development (AHEAD) operation funded by the World Bank (Grant No: AHEAD/RA3/DOR/STEM/No. 63) are highly appreciated by the authors. The authors would like to acknowledge the support provided by the District Engineer of Nanuoya Railway office, and the staff of Nawalapitiya Railway Unit of Department of Railways Sri Lanka for helping to collect railway ballast material.

References

1. Dissanayake D, Kurukulasuriya L, Dissanayake P (2016) Evaluation of shear strength parameters of rail track ballast in Sri Lanka. J Nat Sci Found Sri Lanka 44(1)
2. Ebrahimi A, Tinjum JM, Edil TB (2015) Deformational behavior of fouled railway ballast. Can Geotech J 52(3):344–355
3. Feldman F, Nissen D (2002) Alternative testing method for the measurement of ballast fouling: percentage void contamination. In: CORE 2002: Cost efficient railways through engineering, p 101
4. Indraratna B, Salim W, Rujikiatkamjorn C (2011) Advanced rail geotechnology-ballasted track. CRC Press, Boca Raton
5. Indraratna B, Su L, Rujikiatkamjorn C (2011) A new parameter for classification and evaluation of railway ballast fouling. Can Geotech J 48(2):322–326

6. Indraratna B, Wijewardena L, Balasubramaniam A (1993) Large-scale triaxial testing of grey wacke rockfill. Geotechnique 43(1):37–51
7. Navaratnarajah SK (2017) Application of rubber inclusions to enhance the stability of ballasted rail track under cyclic loading. Ph.D. Thesis. University of Wollongong, Australia
8. Paiva C, Ferreira M, Ferreira A (2015) Ballast drainage in Brazilian railway infrastructures. Constr Build Mater 92:58–63
9. Schmidt S, Shah S, Moaveni M, Landry BJ, Tutumluer E, Basye C, Li D (2017) Railway ballast permeability and cleaning considerations. Transp Res Rec 2607(1):24–32
10. Selig ET, Waters JM (1994) Track geotechnology and substructure management. Thomas Telford, London
11. Tennakoon NC (2012) Geotechnical study of engineering behaviour of fouled ballast. Ph.D. thesis, University of Wollongong
12. Terzaghi K, Peck R (1967) Soil mechanics in engineering practice, 2nd edn. Wiley, New York

A Laboratory Investigation on the Advancement of Railway Ballast Behavior Using Artificial Inclusions

S. Venuja, S. K. Navaratnarajah, T. H. V. P. Wickramasinghe, and D. S. A. Wanigasekara

Abstract Ballasted rail tracks are the most popular and conventional rail track foundation system primarily consists of ballast as a major portion by weight and volume. Ballast is a highly angular, coarser material with high bearing capacity, shear strength, and non-water absorbent, which is obtained by crushing rocks. The ballast layer absorbs and widely distributes the moving train loads from sleepers to the ground. With time, the ballast is deteriorated because of frequent cyclic and impact loads from train movements, which ended up with high-cost maintenance. Artificial inclusions are renowned remedial action to the above-mentioned issue. In this laboratory-based study, the effect of rubber pads and geogrids on the shear and deterioration behavior of ballast was evaluated by conducting large-scale direct shear tests under 30, 60, and 90 kPa normal loads with a shearing rate of 4 mm/min. Based on the experimental results, a combination of shock mats and geogrid is suggested which enhanced the stress, dilation, and deterioration behavior of railway ballast.

Keywords Ballast · Shear strength · Deterioration · Rubber pads · Geogrids

1 Introduction

Ballast is produced by crushing accessible natural rocks such as granite, basalt, dolomite, gneiss, and rheolite. These coarse aggregates are packed below and around the crossties to transmit the stresses from sleepers to the underneath layer such as the capping layer and subgrade. Stresses transferred from the superstructure to the ballast layer depend on dead and live loads from the superstructure, spacing, and properties of sleepers, gradation, and level of compaction of ballast, ballast depth as well as subgrade conditions. These repeated dynamic and impact loads cause ballast deterioration. Ballast aggregates undergo breakage and these crushed materials clog the voids in the ballast layer causing drainage hindrance. Ballast may penetrate the formation and blow away due to excessive loads. This may lead to

S. Venuja (✉) · S. K. Navaratnarajah · T. H. V. P. Wickramasinghe · D. S. A. Wanigasekara
Department of Civil Engineering, Faculty of Engineering, University of Peradeniya, Peradeniya, Sri Lanka
e-mail: venujas@eng.pdn.ac.lk

R. Dissanayake et al. (eds.), *ICSBE 2020*, Lecture Notes in Civil Engineering 174,
https://doi.org/10.1007/978-981-16-4412-2_5

differential track settlement and loss of track geometry thus leads to safety issues. Therefore, regular monitoring and maintenance are required which involves high expenses [9, 15, 17, 25].

Degradation behavior of ballast and enhancement of ballast performance with artificial inclusions were analyzed in many ways such as conducting laboratory tests like direct shear tests, triaxial tests, impact load tests, truncated pyramid load tests, and dynamic load tests [1, 6, 14, 16, 18, 27, 28], numerical simulations using *PLAXIS 2D*, *PLAXIS 3D*, *ABAQUS*, *Midas*, and *DEM* [2, 3, 5, 13, 23] and field tests such as plate load test, single tie push test, static load test, field instrumentation and monitoring [4, 10, 24]. Rubber mats and geosynthetics are the major types of artificial inclusions in the railway industry. Nowadays, rubber elements from the recycling of waste tires also have been studied for the suitability in rail track performance enhancement through absorbing energy and reducing ballast breakage [12, 22].

Rail pads (RPs), under sleeper pads (USPs), and under ballast mats (UBMs) are examples of rubber mats used in the rail track. Rubber mats create a softer interface between various parts of the rail track structure. Also, it increases the contact area and distributes load through a wider area [11, 16, 18, 21]. USP is placed on top of the ballast under the sleepers where UBM is placed below the ballast bed. Geogrid reduces the lateral movement of ballast aggregates via mechanical interlocking and it reduces subgrade stresses through acting as a tensile element. Soft subgrade condition encourages the higher mobilization of tension in the geogrid thus leads to lower sleeper displacement [7, 10, 19, 20, 29].

In this study, a series of large-scale direct shear tests were conducted on ballast with and without rubber mats and geogrid. All samples were tested under 30, 60, and 90 kPa static normal loads with a constant shearing rate of 4 mm/min up to 15% shear strain. Shear, dilation, and breakage behavior of ballast with and without artificial inclusions were discussed in this paper.

2 Materials and Test Mechanism

2.1 Materials

Fresh biotite gneiss ballast material was collected from Nawalapitiya stockyard. The basic physical properties such as bulk specific gravity, water absorption, aggregate crushing value, aggregate impact value, flakiness index, and elongation index were tested and concluded that the ballast sample is a composition of highly rock fragments. Ballast was sieved using 63, 50, 37.5, 25, and 20 mm sieves to separate particles by size to prepare a test sample according to Indian standard limits for ballast gradation which is adapted by Sri Lankan railways. Then, aggregates were washed thoroughly to remove dust or other coatings from its surface and left for drying. Artificial inclusions used in this study are rubber mats and geogrid shown in Fig. 1. The mechanical properties of the rubber mats (UBM and USP) can be found

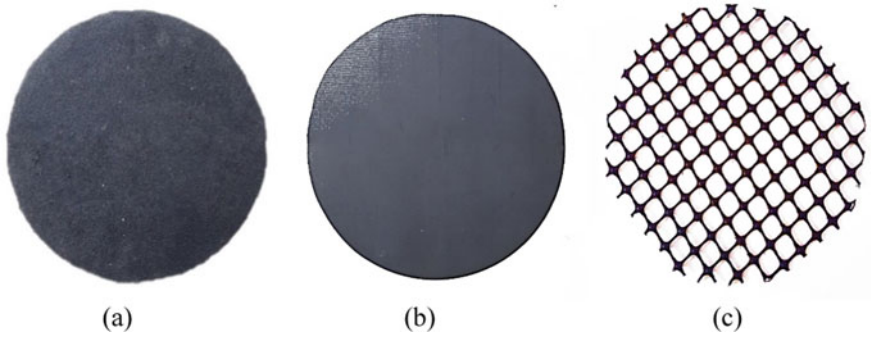

Fig. 1 Artificial inclusions used in this study; **a** UBM; **b** USP; **c** Geogrid

Table 1 Mechanical properties of rubber mats

Material properties	Under ballast mat (UBM)	Under sleeper pad (USP)
Thickness (mm)	10	10
Weight (per unit area) (kg/m^2)	9.2	4.2
Young's modulus (MPa)	6.12	6.0
Bedding modulus, C_{stat} (N/mm^3)	0.20	0.22

in Table 1 [17]. Geogrid has a shear strength of 50 kN/m in both longitudinal and transverse directions as it is an extruded bi-axial polypropylene type.

2.2 Structure of the Large Scale Direct Shear Test Apparatus

As ballast is a large size material, the conventional direct shear apparatus is not capable of analyzing the shear behavior of railway ballast. Therefore, a large-scale direct shear test apparatus was built at the Geotechnical Laboratory of the University of Peradeniya. There are different square-shaped and rectangular-shaped large shear boxes which are discussed by researchers from different countries. Figure 2 illustrates the various parts of the large-scale shear test apparatus used in this study. 400 mm diameter and 300 mm depth hollow cylinder is divided into two equal halves and the top half is fixed in position with the support frame where the bottom part is movable only in the horizontal direction. Shear displacement is applied to the bottom part through a manually operated hydraulic jack. The load cell is used to measure the resistance to shearing where the horizontal transducer is used to measure the shear displacement and both are connected to the bottom half of the apparatus. Surcharge pressure is applied on a top plate mounted on the sample using a lever arm technique.

Fig. 2 The large-scale direct shear apparatus

Another transducer attached to the top plate is used to measure the compression and dilation of the sample during shearing.

2.3 Test Approach

As the aim of this study is to analyze the shear, dilation, and breakage behavior of ballast various layer types of samples were tested under 30, 60, and 90 kPa surcharge stresses. Different layered samples include fresh ballast, ballast with only UBM, ballast with only USP, ballast with a combination of UBM and USP, and ballast with a combination of UBM and USP along with geogrid. The ballast was filled in three layers into the ballast box. Thus, ballast for each layer was prepared according to the particle size distribution (PSD) shown in Fig. 3 by adding the predetermined mass of different sized particles and mixing with a hand shovel. Each layer was compacted using a rubber-padded hammer to required density to attain a 100 mm overall height.

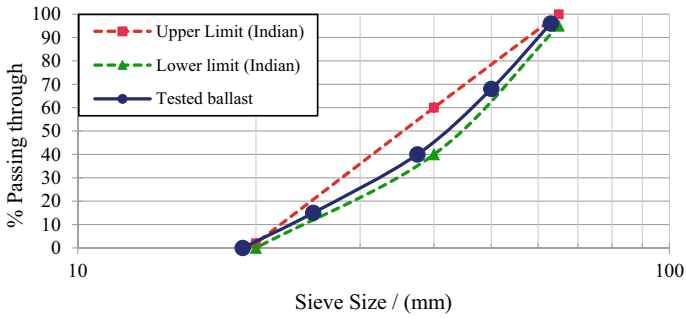

Fig. 3 PSD of tested ballast

UBM was placed at the bottom of the ballast, USP was placed at the top of the ballast, and geogrid was placed on top of the UBM for selected tests. A constant shearing rate of 4 mm/min up to a shear displacement of 60 mm was achieved. The outcomes were obtained from a computer connected with a data logger for automatic recording of shear load, vertical displacement, and shear displacement.

3 Analysis of Experimental Outcomes

3.1 Influence of Artificial Inclusions on Shear and Dilation Behavior of Ballast

Shear load, shear displacement, and vertical displacement were obtained from the data logger for each type of sample. Then, shear stresses of each sample were plotted against the corresponding shear strain (see Fig. 4). An increasing trend up to maximum shear stress was observed in all plots in between 13 and 15% shear strain. With the increase in surcharge load, shear stress increased as higher interlocking between granular particles under greater loads lead to improved frictional resistance.

Under all normal loads, fresh ballast had higher shear stress than the samples with rubber mats and geogrid. Fresh ballast with a combination of UBM, USP, and geogrid showed the second-highest shear stress as the geogrid provides mechanical interlocking to ballast particles [26]. Comparing UBM and USP installed samples, ballast with UBM showed higher shear stress than with USP due to the ballast particle gripping on the UBM and resulted in improved shear resistance. Further, Mohr–Coulomb failure envelopes were developed for each type of sample using the highest shear stress from each test as illustrated in Fig. 5. The friction angle of the ballast was 68° and the lowest value of 59° was obtained for ballast with USP.

3.2 Influence of Artificial Inclusions on Breakage Behavior of Ballast

Ballast particles experienced angular corner breakage, fracture, grinding, and breaking into minor particles as shearing and normal stress applied to the ballast sample. The method proposed by Indraratna et al. [8] was adopted in this study to calculate the ballast breakage index (BBI). The bar graph of BBI of various samples under three normal loads is elaborated in Fig. 6. Higher normal loads compress the ballast sample thus the possibility of higher breakage and higher BBI. BBI values indicated that the ballast breakage is minimal when a combination of USP and UBM is installed. Resilient rubber pads allow ballast particles to partially compress into the smooth surface and USP resulted in a uniform distribution of normal load to the

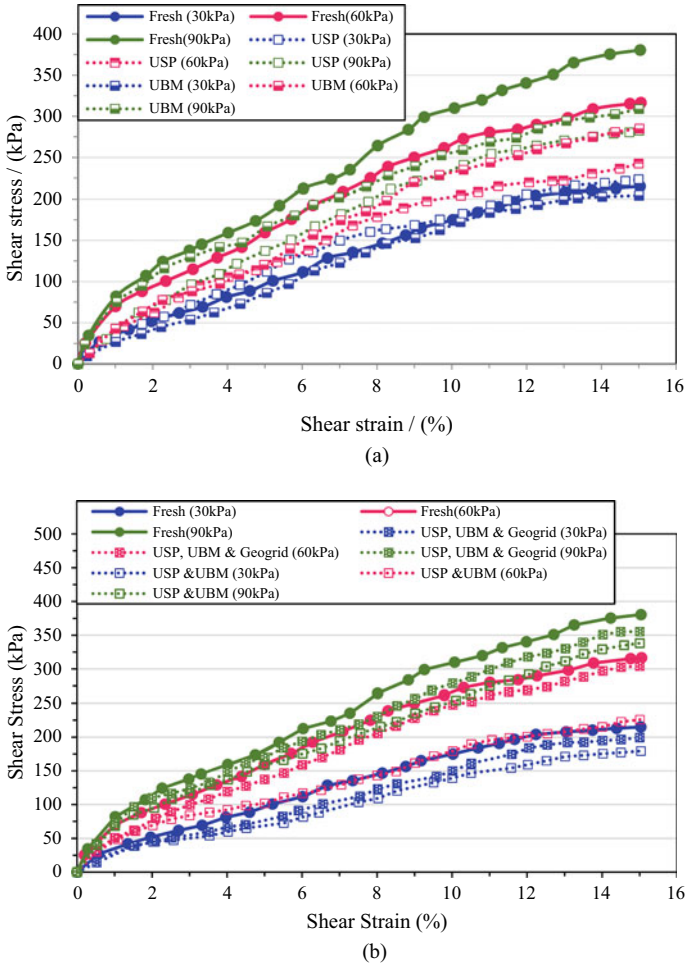

Fig. 4 Shear stress variation with shear strain of ballast; **a** only one artificial inclusion; **b** a combination of artificial inclusions

ballast in a wider area thus lower BBI [22]. The inclusion of geogrid on top of UBM did not influence the change in BBI compared to ballast with both USP and UBM.

As the shear displacement is applied at the bottom part and normal load varies with the depth, the variation in breakage potential was examined by calculating BBI of three layers like top, middle and bottom layers separated using painting each layer in different colors. Higher BBI was observed in the middle layer as the shear plane is fixed in the middle of the test apparatus.

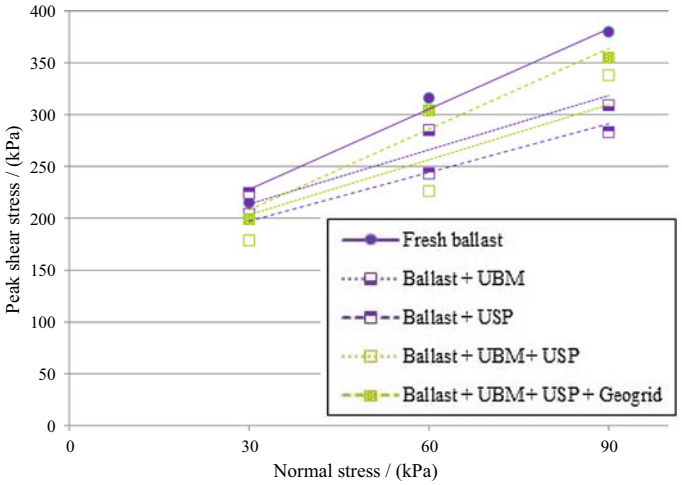

Fig. 5 Peak shear stress variation with normal stresses

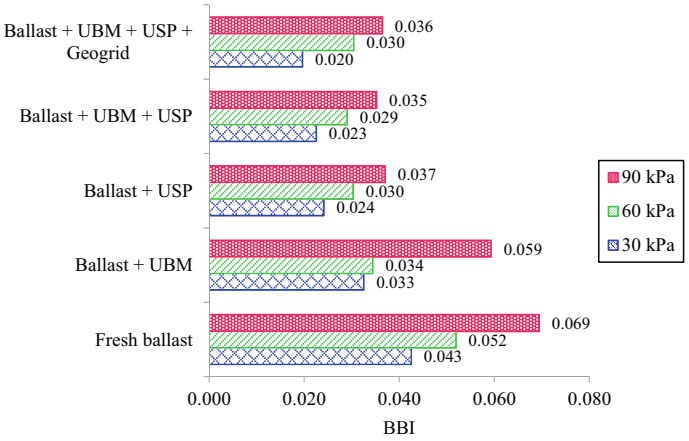

Fig. 6 BBI of various samples under different normal stresses

4 Conclusions

The conducted static load tests on ballast clearly showed that the artificial inclusions, as well as applied normal stress, have an impact on the shear and breakage behavior of ballast. Shear stress and friction angle of fresh ballast were greater than that for ballast with artificial inclusions. Ballast with a combination of rubber pads and geogrid showed closer shear stress values as of fresh ballast and reduced the ballast breakage nearly half of fresh ballast. Further, ballast breakage significantly reduced with a combination of artificial inclusions as the rubber element acted as a cushion

and distributed the load more uniformly to the ballast. A combination of rubber mats along with geogrid is suggested as it gives nearly the same shear behavior as ballast and drastically reduces the ballast breakage. This study is limited to check the influence of artificial inclusions under static loads.

Acknowledgements This research work is supported by Accelerating Higher Education Expansion and Development (AHEAD) Operation of the Ministry of Higher Education funded by the World Bank (Grant No: AHEAD/RA3/DOR/STEM/No. 63) and the University of Peradeniya Research Grant (Grant No: URG-2017-29-E) are acknowledged with the appreciation by the Authors. The authors especially appreciate the staff from Nawalapitiya for their support in the material collection.

References

1. Biabani MM, Indraratna B, Nimbalkar S (2016) Assessment of interface shear behaviour of sub-ballast with geosynthetics by large-scale direct shear test. Procedia Eng 143:1007–1015
2. Chawla S, Banerjee L, Dash SK (2018) Three dimensional finite element analyses of geocell reinforced railway tracks. In: Indian geotechnical conference, Bengaluru, India, pp 1–5
3. Chen C, McDowell GR, Thom N (2013) A study of geogrid-reinforced ballast using laboratory pull-out tests and discrete element modelling. Geomech Geoeng 8(4):244–253
4. Esmaeili M, Zakeri JA, Babaei M (2017) Laboratory and field investigation of the effect of geogrid-reinforced ballast on railway track lateral resistance. Geotext Geomembr 45(2):23–33
5. Fattah MY, Mahmood MR, Aswad MF (2017) Experimental and numerical behavior of railway track over geogrid reinforced ballast underlain by soft clay. In: International Congress and Exhibition Sustainable Civil Infrastructures: Innovative Infrastructure Geotechnology. Springer, Berlin, pp 1–26
6. Huang H, Tutumluer E, Dombrow W (2009) Laboratory characterization of fouled railroad ballast behavior. Transp Res Rec 2117(1):93–101
7. Hussaini SKK, Indraratna B, Vinod J (2018) A Critical review of the performance of geosynthetic-reinforced railroad ballast. Geotech Eng 49(4):31–41
8. Indraratna B, Lackenby J, Christie D (2005) Effect of confining pressure on the degradation of ballast under cyclic loading. Geotech Inst Civil Eng 55(4):325–328
9. Indraratna B, Navaratnarajah SK, Nimbalkar S, Rujikiatkamjiorn C (2014) Use of shock mats for enhanced stability of railroad track foundation. Austr Geomech J 49(4):101–110
10. Indraratna B, Navaratnarajah SK, Nimbalkar S, Rujikiatkamjorn C, Neville T (2015) Performance monitoring: case studies of tracks stabilised by geosynthetic grids and prefabricated vertical drains. In: Field measurements in geomechanics, Sydney, pp 233–246
11. Indraratna B, Qi Y, Tawk M, Heitor A, Rujikiatkamjorn C, Navaratnarajah SK (2020) Advances in ground improvement using waste materials for transportation infrastructure. In: Proceedings of the Institution of Civil Engineers—Ground Improvement, pp 1–44
12. Jayasuriya C, Indraratna B, Rujikiatkamjorn C, Navaratnarajah SK (2020) Application of elastic inclusions to improve the performance of ballasted track. In: Geo-Congress 2020: Engineering, Monitoring, and Management of Geotechnical Infrastructure. American Society of Civil Engineers Reston, VA, pp 364–373
13. Jiang Y, Nimbalkar SS (2019) Finite element modelling of ballasted rail track capturing effects of geosynthetic inclusions. Front Built Environ 5:69(1–11)
14. Leshchinsky BA (2011) Enhancing ballast performance using geocell confinement. In: Geofrontiers 2011: advances in geotechnical engineering, pp 4693–4702
15. Mishra A, Goyal S, Muttharam M, Nanthakumar S (2018) Study on the performance of railway ballasted track reinforced with geogrid. Indian J Sci Technol 11(23):1–4

16. Navaratnarajah S, Indraratna B, Nimbalkar S (2015) Performance of rail ballast stabilized with resilient rubber pads under cyclic and impact loading. In: International conference on geotechnical engineering, Colombo, pp 617–620
17. Navaratnarajah SK (2017) Application of rubber inclusions to enhance the stability of ballasted rail track under cyclic loading. Ph.D. thesis, University of Wollongong. Available at: https://ro.uow.edu.au/theses1/51
18. Navaratnarajah SK (2019) Resilient element attached under the concrete sleepers to improve the rail track performances. J Eastern Asia Soc Transport Stud 13:2506–2520
19. Navaratnarajah SK, Gunawardhana KRCM, Gunawardhana MASP (2020) Influence of type of interfaces on railway ballast behavior. In: ICSECM 2019, Lecture notes in civil engineering. Springer, Berlin, pp 243–251
20. Navaratnarajah SK, Indraratna B (2017) Use of rubber mats to improve the deformation and degradation behavior of rail ballast under cyclic loading. J Geotech Geoenviron Eng 143(6):1–15
21. Navaratnarajah SK, Indraratna B (2018) Application of under sleeper pads to enhance the sleeper-ballast interface behaviours. In: Indian geotechnical conference, Bengaluru, pp 1–8
22. Navaratnarajah SK, Indraratna B (2020) Stabilisation of stiffer rail track substructure using artificial inclusion. Indian Geotech J 50(2):196–203
23. Navaratnarajah SK, Indraratna B, Ngo NT (2018) Influence of under sleeper pads on ballast behavior under cyclic loading: experimental and numerical studies. J Geotech Geoenviron Eng 144(9):1–16
24. Ngo NT, Indraratna B, Bessa Ferreira F, Rujikiatkamjorn C (2018) Improved performance of geosynthetics enhanced ballast: laboratory and numerical studies. Proc Inst Civil Eng Ground Improve 171(4):202–222
25. Sun Q (2020) Numerical simulation of the dynamic response of ballasted track overlying a tire-reinforced capping layer. Front Built Environ 6:1–15
26. Sweta K, Hussaini SKK (2018) Effect of shearing rate on the behavior of geogrid-reinforced railroad ballast under direct shear conditions. Geotext Geomembr 46(3):251–256
27. Sweta K, Hussaini SKK (2019) Behavior evaluation of geogrid-reinforced ballast-subballast interface under shear condition. Geotext Geomembr 47(1):23–31
28. Tennakoon N, Indraratna B, Rujikiatkamjorn C, Nimbalkar S (2012) Assessment of ballast fouling and its implications on track drainage. In: 11th Australia–New Zealand conference on geomechanics: ground engineering in a changing world, pp 421–426
29. Venuja S, Navaratnarajah SK, Bandara CS, Jayasinghe JASC (2020) Review on geosynthetic inclusions for the enhancement of ballasted rail tracks. In: ICSECM 2019, Lecture notes in civil engineering. Springer, Berlin, pp 459–468

Numerical Modeling of the Effect of Fine Materials on Shear Behavior of Fouled Railway Ballast

R. M. D. L. Rathnayake, S. K. Navaratnarajah, M. Daxsan, and H. K. K. A. Jayasekara

Abstract Railway network has become the most economical and widely used transportation mode in many countries. This is mainly due to the frequent congestion of major highways which is caused by rapid urbanization. With this increasing demand for railway transportation, the need for heavier and faster trains too has increased. Introducing high-speed trains with heavy axel loads creates high stresses in the track layers and causes excessive settlement and degradation. Therefore, special attention must be given in understanding the behavior of track layers due to vibrations under dynamic loading. The ballast layer plays a crucial part in transmitting and distributing the wheel load from sleepers to the underlying sub-ballast and subgrade. Ballast becomes degraded and fouled by the progressive accumulation of fines between ballast voids due to repeated train loading and various external factors. This phenomenon leads to a change in ballast behavior such as shear and dilation. This study concentrates on analyzing the effect of fine material on the shear behavior of railway ballast material. To achieve this goal a 3D finite element model of ballast during large-scale direct shear test is developed using ABAQUS software. The model is calibrated and validated using data obtained during a previous study. A parametric study is carried on the shear behavior of ballast by varying normal stress and the percentage of fines. This model is then used to predict the effect of fine materials on the shear behavior of ballast.

Keywords Ballast · Shear behavior · Foul material · Numerical modeling

1 Introduction

The ballasted track is the most conventional and popular track system all over the world. The use of ballasted railway track for transportation has increased due to the increasing traffic congestion of highways. Therefore, high-speed trains with heavy axel loads are being introduced. Since the degradation of ballast increases due to the

R. M. D. L. Rathnayake (✉) · S. K. Navaratnarajah · M. Daxsan · H. K. K. A. Jayasekara
Department of Civil Engineering, Faculty of Engineering, University of Peradeniya, Peradeniya, Sri Lanka
e-mail: dimalir@eng.pdn.ac.lk

R. Dissanayake et al. (eds.), *ICSBE 2020*, Lecture Notes in Civil Engineering 174,
https://doi.org/10.1007/978-981-16-4412-2_6

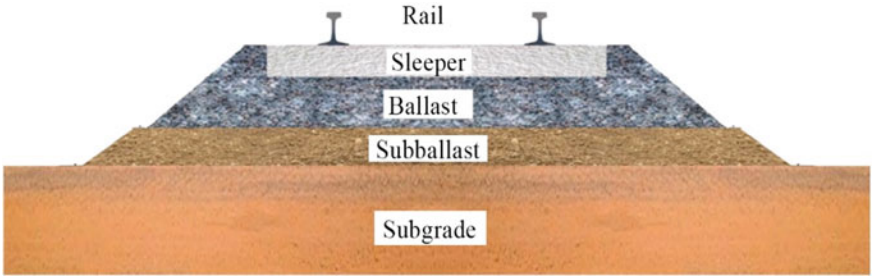

Fig. 1 Typical geometry of ballasted railway track

heavy loads, it is important to study the strength properties of ballast and apply the results in the design and maintenance of ballasted railway tracks [8, 11, 17].

The ballasted railway track consists of superstructure and substructure. The track superstructure contains sleepers, rails, and a fastening system. the track substructure consists of three layers namely ballast, sub-ballast, and subgrade [13]. The ballast layer is made of coarse angular aggregates (size 10–70 mm). Sub-ballast has much finer aggregate (size 0.3–20 mm) and subgrade is usually a compacted soil embankment. Figure 1 shows the geometry of a conventional ballasted track.

The ballast layer transmits the loads from sleepers to the foundation and absorbs energy and vibrations transferred from a moving train [5, 7, 10, 12, 14]. Ballast has a high resistance to weather changes and provides adequate drainage during flood season. The durability of the tracks depends on the quality of the ballast material used. Ballast material tends to be fouled with the intrusion of foreign material such as fine silt, very fine sand, and clay. This is due to various external factors such as floods, wind, and mud pumping. When the ballast layer is contaminated with fines it changes its physical and mechanical properties and that changes the shear strength of the ballast layer. Therefore, it is important to understand the effects of fine materials on the shear strength of ballast for the design and maintenance of ballasted railway track.

Huang et al. [6] has measured strength and deformation characteristics of fresh ballast and fouled ballast with coal dust, plastic clay, and non-plastic mineral filler using a large direct shear device. Esmaeili et al. [4] has done a field experiment by monitoring a railway track for 6 months to analyze the effect of sand-fouled ballast on train induced vibrations. Even though the behaviour of fouled ballast has been analysed by doing field experiments and laboratory tests as found in literature, very few number of numerical models are developed to simulate the direct shear test done on ballast and fouled ballast. In this research, the numerical model developed to simulate large scale direct shear test is used to do a parametric study changing normal load and foul material.

Fig. 2 Large scale direct shear test apparatus

2 Experimental Data

Navaratnarajah et al. [16] has conducted a study on the influence of different types of fine material intrusion on shear and degradation behavior by performing a series of large-scale direct shear tests using clay and fine sand as fouling material. The laboratory experiment data from Navaratnarajah et al. Navaratnarajah et al. [16] is used to calibrate and validate the model development in this study. Previous laboratory study has been conducted using large scale shear test apparatus which is capable of conducting direct shear tests on ballast material without downsizing the ballast material.

The apparatus consists of two rings with each 400 mm diameter and 150 mm height. The top ring is fixed and the bottom ring is movable. A normal load is applied to the setup using the loading plate. A lateral load is applied at a constant loading rate to the bottom ring using a hydraulic loading system. The horizontal displacement, vertical displacement, and horizontal load readings were obtained using displacement gauges and a load cell. Tests have been conducted using fresh ballast, 10% sand fouled ballast, 15% sand fouled ballast, and 5% clay fouled ballast for 30, 60 , and 90 kPa normal loads. The test apparatus is shown in Fig. 2.

3 Numerical Modeling

Railway substructure and the components including ballast have been numerically modeled using various techniques by many researchers. In Navaratnarajah et al.

[15] a finite element model of ballast, sleeper, and under ballast mat is modeled to simulate the effect of repeated cyclic loading. Biabani et al. [1] has modeled a finite element model of ballast, sub-ballast, and geocell to study geocell-reinforced sub-ballast subjected to cyclic loading. In Navaratnarajah et al. [15] and Biabani et al. [1] ballast is modeled as elastic–plastic material by using the Drucker-Prager yield criterion [3]. The material type used in both these studies is C3D8R hexahedral elements. Leshchinsky and Ling [9] also have used the Drucker-Prager yield criterion as ballast material property but instead of C3D8R hexahedral elements, they have used tetrahedral 4-noded elements with reduced integration (C3D4R) for the ballast and sub-ballast material in their finite element model. Chawla and Shahu [2] did a non-linear analysis for ballast, sub-ballast, and subgrade soils using Duncan Chang constitutive relationship and linear analysis using Mohr–Coulomb constitutive relationship using Midas/GTS software. They have used 10-noded tetrahedral elements to model ballast material. In all the above studies material properties such as mass density, elastic modulus, Poisson's ratio, internal friction and angle of dilation were either obtained via lab experiments or previous literature and researches.

4 Finite Element Model

After a thorough understanding of the experimental procedure and the results, a numerical model of the direct shear test was developed and validated using the experimental results. Then a parametric study was done by analyzing the shear variation of the ballast by increasing normal stress and fine percentage.

The model consists of three main parts namely the top ring, the bottom ring, and the ballast. The ballast was modeled as one continuum.

4.1 Finite Element Mesh

3D, 8-noded linear brick, (C3D8R) hexahedral elements chosen for the model as this element type is the most preferable element type to model cylindrical and cubical parts. The local and global coordinate systems of these elements are the same and results can be obtained easily. A mesh convergence was done and a 20 mm mesh size was selected depending on the converged numerical model for displacement. The number of elements in the model is 8200. Figure 3 shows the meshed finite element model.

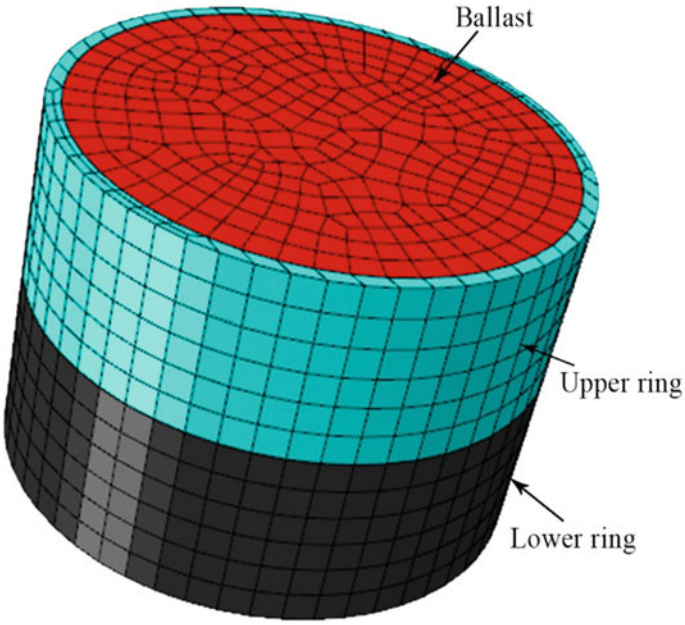

Fig. 3 Meshed finite element model

4.2 Material Properties

As ballast is modeled as a continuum instead of using discrete elements the material properties assigned to ballast should be equal to the overall properties of mixed ballast with fine. In this model Drucker–Pager yield criterion was used for the material model because this is a pressure-dependent analysis. Also, this criterion is preferable for the analysis of the plastic shear behavior of large particles. Steel rings were modeled as rigid parts because the aim is to analyze ballast shear behavior. Modeling the rings as rigid parts also save computational time.

4.3 Boundary Conditions and Loading

The boundary conditions of the experimental setup are implemented in the numerical model. The Upper ring is fixed by restricting motion from every direction. The bottom ring is allowed to move horizontally at the rate of 4 mm/min in the X-direction. The bottom surface of the ballast is restricted in the Y direction. The normal load is applied to the top of the ballast surface as pressures of 30, 60, and 90 kPa. Penalty interaction was defined with friction coefficients in the range of 0.4–0.8 for different ballast mixes.

5 Results and Discussion

Figure 4 shows the shear stress of ballast at the midplane of the ballast layer in the X-direction for three cut sections. Shear stress is lower at the area near the point where horizontal displacement is applied. The three planes are cross-sections of ballast at 75, 150, and 225 mm measuring from the top surface. Figure 5 shows the maximum principal stress variation of ballast in three planes.

5.1 Model Validation

FEM analysis were done for fresh ballast, 10% sand fouled ballast, 15% sand fouled ballast, and 5% clay fouled ballast for 30, 60, and 90 kPa normal loads and compared with experimental results for the validation of the FEM models.

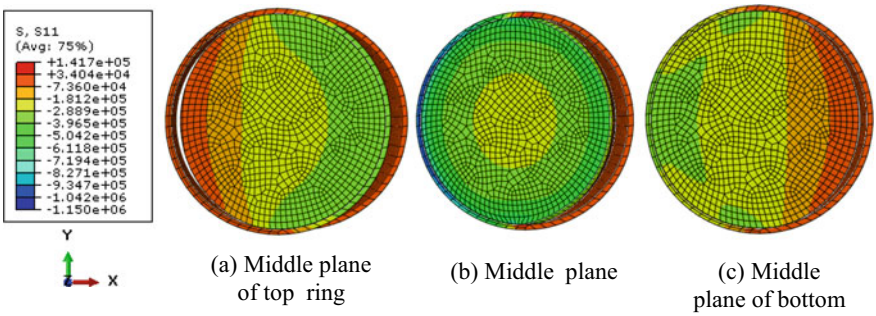

Fig. 4 Shear stress variation of ballast at **a** middle plane of top ring; **b** middle plane of assembly; **c** middle plane of bottom ring

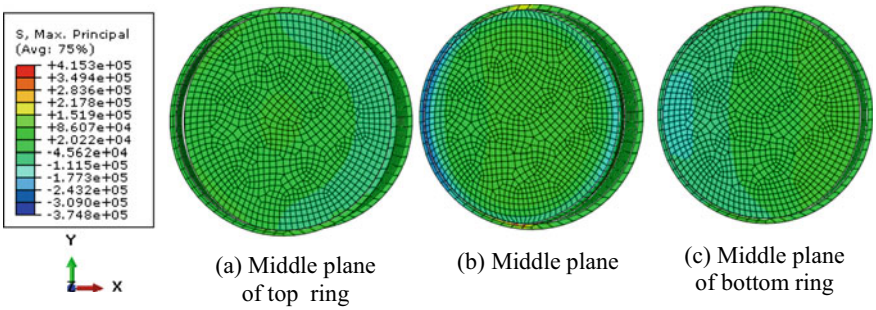

Fig. 5 Maximum principal stress variation of ballast at **a** Middle plane of top ring; **b** middle plane of assembly; **c** middle plane of bottom ring

Shear stress–strain behavior of ballast obtained during experimental analysis and FE analysis are comparatively plotted in Figs. 7a, b and 8a, b. The material properties used in the FEM model for the model validation process are tabulated in Table 1.

Figure 6a shows the shear stress vs shear strain of fresh ballast during experimental and FE analysis. It can be observed that during the application of 30 kPa normal pressure the experimental values tally with the numerical model analysis with considerable accuracy. During the application of 90 kPa pressure, experimental results and numerical analysis results tally only after gaining 6% of the shear strain. It is also observed that the shear stress is increasing with vertical pressure. This behavior is obtained during both experimental and numerical analysis. The major deviation between the experimental and numerical results during the application of 60 and 90 kPa can be due to the discrete nature of ballast and voids which cannot be captured by the continuum numerical model of ballast.

Figure 6b shows the shear stress–strain behavior of ballast when 5% clay mixed with ballast. The shear strength of the ballast is reduced during the analysis of the experimental results. The clay particles acts as a lubricant between ballast particles and reduce the friction between ballast. Then the angle of repose of the mixed material is reduced. This leads to reduction of shear strength. Also, Young's modulus and friction angle of the ballast fouled with clay is reduced. Using the altered material property for ballast fouled with clay the behavior of the clay fouled ballast is captured during the numerical simulation.

The results of experimental analysis and numerical analysis show a considerable similarity during the application of 30 and 60 kPa normal loads after gaining 3% of shear strain.

To study the behavior of ballast when fouled by sand, large-scale direct shear tests were done using ballast fouled with 10% sand and 15% sand. Figure 7 shows the shear stress and shear strain behavior of sand fouled ballast when increasing the normal load. When sand is mix with fresh ballast overall weight and density of ballast increases. Therefore, the young's modulus of the ballast increases with the fines percentage.

Table 1 Material properties used in the FEM model

Material Properties	Fresh ballast	Ballast fouled with 5% clay	Ballast fouled with 10% sand	Ballast fouled with 15% sand
Density (kg/m3)	1640	1750	1805	1900
Young's modulus	3	1.56	6	7.5
Friction angle	40	38	43	45
Dilation angle	15	15	15	15
Poisson's ratio	0.25	0.25	0.28	0.29

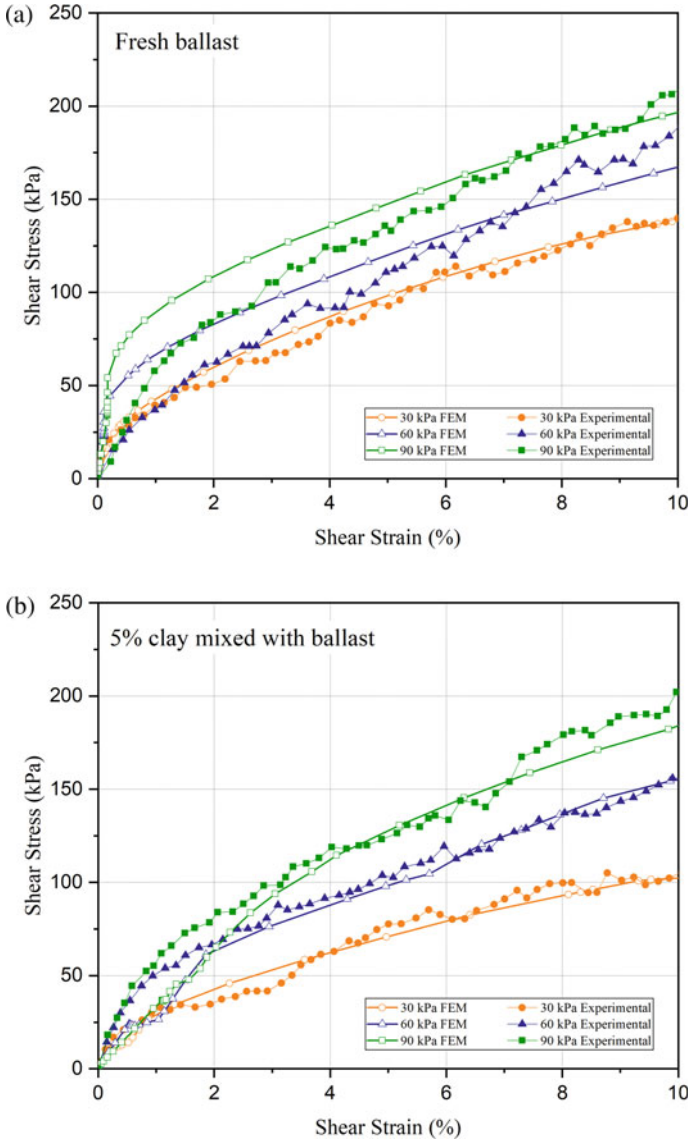

Fig. 6 Shear stress versus shear strain behavior of ballast under 30, 60, and 90 kPa normal stress loads **a** fresh ballast; **b** 5% clay mixed with ballast

5.2 Parametric Study

A parametric study was done using the numerical model after validating the model. Shear stress–strain behavior of ballast mixed with 10% sand and 15% sand was

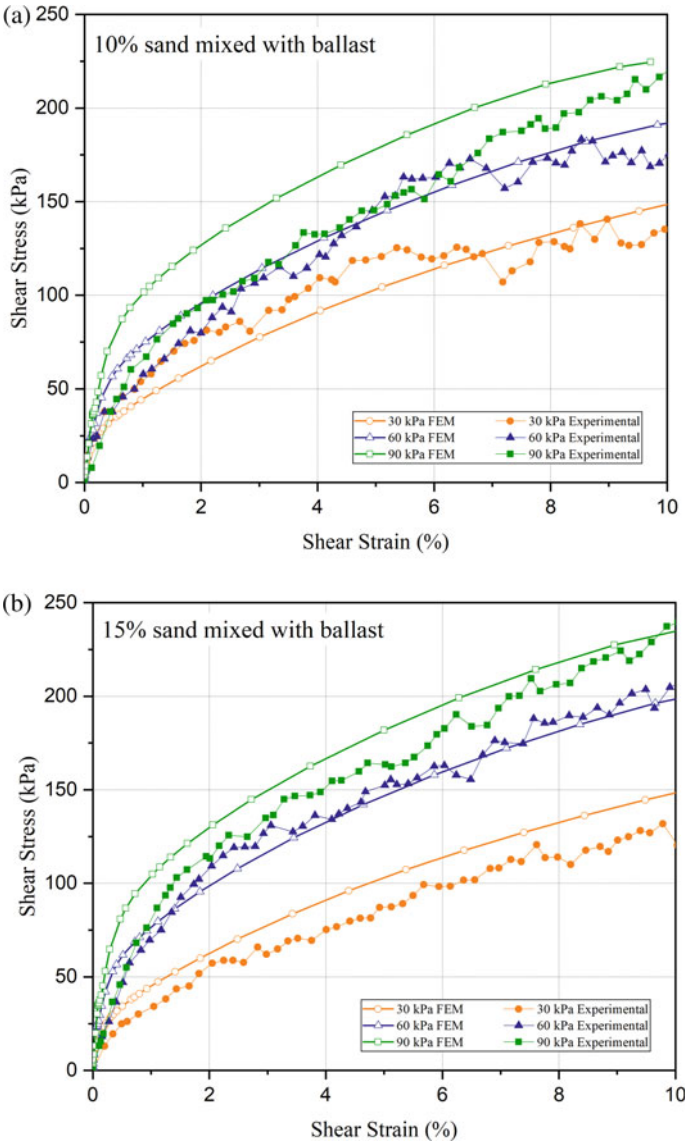

Fig. 7 Shear stress versus shear strain behavior of ballast under 30, 60, and 90 kPa normal stress loads **a** 10% sand mixed with ballast; **b** 15% sand mixed with ballast

analyzed by increasing normal pressure up to 120 and 150 kPa. The results are shown in Fig. 8a, b. Also, another parametric study was done by changing the material properties of ballast to achieve the properties of ballast mixture having 20 and 25% sand fines weight percentages. Then the models were simulated under 30, 60, and 90 kPa normal pressure.

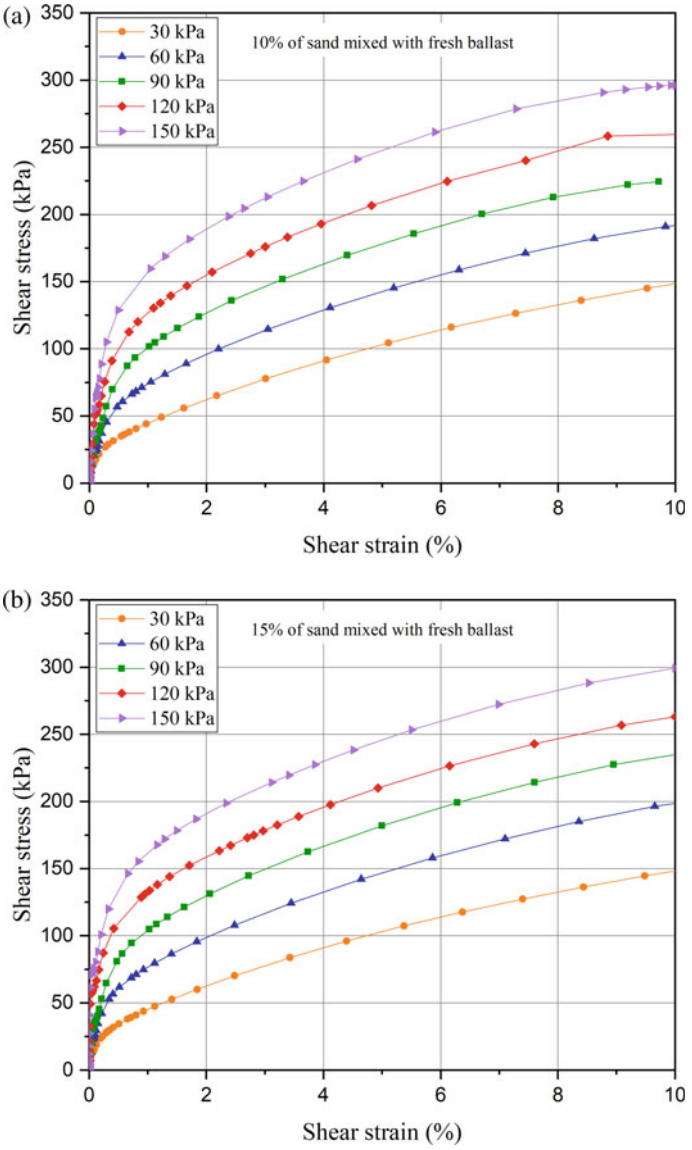

Fig. 8 Shear stress versus shear strain behavior of sand fouled ballast under 30, 60, 90, 120, and 150 kPa normal stress loads a 10% of sand mixed with fresh ballast, b 15% of sand mixed with fresh ballast

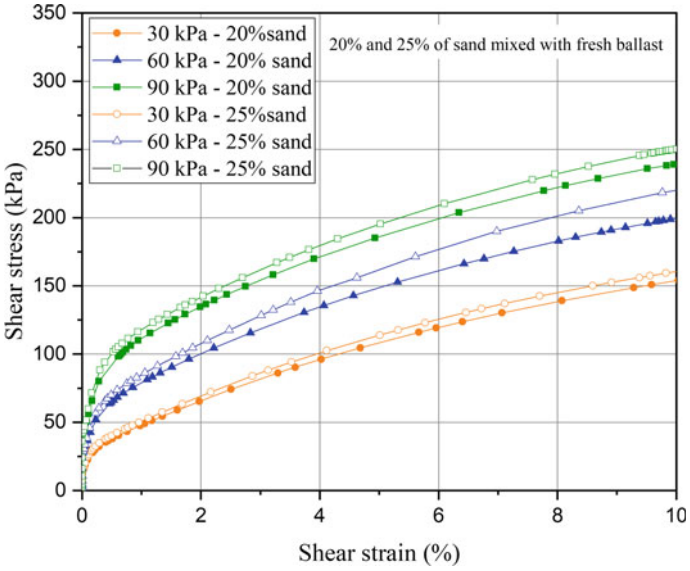

Fig. 9 Shear stress vs shear strain behavior of 20 and 25% weight of sand fines mixed with fresh ballast under 30, 60, 90 kPa, normal stress loads

When the ballast is mixed with clay, the strength of the ballast decreases leading to failure at the shear plane at low strain values when vertical pressure is increased. Therefore, a parametric study was continued with sand fouled ballast. Figure 8a, b show the stress–strain behavior of sand fouled ballast with 10 and 15% sand fines weight. Sand mixed ballast have high strength than fresh and clay mixed ballasts. Therefore, this sand mixed ballast has a strong shear plan to carry the 120 and 150 kPa normal stress loads.

By observing the numerical and experimental results of sand fouled ballast with 10 and 15% weight sand mixed ballast, material properties were determined for fouled ballast with 20 and 25% sand weight. Young's modulus was increased. The shear strength versus shear strain behavior obtained under vertical pressures 30, 60, and 90 kPa are shown in Fig. 9.

6 Conclusion

This study presents a numerical model to perform finite element analysis of large-scale direct shear tests on ballast material. The model is developed using ABAQUS finite element software. The material properties of fouled ballast are determined by considering the fouled ballast with clay or sand fines as one material. The large-scale direct shear test is performed in the laboratory and the results available in literature were used to validate the numerical model. The validated numerical models with

sand fouled ballast can be used to predict the shear stress–strain behavior of sand fouled ballast with increased normal stresses. Also, the presented model can be used to predict the shear behavior of ballast when the fine percentage is increased by using carefully determining material properties.

Acknowledgements The support provided by the Accelerating Higher Education Expansion and Development (AHEAD) operation funded by the World Bank (Grant No: AHEAD/RA3/DOR/STEM/No.63) and University of Peradeniya Research Grant (Grant No: URG 2017/29/E) are highly appreciated by the authors.

References

1. Biabani MM, Indraratna B, Ngo NT (2016) Modelling of geocell-reinforced subballast subjected to cyclic loading. Geotext Geomembr 44(4):489–503
2. Chawla S, Shahu J (2016) Reinforcement and mud-pumping benefits of geosynthetics in railway tracks: model tests. Geotext Geomembr 44(3):366–380
3. Drucker DC, Prager W (1952) Soil mechanics and plastic analysis or limit design. Q Appl Math 10(2):157–165
4. Esmaeili M, Zakeri JA, Mosayebi SA (2014) Effect of sand-fouled ballast on train-induced vibration. Int J Pavement Eng 15(7):635–644
5. Feng H (2011) 3D-models of railway track for dynamic analysis. M. sc thesis, Royal Institute of Technology (KTH)
6. Huang H, Tutumluer E, Dombrow W (2009) Laboratory characterization of fouled railroad ballast behavior. Transp Res Rec 2117(1):93–101
7. Indraratna B, Qi Y, Tawk M, Heitor A, Rujikiatkamjorn C, Navaratnarajah SK (2020) Advances in ground improvement using waste materials for transportation infrastructure. In: Proceedings of the Institution of Civil Engineers-Ground Improvement, pp 1–44
8. Kouroussis G, Verlinden O (2013) Prediction of railway induced ground vibration through multibody and finite element modelling. Mech Sci 4(1):167–183
9. Leshchinsky B, Ling H (2013) Effects of geocell confinement on strength and deformation behavior of gravel. J Geotech Geoenviron Eng 139(2):340–352
10. Mosayebi S-A, Esmaeili M, Zakeri J-A (2020) Dynamic train-track interactions and stress distribution patterns in ballasted track layers. J Transport Eng Part B: Pavements 146(1):04019042
11. Navaratnarajah S, Indraratna B (2020a) Stabilisation of Stiffer Rail Track Substructure Using Artificial Inclusion. Indian Geotech J 1–8
12. Navaratnarajah S, Indraratna B, Nimbalkar S (2015) Performance of rail ballast stabilized with resilient rubber pads under cyclic and impact loading. In: International conference on geotechnical engineering, Colombo, Sri Lanka
13. Navaratnarajah SK (2017) Application of rubber inclusions to enhance the stability of ballasted rail track under cyclic loading. Ph.D. thesis, University of Wollongong
14. Navaratnarajah SK, Indraratna B (2020) Application of under sleeper pads to enhance the sleeper-ballast interface behaviors. In: Construction in geotechnical engineering. Springer, pp 619–636
15. Navaratnarajah SK, Indraratna B, Ngo NT (2018) Influence of under sleeper pads on ballast behavior under cyclic loading: experimental and numerical studies. J Geotech Geoenviron Eng 144(9):04018068
16. Navaratnarajah SK, Venuja S, Shahmi NM., Rimas NM (2019) Influence of fine materials on stress-strain and degradation behavior of railway ballast under static loading conditions. In:

10th international conference on structural engineering and construction management, Kandy, Sri Lanka
17. Sayeed MA, Shahin MA (2016) Three-dimensional numerical modelling of ballasted railway track foundations for high-speed trains with special reference to critical speed. Transport Geotech 6:55–65

Potential of Waste Rice Husk Ash to Reduce Propagation of Ground Vibration from Impact Piling: Characteristics of In-Filled Trenches

G. H. M. J. Subashi De Silva, S. Thoradeniya, and K. M. G. C. J. Thilakasiri

Abstract Impact pilling inevitably generates seismic disturbance to the surroundings that can cause discomfort to occupants in nearby buildings, disturbance to the activities undertaken in the buildings, and possible damage to nearby structures. To reduce the disturbances to occupants and damages to structures, the propagation of the impact pilling induced ground vibration needs to be assessed and controlled. The objectives of this study are to investigate the characteristics of ground vibration induced by impact piling, and assess impact pile induced vibration based on the available standards and evaluate the effectiveness of trench characteristics (i.e., shape of the trench, multiple trenches, infilled trenches) in reducing the propagation of ground vibration. The ground vibrations were measured by using a four-channel seismograph and a six-channel seismograph. The measured ground vibrations induced by the impact piling were compared with local and international standards. A damping layer was introduced by using six different types of trenches: Rectangular open single trench, rectangular open double trench, trapezoidal open single trench, trapezoidal open double trench, a single trench filled with RHA, and a double trench filled with rice husk ash (RHA). It was found that the magnitude and frequency of ground vibration induced by impact piling in hard soil was greater than that of soft soil. When the excavations were carried out in hard soil the magnitude of ground vibration exceeded the permissible values recommended in local and international standards, implying a necessity of having a method to reduce the propagation of ground vibration to far-field. It was found that rectangular open double trench reduced ground vibration by 82.9% in the transverse direction and 78.8% in the vertical direction. Double trench filled with waste rice husk ash reduced ground vibration by 76.3% in a longitudinal direction. This study concludes that in-filled trenches with waste RHA, an agricultural by-product, has the potential to reduce the propagation of ground vibration induced by impact pilling.

Keywords Ground vibration · Damping layer · In-filled trenches · Rice husk ash

G. H. M. J. S. De Silva (✉) · S. Thoradeniya · K. M. G. C. J. Thilakasiri
Department of Civil and Environmental Engineering, Faculty of Engineering, University of Ruhuna, Matara, Sri Lanka
e-mail: subashi@cee.ruh.ac.lk

R. Dissanayake et al. (eds.), *ICSBE 2020*, Lecture Notes in Civil Engineering 174,
https://doi.org/10.1007/978-981-16-4412-2_7

1 Introduction

Piling is the common type of foundation used in the construction of high-rise buildings, larger and smaller span bridges and expressways. Pile driving inevitably generates seismic disturbance to the surroundings that can cause discomfort to occupants in nearby buildings, disturbance to the activities undertaken in the buildings and possible damage to nearby structures. Based on the method of construction, piling can be categorized into two: bored piling and impact piling. Among these two types of piling, the impact piling is more popular over the bored pilling due to various reasons including less time consumption, less cost and less requirement of high technology and machineries. However, it has been found that impact piling induces ground vibration with a high magnitude (i.e., 3 mm/s) and at low frequency (i.e., 20 Hz) [1]. High magnitude at low frequency can damage structures and are felt by the occupants easily, because the resonance of human body generally lies at low frequencies (i.e., around 5–12 Hz for vertical vibration, 1–4 Hz for horizontal vibration) [15]. In order to reduce the disturbances to occupants and damages to structures, the propagation of impact piling induced ground vibration needs to be assessed and controlled.

Ground vibration has been assessed using different vibration standards: ONORMS of Austria, DGMS of India, Australian Standards, USSR of Union of Soviet Republic and Swiss Standards. In these standards, the structures are classified as domestic houses, industrial buildings and objects of historic importance and sensitive structures. The vibration standards for Sri Lanka are given by the Central Environmental Authority [4] based on ISO 4966: 1990E. They have classified structures into four types (Table 1). Therefore, it is an increasingly important need to reduce the ground vibration induced by pilling to satisfy the limits specified in standards.

Table 1 Categorization of structures according to the type of building (from ISO-4966: 1990E)

Category of the structure of the building	Description
Type 1	Multi-storey buildings of reinforced concrete or structural steel, with in filling panels of block work, brick work or precast units not designed to resist earthquakes
Type 2	Two-storey domestic houses and buildings constructed of reinforced block work, precast units, and with reinforced floor and roof construction, or wholly of reinforced concepts or similar, not designed to resist earthquakes
Type 3	Single and two-storey houses and buildings made of lighter construction, using lightweight materials such as bricks, cement blocks etc., not designed to resist earthquakes
Type 4	Structures that, because of their sensitivity to vibration, do not correspond to those listed above 1, 2 and 3, and declared as archeologically preserved structures by the Department of Archaeology

Propagation of vibration can be controlled by passive damping, which is provided through energy dissipation by using materials. This method is attractive because of its low cost and easy maintenance. To reduce the ground vibration induced by piling activities, ground barriers have often been used [16]. The open trenches are more effective and cost effective than in-filled trenches or soil stiffening [5, 16]. However, the main disadvantage of the open trench is amplification of response inside trenches and requirement in stabilizing the sides of the open trench. As the maintenance of open trenches is difficult providing in-filled trenches are attractive [8]. However, the characteristics of the trench and the in-filled materials should be carefully selected because the trench characteristics and the materials that are effective with controlling the vibration may not be stable physically.

For the filling, low-cost materials, probably, waste materail would be attractive because of the sustainability. The materials having high stiffness has been identified as effective while some researchers have found lower the stiffness the damping performance is high. Bottom ash, rice husk in both compacted and uncompacted forms have been used previously [8]. Among the three forms of materials, bottom ash has shown the best results due to its cementitious properties.

Rice husk ash often identified as a cementitious material. Rice is the staple food in many countries, resulting to produce a large amount of rice husk. For example, out of 579, 476, 722 tons of world annual paddy production in 2002, Sri Lanka produces 2, 794,000 tons was placed at the 18^{th} highest paddy producing country in the world [7]. Husk to Paddy Ratio is 0.1 by weight and about 20% of rice husk becomes RHA [2], as a result 279,400 tons of rice husk are produced by rice milling industry. In Sri Lanka, Rice husks are often used as a fuel in brick manufacturing industry; as a result, a considerable amount of rice husk ash (RHA) accumulates in the environment without having a proper usage. Rice husk ash (RHA), a waste of brick firing process, is unusually high in silica (around 90%), highly porous and light weight, with a large external surface area [5]. The silicate available in the waste RHA is amorphous form [6] and provide stability to trench. Zoccali [17] stated that concrete is currently the best material to use, although in some frequency ranges it can actually increase the vibration levels and therefore this should be analyzed based on critical frequencies of the receiver. Although a concrete has been identified as the best in-filled materials to be used in wave trench [17], it would not be a cost effective method, especially for ground vibration induced by construction activities, as the requirement is only during the period of construction. Therefore, in the current study attempts have been given to utilize waste RHA, a cementitious material, as in-filled material for screening ground vibration.

The objectives of this study are:

- To investigate the characteristics of ground vibration induced by impact piling
- To asses impact pile induced vibration based on the available standards.
- To evaluate effectiveness of trench characteristics (i.e., shape of the trench, multiple trenches, in filled trenches) in reducing the propagation of ground vibration.

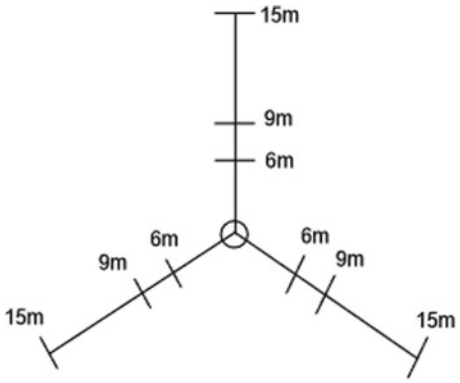

Fig. 1 Ground vibration monitoring locations

2 Methodology

2.1 Site Selection

Impact piling sites were selected for measuring the ground vibration. The measurements were recorded in three radial directions at 6, 9 and 15 m distance as shown in Fig. 1.

2.2 Vibration Measurement

The ground vibrations were measured by using two seismographs (Fig. 2): four channel seismograph and six channel seismograph. One tri-axial geophone was connected to four channel seismograph while two tri-axial geophones were connected to the six channel seismograph. These seismographs have the ability to measure vibration in transverse (direction parallel to the source), vertical and longitudinal directions (the direction perpendicular to the source) with a resolution of 0.127 mm/s in the frequency range of 2–250 Hz. Each geophone was placed on the ground and its ground spikes were inserted to a length of 65 mm. Before measuring, the geophone was programmed to record vibration in the continuous mode and the fixed time stop mode. Magnitudes and dominant frequencies of the ground vibration of each location from the source were measured with sampling time equal to 1/1024 s.

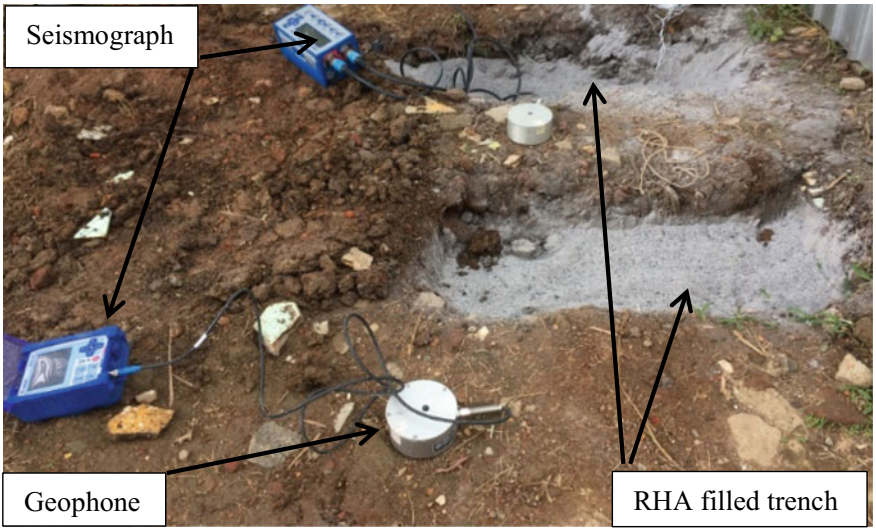

Fig. 2 Measuring ground vibration with the damping layer

2.3 Assessment of the Ground Vibration

The ground vibrations obtained from the impact piling sites were compared with local (i.e., Central environmental Authority (CEA) standard and other available international standards (i.e., DGMS, ONORMS, Australian, DIN4150, USSR and Swiss standards). Permissible vibration magnitudes and frequencies recommended in local standard and international standards are summarised in Tables 2 and 3, respectively.

2.4 Effectiveness of the Trench Filled with Waste RHA

A damping layer was introduced by using six different types of trenches four types of open trenches and two types of in-filled trenches. Four open type trenches include two different shapes (i.e., rectangular and trapezoidal) and two different arrangements (i.e., single trench and double trenches): open single rectangular trench, open double rectangular trenches, open single trapezoidal trench, open trapezoidal double trench. Two in-filled type trenches include trapezoidal single trench filled with waste rice husk ash (RHA), and trapezoidal double trench filled with waste rice husk ash (RHA). Types of trenches investigated are listed in Table 4. The trenches were introduced at about 4 m away from the source of vibration across the path of wave propagation. The dimensions and arrangement of the trenches are shown in Fig. 3.

Table 2 Interim Standards for vibration of the Operation of Machinery, Construction Activities and Vehicle Movements Traffic (*Source* Central Environmental Authority, Sri Lanka)

Category of the structure as given in Table 1	Type of Vibration	Frequency of Vibration (Hz)	Vibration in Peak Particle Velocity (PPV) (mm/s)
Type 1	Continuous	0–10	5
		10–50	7.5
		Over 50	15
	Intermittent	0–10	10
		10–50	15
		Over 50	30
	Continuous	0–10	2
		10–50	4
		Over 50	8
Type 2	Intermittent	0–10	4
		10–50	8
		Over 50	16
	Continuous	0–10	1
		10–50	2
		Over 50	4
Type 3	Intermittent	0–10	2
		10–50	4
		Over 50	8
	Continuous	0–10	0.25
		10–50	0.5
		Over 50	1
Type 4	Intermittent	0–10	0.5
		10–50	1
		Over 50	2

To determine the effectiveness of the in-filled trench a six channel seismograph along with two geophones were used for simultaneous measurement of ground vibrations. For measuring the ground vibration in transverse direction, the geophone was placed parallel to the length of the trench while for measuring the ground vibration in the longitudinal direction the geophone was placed perpendicular to the length of the trench.

Effectiveness of open trench /trenches and in-filled trench/trenches with difference arrangements (i., shape, single trench, double trenches) in screening the ground vibration was investigated by determining the reduction in Peak Particle Velocity (PPV) of ground vibration. The reduction in the ground vibration compared with the vibration that was measured before the trench at a particular location.

Table 3 Vibration standards for different countries/researches

Standard		Domestic houses (PPV) (mm/s)		Industrial building (PPV) (mm/s)		Objects of historic importance and sensitive structures (PPV) (mm/s)		Dominant excitation frequency (Hz)
DGMS (Standards Association of India)	Buildings/structures not belong to the owner	5		10		2		< 8
		10		20		5		8–25
		15		25		10		> 25
	Buildings belonging to the owner with limited span of life	10		15				< 8
		15		25				8–25
		20		50				> 25
ONORMS 9020 [10]		20		30		5		< 24
Australian Standard [9]		10		25		2		
DIN 4150 [12]		5		20		3		0–10
		5–15		20–40		3–8		10–50
		15–20		40–50		8–10		50–100
USSR Standard [14]		Repeated - 30		Repeated- 60				
		One-fold-60		One-fold-120				
Swiss Standard [13]		Blast induced	Traffic/machine induced	Blast induced	Traffic/machine induced	Blast induced	Traffic/machine induced	
		12		30		8		10–60
		12–18		30–40		8–12		60–90
			5		12		3	10–30
			5–8		12–18			30–60

Table 4 Types of trenches used for the study

Types of trench barrier	Open trenches	In-filled trenches
Type 1	Open single rectangular trench	
Type 2	Open double rectangular trenches	
Type 3	Open single trapezoidal trench	
Type 4	Open double trapezoidal trenches	
Type 5		In-filled single rectangular trench
Type 6		In-filled double rectangular trenches

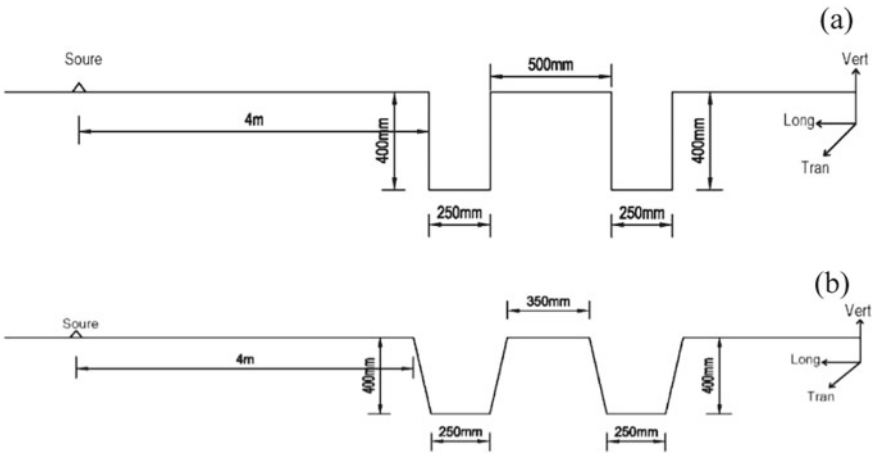

Fig. 3 Arrangement of trenches in the site **a** rectangular trenches **b** trapezoidal trenches

In order to further determination of the attenuation of ground vibration due to the presence of barriers, the ground velocity measurements were converted into ground acceleration. For each filling material, ground vibration particle velocity that was measured were converted into acceleration (a_i: acceleration value of particular time step) using Eq. (1).

$$ai = \frac{v_{i+1} - v_i}{\Delta t} \tag{1}$$

where v_i and v_{i+1} are particles velocity readings at time step i and $i + 1$, respectively, and Δt is the sampling time (i.e., 1/1024 s). The ground acceleration before the barrier was compared with the ground acceleration measured after the barrier.

3 Results and Discussion

3.1 Hard Soil

Figure 4 shows the average PPV of ground vibration induced in transverse, vertical and longitudinal directions for driving of 5 piles. Associated frequencies of ground vibration are compared in Table 5.

Longitudinal direction wave has the highest magnitude (PPV) compared to vertical and transverse directions (Fig. 4). PPV of ground vibration in all three orthogonal directions reduces with increasing the distance from the source (Fig. 4). With the distance, ground vibration decreases at a rate of 0.9, 0.69 and 0.59 ms^{-1}/m for longitudinal, vertical and transverse directions, respectively, indicating that the rate of decrease in ground vibration is higher in longitudinal direction than that in the other two directions.

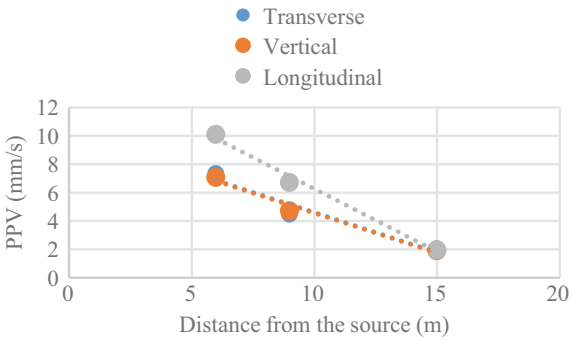

Fig. 4 Average PPV variation with distance in hard soil (without trench)

Table 5 Frequency range and PPV variation with distance from the source in hard soil

Magnitude and frequency of the vibration		Distance from the source		
		6 m	9 m	15 m
Transverse	Fre (Hz)	17–47	14–47	20–85
	PPV (mm/s)	7.34	4.44	2.02
Vertical	Fre (Hz)	20–43	34–100	22–100
	PPV (mm/s)	8.07	4.7	1.88
Longitudinal	Fre (Hz)	15–47	22–100	17–100
	PPV (mm/s)	10.09	6.69	1.96

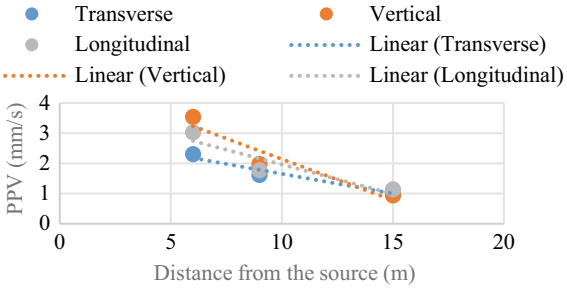

Fig. 5 Average PPV variation with distance in soft soil (without trench)

Table 6 Frequency and average PPV variation with distance in soft soil

Magnitude and frequency of the vibration PPV		Distance from the source (m)		
		6 m	9 m	15 m
Transverse	Fre (Hz)	3.4–11	3–17	3.5–15
	PPV (mm/s)	1.757	1.755	1.21
Vertical	Fre (Hz)	2.8–23	3.5–20	3.5–13
	PPV (mm/s)	3.55	2.255	1.025
Longitudinal	Fre(Hz)	3.1–13	3.3–20	4–16
	PPV (mm/s)	2.214	1.98	1.624

3.2 Soft Soil

Figure 5 shows the average PPV of ground vibration induced in transverse, vertical and longitudinal directions for driving of 7 piles each at a time. Associated frequencies of ground vibration are compared in Table 6.

According to Fig. 5, it can be seen that PPV in all three directions decay with the distance from the source, similar to that observed for pilling in hard soil. Vertical direction wave has the highest magnitude compared to longitudinal and transverse directions. However, with the distance the rate of decrease of vertical (0.28 ms^{-1}/m) ground vibration is greater than that of longitudinal (0.07 ms^{-1}/m) and transverse (0.06 ms^{-1}/m) ground vibration.

3.3 Comparison of Level of Vibration Induced by Impact Piling in Hard Soil and Soft Soil

Figure 6 compares the values of PPV in soft soil and hard soil excavations for transverse, vertical and longitudinal directions.

It can be clearly identified that the PPV is higher when excavating the hard soil than that of soft soil, irrespective of the direction of ground vibration. However,

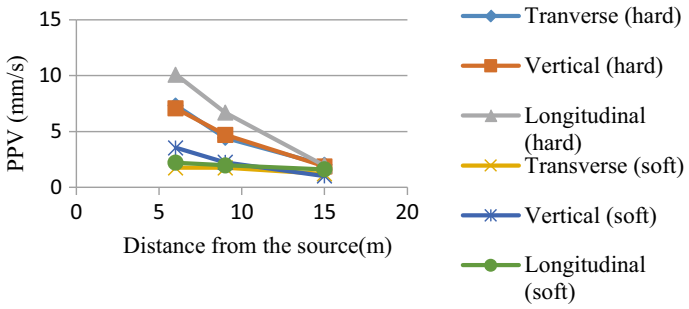

Fig. 6 Comparison of magnitude of transverse, vertical and longitudinal waves during the excavation of hard soil and soft soil

difference in this PPV of ground vibration between hard soil excavation and soft soil excavation reduces with increasing the distance from the source**.**

3.4 Assessment of Ground Vibration Level

3.4.1 Hard Soil

At 6 m distance, for transverse, vertical and longitudinal directions the PPV's are greater than that specified in the standards (Tables 2 and 3). At about 9 m distance. PPV in the transverse direction is greater than that specified in the standards except from Australian, DIN and Swiss standards (Tables 2 and 3).

3.4.2 Soft Soil

In soft soil, PPV in transverse, vertical and longitudinal direction are within the maximum permissible level in standards of CEA, DGMS, ONORMS, Australian and Swiss standards. However, these values are lesser than that of DIN standards of Germany: for the frequency between 10–50 Hz the PPV should be between 5 and 15 mm/s.

3.5 Effectiveness of Trench Characteristics and Waste RHA

Open trenches have shown better performance than infilled trenches in transverse and vertical directions (Fig. 7). Similar trend has been observed previously by Jayawardane et al. [8]. However, in longitudinal direction, in which PPV is a high (Fig. 7) in-filled trench performed better than open trenches.

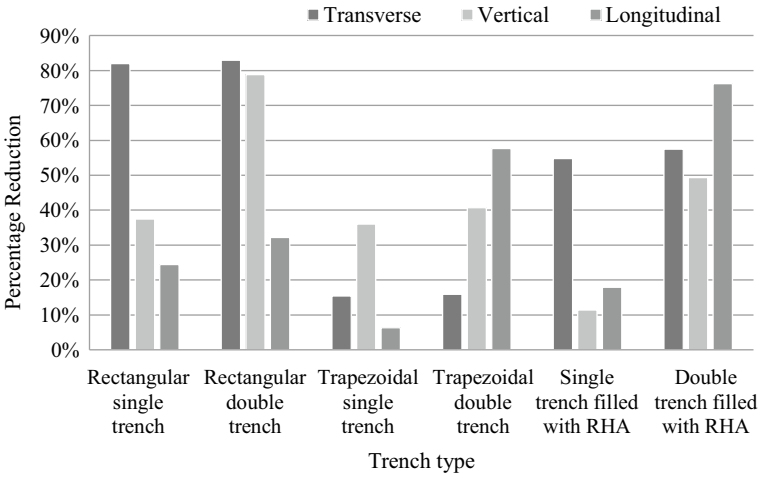

Fig. 7 Percentage reduction in PPV of ground vibration by different types of trenches

Comparing with the two shapes of the trench investigated, rectangular shape performed better than the trapezoidal trench. This was clear in the transverse and vertical directions (Fig. 7). The best performance was achieved with rectangular double trench (Fig. 8). the open trenches performed better in screening the ground vibration, than waste RHA filled trench, in-line with that reported in previous studies [5, 16] (Fig. 9).

When the performances of single and double trenches were compared, the double trench shows better performance than single trench. This was more clear in longitudinal and vertical directions**.** However, in transverse direction, single trench shows better performance (Fig. 10).

When RHA was used as a filling material, there was a significant screening in the vibration propagation. Double trenches filled with waste RHA has shown the best performance in longitudinal direction. Also, double trenches filled with waste RHA were more effective than the single trench filled with waste RHA (Fig. 10). This might be due to the cementations properties of RHA (Silicon dioxide). In a previous study by Jayawardane et al. [8] found that cementitious properties in coal bottom ash contributed to screen ground vibration. In addition to screening the ground vibration, cementitious material would contribute to ground improvement by strengthening the soil. Screening effect of waste RHA was greater while introducing the double trenches.

It was clear that open trenches have shown better performance than infilled trenches in transverse and vertical directions. That is because in open trenches the reflection occurs while in infilled trenches the vibration is transmitted through the

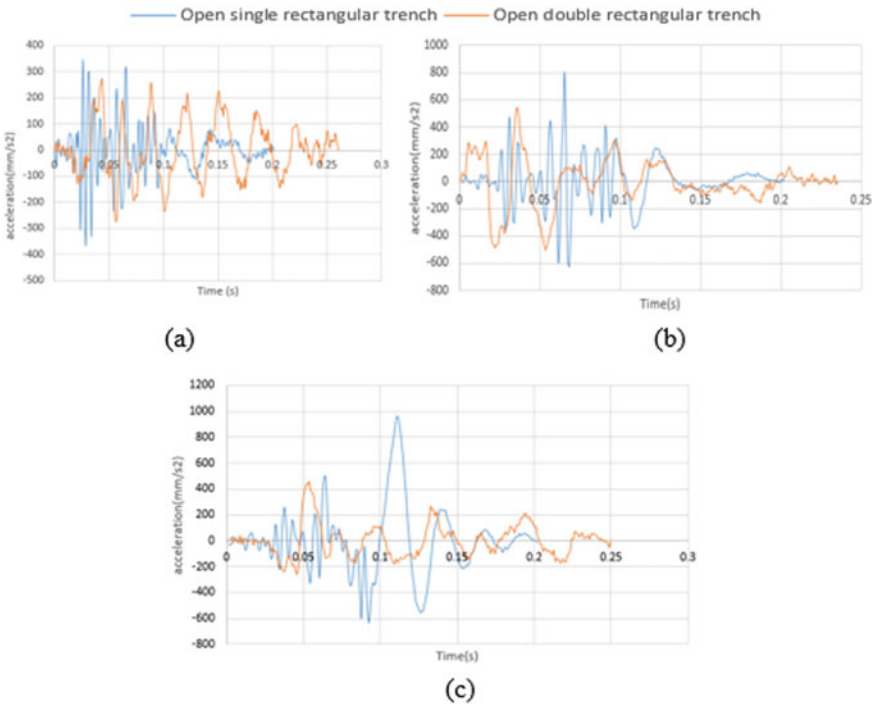

Fig. 8 Acceleration of ground vibration with single and double trench (open rectangular) **a** transverse direction, **b** vertical direction, **c** longitudinal direction

infilled trench as well as it diffracts beneath it. Among the open trenches the rectangular open trenches have shown better performance in transverse and vertical directions than trapezoidal open trenches. This might be attributed by the fact that in rectangular trench the reflection occurs in a vertical surface while in trapezoidal trench reflection occurs in a slanted surface. Therefore, the open rectangular trench shows a better performance in transverse and vertical directions than the open trapezoidal trench.

4 Conclusions

Characteristics of ground vibration induced by impact piling in hard soil and soft soil were investigated and compared. Ground vibration induced by impact piling in different soil medium was compared with local and international standards. In addition, the effectiveness of open trench and trench infilled with RHA in reducing the ground vibration were investigated in this study.

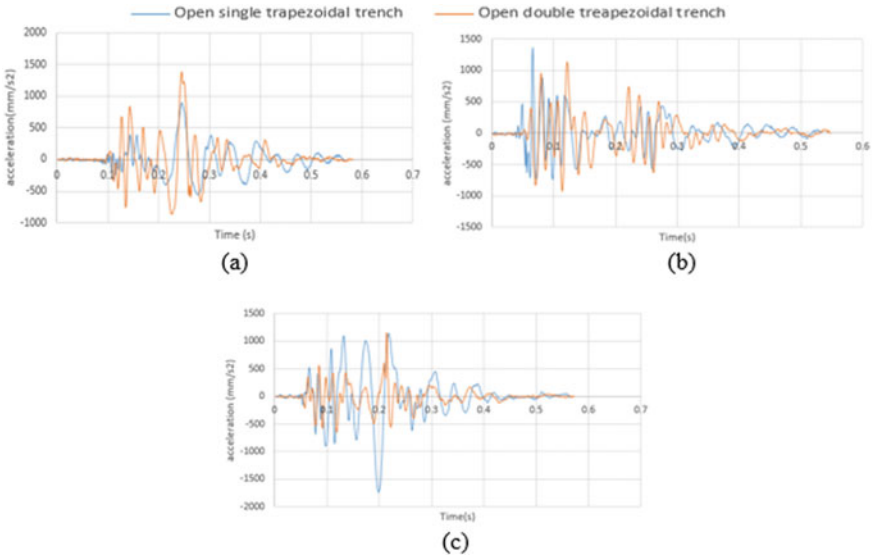

Fig. 9 Acceleration of ground vibration with single and double trench (open trapezoidal) **a** transverse direction, **b** vertical direction, **c** longitudinal direction

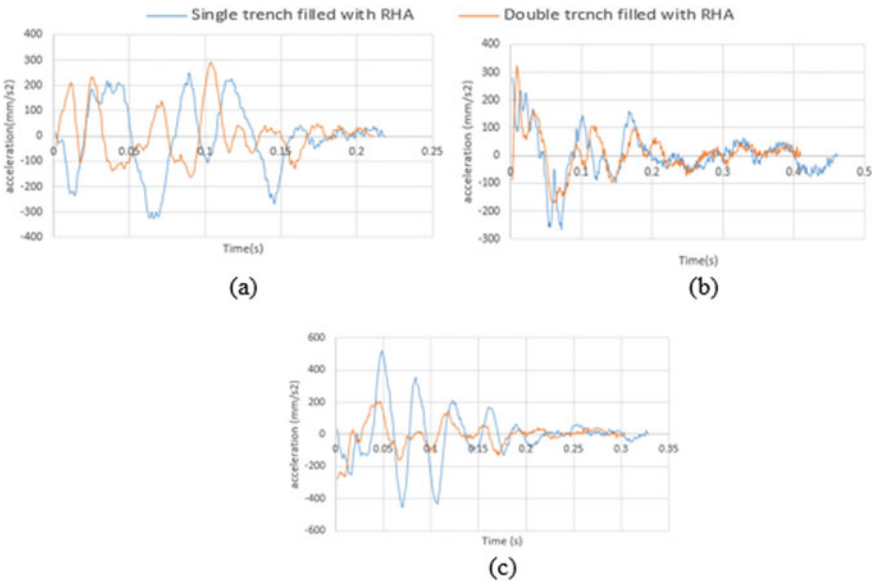

Fig. 10 Acceleration of ground vibration with single and double trapezoidal trenches filled with RHA **a** transverse direction, **b** vertical direction, **c** longitudinal direction

The magnitude and frequency of ground vibration induced in impact piling in hard soil was greater than that of soft soil. When the excavations were carried out in hard soil the magnitude of ground vibration exceeded the permissible values recommended in local and international standards, implying a necessity to investigate a method to reduce the propagation of ground vibration at far field.

Open single rectangular trench, open double rectangular trenches, open single trapezoidal trench, open double trapezoidal trench, single trench filled with waste RHA and double trench filled with waste RHA was introduced in the path of ground vibration propagation. Among six types of trenches, the open double rectangular trenches reduced the ground vibration by 82.9% in transverse direction and 78.9% in vertical direction. In longitudinal direction, double trench filled with waste RHA reduced ground vibration by 76.3%.

References

1. Achchuhan R, Subashi De Silva GHMJ, Sudhira De Silva (2016) Comparison between ground vibrations induced by impact piling and bored piling. In: Proceedings of the 7th international conference on sustainable built environment, Kandy, 16–18 Dec 2016
2. Agus SM (2002) Utilization of uncontrolled burnt rice husk ash in soil improvement. Dimensi Teknik Sipil 4(2):100–105
3. Andersen L, Nielsen SRK (2005) Reduction of ground vibration by means of barriers or soil improvement along a railway track. Soil Dyn Earthq Eng 25:701–716
4. Central Environment Authority (2008) Pollution Control Division amended interim air blast over pressure and vibration standards. Central Environment Authority, Sri Lanka.
5. De Silva GHMJS, Perera BVA (2018) Effect of waste rice husk ash (RHA) on structural, thermal, and acoustic properties of fired clay bricks. J Build Eng 18:252–259
6. De Silva GHMJS, Surangi MLC (2017) Effect of waste rice husk ash on structural, thermal and run-off properties of clay roof tiles. Constr Build Mater 154:251–257
7. Gidde MR, Jivani AP (2007) Waste to wealth—potential of rice husk in India: a literature review. In: Proceedings of the international conference on cleaner technology and environmental management, Pondicherry, India, pp 586–590
8. Jayawardana WAPD, De Silva GHMJS, De Silva GSY (2016) Effectiveness of a trench filled with waste material in reducing the propagation of ground vibration induced by soil roller compaction. Eng J Inst Eng Sri Lanka 49(2):17–24
9. Standards Association of Australia (1987) Australian Standard: Ground vibration induced by construction, (As A-2183). Standards Australia
10. Standards Association of Austria (1986) ONORMS 9020: ground vibration induced by construction, Standards Austria
11. Standards Association of India (1973) DGMS: permissible limit of ground vibration, Standards India
12. Standards Association of Germany (1999) DIN 4150: ground vibration induced by construction, Standards Germany
13. Standards Association of Switzerland. Swiss Standards: ground vibration induced by construction, Standards Switzerland
14. Standards Association of Union of Soviet Republic. USSR Standards: ground vibration induced by construction. Standards Union of Soviet Republic
15. Subashi GHMJ, Nawayseh N, Matsumoto Y, Griffin MJ (2009) Nonlinear subjective and dynamic responses of seated subjects exposed to horizontal whole-body vibration. J Sound Vibr 321(1):416–434

16. Thompson DJ, Jiang J, Toward MGR, Hussein MFM, Ntotsios E, Dijckmans A, Coulier P, Lombaert G, Degrande G (2016) Reducing railway-induced ground-borne vibration by using open trenches and soft-filled barriers. Soil Dyn Earthq Eng 88:45–59
17. Zoccali P, Cantisani G, Loprencipe G (2015) Ground-vibrations induced by trains: filled trenches mitigation capacity and length influence, Constr Build Mater 74

Investigation of Colloidal Transport in Saturated Porous Media: Experimental and Numerical Study

B. G. C. Bombuwala, A. M. E. Karunarathna, B. Banithy, and T. K. K. Chamindu Deepagoda

Abstract Field and laboratory scale observations conducted during last few decades provided ample evidences to prove colloid-facilitated transport of numerous contaminants in porous media including radionuclides, hydrophobic organic compounds (HOCs), heavy metals, pesticides, pathogens, etc. Therefore, it is vital to investigate colloid and colloid-facilitated contaminant transport in porous media and the soil physico-chemical parameters controlling their subsurface fate and transport processes. This study mainly focused on investigating the effect of flow rate (as a physical perturbation) and ionic strength (as a chemical perturbation) on mobilization and transport colloids in saturated porous media. A series of controlled-laboratory column experiments were conducted using a selected sand as the porous medium and colloids with the Stokes' diameter <1 μm extracted from an agricultural soil. The ionic strength was controlled by changing the NaCl concentration in the influent colloidal solution while the flow rate changed by varying the hydraulic head of the column. The turbidity of the effluent solution was measured to estimate the colloid concentration and a series of breakthrough curves were obtained for different combinations of ionic strength and flow rates. The experimental results were numerically characterized based the advection–diffusion/dispersion modelling framework coupled with attachment, detachment and straining parameters which were inversely estimated using the HYDRUS 1D software. Estimated attachment coefficients of soil colloids were significantly higher in low flow rates and higher in high ionic strength. Also, the results of numerical analysis identified attachment as the key retention mechanism in saturated porous sand in an ionic solution.

Keywords Physical and chemical perturbation · Column experiment · Stokes' diameter · Attachment · Detachment · Straining

B. G. C. Bombuwala · A. M. E. Karunarathna · B. Banithy · T. K. K. C. Deepagoda (✉)
Department of Civil Engineering, Faculty of Engineering, University of Peradeniya, Peradeniya, Sri Lanka
e-mail: chaminduk@pdn.ac.lk

R. Dissanayake et al. (eds.), *ICSBE 2020*, Lecture Notes in Civil Engineering 174,
https://doi.org/10.1007/978-981-16-4412-2_8

1 Introduction

Soil is basically a three-phase system; solid, liquid and gas. Solid phase remains static while gaseous and liquid phases are mobile and transient. Further, soil serves as a warehouse for numerous contaminants, including pesticides, heavy metals, radionuclides etc. Such contaminants, if retained such contaminants in soil for a considerable time, cause soil contamination. Plants growing in contaminated soil take up contaminants through their roots and therefore affect the health of the animals who feed on such plants. On the other hand, if contaminants are transported in to groundwater, groundwater contamination takes place. Groundwater contamination is of major concern when considering the public health, as groundwater is the primary source of portable water in many countries. So it is essential to understand the mechanisms controlling transport and retention of contaminants in subsurface environments. The unexpected rapid appearance of some pollutants in groundwater has been frequently observed and reported over the past few decades. Some observations have shown that such pollutants migrated at a faster rate than the mobile water phase. The frequent failure of the two-phase pollution prediction system has forced the search for a potential third mobile phase that is currently recognized as the *colloidal phase*. Colloid is defined as small particles with dimension roughly between 1 μm and 1 nm. The upper limits ensures that colloids are small enough to be in suspension in the solution and the lower limit ensures that colloids are large enough to be distinguished from dissolved solutes. Because of very small size particles can be suspended and dissipated in liquid phase. This occurs for a long period of time by Brownian motion. If particles larger than 1 μm, van der Waals forces are too large to counterbalance the gravitational force. Therefore, they settle out quickly [3]. In order to be a colloid, it is sufficient if one of the characteristic dimensions of the particle falls within above range.

This small moving particles of nanometer scale appear to be everywhere in soil pore waters. They include mineral fragments, microorganisms, humus debris of plants etc. [1]. Extensive research has shown that reactive pollutants can adsorb onto such mobile colloids and easily transport them to groundwater with colloids.

Experimental studies carried out on a field and laboratory scale over the past few decades [2, 4] have provided sufficient evidence to prove that the colloidal fraction plays an important role in transporting numerous contaminants in porous media including radionuclides, hydrophobic organic compounds (HOCs), heavy metals, pesticides, pathogens, etc. In order to the colloid-facilitated transport to take place, three criteria should essentially be met [5]: colloids must be present, contaminants must associate with colloids, and colloids (with associated contaminants) must be transported through the aquifer.

Colloids in groundwater originate from two major sources: mobilization of existing colloid-sized minerals in aquifer sediments and insitu precipitation of super saturation mineral phases. Further, existing colloids are mobilized by some perturbation of the ambient groundwater conditions. Existing minerals in the colloid size

range can be mobilized by perturbation of groundwater chemical and physical conditions [5]. Chemistry of the groundwater may change by decreasing ionic strength, increasing pH, or adsorption of ions and macromolecules that alter mineral surface charge [5]. Also perturbations in the aquifer hydraulics lead to mobilization of colloids. Such physical perturbations give rise to increase of hydrodynamic shear include rapid flow through fractures, rapid infiltration of rainfall, increase in pumping rate during groundwater sampling, differential swelling, slaking, etc.

The governing equation developed for solute transport is used to develop the governing equation of transport of colloid sized particles in porous media. Hence, the complete governing equation for colloid transport in saturated porous media including advection–dispersion-diffusion-attachment/detachment and straining can be written as: [3]

$$\frac{\partial C}{\partial t} = -v_x \frac{\partial C}{\partial x} + D_L \frac{\partial^2 C}{\partial x^2} - \left(k_{att}\psi_s f_s C - \frac{\rho_b}{\theta} k_{\text{det}} S_{att}\right) - k_{str}\psi_{str} C \qquad (1)$$

where C is the concentration of solutes in aqueous phase (nL^{-3}), ν is the pore water velocity (LT^{-1}), D_L is the hydrodynamic dispersion coefficient (L^2T^{-1}), k_{att}, k_{det} and k_{str} are the colloid attachment, detachment and straining coefficient (T^{-1}). Here ψ_s, ψ_{str} and f_s are the dimensionless dynamic blocking function, colloid straining function and the patchwise heterogeneity respectively. ρ_b is the dry bulk density of soil [(M), dry soil/(L^3), soil], θ is the Soil water content [(L^3), water/(L^3), soil] and S_{att} is the colloids concentration on soil phase [(n), Colloids/(M), dry soil].

The main objective of this research study is to characterize, experimentally and numerically, the mobilization and transport of colloid-sized materials in saturated porous media under controlled flow rate and ionic strength conditions. The ionic strength was controlled by changing the NaCl concentration in the influent colloidal solution and the flow rate was changed by varying the hydraulic head of the column. Finally, the experimental results were numerically characterized based the advection–diffusion/dispersion equation coupled with attachment, detachment and straining parameters which were inversely estimated using the Hydrus-1D software package.

2 Material and Method

2.1 Pre-treatment of Porous Media

Sand was used as the porous media material in all column experiments. Sand, collected from a construction site, was first sieved by 2 mm and 425 μm sieves, respectively. The sample passing through 2 mm sieve and retaining on 425 μm was collected. Sieved fraction was washed several times with water until the acidity and turbidity were completely removed and natural pH was maintained. However, the turbidity level of washed sand couldn't be completely removed. Therefore the washed

sand was kept in water for 24 h. After that, washed sand was oven dried at 105 °C for 24 h and then air dry for another 24 h before using in the column experiments.

The measured particle density (ρ_s) and bulk (packing) density were 2.65 g/cm^3 and 1.76 g/cm^3 respectively.

2.2 Preparation of Soil Colloids

The soil samples were taken at 5–10 cm depth in a pasture area belonging to the Faculty of Engineering, University of Peradeniya. The retrieved soil was first oven dried at 105 °C for 24 h and sieved by 2 mm sieve to prepare colloidal solution. To prepare colloidal solution, 150 g of soil was added to water and was shaken manually for 15 min in order to break the soil aggregates. Next the solution was kept undisturbed for 20 h at 25 °C to allow coarser particles to settle. Then the water-dispersible colloid fraction smaller than 2 μm was gently siphoned. Stoke's law (Eq. (2) was used to compute the depth of extraction. Therefore, in 20 h particles of diameter 2 μm travel a distance of 25.93 cm.

$$v = \frac{(\rho_s - \rho_w)d^2 g}{18\eta} \tag{2}$$

where ν is the particle settling velocity (LT^{-1}), ρ_s is the particle density (ML^{-3}), ρ_w is the density of water (ML^{-3}), g is the gravitational acceleration (LT^{-2}), d is the particle diameter (L) and η is the viscosity of the medium ($ML^{-1}\ T^{-1}$).

2.3 Column Apparatus

The experimental apparatus primarily consisted two Marriott tanks and the sand column. The Marriott tanks were made of Perspex with a diameter and a height of 74 mm and 800 mm, respectively. Transparent tubes of similar length were used to hydraulically connect each Mariott tank with the column in order to maintain the same friction loss (and hence the base flow rate) from both tanks. One Marriott tank contained tap water which was primarily used as the base flow. The other tank contained the colloidal solution the properties of which differed according to different ionic strengths.

The sand column, with a diameter and a height of 74 mm and 250 mm, respectively, was prepared using Perspex. O-rings were inserted to grooves at top and bottom caps to ensure watertight closures. Bottom end of each tank was connected to the sand column through a common three-way valve (Fig. 1).

Fig. 1 Packed sand column

2.4 Test Procedure

The column was wet-packed using pre-treated sand incrementally in 5 cm layers. At the top and bottom, a 1 cm thick gravel layer was placed to ensure uniform distribution of the influent solutions. The column was tapped gently to release trapped air and maintain a levelled surface. The column was hydraulically connected at the bottom with the two Mariott tanks via a three-way valve. The water was applied (from 1st Mariott tank) for one pore volume and switched to 4 pore volumes of colloidal solution (from 2nd Mariott tank). The flow was again switched to water flow for several pore volumes (Fig. 2).

Similar application sequence was applied for three different flow rates and ionic strengths. Colloid turbidity and electrical conductivity of effluent samples were measured in parallel to the column experiment. Turbidity was measured using turbidimeter and expressed in NTU, Nephelometric Turbidity Units. Electrical conductivity was measured by using CM-40 V (TOA, Japan) conductivity meter.

2.5 Numerical Analysis

Hydrus 1D (version 4.17) software package was used to parameterize colloid transport. The Hydrus-1D computer software package [6] which simulates water, heat

Fig. 2 The assembly of packed sand column and two Mariott tanks

and multiple solutes movement in one dimensional variably saturated media. The governing flow and transport equations are numerically solved using Galerkin-type linear finite element schemes [7].

After having the experimental results, simulated breakthrough curves were obtained by fitting specific model parameters to the effluent concentration data within Hydrus platform. Finally, parameters that are in colloid transport governing equation were inversely estimated. These parameters are attachment coefficient (k_{att}), detachment coefficient (k_{det}) and straining coefficient (k_{str}) which represent the colloid transport and mobilization behavior under different flow rate and ionic strength conditions.

3 Results and Discussion

3.1 Effect of Flow Rate

The colloid breakthrough curves for the three flow rates (1.291, 2.89, and 4.33 cm^3/s) are illustrated in Fig. 3. The electrical conductivity variation was also monitored. At the lowest flow rate, the colloid retention seemed to be the highest, and with increasing flow rate the colloids seem to have eluted increasingly. This is further evidenced by the simulation parameters shown in Table 1. Note the good agreement observed between observed and simulated data in Figs. 4, 5 and 6.

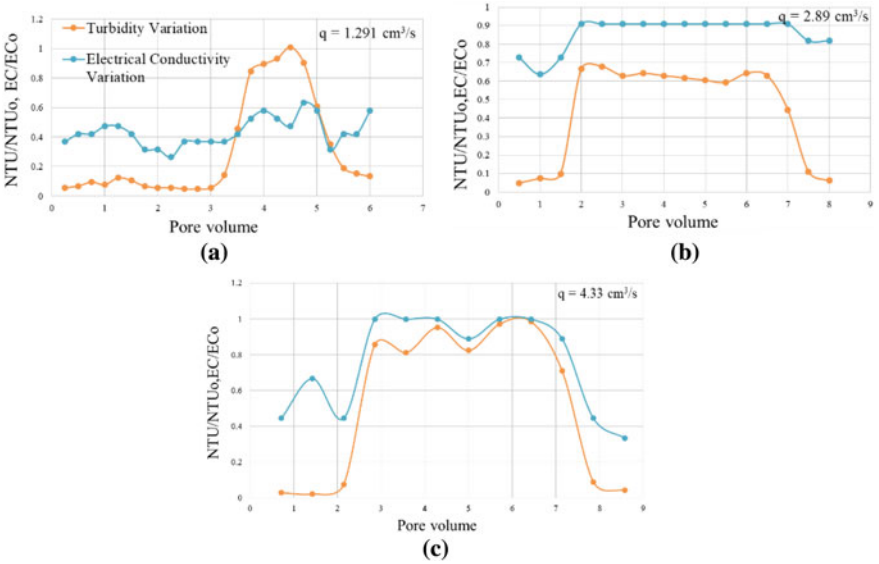

Fig. 3 Variation of turbidity and electrical conductivity ratio with respect to pore volume for **a** 1.29, **b** 2.89 and **c** 4.33 cm^3/s flow rate

Table 1 Estimated transport parameters under varying flow rates

Flow rate (cm^3/s)	Obtained parameters	Value
1.29	Attachment coeff (k_{att}), min^{-1}	2.14
	Detachment coeff (k_{det}), min^{-1}	2.93
	Straining coeff (k_{str}), min^{-1}	1.94
2.89	Attachment coeff (k_{att}), min^{-1}	1.19
	Detachment coeff (k_{det}), min^{-1}	0.641
	Straining coeff (k_{str}), min^{-1}	0.0247
4.33	Attachment coeff (k_{att}), min^{-1}	0.00038
	Detachment coeff (k_{det}), min^{-1}	2.03
	Straining coeff (k_{str}), min^{-1}	1.65

By considering estimated colloid transport parameters under different flow rates condition, the attachment coefficient that confirms the colloid attachment decreases when increasing flow rates.

3.2 Effect of Ionic Strength

Colloid breakthrough curves under three ionic strength values (0.01, 0.05, and 0.1 M) are shown in Fig. 7. With increasing ionic strength, the colloid attachment seems to

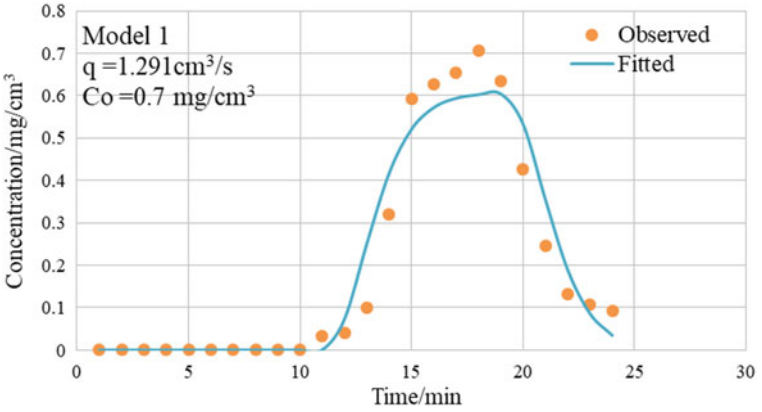

Fig. 4 Simulated breakthrough curve with observe data under 1.291 cm^3/s flow rate

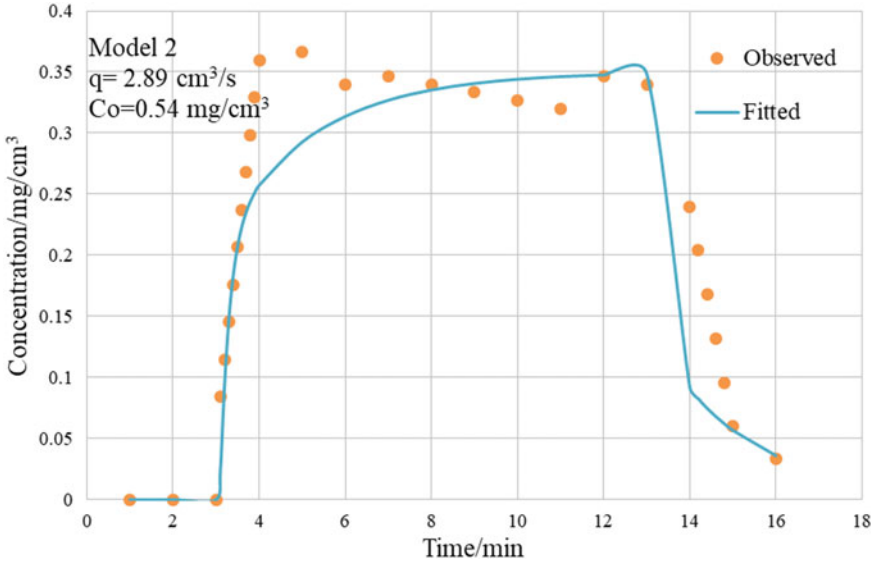

Fig. 5 Simulated breakthrough curve with observe data under 2.89 cm^3/s flow rate

have systematically increased. This is in good agreement with the literature which showed increasing colloid retention due to increasing ionic strength, which was ascribed to the shrink in electrical double layer under increasing ionic strength, resulting in a decline of electrostatic repulsion [5]. This could be further explained by the increasing attachment coefficient in Figs. 8, 9 and 10, while the straining coefficients gave mixed results (Table 2).

Notably, a sudden peak appeared in the 0.1 M breakthrough curve, which was absent in other two breakthrough curves (for 0.01 and 0.05 M). According to the

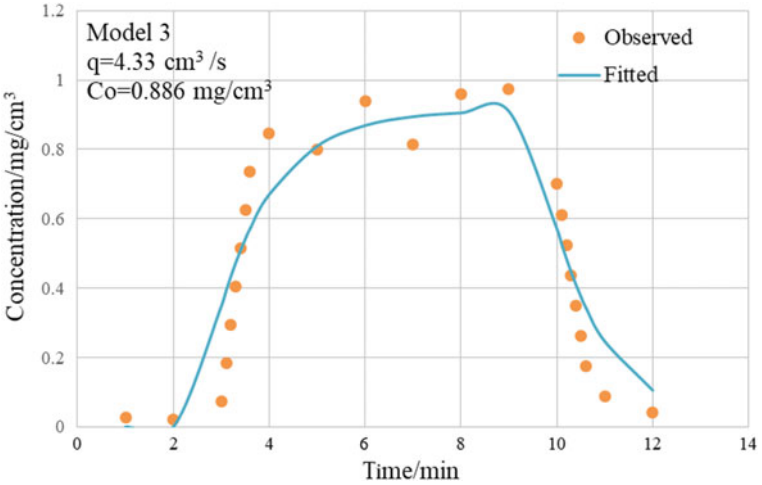

Fig. 6 Simulated breakthrough curve with observe data under 4.33 cm^3/s flow rate

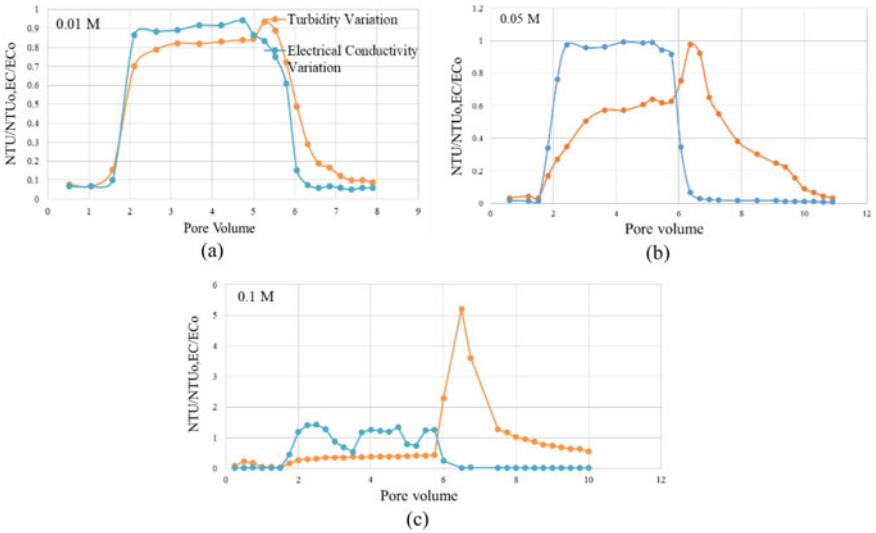

Fig. 7 Variation of turbidity and electrical conductivity ratio with respect to pore volume for **a** 0.01, **b** 0.05 and **c** 0.1 M NaCl concentration of colloidal solution

literature studies, the decreasing in ionic strength is resulted in a large colloid peak in the effluent, indicating a strong increase in the particle release rate at low ionic strength. Also, particle release at low ionic strength is prominent only in the presence of monovalent counter ion at the colloid and matrix surface. When the surfaces are saturated with divalent counter ions, such as Ca^{2+} particle release remains low even at very low ionic strength [3].

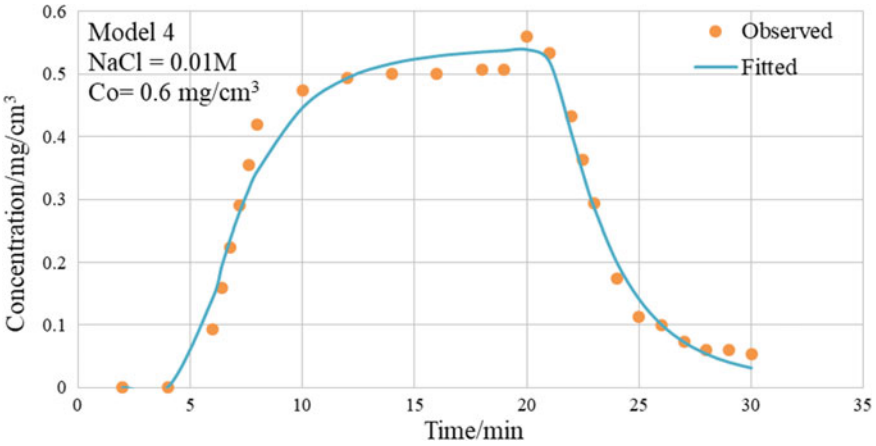

Fig. 8 Simulated breakthrough curves with observed data for 0.01 M ionic strength

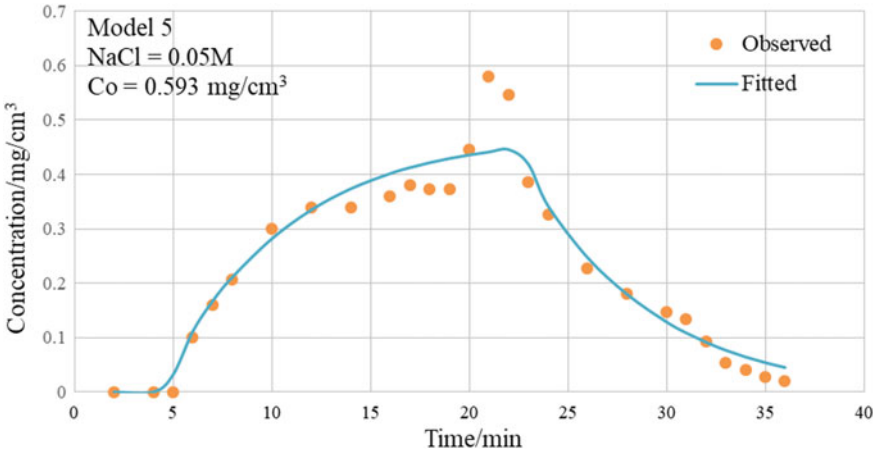

Fig. 9 Simulated breakthrough curves with observed data for 0.05 M ionic strength

Due to a sudden peak in the 0.1 M breakthrough curve, the numerical model was not capable of predicting such chemically-based colloid release and hence mischaracterized the observed data for high ionic strength.

3.3 Implication of Modelled Results in Real Life Application

In order to transfer model results to practical applications, we defined a conceptual real life problem as follows.

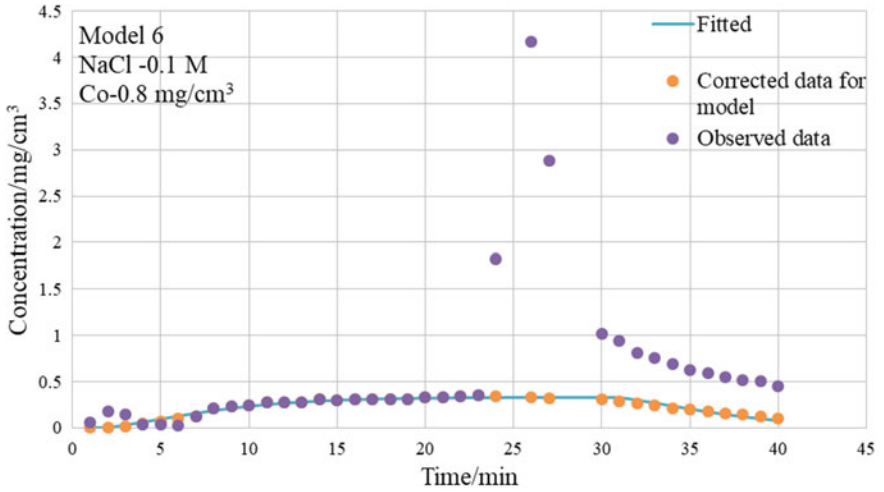

Fig. 10 Simulated breakthrough curves with observed data for 0.1 M ionic strength

Table 2 Estimated transport parameters under selected ionic strengths

Ionic strength (M)	Obtained parameters	Value
0.01	Attachment coeff (k_{att}), min^{-1}	0.0144
	Detachment coeff (k_{det}), min^{-1}	0.0496
	Straining coeff (k_{str}), min^{-1}	0.0026
0.05	Attachment coeff (k_{att}), min^{-1}	0.756
	Detachment coeff (k_{det}), min^{-1}	0.452
	Straining coeff (k_{str}), min^{-1}	2.54
0.10	Attachment coeff (k_{att}), min^{-1}	1.8
	Detachment coeff (k_{det}), min^{-1}	0.759
	Straining coeff (k_{str}), min^{-1}	0.812

A soil profile with 1 m × 1 m area and 10 m in depth was considered to analyse the time taken the colloids (and hence colloid-facilitated contaminants) to reach groundwater table which was assumed at the depth of 10 m (it was assumed that a capillary zone is of negligible height). This soil profile was assumed to contain similar porous media as used in column experiments. An initial colloidal concentration (50 mg/cm^3) was applied to the existing ground for 18 h period, three ionic strength values, 0.01, 0.05 and 0.1 M, in colloidal solutions are considered to mimic the changes in ionic concentrations in the area due the changes in fertilizer applications for agriculture. Hence, this conditions are similar to the column experiments that were done under different ionic strengths. The inversely estimated model parameters for different ionic strength conditions were used for the simulations.

The simulations clearly show that the time taken to migration colloids (and therefore colloid-mediated contaminants) in the conceptual soil profile significantly vary

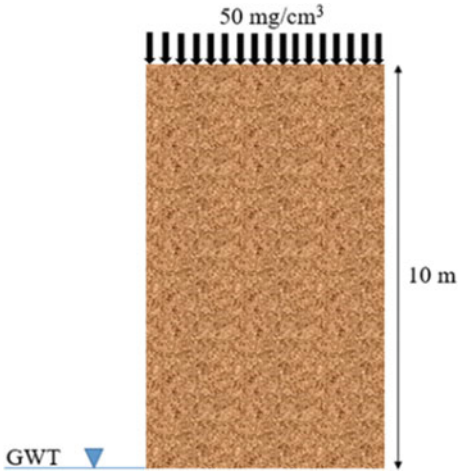

Fig. 11 Schematic Illustration of the conceptual soil profile (not to scale)

with the ionic strength of the colloidal solution. As the ionic strength of the colloidal solution increase from 0.01 to 0.1 M, the time taken for colloids and colloid-facilitated contaminants to reach groundwater table significantly increase (Figs. 11 and 12).

4 Conclusions

This study investigated the transport of colloid-sized materials in saturated porous media for different ionic strengths and at different flow rates by using series of column experiments. Further, colloid transport parameters were numerically estimated. From the results of this study, following conclusions could be drawn.

- Colloid deposition decreased with increasing flow rate.
- Observed high colloid deposition at low flow rates was attributed to the increased mobile-immobile shear interface and to straining of smaller colloids to sand grains.
- Observed breakthrough curves showed increased colloid deposition with increasing ionic strength.
- Estimated straining coefficients of soil colloids were significantly higher in low flow rates and high ionic strength.
- Estimated attachment coefficients were relatively higher at low flow rates and at higher ionic strength.
- Results provided useful implications to estimate colloids (and hence colloid-facilitated transport of contaminants) to reach groundwater under varying ionic strengths.

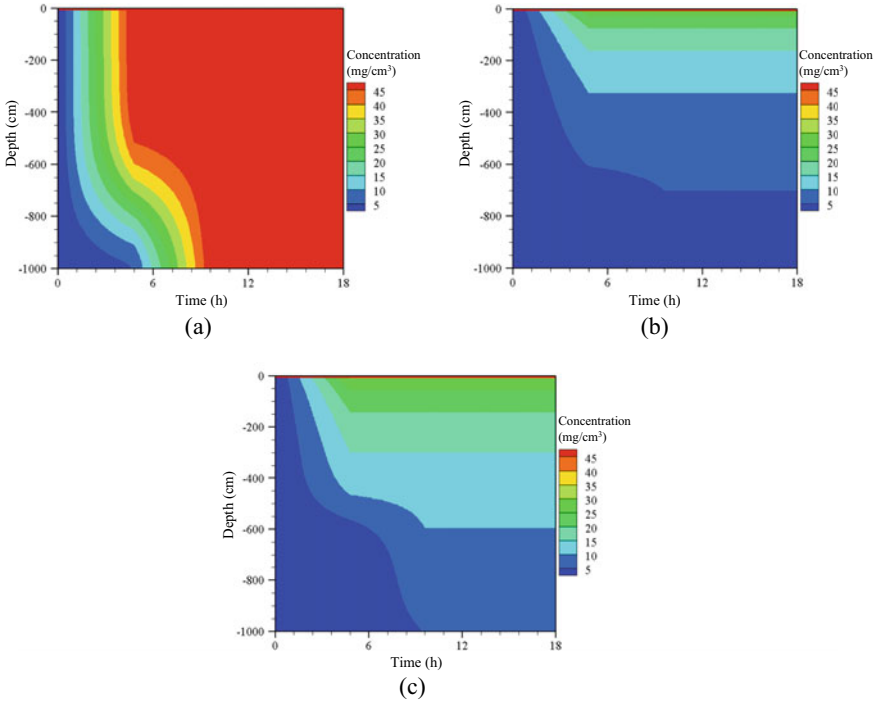

Fig. 12 The variation of applied colloidal concentration (50 mg/cm^3) with time and depth under **a** 0.01 M, **b** 0.05 M and **c** 0.1 M ionic strength

References

1. DeNovio NM, Saiers JE, Ryan JN (2004) Colloid movement in unsaturated porous media: recent advances and future directions. Vadose Zone J 3:338–351
2. Kersting AB, Efurd DW, Finnegan DL, Rokop DJ, Smith DK, Thompson JL (1999) Migration of plutonium in groundwater at the Newada test site. Nature 397
3. Kretzschmar R, Borkovec M, Grolimund D, Elimelech M (1999) Mobile subsurface colloids and their role in contaminant transport. Adv Agron 66:121–194
4. Mackay AA, Gschwend PM (2001) Enhanced concentrations of PAHs at a coal tar site. Environ Sci Technol 35:1320–1328
5. Ryan JN, Elimelech M (1996) Colloid mobilization and transport in groundwater. Coll Surf A 107:1–56
6. Simunek J, Sejna M, Saito H, Sakai M, Van Genuchten MT (2013) The HYDRUS-1D software package for simulating the one-dimensional movement of water, heat and multiple solutes in variably-saturated media. In: HYDRUS technical manual version 4.17
7. Simunek J, He C, Pang L, Bradford SA (2006) Colloid-facilitated solute transport in variably saturated porous media: numerical modeling and experimental verification. Vadose Zone J 05

Utilization of Bottom Ash for Clay Mine Rehabilitation

S. Suloshini, A. S. Ranathunga, S. A. S. Kulathilaka, W. B. Gunawardana, and M. M. S. T. M. Mapa

Abstract At the end of mining activities, clay mines were abandoned due to the cost and non-availability of filling materials. These abandoned clay mines cause adverse environmental and social impacts. In addition, large quantities of bottom ash (BA) are generated as a by-product of coal combustion process. This BA is disposed by open dumping in the lands, which creates severe environmental pollution. Therefore, conducted research on utilization of BA for mine rehabilitation is beneficial. The main focus of this research is applicability of BA generated from Lakvijaya power plant, Sri Lanka as a potential backfill material and a soil amendment during the clay mine rehabilitation. Initially tests were conducted to investigate the basic properties of BA. Next, chemical composition of BA was analysed to select the suitable crops for vegetation. Further pH, electrical conductivity and water holding capacity were checked and micro structural morphology of BA was determined through Scanning Electron Microscope. The results showed that BA has good engineering properties and the potential to improve agronomic characteristics of soil. It has better water holding capacity and permeability. BA can adjust soil pH to a desirable plant growth range. As BA has a very porous structure, the root system can easily develop and helps to uptake nutrients by the plant. However, a considerable percentage of trace metals is accumulated in BA which will increase the bioavailability of some trace metals to levels that poses risk to human. Thus, investigations were carried out to identify the heavy metal concentration in leachate of BA using column leaching test. Results showed that leachability potential of trace metals in BA does not exceed the allowable limits.

Keywords Bottom ash · Clay mines · Compaction · Soil amendment · Trace metals

S. Suloshini (✉) · A. S. Ranathunga · S. A. S. Kulathilaka · W. B. Gunawardana · M. M. S. T. M. Mapa
University of Moratuwa, Moratuwa, Sri Lanka
e-mail: 198034E@uom.lk

R. Dissanayake et al. (eds.), *ICSBE 2020*, Lecture Notes in Civil Engineering 174,
https://doi.org/10.1007/978-981-16-4412-2_9

1 Introduction

1.1 General Background

Clay mining is one of the land degrading methods. As a result of continuous clay mining, many topological changes tend to occur [11]. Most of the clay mining is continued along the river basins due to the availability of quality clay and the most fertile layers are removed due to mining. According to US Geological Survey Department's Mineral report on Sri Lanka, about 70,000 Mt of clay was mined in year 2014 [14]. As the demand for clay bricks and clay roof tiles increasing day by day, it is impossible to erect limitations on the extraction of clay. This has created many abandoned clay mines without any rehabilitation due to the higher cost and lack of suitable filling material. These abandoned clay mines have led to many adverse environmental and social effects such as increasing infectious diseases, soil erosion and slope instability [13]. Hence, an adequate precaution should be taken as soon as possible for the rehabilitation of these abandoned clay pits.

1.2 Bottom Ash (BA)

According to the study of World of Coal Ash (WOCA) the estimated generation of BA from coal thermal power plants in the world has reached to an approximate amount of 730 million Mt per annum [15]. Based on the study of Gimhan et al. [4], Lakvijaya coal power plant in Norochcholai, Sri Lanka produces around 50,000 Mt of BA annually. The method used for the disposal of the BA is open dumping into lands which creates environmental issues such as air, water and soil pollution. Hence, new disposal techniques have to be found. Even though BA has shown the properties which suits for construction material in previous researches, still it is being dumped into the lands in large amounts as waste. Therefore, conducted research on utilizing BA for clay mine rehabilitation will be very beneficial.

1.3 Properties of BA

BA is a granular, coarse and incombustible by product of coal. In general, the particles of BA have porous textures with angular and dark shapes. Generally, particle size of BA is between 0.1 and 10 mm and considered as a well-graded or poorly graded material based on unified soil classification system [5]. These properties of BA depend on the type of burner, operation procedure of the power plant and quality and type of coal burned [1]. In addition, BA exhibits low compressibility characteristics, high strength and higher permeability [19]. BA exhibits relatively good

engineering properties which makes BA as an ideal material for dam design and for other applications in civil engineering.

1.4 Utilization of BA for Geotechnical Applications

According to past studies, BA can be utilized in numerous ways such as coarse aggregates, fine aggregates, for cement production, highway material etc. Apart from this, BA is also used for some geotechnical engineering purposes such as a fill material, to prevent soil erosion, as a soil stabilizer, for geo polymer and soil amendment material [1]. BA is a well-drained material with lower bulk density and hence considered a good fill material [9]. Kim et al. [8] have stated that BA can be used in projects like in highway embankment construction. With the application of BA and lime on soft soils, engineering properties such as strength and bearing capacity have been improved while decreasing compressibility characteristics [4].

According to Sivakumar et al. [16], stabilization of cohesive soil with BA showed better results when compared to cohesive soil without admixtures. As a geo polymer material, BA helps in controlling greenhouse gas emission by replacing cement mortar [9]. The usage of BA in preventing soil erosion has been discussed by the study of Matsumoto et al. [11]. The results show that the possibility of soil erosion can be reduced significantly by adding fly ash and BA with a proportion of more than 85% of sand to top cover soil at the mixing ratio of over 30%. The high water retention capacity of BA due to the microporous structure helps in preventing the soil erosion.

1.5 BA as a Soil Amendment

According to Ranasinghe [13], clay pits have an average total surface area ranging from 10 to 105 acres in different villages in Sri Lanka. Hence, restoration of clay mines with a vegetation cover would be more environmentally friendly and aesthetically pleasing. With the introduction of BA, soil properties can be altered in favour of the environment. BA has the chemical and physical properties which suits the soil in various agricultural applications. Soils mixed with BA have displayed acceptable pH value, electrical conductivity and high water holding capacity which are in desirable for plant growth [18]. Some soils require an addition of lime to preserve its pH value. And BA can be applied as an alternative for those soil. It may increase pH of the soil, improve soil structure, and water infiltration, which is appropriate for crop cultivation [18]. Further, BA contains many essential plant nutrients like, Calcium (Ca), Iron (Fe), Magnesium (Mg), Potassium (K) and Silicon (Si) [18], which will eventually facilitate better growth of plants.

1.6 Problems Related in Using BA

However, some problems are associated with the continuous use of BA as a potential fill material. Due to the mechanized clay mining, large clay pits of about average depth of 8–24 feet are abandoned by the miners without rehabilitating them [13]. When these clay pits are filled with BA, it may cause ground water contamination. Chemical composition of BA is similar to fly ash however typically contain a higher carbon content [10]. The exact composition of the BA might depend on the burner properties (type, size and the operating conditions of the burner) and the raw coal source [5]. Generally, a significant percentage of Sodium (Na), Calcium (Ca), Magnesium (Mg), Potassium (K) and heavy metals such as Arsenic (As), Boron (B), Cadmium (Cd), Chromium (Cr), Copper (Cu), Mercury (Hg), Molybdenum (Mo), Nickel (Ni), Lead (Pb), Antimony (Sb), Selenium (Se), and Zinc (Zn) are accumulated in BA particles [7]. Hence, there is a possibility of leaching these trace metals into soil, groundwater and surface water, when applying high rates of BA for backfilling. It will lead to the increased bioavailability of some trace metals to levels that poses risk to human and ecological health. This cause for negative public perception in the usage of BA due to the health risks associated with it and hence need to be studied prior to the application of BA in the field.

Therefore, the main objective of this research is to investigate the suitability of BA as a fill material for clay mine rehabilitation paying more attention to the suitability as a soil amendment material. It is obtained by conducting appropriate laboratory experiments including particle size distribution, Scanning Electron Microscopy (SEM) analysis, specific gravity, Atterberg limit, Proctor compaction test, permeability test, pH, electrical conductivity, water holding capacity and heavy metal leachability tests.

2 Experimental Methodology

BA generated from the Lakvijaya coal power plant, Sri Lanka was used for this study.

2.1 Investigate the Basic Properties of BA

Particle size distribution was done according to ASTM C-136. Modified Proctor compaction tests were conducted according to ASTM D 678. As BA is a highly porous material, 24 h of saturation period as stated in the ASTM standards were not enough for testing. Hence after conducting several trial tests by standard and modified Proctor tests for different saturation periods, modified Proctor test after one-week saturation period was selected as it gave the optimum results. The cone penetration test was used to determine the liquid limit. The plasticity test was not done for BA as it is considered as non-plastic by referring to the literature [4]. Constant head

permeability test and specific gravity test were done according to ASTM D 2434-19 and ASTM D 854 respectively (three samples were tested for each test).

2.2 Conduct Testing for BA as a Soil Amendment Material

Chemical composition of BA was analysed to select the suitable crops for vegetation. Further pH, electrical conductivity and water holding capacity of BA were checked (three samples were tested for each test). Electrical conductivity and pH were measured using digital meters. Water holding capacity was measured based on the retention percentage of water in BA. A filter paper was placed at the bottom of the funnel. Then, 50 g air-dried sample was placed in a funnel and 100 ml water was added. Sample was kept for 1–2 h of time duration until there was no more visible drainage. After that, the weight of the saturated sample was measured, and sample was oven dried at 105 °C. The weight of the oven dried sample was measured and water holding capacity was calculated. The micro structural morphology of BA was determined through Scanning Electron Microscope (SEM).

2.3 Evaluate the Trace Metal Leachability of BA

The column leaching test was conducted under saturation conditions. The column was made with Perspex. For testing, BA was filled up to 150 mm and BA sample was compacted to its maximum dry density under optimum moisture content to represent field application. Bottom of the column was lined with geotextile to prevent particle loss. A height of 100 mm constant head was maintained. The test was carried out for a period of 96 h as used by Takao et al. [17]. A schematic diagram of the experimental setup of column leaching test apparatus is shown in Fig. 1 (all dimensions are in mm). The collected leachate samples during the testing were analysed using inductively coupled plasma mass spectrometry (ICP–MS) technique facility due to its lower detection limits [1, 17].

3 Results and Discussion

Following sections discuss the results obtained after laboratory tests for BA during the application as a fill material for clay mine rehabilitation.

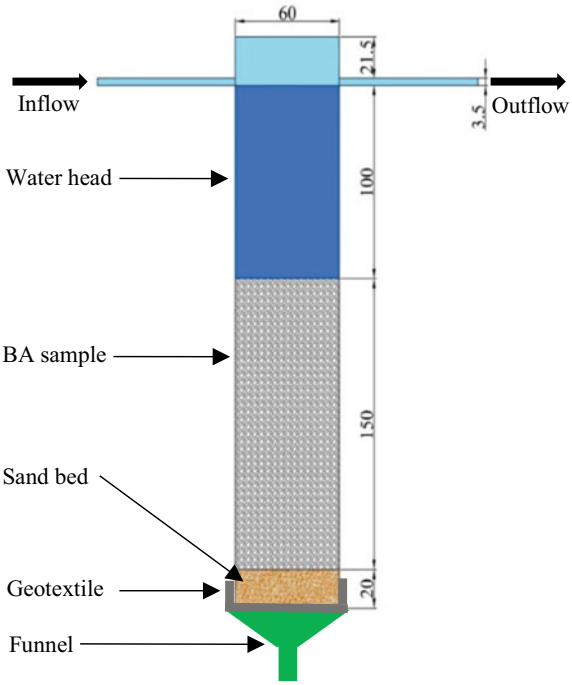

Fig. 1 Schematic diagram of column leaching test set-up

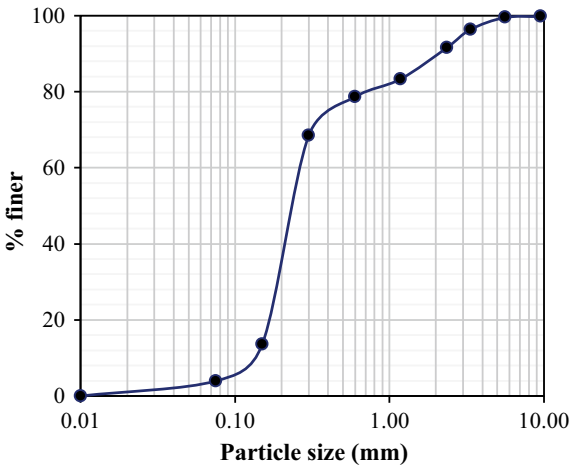

Fig. 2 Particle size distribution of BA

3.1 Suitability of BA as a Fill Material

Particle size distribution curve and modified Proctor compaction curve of BA are presented in Figs. 2 and 3, respectively. And the basic properties of BA are illustrated in Table 1. BA used for the present study is classified as poorly graded sand (SP) and according to Table 1, specific gravity of BA is much lower than that of a normal inorganic soil. Further, BA used for the present study has lower maximum dry density and a comparatively higher optimum moisture content like a soil with higher plasticity. However, during the compaction tests, BA samples mixed with water were non-plastic and workable at all used moisture contents. The porous structure was confirmed through Scanning Electron Microscope (SEM) monographs and is shown in Fig. 4.

Microstructure of the tested BA samples shows freely available scattered popcorn like structure. BA particles exhibit irregular and rough surface texture and internal porous structure is clearly evident (average pore size is around 1.95 μm). These pores

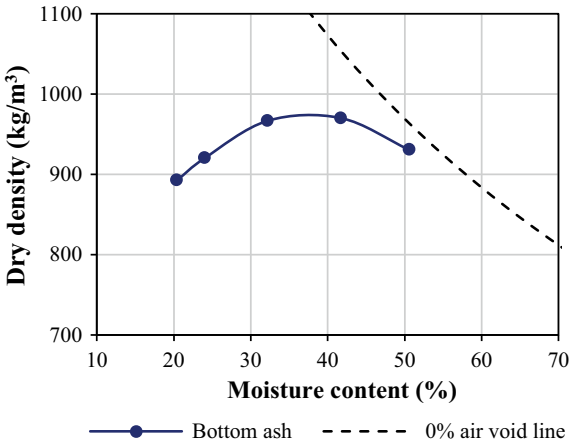

Fig. 3 Modified Proctor compaction curve of BA

Table 1 Properties of BA

Basic properties	Values
Soil classification	Poorly graded sand—SP
Specific gravity	1.88
Liquid limit (%)	20
Maximum dry density (kg/m^3)	975
Optimum moisture content (%)	37
Coefficient of permeability (m/s)	9.9×10^{-5}
pH	8.2
Electrical conductivity (μS/mm)	702
Water holding capacity (%)	66

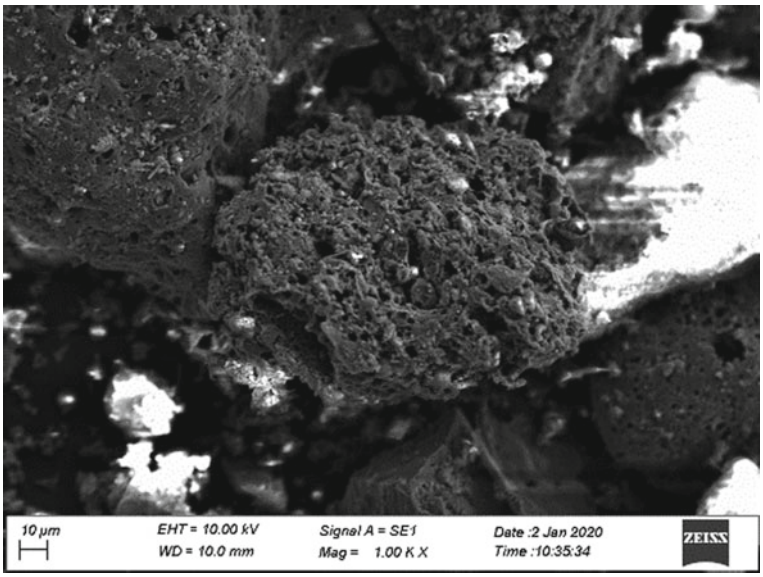

Fig. 4 SEM monograph of BA

are getting filled easily by the moisture added during the compaction, thus requiring more water for the process of compaction. Even with the absorption of large amount of water into this porous structure, the bulk density of the compacted BA at the maximum dry density is still quite low (1336 kg/m^3) compared to conventional fill materials. Hence, BA can be considered as a lightweight fill material and beneficial for construction on soft grounds like the abandoned clay mining areas.

3.2 Suitability of BA for Soil Amendment Material

Chemical composition of the BA sample is shown in Table 2. As witnessed by Wearing et al. [18], the useful plant nutrients can be observed in the BA obtained from Lakvijaya power plant as well, such as Ca, Fe, and Si. BA is an alkaline soil with a pH value of 8.2. Most plant nutrients are available in 6.5–7 pH range and hence, BA can be used to improve the pH of slightly acidic soil and makes it suitable for agriculture. The soluble salt content of BA is 702 µS/mm which represents the moderately saline class based on soil salinity classifications.

Further, the water holding capacity of BA is high (refer Table 1). Therefore, the nutrients can retain in the soil and is good for plant growth. This higher water holding capacity reduces water losses as drainage, improving efficiency in water use and increasing crop yields. With the increase in water holding capacity, decrease in permeability can also be expected. However, higher permeability observed for BA

Table 2 Chemical composition of BA

Chemical composition	Values
Aluminium oxide (Al_2O_3) (%)	17.94
Calcium oxide (CaO) (%)	1.85
Chloride content (Cl) (%)	0.097
Ferrous oxide (Fe_2O_3) (%)	7.85
Silica (SiO_2) (%)	35.79
Sulfuric anhydride (SO_3) (%)	0.04
Total alkali content (Na_2O) (%)	0.37
Arsenic (As) (mg/kg)	0.5
Cadmium (Cd) (mg/kg)	Not detected
Chromium (Cr) (mg/kg)	0.9
Lead (Pb) (mg/kg)	Not detected
Mercury (Hg) (mg/kg)	Not detected

(refer Table 1) will mitigate this problem. The porous structure of BA will be further advantageous to develop the root systems of the plants well and for the solubility of nutrients and ability to uptake nutrients by the plant. Hence, utilizing BA as a soil amendment is favourable during clay mine rehabilitation.

3.3 Trace Metals Leachability of BA

The concentrations of As, Cd, Cr, Cu, Hg, Ni, Pb, Se and Zn obtained from column leaching tests along with allowable limits as per drinking water for United States Environmental Protection Agency (USEPA) guidelines are summarised in Table 3. When compared with the allowable limits, concentrations of selected trace metals were well below the regulatory values.

Table 3 Trace metals concentration after column leaching test of BA

Metal	As	Cd	Cr	Cu	Hg	Ni	Pb	Se	Zn
Concentration (ppm)	–	–	0.017	0.023	–	0.012	0.008	–	0.034
Allowable limits[a] (ppm)	0.01	0.005	0.1	1.3	0.002	0.02	0.015	0.05	5

[a]United States Environmental Protection Agency (USEPA) drinking water standards

3.4 Implications for Field Application

The physical, chemical and geotechnical properties of BA were favourable to be used as a fill material for clay mine rehabilitation. BA is a lightweight fill material which suits to fill the soft grounds like clay mines. This research will therefore help the clay miners to fulfil the regulations of rehabilitating the clay mines at a lower cost after mining. However, different mixtures of locally available soils with BA might improve the compaction properties (maximum dry density and optimum moisture content) as per the need in the field application and should be tested. Further, some preliminary testing should be conducted to check the properties of BA prior to the application in the field as BA is a highly heterogeneous material.

BA has good soil texture, bulk density, water holding capacity and permeability when compared to soil. BA can buffer acidic soils and adjust soil pH to a range that optimizes the availability of most plant nutrients. Therefore, BA can perform as a soil amendment material economically, geologically, chemically and agronomically as stated in Table 4.

BA used as a soil amendment material will be a better way to mitigate the environmental and social impacts due to disposal of BA. In addition, these areas can be converted into recreational areas after restoring with vegetation. With the help of environmental authority and the local governments, these restored quarries can be rehabilitated with native flora and fauna. Plants such as Blue Grama Grass (*Bouteloua gracilis*) and Buffalo Grass (*Buchloe dactyl*oides) grow under tropical conditions and alkaline soils [3]. Hence they can be grown using BA. Further, by adding acid forming materials, pH value of BA can be adjusted to suit other types of plants as well. This will restore the ecological balance and the aesthetics of the area while creating economical advantages for the locals.

4 Conclusions and Recommendations for Future Studies

Following sections list the conclusions of the research and recommendations for future studies.

Table 4 Comparison of BA and agricultural soil

Properties	Agricultural soil	BA soil amendment
pH	6.5–8 [12]	8.2
Electrical conductivity (μS/mm)	240–320 [2]	702
Water holding capacity (%)	20.7–46.5 [6]	66

4.1 Conclusions

According to the findings of the present study, BA has the following properties;

- Lower specific gravity, lower bulk and dry density and therefore, can be considered as a lightweight fill material which is suitable to fill soft grounds like abandoned clay mines.
- Higher water holding capacity, higher electrical conductivity and has necessary plant nutrients which increase crop yields.
- Desirable pH value of 8.2 which suits plant growth and also facilitates as a buffer for slightly acidic soils.
- The trace metal leachability after column leaching test is well below the USEPA standards and therefore, no threat to health, water bodies or environment for utilizing as a backfill material in clay mines.

Hence, BA can be used as a potential fill material for in rehabilitation of abandoned in clay mines.

4.2 Recommendations for Future Studies

Different mixtures of BA and locally available soils need to be tested as it might improve the compaction properties and also for soil amendment purposes to obtain a suitable soil cover for recreational activities. Suitability of BA as a soil amendment needs to be evaluated by seed raising experimental tests to select proper crops for vegetation. It is advised to investigate the long-term effect on utilizing BA for safer application in the field without any threat for health and environment.

Acknowledgements The assistance given by laboratory staff of Geotechnical Engineering and Environmental Engineering Divisions of Department of Civil Engineering, University of Moratuwa and the facilities provided by Industrial Technology Institute (ITI), Sri Lanka to obtain the trace metal concentrations of the samples are acknowledged. This research study is funded by Senate Research Committee Long-term grant (SRC/LT/2019/14) offered by University of Moratuwa, Sri Lanka.

References

1. Chrishanthi JAC (2019) Possible use of bottom ash in embankment construction. MSc Dissertation, University of Moratuwa, Sri Lanka
2. Cropaia (2020) Available at: https://www.cropaia.com/blog/electrical-conductivity/. Accessed 26 Sept 2020
3. De LC (2017) Lawn grasses—a review. Int J Horic 7:82–94

4. Gimhan PGS, Disanayaka JPB, Nasvi MCM (2018) Geotechnical engineering properties of fly ash and bottom ash: use as civil engineering construction material. Eng: J Inst Eng Sri Lanka 51(1):49
5. Jayaranjan MLD, Hullebusch ED, Annachhatre AP (2014) Reuse options for coal fired power plant bottom ash and fly ash. Rev Environ Sci Biotechnol 13(4):467–486
6. Jayanthi M (2007) Engineering aspects of aqua farm design for sustainability of environment and aquaculture. Indian J Fish 54(1):59–65
7. Jones KB, Ruppert LF, Swanson SM (2012) Leaching of elements from bottom ash, economizer fly ash, and fly ash from two coal-fired power plants. Int J Coal Geol 94:337–348
8. Kim B, Prezzi M, Salgado R (2005) Geotechnical properties of fly and bottom ash mixtures for use in highway embankments. J Geotech Geo Environ Eng 131(7):914–924
9. Kim HK, Lee HK (2015) Coal bottom ash in field of civil engineering: a review of advanced applications and environmental considerations. KSCE J Civ Eng 19(6):1802–1818
10. Kumar D, Kumar N, Gupta A (2012) Geotechnical properties of fly ash and bottom ash mixtures in different proportions. Int J Sci Res (IJSR) 3(9)
11. Matsumoto S, Ogata S, Shimada H, Sasaoka T, Kusuma GJ, Gautama RS (2016) Application of coal ash to post mine land for prevention of soil erosion in coal mine in Indonesia: utilization of fly ash and bottom ash. Adv Mater Sci Eng
12. Neina D (2019) The role of soil pH in plant nutrition and soil remediation. Appl Environ Soil Sci 2019:ID 5794869
13. Ranasinghe M (1996) Mine restoration bond for clay mining and its impact on the prices of building materials in Sri Lanka. Constr Manag Econ 14(2):165–174
14. Renaud KM (2014) The mineral industry of Sri Lanka. US Geological Survey, USA
15. Singh N, Shehnazdeep, Bhardwaj A (2020) Reviewing the role of coal bottom ash as an alternative of cement. Constr Build Mater 233:117276
16. Sivakumar D, Ammaiappan M, Anand R, Lavanya V (2015) Importance of bottom ash in preventing soil failure. J Chem Pharm Sci 8(4)
17. Takao T, Kenji N, Masateru N, Jinmei L, Tatsuhiko S (2007) Leaching test of coal fly ash for the landfill. In: Ash facility management I, world coal ash utilization (WOCA) conference, Lexington, KY, USA
18. Wearing C, Birch CJ, Nairn JD (2008) An assessment of Tarong bottom ash for use on agricultural soils. Dev Chem Eng Miner Process 12(5–6):531–543
19. Yuksel I, Genç A (2007) Properties of concrete containing non ground ash and slag as fine aggregate. ACI Mater J 104(4)

Green Technology and Disaster Resilience

A Study on Climate Change Impact on Cooling Energy Demand Patterns for an Existing Office Building

S. V. I. R. V. Serasinghe, M. A. Wijewardane, and I. D. Nissanka

Abstract Energy demand for building heating, ventilation, and air conditioning account for a significant fraction of the global electricity demand. With global average temperatures projected to increase throughout the twenty-first century, building energy demand and consumption are also slated to increase. Even though the importance of climate effect on building energy management has been identified there has been few studies conducted to date to estimate the sensitivity of electricity demand for air conditioning to the climate variability, especially for the tropical weather conditions. The localized studies are of more importance in this regard, as the air conditioning load vary with the local ambient conditions. The impacts of climate change on building air conditioning energy demand for existing buildings can be reduced by establishing future energy demand patterns and using passive cooling strategies. Hence, this research aims to establish a relationship between the current energy demand patterns for air conditioning in a selected existing building and ambient temperature changes, thereby establish energy demand patterns. A suitable sample building was selected for the study and the indoor thermal comfort data, outdoor environment conditions and building energy consumption patterns are monitored and hourly data were collected. Climate conditions and the cooling load variability of the building were studied theoretically and the relation between climate conditions and energy consumption patterns were analysed. The indoor temperature and cooling load showed high sensitivity to the outdoor temperature with maximum of 25% cooling load increase for 1 °C increase in outdoor temperature. Also, it was predicted that the current cooling load of the building will increase by 40–55% in 2050. Further, the effects of the short-term meteorological variability on the cooling degree days are calculated and its impact on the energy demand was established for the selected building, which could be used for predicting future energy demand patterns with the help of different climate change models.

Keywords Energy demand · Air-conditioning · Climate change · Existing buildings · Thermal comfort

S. V. I. R. V. Serasinghe (✉) · M. A. Wijewardane · I. D. Nissanka
Department of Mechanical Engineering, University of Moratuwa, Katubedda, Moratuwa 10400, Sri Lanka
e-mail: serasinghesvirv.20@uom.lk

R. Dissanayake et al. (eds.), *ICSBE 2020*, Lecture Notes in Civil Engineering 174,
https://doi.org/10.1007/978-981-16-4412-2_10

1 Introduction

The current national power generation of Sri Lanka is mainly relying on none-renewable sources such as fossil fuels. The country is planning to towards developing renewable energy sources, while developing a well-managed energy consumption is equally important in in facing the global energy crisis due to the depletion of natural energy reserves. According to a study by Fernando et al. [6], on average 78% of the national energy demand is supplied by non-renewable energy sources. The fact that almost all the non-renewable fuels are being imported into the country imposes a huge burden to the national economy. In tropical countries like Sri Lanka, amid the threats of global warming, increasing energy demand in current infrastructure would be critical for the future national power demand. The building sector in Sri Lanka accounts for 46% of the total energy demand along with the industrial sector and transportation sector consuming 25% and 29% respectively. More than 50% of the energy consumption in Sri Lanka in 2018 was consumed by HVAC systems as calculated by the electricity bills and end-use electricity breakdown [7].

The HVAC energy demand is predicted to increase with the rising global temperatures which will in turn increase the greenhouse gas emissions resulting accelerated global warming creating a cycle of temperature and demand increase. According to the System load profile of Sri Lanka normalized by the peak demand as shown in Fig. 1 [4], the per unit maximum demand at peak hours (1830–2130 h) does not have a significant change in the past 15 years. However, the per unit maximum demand has drastically increased during the daytime (0730–1730 h). This increase could be due to the industrial sector growth as well as the increasing needs of HVAC. The increase of HVAC energy demand can be due to various factors. The economic growth, population growth, technology, increase of cooling degree days and increase

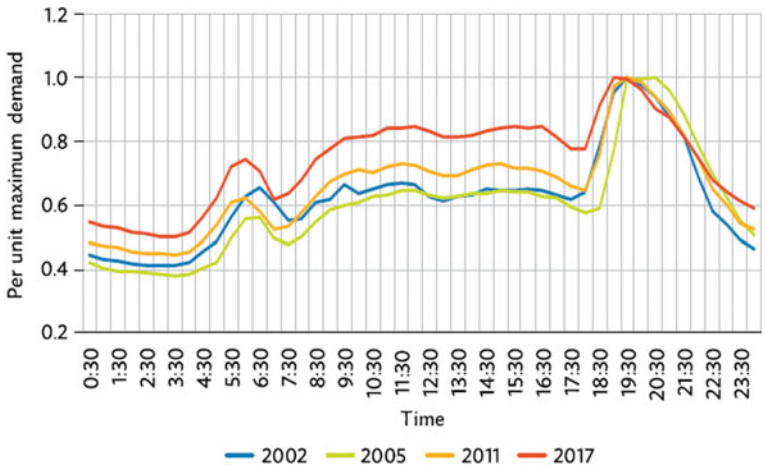

Fig. 1 System load profile of Sri Lanka normalized to peak demand [4]

of global average temperature are the core drivers for this. The global warming has been shown as a critical factor in future energy demand. Research studies showed that the increase of cooling energy requirement due to climate change factors contributes to around 48% of the total cooling energy increase in the USA by the year 2050 [5]. Also, it is predicted that the global net building energy expenditure will increase by 0.1% of the total global income for an increase of 2% in mean surface temperature. This effect is predicted to be higher in tropical countries [5], leading to an incremental change in building energy expenditure. The major fraction of these energy increase would be contributed by the building sector HVAC energy requirements. Thus, there is a clear need of establishing the future energy demand patterns for the existing residential and commercial buildings.

In predicting the future building air conditioning energy demand patterns, localized studies are more important as the energy demand is dependent on the climate zones [8, 12, 19]. The IPCC assessment report, state that the frequency of hot days and hot nights are increasing throughout the globe [9]. These changes are dominant in the Southern and South Eastern Asia region, with the large incremental increase of buildings and also population [13]. A study by Rogner et al. [16] showed that the energy demand for air conditioning in these areas could increase up to 40 times in year of 2100 with an average annual rise of 7%.

In the literature, most of the energy demand quantification were carried out by statistical models, however, these models lack the ability to identify the connection between the ambient conditions and the building thermal properties [21]. Hence, to include the effect of global warming into energy consumption models, the relationship between ambient temperature and the building thermal properties are vital [15]. The sensitivity of a building to the outside air temperature will have a significant impact on the energy demand patterns of the buildings. A study conducted by Watkins and Levermore [20] suggested that an increase of 1 °C of average global temperature would cause an average increase of 10% cooling demand. However, this sensitivity of cooling energy demand of a building is affected by factors such as building architecture, orientation, construction material, and surrounding conditions. Hence, the target of this research is to forecast the energy required by an existing office building in Sri Lanka in the future climate scenarios which will help to develop strategies for the forthcoming energy crisis.

2 Methodology

To calculate the energy demand, a sample building was selected such that the data collected from this building reflects the energy demand patterns of the future buildings, in the area. As the building gets older, the infiltration of outside air into the building through the envelop increases which in turn increases the building energy demand. Thus, a relatively new building was selected for this study so that the effects of the infiltration are minimized. According to a study by Geekiyanage and Ramachandra [7], there are eight factors affecting the cooling energy demand

in buildings: building typology, building density, surface-to-volume-ratio, average building height, surface coverage, the effect of insulation, glazing ratio, and ambient conditions. The area topography of the building location is also an important factor in building energy consumption. The selected study area of the current was a prime development area in the capital city of Sri Lanka where several high-rise buildings were constructed recently. Also, there are several ongoing constructions of high-rise building in this area making it suitable fit to the current study. The selected building for this study was the Western Provincial Council building, situated in Baththaramulla, Sri Lanka which was commissioned in 2018.

In the selected building three key areas were identified for the data collection to accurately represent a typical office building in Sri Lanka. The selected building has three major segments namely office area, cafeteria, and parking space out of which office areas and cafeteria were selected for the data collection. These sampling areas were selected considering different activity levels, occupancy levels, and orientation. The selected sampling areas have different external wall to volume ratios and external walls exposed to different directions of the building. The office area is air conditioned, which allows the study of temperature and other effects in a mechanical ventilated area which will be referred to as "Office area". The second area selected is a cafeteria which is not air-conditioned but with minimal exposure to external sunlit walls. Although this area is not directly air conditioned, there was a significant infiltration of conditioned cool air into this space from neighbouring rooms. From now on this area will be referred to as "Cafeteria" in this paper. Both these selected areas were located in the first floor of the building and thus there is a significant cover fraction from the surrounding buildings. Hence, to identify the variation of cooling load due to orientation and building height, a third area in the top floor of the building with external sunlit walls facing the west side was also selected. This area has no internal heat loads and it was not air conditioned, thus the temperature variation is highly sensitive to outside/ambient conditions. From now on, this area is referred to as "Timber deck" in this study. The geometrical parameters of walls, floor and windows were measured and is tabulated in Table 1.

HOBO U12-012 Temperature and Relative Humidity data loggers were used to collect the indoor temperature data and Relative Humidity (RH). The temperature and RH data for the three selected areas were measured for 1-month period starting from 23rd July 2020 and data were recorded at 10 min intervals. The outdoor temperature and RH of the building for the same period were also collected. The position of data loggers and the floor plans with building orientations are shown in the Fig. 2. The data loggers were positioned such that they were not exposed to direct sunlight through the glasses or direct radiant or conductive heat from nearby appliances. Also, the data logger in the office area was placed avoiding the direct air flow from the air conditioners. The floor and wall areas of the rooms are given in Table 1. The shading coefficient of windows is estimated using the guidelines in ASHRAE pocket guide to air conditioning [2].

Table 1 Geometrical parameters of the selected rooms for data collection

Property	Room		
	Office	Cafeteria	Timber deck
Floor area (m^2)	218.05	550.85	65.03
External wall area (m^2)			
North	0	0	1.17
East	13.35	0	0
South	4.22	5.35	0
West	0	0	0
External window area (m^2)			
North	0	0	19.06
East	82.76	0	0
South	26.13	45.24	0
West	0	0	0
Internal wall area (exposed to air conditioned space) (m^2)	126.46	289.54	0
Internal wall area (exposed to non air conditioned space) (m^2)	0	89.85	136.58
External wall area/total wall area	0.5	0.1176	0.13
External Window area/total External wall area	0.861	0.8943	0.942
Shading coefficient of windows	0.55	0.87	0.87
Total door area (exposed to air conditioned space) (m^2)	4.5	15	0
Total door area (exposed to non air conditioned space)	0	0	3
Maximum number of occupants	35	110	0

The number of Cooling Degree Days (CDD) is an important parameter when calculating the monthly energy consumption of the building using average values. CDD is calculated by the Eq. 1,

$$CDD = \sum_{1}^{d} \left(\frac{\sum_{1}^{24} (T_A - T_P)}{24} \right) \tag{1}$$

where T_P is the preferred temperature and T_A is the hourly average outdoor temperature and d is the number of days in the month.

An equipment survey of the studied areas was conducted to identify the internal loads of theses rooms as shown in Table 2. The usage factors and radiant factors of the equipment were adapted from ASHRAE fundamentals [3].

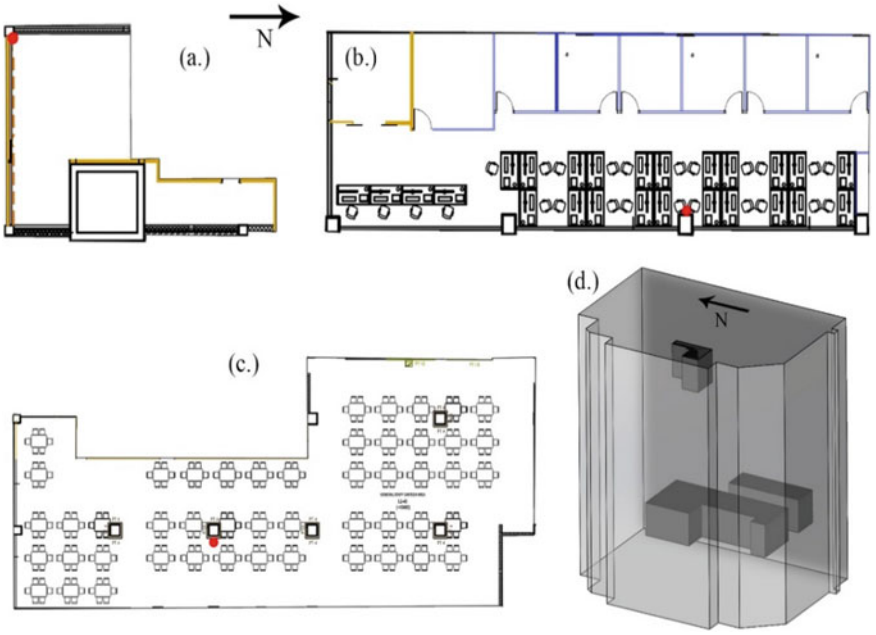

Fig. 2 Floor plans and position of rooms in the building. **a** Timber deck, **b** office, **c** cafeteria, and **d** position of rooms in building. The red dot indicates the position of the data logger in the room

2.1 Calculation of Cooling Load

The cooling load calculation was done according to the ASHARE fundamentals (2017) and, CLTD/CLF (Cooling Load Temperature Difference/Cooling Load Factor) method was used. This method was selected as it allows the values to be adjusted for Sri Lankan conditions using a manual calculation method and modified equations. Heat load through roof, windows and external walls was calculated using Eq. 2 [3].

$$Q_1 = U * A * \mathrm{CLTD}_C \tag{2}$$

where, U is the thermal transmittance, A is the area of the surface concerned, $CLTD_C$ is the corrected cooling load temperature difference. As the CLTD values from 2017 ASHRAE fundamental tables are for internal temperature of 25.5 °C and mean outdoor temperature of 28 °C, these table CLTD ($CLTD_T$) values has been adjusted using Eq. 3 to be used in the Sri Lankan environment [1].

$$\mathrm{CLTD}_C = \mathrm{CLTD}_T + (25.5 - \mathrm{T}_R) + (\mathrm{T}_M - 28) \tag{3}$$

Table 2 Equipment survey results

Room	Equipment	No. of equipment	Rated wattage (W)	Heat gain			Total (W)	Usage factor	Radiant factor
				Sensible convective (W)	Sensible radiant (W)	Latent (W)			
Cafeteria	Microwave oven	3	1700	0	0	0	0	0	0
	Serving cabinet	8	1993	205	821	0	1026	0.51	0.2
	Coffee brewer	5	3810	59	88	205	352	0.08	0.17
	Freezer	6	790	147	176	0	323	0.41	0.45
	Oven	2	5000	718	3214	0	3932	0.79	0.18
	Reach in refrigerator	5	1407	88	264	0	352	0.25	0.25
	Rice cooker	2	1550	14	68	0	82	0.05	0.17
	Boiler (hooded)	8	2450	822	0	0	822	0.84	0.35
	Computers	5	750	83	–	–	83	1	1
	Television	5	240	26	–	–	26	1	1
	Speakers	6	220	15	–	–	15	1	1
	Cash register	5	25	9	–	–	9	1	1
	Mobile phones	35	NA	3	–	–	3	1	1
Office	Coffee brewer	5	3810	59	88	205	352	0.08	0.17
	Computers	36	750	83	–	–	83	1	1
	Television	4	240	26	–	–	26	1	1

(continued)

Table 2 (continued)

Room	Equipment	No. of equipment	Rated wattage (W)	Heat gain			Total (W)	Usage factor	Radiant factor
				Sensible convective (W)	Sensible radiant (W)	Latent (W)			
	Speakers	6	220	15	–	–	15	1	1
	Phone charger	10	NA	5	–	–	5	1	1
	Mobile phones	41	NA	3	–	–	3	1	1
	Photo copier with printer	2	250	28.5	–	–	28.5	1	1
	Printer	4	200	14.5	–	–	14.5	1	1
	Top mounted bottled water cooler	1	1200	172	–	–	172	1	1
Timber deck	–	–	–	–	–	–	–	–	–

where, T_M is the mean outside temperature and T_R is the desired air-conditioned room temperature. The heat due to solar radiation (Q_2) can be calculated by the Eq. (4) where, *SCLF* and *SC* are the solar cooling load factor and shading coefficient.

Heat load from occupants can be calculated by using Eqs. (5) and (6) which gives the sensible heat load (Q_3) and latent heat load (Q_4), respectively. Here, q_S and q_L are the sensible and latent heat load from a typical person according to activity level and N_O is the average number of occupants in the area. Load due to lighting appliances (Q_5) were calculated using the standard LPD (Lighting Power Density) per unit area values. Equation (7) was used to calculate the heat gain through lighting, where the F_U is the usage factor, F_B is the ballast factor and *CLF* is the Cooling Load Factor, and *A* is the area of the room concerned. Load due to other electrical appliances (Q_6) were calculated using the Eq. (8), where *W* is the total heating load, F_U is the usage factor and F_R is the radiant factor as indicated in the Table 1.

$$Q_2 = A * (SCLF) * SC \tag{4}$$

$$Q_3 = N_O * q_S * CLF \tag{5}$$

$$Q_4 = N_O * q_L \tag{6}$$

$$Q_5 = (LPD) * A * F_U * F_B * (CLF) \tag{7}$$

$$Q_6 = W * F_U * F_R * (CLF) \tag{8}$$

3 Results and Discussion

The indoor temperature and relative humidity values of the three selected rooms were logged in 1 min intervals. Figure 3 shows the variations of indoor temperatures and outdoor temperature throughout the month, whereas the Fig. 4 shows the variation of calculated cooling load and outdoor temperature variation throughout the month. For the subsequent analysis, the cooling loads were divided into two categories: external loads (i.e. loads due to external conditions such as heat gain through walls, windows, infiltration) and internal loads (i.e. heat gains due to internal conditions such as heat gain from equipment, lighting and heat gain due to occupants). The highlighted days in both figures (Figs. 3 and 4) are the government holidays during considered study period. In these holidays, most on the internal loads are eliminated thus the cooling loads in these days were comparatively lower than the normal working day which is depicted in Fig. 4. In developing a relationship to understand the sensitivity of the heat load to the outdoor temperature, the ratios of external walls to internal walls, and external wall to window along with the shading coefficient are considered to be

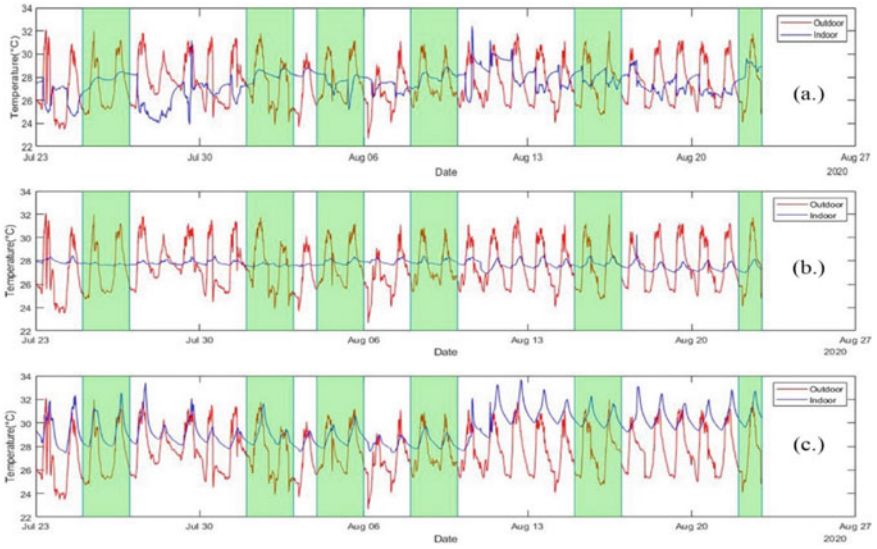

Fig. 3 Indoor temperature and outdoor temperature variation **a** office, **b** cafeteria and **c** timber deck, (highlighted days are holidays)

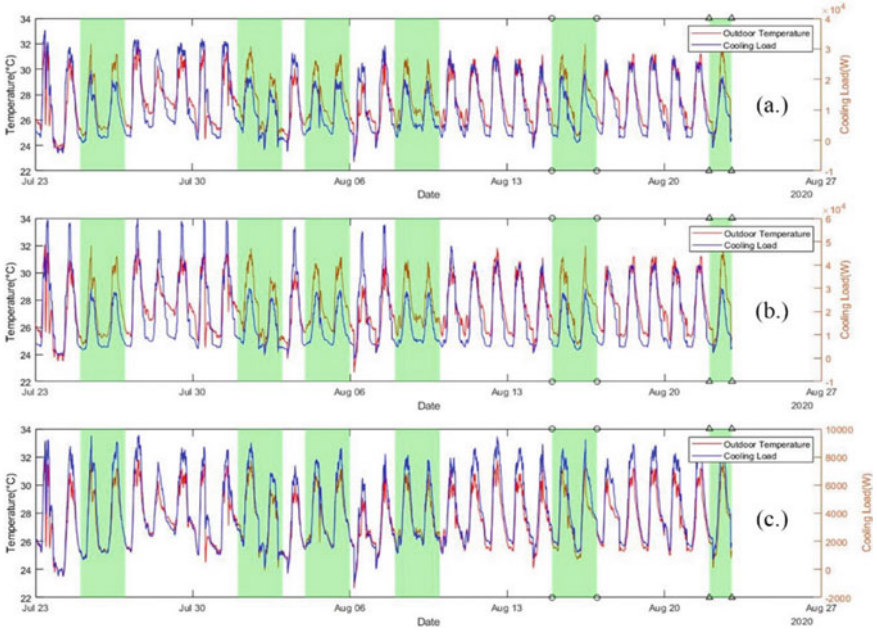

Fig. 4 Cooing load and outdoor temperature variation **a** office, **b** cafeteria and **c** timber deck, (highlighted days are holidays)

the important factors [22]. According the general trends of Figs. 3 and 4, it evident that timber deck having the highest wall to window ratio (Table 1) with very less shading coefficient has the highest sensitivity to outdoor temperature. The timber deck showed a high variation of indoor temperatures during the day and it closely followed the trend of the outdoor temperature. In contrast, cafeteria area which has low external wall ratio has a more stable indoor temperature trend with a slight sensitivity to outdoor temperature. It can also be observed that although the office area is air conditioned, it shows a high sensitivity to the outdoor temperature due to the high ratio of external walls and high ratio of windows.

3.1 Time Lag of Maximum Heat Gain and Peak Outdoor Temperature

To further study the daily variation of the cooling load with the ambient temperature, the average monthly cooling load, outdoor temperatures and external heat gain were calculated by averaging the values over the month. The averaged external heat loads, total cooling load and outdoor temperature were plotted in a single graph as shown in Fig. 5. According to the Fig. 5, the timber deck total cooling load closely followed the outdoor temperature as there were no internal loads. The peak cooling load of timber deck was observed at 1415 h on an average day. The external window of the timber deck was facing the west direction and thus the highest heat gain from surfaces exposed to west direction were around 1300–1530 h as indicated by the *CLTD* values in ASHRAE handbook. The external windows of the office area are exposed to the east side and the peak external load of office area was observed at 1135 h. The *CLTD* values of walls facing the east side record its maximum during 0930–1200 h, which resulted in a higher external heat gain as observed.

Figure 6 shows the variation of indoor and outdoor temperature, their standard deviations, and the standard deviation of peak cooling load. As can be seen from

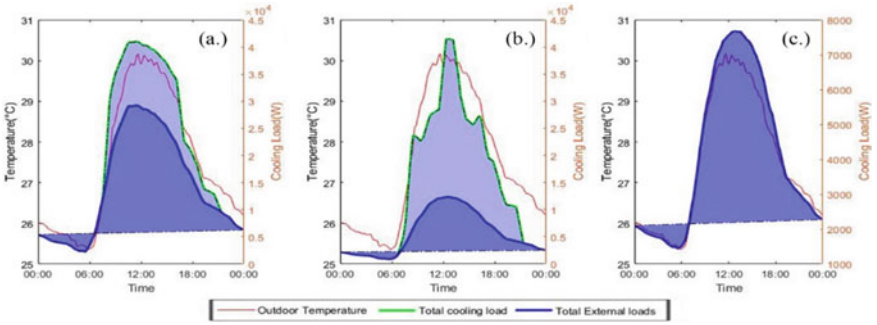

Fig. 5 Average external cooing load, average total heat load and average outdoor temperature variation with the time of the day **a** office, **b** cafeteria and **c** timber deck

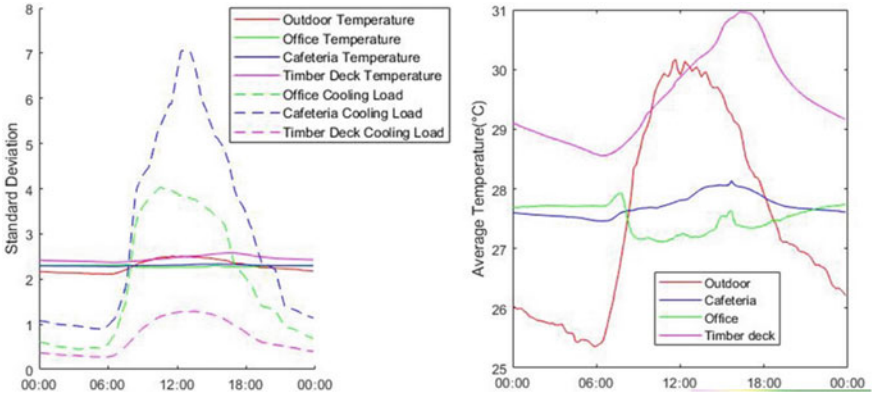

Fig. 6 Standard deviation plot of the selected areas (left) average indoor and outdoor temperature plot for an average day (right)

Fig. 6 the maximum indoor temperature is lagging the peak heat gain. A similar observations have been reported in the published literature [18]. The average indoor temperature variation of office area decreased at 0800 h which is the office starting time when the air conditioner is being turned on. Following this variation, a sudden peak can be seen at 1515 h which can be explained as the impact of the maximum heat gain (lagging of peak heat transfer into the building and the indoor temperature increase). The same phenomenon can be observed in timber deck where the peak heat gain is at 1415 h. And the indoor temperature peaks at 1620 h.

3.2 Measured Sensitivity

The outdoor temperature variation and the relative indoor cooling load increase was calculated taking into account the previously observed time lag. The results were plotted with outdoor temperature variation percentage vs. cooling load increase percentage, which is shown on Fig. 7. The results were fitted to a linear curve with 95% confidence bounds which can be used to interpolate the percentage increase of cooling load per 1 °C increase of outdoor temperature as given in the study by Watkins and Levermore [20]. It is observed that the timber deck has the highest sensitivity to the change in outdoor ambient temperature and cafeteria with lowest sensitivity to the change in outdoor ambient temperature as given in Table 3. The cafeteria cooling load has a lower sensitivity to outdoor temperature as it has a higher surface area and a low ratio of surface area exposed to outer environment.

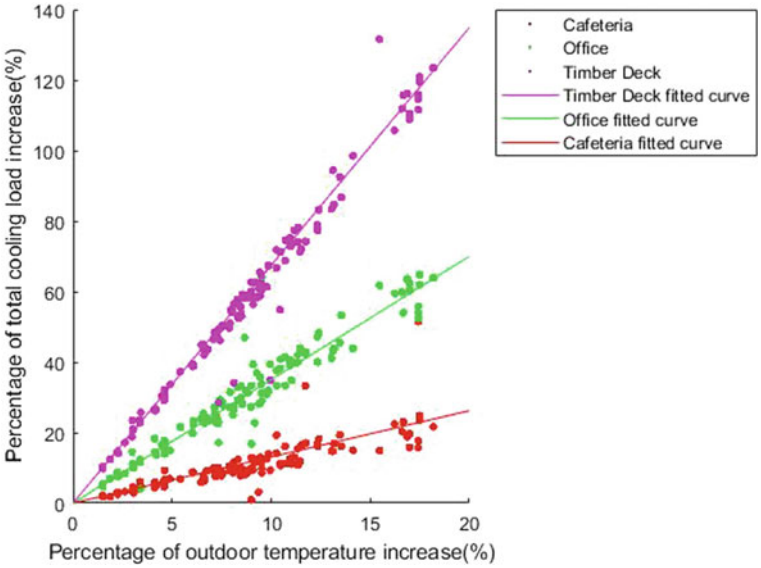

Fig. 7 The correlation between increases of outdoor temperature and increase of cooling load

Table 3 Sensitivity of cooling load to outdoor temperature of rooms

Property	Room		
	Cafeteria	Office	Timber deck
Gradient of graph	1.31	3.5	6.744
R squared of fitted curve	0.6302	0.9053	0.9645
Percentage increasee of cooling load per 1 °C increase of outdoor temperature (%)	5.038	13.462	25.938

3.3 Cooling Load Prediction

In predicting cooling energy demand patterns for a building in the future, three main scenarios should be taken into consideration: the demand change due to the average outdoor temperature rise, the demand due to the increase of number of hot days or cold days, and the demand increase due to the aging of the building. According to the literature [11], under the current emission conditions, the global temperature is predicted to increase by 2 °C by the year 2050 which is a relative increase of 8.69%. Following the trends in Fig. 7, this 2 °C temperature increase in 2050 will roughly return an increase of around 10.076, 26.924 and 51.876% of cooling load in the cafeteria, office area and timber deck, respectively.

Although the number of CDD will not directly affect the peak cooling energy demand of a building, it will affect the total energy consumption. Currently the office area is the only directly air conditioned area, equipped with four 36,000 btu/h

(10.551 kW) split type air conditioners, with a COP of 3.6 for cooling. The current air conditioning system in the office area is capable of handling a maximum cooling load of 42.204 kW. The calculated maximum cooling load of the office area is 36.142 kW. Hence, the existing air conditioning system is capable of cooling the area. The average cooling load for working hours between 8.00 a.m. and 5 p.m. in the office area is calculated to be 19.56 kW, which is roughly 54.12% of the cooling capacity of the air conditioning system. Hence, the average electrical energy consumption calculated is 1268.93 kWh. As Calculated from Eq. (2) for the selected month for this study has a CDD value of 292.8.

Following the CDD increase for past years, Newman [14] has calculated a CDD increase of roughly 33% for the past 30 year time span and projected to increase in the same rate or higher throughout the twenty-first century. Based on this predicted CDD increase rate the estimated CDD in the year 2050 will be 392.4. Adapting from the works of Krese et al. [10], converting this to electrical power consumption, it is notable that the power consumption is projected to increase to 1700.57 kWh in 2050 from 1268.93 kWh in 2020 for the months considered in this study. Also, this increase is only considering the increase of the number of CDDs. The increase due to the other two factors discussed above should also be added on top of this estimate to calculate the total energy demand.

Since the building was commissioned in 2018, Current study assumed that there is no additional infiltration of heat and outside air into the building due to the age of the building. However, in year 2050 building is 32 years old and thus the heat load added due to the air infiltration would be significant. A study conducted by Sherman [17] suggests that a new building will have an increase of around 0.42 ACH (Air Changes per Hour) for 30 year time span. Based on the cooling load calculations, this rate of ACH result in an average increase of 1.89, 12.81 and 5.91 kW of cooling load for timber deck, cafeteria and office, respectively in the year 2050.

4 Conclusion

The observed indoor temperature and the calculated cooling loads have shown a high sensitivity to the outdoor temperature variation. The timber deck area has shown the most sensitivity to outdoor temperature due to the high percentage of sun sit walls and its orientation, followed by the office area and the cafeteria with 25.938, 13.462 and 5.038% increase of cooling load for 1 °C increase of outdoor temperature, respectively. The cooling load sensitivity to the ambient temperature mainly depends on the exposure of the walls and windows to outer sunlight or outer temperature. The time of day when the peak load is achieved depends on the orientation of the walls or windows. Rooms with East facing windows or walls experience the peak cooling load earlier than the rooms with external walls or windows facing west. Therefore, by well planning the building orientation, the heat load stress on the central air conditioning system can be effectively managed. Based on the predicted increase of average global temperature within the next 30 years an additional 40.57, 41.7 and

55.66% of load would be added on to the cooling loads for cafeteria, office and timber deck, respectively. In addition, an estimated 431.64 kWh of electrical energy will be required for the month of August 2050 for office area due to the increase of CDD. Therefore, on average, 41.7% of cooling load plus 431.64 kWh of additional energy per month will be needed only for cooling the office area. The findings of this study highlight the need of further studies to develop strategies in order to manage and reduce this increasing energy demand in building sector due to the global warming which would be the future directions of this research.

Acknowledgements Authors would like to extend their gratitude to Mr. Sameera Jayarathne and Mr. Kamal Priyantha of Central Environment Authority, Sri Lanka for providing outdoor temperature data. Also, authors would like to acknowledge Ms. Thuthiprabha, Mr. Thalangama and Mr. Parakrama from Western Provincial Council, Sri Lanka for granting permission to collect data in their building premises. Further, the authors extend their gratitude to Mr. Amindha Jayasena and Mr. Lihini Tennakoon from Department of Mechanical Engineering, University of Moratuwa for their support. The project was funded by Senate Research Committee (SRC) grant of University of Moratuwa (Grant no: SRC/LT/2020/09).

References

1. Acharya KG et al (2019) Estimation and analysis of cooling load for Indian subcontinent by CLD/SCL/CLF method at part load conditions. J Phys Conf Ser 1240(1). https://doi.org/10.1088/1742-6596/1240/1/012031
2. ASHRAE (1993) Pocket guide for air conditioning, heating, ventilation, refrigeration
3. ASHRAE (2017) Fundamentals
4. Asia Development Bank (2019) Sri Lanka: energy sector assessment, strategy, and road map
5. Clarke L et al (2018) Effects of long-term climate change on global building energy expenditures. Energy Econ 72:667–677. https://doi.org/10.1016/j.eneco.2018.01.003
6. Fernando W, Gupta N, Ozveren CS (2017) The electricity infrastructure in Sri Lanka then, now and hereafter. In: 2017 52nd international universities power engineering conference, UPEC 2017, pp 1–6. https://doi.org/10.1109/UPEC.2017.8231986
7. Geekiyanage D, Ramachandra T (2018) A model for estimating cooling energy demand at early design stage of condominiums in Sri Lanka a model for estimating cooling energy demand at early design stage of condominiums. J Build Eng 17:43–51. https://doi.org/10.1016/j.jobe.2018.01.011
8. Hamdi R et al (2014) Assessment of three dynamical urban climate downscaling methods: Brussels's future urban heat island under an A1B emission scenario. Int J Climatol 34. https://doi.org/10.1002/joc.3734
9. Intergovernmental Panel on Climate Change (2012) Residential and commercial buildings. Clim Change 387–446. https://doi.org/10.1017/cbo9780511546013.010
10. Krese G, Prek M, Butala V (2012) Analysis of building electric energy consumption data using an improved cooling degree day method. Strojniski Vestnik/J Mech Eng 58(2):107–114. https://doi.org/10.5545/sv-jme.2011.160
11. Krinner G et al (2013) Long-term climate change: projections, commitments and irreversibility. In: Climate change 2013 the physical science basis: working group I contribution to the fifth assessment report of the intergovernmental panel on climate change, pp 1029–1136. https://doi.org/10.1017/CBO9781107415324.024

12. Li D, Yang L, Lok C (2012) Impact of climate change on energy use in the built environment in different climate zones—a review. Energy 42:103–112. https://doi.org/10.1016/j.energy.2012.03.044
13. Lundgren K, Kjellstrom T (2013) Sustainability challenges from climate change and air conditioning use in urban areas. Sustain (Switzerland) 5(7):3116–3128. https://doi.org/10.3390/su5073116
14. Newman A (2018) Heat stress: threatens to undermine export economies and disrupt global supply chains, pp 1–9
15. Ortiz L, González JE, Lin W (2018) Climate change impacts on peak building cooling energy demand in a coastal megacity. Environ Res Lett 13(9). https://doi.org/10.1088/1748-9326/aad8d0
16. Rogner H et al (2007) Mitigation. Contribution of working group III to the fourth assessment report of the intergovernmental panel on climate change. In: Introduction. In climate change
17. Sherman MH (2014) Building airtightness: research and practice
18. Sun C et al (2013) Investigation of time lags and decrement factors for different building outside temperatures. Energy Build 61:1–7. https://doi.org/10.1016/j.enbuild.2013.02.003
19. Tewari M et al (2017) Impacts of projected urban expansion and global warming on cooling energy demand over a semiarid region. Atmosp Sci Lett 18(11):419–426. https://doi.org/10.1002/asl.784
20. Watkins R, Levermore GJ (2011) Quantifying the effects of climate change and risk level on peak load design in buildings. Build Serv Eng Res Technol 32(1):9–19. https://doi.org/10.1177/0143624409357122
21. Wonorahardjo S et al (2020) Characterising thermal behaviour of buildings and its effect on urban heat island in tropical areas. Int J Energy Environ Eng 11(1):129–142. https://doi.org/10.1007/s40095-019-00317-0
22. Yang Q et al (2015) Impact analysis of window-wall ratio on heating and cooling energy consumption of residential buildings in hot summer and cold winter zone in China. J Eng (UK). https://doi.org/10.1155/2015/538254

A Case Study on Temporal Variations of the Pavement Thermal Performance Based on Surface Texture for Urban Areas in Sri Lanka

D. M. Senevirathne and V. M. Jayasooriya

Abstract Pavements represent a high fraction of urban land use and contribute to the Urban Heat Island (UHI) in cities. The countries within tropical regions does not experience significant changes in local climate throughout the year similar to temperate regions, however experience differences in ambient temperature conditions due to the changes of the sun path relative to the ground. Identification of the thermal performance variations of pavers in tropical regions will assist landscape planners on selecting the pavers in an optimum way to reduce UHI considering the pavement location and the surrounding structures and direction of shading. The physical attributes of the pavers may also have a significant impact on the thermal performance of pavers. The current study was concentrated on two time periods; (1) where the sun is right above the study area (August–September) and (2) where the sun is relatively positioned furthest to the latitude of study area, (November–December), to assess the thermal performance of pavements within two climatic seasons in Sri Lanka. The study was conducted in an urban environment in Colombo, Sri Lanka by considering 9 sample pavers consisted with a single color (Natural Gray), and three surface roughness levels (Smooth, Rough and Jagged). One-sample t-test was performed to analyze the significant differences among pavers on the thermal performance in two different seasons considered. According to the results obtained, there were no significant differences within the thermal performance between 7.00 AM and 12.00 PM of two time periods, however, after 1.00 PM, pavers have shown a significant difference within the two time periods. The maximum temperature difference within two periods was shown at 4.00 PM as 6.56 °C. The time period of November to December showed lower surface temperature levels and heat emittance. The findings of this study provide valuable insights in pavement designing for urban areas, in order to regulate microclimates and reduce the impacts of UHI.

Keywords Urban Heat Island · Pavements · Temporal variation · Thermal performance

D. M. Senevirathne · V. M. Jayasooriya (✉)
Department of Forestry and Environmental Science, University of Sri Jayewardenepura, Gangodawila, Nugegoda, 10250, Sri Lanka
e-mail: varuni.jayasooriya@sjp.ac.lk

R. Dissanayake et al. (eds.), *ICSBE 2020*, Lecture Notes in Civil Engineering 174,
https://doi.org/10.1007/978-981-16-4412-2_11

1 Introduction

Urbanization has been exacerbating since mid of the twentieth century until today. According to a report of world urbanization prospects by the United Nations [13, 19], by mid-century, roughly two-thirds (68%) of the world's population will be living in urban areas. A study by Ranagala et al. [16] has shown the trends in increasing temperature for the Colombo area from 1997 to 2017. In the current context, green spaces in urban areas are replaced by infrastructure inclusive of concrete buildings, roads, and pavements. Santamouris et al. [18] and Livada et al. [12] explain that the heat energy absorbed by the infrastructure can cause air temperatures of urban areas to be higher than that of nearby rural areas. This phenomenon is called the Urban Heat Island (UHI) effect. Population increase in an area leads to an increase in the number of artificial structures, energy consumption, anthropogenic heat production, and higher emissions due to higher manufacturing processes. Therefore, the population in an area has a positive relationship with the UHI levels. Since the late twentieth century, Colombo district urban area has shown increasing UHI properties throughout the years [16]. This could in turn lead to several consequences such as thermal discomfort, higher air conditioning loads, increasing energy consumption, and smog production.

The rise of temperatures in the urban environment occurs mainly through the contribution of grey infrastructure and anthropogenic activities. The majority of the green spaces in urban areas are replaced by various grey infrastructures such as buildings, roads, pavements, and other impermeable structures [7]. Especially in developing countries, the urban areas have become vital components of the nations' income and many cities are subjected to an acceleration of infrastructure development [4, 8, 14]. The transmittance of loads to the underlying soil or sub-base is the primary function of a pavement. However, they contribute largely to the heat increment in the urban area. In addition, there may be variations of thermal performance of the pavement structures in different seasons [1].

Studies conducted in different geographical regions across the world have reported that there could be a potential for the variation in thermal performances of pavements, governed by the climatic/seasonal change. According to a study done by Buyantuyev and Wu [3] in the Phoenix metropolitan region, USA on the thermal performance of different types of land covers inclusive of pavements shows that, there exists a variation in thermal performance for different land covers within the months of June and October. Furthermore, a research conducted throughout a year in Beijing by Liu et al. [11] showed that the UHI levels vary along the year. According to this study, the minimum levels was shown in the month of July in the mid of summer season which is usually a frequently rainy season. However, maximum UHI was observed towards December and January which is the winter season. Zhang et al. [21] studied the seasonal thermal performance variations in Shanghai. The study states that there are variations in UHI intensity throughout the year. The lowest UHI levels have been recorded in June where the summer heat starts to set in this region and the highest UHI was recorded in October which is at the beginning of the autumn.

A study carried out by Li [9] focused on the seasonal impact on the thermal performance of pavements in California. The author stated that there is a significant difference in thermal performance levels of paver along the year however concluded that, this was due to the variation of solar radiation levels and there is no significant difference in albedo levels with reference to seasonal variations. A study conducted in the Pearl River Delta region in southern China has also shown that there is a significant difference in UHI during different periods of the year. This study region was low in evaporative cooling as it was highly dense with constructions with a population of about 60 million. The study has shown that the temperature difference is the highest with strong solar radiation absorption in summer. Furthermore, it showed that though the temperature levels may be lower in winter, the UHI is rather similar to the UHI in autumn being the lower temperature level seasons [20]. Therefore, it is evident that there are previous studies conducted on different UHI levels in different seasons of the year [21]. However, the studies are not concentrated particularly on the thermal performances of pavements in different seasons with detailed analysis. Balbo and Severi [2] conducted a study in Sao Paulo-Brazil, to identify the impact of seasonal variations for the thermal performance of pavements in tropical countries. The above research revealed that the rates of surface temperature increase ranges from 1.8 °C to 2.5 °C per h during the spring–summer period and from 1.2 °C to 2.0 °C per h during the autumn–winter period.

When focussing on tropical countries such as Sri Lanka with only two predominant seasons with respect to the monsoon characteristics of wet and dry seasons, there are very limited studies could be found in literature related to the pavement thermal performance assessment. Therefore, the current study is focused on assessing the temporal/seasonal variations in thermal performance of pavements with respect to the changes of surface texture, which is one commonly varying physical attribute in pavement block design.

Colombo, Sri Lanka, which is the case study urban area selected for the present research, exhibits a significant rainfall throughout the year. The climate is hot, oppressive humidity, windy, and overcast. The annual temperature varies typically from 23.0 to 33.0 °C with an annual average rainfall of about 2348 mm. Specifically, the selected pavement environment is hot (temperature ranging from 26 to 35 °C), slightly windy with about 1–2 ms^{-1} speed, and the Relative Humidity ranging from 60 to 90. The seasons could be distinguished in to two major periods where the sun is positioned right above the latitude of the region throughout the year. The months of peak positioning occurs in April and August. Therefore, the sun would be most distant to the latitude of the study area in November–December period. Hence, the solar radiation angles would be different in these two seasons. Furthermore, the two periods fall in two different seasons namely the South-West monsoon and the end of the second inter-monsoon season [5]. Thus, the present study has assessed the variations in thermal performance of pavers with respect to its texture within two periods, as August–September and November–December based on the sun position above the latitude of the study area.

The outcomes of the present study will provide guidance for the landscape architects and construction field professionals in deciding the most appropriate pavement

a) Grey Smooth (GS) b) Grey Rough (GR) c) Grey Jagged (GJ)

Fig. 1 Experimental pavement setups

type to be used in an urban environment considering the location of the site and the relative sun movement of the site. The results obtained by this study will assist the professionals to select pavers with an optimum thermal performance for the areas of limited shading, which are getting exposed for the peak daylight throughout the day. In addition, current information will aid in opting for pavements with lower thermal performance when entertaining aesthetic needs for the areas of no exposure to peak sun hours, or periods. Furthermore, this data could provide valuable insights for the future quantifications of the impacts on UHI and to decide measures to counterbalance the effects of microclimatic variations in urban areas.

2 Materials and Methods

2.1 Study Area and Experimental Set Up

Seasonal variations of temperature profiles for three types of pavers with the same material and same colour with different surface textures were compared in this study. These different pavers were selected based on the commonly used physical attributes currently under application. Nine experimental pavement setups (1 ft × 1 ft and three replicates per each texture) were constructed in an open area with no shading, located in Nugegoda, Sri Lanka within the urban area of the Colombo district. The data collection was carried out on sunny days with no precipitation from August 2019 to December 2019 which covered two seasonal variations of the local climate. The three types of pavers used for the data collection are shown in Fig. 1.

2.2 Data Collection

Each sample contained 9 blocks of 100 mm × 100 mm pavers and represented three replicates for each. The topsoil of the area was cleared up to 30 mm and the samples

were placed as shown in Fig. 2 for the time period of August–October and the time period of November–December. The surface temperatures of the experimental pavement setups were measured with use of the Thermal Imager (TESTO 872), hourly during the days with a clear sky with no precipitation. Each hour, the ambient temperature and relative humidity were recorded using Temp./RH Data Logger. The daily wind velocities were obtained from the weather station located within the premises. Table 1 shows the details of instrumentation used for the data collection.

Ambient Temperature, Relative Humidity and Surface Temperature of the pavement block at the center were measured hourly. The data collection was conducted from 9.00 am to 6.00 pm for five days of the week to assess the variations of the hourly thermal profile of the pavers.

To assess the impacts of temporal temperature variations for the pavement thermal performance, the temperature changes of the pavers were compared by considering

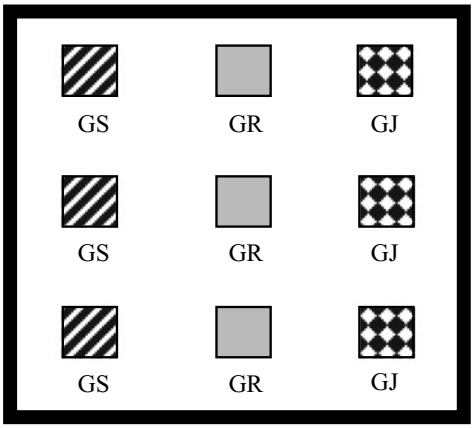

Fig. 2 Sample layout

Table 1 Instrumentation used for the data collection

Instrument	Measurement parameter	Accuracy
Thermal imager *TESTO 872*	Surface temperature	±2% (60 mK sensitivity)
HSETIN Temp./RH data logger	Ambient temperature	±0.6 °C or ±5%
	Relative humidity	±3%
Infrared radiometer *MI-210*	Average surface temperature	±0.5 °C
Automated weather station *Watch Dog 2000 series*	Wind velocity	±0.89 m/s or ±5%
Digital anemometer *Smart sensor AS810*	Wind velocity	±0.1 m/s or ±5%

two seasons. The two seasons compared in this study were: (1) time where sun path directly lies above which is from August to September 2019 and (2) November–December 2019 where ambient temperatures were comparatively recorded lower than the previous season.

The data were analyzed using IRSoft software by analyzing infrared thermal imagery, in order to identify the patterns of the thermal profile variations of the pavers. One-way ANOVA was performed at a 95% confidence interval to determine the significant differences of surface temperatures within the sample types. The differences in surface temperature data for two seasons were compared through independent sample t-test.

3 Results

Two main seasons were considered in the study as, Season 01 (S01); from August to September 2019 and Season 02 (S02); from November to December 2019. The mean Surface Temperatures and the temperature differences between two seasons are given in Table 2. The mean Surface Temperature variation along a day for the two seasons is shown in Figs. 3, 4 and 5 respectively.

As per Figs. 3, 4 and 5 and results of the independent sample t-test, the temperature variations of all the three pavers for both seasons showed temperatures within a similar range until noon. At noon in both seasons; Grey Smooth have reached 42.96–43.37 °C, Grey Rough 45.80 °C-47.97 °C, Grey Jagged 44.69 °C-47.55 °C with no significant difference shown between two seasons. However, after 12.00 pm, the peak temperatures of the paving blocks in Season 01 have shown higher values concerning Season 02. There is a significant difference of 6.71 °C within the two Seasons for thermal performance of block Grey Rough at 3.00 pm.

The data were analyzed using IRSoft software by analyzing infrared thermal imagery, in order to identify the patterns of the thermal profile variations of the pavers. One-way ANOVA was performed at a 95% confidence interval to determine the significant differences of surface temperatures within the sample types. The differences in surface temperature data for two seasons were compared through an independent sample t-test.

Furthermore, all the pavement types show significant differences in thermal performance for two seasons after 2.00 pm. Based on the results of the t-test, it is also evident that, for all the three pavers, there is a significant difference among the temperatures within seasons after 1.00 pm, after achieving the peak temperature. Therefore, it can be observed that even though there are no significant variations in heat gaining within the seasons for the pavers considered, the heat release within seasons have an impact on the pavement thermal performance and therefore contribute differently specifically for the night time UHI.

One-way ANOVA and Tukey Honest Significance Difference tests were conducted to assess whether there is a significant difference in the recorded surface temperatures for the three texture types in each hour separately in Season 02. Sample

Table 2 Comparison of surface temperatures for two seasons

Time	Surface temperatures (°C)					
	GS (n = 15)		GR (n = 15)		GJ (n = 15)	
	Season 01	Season 02	Season 01	Season 02	Season 01	Season 02
09.00	33.15	31.64	35.66	33.88	34.32	33.57
	1.51*		1.78*		0.75	
10.00	36.58	36.81	39.9	39.48	37.66	38.48
	−0.22		0.42		−0.82	
11.00	40.77	40.77	45.11	43.54	42.85	42.47
	−0.01		1.57		0.38	
12.00	43.37	42.96	47.97	45.80	45.38	44.69
	0.41		2.17		0.69	
13.00	45.72	44.39	50.83	47.21	47.55	46.01
	1.33		3.63*		1.54	
14.00	45.39	42.31	49.19	43.41	46.24	42.09
	3.07*		5.79*		4.15*	
15.00	41.22	37.64	44.55	37.84	42.71	37.19
	3.58*		6.71*		5.52*	
16.00	38.91	34.36	41.44	34.88	39.28	34.69
	4.55*		6.56*		4.60*	
17.00	34.67	32.43	36.41	32.78	35.25	32.74
	2.24*		3.62*		2.51*	
18.00	32.34	30.18	33.29	30.19	32.62	30.35
	2.16*		3.10*		2.27*	
19.00			32.51	29.51	31.94	29.68
			3.00*		2.27*	

*Statically significant different at 95% confidence interval ($p < 0.05$)

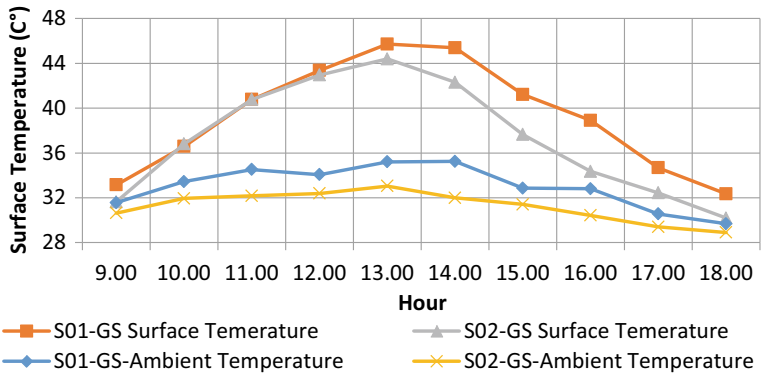

Fig. 3 Surface temperature comparison of grey smooth paver in two seasons

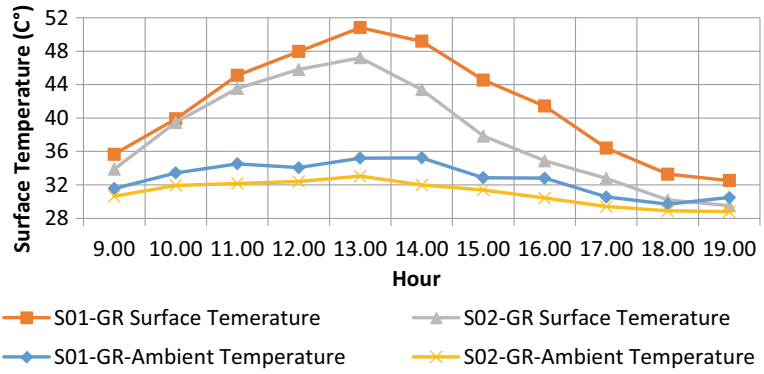

Fig. 4 Surface temperature comparison of grey rough paver in two seasons

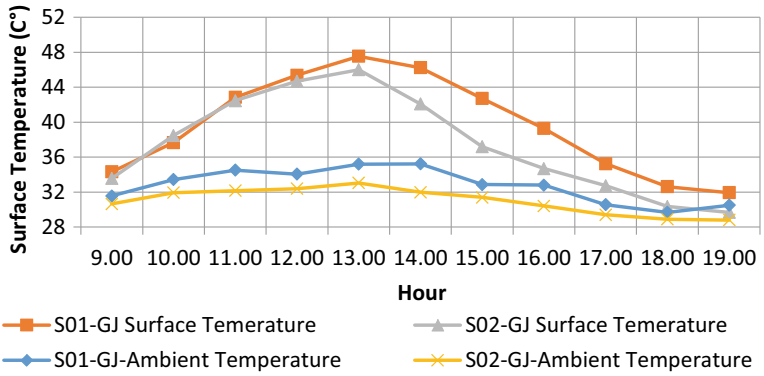

Fig. 5 Surface temperature comparison of grey jagged paver in two seasons

types without significant differences are put into a single subset. The sample type surface temperature mean value is given in the subset columns. If a sample type value is not in a particular subset, that particular sample is significantly different from all the other sample types in that particular subset.

It is further evident that, within the studied hours between 9.00 am and 7.00 pm, the ambient temperature was lower than the surface temperatures of pavement structures. The pavement structures absorb the heat continuously through conductance, convection, and radiation. The pavement structures are able to store the heat energy for a longer period as they are slow in heat emittance into the atmosphere. Therefore, during the daytime, the pavement structures are continuously heated up without the ability to cool down, on clear sky sunny days, having a higher surface temperature level than the ambient temperature (Tables 3, 4, 5 and 6).

The results of selected hours show that there is no significance difference in surface temperature among the sample types in the hour 6.00 am and 6.00 pm. However,

Table 3 Mean surface temperature subsets for 6.00 am

Type	Mean surface temperature (°C)
	Subset for alpha = 0.05
	1
Grey rough	24.6133
Grass paver	24.7533
Grey smooth	24.8067

Table 4 Mean surface temperature subsets for 11.00 am

Sample type	Mean surface temperature (°C)	
	Subset for alpha = 0.05	
	1	2
Grey smooth	41.0540	
Grey jagged	43.1932	43.1932
Grey rough		43.8083

Table 5 Mean surface temperature subsets for 1.00 pm

Type	Mean surface temperature (°C)	
	Subset for alpha = 0.05	
	1	2
Grey smooth	44.6220	
Grey Jagged	46.1294	46.1294
Grey rough		48.2159

Table 6 Mean surface temperature subsets for 6.00 pm

Type	Mean surface temperature (°C)
	Subset for alpha = 0.05
	2
Grey rough	30.1879
Grey smooth	30.1939
Grey jagged	30.3152

in the hours 11.00 am and 1.00 pm, there is a significance difference of 2.8 °C and 3.6 °C surface temperature respectively among the sample types Grey Smooth and Grey Rough.

4 Discussion

The season 01 considered in this study ranged from August 2019 to September 2019. The peak temperature gain for the pavers was higher compared to season 02 of November–December 2019. However, the thermal gain does not show a significant difference until the noon hours. This indicates that the thermal gain of pavers occurs equally in two seasons, however, in Season 01, the pavers heat up continuously at a higher rate than in Season 02 from 12.00 to 1.00 pm. Season 01 is from August to September where the sun is directly overhead of Sri Lanka [5]. This may have influenced the further heating of pavers during this period. Furthermore, after 1.00 pm, in both the seasons, the pavers showed a significant difference in thermal performance which could be also explained by this fact. However, the other environmental components may also absorb higher heat energy and obstruct the cooling down of pavements. There are no comprehensive studies done in Sri Lanka on the impacts of temporal changes for the UHI.

The significant differences shown in thermal performances for the selected two seasons of present study suggest that the utilization of pavements to mitigate UHI could be performed with a better understanding of its temporal variations. The study has further highlighted that there is no significant difference in the heating trends of pavements before 12.00 pm and the significant differences were recorded only after 12.00 pm. This information could provide assistance for landscape architects and other construction professionals in deciding the appropriate pavement types for different locations of the site considering the periods of pavements exposure to the sun.

According to the results among different textures, there is a distinguishable difference in surface temperatures between the smooth textured sample type and the jagged textured sample type in sample types. Furthermore, after 2 pm it can be identified that the surface temperatures are not showing much noticeable difference among the sample types. Different texture types have their unique solar energy reflectance characteristics. This characteristic allows the smooth textured sample type to reflect comparatively more solar radiation and prevent the increase of absorbance to the pavement structure. Therefore, the smooth sample type shows lower surface temperature levels. However, the texture characteristic is largely impacting at noon hours as it is identifiable in the graph. All the texture types cool down to a similar surface temperature level by 2 pm showing that the texture characteristic alone is not sufficient to cool down the sample types, faster. Previous studies suggest that smooth surfaces have a lower impact on UHI due to the higher albedo levels [10, 15, 17]. This has been suggested in reference to the fact that the smooth colors have higher albedo with high reflectivity. The current study also confirms this factor showing significantly lower temperatures in mid-day hours in smooth texture. This reflects that the consideration of texture type in the utilization of pavements is also significant to mitigate UHI.

Even though the present study can be used to draw conclusions on thermal performance seasonal variation of pavers for the better paver design in the future to achieve

the optimum thermal performance, further studies will be required with respect to some of the other factors which may influence the results. Some potential parameters that may contribute to the pavement thermal performance would be the neighboring effects such as the surrounding ambient differences due to built environment Land Use Land Cover (LULC) and the associated structures, other environmental and climatic factors [6].

5 Conclusion

There were no significant differences observed in heat levels until noon for the pavers considered in two seasons. However, the pavers showed a significant difference in heat release after 12.00 pm for both the two seasons considered in the present study. Therefore, it can be concluded that the pavement surfaces influence UHI in various intensities, which is defined by the seasonal climatic variations. It is further concluded that, within the two seasons compared for the current study area, within the period from August to September, the pavers affect the UHI effect at a higher level. This could provide insights to identify additional actions that are needed in pavement designing and construction for the reduction of UHI in the South-West Monsoon season (period of August–September) where the sun is right above the latitude of the case study ground. However, it should be noted that other factors such as anthropogenic heat levels are also vital for the thermal performance of pavements. Therefore, further studies can be recommended to identify different impacts of different other physical attributes of pavements, wind conditions, and other parameters alongside the seasonal variation.

Acknowledgements The research work was supported by the research grant No. ASP/01/RE/SCI/2018/45, funded by University of Sri Jayewardenepura, Sri Lanka.

References

1. Austroads (2007) Guide to pavement technology, part 4b: asphalt. Austroads Inc., Sydney, Australia
2. Balbo J, Severi A (2002) Thermal gradients in concrete pavements in tropical environment: experimental appraisal. Transp Res Rec J Transp Res Board 1809(1):12–22
3. Buyantuyev A, Wu J (2009) Urbanization alters spatiotemporal patterns of ecosystem primary production: a case study of the Phoenix metropolitan region, USA. J Arid Environ 73(4–5):512–520
4. Coppola E, Rouphael Y, De Pascale S, Moccia FD, Cirillo C (2019) Ameliorating a complex urban ecosystem through instrumental use of softscape buffers: proposal for a green infrastructure network in the metropolitan area of Naples. Front Plant Sci 10:410
5. Department of Meteorology (2019) Climate of Sri Lanka (Online). Meteo.gov.lk. Available at: http://www.meteo.gov.lk/index.php?option=com_content&view=article&id=94&Itemid=310&lang=en. Accessed 9 July 2019

6. Dissanayake D (2020) Land use change and its impacts on land surface temperature in Galle City, Sri Lanka. Climate 8(5):65
7. Jayasooriya V, Ng A (2013) Development of a framework for the valuation of eco-system services of green infrastructure. In: Proceedings of the 20th international congress on modelling and simulation, Adelaide, Australia, pp 1–6
8. Jopek D (2018) Water in the city. The development of permeable surfaces in urban areas. In: E3S web of conferences. EDP Sciences, p 00109
9. Li H (2012) Evaluation of cool pavement strategies for Heat Island mitigation, 389p
10. Li H, Harvey JT, Holland TJ, Kayhanian M (2013) Erratum: the use of reflective and permeable pavements as a potential practice for heat island mitigation and stormwater management. Environ Res Lett 8(4):112–113. https://doi.org/10.1088/1748-9326/8/4/049501
11. Liu X, Zhou Y, Yue W, Li X, Liu Y, Lu D (2017) Spatiotemporal patterns of summer urban heat island in Beijing, China using an improved land surface temperature. J Clean Prod 51:141–150
12. Livada I, Santamouris M, Niachou K, Papanikolaou N, Mihalakakou G (2002) Determination of places in the great Athens area where the heat island effect is observed. Theoret Appl Climatol 71(3–4):219–230. https://doi.org/10.1007/s007040200006
13. Martine G (2007) UNFPA State of world population 2007. United Nations Population Fund, New York, p 1
14. Padmanaban R, Bhowmik AK, Cabral P (2019) Satellite image fusion to detect changing surface permeability and emerging urban heat islands in a fast-growing city. PLoS ONE 14(1): e0208949. https://doi.org/10.1371/journal. pone.0208949
15. Radhi H, Assem E, Sharples S (2014) On the colours and properties of building surface materials to mitigate Urban Heat Islands in highly productive solar regions. Build Environ 72:162–172. https://doi.org/10.1016/j.buildenv.2013.11.005
16. Ranagala M, Estoque R, Murayama Y (2017) An urban heat island study of the Colombo Metropolitan Area, Sri Lanka, based on landsat data. Int J Geo-Inform 6:189. https://doi.org/10.3390/ijgi6070189
17. Richard C, Doré G, Lemieux C, Bilodeau JP, Haure-Touzé J (2015) Albedo of pavement surfacing materials: in situ measurements. In: Proceedings of the international conference on cold regions engineering, pp 181–192. https://doi.org/10.1061/9780784479315.017
18. Santamouris M, Papanikolaou N, Livada I, Koronakis I, Georgakis C, Argiriou A, Assimakopoulos DN (2001) On the impact of urban climate on the energy consumption of building. Solar Energy 70(3):201–216. https://doi.org/10.1016/S0038-092X(00)00095-5
19. United Nations, Department of Economic and Social Affairs, Population Division (2019) World urbanization prospects: the 2018 revision (ST/ESA/SER.A/420). United Nations, New York
20. Wu J, Chow K, Fung J, Lau A, Yao T (2010) Urban Heat Island effects of the Pearl River Delta city clusters—their interactions and seasonal variation. Theoret Appl Climatol 103(3–4):489–499
21. Zhang B, Wang B, Shen L (2011) Influence of raw materials on the preparation of terracotta panel. Mater Sci Forum 695:267–270. https://doi.org/10.4028/www.scientific.net/MSF.695.267

Discharge Observations Assimilation to Improve Flood Prediction Skills

W. H. M. Y. D. Bandara, K. H. S. Dinelka, and N. G. P. B. Neluwala

Abstract Flood is one of the most threatening disasters affect the people not only in Sri Lanka but also in the world. Data assimilation is a state-of-the-art technique which can provide accurate analysis in modern day. Accurate flood prediction is essential to reduce damages which are caused by floods. On that topic Sri Lanka is in a very poor position. As a reason for that not using Data assimilation much in Sri Lanka may be have a significant factor. Ensemble Kalman Filter is a popular Data assimilation method widely used to incorporate observation data to model forecast. Most of the research based on this area was done by using MIKE 11 application. Kelani River is one of the major rivers that was affected by floods to the people and properties in past few decades. Study area of the research is selected from Glencourse to Hanwella of Kelani River. This study found that discharge observations assimilation is very effective in updating the entire model to improve flood hydrograph at Hanwella by using MIKE 11 and real data of flood events. Before doing model simulations, calibration was done by using data of May of 2016. Then to demonstrate the Data Assimilation system, multiple 1D simulations with different scenarios were carried out to get the results. Final results show the discharge observation assimilation is very effective to improve flood prediction skills.

Keywords Data assimilation · Ensemble Kalman filter · MIKE 11 · Kelani river

1 Introduction

Flooding is the covering of dry area (normally) with a large water body and also flood is one of the most destructive and frequent natural disaster threatening peoples' lives and properties in the world. Due to floods, thousands of people die and be helpless throughout the world. Flood warning and forecasting systems can be very helpful to reduce the effects of flooding by giving time to the people to be evacuated from the areas at risk and to move vehicles and personal belongings to safety [10]. The global flood losses have grown worldwide to the level of billions of US dollars per year

W. H. M. Y. D. Bandara (✉) · K. H. S. Dinelka · N. G. P. B. Neluwala
Department of Civil Engineering, University of Peradeniya, Peradeniya, Sri Lanka

R. Dissanayake et al. (eds.), *ICSBE 2020*, Lecture Notes in Civil Engineering 174,
https://doi.org/10.1007/978-981-16-4412-2_12

[4]. Strategies for reducing flood losses by flood protection and management include (a) modifying sensitivity to flood damage which is taking actions before a flood (b) modifying flood waters and (c) modifying the impact of flooding (during and after flood). From all of these taking actions before a flood is the most economical and effective action. So that flood forecasting systems play a major part in flood controlling measurement.

Due to the lack of flood prediction and warning systems, the damages happening are no different in Sri Lanka. For an example there were reported 21 deaths, 150,000 people misplaced and 4900 damages occurred due to flooding in Sri Lanka 2017 [11]. There were some major flood events occurred in couple of river catchment areas in last few years. Kelani, Kalu, Gin, Nilwala are some of the mostly flood effected river catchment areas in Sri Lanka. Even though Sri Lanka has some flood prediction and warning systems Data Assimilation method hardy used in any of these system.

Flood protection measures can be divided in to two categories as structural (hard) and non-structural (soft). As structural defences dikes, dams, and flood control reservoirs, diversions, flood ways and improving channel conveyance capacity (widening, deepening, realignment and bank protection) etc. Flood forecasting and warning, watershed management, insurance, awareness programs etc. fall in to the non-structural category. Among them, flood forecasting and warning is very important. Flood prediction based on mathematical modelling which allows to convert information on past and present rainfall, discharge of the river into a river flow forecast. It helps to reduce the damage done by floods by giving a head start to the public to act before the flood level increases to a critical level [7].

Data assimilation is a state of-the-art method to improve model results considering the observation and numerical model errors. DA has already been amply demonstrated in meteorology and oceanography over the past decades. Data assimilation in hydrological model can be used for three main purposes. They are improving soil moisture states, improving streamflow predictions and optimizing models' parameters. It can be carried out by analyzing soil moisture or streamflow data [12, 13]. For example, Reichle et al. [8] assessed the performance of an Extended Kalman Filter (EKF) and an Ensemble Kalman Filter (ENKF) for soil moisture analysis. Rüdiger et al. [9] used a variational data assimilation approaches for assimilating discharge data to retrieve root zone soil moisture. Auber et al. [1] developed an ENKF assimilation system for improving discharge flow prediction over a Seine river sub-basin. Clark et al. [2] used the EnKF in which sates in a distributed hydrological model were updated using discharge observation data. Madsen et al. [5] presented water level and discharge data assimilation in the MIKE 11 Flood forecasting system using EnKF.

This study is a combination of using real data, idealistic data which is presents that discharge observations assimilation is very effective to updating the entire model to improve flood hydrograph at Hanwella by using MIKE 11 and real data of flood events in Kelani river.

2 Study Area

Kelani river is the fourth largest (145 km) rivers in Sri Lanka. It flows through or borders the Sri Lankan districts of Nuwara Eliya, Ratnapura, Kegalle, Gampaha and Colombo [3]. The Kelani river catchment receives an average annual precipitation of 3,718 mm and generating a surface runoff volume of about 8600 million m3 of which nearly 65% discharges into the Indian Ocean [6].

Major portion of the rainfall is received during the South-West monsoon period. However, the catchment receives considerable amount of rainfall during the North-East monsoon and inter-monsoonal periods too. Owing to the heavy rainfall and the steep terrain of the upper catchment, the lower basin of the Kelani River is subjected to heavy floods. In the recent past there were severe floods in Kelani river such as 2016, 2017 and 2018. So that is why Kelani river chosen as the study area.

In the present study, from Glencourse to Pahala Hanwella (18 km) of Kelani river was selected considering the availability of rainfall, cross section data, water level, discharge data and also, that part of river does not have many considerable tributaries.

3 MIKE 11 Ensemble Kalman Filter

According to Madsen et al. [5], The Kalman filter data assimilation algorithm is based on a stochastic representation of the model dynamics and the measurements. The numerical scheme of the MIKE 11 and MIKE FLOOD modelling systems can be written in a state-space form

$$x_k = \Phi(x_{k-1}, u_k) \tag{1}$$

where $\Phi(.)$ is the model operator representing the numerical scheme of MIKE FLOOD, x_k is the state vector representing the state of the modelled system at time step k, and u_k is the forcing of the system. The state vector includes discharges and water levels in the computational grid of the river system as well as depth-averaged x and y velocities and water levels in each potential flood point of the grid representing the flood plain. The forcing includes different boundary conditions for the river model (water level, discharge, rainfall-runoff, rating curves) and possible wind forcing. For modelling the uncertainty of the system, it is assumed that model errors are related to errors in the forcing terms

$$x_k = \Phi(x_{k-1}, u_k + \varepsilon_k) \tag{2}$$

where ε_k is the model error. The model error process is described by defining the model error variance as well as the temporal and spatial correlation structure. If a correlated system noise is defined, an augmented state vector formulation is adopted in the Kalman filter. This formulation provides not only an update of the model state

x_k but also an update of the (erroneous) model forcing. The data assimilation system allows assimilation of flux and water level measurements in the river system and on the floodplain. This is formulated in the measurement equation

$$z_k = C_k x_k + \eta_k \tag{3}$$

where z_k is the vector of measurements, C_k is a matrix that describes the relation between measurements and state variables (a mapping of state space to measurement space), and η_k is the measurement error. This error is assumed unbiased with covariance matrix R_k.

The Kalman filter is a succession of two steps. First, the model is employed to issue a forecast, and then the observed data are meld with the forecast to provide an updated state (analysis step). Denote by x_k^f a one-step ahead forecast of the state of the system, according to the model operator $\Phi(.)$, cf. Eq. (1) and P_k^f the covariance matrix of this forecast. The Kalman filter update of the state vector and the error covariance matrix is given by,

$$x_k^a = x_k^f + K_k\left(z_k - C_k x_k^f\right) \tag{4}$$

$$P_k^a = P_k^f - K_k C_k p_k^f \tag{5}$$

where K_k is the Kalman gain matrix,

$$K_k = P_k^f C_k^T [C_k P_k^f C_k^T + R_k]^{-1} \tag{6}$$

which serves as a weighting function of model forecast and measurements. In Eqs. (4)–(6) superscripts f and a refer to, respectively, forecast and analysis (or update). Finally, those equations extend to Ensemble Kalman Filter.

4 Methodology

For the MIKE 11 application cross section data, Q–h curves, water level data and discharge data need as input data to the model. Then river discharge, Q–h curves and water level data were collected from the Irrigation Department. Both 2016 May and 2017 May flood events were selected for this study. Cross section data was collected from surveying department. Then River network was modelled using MIKE 11.

It is required to calibrate and validate the model to the study area from Glencourse to Pahala Hanwella because the model parameters vary according to the river. River calibration and validation processes were done using data 2016 and 2017 respectively. Three sets of scenarios were done for each analysis.

Scenario 1 (S1)—Reference simulation: model with real boundary conditions.

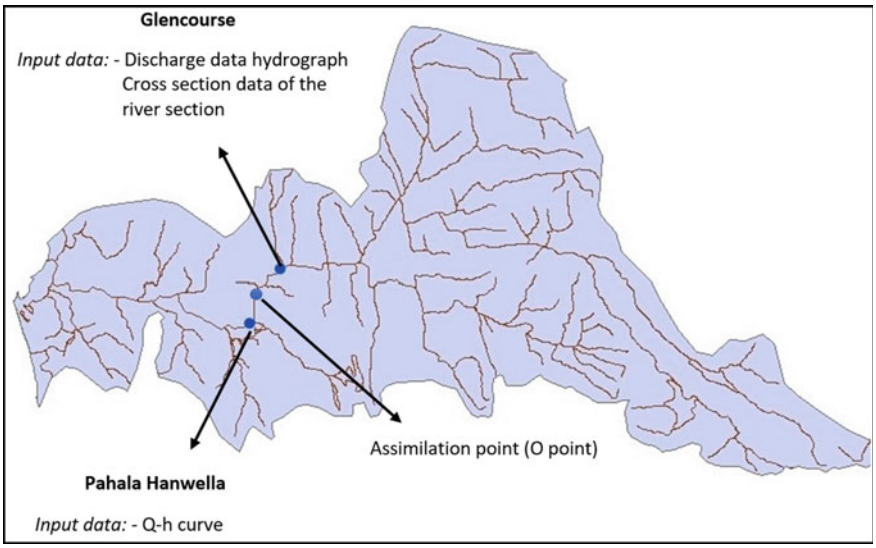

Fig. 1 Kelani River basin

Scenario 2 (S2)—Modelling with wrong boundary condition data (WBC) which is with artificial errors and without DA.
Scenario 3 (S3)—Modelling S2 with observations of O point which are with artificial errors and with DA (Fig. 1).

The observations were created idealistically from the reference simulation due to lack of observations stations in this part of the tributary shown. For this discharge data from point O was extracted from the reference simulation (S1). Then these observations were utilized in the data assimilation simulation.

Then S2 was run and got the discharge at Hanwella. However, discharge data was different from real discharge due to wrong boundary conditions expected. Then the model was updated with Ensemble Kalman Filter (data assimilation part) with wrong boundary conditions. So, an assimilation point O was assigned. For that extracted discharge data at O point was given. In data assimilation editor standard deviations of assimilation points and boundaries can be given.

Then S3 was run and improved results at Hanwella were obtained. So, by changing those values can get the observation discharge at Hanwella. To do that two model errors have to assigned in Data assimilation editor. They are observation (assimilated) data error and error with upstream WBC. Those errors were found using trial and error method for each analyses. Then they were introduced to the model setup.

Two DA analysis were done to discuss the importance of DA to improve flood prediction skills. Ensemble size was given as 50 for these analyses.

1. DA analysis 1—S2 and S3 with having missing discharge period for upstream WBC and correct assimilated data.

2. DA analysis 2—S2 and S3 with having random uniform error for both upstream WBC and assimilated data within the range of ±10% to both actual BC and assimilated data.

5 Results

DA analysis 1.

See Fig. 2.

As in the methodology S2 was run using WBC for the upstream with having missing discharges compared to the correct BC. Then S3 was done by updating with EnKF using correct assimilated data which was extracted from S1 and got some interesting results. Model errors were introduced at the upstream (WBC) with a resulting standard deviation (SD) of 10% and at the O point with a resulting SD of 0.1%. Figure 2 is shown the compared results at Hanwella for third analysis respectively, the reference simulation (Blue curve), the simulation with WBC (Yellow curve) and the EnKF update (dashed Black curve). According to the Fig. 2, can see the S1 and S3 resulted hydrographs are almost same. So, Black curve lies on the Blue curve as in the Fig. 2. Also, according to the NSE and RMSE values of Table 1 it is very effective to update with EnKF.

DA analysis 2.

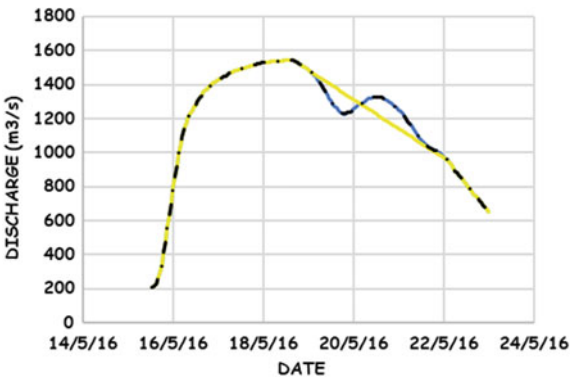

Fig. 2 The comparison of resulted hydrographs at Hanwella, respectively, from three scenarios

Table 1 Comparison of RMSE and NSE values of S2 and S3 with S1 for each analysis

Analysis	Parameter	S2	S3
DA analysis 1	RMSE (m^3/s)	49.29	0.29
	NSE	0.8447	0.999
DA analysis 2	RMSE (m^3/s)	24.38	18.35
	NSE	0.9232	0.9541

Fig. 3 The comparison of resulted hydrographs at Hanwella, respectively, from three scenarios

See Fig. 3.

Usually both upstream boundary and the assimilated discharge data could have errors in real situation. So, in this analysis S2 was done using WBC for the upstream with having random error within the range of $\pm 10\%$ to the correct BC. Then S3 was done by updating with EnKF using assimilated data with having random error within the range of $\pm 10\%$ to the correct assimilated data from S1 and got the resulted hydrographs. Model errors were found and introduced at the upstream and at the O point. Figure 3 is shown the comparison of simulated hydrographs at Hanwella from fourth analysis respectively, the reference simulation (Blue curve), the simulation with WBC (Red curve) and the EnKF update (dashed Black curve). According to the Fig. 3 reference and EnKF update graphs are little bit different due to incorrect inputs. But, according to the NSE and RMSE values of Table 1 it is very effective to update with EnKF even though there are observation errors in the both upstream and the O point.

6 Conclusions

A data assimilation system was implemented in MIKE 11 modelling system and tested for two set of analysis which were mentioned under the results section. The data assimilation system is based on the ensemble Kalman filter allows assimilation of discharge observations showed improved results. The developed model setup can be used to improve discharge data along the Kelani River from Glencourse to Pahala Hanwella when having discharge observations at a O point in addition to other input data.

According to the DA analysis 1, it can be get the almost correct flood hydrograph at downstream using DA when having missing period of discharge data for upstream. Because NSE and RMSE values were found as 0.9990 and 0.29 respectively. According to the DA analysis 2, it is possible to improve the flood hydrograph at downstream when having errors for both assimilation data and upstream

boundary condition. Because NSE and RMSE values were found as 0.9541 and 18.35 respectively.

Finally, the results of above analysis were illustrated that the data assimilation system is very effective in updating the entire model using discharge observations from only one location to improve the flood prediction in the river network.

Acknowledgements Author wishes to acknowledge the Department of Irrigation, Centre for Urban Water and DHI group for giving valuable input data and guidance to standardize the paper.

References

1. Aubert D, Loumagne C, Oudin L (2003) Sequential assimilation of soil moisture and streamflow data in a conceptual rainfall–runoff model. J Hydrol 280(1–4):145–161
2. Clark MP, Rupp DE, Woods RA, Zheng X, Ibbitt RP, Slater AG, Schmidt J, Uddstrom MJ (2008) Hydrological data assimilation with the ensemble Kalman filter: Use of streamflow observations to update states in a distributed hydrological model. Adv Water Resour 31:1309–1324
3. De Silva MMGT, Weerakoon SB, Herath S, Ratnayake UR, Mahanama S (2012) Flood inundation mapping along the lower reach of Kelani river basin under the impact of climatic change. Engineer XXXXV(2):23–29
4. Hallegatte S, Green C, Nicholls RJ, Corfee-Morlot J (2013) Future flood losses in major coastal cities. Nat Clim Chang 3(9):802–806
5. Madsen H, Rosbgerg D, Damgard J, Hansen FS (2003) Data assimilation in the MIKE 11 flood forecasting system using Kalman filtering. In: Water resources systems—hydrological risk, management and development. Proceedings of symposium IlS02b held during IUGG2003 al Sapporo. vol 281. IAHS Publication, July 2003, pp 75–81
6. Mahagamage MGYL, Manage PM (2014) Water quality index (CCME-WQI) based assessment study of water quality in Kelani river basin, Sri Lanka. In: ENRIC (2014) The 1st environment and natural resources international conference. The Sukosol Hotel, Bangkok, Thailand, Nov 2014, pp 200–204
7. Nandalal KDW (2009) Use of a hydrodynamic model to forecast floods of Kalu river in Sri Lanka. J Flood Risk Manag 2:151–158
8. Reichle RH, Walker JP, Koster RD, Houser PR (2002) Extended versus ensemble Kalman filtering for land data assimilation. J Hydrometeorol 3:728–740
9. Rüdiger C, Walker JP, Kalma JD, Willgoose GR, Houser PR (2005) Root zone soil moisture retrieval using streamflow and surface moisture data assimilation in nested catchments. In: MODSIM05—international congress on modelling and simulation: advances and applications for management and decision making, proceedings, pp 1458–1464
10. Sene K (2008) Flood warning, forecasting and emergency response. Springer, Berlin, 307p
11. Sundaytimes, May 2018. http://www.sundaytimes.lk/180527/news/21-die-150000-affected-by-flood-havoc-296126.html. Visited 16 June 2020
12. Thirel G, Martin E, Mahfouf JF, Massart S, Ricci S, Habets F (2010) A past discharges assimilation system for ensemble streamflow forecasts over France—part 1: description and validation of the assimilation system. Hydrol Earth Syst Sci 14:1623–1637
13. Thirel G, Martin E, Mahfouf JF, Massart S, Ricci S, Habets F (2010) A past discharge assimilation system for ensemble streamflow forecasts over France—part 2: impact on the ensemble streamflow forecasts. Hydrol Earth Syst Sci 14:1639–1653

A Device to Determine the Panel Orientation for Best Annual Solar Energy Generation at a Selected Location

S. U. M. Jagoda, W. M. C. Dilanga, D. S. D. S. Jarathne, H. K. G. Punchihewa, V. P. C. Dassanayake, and H. P. Karunathilake

Abstract Within the past few years, solar photovoltaic (PV) power generation has gained popularity along with sustainable concepts around the world. The low efficiency of PV systems could be identified as a leading drawback of energy conversion. Panel tilt angle and direction directly affect the amount of irradiance incident on solar panels, governing the amount of energy generated. Assuming ideal conditions, fixed panels are installed to face the equator, as used in common practice, while the tilt angle is kept equal to the latitude of the location. Due to the uniqueness of geographic and weather conditions in different locations, the irradiance patterns may deviate from the ideal. Thus, the optimum panel orientation may differ from conventional practise. Thus, the objective of this study was to introduce a universal method which can determine the location-specific optimum orientation of solar panels. The in-situ weather and irradiance data were captured for a period of time (approx. 30 weeks) at a given location. In addition, weather data at the location was collected for the past few years via relevant authorities. A mathematical model was developed to extrapolate the irradiance incident on various orientations using available data as a guideline for an average year. The orientation that is expected to capture the highest amount of irradiance was determined as the optimum orientation. Then, a case study was carried out following the above methodology at the department of mechanical engineering, University of Moratuwa. The analytical results showed that the overall efficiency of the PV system was increased by 0.4% compared to that obtained with the generic tilt (i.e. 7°) setup. The efficiency of the entire system could be increased without an additional cost if such analysis is conducted prior installation. The analysis would be more appropriate for large scale solar farms rather than domestic installations.

Keywords Solar PV · Panel orientation · Optimum generation · Irradiance modelling · Fixed orientation

S. U. M. Jagoda (✉) · W. M. C. Dilanga · D. S. D. S. Jarathne · H. K. G. Punchihewa · V. P. C. Dassanayake · H. P. Karunathilake
Department of Mechanical Engineering, University of Moratuwa, 10400 Moratuwa, Sri Lanka
e-mail: himank@uom.lk

R. Dissanayake et al. (eds.), *ICSBE 2020*, Lecture Notes in Civil Engineering 174,
https://doi.org/10.1007/978-981-16-4412-2_13

1 Introduction

The use of renewable resources for harvesting energy has gained increasing attention all over the world in the recent times. Greenhouse gas emissions, depleting fossil fuel resources, and the socio-economic impacts of conventional energy supplies have all contributed to this growing popularity of renewables [9]. In the renewable sector, photovoltaic (PV) power generation has captured the attention of many researchers who are involved in improving renewable energy utilization. The abundant availability of the resource, zero carbon footprint in operation, and lower maintenance requirements are among the major reasons for solar energy to be more popular.

The high cost of installation per single unit of power generated is one of the most significant challenges faced by solar energy generation. The initial cost per single unit of generated power could be minimized if the solar panel efficiency is increased. Hence, the power generation for a given installation capacity can be further increased without actually increasing the economic investment. Studies have been conducted with the aim of increasing the power generation and thus the efficiency of a solar panel [5]. Increasing efficiency falls mainly under three main categories: increasing the efficiency of the solar panel itself, cooling the panel, and increasing the amount of solar irradiance incident on the solar panel [5, 11, 15]. Among them, increasing the amount of incident solar irradiance is the method most commonly used [1, 2]. The irradiance incident angle is adjusted as recommended to increase the power generation.

Currently, solar panel installation is mainly based on three techniques, namely fixed tilt angle, single-axis tracking, and dual-axis tracking [6, 16]. Some technical and economic conditions such as wind loads, site topography and soil conditions, and most importantly, the higher capital costs restrict the usage of single and dual-axis tracking [12]. Additionally, due to the rapid price decrement of solar panels, investors have tended to generate the same amount of power utilizing more panels rather than installing complicated systems with higher efficiencies. Therefore, the demand for the fixed tilt angle panels continues steadily.

There are several mathematical models developed to determine the optimal fixed tilt angle for the PV system [1, 4]. In most cases, the tilt to the horizontal is set to be equal to the latitude of the location, as the "latitude tilt" is generally accepted to be the best orientation to maximise the incident irradiation [7]. The panel is fixed so that it faces the equator all the time for best energy generation. This means that in the northern hemisphere the panel should be south-facing, and for the southern hemisphere, it should be north-facing [4].

For the above conclusions, it has been assumed that the irradiance intensity pattern is independent of the location. Several studies have shown that this assumption is implausible since the amount of irradiance at a location may depend on the weather parameters which are unique to the location. The actual optimal orientation can vary due to shading from adjacent modules, the difference between summer and winter months, and other locational parameters [7]. Thus, research has been conducted in several locations around the world to determine the optimum orientation to capture

the maximum amount of irradiance on solar panels. Since these location-based methods are identical and time-consuming, a universal method to determine the optimum orientation is highly admired.

The objective of this study is to propose a universal method to determine the best panel orientation for maximised power generation at a selected location. The existing methodologies to determine the location-specific optimum orientation were analyzed with respect their strengths and weaknesses. In this study, the irradiance level for the location was determined using mathematical models and captured data. Then the optimum orientation was determined based on the results of the developed mathematical model. A case study was carried out for a site location in University of Moratuwa, Sri Lanka (6.79° N, 79.90° E) to demonstrate and validate the study outcomes. The feasibility of following this method for installing solar systems was analyzed in economical and technical terms using a decision support framework. These findings will be of particular use to the PV industry in regions with high solar energy potential to gain more benefits from the available resource.

Many experiments have been conducted by several researchers to determine the optimum tilt angle for a certain location [8]. These experiments have been conducted almost all over the world considering several models to evaluate the irradiance. The methodologies have used measured values supported by the theoretical models as well.

Research has been conducted in Bilecik, Turkey, to determine the optimum tilt angle on location [8]. A mathematical model was developed using MATLAB, which determines the optimum tilt angles for each month, each season and the entire year. An experimental setup was implemented, containing six solar panels at fixed angles from 10° to 60° at increments of 10°, to measure data for May, June, July, and August. By optimizing the experimental values, it has been determined that 10° would be more optimum. Compared to the values obtained for each month, experimental values show an approximated deviation of 11°. It was finally concluded that the environmental factors such as dust, temperature, and dirt have to be taken into consideration when determining the optimum orientation [8].

Danny Li and Tony Lam have conducted a research considering the sky as a dome with 145 small patches [14]. Here, the irradiance incident on an inclined surface has been calculated as an integration of the irradiance caused by each patch. The optimum tilt angle for the location in Honk Kong had been determined to be around 20° which differs by 3° from its latitude, 23.40°.

A similar research has been conducted in Canada have attempted to determine the optimum orientation in Ontario considering the weather data from four weather stations. Power generation data has been gathered for 130 different configurations and the optimum orientation was determined based on captured data. These measured values have been plotted as in Fig. 1. This research also shows that the tilt for optimum generation differs by 7° to 9° from the latitude in Ottawa and Ontario respectively. The reason for this is concluded as the climate variation which affects the behaviour of irradiance [17].

A research had been done in Kerala, India, to determine the optimum tilt angle for each month, each season and for the entire year [4]. The optimum tilt angle has

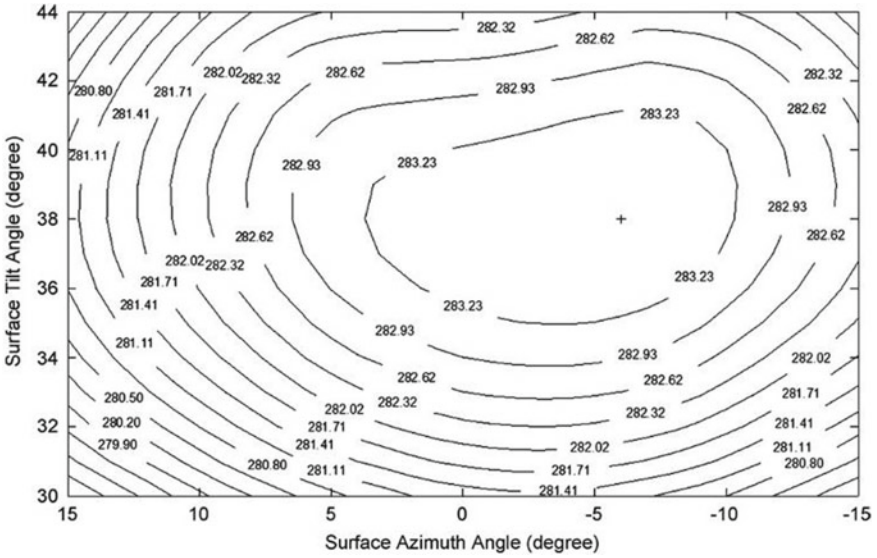

Fig. 1 Orientation versus generated energy for Ottawa [17]

been calculated in several methods based on geographical factors, clearness index and declination angle. Each formula used in determining optimum tilt contains with polynomial functions of each considered factor. This research reveals that a small deviation in tilt angle of 5° may result a power loss of 2% or more.

A research has also been conducted in Madinah, Saudi Arabia for optimizing the tilt angle considering the measured data and theoretical models. Global irradiance, diffuse irradiance, direct normal irradiance, air temperature and relative humidity has been collected from 1998 to 2002 with 5 min time intervals. A second order polynomial function as a function of tilt has been fitted to the data set and the optimum tilt has been calculated by differentiating the polynomial function. Suggested tilt angle for Madinah has been determined as 23.5° where the latitude of the location was 24.5° [1].

Researchers have shown that the PV module temperature and humidity are inversely proportional to the power generated by a solar panel [3, 13]. The amount of irradiance shows a strong relationship to the amount of energy generated. Even the high irradiance level would cause to increase temperature of the panel, still its worthy to increase the amount of irradiance incident on the panel [10]. The correlation between altitude and power generation is also positive since much irradiance is captured by the panels at higher sea level.

2 Research Gap

Based on the above literature review, it was identified that most of the studies have mainly focused on optimizing the power generation depending either on theoretical models or on captured data. There are few major deficiencies that could be seen in these methods.

- The time taken to determine an optimum orientation at a given locations is very high. The data has to be captured for a year and then the orientation is determined by comparing the generated power. Thus, it takes almost a year for the entire process [1].
- Under existing method, only the weather pattern of the considered year is taken into consideration. The weather pattern for that certain year may deviate from the average weather pattern of the location. Thus, there is an uncertainty in the determined orientation [14].
- Usage of number of solar panels throughout a year could be identified as another weakness in the existing methods. Several panels need to be fixed in different angles which are not the optimum orientation [8].
- The research based on measured data are specific to the considered location. Therefore, no universally applicable method has been developed to date.
- In addition, not all the factors that affect energy generation (such as environmental conditions, shading, location) are integrated into mathematical models when predicting the optimal orientation.

Thus, it can be concluded that a method that is universally applicable and also integrates all the pertinent parameters instead on only considering a few of them is missing in the existing knowledge base. This gap needs to be addressed in developing a comprehensive method for determining optimal PV panel orientation.

3 Methodology

Initially, weather parameters such as global irradiance, diffuse irradiance, direct normal irradiance, air temperature and relative humidity were identified as the parameters that impact the panel efficiency and energy generation through the literature. This was followed by experimental data collection and mathematical modelling to determine the best orientation. The entire process followed in this experiment is depicted in Fig. 2.

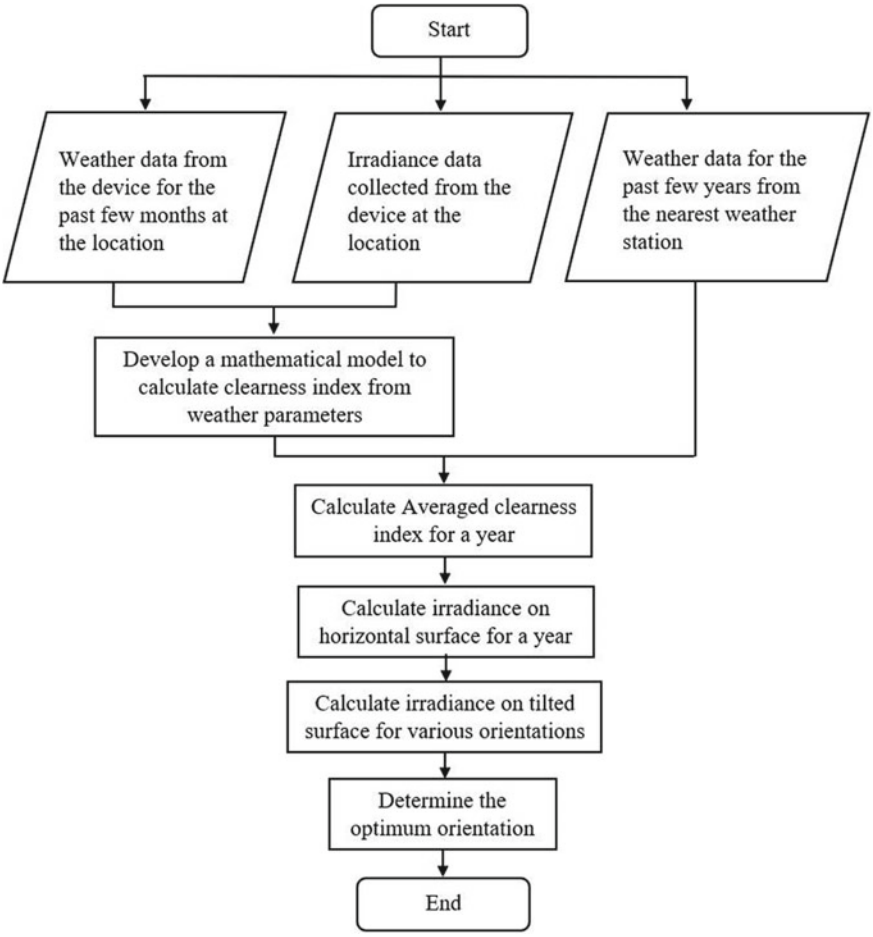

Fig. 2 Process flow chart

3.1 Collecting Data and Determining Parameters to Be Considered

To analyse the power generation patterns which are unique to a location, it is necessary to capture in situ data. Humidity level, temperature and irradiance intensity were measured in 5 min time intervals. Additionally, the power generated by a solar panel at various angles were measured. For that, a two-axis solar panel was utilized to measure the amount of power generated. A stepper motor was used to change the azimuth angle and a linear actuator was used to manipulate the tilt angle as required. The 3D model of the fabricated device is depicted in Fig. 3.

A solar panel was used to measure the voltage values at various orientations and hence validate the mathematical model. An Arduino-based data logger was developed

Fig. 3 Fabricated device

to record the generated voltage, current, and power. The device was installed with the following sensors to capture data at the Department of Mechanical Engineering, University of Moratuwa for the first three months of 2019.

1. Voltage sensor
2. ACS 712 Current sensor
3. DHT11 Humidity sensor module
4. DS18B20 temperature sensor
5. Pyranometer.

In addition, weather data for the past 4 years was collected from the department of meteorology. Weather data that was captured for cloud coverage, minimum and maximum temperature, minimum and maximum humidity and rainfall was collected. In this case study, the data was collected from the Ratmalana station (the nearest weather station to the University of Moratuwa).

The clearness index values were calculated for each irradiance data logged with 5 min time intervals for a period of 30 weeks. The variation of clearness index (K_t) with each weather parameters were analysed using the data collected at the location to identify the parameters to be considered for the mathematical model. The correlation coefficient between irradiance and each of the weather parameters were calculated. The parameters which showed the highest correlation with irradiance were taken into consideration in this study.

3.2 Developing the Mathematical Model to Calculate Clearness Index

Initially, a polynomial equation was developed to calculate the clearness index value using *Jupyter Notebook* (a web-based, interactive computing notebook environment

using python) taking the weather parameters as variables. The clearness index values and the weather data collected at that location were used to develop this equation. The equations were developed for zeroth degree to 5th degree. Since the models displayed an acceptable level of accuracy under a 4th degree polynomial equation, and no significant development in accuracy was shown for higher degree functions, this form was selected for modelling.

The obtained data for the past few years were averaged for one year so that the irradiance patterns for an indicative year could be analysed. After the model to calculate the clearness index was developed, the values for the clearness index were computed using available weather data. Thus, the clearness index values for an average year was obtained.

3.3 Developing the Mathematical Model to Determine Optimum Orientation

After developing the mathematical model to calculate the clearness index value, a mathematical model that calculates the amount of irradiance incident on a tilted surface was developed. Hence, the orientation which the maximum amount of irradiance incident could be determined.

In mathematical modelling, solar irradiance is considered to be caused by three major components [18],

1. Beam irradiance
2. Diffuse irradiance
3. Ground reflected irradiance.

Several models are available for calculating the beam and diffuse irradiance components incident on a horizontal surface developed by researchers. Most of the models were polynomial functions of the clearness index. Several models were developed to calculate each component of irradiance separately.

The models taken into consideration for calculating the beam component are mentioned below.

1. Louche's model
2. Maxwell model
3. Vignola and McDaniel's model.

Then the following existing models to calculate the diffuse fraction were used to determine the diffuse fraction of irradiance incident on a horizontal surface:

1. Lam and Li model
2. Erb's model
3. Chandrasekaran and Kumar model
4. Orgill model
5. Reindl-1 models.

3.3.1 Developing Models to Calculate the Amount of Irradiance Incident on a Horizontal Surface

Determining the most appropriate model to calculate each irradiance component was critical since it was unable to measure each component with the available equipment. Thus, each model to calculate the beam component was combined with each model to calculate the diffuse component. Then, the summation of irradiance components was compared with the measured value. The combination that gave the minimum error values were chosen as the most appropriate model combination for further processing.

Next, the measured and calculated irradiance values were plotted. Even though the selected combination gave the minimum error value, still the calculated irradiance values were much lower than measured ones under both clear and overcast sky conditions. Therefore, it was decided to multiply each irradiance component to get more accurate modelling values. The beam component and diffuse components were multiplied by a factor (C_b, $C_d > 1$) and then the coefficient that gave the minimum error was chosen for modelling purposes.

$$\boldsymbol{Beam\ Irradiance = C_b \times Beam\ irrdiance\ obtained\ from\ model} \quad (1)$$

$$\boldsymbol{Diffuse\ Irradiance = C_d \times Diffuse\ irradiance\ obtained\ from\ model} \quad (2)$$

Then the most appropriate C_d and C_b values were determined.

3.3.2 Developing Models to Calculate Irradiance Incident on Tilted Surfaces

After determining the most appropriate model for each component, the amount of irradiance incident on an inclined surface was determined. The ratio between the irradiance on an inclined surface, to the irradiance on a horizontal surface (R_θ) was calculated.

$$\boldsymbol{R_\theta = \frac{Irradiance\ incident\ on\ inclined\ plane}{Irradiance\ incident\ on\ horizontal\ plane}} \quad (3)$$

The equation to determine the beam irradiance component incident on an inclined surface was based on geometry. Hence, the error incurred was minimum. Still, the models had to be calibrated with the measured data.

There were several models used to determine the diffuse component incident on an inclined surface. Therefore, the best model had to be selected using statistical analysis. Since R_θ values have to be equal to one when the tilt angle is given as zero, the models that returned the values closer to one were selected. (R_θ values were

calculated for each model providing the tilt angle is equal to zero. The model which returns values closer to one was selected as the most appropriate model to be used further.)

Bugler's model gave the minimum error value for a horizontal surface. Thus, it was selected to be used for further reference. Following are the finalized models to be used:

For beam irradiance,

$$I_{b\theta} = \frac{\cos(\theta) I_b}{\cos(\varphi)\cos(\delta)\cos(\omega) + \sin(\varphi)\sin(\delta)} \tag{4}$$

For diffuse irradiance,

$$I_{d\theta} = \left(\frac{1 + \cos(\beta)}{2}\left(I_d - 0.05\frac{I_{b\beta}}{\cos(\theta_Z)}\right)\right) + 0.05 I_{b\beta}\cos(\theta) \tag{5}$$

3.4 Model Validation

The sum of absolute errors was calculated for each model developed using measured values. It was not possible to validate the models where the actual measured values were unavailable. Therefore, the correlation coefficient between the measured voltage and calculated irradiance was calculated.

4 Results

4.1 Parameters to Be Considered

The correlation coefficient between each weather parameter and clearness index values were calculated. The correlation coefficient values are shown in Table 1.

The results show that the cloud coverage, minimum atmospheric temperature and minimum relative humidity for a given day shows the highest amount of correlation with the clearness index values.

Table 1 Correlation coefficient of parameters with K_t

Weather parameter	Correlation factor with K_t
Rainfall	−0.271
Cloud coverage	−0.692
Maximum relative humidity	−0.131
Minimum relative humidity	−0.569
Maximum atmospheric temperature	0.242
Minimum atmospheric temperature	−0.352
Atmospheric pressure	0.021

Fig. 4 K_t variation with day

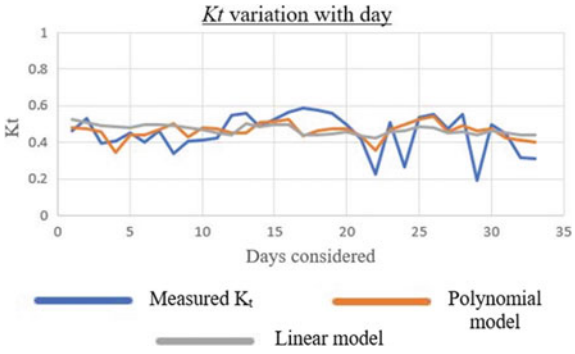

4.2 The Mathematical Model to Calculate Clearness Index Values

The model for calculating clearness index using weather parameters was developed using 80% of data available, and the remaining 20% was used to validate the accuracy of the model. Figure 4 shows the measured clearness index values plotted with calculated clearness index values using the linear model and a 4th-degree polynomial model.

4.3 The Mathematical Model to Determine Optimum Orientation

The results obtained from the mathematical model to determine the optimum orientation is discussed in this section.

4.3.1 Model to Calculate the Irradiance Incident on a Horizontal Surface

Error-values for each combination of beam and diffuse models were calculated as follows. The summation of absolute errors for the first 30 weeks in 2019 are shown in Table 2.

Lam and Li model was selected to calculate the diffuse component while Louche model was selected for the beam component.

Then the sum of absolute error values were obtained for beam and diffuse coefficients. The calculated error values are shown in Table 3.

The coefficient combination which gave the minimum sum of error values were chosen. In this case, it was determined as 1.9 for the beam component and 1.2 for the diffuse component. Figure 5 justifies the results were considerably precise after multiplying each component by the coefficient values. The blue colour line is for calculated values and the orange is for measured values.

Table 2 Squared sum of error values obtained for each beam and diffuse model combination

Diffuse models	Beam models		
	Vignola	Louche	Maxwell
Lam and Li	1.16E+06	**1.19E+04**	1.42E+04
Erbs	1.16E+06	1.48E+04	1.72E+04
Chandrasekaran	1.16E+06	1.37E+04	1.62E+04
Orgill	1.16E+06	1.28E+04	1.52E+04
Reindl	1.16E+06	1.35E+04	1.60E+04

Table 3 The squared sum of error values for each irradiance component coefficients

Cb	Cd		
	1.1	1.2	1.3
1.8	1,806,182	1,126,183	1,209,068
1.9	1,647,522	**1,067,419**	1,283,101
2.0	1,542,398	1,080,502	1,389,447

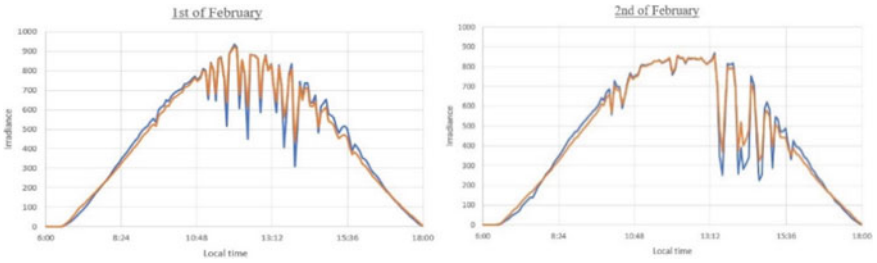

Fig. 5 Calculated versus measured irradiance values

Table 4 Error-values for each model for determining diffuse irradiance on an inclined surface

	Average value	Absolute error
Bugler's model	0.81	0.19
Temps and Coulson's model	1.21	0.22
Liu and Jordan's model	0.07	0.93

Table 5 Correlation between measured and calculated values (for K_t)

Correlation values for each day				
Day 34	Day 35	Day 36	Day 37	Day 38
0.977	0.952	0.945	0.954	0.964

4.3.2 Model to Calculate the Irradiance Incident on an Inclined Surface

The most appropriate model to calculate the irradiance on the tilted surface was chosen by selecting the model that gives R_θ values closer to 1 at zero tilt. An average value and the absolute error of R_θ values for several models at zero tilt are shown in Table 4.

The values from the above table show that Bugler's model gives the minimum error when calculating the amount of diffuse irradiance incident on a horizontal surface. Therefore, this model was taken into consideration in further modelling.

After that, the model was validated using the data captured through the device. The correlation coefficient values between calculated irradiance and measured voltage were taken into consideration and the correlation values between calculated irradiance and measured voltage for the considered five days are as follows (Table 5):

4.4 Model Validation Results

The combined model for calculating irradiance on a horizontal surface was validated using measured values. As a result of the method used to minimize errors, it was able to reduce the error percentage even less than 5%.

$$\begin{aligned} Percentage\,error &= \frac{Absolute\,sum\,of\,errors}{Sum\,of\,measured\,irradiance} \times 100\% \\ &= \frac{1{,}067{,}419}{22{,}576{,}161} \times 100\% \\ &= 4.7\% \end{aligned}$$

Then, the model to calculate the irradiance incident on the inclined surface was validated. The averaged correlation coefficient value was equal to 0.953 for the tilt

angle of 7° and zero azimuth angle. Thus, it can be concluded that the model to calculate the amount of irradiance incident on the inclined surface is performing at an accuracy level of 4%.

After that, the model to calculate the clearness index using weather parameters were validated using 20% of the data collected. The average error percentage was calculated as follows using the 20% of data which was used to validate the model:

$$\begin{aligned} Percentage\,error &= \frac{Absolute\,sum\,of\,errors}{Sum\,of\,measured\,K_t} \times 100\% \\ &= \frac{2.22}{14.94} \times 100\% \\ &= 14.8\% \end{aligned}$$

4.5 Overall Results

The amount of irradiance incident on an inclined surface at various tilt angles and azimuth angles were calculated that is given in Table 6. The calculated irradiance values are divided by 1000 for ease of representation. Table 6 shows that the maximum amount of irradiance is incident on an inclined surface when it is tilted by 1° while it is facing 6° to west from the south for the case considered under this study.

Figure 6 shows the variation of the total amount of irradiance versus tilt angle over a range of azimuth angles. The highest amount of total irradiance is captured when the azimuth angle is closer to 1° with a minimum effect from the tilt angle.

The increment of the amount of irradiance incident on solar panel compared to the current orientation could be calculated as follows:

$$\begin{aligned} Irradiance\,increment &= \frac{Irradiance\,increment}{Amount\,of\,irradiance\,under\,current\,condition} \\ &= \frac{10{,}501{,}196 - 10{,}458{,}402}{10{,}458{,}402} = 0.4\% \end{aligned}$$

The theoretically expected energy generation for a given year by the 5 kW solar system installed at the Department of Mechanical Engineering at 7° tilt angle while the panel is facing south, is as follow. The 1086 kWh is the energy generated for the last year.

$$\begin{aligned} Expected\,energy\,generated\,per\,year &= Current\,energy\,generation \times 1.004 \\ &= 1082\,\text{kWh} \times 1.004 \\ &= 1086\,\text{kWh per year} \end{aligned}$$

Table 6 Amount of irradiance incident on the solar panel at different orientations

Tilt angle (degrees)	Azimuth angle (degrees)									
	12	10	8	6	4	2	0	−2	−4	−6
−3	489,581	490,120	490,626	491,150	496,826	499,067	500,077	500,322	500,347	500,350
−1	498,857	499,143	499,406	499,580	499,747	500,627	500,538	500,352	500,368	500,334
1	500,976	501,072	501,145	501,196	501,173	500,962	500,024	500,493	500,259	500,376
3	497,413	497,117	496,542	496,078	495,610	495,066	492,584	493,825	493,205	493,515
5	497,265	496,830	496,310	485,139	484,365	483,278	478,738	481,008	479,873	480,441
7	467,353	466,052	464,701	463,018	461,506	459,958	458,402	459,180	458,791	458,986
9	443,624	441,806	439,822	437,762	435,801	433,862	431,686	429,628	427,314	425,242
11	413,451	411,024	408,633	406,303	403,728	401,299	398,672	396,143	393,382	390,819
13	376,990	374,184	371,296	368,335	365,492	362,440	359,348	356,296	353,145	350,121

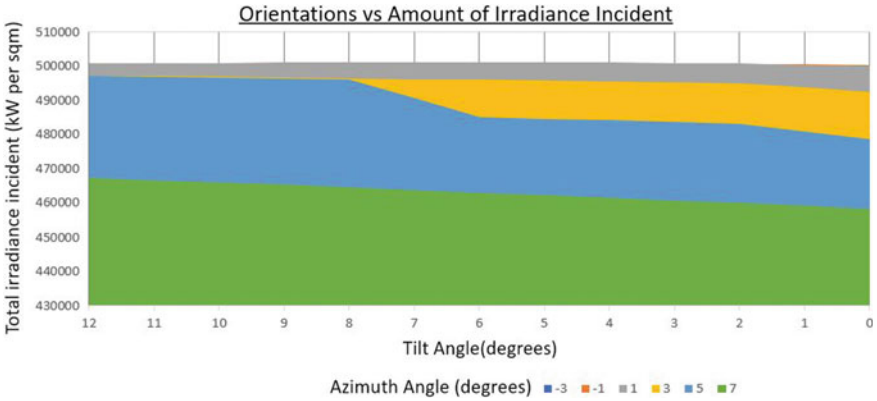

Fig. 6 Total irradiance versus tilt angle

5 Conclusion

The captured irradiance data showed that the measured irradiance pattern vary from the ideal conditions. Additionally, the findings from collected data concluded that some weather parameters showed a correlation (cloud coverage—0.7, minimum humidity—0.6, minimum temperature—0.4) with the amount of irradiance at the location. Thus, considering weather data for the past years, a model was developed to calculate the amount of irradiance incident on inclined surfaces at different orientations. Finally, the orientation which captures the maximum amount of irradiance was determined.

Based on the results of this research, it could be concluded that the maximum amount of irradiance is incident on panel when the azimuth angle is equal to 6° to west from south while tilt angle is equal to 1° to horizontal for the considered location. Thus, the suggested orientation has been deviated approximately by 8° than the current orientation. Even though the amount of increased energy generated (0.4%) is comparatively negligible for the considered case study, the values are significant for some cases found in the literature. An additional 4.3 kWh energy per year could be generated from a 5 kW PV system without an additional effort by setting the orientation as recommended which is equal to the energy generated within 1.5 days on average.

The annual economic benefit would be about 0.4 $ per year under the given rates by the Ceylon Electricity Board that could be almost negligible and unable to justify the amount of money spent on reorientation of panels. If this analysis was done prior to the installation, the panels could have been oriented to capture more energy than the existing orientation. The expected economic benefit is assumed to be linear with the size of the array since extra energy is generated by each extension of the PV system. Since the objective of this work is to determine the panel orientation at the installation stage, the costs incurred could be justified.

The research gap identified has been filled up to a reasonable extent as shown in the results via the suggested methodology. The time taken to determine the amount of irradiance incident at the location was reduced significantly by developing a mathematical model to predict the irradiance level. The model was capable of accommodating data for the past few years thus, utilizing a normalized set of data instead of year specific data. The suggested methodology incorporates several weather parameters and deploy them in the process of determining the irradiance level.

This method would be more efficient and effective for large scale solar systems. Therefore, when it comes to the national level, the amount of power generated using solar farms could be increased by a significant amount.

References

1. Benghanem M (2011) Optimization of tilt angle for solar panel: case study for Madinah, Saudi Arabia. Appl Energy 88(4):1427–1433. https://doi.org/10.1016/j.apenergy.2010.10.001
2. Castelino RV, Jana S, Kumhar R, Singh NK (2018) Optimization and development of solar power system under diffused sunlight condition in rural areas with supercapacitor integration. In: AIP. https://doi.org/10.1063/1.5032045
3. Chikate BV, Sadawarte YA, Sewagram BDCOE (2015) The factors affecting the performance of solar cell. Int J Comput Appl
4. George A, Anto R (2012) Analytical and experimental analysis of optimal tilt angle of solar photovoltaic systems. In: International conference on green technologies (ICGT), 234–39. IEEE. https://doi.org/10.1109/ICGT.2012.6477978
5. Idoko L, Anaya-Lara O, McDonald A (2018) Enhancing PV modules efficiency and power output using multi-concept cooling technique. Energy Rep 4:357–369. https://doi.org/10.1016/j.egyr.2018.05.004
6. IFC (2015) Utility-scale solar photovoltaic power plants
7. Kalogirou SA (2014) Photovoltaic systems. In: Solar energy engineering, 2nd edn. Elsevier, Oxford, pp 481–540. http://doi.org/10.1016/B978-0-12-397270-5.00009-1
8. Karafil A, Ozbay H, Kesler M, Parmaksiz H (2015) Calculation of optimum fixed tilt angle of PV panels depending on solar angles and comparison of the results with experimental study conducted in summer in Bilecik, Turkey. In: 2015—9th international conference on electrical and electronics engineering (ELECO), pp 971–976. http://doi.org/10.1109/ELECO.2015.7394517
9. Karunathilake H, Hewage K, Mérida W, Sadiq R (2019) Renewable energy selection for net-zero energy communities: life cycle based decision making under uncertainty. Renew Energy 130:558–573. https://doi.org/10.1016/j.renene.2018.06.086
10. Kemery BP, Beausoleil-Morrison I, Rowlands IH (2012) Optimal PV orientation and geographic dispersion: a study of 10 Canadian cities and 16 Ontario locations. In: Proceedings of ESim 2012: the Canadian conference on building simulation optimal, pp 136–149
11. Khaligh A, Onar OC (2018) Energy sources. In: Power electronics handbook. Elsevier, Oxford, pp 725–765. http://doi.org/10.1016/B978-0-12-811407-0.00025-8
12. SPW (2021, June 02) Advantages and disadvantages of a solar tracker system [Online]. https://www.solarpowerworldonline.com/2016/05/advantages-disadvantages-solar-tracker-system/
13. Kumar Panjwani M, Bukshsh Narejo G (2014) Effect of humidity on the efficiency of solar cell (photovoltaic). Int J Eng Res Gen Sci 2(4)
14. Li DHW, Lam TNT (2007) Determining the optimum tilt angle and orientation for solar energy collection based on measured solar radiance data. Int J Photoenergy 85402. http://doi.org/10.1155/2007/85402

15. Rajvikram M, Leoponraj S (2018) A method to attain power optimality and efficiency in solar panel. Beni-Suef Univ J Basic Appl Sci 7(4):705–708. https://doi.org/10.1016/j.bjbas.2018.08.004
16. Clean Energy Decision Support Centre (2015) Clean energy project analysis: RETScreen engineering and cases textbook. In: Clean Energy Project Analysis RETScreen Engineering & Cases Textbook, pp 173–216. http://publications.gc.ca/collections/collection_2007/nrcan-rncan/M154-13-2005E.pdf
17. Rowlands IH, Paige B, Beausoleil-Morrison I (2011) Optimal solar-PV tilt angle and azimuth: an Ontario (Canada) case-study. Energy Policy 39(3):1397–1409. https://doi.org/10.1016/j.enpol.2010.12.012
18. Vanek FM, Albright LD (2008) Energy systems engineering: evaluation and implementation. McGraw-Hill, New York. https://doi.org/10.1036/0071495932

The Autonomous Battery-Powered House, Which Energized Through a Solar Power and Reused Hybrid Vehicle Batteries Under Extra Low Voltage Direct Current Installation

H. N. Hikkaduwa

Abstract The life was arose with the lunar energy, and the main source of the energy to earth is solar. The evolution of science from Stone Age, then find fire and now electricity, and tends to find new energy requirements for living. At present, electricity become the basic need in human life. Day by day the electrical sector developing and lifestyle is changing swiftly. Similarly electrical energy demand will boosting with respect to the population growth and changing lifestyle. The strategic setting of Sri Lanka in Indian Ocean, created the immense development and leads for vast electrical demand in power sectors. Thus power generations consumes huge amount of coal and fossils fuel, through a massive environmental damage and loosing of countries foreign remittent. In par the distributional losses will exaggerate further. Electrocution is a critical risk with high and medium voltage supply; even in the domestic supply of 230 V, AC. Presently most house hold electrical appliances are runs with 5–12 V direct current (DC) low voltages, and for step-down it, also creates losses. The life was arose with the lunar energy, and the main source of the energy to earth is solar and accordingly humans were success to absorb the energy of the solar rays as a solar photovoltaic power. Sri Lanka is a tropical country, which close to the equator, and also efficiency of solar PV panels and batteries technology in rapidly in present: therefore solar is the more prominent power source to country. Nonetheless, the cost on solar panels can affordable and price on better batteries are compatibly high. Sri Lankans running with significant amount of electrical and hybrid vehicle, and dispose of its batteries are now be a challenge, due to absent of recovering technologies. Haphazardness disposal of them course huge environmental damage. Thus reusing of them shall eliminate those issue. Hence, this paper assays to elaborate the prospects of autonomous "Battery Powered House", which runs with extra low voltage (12 V) installation and energized thru Solar PV and Reused electrical vehicles (EV) battery bank.

Keywords Battery-powered house · Low voltage electrical installation · Reused hybrid vehicle battery bank · Solar PV

H. N. Hikkaduwa (✉)
Construction Industry Development Authority (CIDA), "Sawsiripaya", 123 Wijerama Mw., Colombo 00700, Sri Lanka

R. Dissanayake et al. (eds.), *ICSBE 2020*, Lecture Notes in Civil Engineering 174,
https://doi.org/10.1007/978-981-16-4412-2_14

1 Introduction

Sri Lanka is the pearl of Indian Ocean, which located at the strategic point of the Indian Ocean. Consists with rich history and natural resources. The culture, hospitality, quality of life and tax flexibility will attract the investments to the country. Thus the immense development stand in the country. The rapid development and urbanization, will boost the national electrical demand. The electrical energy is a basic need to human life, and power sector demand are challenge to the country itself. Earlier, Sri Lanka powered demand covers through hydro power electricity generation. With respect to the demand and climatic conditions Sri Lanka gradually shift to the coal and fossil fuel power generations [1]. The power generation stations are scattered in geographically, and the distributional losses are considerably high. Further expecting to reduce energy losses by improving energy distribution infrastructure and energy saving through introduction of Demand Side Management (DSM) [2, 3]

Sri Lanka, a country vulnerable to climate change impacts, in response to challenges posed by climate change, Sri Lanka has taken several positive steps by introducing national policies, strategies and actions in order to address climate change induced impacts, and presented the Nationally Determined Contributions (NDC) to strengthen the global efforts of both mitigation and adaptation. In an endeavour to embrace renewables more fully, Sri Lanka, while attending the 22nd UNFCCC Conference of Parties in Marrakech, Morocco, as part of the Climate Vulnerable Forum, pledged to use only renewable energy for electricity generation by 2050 (*Assessment of Sri Lanka's Power Sector*, 2017). While fulfilling the increasing national electricity demand and integrating more renewable sources in combination with conventional fossil source based energy sources, a detailed electricity generation expansion plan has been developed. The National Energy Policy and Strategy (NEPS) anticipate increasing share of Other Renewable Energy (ORE) resources. According to the ratified NDCs in September 2016 by UNFCC, among mitigation strategies, Sri Lanka expects 4% unconditional and 16% conditional reduction of greenhouse gas emissions with compared to Reference scenario in 2030 based on Long Term Generation and Expansion Plan (LTGEP) 2015–2034 for the electricity sector. During the preparation of LTGEP 2020–2039, this commitment is compiled to fulfil the Sri Lanka's obligations on Climate Change mitigation from Electricity Sector [4].

Sri Lankan Economy is losing foreign exchange, due to importing of Coal and fossils fuels to power and transportation sectors. The system losses, step-down loses and inefficient appliances will exaggerates further. There are many loss of life due to electrocution, and it is a critical risk with high and medium voltage supply; even in the 230 V, AC domestic supply. Presently most house hold electrical appliances are runs with 5–12 V direct current (DC) low voltages, and to step-down it, also creates losses. Shifting to low voltage installation to house hold is will be an ideal solution to those issues.

Further Sri Lanka wishers to shift electrical vehicles to transport sector development, lined with eliminating pollution control. But it may become purpose less if not power sector not shifted to renewable energy. Further Sri Lanka does not have a proper system to manage their e-waste, thus disposing of EV will be a future environmental issue.

Sri Lanka is a tropical country which close to the equator, and consists with three climatic zones as wet, intermediate and dry. Dry zone of Sri Lanka's occupies three-quarters of the island and it's have more solar potential [5]. According to solar potential maps (Fig. 1), dry zone and intermediate zones is more potentials to solar PV power generation and it covers larger part. The efficiency of solar PV panels and batteries technology is rapid. Nonetheless, the cost on solar panels can affordable and price to better battery storage is compatibly high. Shifting on recondition batteries sources will eliminate it. Especially rural housing sector demands could not be covered due to remote houses and high distribution costs. Therefore solar can be used as a more prominent power source in housing sector demand to said zones.

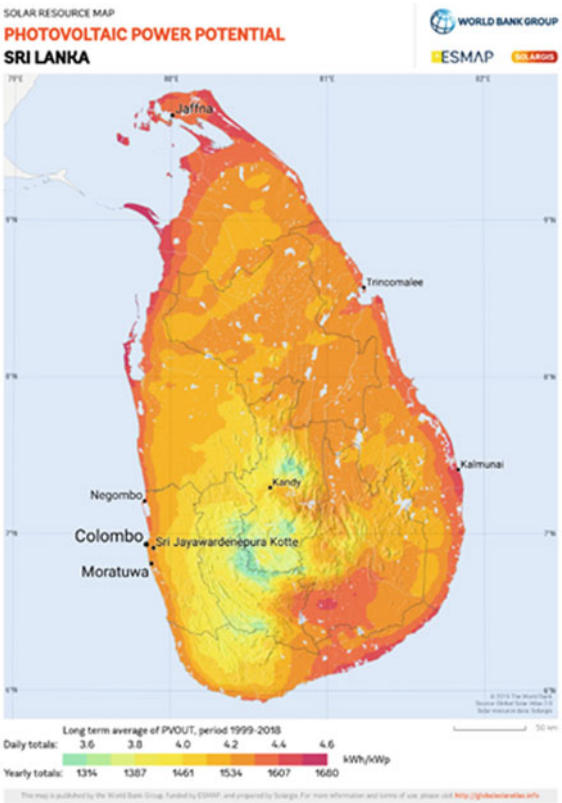

Fig. 1 Photovoltaic power potential, Sri Lanka. *Source* https://globalsolaratlas.info/download/sri-lanka

2 Objective of the Study

The study objective is to develop autonomous, sustainable, affordable, minimum risk, and environmental friendly electrical power source to Housing Sector in Sri Lanka.

3 Methodology

- Survey to identify the suitable renewable energy sources
- Identify the more appropriate energy storage technology, drawbacks and possibility with recycled batteries
- Survey to identified the appliance that are common to law and middle income households
- Identify the present house hold electrical installation risks and possibility of using low voltage installation
- Design a mock-up system with 12 V DC installation, reclaimed battery bank that charged by Solar PV system. with relevant safety and Standards
- Cost analysis of the system
- Run the system as a pilot project in a selected site to identify the gaps and development.

4 The Best Renewable Energy Source to the System

There are different sources of renewable energy technology out of those solar and wind power are more common. The wind power is more suits for very few high wind potential locations in Sri Lanka. Further, it is not suits cover small scale remote household energy requirement. Sri Lanka is a tropical country which close to the equator, and benefiting of having sunlight for more than 12 h per day. Also more area of the country is with high solar PV potential (Fig. 1), and solar PV have less maintenance requirement. Therefore using solar systems to generate electricity is truly beneficial.

Solar panels absorb the energy of the solar rays as photovoltaic (PV). It convert the sun's rays into electricity by exciting electrons in silicon cells using the photons of light from the sun. The efficient of the solar PV system is relies with the sun rise and sun set (i.e. exposure time to sun), cloud cover (i.e. intensity of solar ray), sun path (i.e. to identify the best fixing angle to collect more energy) and the ambient temperature (i.e. efficiency of cells power generation). Therefore in site planning for a solar PV system, those points are essential considerations for the sustainability. Further, there are main two type of solar panels (Fig. 2); that are mono crystalline and poly crystalline the efficiency it is varying. For tropical country like Sri Lanka poly crystalline is more suitable (Fig. 3).

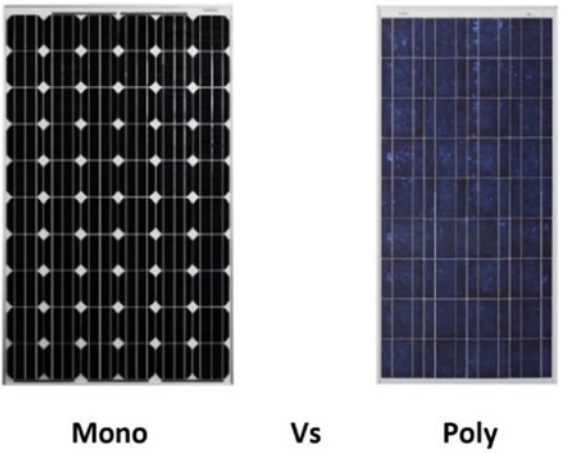

Fig. 2 Mono and poly crystalline solar PV panels

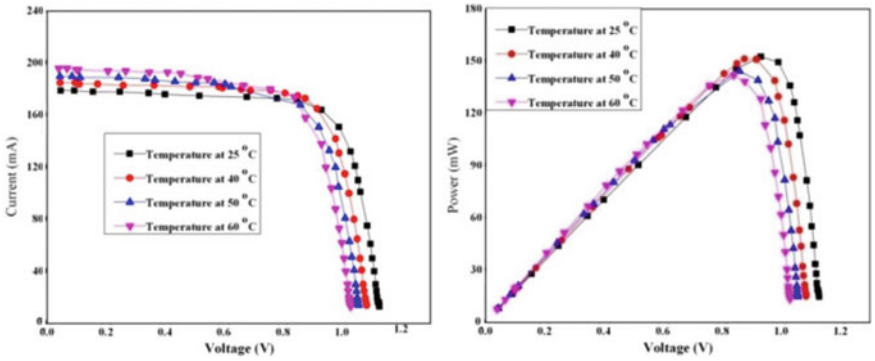

Fig. 3 Poly crystalline solar PV panels performance with temperature. *Source* https://www.sciencedirect.com/

5 Appropriate Energy Storage Capability

When the sunset, it is a requirement to have a storage system to store the excess energy generated from Solar PV panels in day time. The system planning should focus day and night time energy requirements. When compared to current situations night time requirement is higher in domestic houses. Planning on battery banks, have to concerns more suitable and durable batteries. Typically most batteries are made with one of the chemical compositions such as lead-acid, and lithium-ion. The lead-acid batteries are a tested technology that has been used in off-grid energy systems for decades. It have relatively short life and lower depth of discharge than the other battery types, and also the least expensive batteries in the market. The lithium-ion batteries are lighter and more compact than lead-acid batteries. They also have a higher depth of discharge value and longer lifespan when compared to

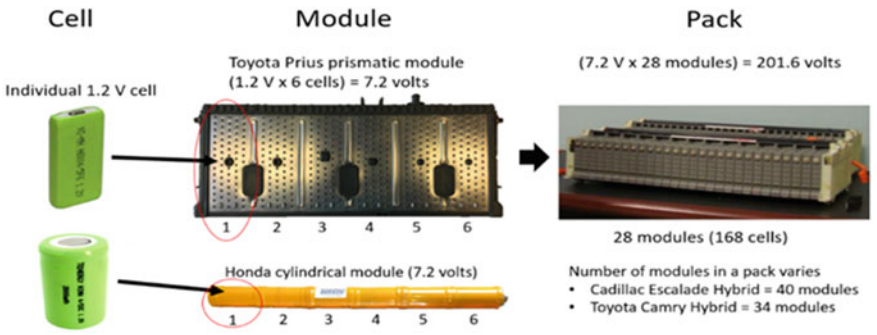

Fig. 4 24 nos of module, battery pack

lead-acid batteries. However, lithium ion batteries are more expensive than the lead acid counterparts. Lithium-ion chemical composition batteries are the most accepted by the new home energy storage technologies. As a developing country, step into fresh lithium-ion battery banks will be an issue. Thus it can be resolved through reclaim batteries (Fig. 4).

Sri Lanka transport sector will shifting to Hybrid Vehicles and Electrical Vehicles (EV) and disposal of EV batteries will be a massive environmental issue, due to absence of proper e-waste management. The non performing batteries on hybrid/EV vehicles can be used as battery banks in proposed system energy storage as a win win solution. The battery performance is depends on its capacity Ampere Hour (Ah) rating. Hence the power of the battery bank will be Volt Ampere Hour (i.e. Wh). The series and paralleled connection of batteries shall fallow the basic principles to minimize risk and optimum power output (Fig. 5). The weather pattern will not unique and receiving of solar not uniform throughout the year. Therefore some days not receive daily energy requirement. Thus the storage system should be planned for 2–3 days to eliminate dark nights.

The charging of a hybrid vehicle battery has a risk on explosion and fire. Hence the batteries modules carefully packed and compressed (Fig. 4), and maintained a cooling system during charging. Further batteries shall charge by a Solar PV panels through relevant charge controller to minimise the risk. The charge controller will protects the batteries on overcharge and explosion and fire. The battery bank shall be designed to the half design Load. This will enhance the battery life (Fig. 6).

6 The Household Electrical Installation

When concerns on existing 230 V Alternative Current, domestic electrical installation that leads to high risk on electrocution or an electric shock to humans. Thus this will become a disaster, according to the report on electrocutions by Public Utilities

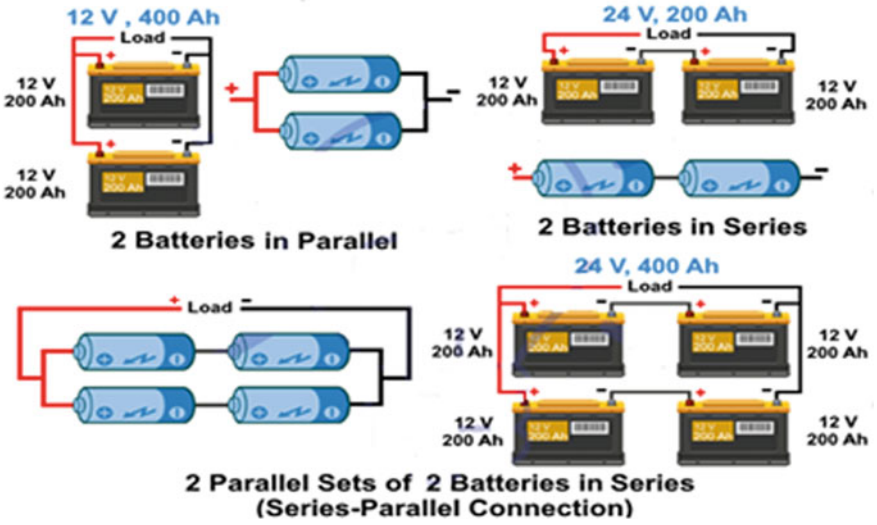

Fig. 5 Battery connection detail. *Source* www.electricaltechnology.org

STORAGE CHARGE TIMES

Battery Type	Capacity at 10 Hr. Rate (Ah)	Charging Time in Hours At 1 Amp	At 1.5 Amps	At 2 Amps
TX4L	3	2-3	-	-
TX5L	4	2-4	-	-
TX7L	6	3-6	2-4	2-3
TZ7S	6			
T7B	6.5			
TX9	8	4-8	3-6	2-4
TZ10S	8,6			
TX12	10	5-10	4-7	3-5
T12B	10			

Battery Type	Capacity at 10 Hr. Rate (Ah)	Charging Time in Hours At 1 Amp	At 1.5 Amps	At 2 Amps
T14B	12	6-12	4-8	3-6
TX14(L)	12			
TX14AH	12			
TX15(L)	13	7-13	5-9	4-7
TX20HL	18	9-18	6-12	5-9
TX20CH	18			
T16L	19	10-19	7-13	5-10
TX24(H)(L)	21	11-21	7-13	6-11
TX30L	30	15-30	10-20	8-15

Fig. 6 Battery charging detail. *Source* www.electricaltechnology.org

Commission of Sri Lanka (PUCSL) the electrocutions are on the rise, and 103 people died due to electrocutions in 2019.

Unfortunately, the prevailing power system infrastructures are based on alternating current (AC) while two of the leading environmentally friendly energies, fuel cells and photovoltaics, produce direct current (DC). Present power system infrastructure, DC sources such as Solar PV that supply to DC loads must implement two converters,

one that first converts the DC to AC and then another to return the AC back to DC. This type of power system can result in significant losses [9]. Therefore DC-DC converters is that the efficiency tends to fall when operated below the rating and the DC-DC converter efficiency was assumed fixed for all operating conditions [7]. Further from studies it was demonstrated that the suitability of DC Distribution Systems [8].

Today's most electrical appliances are operating with law DC voltage, and due to power converters reduces efficiency. These devices essential to converted again from AC back to DC adding further losses and complexity to the power system. Furthermore, an ever increasing number of DC consuming devices today. Several devises at average household, that are running with the AC current such as refrigerator, electric iron/strict and rice cookers.

To satisfy that requirement, it is suits to introduce separate line on those devises or separate power inverts for those points. Currently power inverter prices are affordable and efficiencies are increasing. Other devises such as Television, Computers ….etc. that are convert AC to DC; circuits can be changed DC to DC converters and integrated into the system. Further in the current market we can find DC LEDs, Fans, Radios ….etc. Therefore, the study was focused to do household electrical installation by DC distribution system, with suitable caballing's and protection measures.

7 System Design Calculations

7.1 The Load Calculations

It is identified that the most common appliances of rural house may replace by 12 V DC appliances; such as LED lights 5–9 W, Table/wall mounted fan 12 W, and Radio 3 W. Therefore consider a typical rural housing electrical installation to demand calculations, that based on the survey (Table 1).

Table 1 Calculation of energy demand

Appliance	Watt	Operating hours	No	Wh
Lighting Type 1	5	4	10	200
Lighting Type 2	9	4	5	180
Fans operation type 1	12	5	1	60
Fans operation type 2	12	7	2	168
Electronic item operation (Radio)	3	5	1	15
	Daily energy demand (DD)			623
	Design energy demand (3X DD)			1869
	The half load energy demand (3XDDX2)			3738

7.2 *Design of Solar PV System.*

The selected site for the pilot project is Kalutara, that situated in intermediate zone and have 4.2–4.4 kWh solar potential (Fig. 1). When planning the system the receiving of required amount of solar rays to the Solar PV panels are more important factor to consider. Therefore it is important to consider sunrise and sunset (Fig. 7), cloud cover (Fig. 8), and Sun path. Hence selected site 12 h of sun rays in average day (Fig. 7). In January to April and September to December will have less cloud cover (Fig. 8).

The solar cell operates at a higher temperature than the 25 °C of the standard test conditions, when the temperature increases, the solar cell open circuit voltage, Voc, decreases, so, the output voltage is also reduced. The operating temperature of the solar cell is given by the temperature of the ambient and the solar irradiance or the intensity of the sunlight in the module [6]. Thus the efficiency of the Solar PV system relies with ambient temperature. Hence the cooling system has to plan through sparing water in high temperatures and poly crystalline panels can use to system (Fig. 9).

1. The system will planned with 450 W poly crystalline solar PV array;
2. Actual power output of a PV panel:

$$= \text{Peak power rating} \times \text{operating factor}$$
$$= 450\,\text{W} \times 0.75 = 337.5\,\text{W}$$

3. The power used at the end use is less (due to lower combined efficiency of the system)

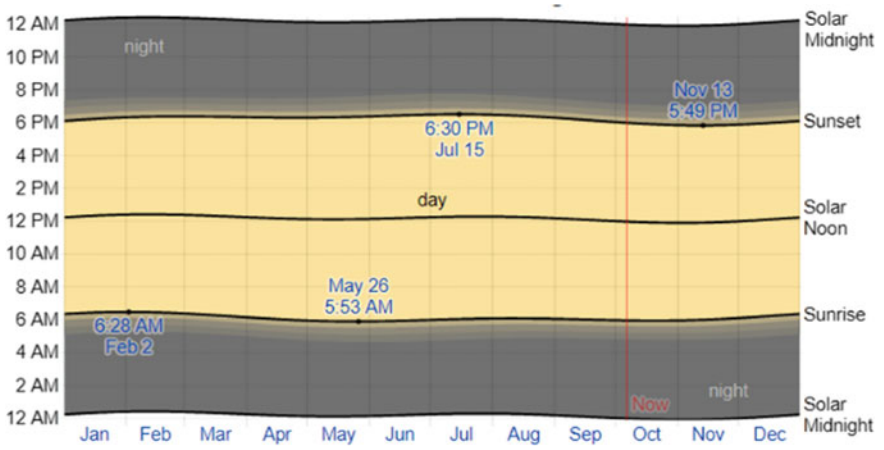

Fig. 7 Sunrise and sunset with twilling, Kalutara District. *Source* https://weatherspark.com/

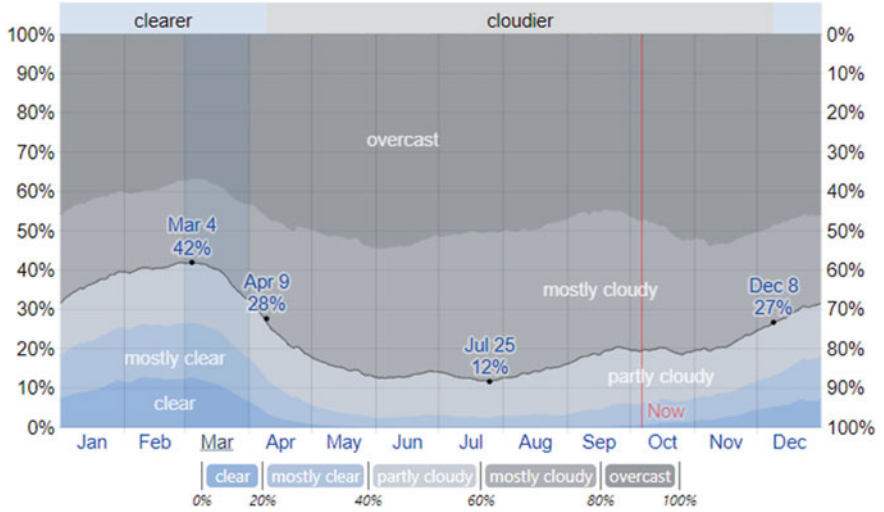

Fig. 8 Cloud cover categories, Kalutara District. *Source* https://weatherspark.com/

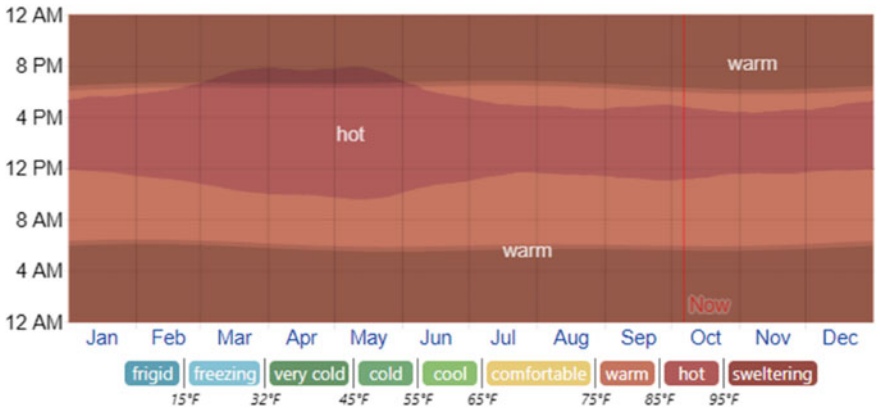

Fig. 9 Average hourly temperature, Kalutara District. *Source* https://weatherspark.com/

$$= \text{Actual power output of a panel} \times \text{combined efficiency}$$
$$= 337.5\,\text{W} \times 0.81 = 273.375\,\text{W (VA)}$$
$$= 273.375\,\text{W}$$

4. Energy produced by one 450 W panel in a day

$$= \text{Actual power output} \times 7\,\text{h per day (peak equivalent)}$$
$$= 273.375 \times 7 = 1914\,\text{Wh}$$

5. Number of solar panels required to satisfy given estimated daily half load:

$$= (\text{Total watt} - \text{hour rating (daily half load)}/(\text{Daily energy produced by a panel})$$
$$= 3738/1914 = 1.95 = 2 \text{ (round figure)}$$

Hence systems runs with 2 Nos × 450 W solar PV panel array.

7.3 Design of Battery Bank

The Hybrid vehicle battery module (Fig. 4) is consists with 6 of 1.2 V, Lithium ion battery cells that have nominal voltage 7.2 V and nominal capacity of 6.5 Ah. The units for the pack is designed, with series of two module that have 14.4 V and 24 of those modules (Fig. 10).

1. The design load under half load = 3738 Wh (VAh)
2. The capacity of battery bank

$$= (\text{design load under half load})/(\text{Cell Voltage} * \text{Cell Ah})$$
$$= (3738)\ \text{VAh}/(7.2 \times 2\ \text{V} \times 6.5 \times 2\ \text{Ah}) = 19.96$$
$$= 20 \text{ Cells. (Round figure)}$$

3. Charge controller requirement:

$$= \text{Solar Array output}/\text{Array Voltage}$$
$$= (1913.625 \times 2)/(37 \times 2)$$
$$= 5.85\ \text{A}$$
$$= 30\ \text{A charge controller}$$

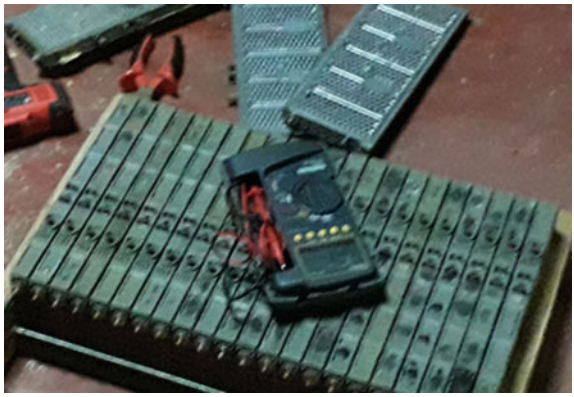

Fig. 10 24 nos of module, battery pack

7.4 Cost Estimation

The cost for solar panels (2 × 450 W)	LKR 50,000
Electrical installation average forecast	LKR 5000
Battery assembly and charge controller 230 A	LKR 4000
Contingencies 10%	LKR 5600
Total	LKR 64,900

8 Discussion

Sri Lanka is the country is a rapid developing country and rich with natural environments. As a developing country that burns considerable amount of foreign exchange to foils fuels and coal for power generation. To earn that money Sri Lanka trade countries most valuable labour force to The Middle Eastern countries, that makes negative effects to the economy in macro levels. Additional the burning of coal and fossils fuel will course huge environmental damage, and this also a negative effect to the country, when concerns the prime income of hospitality industry.

In financial point of view the payback period is comparably high on solar power systems, but if encounter the other aspects such as environmental and climate change protection measures, it is much worth system. The proposed system will also address the disposal issue of vehicle batteries. Further, from 12 V DC household installation, prevent the electrocution hazard and can protect life. Proposed system will be also an answer to those who in inaccessible to electricity. It is more suit to dry and intermediate zones domestic power requirement up to 4 kW.

9 Conclusion

Sri Lanka is a country that is boosting electrical demand and have loops in domestic power supply to isolated areas. Further, vulnerable to climate change impacts and shifting to solar energy will be a prime solution. There are life risk in domestic AC installation and shifting to DC domestic installation will be risk free and the amount of DC loads in our buildings is ever-increasing. Shifting to off-grid solar PV systems are demotivated owing to efficiency, lifecycle and prices of the batteries. The reusing of motor vehicle batteries, that could not perform in vehicles shall eliminate the issue. Further, lithium–ion are the most fitted batteries to the battery storage and price of fresh battery is challenge. Reclaiming of EV batteries will be a win win approach, and it will be a great value to the environment and natural global resources usage. The system can recommended to use totally off-grid or as hybrid. Thus the proposed autonomous “Battery Powered House”, which energized through a solar power and reused hybrid vehicle batteries under extra low voltage direct current installation will

save the country foreign remitters and economic stability, and be a solution for rural power blackouts.

Acknowledgements I wish to convey my special gratitude, Mr. M. P. Hikkaduwa and Mrs. U. S. Thenuwara for the support, cordage and acceptance on pilot site. Further to Sulalitha Motors, Kalutara who supplies used EV batteries and assistance. Finally, I will thanks all who support for success.

References

1. Sri Lanka Energy Balance (2017) Available at: http://www.energy.gov.lk/images/energy-balance/energy-balance-2017.pdf. Accessed 29 Sept 2020
2. Basnayaka WBMCM (2016) Past, present and future of electricity generation in Sri Lanka. Thesis. University of Ruhuna, Sri Lanka. Available at: https://www.researchgate.net/publication/337943282_Past_Present_and_Future_of_Electricity_Generation_in_Sri_Lanka. Accessed 29 Sept 2020
3. Rodrigo Asanka S, Gunatillaka MDPR (2019) An effective method of segregation of losses in distribution systems. J Pap Eng LII(02):1–14
4. Ceylon Electricity Board (2019) Long term generation and expansion plan 2020–2039. Available at: https://www.ceb.lk/front_img/img_reorts/1560836289LTGEP_2020-2039_(Draft).pdf. Accessed 29 Sept 2020
5. Meegahakotuwa US, Nianthi KWGR, Dissanayake DM (2019) Seasonal solar power generation potential for electricity supply in the dry zone of Sri Lanka. In: International research conference of UWU-2019. Uva Wellassa University, Sri Lanka. Available at: http://www.erepo.lib.uwu.ac.lk/handle/123456789/224. Accessed: 29 Sept 2020
6. WENHAM SR et al (2007) Applied photovoltaics, 2nd edn. Earthscan, UK, USA
7. General Motors Corporation (1999) High efficiency power system with plural parallel DC/DC converters. US Patent 6 166 934, June 30, 1999
8. Nilsson D (2005) DC distribution systems. Ph.D. dissertation, Department of Energy and Environment, Chalmers University of Technology, Goteborg, Sweden
9. Starke M, Tolbert LM, Ozpineci B (2008) AC vs. DC distribution: a loss comparison. In: IEEE/PES transmission and distribution conference and exposition. Available at: https://ieeexplore.ieee.org/document/4517256. Accessed: 29 Sept 2020

EPS Blended Cementitious Plaster for Improved Thermal Comfort in Buildings

A. Selvaratnam, J. C. P. H. Gamage, and G. I. P. De Silva

Abstract The use of green materials in building construction has become trendy to improve the thermal comfort within the buildings with minimized natural resources. This paper presents the development of a cementitious insulated plaster using Expanded Polystyrene (EPS) as partial replacement for fine aggregates. An experimental program was conducted by replacing the fine aggregates in the conventional plaster with EPS in the range of 0–200% by volume. A reduction up to 69% and 53% were noted in thermal conductivity and density, respectively due to the replacement of aggregates with EPS in the conventional mortar. From a trial and error process, the mix with 125% replacement by EPS was selected as the ideal mix for optimum thermo-mechanical performance. A numerical model was developed to examine the heat transfer behaviour through a wall/Plaster composite and the predicted results were in a satisfactory agreement with the experimental results. A reduction of 18% in the decrement factor and an increment of 20% in time lag were noted in the wall panels with the developed EPS-Cement plaster.

Keywords EPS · Green insulation · Recycling · Thermal comfort · Wall plaster

1 Introduction

The production of EPS material has rapidly increased due to its frequent application in packaging, thermal insulation, and craft applications. The desire towards the EPS materials has risen because its superior properties such as lightweight, thermal insulation, impact resistance, airtightness, load-bearing capacity at a low weight, and long life [17]. However, EPS is bio-degradable [10] and hence tons of EPS are sent to the landfills every day. Since incorporating the waste materials into building

A. Selvaratnam (✉) · J. C. P. H. Gamage
Department of Civil Engineering, University of Mortuwa, Mortuwa, Sri Lanka
e-mail: aarugas@uom.lk

G. I. P. De Silva
Department of Material Science and Engineering, University of Mortuwa, Mortuwa, Sri Lanka

R. Dissanayake et al. (eds.), *ICSBE 2020*, Lecture Notes in Civil Engineering 174,
https://doi.org/10.1007/978-981-16-4412-2_15

construction has become attractive [13], utilization of the recycled EPS as a building construction material is an excellent solution towards a greener industry.

The research focus on the utilization of EPS in the civil engineering industry has become generic in the last few decades. In such a case, lightweight concrete [18], precast wall panels [4], and sandwich panels [6] are the extensive studies using EPS as a base material. Kaya and Kar et al. [15] have shown that a range of thermal conductivity from 0.048 to 0.390 W/m K can be obtained for the concrete containing waste EPS and natural resin. Schackow et al. [18] have also investigated the mechanical and thermal properties of lightweight concrete with EPS and indicated that 7.7–11.8 MPa of compressive strength and 0.50–0.56 W/m K of thermal conductivity can be achieved with 55–65% of EPS volume fraction and 1% air-entraining agent by weight.

Thermal comfort is a key variable of indoor environment quality which is mainly influenced by the materials used in construction and the design strategies [12, 14]. Therefore, using insulating materials for the building walls or wall plasters could significantly reduce the heat transfer within the buildings. In such a case, addition of thermally insulative materials such as Rice husk ash, bottom ash, fly ash into the concrete and mortar mixes have been studied by many researchers [8, 9, 19].

Few researchers have focused on the EPS-cement mortar and its thermal and mechanical properties. Ferrándiz-Mas et al. [7] have investigated the cement mortar with EPS and paper sludge ash and discovered mortar mixes with a thermal conductivity range of 0.4–0.9 W/m K and compressive strength range of 0.5–8.5 MPa. Dylewski and Adamczyk [5] explored the ecological and economic performance of different types of thermal insulation plaster as EPS plaster one of them. This study has indicated that using EPS plaster is far more beneficial than conventional cement plaster for both economic and ecological reasons. Though few investigations have been made on EPS plaster, no studies have focused on the development and application of the EPS plaster to building walls to date, according to the authors' knowledge. This study focuses on the development of a thermally insulated cementitious wall plaster using EPS as a partial replacement for fine aggregates and on the application of the developed plaster to assess the heat transfer behaviour.

2 Test Program

2.1 Overview

A detailed experimental program was carried out to develop a lightweight cementitious insulated plaster with Expanded Polystyrene (EPS) as the base material. Figure 1 illustrates the test methodology followed in this experimental program. The conventional cement sand mortar with cement: sand weight ratio of 1:3 (1:2.25 volume ratio) was selected as the control specimen for this study and it was modified by the replacement of sand by EPS particles. The thermal conductivity and the compressive

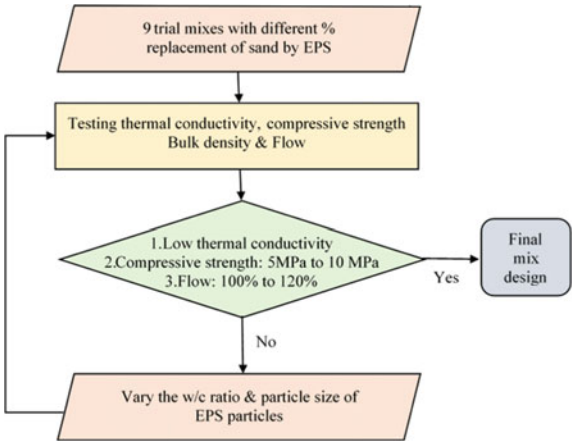

Fig. 1 Methodology of the test program

strength of the trial mixes were used for the selection criteria of the final product to match with the common industry practice for N-type mortar [2].

2.2 Materials and Sample Preparation

Ordinary Portland cement with 28 days average compressive strength of 42.5 MPa as the binding agent, river sand passing through 0.8 mm sieve, recycled EPS resin particles passing through 3.35 and 1.15 mm sieve as fine aggregates were used throughout the test program (Fig. 2). A constant water/cement ratio of 0.45 was used at the first stage of the experimental program. 60 mm diameter and 5 mm thick specimens were prepared to test the thermal conductivities based on Lee's disk method in accordance with ASTM D7340-07 [3]. The compressive strength of the trial mixes was tested in accordance with SLS 107: Part 2 [21]. Figure 3 shows a few test samples and the testing apparatus.

Fig. 2 Materials **a)** cement; **b)** river sand; **c)** EPS—3.35 mm; **d)** EPS—1.15 mm

Fig. 3 Specimen preparation and testing **a)** mixing mortar; **b)** compressive strength test samples; **c** testing thermal conductivity

2.3 Test Results

The obtained thermal and mechanical properties with 3.35 mm grade EPS are listed in Table 1. The test results show that replacing the sand particles with EPS drastically reduces the compressive strength, density, and thermal conductivity where the reduction in compressive strength decrease the mechanical performance and the reduction in the thermal conductivity enhance the thermal performance of the mixes. Figure 4 shows the variation in the compressive strength and thermal conductivity with respect to the volume replacement percentage. Though 62% replacement indicates the optimum performance, a lesser compressive strength value would be sufficient for an N-type mortar mix. Meanwhile, the introduction of EPS particles makes the mortar mix lightweight which adds more benefits to a green mortar mix. The flow table test results indicate that replacement of sand by EPS (E-0 to E-90) increases the flow of the mix and further addition of EPS particles (E-90 to E-200) decreases the flow back again due to the larger volume of aggregate particles.

Table 1 Measured thermal and mechanical properties

Sample	Replacement of sand by EPS (% volume)	Density (kg/m^3)	Compressive strength (MPa)	Thermal conductivity (W/m K)	Flow (%)
E-0	0	2075	28.1	0.692	14
E-30	30	2049	23.9	–	54
E-50	50	1976	18.8	–	65
E-70	70	1690	12.5	–	97
E-90	90	1453	11.1	0.361	128
E-125	125	1282	5.5	0.281	65
E-150	150	1176	5.3	–	20
E-175	175	1145	3.6	–	33
E-200	200	968	2.9	0.216	10

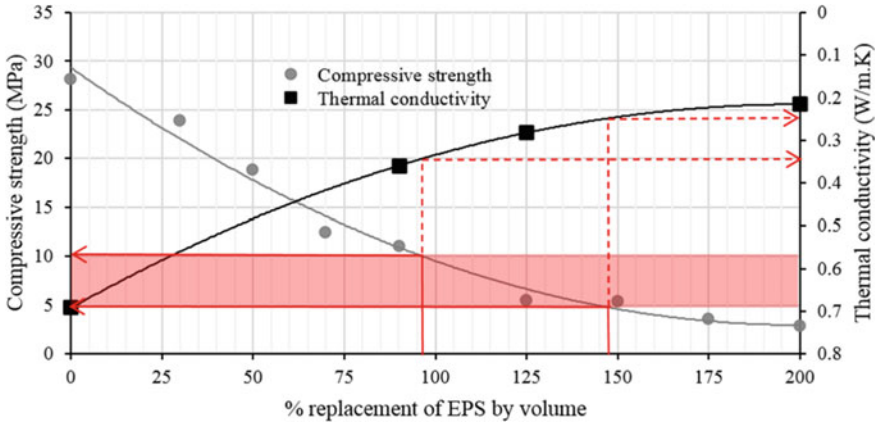

Fig. 4 Thermal and mechanical properties variation with % replacement of sand by EPS

Based on the values obtained for compressive strength, mixes between 100% and 150% replacement lie in the N-type mortar criteria. However, the respective flow table test results do not compile with the flow requirement specified in ASTM C 270-07 (2007). Hence, the E-125 mix was selected for further modification since it is the most ideal mix within the range.

2.4 Modification to the Mortar

Two different particle sizes and a range of w/c ratios were used to modify the mortar in order to compile with the specifications. The selected mix proportions and the measured material properties are listed in Table 2. The test results show that finer EPS particles can enhance the mechanical performance of the mix. Nevertheless, thermal performance and lightweight behaviour reduce with the finer particles. However, to preserve the aesthetic appearance of the building walls, the mix with finer particles were further investigated with changing w/c ratios.

Table 2 Measured properties of the selected mix proportions

Mix ID	Grade of EPS	Water/cement ratio	Density (kg/m^3)	Compressive strength (MPa)	Thermal conductivity (W/m K)	Flow (%)
E-125-1	3.35	0.45	1282	5.5	0.281	65
E-125-2	1.15	0.55	1498	7.12	0.405	55
E-125-3	1.15	0.65	1436	5.43	–	63
E-125-4	1.15	0.75	1417	4.96	0.406	97

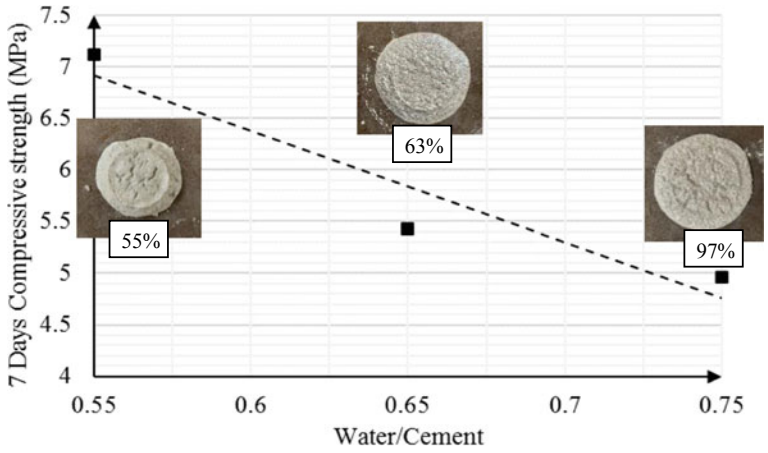

Fig. 5 Relationship between compressive strength and w/c ratio

The effect of the w/c ratio was noted high in the compressive strength values compared to the thermal conductivity and density test results. The relationship between the w/c ratio and compressive strength is shown in Fig. 5. From the three trial mixes, E-125-4 can be chosen as the ideal mix for an insulated wall plaster to enhance the thermal comfort in the buildings while ensuring the integrity of the masonry walls. Hence, a heat transfer analysis through the EPS plaster/wall composite was carried out in the next step of this study. Here onwards, the selected mortar mix will be referred to as EC.

3 Heat Transfer Analysis

A three-dimensional finite element model of the composite wall was developed using an advanced finite element software [1]. A 3 m × 4 m × 0.1 m dimension wall panel with a 25 mm thick external plaster was developed for this study. 8-node linear heat transfer brick elements (DC3D8) were used to model both elements in the composite wall. From a mesh sensitivity analysis, the mesh size was determined as 50 mm. Since no sustained loads were applied, the plaster and the wall panel were assumed to be perfected bonded, and hence a tie constraint was used to represent the bond. Figure 6 shows the finite element mesh of the composite wall.

The thermal performance of masonry walls can be assessed using “decrement factor” and “time lag” in common practice. The decrement factor is referred to as the ratio between the amplitude of temperature wave at the indoor wall surface and the outdoor wall surface [23]. And the time lag refers to the time taken for the peak temperature to propagate from the outdoor surface to the indoor surface [23]. Wall

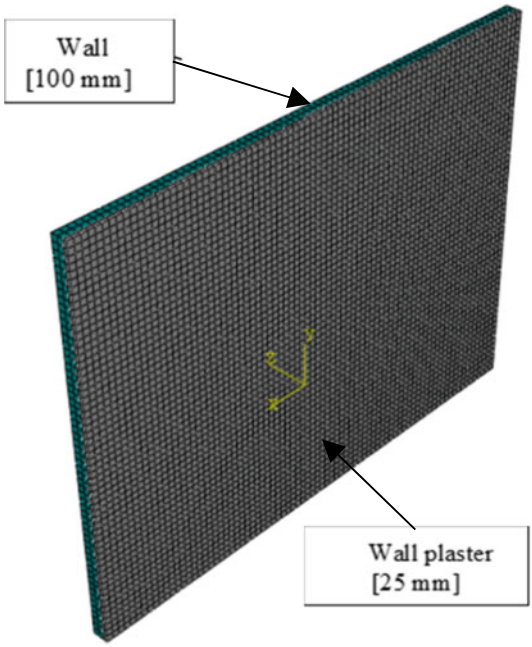

Fig. 6 Discretized model

panels with a low decrement factor and a higher time lag can act to enhance the thermal comfort within the buildings [16].

Two distinct wall panels were simulated to compare the thermal performances and they are (a) Wall panel with a conventional cement-sand plaster (WP_CS), and (b) Wall panel with the EPS-cement plaster developed in this study (WP_EC). The thermal properties of the selected plasters were tested in the laboratory and the properties of the concrete blocks were obtained from available literature [11]. Table 3 shows the material properties used for this simulation. It was assumed that the outdoor air temperature was transferred to the external wall surface through conduction and radiation.

Table 3 Thermal properties of the materials

Material	Thermal conductivity (W/m K)	Specific heat (J/kg K)	Density (kg/m^3)
Concrete blocks	1.263	1000	2000
CS	0.71	840	2011
EC	0.4	1094	1417

3.1 Model Results and Validation

To validate the numerical model, a small-scale building prototype with external wall plaster was built (Fig. 7) and an EPS roof was fixed to avoid the heat transfer from the top of the building. The wall surface temperatures inside and outside were monitored for 6 consecutive hours and compared with the results predicted from the numerical model. Figure 8 shows a comparison of measured surface temperatures and numerically predicted temperatures and it indicates fairly good agreement between the experimental and numerical results. Moreover, the internal wall surface temperature with 'the developed plaster (WP_EC) seems less compared to the wall with conventional plaster (WP_CS). To explore the thermal performance throughout a day, weather data of a random day in Colombo for 24 h [22] was used. The model was simulated for consecutive 3 days to avoid the errors due to the initial boundary condition assumptions. The output for 24 h was extracted beyond the convergence

Fig. 7 Building prototypes

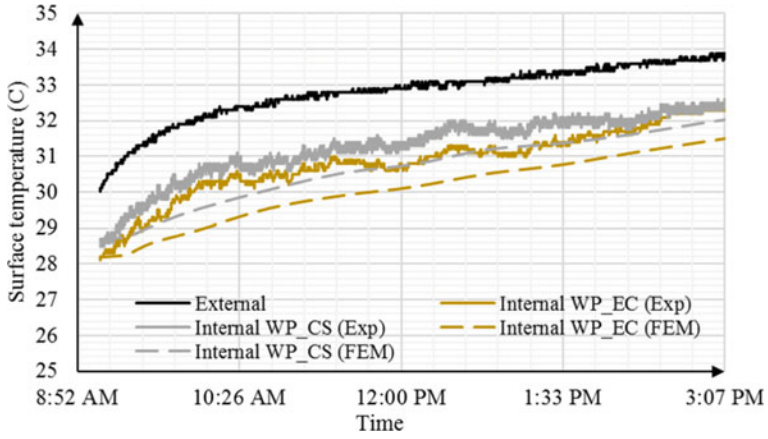

Fig. 8 Comparison of measured temperature and predicted temperature

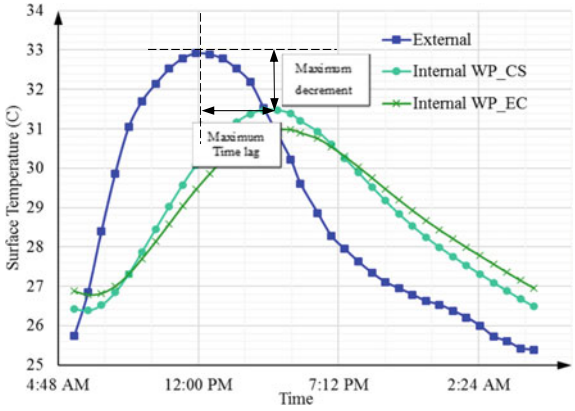

Fig. 9 Predicted temperature profiles

Table 4 Computed decrement factors and time lags

Model ID	Time lag	Decrement factor
WP_CS	3 h 48 min	0.68
WP_EC	4 h 33 min	0.56

which is illustrated in Fig. 9. The computed decrement factors and time lags for both models are listed in Table 4. The predicted results indicate that the buildings with WP_EC wall panels can enhance the thermal comfort compared to the buildings with WP_CS wall panels.

3.2 Parametric Study

3.2.1 Effect of Plaster Thickness

The selection of plaster thickness is a crucial aspect in terms of maintaining thermal comfort within the buildings. Therefore, a range of plaster thickness between 10 and 50 mm was selected in this study. The developed composite wall panel model (WP_EC) was re-analysed with changing plaster thicknesses and the indoor wall surface temperatures were monitored. From the results obtained, the decrement factors and time lags for respective plaster thicknesses were calculated and presented in Fig. 10. The graph indicates that the decrement factor reduces with increasing plaster thickness and it reverses for the time lag. Moreover, it is noted that similar thermal performances can be achieved using 15 mm of EC plaster and 25 mm of CS plaster. This shows the reduced thickness requirement when using the plaster discovered in this study.

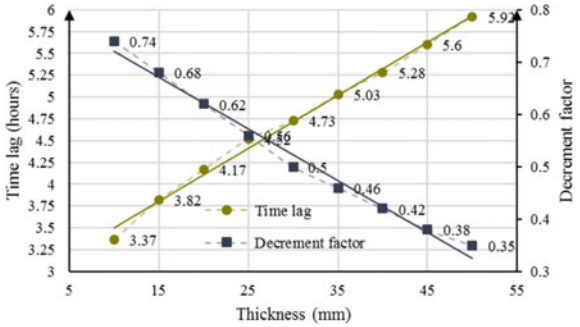

Fig. 10 Effect of plaster thickness on heat transfer

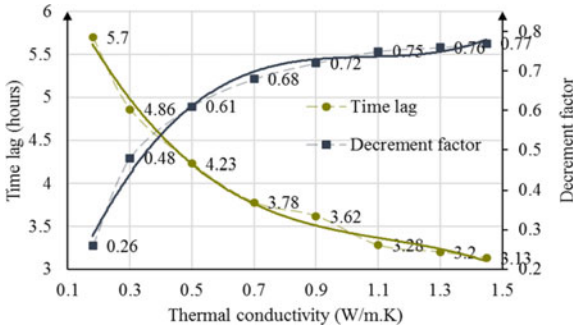

Fig. 11 Effect of thermal conductivity of the plaster thickness on heat transfer

3.2.2 Effect of Thermal Conductivity

The thermal conductivity of a material is a key parameter in deciding the heat transfer process through any materials [20]. Since several mixes were developed in this study, assessing the effect of thermal conductivity of the plaster material on heat transfer analysis is essential. In such a case, a range of thermal conductivities between 0.15 and 1.45 W/m K were selected. By monitoring the indoor and outdoor wall surface temperatures, the relevant factors were calculated (Fig. 11). The plot indicates that a range of decrement factors from 0.26 to 0.76 and a range of time lags from 3.1 to 5.7 h can be achieved with the given range of thermal conductivity mixes. It is also noted that a small change in the thermal conductivity makes a huge change in the heat transfer analysis in the low thermal conductivity materials.

4 Conclusions

An attempt has been made on developing a green insulation system for the building walls to enhance the thermal comfort within the buildings. The following conclusions were drawn:

1. Recycled Expanded Polystyrene (EPS) particles can be incorporated in the construction industry as a base material for the cementitious plasters. On average of 95–145% of the sand can be replaced by coarse EPS particles to achieve a mortar mix match with N-type mortar requirements.
2. The thermal conductivity, compressive strength, and density drastically reduce with the replacement percentage. A thermal conductivity range of 0.22–0.34 W/m K can be obtained for the EPS-cement N-type plaster with 3.35 mm grade EPS.
3. The thermal conductivity of the mortar mixes significantly varies with the particle size distribution of the EPS particles. The mortar mix with 125% replacement by the 1.15 mm grade EPS has been identified as the ideal mix for the insulated wall plaster.
4. A numerical model of a composite wall panel was developed to study the heat transfer process through the wall panel with the developed plaster and the model results were in good agreement with the experimental results.
5. The heat sustains an additional 45 min within the composite wall with EPS plaster compared to the wall with the conventional plaster. The decrement factor of WP_ES is 18% less than the WP_CS which also adds value to the developed plaster in enhancing the thermal performance.
6. The parametric study shows that the plaster thickness and the thermal conductivity of the plaster have an adverse effect on the heat transfer through the composite wall. A similar thermal comfort to the buildings with a 25 mm thick conventional plaster can be expected in the buildings with a 15 mm thick developed plaster (EC).

Acknowledgements The financial support provided by National Research Council; Sri Lanka (PPP 18-01) is greatly appreciated.

References

1. ABAQUS 6.13 (2013) ABAQUS analysis user's guide. Dassault Systems Simula Coorporation
2. ASTM C 270-07 (2010) Standard specification for mortar for unit masonry. ASTM International, West Conshohocken, pp 2–13. https://doi.org/10.1520/C0270-10
3. ASTM D7340 (2018) standard practice for thermal conductivity of leather. ASTM International, West Conshohocken
4. Dissanayake DMKW, Jayasinghe C, Jayasinghe MTR (2017) A comparative embodied energy analysis of a house with recycled expanded polystyrene (EPS) based foam concrete wall panels. Energy Build 135:85–94. https://doi.org/10.1016/j.enbuild.2016.11.044
5. Dylewski R, Adamczyk J (2014) The comparison of thermal insulation types of plaster with cement plaster. J Clean Prod 83:256–262. https://doi.org/10.1016/j.jclepro.2014.07.042
6. Fernando PLN, Jayasinghe MTR, Jayasinghe C (2017) Structural feasibility of Expanded Polystyrene (EPS) based lightweight concrete sandwich wall panels. Constr Build Mater 139:45–51. https://doi.org/10.1016/j.conbuildmat.2017.02.027

7. Ferrándiz-Mas V et al (2014) Lightweight mortars containing expanded polystyrene and paper sludge ash. Constr Build Mater 61:285–292. https://doi.org/10.1016/j.conbuildmat.2014.03.028
8. Ghosh A, Ghosh A, Neogi S (2018) Reuse of fly ash and bottom ash in mortars with improved thermal conductivity performance for buildings. Heliyon 4:1–32. https://doi.org/10.1016/j.heliyon.2018.e00934
9. Gunawardhana DSRSS, Gamage JCPH (2015) Performance of sand cement block produced with partial replacement of cement by rice husk ash. In: 6th international conference on structural engineering and construction management 2015, Kandy, Sri Lanka, pp 172–175
10. Ho BT, Roberts TK, Lucas S (2018) An overview on biodegradation of polystyrene and modified polystyrene: the microbial approach. Crit Rev Biotechnol 38(2):308–320. https://doi.org/10.1080/07388551.2017.1355293
11. Irsyad M et al (2017) Heat transfer characteristics of building walls using phase change material. In: 1st international symposium on green technology for value chains. IOP Publishing. https://doi.org/10.1088/1755-1315/60/1/012028
12. Jannat N et al (2020) A comparative simulation study of the thermal performances of the building envelope wall materials in the tropics. Sustainability 12:1–26. https://doi.org/10.3390/SU12124892
13. Jayasinghe C, Fonseka WMCDJ, Abeygunawardhene YM (2016) Load bearing properties of composite masonry constructed with recycled building demolition waste and cement stabilized rammed earth. Constr Build Mater 102:471–477. https://doi.org/10.1016/j.conbuildmat.2015.10.136
14. Kahandawa Arachchi KADYT, Gamage JCPH, De Silva GIP (2019) Thermal insulaltion systems for CFRP/concrete composites: a review. In: International conference on structural engineering and construction management, Kandy, Sri Lanka
15. Kaya A, Kar F (2016) Properties of concrete containing waste expanded polystyrene and natural resin. Constr Build Mater 105:572–578. https://doi.org/10.1016/j.conbuildmat.2015.12.177
16. Ozel M, Ozel C (2012) Effects of wall orientation and thermal insulation on time lag and decrement factor. In: 9th international conference on heat transfer and thermodynamics, Malta, pp 680–684
17. Ramli Sulong NH, Mustapa SAS, Abdul Rashid MK (2019) Application of expanded polystyrene (EPS) in buildings and constructions: a review. J Appl Polym Sci 136(20):1–11. https://doi.org/10.1002/app.47529
18. Schackow A et al (2014) Mechanical and thermal properties of lightweight concretes with vermiculite and EPS using air-entraining agent. Constr Build Mater 57:190–197. https://doi.org/10.1016/j.conbuildmat.2014.02.009
19. Selvaranjan K et al (2020) Thermal performance of rice husk ash mixed mortar in concrete and masonry buildings. Budownictwo i Architektura 19(4):43–52. https://doi.org/10.35784/budarch.2121
20. Selvaratnam A, Gamage JCPH (2021) A review on thermo-mechanical behaviour of CFRP-concrete composites at elevated temperature and available insulation systems. In: Lecture note in civil engineering, pp 533–541. https://doi.org/10.1007/978-981-15-7222-7_43
21. SLS 107 (1995) Specification for Ordinary Portland cement Part 2: Test methods. Sri Lankan Standards, p 107
22. Time and date (2020) Available at: https://www.timeanddate.com/weather/sri-lanka/sri-jayawardenapura-kotte/hourly
23. Toure PM et al (2019) Experimental determination of time lag and decrement factor. Case Stud Constr Mater 11:e00298. https://doi.org/10.1016/j.cscm.2019.e00298

Investigating the Preparedness of Staff Members in Privately Owned Hospitals in Sri Lanka Against Fire Hazards

W. D. M. Kularatne, H. H. H. Hasalanka, and C. S. A. Siriwardana

Abstract Hospitals have a high potential for fire hazards due to reasons such as the presence of volatile chemicals, large electrical networks, and high waste generation. In addition to taking steps to prevent fire, preparation of staff to face a fire hazard should also be done. This study looks at the current level of fire safety training and preparedness of staff members in privately owned hospitals in Sri Lanka. A structured questionnaire was developed to assess fire safety training and preparedness of hospital staff members. This was used to interview sixty-six staff members of multiple major private hospitals. The staff consisted of various positions ranging from medical staff to security and maintenance staff. The study revealed that over 70% of the staff had training in basic fire management and more responsibility in emergency response had been given to the maintenance and security staff in the hospitals. Overall, the staff in private hospitals were suitably prepared for fire hazards, with each institution holding fire training programs annually. It is recommended that staff preparedness can be increased through actions such as carrying out regular fire safety training and drills, developing a fire action plan for the hospital, and designating a fire safety officer for the hospital.

Keywords Safe hospitals · Disaster risk reduction · Fire safety training · Staff preparedness · Patient evacuation

1 Introduction

Fire hazards, which could originate from within buildings, or as wildfires have the potential to cause serious injuries and even death [5, 48]. In addition, fires can lead to psychological stress and property loss [25]. In the twenty-first century, the world experiences 7–8 million fires annually, resulting in over 500,000 injuries and around 300,000 deaths [5, 48]. In Sri Lanka also, fires account for 5% of recorded disaster events in the country [44].

W. D. M. Kularatne (✉) · H. H. H. Hasalanka · C. S. A. Siriwardana
Department of Civil Engineering, University of Moratuwa, Katubedda, Sri Lanka

R. Dissanayake et al. (eds.), *ICSBE 2020*, Lecture Notes in Civil Engineering 174,
https://doi.org/10.1007/978-981-16-4412-2_16

The fact that healthcare institutions can also experience disasters has come into the focus of the World Health Organization in recent years, leading to the introduction of the Safe Hospital Initiative. In accordance with this, the WHO has introduced disaster risk reduction frameworks for hospitals such as the Hospital Safety Index (HSI) Guide [47].

This study is a part of the Safe Hospital Project which is a collaborative effort between the University of Moratuwa and the Disaster Preparedness and Response Division, Ministry of Health, Sri Lanka. The project was initiated in order to assess hazard risks to hospitals in the country and improve their disaster reduction. The project explores all aspects related to disaster risk reduction; structural safety, non-structural safety, and emergency and disaster management.

Studies have been conducted regarding the adaptation of the Hospital Safety Index Guide developed by the WHO and PAHO to suit Sri Lankan hospitals and the development of a hazard map for government-owned hospitals in the country [18, 16, 24].

In addition to studies related to multi-hazard disaster risk reduction in hospitals, further studies have been conducted to identify the preparedness of hospitals to face specific hazard types in Sri Lanka such as tsunami and fires [13, 17, 23].

From various case studies that have been conducted in government-owned hospitals, in the project, it has been identified that there is much room for improvement in Sri Lankan hospitals, especially in the area of emergency and disaster management [24]. Due to factors such as the high amount of work being carried out and the limitation of staff and budgeting in the hospitals, it has been noticed that work related to disaster management in individual hospitals have been given only a minor role.

In the disaster risk reduction frameworks such as the HSI Guide, fire hazards have been significantly considered. It is evident when looking at the routine functions of a hospital, that hospitals have potential risk for fires. For example, hospitals have a large number of medical equipment that draws a high amount of electricity, which paves an easy path for electric fires from electric overloading [46]. Again, hospitals normally use medical gas supply lines that run throughout the hospital buildings, which means that hospitals have a high concentration of oxygen gas [8]. Hospitals also have large quantities of flammable or combustible material in storage, such as highly concentrated medical solutions and alcohol-based solutions.

The impact on people's lives due to a fire in a hospital can be high due to the type of population present in the hospital, with many patients having mobility issues. Evacuating people who are able-bodied during an emergency is still a difficult task, due to the panic that could set in as well as the traffic that would be created in escape corridors and stairwells. When the majority of people in the building might have mobility issues, the evacuation process is made much harder. A recent study has identified several hospital units as critical units, as they hold the most vulnerable patients who cannot be easily evacuated. These identified units are maternity units, labor rooms, premature baby units, neonatal intensive care units, intensive care units, operating theatres, and pediatric units [13].

The risk of fire in hospitals can be seen more clearly by looking at past incidents. The AMRI hospital in Calcutta, India experienced a fire caused by a short circuit

in 2011 which caused 89 deaths [32, 34]. Another fire hazard in the Ramenskyon Psychiatric Hospital in Moscow, Russia in 2013 was caused by a smoking incident and resulted in 38 deaths [43]. The fire hazard in the Royal Marsden Hospital in England in 2008 caused damages worth GBP 500 million at the time [45].

The risk of fires is equally present in hospitals in Sri Lanka as well. The Anuradhapura Teaching Hospital experienced a fire in 2014 when an MRI Scan machine was being installed. The destroyed machine was worth an equivalent of USD 1.9 million at the time [9]. In early April of 2020, there was a chemical fire at the pharmaceutical storage facility of the Teaching Hospital Kurunegala which destroyed medical supplies stored in three rooms as well the ground floor corridor of the facility [19].

Considering the above-mentioned factors and the high risk of fires in hospitals, fire safety management should be an integral part of the hospital strategy to be a "Safe Hospital". In fire safety management, the concepts of fire prevention and protection from fire should both be adopted [39]. Staff preparedness is a significant part of fire safety management.

The positive effect that fire safety training can have during a fire incident as well as the negative impact due to a lack of training can be understood from the following two examples.

1. The Royal Marsden Hospital fire [1], although it caused a high financial cost, did not experience any casualties. The fire caused the hospital to evacuate over 150 patients and 800 staff members. This impressive safety in terms of human lives was a direct effect of the excellent fire safety training given to staff members [2, 45].
2. The chemical fire at the Teaching Hospital Kurunegala [2] had blazed when the staff had attempted to use water to douse the fire. This shows the negative impact due to the staff members not being trained on the proper suppression methods and material for different types of fires [1].

As can be seen from the two examples, a high level of fire safety training and preparedness directly impact whether the losses from a fire will be major or minor. Therefore, hospital staff members must be well versed in fire safety practices.

Sri Lanka has both government-owned hospitals as well as privately owned hospitals. In this research study, an attempt is made to analyze the fire safety training and preparedness of staff members in privately owned hospitals. The study was preceded by a literature review regarding fire safety training needed for an institution's staff.

2 Literature Review

Providing fire safety training to staff of an institution as well as conducting regular fire drills is an important part of fire risk management. In a hospital, especially, the presence of nursing staff with fire safety training is the best defense in the face of a fire [46]. A study conducted in Malaysia regarding preparedness and resilience in hospitals has shown that human resources and training have been ranked highest in

terms of preparedness and the ability to adapt in a timely manner has been ranked highest in terms of resilience [41].

There are instances that hospitals do not consider fire hazards as a top priority, especially in highly controlled areas such as operating theatres. However, surgical fires have been ranked as the number 3 among the top 10 common technology hazards [29]. Many professionals mistakenly assume that if a fire occurred in an operating theatre, then that fire was not preventable. However, most surgical fires are preventable. Preparing for a fire hazard is important in a hospital, as there will be a large population of weak and vulnerable patients who will be depending on the staff members for their safety [14].

Fire hazards have the potential to occur suddenly and without warning. They can become intense quickly, and therefore requires fast response in order to minimize the losses [11]. If staff members have not had previous training, it is not realistic to expect that they would respond to a fire in an effective way [35]. Although panic behavior is not common in the face of a fire, the lack of knowledge on the fire emergency actions as well as the induced stress can end up causing people to make fatal errors [37]. The lack of staff training in fire safety can increase confusion, which would increase the danger during the time of a fire hazard [6]. In some people, the lack of previous experience can cause the phenomenon of "cognitive paralysis", where people end up not taking any action. This can lead to fatalities that could have been avoided [26, 27].

Fire safety training has been identified as a tool to help improve fire safety knowledge and the response to a fire. This can result in minimizing fire-related casualties [10, 21, 31]. Fire safety is the collective responsibility of all staff members and therefore, it is important that staff members in each department of the hospital are actively involved in fire safety training [15]. The way a person acts during a fire depends on factors such as personality and leadership abilities, decision-making styles, and the amount of fire training received [36]. Therefore, when assigning disaster and emergency duties to the staff members, the above-mentioned factors should be considered.

Fire safety drills should be used in institutions as they are effective in converting fire safety training into an experience that the staff members can use to respond effectively during a fire hazard [40]. This experience helps a person to effectively analyze the situation and correctly understand the information in the surroundings [11]. Previous studies have found that unannounced drills and exercises are often more effective [22].

An experiment done in the Netherlands shows the effectiveness of hospital staff training in an evacuation. The same evacuation procedure was practiced in two rounds for patients of different medical status. It was observed that during the second round of evacuation, the hospital staff managed to achieve a significantly better evacuation rate [20]. The results of the experiment have been illustrated as seen in Fig. 1.

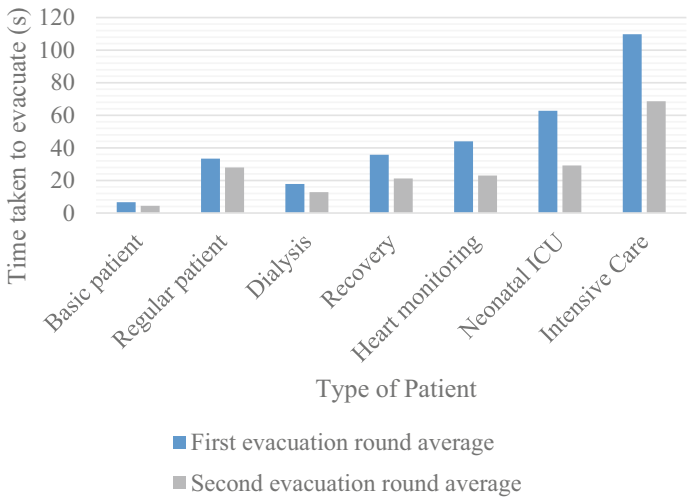

Fig. 1 Influence of trained staff during evacuation [20]

The training given to an institution's staff should be customized to the characteristics of the workplace. The training should [12],

- Provide information about the emergency procedures
- Consider the duties and responsibilities of the staff
- Be understood by the staff
- Consider the results of risk assessments done for the institution.

Fire training should include providing the staff members with a sufficient level of knowledge of operating and maintaining fire safety equipment such as fire extinguishers, fire hose reels, and fire blankets [3, 28]. The training should also include a description of staff duties, emergency evacuation procedures, and contacting the local fire service department [7]. It is important that the training is conducted so that the participants fully understand it and know their roles. Therefore the training should not only include a sufficient amount of time on fire safety training and drills, but it should also be of good quality and tailored to the participant group [38]. Fire safety training should also be conducted at regular periods, so that the staff members continuously review, revise, and reconfigure their knowledge on fire safety [42].

Fire safety preparedness should include developing and maintaining a fire safety plan. Two essential actions for fire safety in an institution is the appointment of a fire safety manager, who is responsible for the overall fire safety management, and the maintenance of a fire safety manual, which will contain all documentation regarding the fire safety planning in the institution [4].

3 Methodology

Sri Lanka has a free healthcare system for all citizens through 1100 primary, secondary, and tertiary level hospitals [30]. Privately owned hospitals, which charge for healthcare services, also operate in the country. Many recent risk assessment studies carried out regarding hospitals in Sri Lanka have only focused on government-owned hospitals. However, when fire risk is concerned, all hospitals whether government-owned or privately owned must be considered. In this study, the focus was given to the fire risk preparedness of staff members in privately owned hospitals in the country.

Staff members of three major privately owned hospitals were interviewed during this study. For confidential reasons, the hospitals shall be referred to as Hospital A, Hospital B, and Hospital C in this paper. Each of the hospitals had a different administration system. Hospital A is headed by the hospital director, while Hospital B's administration is done through a Board of Directors. Hospital C is administrated by a General Manager.

3.1 Survey Development

The first part of the survey looked at the demography of the responders. The elements in the section included the job position of the responders, their gender, age category, number of years they had worked at the hospital, and previous work experience in hospitals.

The second section explored the preparedness of the responders in three different ways which were identified in the literature review: past experience with fire hazards in hospitals, training, and drills regarding fire hazards experienced in the current and previous workplaces, and knowledge regarding the procedures that need to be followed during a fire hazard. The section considered activities regarding sounding the alarm, preliminary firefighting by the staff members, evacuation of self and patients, and contacting the local fire service department. The final question was a self-evaluation of the responder's preparedness regarding fire hazards, using a scale system of 1–5.

3.2 Sampling Method

Hospitals have a large number of staff members, medical and non-medical, who have various types of duties and responsibilities. As a hospital has various areas with a high risk of fire, most staff members have a possibility of experiencing a fire hazard. Therefore, all staff members in a hospital must possess a basic level of preparedness for a fire hazard. Therefore, in this survey, a random sampling method was used, so

as to ensure that staff members of all levels and various job titles were included in the survey.

3.3 Sample Size

The total population of permanent staff members in the three hospitals rounds off at 1500. Assuming a confidence level of 90% and a 10% margin of error, the ideal sample size was calculated.

For 90% confidence level: Z score = 1.65

$$\text{Sample Size} = \frac{z^2 \times p(1-p)}{e2} \Big/ 1 + \frac{z2 \times p(1-p)}{e2N} \tag{1}$$

z = Z Score,
p = Standard Deviation,
e = Margin of Error,
N = Population.

The standard deviation was assumed as 0.5 in order to ensure the sample size was large enough.

$$\text{Sample size} = \frac{1.652 \times 0.5 \times (1-0.5)/0.12}{1 + (1.652 \times 0.5 \times (1-0.5)/0.12 \times 1500)} = 65$$

3.4 Data Collection Method

Each of the responders was interviewed using the structured questionnaire. A total of 66 responses were obtained. The responses were then analyzed to find out the preparedness of the staff against a fire hazard in the hospital.

Each of the hospitals had a specific staff member who was responsible for fire safety management in the hospitals. To gain a better and overall insight into the fire safety practices of each hospital, these staff members were also separately interviewed at a greater depth.

4 Demography of the Responders

From the 66 responses that were obtained, 20 of the respondents were from Hospital A, 30 from Hospital B, and 16 from Hospital C. The responders included various hospital staff members such as nursing staff, maintenance staff, security staff, office

Table 1 Distribution of the responders according to staff position

Staff position	Office	Store	Laboratory	Security	Supportive	Nursing	Maintenance
Percentage of responders (%)	33.8	3.1	6.2	20.0	12.3	15.4	9.2

staff, storage staff, laboratory staff, and supportive staff. The distribution of the responders according to their staff position can be seen in Table 1. A higher percentage of the responders were female with only 38% of the staff members being male.

Looking at the age distribution of the responders, a majority of them were between the ages of 20 and 49. The complete distribution of the responders according to age is described in Table 2.

When considering the number of years of employment of the responders, 21 had worked at the hospitals less than a year, while 18 had worked between 1 and 5 years. Another 13 responders had 6–10 years of employment at the hospitals and 12 had worked 11–20 years. The remaining 2 responders had worked for over 20 years at the hospitals. The complete distribution of the responders according to the period of employment at the hospital is given in Table 3.

Table 2 Distribution of the responders according to age

Age category	20–29	30–39	40–49	50–59	60–69	Above 70
Number of responders	23	14	20	6	2	1

Table 3 Distribution of the responders according to the number of years of employment

Number of years at the hospital	Less than 1 year	1–5 years	6–10 years	11–20 years	More than 20 years
Number of responders	21	18	13	12	2

5 Results of the Questionnaire

Nine of the responders had experience with fires that had occurred in the hospitals. All the fires were minor and extinguished quickly, avoiding the spread of fire. The causes of past fire incidents in the hospitals included electrical failures, lightning, and human errors. There had been electric fires in the kitchen and the electric panel in Hospital A, a fire in the generator caused by lightning and an electric fire in the basement in Hospital B, and an accidental fire in a patient room in Hospital C.

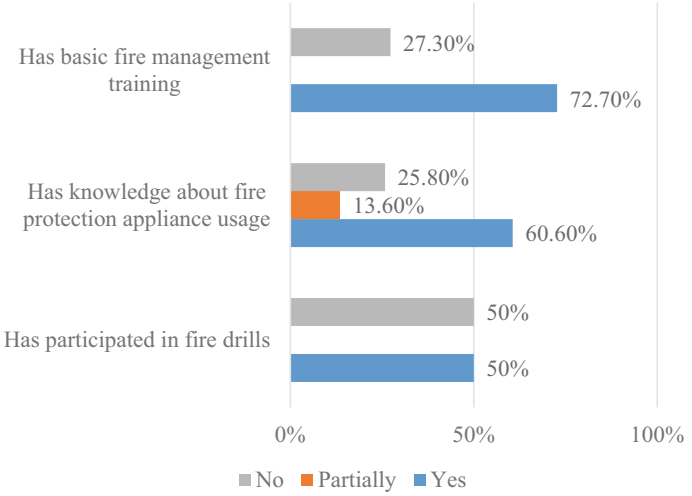

Fig. 2 Fire safety training provided by the hospital to responders

When looking at the fire training provided for the hospital staff, over 70% responded that they had received basic fire management training and a little over 60% had some kind of knowledge regarding the usage of fire protection appliances such as fire extinguishers. The 13.6% of responders who replied to have partial knowledge in fire protection appliance usage denoted the staff members who had received theoretical knowledge in the subject but had not received practical training. Half of the responders had participated in fire safety drills. The statistics can be seen in Fig. 2.

According to the staff personnel in charge of fire safety management in each of the hospitals, fire safety training programs, and fire drills for the staff are held at the hospital at least annually. Hospital A and B both hold fire safety training programs annually. It must however be noted that the program is not attended by all of the staff members. This is for two reasons; the first reason being that the program cannot accommodate all of the staff members in one session and the second reason being that the operation of the hospital during the program requires many staff members to continue with their duties. In Hospital C, these programs are held around 8 times every year, so that all staff members experience the training at least once a year. The regularity of these programs can be credited to the requirement given by the fire service department in the country for privately owned hospitals to obtain a "Fire Safety License" annually to continue the operation of the hospitals.

It must be noted that in both Hospital A and Hospital B, the heads of the maintenance units of the hospitals were in charge of the fire safety management in the hospitals. However, Hospital C had a separate Fire Commander, whose main responsibility was fire safety management in the hospital.

When looking at the collected data, it was observed that the staff who had received most of the training were from the hospitals' maintenance units and security units.

During the interviews, a majority of the responders (who were not maintenance of security staff members) relayed that if a fire were to occur, they would quickly inform the maintenance and security personnel about the incident.

Fire detection and alarm systems had been installed at Hospital B and Hospital C, but not in Hospital A. However, Hospital A had a manual emergency alarm system that was connected to the hospital reception and security office. Regarding sounding the alarm during a fire, a majority of the staff were aware of how to use the manual call points or emergency alarm. Only 3 out of 66 responders were not aware of the alarm systems. In areas where there were no alarm systems installed, the respondents have stated that they would use a mobile phone to send the alarm.

From the interviews, it was observed that the responsibilities during a fire hazard varied for each kind of staff. For office staff, there were no other responsibilities other than evacuation if the fire occurred at another place. In all three hospitals, the office areas were on the upper floors, so this course of action would be best for these staff members. If the fire were to occur in the office areas, the staff must operate the manual call point and try to extinguish the fire.

Considering the nursing staff of the hospitals, they are in charge of evacuating the patients of wards along with their medical files and other necessary materials safely to the designated assembly point or another safe place.

The major responsibility during a fire would fall to the maintenance staff and security staff. They would be in charge of directing the evacuation of the other staff as well as patients and hospital visitors. In Hospital C, there was a designated Emergency Response Team. They have been given advanced training in fire safety and consist of maintenance unit staff, security staff, and kitchen staff.

The staff personnel who will be in charge of notifying the local fire service department if necessary, according to the responders include maintenance staff, security staff, administrative staff, and reception staff.

Considering evacuation, staff members stated that an emergency evacuation without patients would take between 1 and 5 min, and evacuation with patients would take between 5 and 15 min. In reality, this would probably increase due to the traffic in stairways during an emergency.

When looking at the evacuation of patients, especially patients who will have mobility issues, more attention is needed. All staff personnel relevant to the evacuation activities of patients such as nursing staff, security staff, and maintenance staff in each of the hospitals were well aware of the standard procedures. During an emergency, if evacuation of patients who require assistance is necessary, the patients will be transferred to trolleys, stretchers, or wheelchairs and evacuated along safe exit ways and exit staircases. The staff members were well aware of the necessity to avoid using elevators during an emergency. During the evacuation, the responders have stated that the evacuated patients must be accompanied by the patients' medical records as well as other relevant medical supplies necessary for the patients (e.g. oxygen cylinder, saline, etc.).

In Hospitals A and B, where assembly points had not been designated, most of the responders declared that assembly would be done in the open area in front of the hospital buildings or the roadway. This would both put the evacuees in danger as well

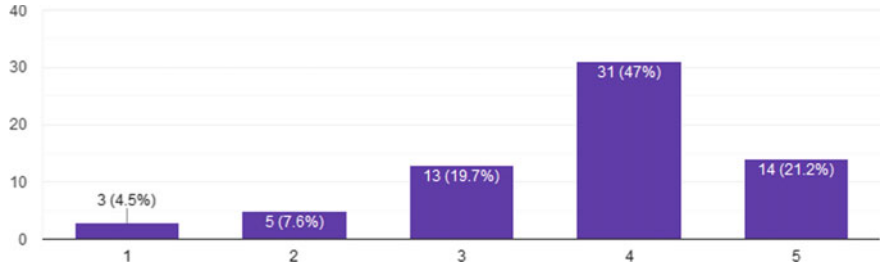

Fig. 3 Self-evaluation of the responders regarding their preparedness to face a fire hazard

as cause trouble for the fire brigades who would come in. The staff in Hospital C all had knowledge of the assembly point of the hospital as it has been clearly designated with a sign.

When asked to self-evaluate their preparedness to face a fire hazard in their workplace on a scale of 1–5, with 5 being extremely prepared, the responders replied as can be seen in Fig. 3. Only 3 responders gave a self-evaluation of 1, while 5 gave a self-evaluation of 2 and 13 gave a self-evaluation of 3. 31 of the responders gave a self-evaluation of 4 and the other 14 gave themselves a score of 5.

The evaluation of 1 was considered as 0% prepared and 5 was considered as 100% prepared. In this case, the evaluation points of 2, 3, and 4 can be converted into preparedness levels of 25%, 50%, and 75% respectively. In this case, over 68% of the responders have evaluated themselves as at least 75% prepared to successfully face a fire.

6 Conclusions and Recommendations

6.1 Conclusions

Carrying out fire prevention practices is the best way to manage the risk of fires. However, there is always the possibility that a fire hazard could occur despite the strictest measures taken to minimize the risks. Therefore, a hospital and its management should always be prepared for fire protection as well. This should include the preparedness of all staff members to face a fire hazard.

From the survey, it has been identified that a majority of staff members in privately owned hospitals are at a high preparedness level in terms of fire with over 60% having training in the use of fire protection equipment and over 70% having received basic fire management training. This is in contrast to government-owned hospitals, as a recent study in two major tertiary hospitals observed a distinct lack of training in fire management for staff members [24]. The survey found that the duties and responsibilities of staff members in Hospitals A, B, and C in the event of a fire hazard had been identified. The major responsibilities in such an event were given to the staff

of the maintenance and security units of the hospitals. These responsibilities include extinguishing the fire, evacuating people in the vicinity of the fire, and notifying the local fire service department. The main responsibility of evacuating patients falls to the nursing staff and supportive medical staff in the respective hospital wards.

Annual fire hazard management training and drills are conducted by each of the three hospitals, as this is a partial requirement in obtaining the annual "Fire Safety License" which is required for the continued operation of a privately owned hospital. The same requirement is not present for government-owned hospitals.

6.2 Recommendations

It is important that a hospital has a fire safety plan, which should include a fire action plan. The fire action plan should include the procedures for initial fire suppression, fire evacuation, and communicating with the local fire service department.

Hospital C, which had its own fire safety officer, performed better in fire safety management compared to Hospitals A and B whose fire safety management was overseen by the heads of maintenance units, who also had other duties to oversee. This better performance can be partially attributed to the presence of a staff member whose main responsibility was the fire safety management in the hospital. It is advised that a hospital has a separate fire safety officer, who will oversee and control the fire safety practices in the hospitals.

When considering fire safety training and fire drills, it is recommended that all staff are required to undergo the programs. However, if this cannot be done, the training should be provided in such a way that at least a few staff members from each department are included. It is important that fire safety training is provided at least annually to the hospital staff. Realistically, it is not possible to hold one program session for all the staff members at the same time, considering the staff size in a major hospital, shift-based duty of hospital staff as well as the regular duties of the staff which are needed at all times of the day. Therefore, it is recommended that fire safety training is provided for groups of the staff in several sessions in order to gain an optimum level of staff preparedness.

When delegating staff responsibilities for a potential fire hazard, the responsibilities should coordinate with the regular responsibilities of each staff member. For example, taking care of patients and evacuating them safely if necessary, should be done by nursing staff and other medical staff. Fire suppression and directing evacuation should be under the responsibility of the hospital's security staff and the maintenance staff.

The action of contacting the local fire service department is important and doing this early can help to minimize property damages and injuries. From the survey it was identified that the hospitals had identified this as the responsibility of the fire safety officer or the administrative staff. This can be dangerous as it would delay the time taken to notify the fire service department and allow the fire to spread. All staff

members in a hospital must be trained to act quickly in informing the fire service department as soon as possible in case of a fire incident.

In a hospital, the evacuation procedures for patients must be taken seriously. Often times during a fire, lives could be saved by remaining in place rather than rushing to evacuate through a smoke dense path. Therefore, the fire safety officer should develop proper emergency evacuation paths and procedures. Also, coordination between staff in different areas of the hospital is important during a fire hazard and should be included in staff preparedness training.

Acknowledgements The authors wish to thank the administrative officials of the three hospitals for providing permission to carry out the research study. Sincere thanks also go out to all the responders of the study.

References

1. Ada Derana (2020) Cause of Kurunegala Hospital drug storage fire uncovered [WWW Document]. http://www.adaderana.lk/news/62296/cause-of-kurunegala-hospital-drug-storage-fire-uncovered. Accessed 30 April 2020
2. Allen N, Cockroft L, Borland S (2008) £500m Royal Marsden blaze cripples services
3. Brennan P (1999) Victims and survivors in fatal residential building fires. Fire Mater 23:305–310
4. British Standards Institution (1997) BS 5588, Fire precautions in the design, construction and use of buildings, Part 11: Code of practice for shops, offices, industrial, storage and other similar buildings. London, UK
5. Brushlinsky NN, Sokolov SV, Wagner P, Hall JR (2006) World fire statistics
6. Cassidy D (1991) Involving the staff in fire safety. Nurs Homes Sr Citiz Care 40:15–18
7. Chow WK (2001) Review on fire safety management and application to Hong Kong. Int J Eng Perform-Based Fire Codes 3:52–58
8. Chowdhury K (2014) Fires in Indian hospitals: root cause analysis and recommendations for their prevention. J Clin Anesth 26:414–424. https://doi.org/10.1016/j.jclinane.2013.12.014
9. Daily Mirror Online (2014) Fire at Anuradhapura Teaching Hospital. Dly. Mirror
10. DiGuiseppi C, Roberts I, Wade A, Sculpher M, Edwards P, Godward C, Pan H, Slater S (2002) Incidence of fires and related injuries after giving out free smoke alarms: cluster randomised controlled trial. Br Med J 325:995
11. Driskell JE, Salas E (eds) (1996) Stress and human performance. Series in applied psychology. Lawrence Erlbaum Associates, Mahwah, NJ
12. Great Britain, Health and Safety Executive (1999) Fire safety: an employer's guide. Stationery Office, London
13. Harisuthan S, Hasalanka H, Kularatne D, Siriwardana C (2020) Applicability of the PTVA-4 model to evaluate the structural vulnerability of hospitals in Sri Lanka against tsunami. Int J Disaster Resil Built Environ. https://doi.org/10.1108/IJDRBE-01-2020-0001 (ahead-of-print)
14. Harrington SS, Walker BL (2003) Is computer-based instruction an effective way to present fire safety training to long-term care staff? J Nurses Prof Dev 9:147–154
15. Hart SR, Yaknik A, Ashford J, Springer R, Harvey S (2011) Operating room fire safety. Ochsner J 11:37–42
16. Hasalanka H, Kularatne D, Siriwardana C, Wijesekara N, Kodituwakku L (2019) A framework to develop multi-hazard maps to identify the natural hazards which affect the safety of Sri Lankan Hospitals. In: 2019 Moratuwa engineering research conference (MERCon). Presented

at the 2019 Moratuwa Engineering Research Conference (MERCon), IEEE, Moratuwa, Sri Lanka, pp 418–423. https://doi.org/10.1109/MERCon.2019.8818863
17. Hasalanka H, Siriwardana C, Kularatne D (2019) Development of a hospital safety assessment for tsunami in the Sri Lankan context. Presented at the International Conference on Structural Engineering and Construction Management, Kandy, Sri Lanka
18. Hasalanka H, Siriwardana C, Wijesekara N, Kodituwakku L (2018) Development of a tool to assess structural safety of Sri Lankan hospitals under disaster conditions. Presented at the International Conference on Sustainable Built Environment
19. Hiru News (2020) Fire at the Kurunegala hospital caused by a chemical—staff evacuated safely [WWW Document]. Hiru News. http://www.hirunews.lk/237996/fire-at-the-kurunegala-hospital-caused-by-a-chemical-staff-evacuated-safely. Accessed 30 April 2020
20. Hoondert PPN (2017) State of the art fire safety concept for evacuation of different types of vulnerable patients in Dutch hospitals. Delft University of Technology, Faculty of Architecture and the Built Environment and Building Technology
21. Huseyin I, Satyen L (2006) Fire safety training: Its importance in enhancing fire safety knowledge and response to fire. Aust J Emerg Manag 21:48–53
22. Kaji AH, Lewis RJ (2006) Hospital disaster preparedness in Los Angeles county. Acad Emerg Med 13:1198–1203. https://doi.org/10.1197/j.aem.2006.05.007
23. Kularatne D, Hasalanka H, Siriwardana C (2019) Conceptual Compilation of activity criteria during the post-disaster stage of a fire hazard in hospitals. Presented at the International Conference on Structural Engineering and Construction Management, Kandy, Sri Lanka
24. Kularatne D, Siriwardana C, Hasalanka H (2019) Evaluating the applicability of the "Hospital Safety Index Guide" for the Sri Lankan context. In: 2019 Moratuwa engineering research conference (MERCon). Presented at the 2019 Moratuwa Engineering Research Conference (MERCon), IEEE, Moratuwa, Sri Lanka, pp 406–411. https://doi.org/10.1109/MERCon.2019.8818932
25. Laugharne J, Van de Watt G, Janca A (2011) After the fire: the mental health consequences of fire disasters. Curr Opin Psychiatry 24:72–77. https://doi.org/10.1097/YCO.0b013e32833f5e4e
26. Leach J (2005) Cognitive paralysis in an emergency: the role of the supervisory attentional system. Aviat Space Environ Med 76:134–136
27. Leach J (2004) Why people 'freeze' in an emergency: temporal and cognitive constraints on survival responses. Aviat Space Environ Med 75:539–542
28. Mallonee S, Istre GR, Rosengberg M, Reddish-Douglas M, Jordan F, Silverstien P, Tunell W (1996) Surveillance and prevention of residential fire injuries. N Engl J Med 335:27–31
29. Marion J (2009) ECRI identifies top 10 health technology hazards for 2010 [WWW Document]. Healthc. IT News. https://www.healthcareitnews.com/news/ecri-identifies-top-10-health-technology-hazards-2010. Accessed 30 April 2020
30. Ministry of Health and Indigenous Medical Services Sri Lanka (2019) Summary of government hospitals [WWW Document]. Minist. Health Indig. Med. Serv. Sri Lanka. http://www.health.gov.lk/moh_final/english/others.php?pid=92. Accessed 10 June 2020
31. National Fire Protection Association (NFPA) (2000) Reducing the number of deaths and injuries from residential fires. Am Acad Pediatr 105:1355–1357
32. NDTV (2011) Kolkata: 89 killed in AMRI hospital fire; six board members arrested. NDTV.com
33. Nimlyat PS, Audu AU, Ola-Adisa EO, Gwatau D (2017) An evaluation of fire safety measures in high-rise buildings in Nigeria. Sustain Cities Soc 35:774–785. https://doi.org/10.1016/j.scs.2017.08.035
34. Pal I, Ghosh T (2014) Fire incident at AMRI Hospital, Kolkata (India): a real time assessment for urban fire. J Bus Manag 3:6
35. Phillips R (1994) Fire prevention: improving staff readiness. Nurs Homes 43:31–33
36. Proulx G (2003) Playing with fire: understanding human behavior in burning buildings. Am Soc Heat Refrig Air-Cond Eng ASHRAE J 45:33–35
37. Proulx G (1993) Occupant behavior and evacuation. In: Proceedings of the 9th international fire protection symposium, vol 1, pp 21–41

38. Proulx G, Reid IMA (2006) Occupant behavior and evacuation during the Chicago Cook County Administration building fire. J Fire Prot Eng 16:283–309. https://doi.org/10.1177/10423915065065951
39. Ramachandran G (1980) Statistical methods in risk evaluation. Fire Saf J 2:125–145. https://doi.org/10.1016/0379-7112(79)90039-0
40. Robotham G (2001) Safety training that works. Prof Saf 46:33
41. Samsuddin NM, Takim R, Nawawi AH, Syed Alwee SNA (2018) Disaster preparedness attributes and hospital's resilience in Malaysia. Procedia Eng 212:371–378. https://doi.org/10.1016/j.proeng.2018.01.048
42. Subramaniam C (2004) Human factors influencing fire safety measures. Disaster Prev Manag Int J 13:110–116. https://doi.org/10.1108/09653560410534243
43. The Guardian (2013) Moscow psychiatric hospital fire kills 38. The Guardian
44. UNDRR (2020) Sri Lanka [WWW Document]. DesInventar Sendai. https://www.desinventar.net/DesInventar/profiletab.jsp?countrycode=lka&continue=y. Accessed 17 May 2020
45. Wapling A, Heggle C, Murray V, Bagaria J, Philpott C (2009) Review of five London hospital fires and their management. National Health Service (NHS), London, UK
46. Wei-Wen T, Kuo-Hsiung P, Che-Ming H (2011) Performance-based fire safety design for existing small-scale hospitals. Procedia Eng 11:514–521. https://doi.org/10.1016/j.proeng.2011.04.690
47. World Health Organization, Pan American Health Organization (2015) Hospital safety index guide for evaluators, 2nd ed. World Health Organization
48. World Health Organization (WHO) (ed) (2004) Changing history. The world health report. Geneva

Redesigning and Repurposing Healthcare Facilities for the New Normal, COVID-19: A Review on New Approaches in Hospital Systems

J. H. P. R. U. Jayasekara, C. S. A. Siriwardana, D. Amaratunga, and R. Haigh

Abstract Without any doubt, the outbreak of novel coronavirus; mostly known as COVID-19 has divided the recent timeline of world into three periods namely, before COVID-19, during COVID-19 and after COVID-19. The devastating impacts that occurred during COVID-19 have already been a wake-up call towards how the existing systems should be strengthened for the period after COVID-19 to mitigate the risk of future pandemics. During the pandemic, functionality of healthcare facilities started to fail in a cascading manner highlighting the need for addressing the systemic nature of risks with novel approaches. Architects, engineers, healthcare professionals, and policymakers have started to plan on how the future healthcare facilities have to be altered for the new normal, COVID-19. This paper delves into the challenges rendered on healthcare facilities during COVID-19, immediate actions taken to mitigate the impacts, and new approaches suggested for the period after COVID-19. The study has drawn on a review of recently published scholarly articles, reports, international and national policy and frameworks, news items, magazine articles, etc. pertaining to the behavior of healthcare facilities during the crisis and future hospital designs. Apart from the challenges and immediate actions in mitigating the negative impacts, this paper has summarized new approaches for future hospital designs under two categories namely, hospital design and built environment, and hospital management and operation. It is evident that pandemic has highlighted the paramount importance of sustainable Disaster Risk Reduction (DRR) strategies towards more resilient healthcare facilities in the future. But still, these new approaches have to be further validated through multi-sectoral approaches since the crisis is not still over.

Keywords COVID-19 · Hospitals · Disaster Risk Reduction · Systemic risks

J. H. P. R. U. Jayasekara · C. S. A. Siriwardana (✉)
University of Moratuwa, Moratuwa, Sri Lanka

D. Amaratunga · R. Haigh
Global Disaster Resilience Centre, University of Huddersfield, Huddersfield, UK

R. Dissanayake et al. (eds.), *ICSBE 2020*, Lecture Notes in Civil Engineering 174,
https://doi.org/10.1007/978-981-16-4412-2_17

1 Introduction

Infectious diseases have rendered severe disruptions throughout history engulfing the world from time to time [71]. Highlighting its devastating impacts and severity, the World Economy Forum has included infectious diseases within the ten hazards with the highest risk [75]. Since the end of the twentieth century, risk driving factors such as more human to animal contact, lack of hygiene, international travel in bulk volume, and threat of bioterrorism have heightened the frequency of these biological hazards [25]. The rising severe effects of the COVID-19 outbreak have already called the need for heightening the concerns of the authorities on preparedness and response of the entire world since the pandemic exposed the immanent gaps in the system.

Since the first cluster of cases reported in Wuhan, China at the end of 2019, the coronavirus has affected almost the whole world recording over 42 million infected cases at the time of writing (WHO Situation Report, 2020). The entire health system has been grossly upended by the pandemic due to the continuously rising number of cases. Not limiting to the engulfed health sector, the effects of COVID-19 have cascaded into the socio-economic aspects as well, thus responding to the pandemic has become a global agenda [35]. This unseen catalyst has dragged the global economy into a deep recession. The International Monetary Fund (IMF) has warned that the global economy will shrink by 3% in 2020 [26]. A number of industries except the pharmaceutical companies had to go through huge downfalls. International travel, entertainment, oil, agriculture, and tourism are such industries that experienced unprecedented lows during the pandemic [6]. Further the pandemic has caused adverse social implications by affecting marginalized communities such as the poor and elderly people and increasing unemployment, poverty, public unrest, and inequalities. Such devastations across the health, economic, social, political, and environmental aspects have evidenced the systemic nature of risks. Therefore, the authorities have been already vested with a pivotal role in rethinking and improving the resilience of the entire system against the effects of biological hazards.

Illustrating the enormous pressure put on the health system, healthcare infrastructures such as hospitals were severely affected by the pandemic. Due to the surge of infected patients, hospitals ran out of enough space and resources to treat even patients with severe symptoms [55]. It has called for the need for building up new treating centers and temporary units. Existing facilities such as hotels, stadiums, and auditoriums were converted into treating facilities for COVID-19 while new hospital complexes were built rapidly [12, 34, 49]. These overcrowded hospitals became a reason for COVID-19 to be turned into a nosocomial disease, thus emerged as an alarming threat that infects Healthcare Workers (HCWs) and other patients. Keeping HCWs away from their service was one of the major catalysts that caused the failure of hospital systems [56]. Such failures that occurred in a cascading manner paved the way for hospitals to be turned into a repository of spreading the disease.

Stakeholders of healthcare systems were dragged to address these cascading failures with immediate and long-term solutions. Since the healthcare sector has to cope

with the new realities of the pandemic, these changes have varied from the operation and management to the built environment of hospitals [4, 23]. Policymakers who were vest with the power of governance in the healthcare field have altered policies and regulations affecting the hospital management and operation to cater to issues arising during the crisis. Provisions for clinical management, changes in the allocation of infrastructures, changes in supply chain management, and more use of technology are a few of such alterations that optimized the hospital management and operation to alleviate the stresses put on hospitals [11, 72]. Furthermore, architects, engineers, and interior designs were called for reimaging and redesigning the hospital-built environment with immediate and long-term measures. Increasing the healthcare spaces with alternative units and split up treating and triage areas for COVID-19 infected patients were among the immediate interventions within the hospital setting [16]. Furthermore, professionals have been concerned with reviewing air condition systems, use of anti-bacterial materials, touch-free controls, and flexibility in designs in order to ensure the safety of HCWs and patients in a world living with COVID-19 and other pandemics [61]. Most of the fields have now resumed their activities with new sustainable approaches that can mitigate the risk of future biological hazards. The healthcare system also needs to delve into the impacts of the ongoing pandemic, COVID-19, and start repurposing and redesigning the hospital system.

In such a context this paper aims to identify the challenges that global healthcare facilities have faced during COVID-19 and to explore the immediate measures which have been taken inside hospital systems. When analyzing the immediate measures taken by the authorities, the Hierarchy of Controls (HOC) developed by the National Institute for Occupational and Health (NIOSH) has been incorporated. Furthermore, another major focus was given to explore possible new approaches and suggestions to reshape healthcare facilities in the future. The scope of new approaches and suggestions identified in this study was further broadened under two sectors namely, hospital-design and built environment, and hospital management and operations. And also, the study has addressed the use of sustainable and innovative techniques for future hospital designs. The outcomes of this study can be used as an initial guideline for national and local policymakers to start planning on how hospital systems have to be altered in the future.

2 Methodology

This study has drawn on an extended literature review including scholarly articles, global and national reports, policy, and legal frameworks, news items, and internet sources. In selecting scholarly articles, a systemic approach was used. Google Scholar, ScienceDirect, and Wiley Open Library databases were searched for articles published on challenges and changes in hospital systems during COVID-19. The Boolean strategy shown in Table 1 was used in searching for articles. Google Scholar, ScienceDirect, and Wiley Open Library have yielded respectively 133, 45,

Table 1 Boolean search strategy

AND		
Hospital design	COVID-19	
OR		
Changes	Isolation rooms	PPE
Healthcare workers	Negative pressure rooms	Operations
ICU		

and 8 articles published in 2020. Papers were retained for this study if those papers have discussed challenges and changes related to hospital management, operations, functionality, and built environment during COVID-19. Furthermore, publications done only in English were selected for the review. In addition to these retained articles, another set of articles was also added to the review by manual search. Furthermore, global and national reports, policy, and legal frameworks, news items, and internet sources were used for the review. Finally, 75 sources were incorporated in this study based on the aforementioned inclusion and exclusion criteria.

3 Challenges for Healthcare Facilities During COVID-19

It is clearly evident that the COVID-19 disease has placed enormous, unprecedented stresses on the healthcare system due to the continuously increasing number of infected cases. It called for the need for assessing the resources of healthcare facilities, identifying the gaps, and implementing strategies for increasing the surge capacity [2]. In responding to COVID-19, healthcare facilities have been vested with the responsibility of two major aspects. Hospitals had to first treat infected patients with severe symptoms while treating patients with mild symptoms and suspected cases. Further, these treatments were supposed to be carried out while stopping the transmission of virus to HCWs and other patients. With the absence of enough scientifically validated information and evidence-based measures, containment of the virus became a severe problem [14]. Furthermore, hospitals were supposed to withstand concurrent hazards amidst responding to the COVID-19 and safeguard HCWs and patients. For an instance, Croatia experienced an earthquake with magnitude of 5.3 on the Richter scale, followed by 57 aftershocks. The severe property damages necessitated the evacuation of several hospitals in the capital of Croatia [17]. Furthermore, a fire has broken out in an intensive care unit in Romania causing the death of 10 COVID-19 patients. 7 others, including the on-call doctor were severely injured [50]. Therefore, during these endeavors of safeguarding the patients and HCWs and addressing the potential systemic risks, hospitals had to overcome several other challenges as well.

Elaborating on challenges related to the capacity of hospitals, due to the sudden spikes in COVID-19 positive cases, hospitals ran out of beds and isolation units required to treat the infected patients. Especially the shortage of ICU beds became an alarming threat though critically ill patients required weeks of treatment in ICUs. This

Table 2 Summary of the available number of ICU beds per 100,000 habitants in several selected countries [65]

Country	Number of ICU beds per 100,000 inhabitants
United States	34.7
Germany	29.2
Italy	12.5
France	11.6
South Korea	10.6
Spain	9.7
Japan	7.3
United Kingdom	6.6
China	3.6
India	2.3

issue has gained the potency of amplifying death rates in underdeveloped countries where healthcare infrastructures are fragile. For an instance, the whole sub-Saharan African region excluding South Africa only had just over 2000 ICU beds where New York City had 1600 beds [39]. Table 2 shows the available number of ICU beds per capita in several selected countries. A clear deviation is evident in the number of ICU beds available in countries worldwide. Repercussions of COVID-19 have been expected to be major when the outbreak's peak hits such countries that lack intensive care facilities. Even before the COVID-19 outbreak, a study carried out in France has highlighted the fact that lack of ICU beds can lead to preventable deaths [60]. Furthermore, the deficiency in ICU facilities has raised major ethical dilemmas as well since the hospitals were not capable of treating the entire group of patients who need intensive care [66]. The insufficient number of ventilators available in hospitals has been another risk driving factor. As the coronavirus is damaging patients' lungs causing breathing difficulties, critically ill patients need respiratory support, thus ventilators are needed for assisting their breathing. In such a context, the dreadful shortage of ventilators and their high cost have paved the way for increasing fatalities rates in severely affected countries by the pandemic [31].

Lack of Personal Protection Equipment (PPE) has become another distressing challenge to stakeholders of hospital systems. Inadequate respirators, gloves, shields, and hand sanitizers for frontline HCWs have increased the rates of infections and deaths among HCWs [32]. Before the pandemic starts in China, they have produced almost half of the world's demand for facemasks. Those exports of masks in bulk volumes were paused when China was severely hit at the start of the outbreak [9]. Furthermore, healthcare supply chains for pharmaceuticals, medical supplies such as testing materials and laboratory and intravenous kits experienced severe disruptions amidst of COVID-19 crisis. International travel restrictions were not the sole reason for breakdowns in these logistics supply chains. Grass root level issues compromising the migration of laborers working in industrial units, domestic travel bans, especially trucks, lack of cooperation between different administrations, and transporters and couriers not functioning timely have rendered commotions [64]. Especially drugs that

have a global supply chain and long-life cycles had to surpass unforeseen barricades [48].

Considering the challenges related to human resources, the loss of HCWs became a major factor that provoked healthcare facilities to become dysfunctional during the COVID-19. It was clearly evident that without the safety of HCWs, the safety of patients becomes an illusion. From the start of the pandemic HCWs and their families were stressed with unprecedented risks. Statistics from WHO has highlighted that a larger portion of infected cases has been reported from HCWs. In some countries, the proportion has exceeded even 30% [67]. Apart from infections of the virus, the outbreak has put on enormous psychological stresses on HCWs who were exposed to high-demand settings for long hours and living in constant fear of disease exposure. Furthermore, during lockdown periods, transportation became a severe issue for HCWs in underdeveloped countries. A recent study has presented that a considerable portion of healthcare professionals have found depression, anxiety, and insomnia during COVID-19 [57]. Furthermore, WHO has highlighted an increasing threat of attacks on HCWs such as verbal harassment, discrimination, physical violence amidst the pandemic [68].

Healthcare-associated infections have become an alarming threat due to the overcrowded healthcare facilities because of increasing hospitalization rates. As reported by [27], healthcare-associated infections have risen considerably in the United Kingdom, since there has been a surge in infected cases with the second wave in the country. This has become a common phenomenon in countries like South Korea as well [27, 37]. Apart from that, mental health issues among the COVID-19 patients and other patients have risen considerably due to the factors such as uncertainty, low predictability, and imminent risk of transmission and mortality by the pandemic [33].

Furthermore, the consequences of the sudden surge of infected cases paved the way for disruptions and breakdowns in the non-COVID-19 related functions within healthcare facilities. There were considerable drops in the number of non-infected patients turning to hospitals because of the fear of contracting COVID-19. It has the potency of leading to far worse consequences because of heart problems and cancers [8, 30]. On some occasions, patients even with severe symptoms have not arrived in hospitals because of the uncertainty and fear created, and finally met death. For an instance, a considerable portion of the COVID-19 related deaths during the second wave in Sri Lanka have occurred at homes [20]. Likewise, hospital systems have been experiencing a fair share of direct and cascading impacts of COVID-19 highlighting the systemic nature of risks pertaining to highly contagious diseases.

4 Immediate Changes in Hospital Settings During COVID-19

Since the sudden surge of infected patients has overwhelmed the functionality of healthcare facilities systemically, authorities implemented immediate measures to

mitigate the synergized effects. Those immediate actions have been structured in this study according to the Hierarchy of Controls (HOC) defined by the National Institute for Occupational and Health (NIOSH), US for mitigating the impacts of a particular hazard. The HOC consists of five levels namely; Elimination, Substitution, Engineering Controls, Administrative Controls, and Personal Protective Equipment (PPE) in an order where Elimination is the most effective and PPE is the least effective [51].

Following the hierarchy of controls, health authorities have looked into eliminating and substituting the hazards of the COVID-19 virus by implementing measures like stratification and repurposing of the existing healthcare facilities. Moving into engineering controls, several changes such as isolation rooms and split respiratory care units were launched at the hospital settings. Furthermore, policymakers have addressed the step administrative controls through the protocols and algorithms developed for work routines and surveillance of HCWS. Last but not least, the use of PPE in hospital settings has rendered a great service by limiting the unnecessary contacts of the virus.

1. Elimination and Substitution—Stratification of healthcare facilities

Under the concepts of elimination and substitution, the hazard is physically removed or substituted by another at the vulnerable community. In the context of COVID-19, authorities have limited the arrival of COVID-19 contracted patients to every healthcare facility. Therefore, most of the countries have repurposed and reshaped their hospital system and established dedicated healthcare facilities for COVID-19 infections. Furthermore, healthcare professionals have identified the paramount importance of providing optimal healthcare by reallocating HCWs and resources and increasing bed capacities. The allocation of COVID-19 contracted cases to these facilities has been taking place based on the legal policies and frameworks issued by the relevant government authorities.

In South Korea, the government has declared five types of treatment facilities namely, COVID-19 community facilities, dedicated COVID-19 hospitals, and primary, secondary, and tertiary hospitals in stratifying the hospital structure. A COVID-19 task force team and regional COVID-19 management have been established. These two units have assigned the patients to the hospitals based on room availability and disease severity as shown in Fig. 1 [28].

The Sri Lankan government has launched a 3-level approach that consists of intermediate care centers, COVID-19 designated Divisional/Base hospitals, and territory hospitals. Authorities have performed allocation of the infected patients was done based on the criteria for case definition developed by the Ministry of Health, Sri Lanka [44] (see Fig. 2).

Furthermore, in India, the government authorities have developed a classification of health facilities including three categories namely, COVID Care Centre, Dedicated COVID Health Centre, and Dedicated COVID Hospital. Contracted patients have been allocated based on the severity of the symptoms as shown in Fig. 3 [43].

2. Engineering controls

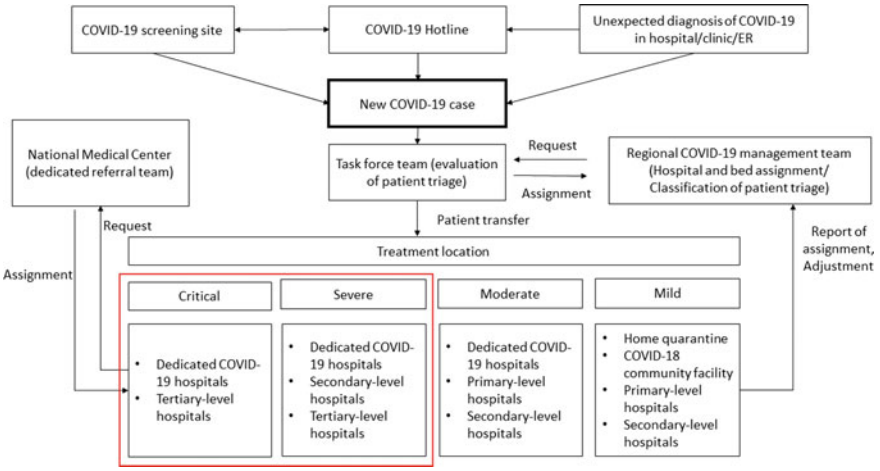

Fig. 1 Stratification of hospitals/rooms assignments in South Korea (adapted from [28])

Elaborating on the concept of engineering controls, health authorities have taken several measures to isolate HCWs and non-infected patients from the virus. Split respiratory care units and isolation rooms/negative pressure rooms are among those immediate measures.

- Split respiratory care units

During recent pandemics such as SARS (2003) and MERS (2015), nosocomial infections have turned out to be a critical factor and several super spreaders have been reported in hospitals [54]. COVID-19 also had the likelihood of being a nosocomial disease which can render bleak effects on health systems [15, 59]. In addressing this disastrous issue, hospital management has taken initial measures in advance. Patients with respiratory symptoms have been separated from patients without respiratory symptoms at the initial triage area. The objective of this measure has been to minimize unnecessary contacts between the suspected cases of COVID-19 and other patients, thus limiting the rate of hospital-associated infections [28]. Illustrating on separating patients at the entrance to hospital premises, in Sri Lanka there were separate triage areas for COVID-19 suspects and other respiratory patients as well. The ministry of health, Sri Lanka has devised and issued the provisional guidelines on infection prevention and control in these triage areas [46]. Hospitals ranging from National Hospital to Base Hospitals in the hierarchy of hospitals in Sri Lanka have reshaped themselves into respiratory care split hospitals [47]. Furthermore, internal circulation routes within these split care hospitals for the two sets of patients have been separated to avoid unnecessary contacts.

- Isolation rooms/negative pressure rooms

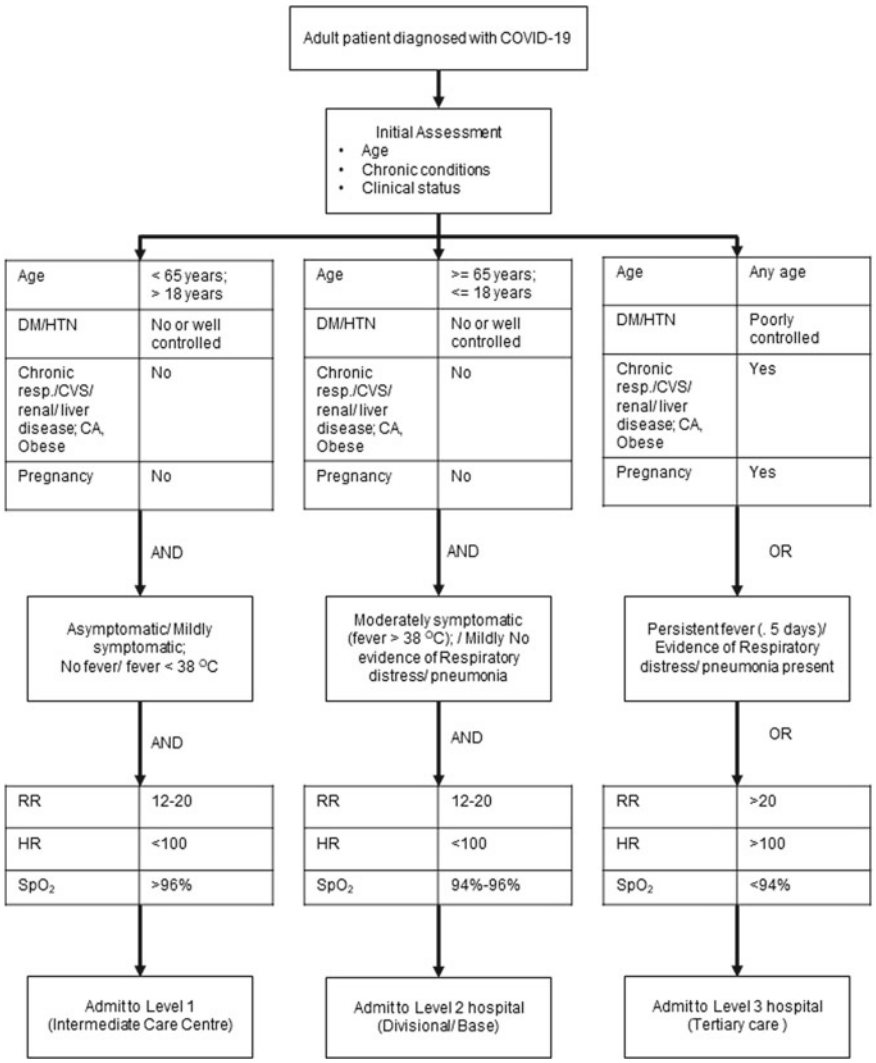

Fig. 2 Stratification of hospital/room assignments in Sri Lanka (adapted from [44])

The paramount importance of isolation rooms was greatly highlighted during the COVID-19 outbreak for limiting the nosocomial transmission of this invisible cause of death. Since SAR-Cov-2 is a novel strain of the coronavirus, it transmits among humans when it enters the body through the mouth and nose or eyes [73]. Droplets, surfaces, and aerosols have become the main modes of virus transmission. Therefore, the potency of COVID-19 to be an airborne disease has been continuously increasing [10]. An isolation room aims on controlling the airflow in the room, thus reduces airborne infectious particles. Since COVID-19 is also turning out to

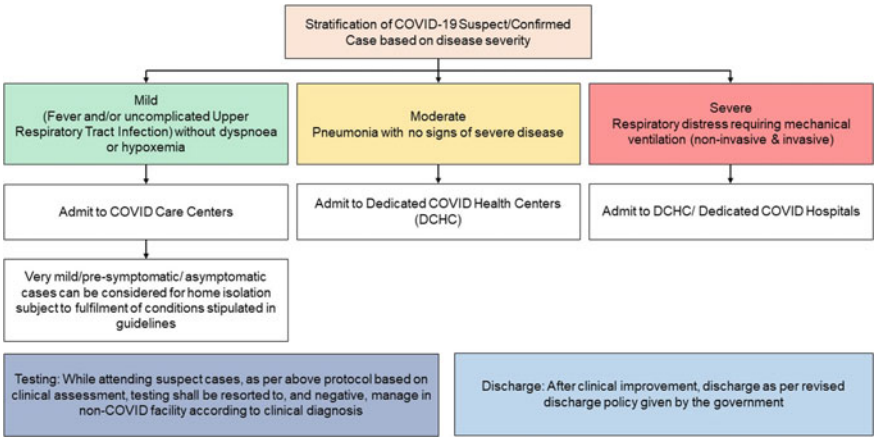

Fig. 3 Structure of hospital facilities for treating COVID-19 cases in India (adapted from [43])

be an airborne disease, the use of isolation rooms for treating infected patients was recommended by the professionals [62]. Negative pressure rooms are one kind of isolation rooms where the pressure is negative relative to the surrounding environment. The contagious diseases are trapped inside these rooms without letting them escape and infect outsiders. Use of negative pressure rooms at COVID-19 treatment centers became a global concern with the unprecedented behavior of the virus. For an instance, Australian Government recommended the use of negative pressure rooms for isolation of patients with severe acute respiratory symptoms. In case of running out of negative pressure rooms, it was indorsed to use empty, well-ventilated rooms for isolation of such patients [21]. Due to the lack of isolation rooms, most of the healthcare facilities around the world have stepped towards increasing their number of isolation rooms by adding temporary structures.

3. Administrative controls

Elaborating on how the next step of the HOC; administrative controls were used in relation to HCWs' safety, authorities have published several policies and frameworks. During COVID-19, the consequences of keeping the HCWs away from the healthcare facilities have emerged as an alarming threat. Aiming at improvements in the safety of HCWs, global organizations such as WHO and Occupational Safety and Health Administration (OSHA) devised and published relevant guidelines to provoke the authorities to implement necessary actions [53, 67]. These guidelines were mainly focusing on protecting HCWs from physical and biological hazards, developing and implementing national programs for occupational health and safety of health workers, protecting HCWs from violence in the workplace, and improving the mental health and psychological well-being of HCWs. Most of the hospitals have canceled their elective procedures and free up HCWs and reallocated efficiently. Further, they

have developed an inventory of staff who might play unconventional roles in their COVID-19 response to ensure safety by limiting unnecessary contacts [2].

Governments have developed guidelines for the effective screening of HCWs for COVID-19. For an instance, India has established a district-level facility-based surveillance system for COVID-19. Under this system, 100 samples of swabs have been collected from 10 healthcare facilities from each district per week and tested. They have identified HCWs as a high-risk population [43]. In Sri Lanka, the Ministry of Health has developed a system of screening and managing HCWs following exposure to a confirmed or suspected case of COVID-19. According to this system, three risk levels have been defined based on the degree of exposure, thus measures to be taken at each risk level have been clearly identified (see Fig. 4) [44]. With the objective of limiting the nosocomial infection of HCWs, they have been provided with a safe zone and a separate entrance for every ward with COVID-19 suspected/confirmed cases. Furthermore, the mental health of HCWs was one of the major concerns during the crisis. Authorities have implemented polices to ensure appropriate and fair duration of working hours, rest break and minimized the administrative burden on HCWs. Moreover, mental well-being and social support services have been activated for HCWs during the crisis.

4. PPE

As the last line of defense, healthcare Authorities have identified the paramount importance of the use of PPE and healthcare facilities to protect HCWs and prevent transmission of the virus. Currently, available information indicates that the virus is basically transmitted through respiratory droplets and close contacts. The possibility of airborne transmission is also considered by the authorities at the moment [73, 74]. Governments all over the world have issued several guidelines related to the use of PPE and updated them according to trends of the virus. For an instance, the government of South Korea issued guidelines for infection prevention and control at the hospital settings at the early stage of the pandemic. In those issued guidelines the selection of PPE was completely based on the guidelines used for the MERS outbreak in 2015. But after that several updates were released by the government for the proper use of PPE at the hospitals [58]. Elaborating further on the use of PPE, the Ministry of Health Sri Lanka has developed and published a guiding document on the rational use of PPE in hospitals during the COVID-19 disease. This guidance has identified the various settings in a hospital and recommended the proper types of PPE and procedures to be followed in particular settings. Furthermore, the settings where no PPE are required also have been clearly mentioned under the guidelines [45].

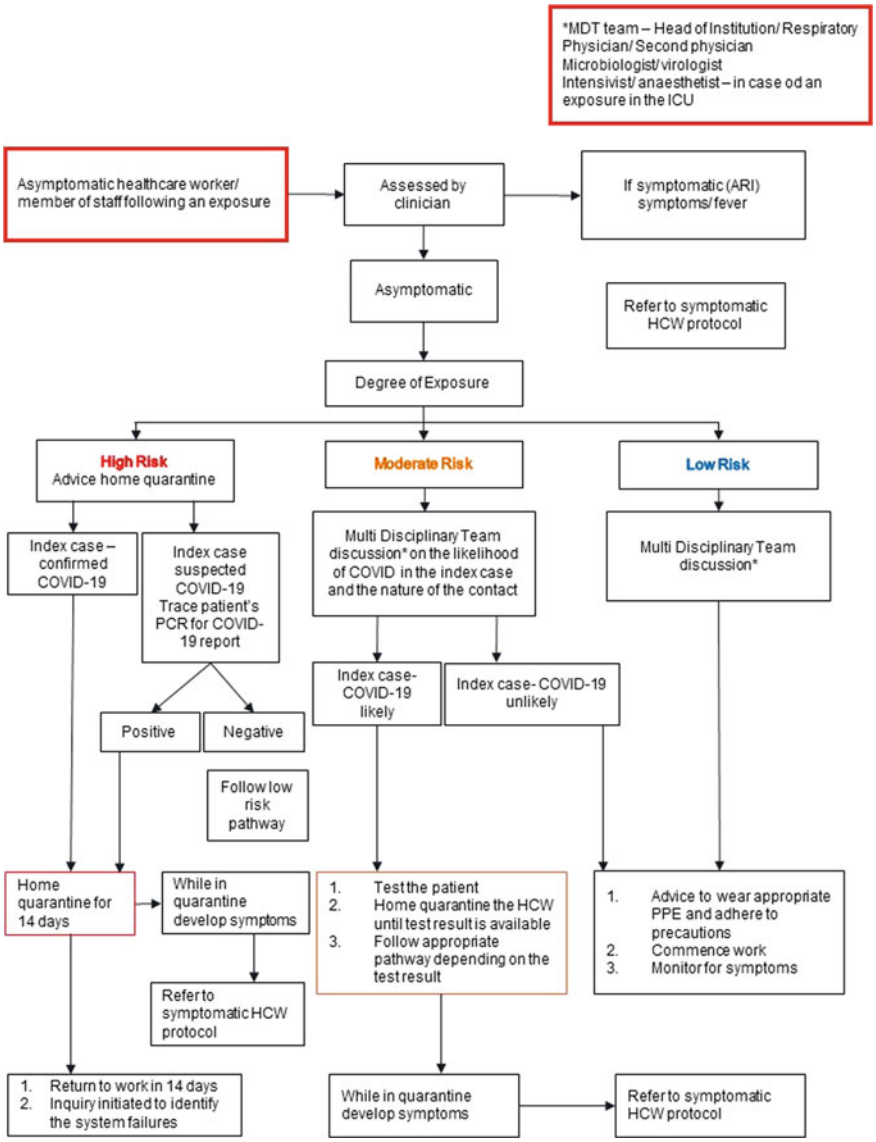

Fig. 4 Testing algorithm for exposed HCWs to suspected/confirmed cases (adapted from [45])

5 Suggestions and Improvements in Hospital Settings for the New Normal; COVID-19

Since the start of the COVID-19 outbreak at the end of December 2019, healthcare facilities have undergone numerous changes immediately to address the spikes

in hospitalization and associated cascading impacts. These devastating impacts of COVID-19 on the health system have called for the need for long term interventions in addition to the immediate actions taken during the outbreak. Since the world is now more concerned about systemic risk and Disaster Risk Reduction (DRR), the relevant authorities are vested with the responsibility of delving into DRR strategies for biological hazards and implement them accordingly. Enhancing the resilience of hospitals has become the foremost objective of such strategies. These long-term interventions can be categories into two categories namely, hospital design and built environment, and operation and management.

5.1 Hospital Design and Built Environment

There is a huge number of alternations that can be implemented during the design phase of hospitals and the built environment. Starting from suggestions on the location of healthcare facilities this set of suggestions consists of changes to man-made structures, facilities, and features of healthcare facilities. Table 3 shows suggested alterations for hospital design and built environment categorizing them into the relevant step in the Hierarchy of Control (HOC).

5.2 Hospital Management and Operation

In addition to the changes in the hospital design and built environment, several alternations have been suggested to implement reshaping the hospital operation and management. Table 4 shows the suggestions found out in this study.

6 Conclusion

The prevailing impacts of COVID-19 have created enormous pressure on the health sector since the hospital systems were overwhelmed and HCWs were kept away from the hospitals. Starting from the overcrowded treatment areas, the impacts of the pandemic have cascaded down step by step rendering the failure of the whole hospital system. These cascading impacts have highlighted the need for addressing the systemic nature of risks using DRR strategies pertaining to biological hazards. Therefore, preparedness and response planning in hospitals for biological hazards has become a multi-sectoral approach that needs input from several sectors such as health, engineering, and information and technology. COVID-19 is becoming a new normal in the current world which has called for new approaches to designing hospital systems apart from the immediate measures taken to flatten the curve; mitigate the impact of mortality and morbidity. These measures are ranging from the design

Table 3 Suggested alterations for hospital design and built environment

Suggestions	Remarks	Step in HOC	References
Location	The location of a healthcare facility affects its sustainability and efficiency. Nowadays though the hospitals are located in central urban areas, it has become a vulnerability during infectious disease outbreaks like COVID-19. Changing hospitals' locations in a crisis is not feasible. Therefore, in the design and planning process of hospitals should be located closer to the city boundaries to ensure the containment of viruses and treat the patients in bulk volumes	Elimination	[18, 19]
Flexibility in Design	Even before the COVID-19 flexibility of hospital design has been a major concern. According to what is meant by flexibility, a hospital should be adaptable, convertible, and expandable. Since the authorities were urging to increase the ward and ICU capacities to treat the increasing number of hospitalized infected patients, the paramount importance of hospital designs was highlighted greatly. Wider column spacings, more ceiling heights, standby mechanical and electrical services, and open building concepts are a few strategies that can increase the flexibility of hospital designs	Engineering controls	[7, 24]

(continued)

Table 3 (continued)

Suggestions	Remarks	Step in HOC	References
Functional programs and access	The functionality of hospitals should be increased in terms of a strong connection between the critical units in the hospitals. It is a vital factor for the fast movement of patients between the respective units. Furthermore, the hospital designs should have separate access for HCWs. It reduced the chances of nosocomial infections. And also, the emergency units of the hospitals should have two separate access for patients with respiratory symptoms and others. In the case of ambulances, there should be separate areas for decontamination	Engineering controls	[1, 52]
Internal circulation	The internal circulation system in a hospital should be further developed to increase the resilience of hospitals for biological hazards. In that case, the wider corridors have a greater impact on increasing the level of internal circulation. Narrow corridors can cause bleak effects such as nosocomial infections. Further the location of vertical transportation also a major factor in internal circulation	Engineering controls	[5]
Maximize the number of single rooms	The use of single rooms more can limit unnecessary contacts among the infected and non-infected. The future hospital designs should be strengthened with more single rooms for isolation purposes	Engineering controls	[14]

(continued)

Table 3 (continued)

Suggestions	Remarks	Step in HOC	References
Reviewing ventilation systems	Experts have warned the recirculation of air-conditioned air may increase the spread of the virus. Still, there is only a fewer number of studies conducted on the role of HAVC systems towards the spread of novel coronavirus. But there is a need to review and redesign the HAVC systems still. Currently, scientists are engaging in various experiments to develop a more reliable arrangement for HAVC systems for hospitals to avoid cross-infection. The air quality should be maintained well especially inside the ICUs	Engineering controls	[3]
Use of anti-bacterial/non-porous material	Handrails, doorknobs, elevator controls, and seats can be identified as frequently touched points by the patients, HCWs, and visitors of the hospitals. The use of anti-bacterial materials for such points can be identified as one of the design strategies for living with the new normal; COVID-19. Furthermore, anti-bacterial materials can be used for furniture and paints as well. Copper and silver are such metallic antibacterial agents which can be used for frequently touched points	Engineering controls	[29, 63]

(continued)

Table 3 (continued)

Suggestions	Remarks	Step in HOC	References
Touch-free controls	Architects and engineers are now more focusing on touch-free controls within hospitals to limit the transmission of the virus through unnecessary contacts. Sensor-based water appliances, automatic doors, temperature detectors, and touch-free dispensers are a few of such measures that can be incorporated in future hospital designs	Engineering controls	[22]
Presence of additional storage	Additional storage within a hospital facility can be utilized during a crisis for multi-purposes. For an instance, those storing areas can be used as a PPE, and sanitary material storage. Furthermore, these areas can be utilized as storage for containment waste during a crisis	Engineering controls	[14]
Modular designs/prefabricated units	During COVID-19, prefabricated units were vastly utilized for expanding the surge capacities of hospitals. The use of prefabricated units and modular designs becomes a sustainable solution due to their cost, time, and resource-saving benefits. Therefore, future hospital designs should allow those alternative units to be added to the design there is a need of expanding capacities	Engineering controls	[42, 77]

Table 4 Suggested alterations for hospital management and operation

Suggestions	Remarks	Step in HOC	Reference
Strengthening the network between healthcare facilities and other critical infrastructures	The proper coordination between healthcare facilities and the other critical infrastructures such as electricity, telecommunication, and food supplies within a particular area plays a vital role in any kind of emergency. But its significance is greatly highlighted during a crisis like COVID-19 since it lasts for a longer period. Furthermore, establishing more primary care units also can reduce the number of people arriving in hospitals by managing patients with low risk	Administrative controls	[13, 41]
Improvement of patient safety	Hospitals should be a safe place for patients while they are receiving their treatments. A safe hospital is defined as a healthcare facility that remains functional in its maximum capacity during and immediately after a disaster. During a long-lasting disaster like a pandemic, there are ample changes happening in a hospital. Those changes should ensure the patients' safety. Furthermore, there can be concurrent hazards amidst a pandemic. The hospital management has been vested with the responsibility of ensuring that all changes in the hospital setting improve the patients' safety	Engineering/administrative controls	[69]

(continued)

Table 4 (continued)

Suggestions	Remarks	Step in HOC	Reference
Use of modern technology for treatments	Admission of patients who are not infected with COVID-19 to hospitals has dropped considerably down due to the fear of COVID-19. In order to address these issues telemedicine can be utilized in a more sustainable way. Further, video conferencing facilities for OPD consultation can be used to limit the transmission of infectious viruses from the hospital. In the future, people will not arrive in hospitals unless there is a serious issue. In addition to these modern technological developments such as robots can be incorporated in limiting the contact of HCWs with the infected patients while they are being treated at the hospital	Engineering controls	[38, 76]
Emergency funds	Allocating more funds stresses authorities without any doubt. But the implications of COVID-19 have provoked governments and health professionals to do major allocations in the present. It highlights the significance of emergency funds to survive during a crisis like COVID-19. Especially for infection prevention and control measures, the availability of emergency funds is crucial	Administrative controls	[36, 40]

(continued)

of the hospital to the management of the hospital. This paper has presented a set of suggestions that have to be included in the hospital designs to tackle invisible enemies like COVID-19 in the future. The existing healthcare facilities must be altered accordingly while the new facilities can incorporate them from the phase of planning. Since the world is now moving towards sustainability and disaster risk reduction, these long-term interventions should be aligned with them as well. Similar

Table 4 (continued)

Suggestions	Remarks	Step in HOC	Reference
Improvements in emergency plans	During COVID-19, providing surge capacity by converting stadiums, hotels and auditoriums were among immediate responses. But in the future, this strategy should be performed within hospital premises or very close proximity, thus accessing staff and equipment become easy. Therefore, hospitals should be able to switch into the pandemic mode by executing emergency plans developed for emergencies like COVID-19. The bleak effects of COVID-19 on healthcare facilities have highlighted the gaps in the existing emergency plans. So, there is a need for major improvements in areas such as increasing surge capacity, infection prevention, and control, the safety of HCWs	Administrative controls	[70]

to the developments in the other processes, the pandemic has triggered the use of innovation and technology in the field of healthcare. Innovative techniques such as modular construction, prefabricated healthcare units, expandable built environment need to be utilized more frequently in future hospital designs. In addition to that, the use of telecommunication for medical care services is now becoming a new trend. Therefore, modern hospital designs should allocate more facilities for innovative trends like that. The crowded hospitals and their consequences have questioned the locations of the current healthcare facilities since most of them are located in highly urbanized areas. This issue has been an eyeopener for authorities to select the best locations for future healthcare facilities. Last but not least availability of enough funding for the immediate response stage in biological hazards like pandemic has been greatly highlighted. It is clearly evident that the devastating impacts of COVID-19 have been a wake-up call for humans to integrate sustainable approaches into the healthcare system.

Acknowledgements This project is funded by UK research and innovation through the UK government's global challenges research fund (GCRF) and the Newton fund [grant number EP/V026038/1]. UK research and innovation ac-cepts no liability, financial or otherwise, for expenditure or liability

aris-ing from the research funded by the grant except as set out in the terms and conditions, or otherwise agreed in writing.

References

1. Beusekom M, Van (2020) Indoor spread of COVID-19 can be lessened, experts say [WWW Document]. Cent. Infect. Dis. Res. Policy, Univ. Minnesota. https://www.cidrap.umn.edu/news-perspective/2020/05/indoor-spread-covid-19-can-belessened-experts-say. Accessed 11 Nov 2020
2. Abir M, Nelson C, Chan E, Al-Ibrahim H, Cutter C, Patel K, Bogart A (2020) Critical care surge response strategies for the 2020 COVID-19 outbreak in the United States. RAND Corporation, Santa Monica, CA. https://doi.org/10.7249/rra164-1
3. Angarai R, Sharma K (2020) The need to redesign the hospital ICUs for Covid-19 patients to save the medical fraternity [WWW Document]. https://doi.org/10.35543/osf.io/k4vqe. Accessed 11 Nov 20
4. Arango C (2020) Lessons learned from the coronavirus health crisis in Madrid, Spain: how COVID-19 has changed our lives in the last 2 weeks. Biol Psychiatry 88 e33–e34.https://doi.org/10.1016/j.biopsych.2020.04.003
5. Architects and Designers (2020) Hospital corridor safety a better way to store beds & save space [WWW Document]. South West Solut Gr.https://www.southwestsolutions.com/ssg/hospital-corridor-safety-a-better-way-to-store-beds-save-space. Accessed 11 Nov 2020
6. BBC News (2021) Coronavirus: how the pandemic has changed the world economy [WWW Document]. https://www.bbc.com/news/business-51706225. Accessed 3 Nov 2020
7. Babbu AH (2016) "Flexibility": a key concept in hospital design. Int J Appl Innov Eng Manag 5:24–28
8. Baral S (2020) Fear of infection still keeping patients away from hospitals across the country [WWW Document]. Kathmandu Post. https://kathmandupost.com/health/2020/09/25/fear-of-infection-still-keeping-patients-away-from-hospitals-across-the-country. Accessed 11 Sep 20
9. Bradhser K, Adherman L (2020) The world needs masks. China makes them, but has been hoarding them. The New York Times [WWW Document]. New York Times. https://www.nytimes.com/2020/03/13/business/masks-chinacoronavirus.html. Accessed 11 Sep 2020
10. Buonanno G, Morawska L, Stabile L (2020) Quantitative assessment of the risk of airborne transmission of SARS-CoV-2 infection: prospective and retrospective applications. Environ Int 145:106112. https://doi.org/10.1016/j.envint.2020.106112
11. CDC (2020) Healthcare facilities: managing operations during the COVID-19 pandemic | CDC [WWW Document]. Centers Dis. Control Prev. US. https://www.cdc.gov/coronavirus/2019-ncov/hcp/guidance-hcf.html. Accessed 11 Jul 2020
12. CGTN (2020) Hong Kong's first COVID-19 temporary hospital starts operation. CGTN [WWW Document]. https://news.cgtn.com/news/2020-08-01/Hong-Kong-s-first-temporary-hospital-to-start-operation-on-Saturday-SB3IOM8kko/index.html. Accessed 6 Nov 2020
13. Capolongo S, Mauri M, Peretti G, Pollo R, Tognolo C (2015) Facilities for Territorial Medicine: the experiences of Piedmont and Lombardy regions. J Technol Archit Environ 9:230–236
14. Capolongo S, Gola M, Brambilla A, Morganti A, Mosca EI, Barach P (2020) COVID-19 and healthcare facilities: a decalogue of design strategies for resilient hospitals. Acta Biomed 91 (9-S):50–60. https://doi.org/10.23750/abm.v91i9-S.10117
15. Carter B, Collins JT, Barlow-Pay F, Rickard F, Bruce E, Verduri A, Quinn TJ, Mitchell E, Price A, Vilches-Moraga A, Stechman MJ, Short R, Einarsson A, Braude P, Moug S, Myint PK, Hewitt J, Pearce L, McCarthy K, Davey C, Jones S, Lunstone K, Cavenagh A, Silver C, Telford T, Simmons R, Holloway M, Hesford J, El Jichi Mutasem T, Singh S, Paxton D, Harris W, Galbraith N, Bhatti E, Edwards J, Duffy S, Kelly J, Murphy C, Bisset C, Alexander R,

Garcia M, Sangani S, Kneen T, Lee T, McGovern A, Guaraldi G, Clini E (2020) Nosocomial COVID-19 infection: examining the risk of mortality. The COPE-Nosocomial Study (COVID in Older PEople). J Hosp Infect 106:376–384. https://doi.org/10.1016/j.jhin.2020.07.013
16. Chopra V, Toner E, Waldhorn R, Washer L (2020) How should U.S. hospitals prepare for coronavirus disease 2019 (COVID-19)? Ann Intern Med 172:621–623 https://doi.org/10.7326/M20-0907
17. Čivljak R, Markotić A, Capak K (2020) Earthquake in the time of COVID-19: the story from Croatia (CroVID-20). J Glob Health 10. https://doi.org/10.7189/JOGH.10.010349
18. Dell'Ovo M, Capolongo S, Oppio A (2018) Combining spatial analysis with MCDA for the siting of healthcare facilities. Land Use Policy 76:634–644
19. Dell'Ovo M, Frej EA, Oppio A, Capolongo S, Morais DC, de Almeida AT (2018b) FITradeoff method for the location of healthcare facilities based on multiple stakeholders' preferences. In: Chen Y, Kersten G, Vetschera R, Xu H (Eds) Group decision and negotiation in an uncertain world. Springer International Publishing, Springer, pp 97–112
20. Department of Government Information (2020) DoGI, Sri Lanka [WWW Document]. https://www.dgi.gov.lk/. Accessed 13 Nov 2020
21. Department of Health Australia (2020) CDNA National guidelines for public health units version 3.10 [WWW Document]. https://www1.health.gov.au/internet/main/publishing.nsf/Content/cdna-song-novel-coronavirus.htm. Accessed 10 Nov 2020
22. Eagle A (2015) Designing hospital public spaces | HFM. ASHE Heal. Facil. Manag.
23. Emmanuel U, Osondu ED, Kalu KC (2020) Architectural design strategies for infection prevention and control (IPC) in health-care facilities: towards curbing the spread of Covid-19. J Environ Health Sci Eng 18:1699–1707. https://doi.org/10.1007/s40201-020-00580-y
24. Fabris P (2020) COVID-19 epidemic demonstrates value of flexible hospital space [WWW Document]. Build. Des. Constr. https://www.bdcnetwork.com/covid-19-epidemic-demonstrates-value-flexible-hospital-space. Accessed 11 Nov 2020
25. Gesser-Edelsburg A, Mordini E, James JJ, Greco D, Green MS (2014) Risk communication recommendations and implementation during emerging infectious diseases: a case study of the 2009 H1N1 influenza pandemic. Disaster Med Public Health Prep 8:158–169. https://doi.org/10.1017/dmp.2014.27
26. Gopinath G (2020) The great lockdown: worst economic downturn since the great depression [WWW Document]. https://blogs.imf.org/2020/04/14/the-great-lockdown-worst-economic-downturn-since-the-great-depression/. Accessed 6 Nov 2020
27. Heneghan C, Howdon D, Oke J, Jefferson T (2020) The ongoing problem of UK hospital acquired infections—the centre for evidence-based medicine. Cent. Evidence-Based Med.—Univ, Oxford
28. Her M (2020) Repurposing and reshaping of hospitals during the COVID-19 outbreak in South Korea. One Heal. https://doi.org/10.1016/j.onehlt.2020.100137
29. Hua T (2020) Antimicrobial coatings at the front line of COVID-19 [WWW Document]. LUX Tech Signal. https://www.luxresearchinc.com/blog/antimicrobial-coatings-at-the-front-line-of-covid-19. Accessed 11 Nov 2020
30. Hurdle J (2020) Fear of COVID-19 infection is keeping many other patients away from hospitals, officials say [WWW Document]. NJ Spotlight News. NJ Spotlight News. https://www.njspotlight.com/2020/05/fear-of-covid-19-infection-is-keeping-many-otherpatients- away-from-hospitals-officials-say/. Accessed 9 Nov 2020
31. Iyengar K, Bahl S, Vaishya R, Vaish A (2020) Challenges and solutions in meeting up the urgent requirement of ventilators for COVID-19 patients. In: Diabetes and metabolic syndrome: clinical research and reviews. Elsevier Ltd, pp 499–501. https://doi.org/10.1016/j.dsx.2020.04.048
32. Jacobs A, Richtel M, Baker M (2020) Doctors say shortage of protective gear is dire during coronavirus pandemic. New York Times
33. Jakovljevic M, Bjedov S, Jaksic N, Jakovljevic I (2020) Covid-19 pandemia and public and global mental health from the perspective of global health security. Psychiatr Danub 32:6–14. https://doi.org/10.24869/psyd.2020.6

34. Janes C, Stanley-Becker I, Bernstein L, Partlow J (2020) Surge in virus hospitalizations strains hospitals in several states—The Washington Post. Washington Post
35. Khetrapal S, Bhatia R (2020) Impact of COVID-19 pandemic on health system & Sustainable Development Goal 3. Indian J Med Res 151:395–399. https://doi.org/10.4103/ijmr.IJMR_1920_20
36. Khullar D, Bond AM, Schpero WL (2020) COVID-19 and the financial health of US hospitals. JAMA—J Am Med Assoc 323:2127–2128. https://doi.org/10.1001/jama.2020.6269
37. Kim SW, Jo SJ, Lee H, Oh JH, Lim J, Lee SH, Choi JH, Lee J (2020) Containment of a healthcare-associated COVID-19 outbreak in a university hospital in Seoul, Korea: a single-center experience. PLoS ONE 15:e0237692. https://doi.org/10.1371/journal.pone.0237692
38. Leite H, Hodgkinson IR, Gruber T (2020) New development: 'healing at a distance'—telemedicine and COVID-19. Public Money Manag 40:483–485. https://doi.org/10.1080/09540962.2020.1748855
39. Ma X, Vervoot D (2020) Critical care capacity during the COVID-19 pandemic: global availability of intensive care beds. J Crit Care 58:96–97. https://doi.org/10.1016/j.jcrc.2020.04.012
40. Maina M, Tosas-Auguet O, English M, Schultsz C, McKnight J (2020) Infection prevention and control during the COVID-19 pandemic: challenges and opportunities for Kenyan public hospitals [version 1; peer review: 2 approved]. Wellcome Open Res 5:211. https://doi.org/10.12688/wellcomeopenres.16222.1
41. Mauri M (2015) The future of the hospital and the structures of the NHS. J Technol Archit Environ 9:27–34
42. Megahed NA, Ghoneim EM (2020) Antivirus-built environment: lessons learned from Covid-19 pandemic. Sustain Cities Soc 61:102350. https://doi.org/10.1016/j.scs.2020.102350
43. Ministry of Health and Family Welfare Government of India (2020) MoHFW | Home [WWW Document]. https://www.mohfw.gov.in/. Accessed 11 Nov 2020
44. Ministry of Health and Indigenous Medical Services Sri Lanka (2020) Provisional guidelines for clinical management of COVID-19. Colombo, Sri Lanka
45. Ministry of Health Sri Lanka (2020) Guidance on the rational use of personal protective equipment (PPE) in hospitals in the context of COVID-19 disease
46. Minstry of Health (2020) Hospital preparedness for COVID-19; a practical manual. Colombo, Sri Lanka
47. Minstry of Health Sri Lanka (2017) Healthcare bulletin 2017. Colombo, Sri Lanka
48. Mirchandani P (2020) Health care supply chains: COVID-19 challenges and pressing actions. Ann Intern Med 173:300–301. https://doi.org/10.7326/M20-1326
49. Moore A (2020) Mapped: the temporary hospitals created for coronavirus, For Healthcare Leaders
50. NDTV (2020) Fire kills 10 at Romanian COVID-19 hospital [WWW Document]. https://www.ndtv.com/world-news/fire-kills-10-at-romanian-covid-19-hospital-2325331. Accessed 15 Nov 2020
51. NIOSH (2020) Hierarchy of controls WWW Document]. Natl. Inst. Occup. Saf. Heal. https://www.cdc.gov/niosh/topics/hierarchy/default.html. Accessed 13 Nov 2020
52. Nazarian M, Price ADF, Demian P (2011) A review of different approaches to access and people circulation within health-care facilities and the application of modelling, simulation and visualisation. Loughborough University
53. OSHA (2020) COVID-19—control and prevention | Healthcare Workers and Employers | Occupational Safety and Health Administration [WWW Document]. Occup. Saf. Heal. Adm. https://www.osha.gov/SLTC/covid-19/healthcare-workers.html. Accessed 11 Nov 2020
54. Oh MD, Park WB, Park SW, Choe PG, Bang JH, Song KH, Kim ES, Kim HB, Kim NJ (2018) Middle East respiratory syndrome: what we learned from the 2015 outbreak in the republic of Korea. Korean J Intern Med 33:233–246. https://doi.org/10.3904/kjim.2018.031
55. Ornstein C, Hixenbaugh M (2020) "All the hospitals are full": in Houston, overwhelmed ICUs leave COVID-19 patients waiting in ERs—ProPublica. ProPublica [WWW Document]. https://www.propublica.org/article/all-the-hospitalsare-full-in-houston-overwhelmed-icus-leave-covid-19-patients-waiting-in-ers. Accessed 6 Nov 2020

56. PAHO W (2020) COVID-19 has infected some 570,000 health workers and killed 2,500 in the Americas. PAHO Director says, Pan American Health Organization
57. Pappa S, Ntella V, Giannakas T, Giannakoulis VG, Papoutsi E, Katsaounou P (2020) Prevalence of depression, anxiety, and insomnia among healthcare workers during the COVID-19 pandemic: a systematic review and meta-analysis. Brain Behav Immun 88:901–907. https://doi.org/10.1016/j.bbi.2020.05.026
58. Park SH (2020) Personal protective equipment for healthcare workers during the COVID-19 pandemic. Infect Chemother 52:165–182. https://doi.org/10.3947/ic.2020.52.2.165
59. Rhee C, Baker M, Vaidya V, Tucker R, Resnick A, Morris CA, Klompas M (2020) Incidence of nosocomial COVID-19 in patients hospitalized at a large US Academic Medical Center. JAMA Netw Open 3:e2020498. https://doi.org/10.1001/jamanetworkopen.2020.20498
60. Robert R (2012) Shortage of ICU beds leads to patient deaths—HealthManagement.org. ICU Manag Pract 12
61. Roychowdhury V (2020) How COVID-19 is transforming hospital design. Express Healthcare
62. Safe Care, 2020. COVID-19 hospital preparedness guideline. Amsterdam, Netherlands
63. Schettler T (2016) Antimicrobials in hospital furnishings: do they help reduce healthcare-associated infections? Health Care Without Harm US, Reston, USA
64. Sharma A, Gupta P, Jha R (2020) COVID-19: impact on health supply chain and lessons to be learnt. J Health Manag 22:248–261. https://doi.org/10.1177/0972063420935653
65. Statista (2020) The countries with the most critical care beds per capita | Statista [WWW Document]. https://www.statista.com/chart/21105/number-of-critical-care-beds-per-100000-inhabitants/. Accessed 13 Nov 2020
66. Vincent JL, Creteur J (2020) Ethical aspects of the COVID-19 crisis: how to deal with an overwhelming shortage of acute beds. Eur Heart J Acute Cardiovasc Care9:18–23. https://doi.org/10.1177/2048872620922788
67. WHO (2020) Keep health workers safe to keep patients safe: WHO. New Releases-World Heal. Organ. https://www.who.int/news/item/17-09-2020-keep-health-workers-safe-to-keep-patients-safe-who. Accessed 07 Nov 20
68. WHO (2020) Attacks on health care in the context of COVID-19 [WWW Document]. https://www.who.int/news-room/feature-stories/detail/attacks-on-health-care-in-the-context-of-covid-19. Accessed 9 Nov 2020
69. WHO (2015) Comprehensive safe hospital famework. World Health Organization, Geneva, Switzerland
70. WSP (2020) Hospitals after COVID-19: how do we design for an uncertain future? | WSP [WWW Document]. https://www.wsp.com/en-AE/insights/hospitals-after-covid-19-how-do-we-design-for-an-uncertain-future. Accessed 11 Nov 2020
71. Walsh B (2020) Covid-19: The history of pandemics, BBC. Available at: https://www.bbc.com/future/article/20200325-covid-19-the-history-of-pandemics (accessed: 2.11.2020)
72. Weiss YG, Buda I, Alon R, Adar Y, Lavi B, Rothstein Z (2020) Long-term hospital management in the presence of COVID-19: a practical perspective. J Hosp Adm 9:18–23. https://doi.org/10.5430/jha.v9n3p18
73. World Health Organization (2020b) Modes of transmission of virus causing COVID-19: implications for IPC precaution recommendations: scientific brief [WWW Document]. https://apps.who.int/iris/handle/10665/331616. Accessed 05 Nov 20
74. World Health Organization (2020) Infection prevention and control during health care when COVID-19 is suspected: interim guidance. Geneva, Switzerland
75. World Economic Forum (2020) The global risks report 2020. Geneva, Switzerland
76. Yang GZ, Nelson BJ, Murphy RR, Choset H, Christensen H, Collins SH, Dario P, Goldberg K, Ikuta K, Jacobstein N, Kragic D, Taylor RH, McNutt M (2020) Combating COVID-19—the role of robotics in managing public health and infectious diseases. Sci Robot 5:55–89. https://doi.org/10.1126/scirobotics.abb5589
77. Zhou Y, Zhang Z, Wang B, Ren G, Qi H, Wang X (2020) Construction time, cost and testing data of a prefabricated isolation medical unit for COVID-19. Data Brief 32:106068. https://doi.org/10.1016/j.dib.2020.106068

Development of a Framework to Examine the Transportation Infrastructure Resilience; Sri Lankan Context

P. L. A. I. Shehara, C. S. A. Siriwardana, D. Amaratunga, and R. Haigh

Abstract Critical Infrastructures can be considered as backbones in the societal and economic well-being of the countries. In many of the countries, natural hazards turning to disasters have become a massive threat in reducing the continuous functionality and delivery of the service. Due to the systematic behaviour of these Critical Infrastructures, the failure or disruption of one infrastructure system disturbs the functioning of the whole infrastructure system network. This induces with the cascading effects triggering on one infrastructure system, impacting the other infrastructure systems in the long run. For this to mitigate, the focus on integrating Disaster Risk Reduction strategies towards reducing the disaster damages on Critical Infrastructure emerged with time. In the Sri Lankan context, each year, the disaster damages to Critical Infrastructures are rapidly increasing making a huge impact on the country's economic development. Among them, there seems a rise in disaster damage to the transportation infrastructure sector, in which the highest damage was incurred from the 2004 Indian Ocean Tsunami incident. Here, the damage occurred on Peraliya railway infrastructure recorded as the largest single rail disaster in the world history with loss of nearly 1700 people lives and about million cost of damage to the railway assets. Based on these background aspects, the research study outlines the development of the transportation infrastructure management framework with a focus on climate resilience aspects in Sri Lanka. The impact of each of the determinant aspects of infrastructure resilience which are interlinked with the community and organizational resilience aspects were examined with the review of the literature and as well as the questionnaire survey analysis. A field survey was conducted to examine the community resilience aspects and a telephone interview survey was conducted to examine the organizational resilience aspects from the Sri Lankan perspective. From the 323 responses obtained from the community field survey and 1004 responses obtained from the telephone interviewing, the extent of perception for each defined resilience parameters were examined. From these survey results and the review of similar framework studies, the identified parameters were outlined into a framework.

P. L. A. I. Shehara (✉) · C. S. A. Siriwardana
University of Moratuwa, Colombo, Sri Lanka

D. Amaratunga · R. Haigh
University of Huddersfield, Huddersfield, UK

R. Dissanayake et al. (eds.), *ICSBE 2020*, Lecture Notes in Civil Engineering 174,
https://doi.org/10.1007/978-981-16-4412-2_18

This developed framework is suggested to further verify and define weightages for each parameters in the future studies.

Keywords Critical infrastructure (CI) · Resilience · Natural hazards · Transport infrastructure · Disaster risk reduction (DRR)

1 Introduction

Natural hazards triggering extreme disaster situations are the biggest threats to the built environment. The Indian Ocean Tsunami in 2004, Hurricane Katrina in 2005, Sichuan Earthquake in 2008, Haiti Earthquake in 2010 and Tohoku Earthquake in 2011 are some such extreme disaster incidents that have caused massive destructions in the Critical Infrastructure sector. These have become the costliest disaster incidents which have induced high economic losses in countries over the world.

Critical Infrastructures (CI) are defined generally as the primary physical structures, technical facilities and systems which are socially, economically and operationally vital to the proper functioning of the community [27]. The failure or disruption of these CIs impacts the societal well-being of the people and the economic development of the country. Different sector classifications have been defined based on their significance on the national economic security, public health and safety and national morale [20]. These were mainly inclusive of sectors such as transportation infrastructure sector, water and sanitation infrastructure sector, power and energy infrastructure sector, telecommunication infrastructure sector and food and agriculture sector. Among these, the transport infrastructure sector is highly significant in providing accessibility and related facilities towards the society which directly influences the economic development of the country. The damages that have been triggered in the transportation infrastructure sector are highly critical when compared with the other infrastructure sectors. Some such massive destructions which had incurred in the transportation infrastructure are represented under Table 1.

Based on these, the necessity to mitigate the damage content towards the economic loss of the country along with enhancing the resilience capacities of the transportation infrastructures emerged with time. In dealing with this, the strategic implementation of the Disaster Risk Reduction (DRR) strategies was highlighted in many of the global level policy frameworks [27]. Target 4 of the Sendai Framework for Disaster Risk Reduction 2015–2030 focuses the significance of minimizing the disaster damages to CIs [43]. Here, they have aimed at initiating strategies to substantially decrease the damages and disruptions to CIs by 2030 [17]. Based on these, the new designing aspects of CIs needed to be effectively designed to resist the barriers from natural hazards and as well as the existing CIs needed to be effective managed with necessary measures.

In the Sri Lankan context, the damage to economic loss of the country from transportation infrastructure from 2016 to 2017 denotes a rapid increment when compared with other infrastructure sectors [33]. The criticality of the transportation

Table 1 Disaster damages to economic loss from the transportation infrastructures

Disaster event	Year	Country	Infrastructure damage to the economic loss of the country	References
Indian Ocean Tsunami	2004	Sri Lanka	15$ million damage of railway infrastructure assets 60$ million damage of road infrastructure assets	[36, 35]
Hurricane Katrina	2005	USA	Shut down of the airports Disruption to railway infrastructure due to flooding caused	[1]
Sichuan Earthquake	2008	China	34,000 km highway damage and transport infrastructure failures	[57]
Typhoon Morakot	2009	Taiwan	More than 600 km of highway length and 196 bridges failed	[50]
Haiti Earthquake	2010	Haiti	Loss of communication lines Road blockages from debris	[5]
Pakistan floods	2010	Pakistan	Infrastructure damage $4 billions	[23]
Tohoku Earthquake	2011	Japan	1 million USD damage on transport infrastructure	[21, 31]
Hurricane Sandy	2012	USA	Shut down of all the airports, ports and public transit systems of the region	[25, 55]

Fig. 1 Some captures of Peraliya rail disaster in 2004

infrastructures with respect to economic damage in the country and ability of response and recovery was further highlighted through the massive destruction which had occurred to the Peraliya railway infrastructure from the 2004 Indian Ocean Tsunami incident [35]. This was recorded as the worst single rail catastrophe ever in the history, which induced a loss of nearly 1700 lives of people and about 15$ million infrastructure damage to the railway assets [36]. With the force triggered by the waves towards the resistance of the train, the railway line has overtopped leading to

an extreme catastrophe situation [13]. Figure 1 denotes the pictographic view of the extent of the massive damage occurred in this scenario [10].

Based on these, the necessity to enhance the resilience of transportation infrastructures in Sri Lanka was identified. This can be proceeded with a development of the CI resilience framework with the focus of transportation infrastructures in the Sri Lankan context.

2 Literature Review

2.1 Overview of Transportation Infrastructure

The continuous functionality of the CIs is essential in the economic and national prosperity of the communities. As a result, CIs are considered as the backbones in the societal prevalence. Among these CI sectors, the transportation infrastructure sector has become extremely important as well as critical in many of the country sector identifications. This has emerged critical with the exposure of criticality based on time, quality and as well as proportion. In providing accessibility facilities towards the community to reach other infrastructure facilities and fulfill their day today activities, the transportation infrastructures render a massive service. Based on the Transportation sector specific plan by the FEMA, the main asset classification of the transportation infrastructures are represented in the below list [28].

- Aviation—Airports, heliports, seaplane bases, support services, air traffic control and navigation facilities
- Maritime—Waterways, ports and intermodal landside connections
- Freight rail—Rail tracks, freights, coal shipments
- Highway and motor carrier—Bridges, tunnels, commercial vehicles and roadway
- Pipeline—Compressor stations, pumping stations and pipelines
- Postal and shipping—Courier service providers, mail management firms and delivery services
- Mass transit—transit buses, monorails, light rails, passenger rails and commuters.

The criticality of the behavior of these assets in transportation infrastructures depend on factors such as maintenance capability, time and cost incurring on the repairing of the assets, impact to the economy of the country, capability of response and recovery, subsequent consequences and detection capabilities [19]. To make these CIs critical in nature, different threats such as cyber threats, terrorist attacks, natural hazards triggering into disasters and aging of infrastructures mainly influence [28]. Among the major threats which disrupt the transportation infrastructure functioning, the disasters which trigger the natural hazards are identified as a major threat which influence through natural occurrence [53]. When reviewing past disaster incidents, the extreme level of destruction has occurred in the transportation infrastructure network in many of the countries. Some such impacts which trigger from the climate

change occurrences on transportation infrastructures are listed in Table 2 [16, 22, 29, 50, 54].

Accordingly, the measures needed to be undertaken in the disaster preparedness stage to mitigate these damages which trigger extreme disaster situations to the transportation infrastructures.

Table 2 Natural hazard impacts on transportation infrastructure

Natural hazard impacts	Impact on transportation infrastructure	Measurable parameters
Extreme rainfall	• Roadway washout and overtopping • Disrupt transportation in roadways • Bridge scouring • Disrupt transportation in inland waterways • Increase of seepage and infiltration into pavement and subgrade • Overloading of drainage systems	• Extent of the use of resilient construction materials • Extent of periodic maintenance of drainage paths • Capacity of the drainage paths (Hydraulic size or gradient of culverts) • Availability of bridge scour protecting measures for high velocity flows
Increase in maximum temperature	• Thermal expansion in bridge expansion joins and paved surfaces • Asphalt cracking • Railway buckling • Asphalt rutting • Failed expansion joints • Pavement softening	• Extent of the use of thermal resilient pavement material • Extent of handling proper routine maintenance • Provision of adequate expansion joints
Sea level rise	• Erosion of the road base • Erosion of bridge scours • Inundation of coastal infrastructure • Flooding of underground tunnels and low lying infrastructure • Decrease of the expected lifetime of highways • Reduced clearance under bridges	• Extent of providing adequate scour protection for bridge sub structures • Availability of protective sea wall barriers • Performance of periodic maintenance routines
Extreme wind speed	• Damage to signboards, lighting fixtures and supports • Threat to the stability of bridge decks • Disruption to ports and airports • Increased probability of infrastructure failure	• Availability of backup facilities and communication mechanisms • Ensure of redundancy of CIs (e.g. navigation of planes) • Strategies for cross wind effects

2.2 Transportation Infrastructure Resilience

The resilience concept of CIs emerged with the initial focus of CI protection in many of the countries in the global context. With this, the strategy implementation focusing the resilience targets at minimizing the consequences which are triggered from disruption of the infrastructure assets rather than avoiding the complete failures [42]. The new infrastructure assets should be planned, designed, built and operated to account for the extreme changes in climate conditions and the existing assets need to be retrofitted and managed effectively [22]. The concept of resilience is defined in the literature as the ability to absorb, adapt to and rapidly recover the Critical Infrastructures from potentially disruptive events such as extreme disaster situations [26, 38]. The resilience aspects are needed to be initiated from the initial phase of the disaster management mechanism.

Based on this, the resilience measure has being determined under the cyclic prevention, absorption, recovery and adaptation phases [41]. The prevention phase of the resilience cycle needed to be initially concerned with the adoption of preventive measures to safeguard the CIs. The CI system then needs to adapt to the absorption phase as with the disaster situations strikes the system. For this to be adopted, the absorption measures needed to be initiated which are featured with the robustness capacity of the system. Followed with this, the recovery phase is initiated through the capability of the system to function back its activities towards the normal behaviours. For this to be achieved, the minimum recovery period needed to be capable of facilitating the CI system. As the final phase, the adaptation phase initiates with the representation of the potential of the CI system towards adapting towards the changing environment which is triggered by the disruptive disaster incidents.

Accordingly, for a CI system that needs to be potential enough to sustain the extreme disaster situation, adequate measures needed to be initiated with the system to mitigate the damages and service disruption [37]. The factors which determine the resilience capacities of CIs are categorized such as organizational, technical and community factors [26]. To effectively initiate the resilience capacities of the CI systems, these need to be well initiated and well managed.

2.3 Mainstreaming Disaster Risk Reduction Strategies

With the aforementioned focus on the disaster damages on CIs, the immediate focus on implementing strategies to reduce them has emerged all over the world. Under this consideration, the integration of Disaster Risk Reduction (DRR) strategies with enhancing the resilience of CI has a major concern. The concept of Multi-Hazard Early Warning (MHEW) mechanism is one of the prominent concepts which has highlighted as a key component in the DRR strategy implementation [43]. This aims at initiating the ability to address several hazards or impacts of a similar or different

type in situations where these events may occur alone, simultaneously or cascading with time [15].

The technological aspects have widened the functional capabilities and resilience capacities of the infrastructure systems to face the challenges triggering from natural hazards [45, 47]. In this context, the digitalized mobile-based technologies are highly significant in adapting towards the novel technological aspects in the world [46, 48]. The delivery of EWs through mobile-based platforms are massively used in many of the developed and developing countries over the world. In this context, the resilience level of the community is possible to enhance higher capacities with the adaptation towards these novel technological developments. The adaptation of community and as well as the stakeholder perspectives too can be altered through the novel digital platforms which are focussed at effective and timely delivery of the MHEWs [45–48]. For this to be adequately initiated, the community and stakeholder level trust and awareness needed to be fulfilled towards the novel communication platforms [46, 48].

Further, the mapping of infrastructure assets can be manipulated with novel technologies such as Geographical Information Modelling (GIS) [54]. These can be altered by safeguarding and effectively managing the infrastructure assets with time. Accordingly, it is of vital importance to focus on initiating the CI resilience strategies with the integration of the DRR measures to face the threats triggering from extreme disaster situations.

Along with this, different countries have used modern approaches to initiate these DRR strategies in enhancing the resilience of the transportation infrastructure assets. Some such strategies are more broadly discussed Table 3.

2.4 Transportation Infrastructure Resilience Frameworks

With the focus of enhancing the resilience capacities in the countries, the policy development measures and frameworks have been implemented at the national level. Here the national level infrastructures are identified as critical in which transportation infrastructure has become extremely critical in this among the other sectors. The significance of initiating measures on safeguarding transportation infrastructures was highlighted in many of these frameworks and policy guidelines. Summary of such developed frameworks and policy guidelines that mainly focus on transportation infrastructure resilience are listed in Table 4.

Under these frameworks, the integrated factors which determine the transportation infrastructure resilience are majorly highlighted. The measures which needed to be focussed in each phase of the CI resilience cycle have elaborated with the representation of the significance of each of them. In effectively managing the transportation infrastructures, adequate measures needed to be followed in infrastructure planning, designing and as well as in operational and management stages [22]. Further, the CI system interlinked factors such as organizational, community and technical capacities of CI systems needed to be well focussed [26].

Table 3 Overview of DRR strategies implicated in the past disasters

Disaster situation	Major issues	Strategies undertaken	References
Kosi floods in 2008 in India	Institutional dysfunction Lack of monitoring and maintenance of the embankments Lack of Awareness, Warning and Preparedness for Flood Disaster	Development of adaptive institutions and distributed responsibilities among the authorities Improve of local level community awareness Establishment of improved EW mechanisms Improve the monitoring and maintenance routines	[14, 49]
Hurricane Katrina in 2005 in USA	Lack of preparedness Poor response of the federal government Absence of routine maintenance facilities for the infrastructure assets	Establishment of high protection structures to resist in heavy winds Frequent and adequate monitoring of levees and flood barriers Periodic maintenance of the infrastructure assets Establishment of separate evaculanes for the safe evacuation of community	[7, 1]
Great East Japan Earthquake in 2011	Inadequate capacity of the railway lines to resist the Earthquakes	Initiating of anti-derailing system for railway Design of sea wall barriers in the coastal belt	[31, 56]
Hurricane Floyd in 1999 in Bahamas islands	Lack of adequate protective measures to control sea water flooding	Reconstruction of timber jetties in which the timber decking was designed as drop in removable panels	[11, 12]
Landslide and rockfall in Cascadia subduction zone in USA	Lack of adequate measures to resist the landslides	Establishment of routine maintenance for drainage facilities Flattening the slope to decrease driving force Construction of retaining walls	[54]

3 Framework Development

Different frameworks and policy guidelines have developed with the basis of enhancing CI resilience in the national level perspectives. Some such frameworks are the Federal Emergency Management Agency (FEMA) national CI guideline, Australian CI resilience strategy, Canadian National Strategy for Critical Infrastructure, Belgium Critical Infrastructure Protection strategy and NIPP 2013: Partnering for Critical Infrastructure Security and Resilience and 2015 Sector-Specific Plans

Table 4 Summary of frameworks and guidelines with the focus on transport infrastructure resilience

Framework/policy guideline	Country/authority	References
Guide for climate resilient road construction	USAID	[30]
Guide for climate resilient bridge construction	USAID	[9]
Climate resilient design standards and guidelines	USA	[32]
City resilience framework	Canada	[39]
Transportation infrastructure resilience framework	New Zealand	[52]
Critical infrastructure resilience strategy	Australia	[26]
Moving towards climate-resilient transport	World Bank	[54]
Towards climate resilient transportation infrastructure	Smart Transportation Alliance	[29]
Policy perspectives for climate resilient infrastructure	OECD	[22]
Adapting transport to climate change and extreme weather	ITF	[42]
Paving the way for climate resilient infrastructure	UNDP	[51]
Adaptation methodologies and strategies to increase the resilience of roads to climate change	PIARC	[24]

in the United States of America. Under the review of these CI resilience strategic frameworks, the basic core structure which has used in the Australian national guidelines were selected in adopting in the Sri Lankan context. This was chosen with the similarity in the Sri Lankan context CI sector classification and as well as from the focus of emergency disaster situations which are mostly similar to the Sri Lankan context from the perspective of natural hazards.

Under this, the basic outline was mapped among the integrated mechanism on community, organizational and infrastructure resilience determinant factors as denoted in Fig. 2.

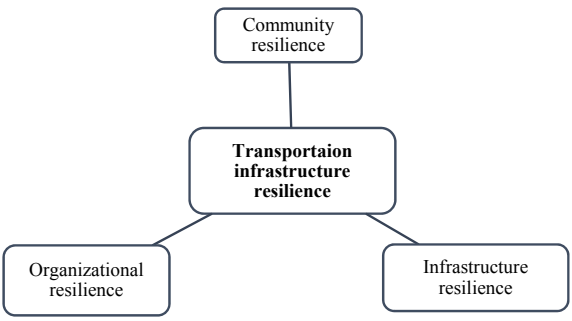

Fig. 2 Basic outline of the framework

Accordingly, the framework here outlines, the integration of the identified parameters which determines the resilience of transportation infrastructure systems in Sri Lanka with the narrowed focus on the road infrastructure sector. Through this the research objectives of identification of community resilience measures, identification of organizational resilience measures, identification of transportation resilience measures and integration of the identified measures in framework development are expected to be attained. Basically, to follow up these research objectives, the community resilience aspects were mainly examined through the community field survey and organizational resilience aspects were examined through telephone interviewing of the stakeholder categories and infrastructure resilience aspects through reviewing the similar global frameworks. The review of each of the studies are discussed more broadly in the below sections.

3.1 Identification of Parameters to Determine Community Resilience

Community resilience is the major influencing key factor which influences the infrastructure resilience capacity. The contribution delivered by the relevant community groups in a particular geographical area is massively important in safeguarding the resilience aspects of the transportation infrastructure. The adaptability of the community towards extreme disaster situations, make the infrastructure resilience of the community to a higher level of capacity.

To examine this extent of community resilience level, a field questionnaire survey was conducted in the Sri Lankan context [46, 48]. The resilience level of the selected communities in Sri Lanka was examined with the focus of DRR strategy implementation through this field questionnaire survey. Overall 323 responses have been collected through the responses obtained covering 10 Grama Niladari divisions in Sri Lanka. Here, the community level adaptation towards the MHEW mechanisms was examined where the technology has incorporated in defining the novel communication mechanisms [46, 48]. The summary of the community resilience parameters which were examined with the extent of resilience level is represented in Table 5.

Apart from these examined parameters of community resilience aspects, the review of recent frameworks and guidelines was conducted with the focus of enhancing transportation resilience capacity. It has revealed that the effective communication mechanism in the community massively contributes to enhancing the resilience capacities of the communities [53]. In supporting this, a sufficient level of community trust and community awareness needed to be enriched with the community [4]. The effective service delivery platforms which are developed with the technological aspects are effectively used in community alerting in extreme disaster situations [46, 48]. For these to be adopted in the communities, the adequate level of trust and awareness needs to be ensured.

Table 5 Summary of extent of community resilience level

Perception level	Very high (80–100%)	High (60–80%)	Moderate (40–60%)	Low (20–40%)	Very low (0–20%)
Community trust level				Low	
Efficiency of delivering EW messages	Traditional modes				
Modes of EW message dissemination		SMS alert through mobile phones			
Authority level issuing the message	DMC, police, media				
Usage level—modern technological platforms					Very low
Trust level—modern technological platforms					Very low
Level of awareness—modern technological platforms				Low	

Further, in effectively managing and reducing the service disruptions in the CI systems which are triggering from the extreme disaster situations, the community level experience is highly useful [40]. The experience in adjusting and adapting to the alternative mechanisms and pathways are highly significant [18]. For example, the use of alternative routes to access other emergency service facilities can be done with the enrichment of past such disaster situations. Further, community partnerships are considered highly significant in effectively managing disaster events in highly resilient communities [44]. The community engagement in training and drills are of major concern under this community resilience enhancement. Through these training and practice sessions, awareness among the community on adapting to disaster situations becomes increased.

Under this perspective, the following parameters were summarized as the key parameters and measurable indicators which determine the community resilience level in focusing on the resilient transportation infrastructures. The identified parameters were mainly classified as under Table 6.

Table 6 Summary of the community resilience parameters

Key parameter	Measurable indicators	References
Community information sharing	Capability of reaching the community alerting through existing communication modes	[18, 53], community field survey
	Trustworthiness on existing Early Warning mechanisms	[4], community field survey
	Availability of community risk register and preparedness level of the community	[4, 18]
	Awareness and usability on existing Early Warning mechanisms	[4], community field survey
Reducing service disruption	Community awareness on adaptation towards service disruptions	[40]
	Community experience on adaptation towards service disruptions	[18]
Managing service disruptions	Availability of alternative communication mechanisms and awareness on emergency plans and updating	[18], community field survey
	Restoration speed or availability of temporary precautions	[8]
Community partnerships	Availability of integrated platforms of governmental and non-governmental organizations to support the community	[44]
	Community participation to preparedness trainings and drills	[4, 18]

3.2 Identification of Parameters to Determine Organizational Resilience

Organizational resilience aspects too are considered a vital sector in enhancing the resilience aspects of the transportation infrastructure sector. It is not only required to enhance the technical resilience level of the CIs, but the adaptability of the authorities which are managing these CIs [41]. The necessity to strengthen the organization's resilience capacity in enhancing the CI resilience level was examined in many of the recent research studies [6]. Under that, the main influencing factors which determine organizational resilience were categorized as risk management factors, organizational innovation processes and educational and development processes [37]. Based on these, the strength of CIs was determined through the determination of organizational resilience level. These are vital in the determination of the preparedness level of the

organizations which are interlinked with CIs in the community. Further, these are adopted in increasing the level of feasibility in adapting the CIs to the extensive disaster situations.

To examine the organizational resilience aspects in the Sri Lankan context, a questionnaire survey was conducted through telephone interviewing [46, 48]. Here, the responses among the stakeholders who are identified as the first responders in the communication mechanism of disaster Early Warnings were collected. Overall 1004 responses were collected through these opinion gathering from the first responders. The extent of perception towards the existing communication mechanisms and as well as the novel communication platforms was examined using this telephone interviewing of the responders. The data could be gathered covering all districts in Sri Lanka and the summary of the perception towards the organizational resilience parameters are represented in Table 7.

From the review of literature of similar organizational resilience focussed frameworks, it has identified that the parameters can be mainly classified as emergency preparedness parameters, effective risk management parameters, parameters which determine improved planning levels and response and recovery related parameters [26]. Under emergency preparedness, the organizational resilience aspects can be enhanced through conducting awareness and training sessions and enhancing the trust level of the authorities which issue Early Warning alerts. Further, it has been recognized that the job role performed by the first responders are highly significant in enhancing the organizational resilience levels [2]. This variates with the

Table 7 Summary of organizational resilience level

Perception level	Very high (80–100%)	High (60–80%)	Moderate (40–60%)	Low (20–40%)	Very low (0–20%)
Perception of being a first responder		High			
Efficiency of delivering EW messages	Mobile based platforms	Traditional modes			
Modes of EW message dissemination	Mobile phone based				
Authority level issuing the message	Disaster Management Center				
Usage level—novel technological aspects					Very low
Trust level—novel technological aspects		High			
Level of awareness—modern technological platforms					Very low

capability level of these first responders who are identified as the personnel who are responsible for disseminating the disaster alerts towards the vulnerable communities. Further, the effective risk management of the organizations can be achieved through assigning defined roles and responsibilities to each of the stakeholders to perform during the emergency disaster situations [18]. The improved hazard mitigation and emergency operation plans are highly significant in adapting to a higher level of the organizational resilient environment [18]. The organizational partnerships with the government and private authorities are highly significant in this aspect of acting responsibly in emergency disaster situations. Further, the updated mitigation and disaster response plans are highly useful in coordinating during these emergencies [6].

Accordingly, based on the above reviews, the following summarized parameters in Table 8 are identified in dealing with the organizational resilience level which leads towards effective management of the transport infrastructures.

Table 8 Summary of the organization resilience parameters

Main parameter	Measurable indicator	References
Emergency preparedness	Organizing training programs and exercises to enhance the preparedness capacities of the community	[26, 28, 18]
	Initiate policies and coordination mechanisms explicitly addressing climate change and resilience of transportation infrastructure	[28, 54]
	Trustworthiness on existing information sources and awareness on modern sources	First responder survey [4]
	Capability of first responders to make aware the community in emergency disaster situations	First responder survey [26]
Effective risk management	Availability of defined roles and responsibilities during emergency situations	First responder survey [26]
	Availability of risk assessment frameworks	[28, 58]
Improved planning	Availability of updated hazard mitigation plans	[28, 58]
	Availability of updated emergency operation plans	[18, 54]
Response and recovery	Availability of updated restoration and rehabilitation plans	[28, 18]
	Improved partnerships for coordination of response and recovery activities	[28, 18]

3.3 *Identification of Parameters to Determine Infrastructure Resilience*

In enhancing the resilience aspects of the transportation infrastructures, the necessity to focus on the technical resilience aspects in planning, designing and operational and maintenance practices has become more prominent. These contribute highly to effective management and adapting to extreme disaster situations.

Under the infrastructure planning stage, the safety protocols needed to be followed such as past historic data regarding the disaster risks in the respective geographical location and identify the probable risks [28, 18]. Further, the infrastructure planning needed to be done with the availability to access to the backup temporary structures and as well as it is needed to have backup plans in providing alterations when the access routes are blocked or damaged by the extreme disaster situations [40].

Further, it is required to focus thoroughly on the infrastructure designing stage which needed to be designed with the fulfilment of the resilience designing strategies. It is required to use resilient construction materials for the design of pavement structure [26]. This can be undertaken with the use of heat resistant asphalt materials which can sustain the extreme thermal impacts. Another main aspect is the design and upgrading of the drainage facilities in accordance to the design criteria [32, 59]. The infiltration and drainage impacts are needed to be thoroughly investigated in the designing stage of the pavements. It is required to maintain the positive cross slope levels as well to facilitate the drainage path more effectively [28]. These are required to effectively manage the flooding impact and properly manage the stormwater which occurs from extreme precipitation levels. Another major aspect is the consideration of resilient design strategies to enhance protection in pavement designing [3]. These are needed to be incorporated with enhancing the resilience capacity of the pavement structure. In low lying areas, cement concrete geo-cells can be used to resist flooding situations. Further, revegetation too can be considered in implicating in the flooding areas as resilience measurements [54].

Another major aspect is the Use of flood protection barriers to ensure the damage mitigation to road pavement and infrastructures. These are identified as rock armor structures, Concrete Masonry Block (CMB) Revetment, Geo-synthetic Container Revetment, dikes, seawalls, rocky aprons and breakwater systems [32, 3]. The significant of these measures were highlighted through the expert opinions as well. Further it was highlighted to elevate the transportation infrastructure assets such as mechanical and electrical equipment in providing operations or maintenance facilities [32].

Apart from these aspects, the existing infrastructure assets need to be effectively managed and coordinated towards safe performance during emergency disaster situations. Under routine maintenance plans, the defects and deteriorations which have been triggered in the bridge structures and pavement structures needed to be monitored and provided with suitable measures [26, 28]. Further, the existing plans must be sufficient with providing measures with restoring the routes and services with normal performances [28].

Storm water management is another main area which is needed with a higher focus level [32]. This needs to be concerned with much attention as the extreme precipitation situations can damage the pavement structures and disrupt the facilities. For this to be maintained, the drainage paths need to be routinely inspected and obtained required actions.

Another aspect is converting the unpaved roads to paved roads which can safeguard the level of disruptions and enhance the resilience levels [32]. Through these, the capacity level of the pavement structures to sustain extreme disaster situations such as floods and landslides can be altered. Based on the above concerns, the summarized parameter list which determines the infrastructure resilience level of the transportation infrastructures is represented in Table 9.

3.4 Overview of the Developed Framework

Based on the above examination and review of framework studies, the key influencing factors which are needed to be highly concerned in managing transportation infrastructures have been identified. The results obtained from the field questionnaire survey and as well as from the telephone interviewing of the stakeholders who are interlinked with the Disaster Management mechanism in Sri Lanka were highly useful in the identification of these parameters.

Through the integration of the above identified key parameters and their measurable indicators relevant to community, organizational and infrastructure resilience aspects, the framework development can proceed. Here the integrated framework is represented as in Table 10.

The above summarized list of parameters that determines the transportation infrastructure resilience level is mainly elaborated through the systematic influence of the functioning of the transportation system. In the further modification of this model, the assigning of the weights can proceed towards the quantification of the resilience capacity of the overall transportation infrastructure system.

4 Discussion

Under the challenging environment for the threats triggering from the extreme disaster situations, it is vital to enhance the resilience capacities of national level Critical Infrastructures. For this, the necessary frameworks and policy guidelines are needed to be initiated with the focus on examining existing resilience capacities and enhancing them to a safer level. Accordingly, in the Sri Lankan perspective, the necessity to develop such frameworks with the focus of CI resilience has emerged with the focus group meetings which were held with the CI related authorities. With this concern, the transport infrastructure seems to be in a critical condition, where

Table 9 Summary of parameters to determine infrastructure resilience

Main parameter	Measurable indicator	References
Infrastructure planning	Conducting risk assessments and use of hazard maps in new transport developments	[28, 18]
	Having backup temporary components (motor boats facilities) or plans	[40, 54]
	Having planned evacuation routes or alternative access roads	[40, 54]
	Availability of mapping of inventory and assets using new technologies (e.g. GIS)	[28, 54]
Infrastructure design	Use of resilient construction materials for pavement construction (e.g. Heat resilient paving asphalt)	[26, 28]
	Upgrading drainage facilities (annullay)	[59]
	Considering resilient design strategies to enhance protection (e.g. Cement concrete geocell, revegetation)	[28, 3]
	Using protective measures for bridge scouring (Geosynthetic Reinforced Soil (GRS) technology for bridges)	[28, 54]
	Use of flood protection barriers to ensure the damage mitigation to road pavement and infrastructure (e.g. rock armor structures, Concrete Masonry Block (CMB) Revetment, Geosynthetic Container Revetment, dikes, seawalls, rocky aprons, breakwater systems)	[32, 3]
	Elevate mechanical and electrical equipment in operations or maintenance facilities	[32]
	Raise elevation of roadway or bridge touchdown on embankments or levees	[30]
Infrastructure operations and maintenance	Frequency of monitoring performance and routine maintenance activities like repairs and retrofitting (annually)	[26, 28, 54]
	Performing repairs like potholes and pavement deteriorations (annually)	[26, 28, 54]
	Capability of restoring the routes/services with existing plans	[28, 18]
	Availability of bridge rehabilitation and maintenance routine plans	[9]
	Availability of storm water management mechanisms or plans to implement frequently	[32, 30]
	Conversion of unpaved roads into paved roads	[30]

Table 10 Summary of the framework

Resilience aspect	Main parameter	Measurable indicator
Community resilience	Community information sharing	Capability of reaching the community alerting through existing communication modes
		Trustworthiness on existing Early Warning mechanisms
		Availability of community risk register and preparedness level of the community
		Awareness and usability on existing Early Warning mechanisms
	Reducing service disruption	Community awareness on adaptation towards service disruptions
		Community experience on adaptation towards service disruptions
	Managing service disruptions	Availability of alternative communication mechanisms and awareness on emergency plans and updating
		Restoration speed or availability of temporary precautions
	Community partnerships	Availability of integrated platforms of governmental and non-governmental organizations to support the community
		Community participation to preparedness trainings and drills
Organizational resilience	Emergency preparedness	Organizing training programs and exercises to enhance the preparedness capacities of the community
		Initiate policies and coordination mechanisms explicitly addressing climate change and resilience of transportation infrastructure
		Trustworthiness on existing information sources and awareness on modern sources
		Capability of first responders to make aware the community in emergency disaster situations

(continued)

Table 10 (continued)

Resilience aspect	Main parameter	Measurable indicator
	Effective risk management	Availability of defined roles and responsibilities during emergency situations
		Availability of risk assessment frameworks
	Improved planning	Availability of updated hazard mitigation plans
		Availability of updated emergency operation plans
	Response and recovery	Availability of updated restoration and rehabilitation plans
		Improved partnerships for coordination of response and recovery activities
Infrastructure resilience	Infrastructure planning	Conducting risk assessments and use of hazard maps in new transport developments
		Having backup temporary components (motor boats facilities) or plans
		Having planned evacuation routes or alternative access roads
		Availability of mapping of inventory and assets using new technologies (e.g. GIS)
	Infrastructure design	Use of resilient construction materials for pavement construction (e.g. Heat resilient paving asphalt)
		Upgrading drainage facilities (annullay)
		Considering resilient design strategies to enhance protection (e.g. Cement concrete geocell, revegetation)
		Using protective measures for bridge scouring (Geosynthetic Reinforced Soil (GRS) technology for bridges)

(continued)

Table 10 (continued)

Resilience aspect	Main parameter	Measurable indicator
		Use of flood protection barriers to ensure the damage mitigation to road pavement and infrastructure (e.g. rock armor structures, Concrete Masonry Block (CMB) Revetment, Geosynthetic Container Revetment, dikes, seawalls, rocky aprons, breakwater systems)
		Elevate mechanical and electrical equipment in operations or maintenance facilities
		Raise elevation of roadway or bridge touchdown on embankments or levees
	Infrastructure operations and maintenance	Frequency of monitoring performance and routine maintenance activities like repairs and retrofitting (annually)
		Performing repairs like potholes and pavement deteriorations (annually)
		Capability of restoring the routes/services with existing plans
		Availability of bridge rehabilitation and maintenance routine plans
		Availability of storm water management mechanisms or plans to implement frequently
		Conversion of unpaved roads into paved roads

it had shown a higher level of damage increasing from the disaster impacts which triggered in 2016–2017.

Accordingly, the framework development was undertaken with the focus of enhancing transportation infrastructure resilience under the road sector. As the initial approach, the identification of the parameters which determines the resilience level of the infrastructures with the basis of CI resilience guidelines was undertaken in this study. Here, the parameters were identified from the similar transportation infrastructure resilient frameworks that were developed in countries like USA, Australia, UK, Canada, New Zealand etc.

The initial framework development was outlined under main sectors of the community, organizational and infrastructure resilience segments which are to

integrate with the overall transport infrastructure resilience. Here, the identified parameters were filtered to be categorized in a summarized manner.

In the further studies of this research focus, the verification of the framework with expert opinion reviews are needed to be undertaken. Moreover, the weightings for each of the measurable indicators are possible to be defined with multi criteria decision making approaches.

With this, the overall transportation infrastructure resilience capacity measurement can be determined for a considered geographical area. The integrated resilience aspects related to transportation infrastructures are then interlinked towards the determination through the resilience index measurement. This measurement is to be determined mainly through each of the community, organizational and infrastructure resilience which are bound around a certain infrastructure system.

Acknowledgements The authors here gratefully acknowledge Erasmus+ Capacity Building for Higher Education Grant, CApacity Building in Asia for Resilience EducaTion (CABARET) for providing funds and expertise in carrying out this research study. Further, the immense support provided by Dialog Axiata PLC Sustainability division in undertaking the survey studies is highly appreciated.

References

1. Abdelhafez MA, Ellingwood B, Mahmoud H (2021) Vulnerability of seaports to hurricanes and sea level rise in a changing climate: a case study for mobile, AL. Coast Eng 167:103884. https://doi.org/10.1016/j.coastaleng.2021.103884
2. Alexander DA, Klein S (2009) First responders after disasters: a review of stress reactions, at-risk, vulnerability, and resilience factors. Prehosp Disaster Med 24:87–94. https://doi.org/10.1017/S1049023X00006610
3. Asariotis R (2020) Climate change impacts and adaptation for coastal transportation infrastructure: a sustainable development challenge for SIDS in the Caribbean and Beyond. In: Coastal and Marine Environments. CRC Press
4. Becker D, Schneiderbauer S, Forrester JM, Pedoth L (2015) Guidelines for development of indicators, indicator systems and provide challenges. CRED, Louvain
5. Bilham R (2010) Lessons from the Haiti Earthquake. Nature 463:878–879. https://doi.org/10.1038/463878a
6. Brown C, Seville E, Vargo J (2017) Measuring the organizational resilience of critical infrastructure providers: a New Zealand case study. Int J Crit Infrastruct Prot 18:37–49. https://doi.org/10.1016/j.ijcip.2017.05.002
7. Burby RJ (2006) Hurricane Katrina and the paradoxes of government disaster policy: bringing about wise governmental decisions for Hazardous areas. Ann Am Acad Pol Soc Sci 604:171–191. https://doi.org/10.1177/0002716205284676
8. Chandra A (ed) (2011) Building community resilience to disasters: a way forward to enhance national health security. RAND, Santa Monica, CA
9. Cuevas SC, Peterson A, Morrison T, Robinson C (2016) Methodology for examining the challenges in mainstreaming climate change adaptation. Int J Clim Chang Strateg Manag 8:418–439. https://doi.org/10.1108/IJCCSM-07-2015-0091
10. Dawson D, Shaw J, Roland Gehrels W (2016) Sea-level rise impacts on transport infrastructure: the notorious case of the coastal railway line at Dawlish, England. J Transp Geograp 51:97–109. https://doi.org/10.1016/j.jtrangeo.2015.11.009

11. Domino ME, Fried B, Moon Y, Olinick J, Yoon J (2003) Disasters and the public health safety net: hurricane floyd hits the North Carolina medicaid program. Am J Public Health 93:1122–1127
12. Dow K, Cutter SL (2002) Emerging hurricane evacuation issues: hurricane Floyd and South Carolina. Nat Hazard Rev 3:12–18. https://doi.org/10.1061/(ASCE)1527-6988(2002)3:1(12)
13. Goff J (2005) Survey of the december 26th 2004 Indian ocean Tsunami in Sri Lanka. Bull N Z Soc Earthq Eng 38:235–244. https://doi.org/10.5459/bnzsee.38.4.235-244
14. Gupta N, Dahal S, Kumar A, Kumar C, Kumar M, Maharjan A, Mishra D, Mohanty A, Navaraj A, Pandey S, Prakash A, Prasad E, Shrestha K, Shrestha MS, Subedi R, Subedi T, Tiwary R, Tuladhar R, Unni A (2021) Rich water, poor people: potential for transboundary flood management between Nepal and India. Curr Res Environ Sustain 3:100031. https://doi.org/10.1016/j.crsust.2021.100031
15. Haigh R, Amaratunga D, Hemachandra K (2018) A capacity analysis framework for multi-hazard early warning in coastal communities. In: Procedia Engineering, 7th International Conference on Building Resilience: Using Scientific Knowledge to Inform Policy and Practice in Disaster Risk Reduction, vol 212, pp 1139–1146. https://doi.org/10.1016/j.proeng.2018.01.147
16. Iloeje AF, Aniagolu CO (2015) Impacts of flooding on road transport infrastructure in enugu metropolitan city, Nigeria. [WWW Document]. https://www.ingentaconnect.com/content/doaj/22489622/2015/00000005/00000006/art00083 (accessed 6.25.19)
17. Innocenti D, Albrito P (2011) Reducing the risks posed by natural hazards and climate change: the need for a participatory dialogue between the scientific community and policy makers. Environ Sci Policy 14:730–733. Adapting to Climate Change: Reducing Water-related Risks in Europe. https://doi.org/10.1016/j.envsci.2010.12.010
18. Jones K, Pascale F, Wanigarathna N, Morga M, Sargin S (2021) Critical evaluation of the customisation process of the UNDRR disaster resilience scorecard for cities to earthquake-induced soil liquefaction disaster events. Bull Earthquake Eng 19:4115–4143. https://doi.org/10.1007/s10518-020-00993-y
19. Katina P, Hester P (2013) Systemic determination of infrastructure criticality. Int J Crit Infrastruct 9:211–225. https://doi.org/10.1504/IJCIS.2013.054980
20. Katina P, Hester P (2013) Systemic determination of infrastructure criticality. Int J Crit Infrast 9:211–225. https://doi.org/10.1504/IJCIS.2013.054980
21. Kazama M, Noda T (2012) Damage statistics (Summary of the 2011 off the Pacific Coast of Tohoku Earthquake damage). Soils Found 52:780–792, Special Issue on Geotechnical Aspects of the 2011 off the Pacific Coast of Tohoku Earthquake. https://doi.org/10.1016/j.sandf.2012.11.003
22. Kennedy C, Corfee-Morlot J (2013) Past performance and future needs for low carbon climate resilient infrastructure– An investment perspective. Energ Policy 59:773–783. https://doi.org/10.1016/j.enpol.2013.04.031
23. Kirsch TD, Wadhwani C, Sauer L, Doocy S, Catlett C (2012) Impact of the 2010 Pakistan floods on rural and urban populations at six months. PLoS Curr 4. https://doi.org/10.1371/4fdfb212d2432
24. Kovarik J-B, Evans C, Godart B, Mendoza JF, Palhol F, Starnes M (2020) Evaluating resilient infrastructure systems: task force 3 infrastructure investment and financing. In: U20, Urban 20 Mayors Summit. Royal Commission for Riyadh City in the Kingdom of Saudi Arabia, Riyad, France, p 28
25. Kwasinski A (2011) Effects of notable natural disasters from 2005 to 2011 on telecommunications infrastructure: lessons from onsite damage assessments. In: 2011 IEEE 33rd International Telecommunications Energy Conference (INTELEC). Presented at the 2011 IEEE 33rd International Telecommunications Energy Conference (INTELEC), pp 1–9. https://doi.org/10.1109/INTLEC.2011.6099777
26. Labaka L, Hernantes J, Sarriegi JM (2016) A holistic framework for building critical infrastructure resilience. Technol Forecast Soc Change 103:21–33. https://doi.org/10.1016/j.techfore.2015.11.005

27. Lamont A (2021) Reflections from the 2019 UNDRR global platform. Aust J Emerg Manag 34:34–35. https://doi.org/10.3316/ielapa.576677532286618
28. Lendholt M, Hammitzsch M (2012) Towards an integrated information logistics for multi hazard early warning systems. Open Environ Eng J 5
29. Lomba-Fernández C, Hernantes J, Labaka L (2019) Guide for climate-resilient cities: an urban critical infrastructures approach. Sustainability 11:4727. https://doi.org/10.3390/su11174727
30. Martin E, Perine C, Lee V, Ratcliffe J (2018) Decentralized governance and climate change adaptation: working locally to address community resilience priorities. In: Alves F, Leal Filho W, Azeiteiro U (Eds.), Theory and Practice of Climate Adaptation, Climate Change Management. Springer International Publishing, Cham, pp 3–22. https://doi.org/10.1007/978-3-319-72874-2_1
31. Mimura N, Yasuhara K, Kawagoe S, Yokoki H, Kazama S (2011) Damage from the Great East Japan Earthquake and Tsunami—a quick report. Mitig Adapt Strateg Glob Change 16:803–818. https://doi.org/10.1007/s11027-011-9297-7
32. Paseka S, Kapelan Z, Marton D (2018) Multi-objective optimization of resilient design of the multipurpose reservoir in conditions of uncertain climate change. Water 10:1110. https://doi.org/10.3390/w10091110
33. Perera C, Jayasooriya D, Jayasiri G, Randil C, Bandara C, Siriwardana C, Dissanayake R, Hippola S, Sylva K, Kamalrathne T, Kulatunga A (2020) Evaluation of gaps in early warning mechanisms and evacuation procedures for coastal communities in Sri Lanka. Int J Disaster Resil Built Environ 11:415–433. https://doi.org/10.1108/IJDRBE-07-2019-0048
34. Pitigala Liyana Arachchi IS, Siriwardana C, Amaratunga D, Haigh R (2021) Evaluation of societal trust on multi-hazard early warning (MHEW) mechanism: Sri Lankan context. Int J Disaster Resil Built Environ ahead-ofprint. https://doi.org/10.1108/IJDRBE-01-2021-0010
35. Ramalanjaona G (2011) Impact of 2004 Tsunami in the Islands of Indian Ocean: lessons learned (WWW document). Emerg Med Int. https://doi.org/10.1155/2011/920813
36. Rathnayake DK, Kularatne D, Abeysinghe S, Shehara I, Fonseka T, Edirisinghe Mudiyanselage SDJ, Kamalrathne WGCT, Siriwardana C, Alagiyawanna Mohotti Appuhamilage CSB, Dissanayake R (2020) Barriers and enablers of coastal disaster resilience – lessons learned from tsunami in Sri Lanka. Int J Disaster Resil Built Environ 11:275–288. https://doi.org/10.1108/IJDRBE-07-2019-0050
37. Rehak D (2020) Assessing and strengthening organisational resilience in a critical infrastructure system: case study of the Slovak Republic. Saf Sci 123:104573. https://doi.org/10.1016/j.ssci.2019.104573
38. Rehak D, Senovsky P, Hromada M, Lovecek T (2019) Complex approach to assessing resilience of critical infrastructure elements. Int J Crit Infrastruct Prot 25:125–138. https://doi.org/10.1016/j.ijcip.2019.03.003
39. Reiner M, McElvaney L (2017) Foundational infrastructure framework for city resilience. Sustain Resil Infrast 2:1–7. https://doi.org/10.1080/23789689.2017.1278994
40. Renne J, Wolshon B, Murray-Tuite P, Pande A (2020) Emergence of resilience as a framework for state Departments of Transportation (DOTs) in the United States. Transport Res Part D: Trans Environ 82:102178. https://doi.org/10.1016/j.trd.2019.11.007
41. Rød B, Lange D, Theocharidou M, Pursiainen C (2020) From risk management to resilience management in critical infrastructure. J Manag Eng 36:04020039. https://doi.org/10.1061/(ASCE)ME.1943-5479.0000795
42. Rowan E, Evans C, Riley-Gilbert M, Hyman R, Kafalenos R, Beucler B, Rodehorst B, Choate A, Schultz P (2013) Assessing the sensitivity of transportation assets to extreme weather events and climate change. Transport Res Rec 2326:16–23. https://doi.org/10.3141/2326-03
43. Saja AMA, Sahid MSL, Sutharshanan M (2020) Implementing Sendai framework priorities through risk-sensitive development planning—a case study from Sri Lanka. Prog Disaster Sci 5:100051. https://doi.org/10.1016/j.pdisas.2019.100051
44. Setola R, Theocharidou M (2016) Modelling dependencies between critical infrastructures. In: Setola R, Rosato V, Kyriakides E, Rome E (Eds.), Managing the Complexity of Critical Infrastructures: A Modelling and Simulation Approach, Studies in Systems, Decision and

Control. Springer International Publishing, Cham, pp 19–41. https://doi.org/10.1007/978-3-319-51043-9_2
45. Shehara I, Siriwardana C, Amaratunga D, Haigh R (2019) An overview of existing digital platforms in disaster emergency response stage. Presented at the SBE19 Malta international conference, Malta
46. Shehara PLAI, Siriwardana CSA, Amaratunga D, Haigh R (2020) Examining the community perception towards communication modes of issuing Multi-Hazard Early Warning (MHEW) in Sri Lanka. In: 2020 Moratuwa Engineering Research Conference (MERCon). Presented at the 2020 Moratuwa Engineering Research Conference (MERCon), pp 60–65. https://doi.org/10.1109/MERCon50084.2020.9185325
47. Shehara PLAI, Siriwardana CSA, Amaratunga D, Haigh R (2019) Application of social network analysis (SNA) to identify communication network associated with Multi-Hazard Early Warning (MHEW) in Sri Lanka. In: 2019 Moratuwa Engineering Research Conference (MERCon). Presented at the 2019 Moratuwa Engineering Research Conference (MERCon), pp 141–146. https://doi.org/10.1109/MERCon.2019.8818902
48. Shehara PLAI, Siriwardana CSA, Amaratunga D, Haigh R, Fonseka T (2020) Feasibility of using mobile apps in communication and dissemination process of Multi-Hazard Early Warning (MHEW) mechanism in Sri Lankan context. In: Dissanayake R, Mendis P, Weerasekera K, De Silva S, Fernando S (eds) ICSECM 2019. Lecture Notes in Civil Engineering. Springer, Singapore, pp 177–189. https://doi.org/10.1007/978-981-15-7222-7_16
49. Shrestha RK, Ahlers R, Bakker M, Gupta J (2010) Institutional dysfunction and challenges in flood control: a case study of the Kosi flood 2008. Econ Political Wkly 45:45–53
50. Teng M-C, Su J-L, Chien S-W (2012) Transportation infrastructure disaster impact and lessons learned after Typhoon MORAKOT 395–403. https://doi.org/10.1061/9780784412299.0048
51. Tessa B, Kurukulasuriya P (2010) Technologies for climate change adaptation: emerging lessons from developing countries supported by UNDP. J Int Affairs 64:17–31
52. Tonn G, Czajkowski J, Kunreuther H, Angotti K, Gelman K (2020) Measuring transportation infrastructure resilience: case study with amtrak. J Infrast Sys 26:05020001. https://doi.org/10.1061/(ASCE)IS.1943-555X.0000526
53. Weilant S, Strong A, Miller B (2019) Incorporating resilience into transportation planning and assessment. RAND Corporation. https://doi.org/10.7249/RR3038
54. World Bank (2015) Moving towards climate resilient transport
55. Xian S, Lin N, Hatzikyriakou A (2015) Storm surge damage to residential areas: a quantitative analysis for Hurricane Sandy in comparison with FEMA flood map. Nat Hazards 79:1867–1888. https://doi.org/10.1007/s11069-015-1937-x
56. Yamamura H, Kaneda K, Mizobata Y (2014) Communication problems after the Great East Japan Earthquake of 2011. Disaster Med Public Health Prep 8:293–296. https://doi.org/10.1017/dmp.2014.49
57. Yen W-H, Chen G, Yashinski M, Hashash Y, Holub C, Wang K, Guo X (2011) China earthquake reconnaissance report: performance of transportation structures during the May 12, 2008, M7.9 Wenchuan Earthquake. Civil, Architectural and Environmental Engineering Faculty Research & Creative Works
58. Zhao Y, Szpiro S, Azenkot S (2015) ForeSee: a customizable head-mounted vision enhancement system for people with low vision. In: Proceedings of the 17th International ACM SIGACCESS Conference on Computers & Accessibility, ASSETS'15. Association for Computing Machinery, New York, NY, USA, pp. 239–249. https://doi.org/10.1145/2700648.2809865
59. Zimmerman R, Faris C (2010) Infrastructure impacts and adaptation challenges. Ann N Y Acad Sci 1196:63–86. https://doi.org/10.1111/j.1749-6632.2009.05318.x

Investigating the Variables that Influence the Use of Social Media for Disaster Risk Communication in Sri Lanka

H. A. D. G. S. Jayathilaka, C. S. A. Siriwardana, D. Amaratunga, R. P. Haigh, and N. Dias

Abstract Sri Lanka has been experiencing various types of hazards which have turn into disasters over the past years. A considerable amount of human lives and properties have been impacted due to these disasters. Establishing proper communication channels for effective dissemination of disaster-related information is one of the key strategies of reducing and preventing the impact of disasters. As an emerging communication technology, new attention has been drawn to use social media as a communication channel during disasters to disseminate disaster-related information to the general public. It has previously been identified that there are several variables that affect the use of social media by the general public during disasters. The primary objective of this study is to investigate these variables and their variation for the Sri Lankan context. To conduct this study, an online questionnaire was circulated among the community and 408 responses were collected. Data were analysed under two phases. In the first phase, descriptive statistics for the data were obtained to identify the demography of the respondents. Secondly, binary logistic regression analysis was conducted to identify the variation of the independent variables (predictors) associated with the use of social media during disasters. It has been identified that there is a positive relationship between the respondents' previous experiences of disasters and their social media usage during disasters. There is no meaningful relationship between gender and the use of social media during disasters. The age group to which the respondents belonged was also identified as having a significant impact on their use of social media during disasters. People who belong to the age group of 18–24 are more likely to use social media during disasters than other age groups. A significant increase in the use of social media during of disaster can be observed among the adult community in Sri Lanka.

H. A. D. G. S. Jayathilaka (✉) · C. S. A. Siriwardana
Department of Civil Engineering, University of Moratuwa, Colombo, Sri Lanka

D. Amaratunga · R. P. Haigh
Global Disaster Resilience Center, University of Huddersfield, Huddersfield, UK

N. Dias
Department of Biological and Geographical Sciences, School of Applied Sciences, University of Huddersfield, Huddersfield, UK

R. Dissanayake et al. (eds.), *ICSBE 2020*, Lecture Notes in Civil Engineering 174,
https://doi.org/10.1007/978-981-16-4412-2_19

Keywords Disasters · Disaster risk management · Disaster risk communication · Social media

1 Introduction

A disaster is a significant disruption of the functioning of a community or society at any level due to hazardous events that interfere with exposure, vulnerability and capability which resulting in losses and damages on lives, properties, economic and environmental factors [37]. Sri Lanka has been undergoing several natural and man-made hazardous events and their subsequent disasters which have been made a catastrophic impact on human lives and properties [7, 26, 34]. The Disaster Management Act No. 13 of 2005 which is the main legal document for disaster management in Sri Lanka has been listed 21 natural and man-made hazardous events that threaten human lives, properties and the environment in the territory of Sri Lanka [33]. Floods, landslides, cyclones, droughts, lightning strikes, coastal erosion, epidemics are the major natural hazards which have caused to happen adverse impacts on Sri Lanka [10]. Localized and seasonal floods and associated landslides are the common hazards that have been reporting from Sri Lanka while droughts, cyclones and tsunamis are some other hazards which have been occurring less frequently but causing for considerable damage [2]. Highest and the most crucial impact has been occurred in Sri Lanka due to the 2004 Indian ocean tsunami which is considered as one of the infrequent hazards in Sri Lanka and it shattered the lives of more than one million people and caused much damage to the infrastructure in the coastal belt [1]. Vector-borne epidemics like dengue, influenza have been also reported over the country and recently Sri Lanka is being seriously affected by the global pandemic of COVID-19. According to the Epidemiology Unit of Sri Lanka, 10,663 cases of coronavirus infection and 20 deaths due to coronavirus infection have been reported in Sri Lanka as at 31/10/2010 [12]. Sri Lanka has been also affecting with several man-made hazards and their subsequent disasters such as traffic accidents, industrial accidents, terrorism, fire, etc. which is caused massive damages and losses on human lives and properties. Annual average cost due to disasters in Sri Lanka has been calculated as LKR 50 billion which is around 0.4% of the Gross Domestic Product of the country. In order to reduce the impact from the disasters, disaster risk communication is played a vital role in disaster risk management. Several types communication channels can be involved for the disaster risk communication and in this study, it is expected to the investigate the variables that influence the use of social media for disaster risk communication Sri Lanka.

2 Disaster Risk Management and Disaster Risk Communication

According to the UNDRR terminology, Disaster Risk Management is the implementation of disaster risk reduction policies and techniques to avoid new disaster risk, minimize existing disaster risk and mitigate residual risk while increasing the resilience and minimizing disaster losses [9]. Communication can be introduced as a key component of disaster risk management because it has a high potential to minimize and minimize the damage caused by disasters [4]. Communication improved the perceptions of the community about disaster risk and affects their behaviour in terms of disaster preparedness and disaster response [28]. Under the Disaster Risk Management, Disaster Risk Management Cycle has been developed which describes the activities in disaster management that have to be taken place under several distinct phases of the disaster [5]. Communication can be linked to each of these disaster phases which describes in Disaster Risk Management Cycle [23, 38].

In the context of Sri Lanka, the leading agency for Disaster Risk Management in Sri Lanka is the Disaster Management Centre (DMC). It is mandated with the responsibility of implementing and coordinating national and sub-national level disaster risk reduction programs with the participation of all related stakeholders. Research and development, mitigation, preparation for planning, dissemination of early warning for the vulnerable community, emergency response, coordination of relief and post-disaster activities in collaboration with other key agencies are the core activities of the Disaster Management Centre (DMC) [11]. Disaster Management Centre (DMC) has been communicating the disaster risk information to the general community under three levels such as national level, provincial/district level and divisional secretariat/village level.

As the aforementioned, communication has been identified as a key component in the Disaster Risk Management. Through examining the literature, several terms that describes the several types of communication can be identified which is related to the Disaster Risk Management. Disaster Communication involves the dissemination of the disaster information to the public by governments, emergency management organizations and disaster respondents, as well as disaster information generated and published by journalists and the media [15]. Disaster communication is closely related to Risk and Crisis Communication [22]. Crisis and Emergency Risk Communication (CERC) is another term which is the use of risk and crisis communication in emergencies to inform the public about an event or issue to empower members of a community to protect themselves [4, 25].

By considering all the aforementioned, the term Disaster Risk Communication has been introduced which is basically involves the disseminating and receiving of Disaster Risk Information which can be defined as comprehensive information which include hazards, exposure, vulnerability and capacity, on all dimensions of disaster risk relevant to persons, communities, organizations and countries and their properties [8].

Table 1 Conventional and modern communication channels which used for communication in disaster

Conventional communication channels	Modern or digital communication channels
Television	Social media
Radio	Mobile apps
Newspaper	Alert messages
Tone alert, radio siren	
Conversation between two people, group conversation or presentation	
Disseminating warning messages from moving vehicle	

3 Communication Channels

Furthermore, it has been identified that during in literature survey, Disaster Risk Communication (including all the other terms of communication) can be taken place via various communication channels. And also, the previous literature has been explored that in order to have an effective communication in disaster, there should be a synergy of different communication modes including conventional and modern or digital communication channels [31]. Table 1 provides some examples for the conventional and modern or digital communication channels which can be used for communication during disasters [6, 13, 21, 29, 30, 36].

Various communication channels such as television, radio, early warning towers, police and military communication systems, SMS alerts and telephone calls are used by the DMC to disseminate disaster risk information to the national level. In the provincial/district level, radio, telephone, police and military communication are the most prominent communication channels which are used and at divisional secretariat/village level, DMC are used telephones, police vehicles for announcements, sirens, temple and church bells, and messengers [11].

With the rapid development of the Information and Communication Technology, people have been tended to utilize modern or digital communication modes which are internet-based communication media as an alternative means of communication in disaster situations due to various reasons such as conveniences, interactive and time communication. As an advanced technical facility, nowadays, use of social media for communication in disasters has become common practice among the public.

4 Social Media

With the rapid development over time, social media has become an advanced communication technology and today it is a popular phenomenon among internet users and has gained considerable popularity around the world in recent years [18]. Social

media has been developed with the basis of Web 1.0 and Web 2.0 concepts and it can be defined as set of internet-based applications that allow and encourage its users to create, share the user-generated content in a participatory and collaborative way [19]. As of today, the latest data shows that social media is being used actively by around 4.14 billion people around the world by October 2020 which is equating to 53% of global population approximately [24]. Many forms of applications in the context of the social media have been developed such as Social media platform (social networks), Messenger apps as well as there are some other forms of applications such as blogs, microblogs, forums, social gaming and etc. At present, Facebook has become the most popular social media platform (social network) around the world and base on publicly available data up to October 2020 Facebook has nearly 2.7 billion monthly active users while there are other social media platforms that claim more than one billion monthly active users each. WhatsApp has become the most popular global messenger apps as of October 2020 which has 2 billon monthly active users approximately [32].

In 2019, a questionnaire survey was conducted to identify the possibility of using mobile apps in the Sri Lankan context of the Early Warning disaster mechanism. The survey was conducted in Sri Lanka within the 10 GN divisions ("Grama Niladhari") and 323 responses were collected and analysed. Through this study, it was found that 32% of respondents have frequently used social media platforms in daily use, while 68% of respondents have not used social media platforms in daily use. And also, the level of frequency of using different social media platforms by the respondents has been identified and the use of Facebook and Twitter by the respondents based on the age category has been also identified in this study. The overall survey summarized that there is a low frequency of community use of digital technology sites and low adaptability of them to digital tools and technologies [29].

5 Use of Social Media for Disaster Risk Communication

5.1 Reasons to Use Social Media for Disaster Risk Communication

Besides the conventional communication modes such as traditional media, communication in disasters have been increasingly taking place via social media due to the timely and interactive communication of user-generated content. Traditional media primarily facilitate one-way information dissemination while social media creates two-way communication opportunities among organizations, the public, and individuals. Traditional media primarily facilitate one-way information dissemination while social media can create opportunities for two-way communication for users because both content creators and consumers in traditional media can disseminate information via social media [3]. During the literature survey, many reasons can be

identified that led the community to use using social media for communication in disasters, some of which are listed below.

- Advanced facilities providing by the various social media platforms (e.g. Facebook safety check, Twitter alerts, Facts about COVID-19) [17, 20].
- Multi-directional communication mechanism provided by the social media [16].
- Through social media, communication can be done via several interfaces such as photographs, video clips, live videos, text, voice recordings and etc. Therefore, situational awareness can be increased by using social media [14].
- In the context of the traditional media, many other utilities such as electricity, telephone connection, a considerable space are needed to get their services. But during a disaster power breakup, telephone line breakups and other cascading impacts can be occurred and because of that communication process via traditional media cannot be get success. But social media can be used in disasters without aforementioned utilities and users can use social media via portable devices such as smart mobile phone, laptop and tablet [35].
- Convenience of the using social media and timely information sharing.

5.2 Use of Social Media for Disaster Risk Communication in Sri Lanka

Disaster Management Centre (DMC), which is the leading risk management agency in Sri Lanka are used system called "Disaster and Emergency Warning Network" (DEWN) to disseminate warning messages (SMS) among the public The DEWN system issues alert "through a secure computer application where the text, geographical area and the recipients (individual or groups) can be selected for the message". Due to region specificity of the DWEN system, it was not a successful disaster communication method throughout the 2016 flood in Sri Lanka [18].

During the flood, which occurred in Sri Lanka in May 2016, social media was the main source of communication and Facebook was the most popular social media platform. Considering COVID-19 pandemic situation in Sri Lanka, social media has been playing a vital role to disseminate the risk information and updates about the COVID-19 pandemic to the general public. Many of Facebook pages, Facebook groups, WhatsApp groups has been created with the purpose of disseminating COVID-19 information by the various stakeholders such as news media, community groups, influencers, researchers, etc. In order to investigate usage of social media platforms to disseminate disaster risk information in Sri Lanka, the primary objective of this study is to investigate the use of social media platforms by the Sri Lankan community to distribute COVID-19 information. Since, Facebook is identified as the most popular social media platform to disseminate COVID-19 information in Sri Lanka this study was conducted by investigating the use of major Facebook pages by the Sri Lankan community that disseminates COVID-19 information to the public.

Considering the above information, it can be concluded that there is a considerable potential to develop and enhance the use of social media as a communication channel for disaster risk communication in Sri Lanka. Several gaps and barriers can be able to identified from the literature in the context of the use of social media for disaster risk communication worldwide which can be useful in enhancing and developing the use of social media for disaster risk communication in Sri Lanka. Several literatures have been revealed that there are different types of variables which are affected for the use of social media for disaster risk communication [13]. Therefore, as the primary objective of this study, it is expected to investigate variables that influence the use of social media for disaster risk communication n Sri Lanka.

6 Methodology

As the commencing part of this study, a comprehensive literature review was carried out in order to identify the key parameters of using social media in disaster communication. Use of social media during disasters around the world was considered for the literature review. Through the literature review key parameters were identified based in the "Users" and the "Uses" of Social Media in disaster risk communication. Furthermore, from the literature review, major criteria that should need to be considered for using social media in disaster risk communication were identified. In order to enhancing the use of social media in disaster communication in Sri Lanka, it was needed to identify the current condition of the using social in disaster communication by the Sri Lankan community. Therefore, an online questionnaire was developed with the purpose of identifying the existing condition of use of social media in disaster communication in Sri Lanka. The online questionnaire was developed by using Survey Monkey which paid online survey software that helps to create and run professional online questionnaires. Online questionnaire was prepared following an ethical procedure and it was circulated among the general public through the social media applications. The estimated average time to complete this survey was about 15–20 min. It was disseminated via Facebook my publishing it as Facebook Posts in several groups and pages and also it was disseminated via WhatsApp by sharing the link to the online questionnaire with several public groups. Furthermore, this online questionnaire was directly share with the individual persons by sharing the link to the survey via Facebook Messenger and WhatsApp directly. Through all these circulating processes ultimately 408 responses were collected and only 352 (86.27%) respondents were fully completed the questionnaire.

As previously described, the main purpose of this questionnaire survey is to gather information about the current condition of the use of social media in disaster communication in Sri Lanka. Accordingly, about 55 questions were asked and all these questions were developed based on the previous studies and the questionnaires previously developed in the context of use of social media and technological applications in disaster communication. The main objective of this study is to identify the variables that affects the use of social media in disaster communication by the

Sri Lankans and how those variables are varying with the context of use of social media for disaster risk communication in Sri Lanka. In order to conduct this study few questions have been added to the questionnaire at the beginning and all the respondents were responded to these questions. From the literature review, several variables have been identified that can have an impact on the use of social media in disaster communication. From the previous studies, it has been identified that the sources utilized by the general community for the disaster communication may vary considerably according to the demographic characteristics. Hence the demographic variables such as age, gender, profession, living area and additionally the previous experiences with disasters. Specifically, respondents were asked to rank the frequency of the occurrence of common natural and mand-made hazards in their areas and a numerical value is allocated for each respondent according to the severity of the respondent's previous experiences.

7 Analytical Study of the Results

Analysis of this study has been carried out in two phases. In the first phase of the analysis, descriptive basic statistics were calculated to assess the demographic information obtained from the respondents. Secondly, logistic regression analysis was carried out to identify the variations of the different predictors (independent variables) associated with the use of social media in disaster communication (dependent variable). All the statistical analyses were done by using IBM SPSS Statistics 26 software (henceforth it is called as SPSS). As the initial step of the analysis all the variables used were identified and categorized according to the data types in SPSS as shown in Table 2.

7.1 Descriptive Statistics

As the first phase of the analysis of this study, descriptive statistic was conducted for the categorical variables such as V1, V2 and V3. In the descriptive statistics of these kinds of categorical variables, the distribution of the data for each category of each

Table 2 Classification of the variables used for the analysis

Dependent variable			Independent variable		
Categorical (qualitative)		Scale (quantitative)	Categorical (qualitative)		Scale (quantitative)
Nominal	Ordinal		Nominal	Ordinal	
Use of social media during disasters (V1)	–	–	Gender (V2)	Age group (V3)	Previous experiences of disasters (V4)

Table 3 Results of the descriptive statistics for the categorical variables

Variable	Number of responses		Mean	Description		Frequency	Percent
				Label	Value		
V1	Valid	408	0.81	No	0	79	19.4
	Missing	0		Yes	1	329	80.6
				Total		**408**	**100**
V2	Valid	408	1.58 (No meaning)	Female	1	173	42.4
	Missing	0		Male	2	235	57.6
				Total		**408**	**100**
V3	Valid	408	3.11 (No meaning)	Under 18	1	12	2.9
				18–24	2	113	27.7
				25–34	3	191	46.8
	Missing	0		35–44	4	37	9.1
				45–54	5	29	7.1
				55–64	6	19	4.7
				65+	7	7	1.7
				Total		**408**	**100**

variable was calculated. Unlike scale data, it is not required to calculate the statistics for categorical variables such as mean, quartiles, standard deviation etc. because no meaningful outcome will be produced with them except for the mean value for V1. Results of the descriptive statistics for the categorical variables (phase 1) are shown in Table 3. The coding description for the variables used for the analysis in SPSS are also given in Table 3.

According to Table 3 it can be seen that 80.6% of the respondents are used social media during disasters. The mean value for the V1 also representing the same as the proportion of respondents answering yes to using the social media during disasters in Sri Lanka.

The descriptive statistics of this study basically describes the demographic characteristics of the respondents. As previously mentioned, 408 people have been responded to the questionnaire in total. According to Table 3, 235 of them were male and 173 of them were female. Also, Table 3 presents the distribution of the respondents for each age group category. 46.81% of the respondents were between the ages of 25–34 and 27.7% were between 35 and 44.

In order to have an idea about the social status of the respondents, they were asked to state their professional/educational status during questionnaire. In there, according to the results of the questionnaire it was identified that respondents are representing the different levels of educational and professional status in Sri Lanka. Figure 1 graphically presents the distribution of the educational/professional status of the respondents.

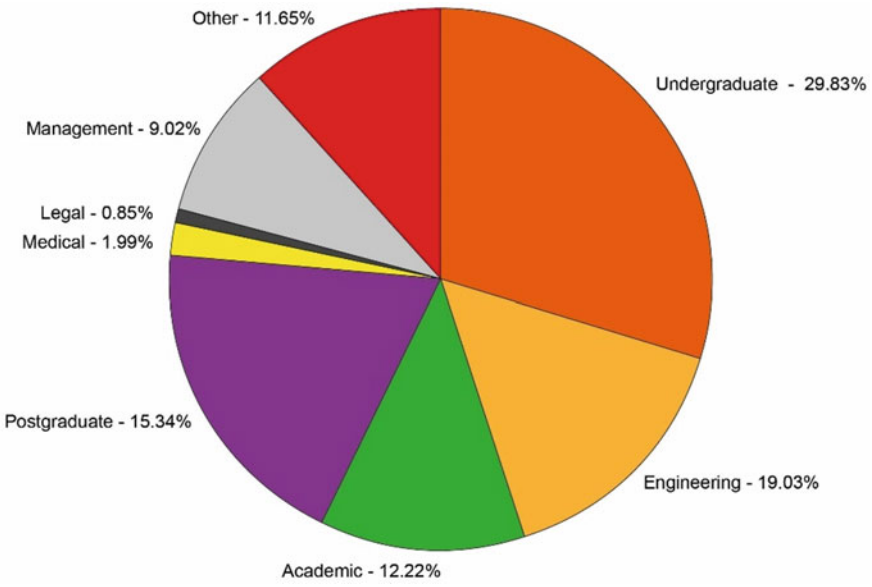

Fig. 1 Educational/professional status of the respondents

In the "Other" category, several educational /professional statues have been included such school students (Advanced level and Ordinary level), Army officers, Quantity surveyors, Architects, Government officers etc.

In this study, it is important to identify how respondents were distributed within the country. Results shows that the all most all the districts (except Mannar and Mullaitivu) have been represented by the respondents (at least one from a district). 30.88% of the total respondents are from the Colombo district and 20.10% of them are from Gampaha district. Furthermore, Fig. 2 shows how the respondents have been divided for each district.

7.2 Binary Logistic Regression

The second phase of the analysis was to investigate the variation of the different predictors (independent variables) associated with the use of social media in disaster communication. Binary logistic regression is used to model the relationship between one or more predictor variables (independent variable) and binary dependent variable. Furthermore, it defines the probability that a given case falls into one of two categories on the dependent variable, given the predictors in the model. In the context of the Binary Logistic Regression, there are four requirements that should not be violated before doing the analysis.

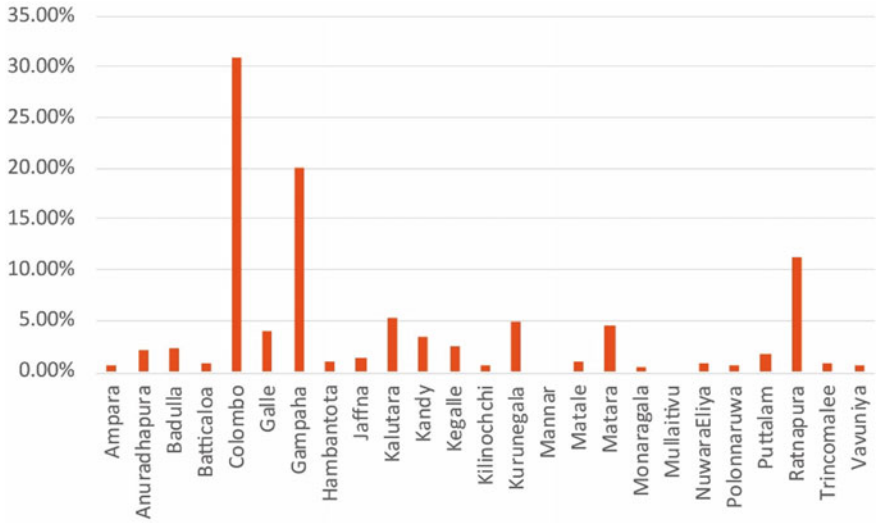

Fig. 2 District representation of the respondents

I. Dependent variable should be measured on a dichotomous scale (i.e. dependent variable should be categorical and it should be consisted with exactly two levels).
II. There should be one or more independent variables, which can be either scale or categorical.
III. Observations should be independence and the dependent variable should have mutually exclusive and exhaustive categories.
IV. There needs to be a linear relationship between any continuous independent variables and the logit transformation of the dependent variable.

In this study, use of social media in disaster communication (V1) was selected as the independent variable which is a categorical variable with exactly two levels. (1 = 'No', 2 = 'Yes'). Gender (V2), Age group (V3) and the previous experiences of disasters (V4) were taken as the predictor variables (independent variables) for this analysis. For this study independent observations were taken and the dependent variable has mutually exclusive and exhaustive categories.

For the binary logistic regression analysis, 'Female' was selected as the reference category in Gender (V2) variable and 'Under 18' was selected as the reference category for the Age (V3) variable. Output results of the binary logistic regression analysis are shown in below.

7.2.1 Results of the Binary Logistic Regression Analysis

Output results of the Binary Logistic Regression analysis presented in blocks.

Table 4 Results of the block 0

Classification table[a, b]					
	Observed		Predicted		
			Using social media in disaster		Percentage correct
			No	Yes	
Step 0	Using social media in disaster	No	0	79	0.0
		Yes	0	329	100.0
	Overall percentage				80.6

[a]Constant is included in the model
[b]The cut value is 0.500

Table 5 Results of the block 0

Variables in the equation							
		B	S.E.	Wald	df	Sig.	Exp (B)
Step 0	Constant	1.427	0.125	129.650	1	0.000	4.165

I. Block 0: Beginning Block
Block 0 (Beginning Block) contains the results from a null model which any independent variable has not been considered. Since the block 0 provides the results for the null model which is the model that does not contain any independent variable (predictors), so the results shown in block 0 are not useful in making decisions in this study. Results are presented in Tables 4 and 5 as given in SPSS.

II. Block
Block 1 contains the results from a full model which has been considered all the predictor variables for the analysis. In this block, contribution of each predictor (independent) variable to the model and its statistical significance have been calculated. Several tests were carried out in order to conduct this analysis in block 1 and the final results of the analysis are presented in Table 6 as given in SPSS.

According to Table 6 the followings can be identified for the variations of the predictor variables associated with the use of social media during disasters in Sri Lanka.

Previous Experience is a positive and significant (B = 0.017, S.E. = 0.013, Sig. = 0.174) predictor of the use of social media during the disasters in Sri Lanka, with the Exp (B) (Odds Ratio) indicating that for every one unit increase on this predictor the odds of use of social media during disasters in Sri Lanka is changed by a factor of 1.018 (meaning the odds are increasing).

Gender is a non-significant predictor of use of social media during disasters in Sri Lanka (B = −0.042, S.E. = 0.262, Sig. = 0.873). If the predictor been significant, then the negative regression coefficient (B) would be taken as an indicator that females

Table 6 Results of the block 1

Variables in the equation									
Variables		B	S.E.	Wald	df	Sig.	Exp (B)	95% C.I. for Exp (B)	
								Lower	Upper
Step 1[a]	Age			12.890	6	0.045			
	Age (1)	1.162	0.681	2.914	1	0.088	3.197	0.842	12.143
	Age (2)	0.718	0.649	1.224	1	0.269	2.051	0.574	7.322
	Age (3)	−0.005	0.724	0.000	1	0.994	0.995	0.241	4.107
	Age (4)	−0.214	0.740	0.084	1	0.772	0.807	0.189	3.441
	Age (5)	0.174	0.818	0.045	1	0.832	1.190	0.240	5.907
	Age (6)	1.063	1.248	0.725	1	0.394	2.894	0.251	33.371
	Gender (1)	−0.042	0.262	0.025	1	0.873	0.959	0.574	1.603
	Previous experience	0.017	0.013	1.851	1	0.174	1.018	0.992	1.043
	Constant	0.310	0.695	0.199	1	0.655	1.364		

[a]Variable(s) entered on step 1: age, gender, previous experience

(coded as 1) are less likely to use of social media during disasters in Sri Lanka than males.

Age has been represented by six dummy variables in this analysis. The first dummy variable is a comparison of the 18–24 (coded 2 on the variable) and Under 18 (reference category coded 1 on the variable) age groups. The positive coefficient suggests that persons in the 18–24 age group category were more likely to use social media than those in the Under 18 age group category. Nevertheless, the difference is not significant (B = 1.162, S.E. = 0.0.681, Sig. = 0.088). The second dummy variable compares the 25–34 age group (coded 3 on the variable) and the Under 18 group (again, the reference category; coded 1). The difference between the groups is not significant, (B = 0.718, S.E. = 0.649, Sig. = 0.269). The positive coefficient suggests that persons in the 25–34 age group category were more likely to use social media than those in the Under 18 age group category but less than the persons in the 18–24 age groups. The third dummy variable is a comparison of the 35–44 (coded 4 on the variable) and Under 18 (reference category coded 1 on the variable) age groups. The negative coefficient suggests that persons in the 35–44 age groups were less likely to use social media during disasters than those in the Under 18 category. However, the difference is not significant (B = −0.05, S.E. = 0.724, Sig. = 0.994). Similarly, other dummy variables can be explained.

8 Discussion

Currently, Sri Lanka has been experiencing several types of natural and man-made hazards and their subsequent disasters in a considerable way. Several strategies have been taken out to reduce the impact of disasters. Having a proper communication system to disseminate the disaster-related information is one of the key strategies which has been suggested by several studies to reduce the severity of the impact of disasters. As an example, in the Sendai Framework for Disaster Risk Reduction 2015–2030 [27], it has been identified that the substantially increase the availability of and access to multi-hazard early warning systems and disaster risk information and assessments to people by 2030 as one of the seven global targets to support the achieving the outcome and goal of Sendai Framework which is reducing and preventing the existing and new disaster risk [27].

As an advanced and developed communication channel, social media enables users to create, consume and share information with a broader community. Several studies have been identified that there are a huge capacity and the potential of the use of social media as a communication tool during disasters to establish a proper communication system as a key strategy to reduce the impact from disasters. With social media, it has been concluded that during the disasters, disaster-related information can be disseminated to the general public effectively in terms of timeliness, accuracy, attractivity etc. As the lessons learnt from the previous studies, there are several variables (predictors) can be identified which have been affected for the use

of social media during disasters by the general public. Investigating those variables for the Sri Lankan context is the primary objective of this study.

In order to conduct this study, an online questionnaire was conducted and 408 responses were collected. Results were analyzed by using the IBM SPSS Statistics 26 software and several conclusions were made up with the analytical approach of the results. According to the descriptive statistics, it has been revealed that 80.6% of the respondents are used social media during disasters to receive disaster-related information. Hence it can be concluded that a considerable number of respondents are used social media currently during disasters. According to the respondent demographic information, it is clearly revealed that the respondents are represented every possible age categories, professionals and districts (except Mannar and Mullaitivu) in Sri Lanka in a certain way. Hence this study can be used to identify and investigate the variables affecting the use of social media during disasters to receive disaster-related information by the general public in Sri Lanka.

As the second phase of the analysis, Binary Logistic Regression analysis was carried out to investigate the variations of the predictor variables with the use of social media during disasters in the Sri Lankan context. Age (V2), gender (V3), previous experiences of the disaster (V4) were taken as the predictor variables (independent variables). The use of social media during disasters by the respondent (V1) was considered as the dependent variable for this study.

9 Conclusion

With the results of the binary logistic regression analysis, several conclusions were made to identify the variation of the predictor variables associated with the use of social media during disasters. It was identified that gender is a non-significant predictor which means that there is no relationship between the use of social media and gender. Also, this study has been revealed that the respondent's previous experiences of disasters are caused to increase in the use of social media during the disasters in Sri Lanka. Considering the age groups variables, it can be concluded that the community who are in age groups of 18–24 are more likely to use social media during disasters than the other age groups. People between the ages of 25–34 are also used social media in a significant way during disasters. By considering the value of the regression coefficient (B), it can be seen that with the increase in the age group from 18–24 to 45–54, the use of social media has decreased. But it has been again shown an increase in the use of social media during disasters in Sri Lanka among the people who are in 55–64 and 65+ age groups. Most of the people who belong to these age groups in Sri Lanka are retired from the jobs and staying their homes restfully. Therefore, a considerable amount of time can be spent by them to study and reveal the opportunities for using social media during disasters. This might be the reason for the increase of social media usage among the people of these adults age groups during disasters in Sri Lanka.

Finally, this analysis concludes that the Sri Lankan community in the 18–24, 25–34, 55–64 and 65+ age groups can be considered as the targeted groups which should be paid more attention, to enhance and develop the use of social media for disaster risk communication in Sri Lanka. These conclusions will be useful for future studies in the context of developing and enhancing the use of social media during the disasters in Sri Lanka.

In disasters occurring in Sri Lanka, there are multiple social, economic and political factors which are of their magnitude and the multiple consequences have been generated by them to different demographic groups. These factors are affected to select the communication channels by the general public to receive disaster-related information. And also, there are some other factors such as accuracy, timeliness, usefulness, information source etc. which are caused for the effectiveness of the communication channels during disasters. These kinds of factors have not been addressed in this study. As the recommendation for the future studies, it can be suggested that it is important to understand how these factors can be affected for the preference of Sri Lankan community in the context using of social media as communication channel during disasters.

References

1. Arnold M (2006) Natural disaster hotspots case studies. World Bank Publications
2. Asian Disaster Reduction Center (ADRC) (2019) (WWW document). https://www.adrc.asia/nationinformation.php?NationCode=144&Lang=en&NationNum=08. Accessed 4 Dec 2020
3. Bortree DS, Seltzer T (2009) Dialogic strategies and outcomes: an analysis of environmental advocacy groups' Facebook profiles. Publ Relat Rev 35:317–319
4. Bradley D, Mcfarland M, Clarke M (2014) The effectiveness of disaster risk communication: a systematic review of intervention studies. PLoS Curr 6. https://doi.org/10.1371/currents.dis.349062e0db1048bb9fc3a3fa67d8a4f8
5. Coppola D (2015) Introduction to international disaster management, 3rd edn (WWW document). https://www.elsevier.com/books/introduction-to-international-disaster-management/coppola/978-0-12-801477-6. Accessed 30 Oct 2020
6. Danaher PJ, Rossiter JR (2011) Comparing perceptions of marketing communication channels. Eur J Mark 45:6–42. https://doi.org/10.1108/03090561111095586
7. Data Collection Survey on Disaster Risk Reduction Sector in Sri Lanka: Final Report (2017) (WWW document). https://openjicareport.jica.go.jp/216/216/216_120_12291944.html. Accessed 4 Dec 2020
8. Disaster Risk Information (2017) (WWW document). https://www.undrr.org/terminology/disaster-risk-information. Accessed 1 Nov 2020
9. Disaster Risk Management (2017) (WWW document). https://www.undrr.org/terminology/disaster-risk-management. Accessed 1 Nov 2020
10. Disaster Risk Reduction in Sri Lanka | UNDRR (2019) (WWW document). https://www.undrr.org/publication/disaster-risk-reduction-sri-lanka. Accessed 1 Oct 2020
11. DMC Profile (2020) (WWW document). http://www.dmc.gov.lk/index.php?option=com_content&view=article&id=72&Itemid=234&lang=en. Accessed 1 Oct 2020
12. Epidemiology Unit (2020) (WWW document). https://www.epid.gov.lk/web/. Accessed 1 Nov 2020
13. Feldman D, Contreras S, Karlin B, Basolo V, Matthew R, Sanders B, Houston D, Cheung W, Goodrich K, Reyes A, Serrano K, Schubert J, Luke A (2016) Communicating flood risk:

looking back and forward at traditional and social media outlets. Int J Disaster Risk Reduct 15:43–51. https://doi.org/10.1016/j.ijdrr.2015.12.004
14. Freberg K, Saling K, Vidoloff KG, Eosco G (2013) Using value modeling to evaluate social media messages: the case of Hurricane Irene. Public Relat Rev 39:185–192
15. Hall S, Park C (2012) National consortium for the study of terrorism and responses to terrorism, p 39
16. Houston JB, Hawthorne J, Perreault MF, Park EH, Goldstein Hode M, Halliwell MR, Turner McGowen SE, Davis R, Vaid S, McElderry JA, Griffith SA (2015) Social media and disasters: a functional framework for social media use in disaster planning, response, and research. Disasters 39:1–22. https://doi.org/10.1111/disa.12092
17. Introducing Safety Check (2014) Facebook. https://about.fb.com/news/2014/10/introducing-safety-check/. Accessed 2 Oct 2020
18. Jayasekara PK (2019) Role of Facebook as a disaster communication media. Int J Emerg Serv 8:191–204. https://doi.org/10.1108/IJES-04-2018-0024
19. Kaplan AM, Haenlein M (2010) Users of the world, unite! the challenges and opportunities of social media. Bus Horiz 53:59–68. https://doi.org/10.1016/j.bushor.2009.09.003
20. Keeping People Safe and Informed About the Coronavirus (2020) Facebook. https://about.fb.com/news/2020/10/coronavirus/. Accessed 11 Oct 2020
21. Lindell MK, Perry RW (2012) The protective action decision model: theoretical modifications and additional evidence. Risk Anal 32:616–632. https://doi.org/10.1111/j.1539-6924.2011.01647.x
22. Mason A, Flores L, Liu P, Tims K, Spencer E, Gire TG (2019) Disaster communication: an analysis of the digital communication strategies used by the medical tourism industry during the 2017 Caribbean hurricane season. J Hosp Tour Insights 2:241–259. https://doi.org/10.1108/JHTI-03-2018-0021
23. Mauroner O, Heudorfer A (2016) Social media in disaster management: how social media impact the work of volunteer groups and aid organisations in disaster preparation and response. Int J Emerg Manag 12:196. https://doi.org/10.1504/IJEM.2016.076625
24. Most Used Social Media (2020). Statista (WWW document). https://www.statista.com/statistics/272014/global-social-networks-ranked-by-number-of-users/. Accessed 31 Oct 2020
25. Reynolds B, Seeger MW (2005) Crisis and emergency risk communication as an integrative model. J Health Commun 10:43–55. https://doi.org/10.1080/10810730590904571
26. Salawa-Wisalawa and Man-Made Disasters—Colombo Telegraph (2016) (WWW document). https://www.colombotelegraph.com/index.php/salawa-wisalawa-man-made-disasters/. Accessed 28 Sept 2020
27. Sendai Framework for Disaster Risk Reduction 2015–2030 (2015) (WWW document). https://www.undrr.org/publication/sendai-framework-disaster-risk-reduction-2015-2030. Accessed 5 Oct 2020
28. Shaw R, Takeuchi Y, Matsuura S, Saito K (2013) Risk communication
29. Shehara I, Siriwardana C, Amaratunga D, Haigh R (2019) An overview of existing digital platforms in disaster emergency response stage. In: SBE19 Malta international conference, Malta
30. Shehara P, Siriwardana CSA, Amaratunga D, Haigh R, Fonseka T (2020) Feasibility of using mobile apps in communication and dissemination process of Multi-Hazard Early Warning (MHEW) mechanism in Sri Lankan context. In: ICSECM 2019. Springer, pp 177–189
31. Sjoraida DF, Anwar RK (2018) The effectiveness of risk communications as a disaster risk reduction strategy in Taragong Garut. AIP Conf Proc 1987:020041. https://doi.org/10.1063/1.5047326
32. Social Media Users (2020). DataReportal—global digitial insights (WWW document). https://datareportal.com/social-media-users. Accessed 31 Oct 2020
33. Sri Lanka Disaster Management Act, No. 13 of 2005 (2005), p 19
34. Sri Lanka Experiences a Series of Man-Made Disasters—Life Online (2017) (WWW document). http://www.life.lk/article/lifestyle/Sri-Lanka-Experiences-A-Series-Of-Man-made-Disasters/45/16950. Accessed 1 Nov 2020

35. Takahashi B, Tandoc EC, Carmichael C (2015) Communicating on Twitter during a disaster: an analysis of tweets during Typhoon Haiyan in the Philippines. Comput Hum Behav 50:392–398. https://doi.org/10.1016/j.chb.2015.04.020
36. Tang Z, Zhang L, Xu F, Vo H (2015) Examining the role of social media in California's drought risk management in 2014. Nat Hazards 79:171–193. https://doi.org/10.1007/s11069-015-1835-2
37. Terminology (2017) (WWW document). https://www.undrr.org/terminology. Accessed 27 Oct 2020
38. Young CE, Kuligowski ED, Pradhan A (2020) A review of social media use during disaster response and recovery phases

Incorparation of Disasater Risk Reduction and Disasater Resilient Mechanisms into the Building Tool of GREENSL® Rating System for Built Environment

A. A. S. E. Abeysinghe, C. S. A. Siriwardane, C. S. Bandara, P. B. R. Dissanayake, R. Haigh, and D. Amarathunga

Abstract Disaster risk in Sri Lanka has been increasing mainly due to rapid unplanned commercialization and development of cities, infrastructure with poor quality, and the impacts of climate change which has exposed the built environment severely to natural hazards. Out of all the hazards, floods, landslides, heavy winds and tsunamis have caused the highest number of damages to buildings and loss of human lives during the period of 1965–2019. Although the Green Building Council of Sri Lanka (GBCSL) has initiated many resilient measures in energy and resources usage in buildings, it has not specifically identified the requirement of integrating Disaster Risk Reduction (DRR) mechanisms into their green rating tools. This research study is focused on identifying structural and non-structural DRR measures for the three disasters; floods, landslides and high winds, developing guidelines and finally proposing a new disaster resilient building tool under the main eight categories of the existing building tool for GREENSL® Rating System for Built Environment V2.0 with expert committee inputs; followed by eleven surveys carried out in green certified buildings situated in flood, landslide and high wind prone areas and less or no hazard prone areas for validation. It is highly recommended to use new disaster resilient building tool in certifying buildings situated in flood and landslide prone areas, moderately recommended to use in high wind areas and finally it is acceptable to use the existing building tool for GREENSL® Rating System for Built Environment V2.0 for the buildings situated in less or no hazard prone areas. However, it can be advised to use the new disaster resilient building tool even for the buildings situated in less or no hazard prone areas as it addresses the general DRR measures to combat adverse climatic trends in future.

A. A. S. E. Abeysinghe (✉) · C. S. A. Siriwardane
Department of Civil Engineering, University of Moratuwa, Katubedda, Sri Lanka
e-mail: sonali.abeysinghe@eng.pdn.ac.lk

C. S. Bandara · P. B. R. Dissanayake
Department of Civil Engineering, University of Peradeniya, Peradeniya, Sri Lanka

R. Haigh · D. Amarathunga
University of Huddersfield, Huddersfield, UK

R. Dissanayake et al. (eds.), *ICSBE 2020*, Lecture Notes in Civil Engineering 174,
https://doi.org/10.1007/978-981-16-4412-2_20

Keywords Natural hazards · Disaster risk reduction · Green rating systems · Green buildings · Disaster resilient building

1 Introduction

Catastrophic disasters induced by natural and man-made hazards are inevitable, but prevention measures will help to reduce the social, environmental and economical adverse impacts immensely. World Health Organization declares that globally, the number of people killed by natural disasters exceeds 90,000 and nearly 160 million people are affected annually. Natural disasters such as floods, droughts, earthquakes, tsunamis, landslides, hurricanes, volcanic eruptions, wildfires, and heat waves not only cause immediate destructions to the physical, biological and social environment, but also impose a long-term threat on the health and well-being of its people [1]. Also, the report 'Economic losses, Poverty and Disaster—1998 and 2017' highlights that geophysical and climate-related disasters have killed around 1.3 million people and made another 4.4 billion people injured, disabled, displaced or in need of assistance during the period of 1998 and 2017. During 1998–2017, the countries hit by natural disasters have gone through direct economic losses valued at US$ 2,908 billion [2]. The Munich Re NatCatSERVICE, reports about 850 natural hazard induced disasters occurred in 2018 only. Out of them, 5% was reported to be Geophysical disasters such as earthquakes, volcanic eruptions and tsunamis, 42%, to be storms, 46% to be floods, flash floods and landslides and 7% to be wildfire, cold and heat. 43% of all the disasters have been reported from Asia, 20% from North America, 14% from Europe, 13% from Africa and 10% from other regions [3].

As Sri Lanka is a tropical country, it often meets with frequent rainfalls and increased temperatures throughout the year. Sri Lanka's climate is governed by the Southwest and Northeast monsoons and two inter monsoon seasons. Behavioral patterns of the Bay of Bengal widely affect the changes in wind patterns and changes in durations of occurrence [4]. Majority of Sri Lankan natural hazards are identified to be hydro-meteorological hazards like floods, high winds, landslides, etc. of which floods are most critical. River floods, urban and flash floods, landslides, cyclones, wildfires are considered to be the main hazards with high risk and coastal erosion, tsunami and droughts are considered to be of medium risk [5]. Out of all, floods and landslides are the most common natural hazards effective for Sri Lanka. Cyclones, droughts, and tsunamis are considered to be severe hazards though their occurrences are of less frequency [5]. Since 1965, 224,760 houses have been damaged due to floods while 128,705 houses have been affected severely from high winds, 105,293 houses have been damaged due to tsunami and 14,761 houses from landslides [6]. Economic losses caused due to natural disasters, accounts for an average annual loss of $380 million which is averagely 3% of total government expenditure, according to World Bank estimates. As a distribution 33.3% accounts for Tsunamis, 30.8% for floods, 29.6% for cyclones and heavy winds and 6.3% due to other hazards during the period of 1990 to 2014 in Sri Lanka [5].

Skyrocketing catastrophic losses and destructions imposed by natural hazards are mainly due to rapid rate of urban growth, unplanned urbanization, poor quality buildings and infrastructure, and the adverse impacts of climate change [7]. A study carried out by the AIT in 2012 has examined on integrating of DRR measures into the national building codes of Sri Lanka for wind, rain and flood and landslides [8]. It manifests that a comprehensive disaster resilient building code could not be found yet in Sri Lanka, which is an essential need to be met in transforming the existing construction industry into a sustainable one. There is an unfilled gap in the GREENSL® Rating System for Built Environment where it could incorporate disaster risk reduction mechanisms. Even a platinum rated green building constructed in a sustainable manner is still prone to damages from natural disasters if proper DRR measures have not been incorporated. As floods, landslides and heavy winds are the most frequent, highly vulnerable and which have caused significant building damages around the country, only the DRR measures related to above three hazards are considered in developing the disaster resilient green rating building tool. There are two types of DRR mechanisms for hazard preparation and mitigation namely structural (hard) and non-structural (soft) measures. Apart from the DRR and disaster resilient global and local frameworks, five green rating tools from four countries were selected based on the factors of, usage and popularity of the tools, vulnerability level of the counties for natural hazards and their world risk index. This research study aims in identifying structural and non-structural DRR mechanisms for floods, landslides and heavy winds aligned with the local and global frameworks for DRR and disaster resilience, developing a set of guidelines using the identified structural and non-structural DRR mechanisms and finally developing a new disaster resilient building tool through incorporating the developed DRR and disaster resilient guidelines into the GREENSL® Rating System for Built Environment.

2 Literature Review

2.1 Global Frameworks for Disaster Risk Reduction

In 2015 three international policy frameworks were established namely Sendai Framework for Disaster Risk Reduction (SFDRR) 2015–2030 (March 2015), the Sustainable Development Goals (SDGs; September 2015) and the Climate Change Agreement (December 2015). Before the development and implementation of the SFDRR 2015–2030, Millennium Declaration (2000) and Hyogo Framework for Action (HFA; 2005–2015) were the frameworks used by the countries to manage and prepare for the natural hazards and the induced disaster risks.

As SFDRR was the latest and most updated international policy framework on DRR, it was considered in selecting guidelines required for the disaster resilient green building tool. The main aim of the SFDRR is to prevent new and reduce existing

disaster risk through the implementation of integrated and inclusive economic, structural, legal, social, health, cultural, educational, environmental, technological, political and institutional measures that prevent and reduce hazard exposure and vulnerability to disaster, increase preparedness for response and recovery, and thus strengthen resilience [9]. Out of the seven global targets, target 3; Reduce direct disaster economic loss in relation to global gross domestic product (GDP) by 2030 and target 4; Substantially reduce disaster damage to critical infrastructure and disruption of basic services, among them health and educational facilities, including through developing their resilience by 2030 were considered in developing guidelines. Similarly, out of four priorities for action, priority 3; Investing in disaster risk reduction for resilience and out of the twelve guiding principles principle 3, 8 and 9 were considered in developing guidelines for green rating systems. SDGs are a collection of 17 global goals introduced by United Nations [10]. Targets under SDG 11; Sustainable cities and under SDG 9; Building resilient infrastructure have a strong interrelationship between DRR and sustainable development. Resilient Construction, sustainable and inclusive industrialization, innovative, resilient, safe and sustainable human settlements and cities are the main goals of the above two SDGs [11].

2.2 Green Building Councils and Green Rating Systems

A 'green' building is a building that, minimizes negative impacts, and make positive impacts, on the environment throughout its life cycle in planning, designing, constructing, or operating [12]. The World Green Building Council (WGBC) is a global leader comprised with nearly 80 green building councils around the world. Green Building Councils develop and lead many of world's green rating tools. Green building rating systems can be defined as a set of guidelines and criteria which a building or a structure is used to assess and recognize when certain green requirements or standards are met [12]. Out of 100 s of existing green rating tools, this literature review is narrowed down into few rating systems, namely, Leadership in Energy and Environmental Design (LEED) and ReLi of Green Building Council of United States, Comprehensive Assessment System for Built Environment Efficiency (CASBEE) of Japanese Green Building Council, GREENSHIP of Green Building Council of Indonesia and Building for Ecologically Responsive Design Excellence (BERDE) of Green Building Council of Philippines for this research. Table 1 summarizes the existing DRR and disaster resilient mechanisms incorporated into the building tools of the above-mentioned green rating systems.

Due to the very high disaster risk profile of Philippines, international, local, government and private organizations have developed many guidelines and frameworks aligned with global frameworks. But the integration of these DRR and disaster resilient mechanisms into the construction industry and BERDE green rating tool is very minimal. The only consideration it has taken is that, during the predesign phase, it is determined whether Environmental Impact Assessment (EIA) and Engineering, Geological, and Geo-Hazard Assessment (EGGA) are needed to be conducted to

Table 1 Existing DRR and disaster resilient measures in different green rating tools

Green rating	Main category	Sub-category	Existing DRR measures available
LEED v4.1 for new construction and design rating tool [11]	Location and Transportation (LT)	Sensitive land protection	Flood hazard areas shown on a legally adopted flood hazard map or designated by local jurisdiction or the state
			Management of areas with wetlands
	Sustainable Sites (SS)	Construction activity pollution prevention	Reduce pollution from construction activities by controlling soil erosion, waterway sedimentation, and airborne dust
		Site assessment	Topography and Hydrography
RELi 2.0 Rating System [12]	Panoramic Approach (AP)	Short-term hazard preparedness + mitigation	Potential actions that can be to mitigate short-term hazards to the building and community occupants, physical property + infrastructure
		Long-term adaptability, diversity + redundancy	Restore the effects due to desertification, beach erosion, and loss of wetlands
			Implement plans to prepare for long-term climatic changes
	Hazard Preparedness (HP)	Emergency planning for hazards	Fundamental safety for occupants during disaster and emergency by developing an Emergency Preparedness Plan
		Fundamental access to: first aid, emergency supplies, water, food, communications	Fundamental safety for occupants during emergencies for at least 96-h with first aid kit and training

(continued)

Table 1 (continued)

Green rating	Main category	Sub-category	Existing DRR measures available
			Provide at least a telephone landline along a cell phone with text message capabilities and an emergency alert radio + walkie-talkies
		Emergency planning for common hazards + extreme events	Enhanced Emergency Planning for Common Hazards + Extreme Events using, communications, life safety, property protection and community outreach
			Expand FEMA Guide 141 Planning Considerations
		Enhanced Access: Emergency Care + Supplies, Water, Food, Communications	Provide safety for occupants during disasters and/or emergencies such as, first aid, short supply items, access to emergency care, sanitation, communication capacity + equipment, emergency back-up power and portable emergency lighting
		Community Education: Weather, Safety + Risks	Inform and educate the public and authorities about increasing weather, safety and resiliency risks
	Hazard Adaptation & Mitigation (HA)	Sites of Avoidance + Repair: 500-Year Floodplain, Storm Surge + Sea Rise	Avoid areas within 500-year floodplains
			Building on green field sites below the 500-year floodplain is not permitted
			Avoid coastal zones inundated by 2″-6″ of sea level rise, or provide a solution

(continued)

Table 1 (continued)

Green rating	Main category	Sub-category	Existing DRR measures available
		Emergency Operations: Back-up Power + Operations	Design for power outages from grid
			Provide back-up power, switching gear, power hook-ups and temporary generators to provide power for critical utilities
			Locate equipment and infrastructure above 500-year floodplain
			If equipment is not sufficiently elevated then apply dry flood protection techniques
		Transit + Transportation System Protection + Continuous Operations	Provide and Maintain Flood Protection + Energy Resiliency in transportation systems for short-term and long-term resiliency
	Energy, Water & Food (EW)	Plan for Rainwater Harvesting, Resilient Landscapes + Food Production	Plan a minimum of 50% of the roof area to capture water for reuse
			Plan structure and site for roof and/or ground level collection of rainwater for project
		Water Efficiency + Resilient Water + Landscapes	Provide on-site rainwater or recycled water storage to cover toilet flushing and mechanical for emergency operations for at least 96 h
CASBEE-UD Rating System [13]	Society	Security/Safety	Disaster Prevention: Use hazard maps and preparedness with communication, water & energy supply during an emergency

(continued)

Table 1 (continued)

Green rating	Main category	Sub-category	Existing DRR measures available
			Disaster Response: Formation of evacuation routes and sites/shelters and emergency operations for continuity of operations
GREENSHIP New Building Version 1.0 Rating Tool [14]	Appropriate Site Development (ASD)	Storm Water Management	Integrated rainwater management system which will reduce runoff volume into the city drainage network from building sites and reduce flooding
	Energy Efficiency & Conservation (EEC)	Climate Change Impact	To provide and increase the knowledge related to the effect of excessive energy consumption towards climate change

comply with the requirements in securing Environmental Compliance Certificate (ECC) [15].

2.3 GREENSL® Rating Systems for Built Environment

GBCSL is the pioneer in certifying the green buildings and infrastructures in Sri Lanka using their developed tools such that; GREENSL® Rating System for New Buildings, GREENSL® Rating System for Existing Buildings, GREENSL® Rating System for Cities, GREENSL® Rating System for Transportation Infrastructure and GREENSL® Rating System for Green Products [16]. The GREENSL® Rating System for New Buildings hich is the main focus of the literature survey consists of main 8 categories with prerequisites (mandatory requirements to fulfill without points) and credits (optional requirements to earn points). Eight categories are, Management (4 Points), Sustainable Sites (25 Points), Water Efficiency (14 Points), Energy and Atmosphere (22 Points), Materials and Resources (14 Points), Indoor Environmental Quality (13 Points), Innovation and Design Process (4 Points) and Social and Cultural Awareness (4 Points) [17]. Table 2 summarizes the current extent of integration of DRR measures in this tool.

Table 2 Existing DRR and disaster resilient measures in GREENSL® rating system for new buildings tool [17]

Main category	Sub-category	Existing DRR measures available
Sustainable Sites (SS)	Site selection	Land whose elevation is lower than 1.5 m above the elevation of the 50-year flood level
		Land which is prior to acquisition for the project was public parkland or land identified as landslide-prone areas
	Site assessment and development	Hydrology: Flood hazard areas, delineated wetlands, lakes, streams, shorelines, rainwater collection and reuse opportunities and initial water storage capacity on site

2.4 Disaster Risk Reduction (DRR) Mechanisms and Disaster Resilient Local Guidelines

This subsection is focused on the DRR mechanisms and disaster resilient local guidelines for floods, landslides and heavy winds which can be divided into two major aspects as; Structural (hard) DRR measures and Non-Structural (soft) DRR measures. Table 3 illustrates the structural and non-structural DRR and disaster resilient local guidelines and mechanism for floods, landslides and heavy winds.

3 Methodology

Research methodology used for this research study in developing a disaster resilient building tool of the GREENSL® Rating System is illustrated in Fig. 1 which consists of five major steps.

According to Fig. 1, after the literature review the guidelines identified and developed were incorporated into the existing 8 categories and subcategories of the building tool of the GREENSL® Rating System. Guidelines were incorporated in to the 8 categories under different levels such as incorporated as a new subcategory, incorporated as a new sub-prerequisite or a sub-credit under the existing credits and prerequisites and incorporated as a new minor improvement or an amendment done to sub-prerequisites & sub-credits. After the development and incorporation of guidelines into the existing 8 categories of the building tool of the GREENSL® Rating System, evaluation of those incorporated guidelines was carried out using expert committee meetings. 8 consecutive expert committee meetings were carried out with the participation of 10 experts and professionals from diverse disciplines and backgrounds related to research study such as green building and built environment

professionals, green accredited professionals, disaster management experts, civil engineers, electrical and mechanical engineers, architects and engineering-based academics.

Many comments and inputs were suggested by the expert committee throughout the series of meetings for the improvement of the building tool of the GREENSL® Rating System for Built Environment as a disaster resilient tool. Those comments are, (1) Input DRR measures to reduce the risk caused due to lightening hazards, (2) Change few categories which the guidelines were directed and listed based on their relativity and most suitability while listing some guidelines under more than one category or credit/prerequisite (structural health monitoring checks in both commissioning and additional commissioning sub-categories), (3) Remove some guidelines which are already in the building codes, (4) Change criteria limits under certain credits and prerequisites (eg: 150% of rainwater harvesting storage) which will

Table 3 Structural and non-structural DRR and disaster resilient local guidelines and measures for floods, landslides and heavy winds

Natural hazard	Structural DRR measures	Non-structural DRR measures
Floods	Orientation: Placing short edge of the building to face flooding direction [18]	Health monitoring and maintenance of the building A separate section/chapter about emergency handling mechanisms during a hazard (including fire) to be incorporated in to the building user guide [12] Develop an emergency preparedness information and instruction manual [12, 22] Implement sediment and erosion control plan to reduce the risk of occurrence and damage due to natural hazards [20, 23] Avoid constructions in inappropriate sites to reduce the vulnerability from natural hazards and carryout site assessment using hazard maps, topography and hydrology, etc. [11, 17] Identify the transportation needs of the people in an emergency by allocating required transportation facilities, resources and alternative evacuation routes [12] Enhancing the connectivity of community and transportation needs during an emergency through building alternative connections [12]
	Plan: aligning openings on opposite walls to generate a flow path for storm water [18]	
	Slabs and foundations: concrete [19]	
	Foundation: for problematic sub soil conditions pile foundations are suggested [19]	
	Elevated buildings: raised plinth by building on higher grounds, creating elevated grounds and on silts [18]	

(continued)

Table 3 (continued)

Natural hazard	Structural DRR measures	Non-structural DRR measures
	Building superstructure: cross walls, heavy and the hollow blocks for wall construction, lintels on openings [18]	
	Amphibious buildings: boat type and lift type [20]	
	Flood proof construction materials: concrete, reinforced concrete framing, lime plastering or using magnesium oxide board as finishing [19]	
	Design wall to floor junction with two layers of waterproofing [20]	
	Use wet flood proofing technique [21]	
	Post-Flood Drainage Systems [20]	
	Water proof/tight construction (lower levels of buildings) [18, 20]	
Landslides	Site selection: ground slope (S) stability ($S < 5^0$: suitable for construction, $5^0 < S < 31^0$: apply engineering techniques, $S > 31^0$: not suitable for construction [18]	Limit disruption of natural water hydrology through watershed management technique [24] Provide access to public portable water transmission systems and wastewater conveyance networks during emergency situations [12] Rain water management systems should be adopted based on the future climate predictions and rain fall patterns [23] Installation of storm water collection and storage systems combined to rain water harvesting tanks with greater capacities, intensity and precipitation [12, 17] Design HVAC systems based on future climate changes and temperature variances, highlighting the energy resilience and natural hazards aspect All buildings in disaster prone areas shall use backup & emergency power sources and reliable communication systems [12] Install a wireless fire communication system to all large buildings in hazard zone areas as a backup system [12]
	Orientation: longer sides of the building should be parallel to the natural contour lines of the slope in a single platform [18]	
	Shape: simple and symmetrical shapes such as square or rectangular [18]	
	Earthworks: stable cut slopes in different soil types with or without a retaining wall [18]	
	Foundation: size and depth should be decided based on the type of subsoil and the bearing capacity of the soil and footings shall be constructed with enough edge distance for protection against erosion [18]	
	Construction of suitable earth retaining & slope stabilization structures [18]	

(continued)

Table 3 (continued)

Natural hazard	Structural DRR measures	Non-structural DRR measures
	Design and development of surface & sub-surface drainage networks along the slopes [18]	
	Landslide resilient construction: terraced buildings, elevated buildings on columns or raised footings [18]	
Heavy winds	Site selection: identification of the expected average wind speeds of the site location based on wind loading zonation maps; zone1: 50 m/s, zone 2: 42 m/s, zone 3: 38 m/s [18]	Use 100% renewable energy sources such as cogeneration & solar as reliable backup & emergency power sources during blackouts Take appropriate measures to safeguard toxic waste materials stored in flood prone zones [20] Install an emergency lighting control system to keep commercial & residential building stairwells, hallways and emergency exits lit during blackouts [12] Evacuation routes are developed as a part of public transportation systems [12] Design open public spaces in disaster risk areas and in vulnerable building premises [12] Emergency & First aid Kit to be stored in first floor to be used during an emergency [12, 22] Awareness programs for general public on natural disasters and their mitigation measures along with techniques related to preparedness Investing in disaster resilience by the local businesses and corporate citizens as a part of their corporate social responsibility are recognized and supported by the government [12] Hazard risk in land profiles are incorporated into land pricing [12] A tailored resource base is available to support disaster management plans in hazardous situations [12]
	Building sheltered using other structures or trees as a wind barrier. In hilly terrains, building should be located in a valley [18]	
	Orientation: shorter side of the building facing wind direction [18]	
	Plan: building openings on opposite walls creating flow path for wind [18]	
	Building shape: Avoid irregular shapes and go for simple regular shapes [18]	
	Walls: supported on all four sides with columns and beams, providing a stiffer wall against lateral wind forces [18]	
	Doors: provided with adequate connection to the walls on either sides and brickwork construction around the door frame [18]	
	Roof structure: avoid mono-pitch roofs and install hipped roofs and reinforced concrete flat roofs for high wind [18]	
	Roof connections: Roof connections between rafter, wall plate, reeper, ridge board, under-purlin & at roof should be properly chosen, designed and fixed according to standard guidelines based on the wind load, wind zone, building height and number of stories, etc. to increase the strength of the roof structure against high winds [18]	

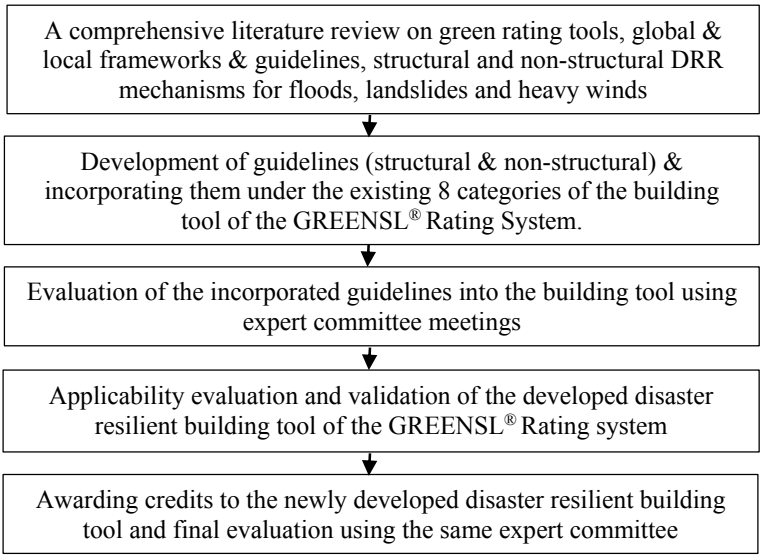

Fig. 1 Methodology used for developing a disaster resilient building tool of the GREENSL® rating system

result in enhancing the DRR and sustainability of the rating tool, (5) fire protection & detection mechanisms are suggested to include under commissioning clauses as a prerequisite as it was not an important aspect in the present rating tool, (6) Input a guideline to reduce the risks and enhance the resilience due to infections deceases like COVID-19, (7) Include some difficult achievables as 'Exemplary Performance' which may be difficult for the majority of green buildings, (8) Remove some criteria from the building tool due to the difficulty in achieving and transfer them to either city tool or transportation infrastructure tool or both based on the applicability and (9) Better not to mention about certain criteria such as slope stabilization criteria as they may vary with new research studies, instead mention only the link to refer the criteria.

After addressing the comments received from the expert committee, the new disaster resilient building tool of the GREENSL® Rating System for Built Environment consists of 2 new subcategories, 11 new sub-prerequisite or a sub-credit under the existing credits and prerequisites and 9 new minor improvement or an amendment done to sub-prerequisites & sub-credits. Initially the credits were awarded with points (starting from 1 point) depending on the importance and weightage of the DRR and disaster resilient guideline towards the greenery and sustainability of the building. Then the credited rating system was evaluated and reviewed using the same expert committee involved in evaluation of the incorporated guidelines. After the inputs and comments received from the expert committee, the rating system was re-credited with the suggested amendments and directed for the next round of review process. After couple of rounds of reviews by the expert committee, the credited rating system

was ready for validation. Building Tool of the GREENSL® Rating system for Built Environment, incorporated with DRR and disaster resilient measures was comprised of extra 20 points, summing the total number of points into 120 points. The score card of the credited, disaster resilient building tool is shown in Table 4. Newly added content and the amendments done are underlined for better and clear identification purposes.

The credited new disaster resilient building tool was then directed for applicability evaluation and validation process. Applicability evaluation and validation were carried out through a series of surveys carried out using green certified buildings by GBCSL. Eleven certified buildings were chosen depending on their geographical location based on hazards and rating levels such that, 2 buildings located in flood prone areas, 3 based in landslide prone areas, another 3 in high wind areas and final 3 buildings located in less or zero hazard prone areas. Then the certified and scored project/building reports of above 11 buildings together with the building tool and newly developed disaster resilient building tool were used for the validation surveys. Score cards of the newly developed disaster resilient building tool were filled based on the current conditions and hazard vulnerability of the buildings. Then the new score card with the new certification type received based on new disaster resilient building tool was compared with the original or old score card with its certification type based on the existing building tool.

4 Results and Discussion

Although 20 points are allocated for DRR in this tool, points are allocated based on the applicable hazards for the respective building site. Therefore, number of applicable points may be varied depending on the location and vulnerable hazards. The summary of the 11 surveys conducted using the new disaster resilient building tool are analyzed and tabulated in Table 5. Points earned and the certification obtained using the existing building tool and the new disaster resilient building tool are compered while suggesting the possible and most effective applications of the tools.

According to Table 5, buildings situated in flood prone areas have dropped their certification at least by one level. Droppage of points has also varied between 8 and 9 points, highlighting the considerable impact on the certification obtained using the existing building tool. Therefore, it is better to use the new disaster resilient building tool in certifying the buildings situated in flood prone areas due to the high frequency and impact created by flood hazards on built environment in Sri Lanka. Same observation can be noticed the buildings situated in landslide prone areas as well. 7 to 8 points have dropped in all 3 surveys carried out while dropping the certification also by one level. Therefore, it can also be recommended to use the newly developed disaster resilient building tool to certify the buildings which are prone to landslides. One special aspect which can be noticed here is that all 3 buildings considered here have incorporated the basic design principles applicable to land slide hazard in constructing the buildings. There is a slight difference in the

Table 4 The score card of the credited, disaster resilient building tool of the GREENSL® rating system for built environment [17]

Prerequisite/credit	Criteria	Points	DRR points
1.0 MANAGEMENT (MN): 4 Total Points Available			
Prerequisite 1	Green Building Accredited Professional	Required	
Prerequisite 2	Commissioning Clauses	Required	
Prerequisite 3	Building users guide	Required	
Prerequisite 4	Emergency Preparedness and Information Manual		Required
Credit 1.1	Building Tuning [1 Point]		
	1.1.1. Occupant comfort and Energy Efficiency	1 Point	
Credit 1.2	Environmental Management [3 Points]		
	1.2.1. Involve Ecologist	1 Point	
	1.2.2. Environmental Management Plan	1 Point	
	1.2.3. Environment Mgt. System (ISO 14001)	1 Point	
2.0 SUSTAINABLE SITES (SS): 25 Total Points Available + Extra 10 Points for DRR			
Prerequisite 1	Erosion and Sedimentation Control	Required	
Credit 2.1	Site Selection [4 Points + 4 Points]		
	2.1.1. Inappropriate site avoidance to reduce environment impacts	4 Points	
	2.2.2. Inappropriate site avoidance to reduce the vulnerability		2 Points
Credit 2.2	Site Assessment and development [2 Points + 6 Points]		
	2.2.1. Site Assessment	2 Points	
	2.2.2. Architectural and design aspects which can withstand natural hazards		2 Points
	2.2.3. All hazard prone should use relevant hazard mitigation and preparedness measures		2 Points
Credit 2.3	Development Density and Community Connectivity	2 Points	
Credit 2.4	Brownfield Redevelopment and allowance for connectivity of Green Lands [1 Point + 2 Points]		
	2.4.1. Develop on a brownfield with required remediations	1 Point	

(continued)

Table 4 (continued)

Prerequisite/credit	Criteria	Points	DRR points
	2.4.2. Check the resilience of brownfield lands for potential hazards before redevelopment		1 Point
	2.4.3. Increase the resilience of the brownfield land		1 Point
Credit 2.5	Alternative Transportation [3 Points + 1 Point]		
	2.5.1 Public Transportation Access	1 Point	
	2.5.2. Parking Capacity	1 Point	
	2.5.3. Encourage use of green modes of transport	1 Point	
	2.5.4. Transportation during an emergency		1 Point
Credit 2.6	Reduced Site Disturbance [6 Points]		
	2.6.1. Protec/restore Habitat	2 Points	
	2.6.2. Vertical greening	2 Points	
	2.6.3. Development footprint	2 Points	
Credit 2.7	Storm Water Design, Quantity Control	2 Points	1 Point
Credit 2.8	Storm Water Design, Quality Control	2 Points	
Credit 2.9	Heat Island Effect, Non – Roof	1 Point	
Credit 2.10	Heat Island Effect, Roof	1 Point	
Credit 2.11	Light Pollution Reduction	1 Point	
3.0 WATER EFFICIENCY (WE): 14 Total Points Available			
Prerequisite 1	Eliminate potable water consumption for irrigation	Required	
Credit 3.1	Use of alternative water sources	1 Point	
Credit 3.2	Use of water-saving performances	1 Point	
	Exemplary Performance Marks (1)		√
Credit 3.3	Indoor water use reduction	1–4 Point	
Credit 3.4	Water Efficiency in air conditioning system	1 Point	
Credit 3.5	Innovative Wastewater Technologies [1–5 Points]		
	3.5.1. Reduce Potable Water Use	1 Point	

(continued)

Table 4 (continued)

Prerequisite/credit	Criteria	Points	DRR points
	3.5.2. Reduce potable water use or treat wastewater	1 Point	
	3.5.3. Harvested rainwater	2 Points	
	Exemplary Performance Marks (2)		√
	3.5.4. Aquifer Recharge	1 Point	
Credit 3.6	Innovative Water Transmission	1 Point	
Credit 3.7	Ground water recharge, if ground water is tapped	1 Point	
4.0 ENERGY AND ATMOSPHERE (EA): 22 Total Points Available + Extra 2 Points for DRR			
Prerequisite 1	Fundamental Building Systems Commissioning	Required	
Prerequisite 2	Minimum Energy Performance	Required	
Prerequisite 3	CFC Reduction in HVAC & R Equipment	Required	
Credit 4.1	Optimize Energy Performance	1–10 Points	
Credit 4.2	Renewable Energy [1 – 6 Points + 1 Point]		
	4.2.1. Renewable energy usage	1–6 Points	
	4.2.2. Renewable energy usage during emergencies		1 Point
Credit 4.3	Additional Commissioning	1 Point	1 Point
Credit 4.4	Ozone Depletion	1 Point	
Credit 4.5	Measurement & Verifications	1–2 Points	
Credit 4.6	Green Power	1 Point	
Credit 4.7	Certified Energy Auditor	1 Point	
5.0 MATERIAL, RESOURCE & WASTE MANAGEMENT (MR): 14 Points Available + 1 Point for DRR			
5.1 MATERIALS AND RESOURCES			
Prerequisite 1	Storage and collection of recyclables	Required	
Credit 5.1.1	Building Reuse [1–2 Points]		
	5.1.1.1. Maintain 75% of existing building and shell	1 Point	
	5.1.1.2. Maintain 75% of existing building structure and shell and 25% of non-shell areas	2 Points	
Credit 5.1.2	Resource reuse [1–2 Points]		

(continued)

Table 4 (continued)

Prerequisite/credit	Criteria	Points	DRR points
	5.1.2.1. for at least 10% of the Building	1 Point	
	5.1.2.2. for at least 20% of the Building	2 Points	
Credit 5.1.3	Recycled Content	1 Point	
Credit 5.1.4	Local/ Regional Materials	1 Point	
Credit 5.1.5	Rapidly Renewable materials	1 Point	
Credit 5.1.6	Certified wood and other building materials	1 Point	
Credit 5.1.7	Global Warming Potential of buildings	1 Point	
Credit 5.1.8	Materials Produced with Waste materials	1 Point	
Credit 5.1.8	Hazard Resilient Building Materials		1 Point
5.2 WASTE MANAGEMENT			
Credit 5.2.1	Construction Waste Management [1–2 Points]		
	5.2.1.1. for 50% recycling	1 Point	
	5.2.1.2. for 75% Recycling	2 Points	
Credit 5.2.2	Operational solid waste management	1 Point	
Credit 5.2.3	Hazardous Waste Management	1 Point	
6.0 INDOOR ENVIRONMENTAL QUALITY (EQ): 13 Total Points Available + Extra 3 Points for DRR			
Prerequisite 1	Minimum IAQ Performance	Required	
Prerequisite 2	Smoke (ETS) Control	Required	
Prerequisite 3	Minimum Acoustic Performance	Required	
Credit 6.1	Outdoor air delivering Monitoring	1 Point	
Credit 6.2	Increased Ventilation	1 Point	
Credit 6.3	Construction IAQ Management Plan	1 Point	
Credit 6.4	Low- Emitting Materials [1–3 Points]		
	6.4.1. Paints and Coatings	1 Point	
	6.4.2. Carpet Systems	1 Point	
	6.4.3. Composite Timber and Agrifibre Products	1 Point	

(continued)

Table 4 (continued)

Prerequisite/credit	Criteria	Points	DRR points
Credit 6.5	Indoor Chemical & Pollutant Source Control	1 Point	1 Point
Credit 6.6	Controllability of systems [1–2 Points + 1 Point]		
	6.6.1 Lighting controls	1 Point	
	6.6.2 Comfort controls	1 Point	
	6.6.3. Emergency Lighting		1 Point
Credit 6.7	Thermal comfort, design	1 Point	1 Point
Credit 6.8	Thermal comfort, verification	1 Point	
Credit 6.9	Daylight & Views [2 Points]		
	6.9.1 Daylight	1 Point	
	6.9.2 Views	1 Point	
7.0 INNOVATION & DESIGN PROCESS (ID): 4 Total Points Available + Extra 2 Points for DRR			
Credit 7.1	Innovation in Design [1–4 Points + 1–2 Points]		
	7.1.1 Innovation in design	1–2 Point	
	7.1.2 Exemplary performance	1–2 Points	1–2 Points
8.0 SOCIAL & CULTURAL AWARENESS (SC): 4 Total Points Available + Extra 2 Points for DRR			
Prerequisite 1	Archaeological sites & Heritage buildings	Required	
Credit 8.1	Social Wellbeing, Public Health & Safety [1–2 Points + 1–2 Points]		
	8.1.1. Enhance social wellbeing & public health	1–2 Points	
	8.1.2. Enchase public safety during emergencies		1–2 Points
	Exemplary Performance Marks (3)		√
Credit 8.2	Cultural Identity	1–2 Point	
Total Number of Points		100	20

scores and certification variation with the buildings situated in high wind areas. As most of the buildings considered here are placed in the east coastal belt of Sri Lanka, those buildings are also highly vulnerable to Tsunami risk as well. Although the scope of the research study was out of tsunami risks, during awarding the points, this aspect was taken into consideration. One of the positive aspects noticed in these selected green certified buildings are that they have considered the wind effect and alkaline effect (due to the locations are near the sea) in architectural and structural design aspects of the building. In these scenarios, points have been dropped by 6 or 7 points due to the moderate consideration of DRR measures against high winds in the

Table 5 Summary of the 11 surveys conducted using the new disaster resilient building tool of GREENSL® rating system for built environment

Project	Building type & location	Hazard vulnerability	Existing building tool		New disaster resilient tool	
			Points (%)	Certification	Points (%)	Certification
A	Factory & Stores—Badalgama	Floods	68	Gold	59	Silver
B	Factory—Millewa	Floods	74	Platinum	66	Gold
C	Administrative Building—Badulla	Landslides	64	Gold	56	Silver
D	Supermarket—Kegalle	Landslides	71	Platinum	64	Gold
E	Goods Factory—Pannala	Landslides	63	Gold	55	Silver
F	Cement Factory—Trincomalee	HW&T[a]	72	Platinum	65	Gold
G	Hospital—Batticaloa	HW&T[a]	67	Gold	60	Gold
H	Bank—Kalmunai	HW&T[a]	72	Platinum	66	Gold
I	University Building—Homagama	No vulnerability	68	Gold	65	Gold
J	Fuel Station Building—Pepiliyana	No Vulnerability	56	Silver	52	Silver
K	Hotel—Galgamuwa	No vulnerability	71	Platinum	68	Gold

[a]HW&T—Heavy Winds and Tsunamis

selected 3 buildings compared with their existing green certification. Other than one building, the certification level of the rest of the 2 buildings have dropped by one level. Therefore, it also can be recommended to use the building tool incorporated with DRR in certifying the buildings in high wind areas. If we have a look at the buildings which are situated out of any hazard vulnerable zones, the droppage of points were only limited to 3 or 4 points. Apart from one building, the rest of the certification levels remained same in the rest of the 2 buildings which the survey was conducted. Even that certification level drop was mainly due to the certification level being marginal to the lower limit of the certification. Therefore, it can be recommended to use the existing building tool in certifying the buildings which are not situated in hazard prone areas. However, incorporating the applicable general DRR measures of the new building tool incorporated with DRR measures is encouraged due to the increasing treads of natural hazards and climate change conditions in the present world and Sri Lanka which will be beneficial in transforming the green buildings into sustainable buildings.

5 Conclusions

Disasters induced by natural hazards are inevitable. Yet taking necessary DRR and disaster resilient measures become a vital necessity with the rapid increment in natural disasters which brings catastrophic damages to the environment, society and the economy. Disaster risk in Sri Lanka has been increasing mainly due to rapid unplanned commercialization and development of cities, infrastructure with poor quality, and the impacts of climate change which has exposed the built environment severely vulnerable to natural hazards. Out of all the hazards, floods, landslides, heavy winds and tsunamis are considered to be the events with highest number of occurrence and also with the highest number of losses and damages during last 30 years in Sri Lanka.

Although GBCSL has initiated encouraging sustainability and reduced consumption of energy and other resources usage in buildings, it could not specifically identify the need of integrating DRR mechanisms into their green rating tools. Even a platinum rated green buildings with lot of sustainable and green related concepts, cannot be sustainable in nature if they are not withstanding against the natural hazards. Therefore, incorporation of DRR and disaster resilient mechanisms into the residential and other buildings, is a transformation towards a sustainable built environment. This research concerns the recognition of structural and non-structural DRR measures for floods, landslides and high winds, developing guidelines and then coming up with a new disaster resilient building tool for GREENSL® Rating System for Built Environment under main 8 categories of the existing building tool for GREENSL® Rating System for Built Environment V2.0.

After developing the new disaster resilient building tool for GREENSL® Rating System, eleven surveys were carried out in green certified buildings situated in hazard vulnerable areas for the floods, landslides and high winds as well as less or no hazard prone areas. Those surveys reveled that, it is highly recommended to use new disaster resilient building tool in certifying buildings situated in floods and landslides prone areas, moderately recommended to use the new tool for certification in high wind areas and finally it is acceptable to use the existing building tool for GREENSL® Rating System for Built Environment V2.0 for the buildings situated in less or no hazard prone areas. However, it is advised that the new disaster resilient building tool is in use even for the buildings situated in less or no hazard prone areas by at least incorporating general DRR measures due to the increase of natural hazards and climate change conditions in the modern world and Sri Lanka which will be beneficial in the process of transforming normal buildings to green buildings.

6 Recommendations

There are number of important recommendations to be suggested at the end of my research work for future references and continuation of this research as follows,

- Some DRR guidelines may be difficult to achieve for a developing nation like Sri Lanka, where greening is also not a very popular concept due to the extra cost incurred. Therefore, incorporating DRR measures may incur another extra cost apart from greening.
- Some DRR measures contradict with greening and sustainability concepts such as zero-carbon emission, life cycle assessment and resources and energy resilience. As an example, use of concrete as a hazard resilient construction material and installation of HVAC systems predicting future climatic changes may consume more energy and recourses as well as emit more carbon to the environment which will contradict with green building concepts. Therefore, it's better to carry out a proper analysis to identify most sustainable options out of these concepts.
- Only 11 surveys were carried out due to lack of green certified buildings situated in hazard prone areas. Also, the recommendations to use the new disaster resilient building tool is in high, moderate, and no or low levels for different hazards or less or no hazard prone areas, it can vary depends on building type and its usage as well. Therefore, this tool can be further developed as a more practical tool if more surveys can be conducted.

Acknowledgements This study was conducted with the help, support and directions of Green Building Council of Sri Lanka (GBCSL). They immensely supported by providing their resources such as green rating tools and systems, green certified building information, green certified project reports and their professionals as well.

References

1. World Health Organization, viewed 25 Nov 2019. https://www.who.int/environmental_health_emergencies/natural_events/en/
2. Economic losses, Poverty and Disaster—1998 and 2017 of UNISDR, viewed 25 Nov 2019. https://www.unisdr.org/we/inform/publications/61119
3. Low P (2019) The natural disasters of 2018 in figures. Munichre, Aug. 01, 2019. https://www.munichre.com/topics-online/en/climate-change-and-natural-disasters/natural-disasters/the-natural-disasters-of-2018-in-figures.html
4. Department of Meteorology—Sri Lanka (2016) Climate of Sri Lanka. http://www.meteo.gov.lk/index.php?option=com_content&view=article&id=94&Itemid=310&lang=en. Accessed 15 Oct 2018
5. PreventionWeb, Sri Lanka Disaster & Risk Profile, viewed 25 Nov 2019. https://www.preventionweb.net/english/
6. DesInventar official website by UNISDR, http://www.desinventar.lk:8081/DesInventar/country_profile.jspcountrycode=sl&lang=EN
7. Amaratunga D, Haigh R, Malalgoda C, Keraminiyage K (eds) (2017) Mainstreaming disaster resilience in the construction process: Professional education for a resilient built environment. A report of the CADRE project: Collaborative Action towards Disaster Resilience Education. www.disaster-resilience.net/cadre
8. Asian Disaster Preparedness Center (ADPC) (2013) Mainstreaming Disaster Risk Reduction into Housing Sector in Sri Lanka

9. Sendai Framework, Viewed on 30 Nov 2019, https://www.undrr.org/implementing-sendai-framework/
10. Le Cozannet G et al (2020) Space-based earth observations for disaster risk management. Surv Geophys. https://doi.org/10.1007/s10712-020-09586-5
11. United Nations. Sustainable development goals. Available: https://www.un.org/sustainabledevelopment/sustainable-development-goals/24
12. Official Website of World Green Building Council, Viewed on 5 Dec 2019. https://www.worldgbc.org
13. LEED v4.1 building design and construction Rating System | U.S. Green Building Council. www.usgbc.org
14. RELi 2.0—Rating Guidelines for Resilient Design + Construction —December 2018
15. CASBEE for CASBEE for Urban Development (CASBEE-UD) Rating System
16. GREENSHIP for New Buildings—Version 1.1. https://www.gbcindonesia.org/greenship
17. Official Website of Green Building Council of Indonesia. https://www.gbcindonesia.org/
18. Official Website of Green Building Council of Sri Lanka. https://srilankagbc.org/
19. GREEN$^{SL®}$ Rating System for Built Environment—New Buildings—Version 2.0
20. Hazard Resilient Housing Construction Manual | Resilient Construction Series No. 1, National Building Research Organization (NBRO)
21. Guidelines for buildings at risk from natural disasters | A response to the tsunami of 26/12/2004 & A contribution to the task of reconstruction July 2005, Society of Structural Engineers—Sri Lanka
22. Khan MK, Ahmad S (2017) Flood resistant buildings: a requirement for sustainable development in flood prone areas (2017)
23. Future–proofing New and Existing Buildings—Flood Resilient Design and Construction Technique, Katy Hunter BRE Scotland. https://www.climatenorthernireland.org/cmsfiles/3-Katy-Hunter---Flood-resilient-design.pdf
24. Your Emergency Preparedness Guide, Office of Public Safety, Prince Edward Island, Canada. www.peipublicsafety.ca

Sustainable Construction of Building and Infrastructure

Improvement of an ADT Estimation Model Developed for A-Class Roads in Sri Lanka by Incorporating National Expressways and Important B-Class Links

P. M. Jayarathne, R. D. N. D. Kumari, W. R. S. S. Dharmarathna, and I. M. S. Sathyaprasad

Abstract Estimates of Average Daily Traffic (ADT) are important in the operations of state highway departments for new constructions, improving existing facilities and maintenance. The available manual survey methods to calculate ADT are costly and time consuming. There have been several previous attempts to develop ADT estimation models for the A-class road network in Sri Lanka. One of the serious shortcomings of these models is that the contribution of important class B roads and expressways in transferring inter-district trips is not represented. Hence, this study aims to improve ADT estimation model for the A-class road network including key B-class links and current expressways (E01, E02, E03). Six independent variables were selected in order to represent three main contributors to the ADT through the location; local, regional and inter-district trips, as build-up areas of cities and, distance to the counting stations, population density in the administrative district and the network connectivity factor. Network connectivity factors were calculated based on a link-node system with 96 nodes and 162 links. Road junctions, interchanges of expressways and district capitals are also selected as nodes in the link-node system. Important B-class road links were selected based on average ADT in B-class links in each district, google maps and, local knowledge. Furthermore, B-class links connected with expressway interchanges are also selected based on ADT values. Assuming the rational behaviour of trip makers that try to reduce fuel, toll cost, travel time, travel distance, etc. the network connectivity factor is derived based on a generalized cost function. Generalized cost matrix was used as an input for analyzing the cheapest path using Dijkstra's Algorithm in Python platform. A regression analysis is done for obtaining the respective parameters of the ADT model with Minitab 19 software. Model resulted a R-square value of 0.71. Percentage bias (PBIAS) was checked for calibration and validation data. For the calibration data, PBIAS is −0.00937% and for the validation data, PBIAS is 1.8%. Hence, the model is not biased and there is a significant improvement of the model, while using generalized cost instead of distance or travel time.

P. M. Jayarathne (✉) · R. D. N. D. Kumari · W. R. S. S. Dharmarathna · I. M. S. Sathyaprasad
Department of Civil Engineering, University of Peradeniya, Peradeniya, Sri Lanka

R. Dissanayake et al. (eds.), *ICSBE 2020*, Lecture Notes in Civil Engineering 174,
https://doi.org/10.1007/978-981-16-4412-2_21

Keywords ADT · Network connectivity factor · Generalized cost function · Regression analysis

1 Introduction

ADT is the volume of vehicles counted over a time period, greater than one day but less than one year, divided by the number of days in that time period. ADT data are mostly used in transportation engineering in order to design roads, pavement capacity analysis and developing transportation infrastructures, computing accident rates etc. Hence studying ADT plays an important role in transport sector. Predicting exact ADT value at a certain location is not a simple task. ADT at a location is governed by nature and function of the road, relative location and size of urban centers, local land use setup, etc. In addition to the aforementioned factors, some adverse conditions also can affect the ADT value such as road closure, accidents, floods, etc.

There are some manual techniques to calculate or find ADT. But those methods are costly and time consuming, and measuring ADT would incur a large cost of implementing equipment and people for surveys. Therefore, forecasting or estimating ADT will solve most of the problems. Estimated ADT value will not be always accurate but to have an initial judgment, estimated value will be more effective.

This research focuses on developing an effective ADT estimation model which can be modeled by using easily found inputs. It can be used for any location of A-class road network, some B-class links which are important while travelling inter district trips and expressways in Sri Lanka (only the available expressways by the time of this research is considered) road network by a simple desk study.

2 Literature Review

Different input variables have been identified by past researchers in various ways to represent the ADT. Build-up areas of the two nearby cities, distance to the counting stations from two cities were observed as the input variable. From that variables, population and urbanization effects were denoted by build-up area of the cities. Building and houses land area were defined as build-up area. Two other input variables were introduced to incorporate the intra district trips and inter district trips through the locations. Trip Attraction Factor was introduced to consider the inter-district trips which could have many origins as well as many destinations [1].

Yu-qin [6] considered emission factors, length, and travel time, and travel time fluctuation of respective road segment in order to construct a generalized cost function. Each weight of the generalized cost function was determined by using a stated preferences survey. In travel cost estimation there were two variables such as travel time cost and fuel consumption.

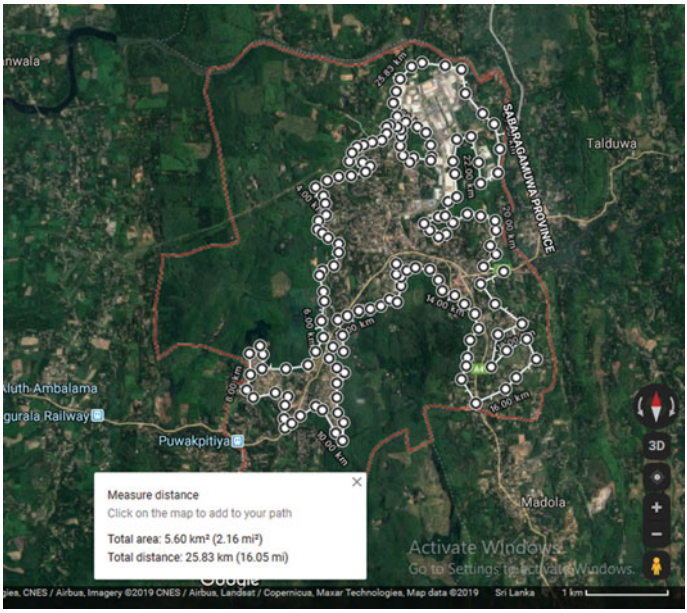

Fig. 1 An example of a build-up area (Awissawella city)

Sliupas [5] observed various methods to forecast Annual Average Daily Traffic (AADT). Linear regression, multiple regression, Idaho (USA) method and growth factor method were used to find out the better method. Maximum absolute error and average absolute error were used to compare methods.

3 Methodology

3.1 Build-up Input Variables

Current research aim is to improve the existing ADT model [4] including important B-class links and expressways. Six input variables were selected to represent urban, intra-district trips and inter-district trips. Those input variables are build-up area of the cities either side of the counting station measured in km^2, distance to the counting station from each city center measured in km, district population density measured in the 2019 (people/ km^2) and the Network Connectivity Factor (NCF). The built-up area of a city consists the area of land including the building and houses located excluding the unused land area. It represents how much cities are urbanized and popularized. Distance to the count location is a measure of the intensity of the city size affecting a certain location. The build-up area of cities and the distance to the

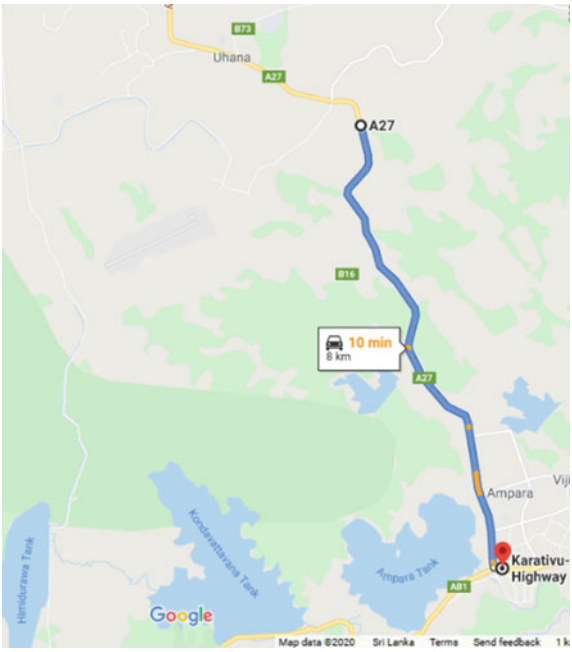

Fig. 2 An example of a distance to the counting locations (on A27 road)

counting locations were determined with the aid of google maps as shown in Figs. 1 and 2.

There are some trips which are originated and ended in the same district. Those trips are dependent on the number of people within the district. Hence in order to represent the regional traffic, District Population Density (DPD) was selected as an input variable. DPD is collected from the census report of population and housing, 2012 by the Department of Census and Statistics, Sri Lanka as the available latest. Yearly growth rate of 2012 as 0.66% was added to convert it to 2019.

$$P = P_0(1 + r)^t \tag{1}$$

P Population in 2019.
P_0 Initial population density in 2012.
R Growth rate.
T Time (years).

This research is mainly focused to find out NCF which represents the national level traffic using inter district trips from the total trips.

3.1.1 Modeling Road Network as a Link Node System

To model the road network, link node system was created, including A-class road, important B-class links and expressways. A-class road junctions, district capitals used [4], important B-class roads, junction and interchanges on expressways which have been completed by the time of this research (E01, E02, E03), were used as nodes. In order to finalize the link-node system, important B-class links were identified with below-mentioned limitation.

1. ADT data were tabulated with km post (permanent location) based on the respective road links and separated into district. Then the higher ADT value road links (greater than the average value) were identified as important B-class links.
2. Based on given origin and destination, many alternative routes can be observed through google map. Accordingly, the quickest and the shortest path were identified and the respective important B-class links were found based on the average district B-class ADT values.
3. Some of important B-class links were selected based on the sense, through the guidance of responsible people and local knowledge.
4. Further, B class road links which connected with the expressway interchanges were also selected based on the respective ADT values.

Based on the above points, road network was finalized with 25 B-class road links as shown in Table 1. In addition, AB044 road also added to the system as it plays an important role in inter district trips.

Table 1 Important B-links

Route No	Starting node	Ending node	Route No	Starting node	Ending node
AB044	Mahiyanganaya	Manampitiya	B213	Kakirawa	Talawa
B001	Akkareipaththu	Ampara	B240	Rajagiriya	Athurugiriya Int
B014	Ambalangoda	Kurundugahahethakma int	B247	Kurunrgala	Chilaw
B036	Mahiyanganaya	Hali-Ela	B296	Mullativu	Puliyankulam
B044	Bandarawela	Welimada	B297	Mullativu	Welioya
B056	Bibile	Monaragala	B304	Kaluthara	Horana
B057	Mahiyanganaya	Bibile	B308	Kurunegala	Katunayaka
B079	Padeniya	Chilaw	B413	Kandy	Kandehandiya
B084	Colombo	Horana	B424	Welioya	Trinco
B111	Ja-Ela	Giriulla	B427	Udawalawa	Thanamalwila
B127	Galigamuwa	Karawanella	B435	Rajagiriya	Kaduwela int
B128	Galle	Baddegama int	B465	Weligama	Kokmaduwa Int
B208	Katunayaka	Veyangoda	B492	Kandehandiya	Andaulpatha

Link-node system was created using A-class road links, important B-class road links and selected expressways. The respective schematic diagram of the road network is shown in Fig. 3.

NCF was calculated based on the above link node system. NCF is a parameter that indicate the total number of inter district trips and it represent the importance of a given road link in transferring inter-district traffic between districts. For each origin and destination pairs (i, j) the least generalized cost path is found using distance, travel time and the travel cost (toll for expressways) by applying Dijkstra's Algorithm [2]. The total inter district traffic volume can be computed according to the Gravity Model

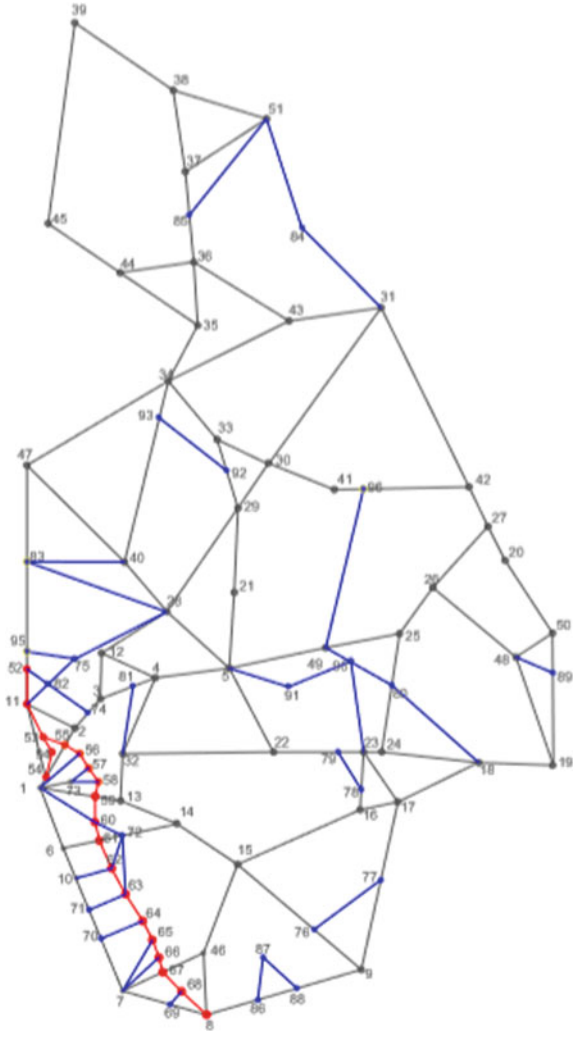

Fig. 3 Schematic diagram of road network

of trip attraction using district population densities ($P_i P_j$) and least generalized cost x_{ij}.

The number of trips between any given two nodes (district i, j) can be expressed as,

$$n_{ij} = k\frac{P_i * P_j}{x_{ij}^2} \tag{2}$$

where,

k	Calibrating coefficient.
P_i, P_j	Population densities of districts i and j.
x_{ij}	Total cost from i to j.

Moreover, if, T_l is the total number of inter district trips across link PQ as shown in Fig. 4, and then;

$$T_l = k\sum_i \sum_j \left(\frac{P_i * P_j}{x_{ij}^2}\right) C_{ijl} \tag{3}$$

where,

$C_{ijl} = 1$ if quickest path from i-j goes through $\boldsymbol{l}$.
$C_{ijl} = 0$ if quickest path from i-j does not go through $\boldsymbol{l}$.

Trip makers are trying to maximize their utility or on other words trying to reduce total travel time, total travel distance, fuel cost, toll cost, when they are travelling between any given two nodes. Accordingly, the travelers are trying to reduce the total generalized cost. Therefore, the travel cost function must be able to represent a relationship among the aforementioned variables. The generalized cost function discussed in the final report of economic feasibility analysis for central expressway

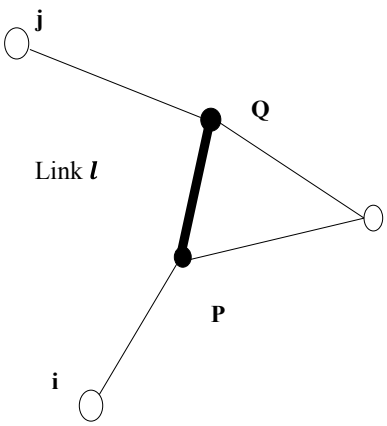

Fig. 4 Least generalized cost path from node i to node j goes through the link $\boldsymbol{l}$

was used for the calculation [3].

$$GC = \text{Time} + \text{Distance} \times \left(\frac{\text{VOC}}{\text{VOT}}\right) \times 60 + \text{Toll} \times \left(\frac{1}{\text{VOT}}\right) \times 60 \quad (4)$$

where,

Time	Travel time (min).
Distance	Travel distance (km).
VOC	Perceived vehicle operating cost (Rs/km).
VOT	Perceived value of time (Rs/h).
Toll	Toll cost (Rs).

Considering the all type of vehicles as a passenger car unit,

VOC	29.33 Rs/km.
VOT	514 Rs/h.

Accordingly, generalized cost was found for all links in the link-node system and identified the respective cheapest paths by using Anaconda software. Correspondingly, NCFs were calculated for all links.

4 Result and Discussion

Using the Minitab statistical software, following analysis was made considering backward elimination method with 95% confidence level.

$$\begin{aligned} ADT = {} & 8303 + 1581 \ln(A1) + 2185 \ln(A2) - 69.3D1 \\ & - 169.6D2 + 5.260DPD + 239.6NCF \end{aligned} \quad (5)$$

ADT	Average Daily Traffic.
D1	Longest distance from counting location.
D2	Opposite distance from counting location.
A1	Buildup area of the city that belongs to longest distance (D1).
A2	Buildup area of the city that belongs to opposite distance (D2).
DPD	District Population Density of the district in which measurement station is located.
NCF	Network Connectivity Factor of the link on which the measurement station is located.

Both model calibration and validation resulted a R-square value of 0.71. Percentage bias (PBIAS) for the calibration data, is −0.00937% and for the validation data, is 1.8%. Hence, the model is not biased. For the above model, D1 and A1 should always correspond to the distance which is longer.

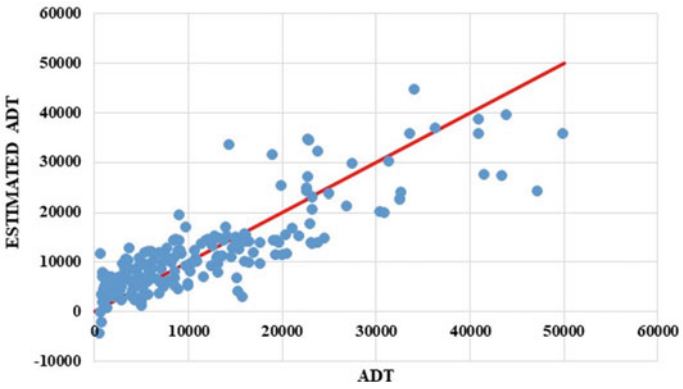

Fig. 5 Estimated ADT versus actual ADT

In output model, the distance coefficients have negative values and it suggests that ADT values reduces when going away from the urban centers. ADT increases when increasing the area of the cities and district population density.

Typically, the coefficient P-values to determine which terms to keep in the regression model. Resulted P-values for the all variables are less than 0.05 and hence, all input variables are statically significant.

As shown in Fig. 5, the estimated ADT values and the observed ADT values showed a significant relationship. Normalized objective function for above graph, is 0.47. It is less than 0.5. Hence, it can be taken as acceptable. In some locations, the estimated ADT shows a lower value than the observed. The reason for this deviation is due to the lesser presentation of build-up areas in vertical direction while capturing from the satellite maps. For some locations with low ADT, the model has estimated moderately high values. It occurs, because of the built-up areas are covered with vegetation and agricultural lands would not contribute to the trip generation as considered.

There are few negative ADT values in the estimated results. It is possible, if the urban centers are smaller in size and far away from the measurement location. Also, the road link may have a lower population density.

5 Conclusions

NCF was calculated based on distance in past studies [1, 4]. But when using the expressways, it is necessary to consider the toll cost. The model predictions showed very low percentage BIAS of −0.00937% and 1.8% in calibration and validation respectively. Hence, the model predictions are unbiased. In addition, some important B-class road links, expressways, and AB road links to the previously discussed model

and correspondingly, a broad range of road network can be investigated through the developed model.

Acknowledgements We thank Eng. (Mrs.) D. N. Siyambalapitiya, Director (Planning), RDA and staff of the planning branch for their assistance in arranging traffic data for model development and calibration. Further we shall also acknowledge Ms. M. M. F Hafza, Ms. W. P. M. T. Jayathilaka, Mr. B. M. A. S. M. Balasooriya and Mr. A. B. M. S. B. Wijekoon, the previous researchers who involved in the earlier developments of the model, for providing information and assistance.

References

1. Balasooriya B, Wijekoon A, Sathyaprasad I (2017) Estimation of average daily traffic based on urbanization effect and network connectivity. ICSECM2017-151
2. Dikstra E (1959) A note on problem in connexion with graphs. Numer Math 1:269–271
3. Economic Feasibility Analysis for Central Expressway Project (2016) Economic feasibility analysis for central expressway project. Colombo, Sri Lanka
4. Hafza M, Jayathilaka W, Sathyaprasad I (2018) A comparative study travel time and distance in the estimation of inter district trips. ICSBE1018-492
5. Sliupas T (2006) Annual average daily traffic Forecasting using different techniques. Transport 38–43
6. Yu-qin F, Jun-qiang L, Gui-e X, He YH (2013) Route choice model considering generalized travel cost based on game theory. Math Probl Eng 2013(5)

Finite Element Analysis of Shear Strength Degradation of Reinforced Concrete Members with Corrosion

R. A. C. G. Ranasinghe and J. M. R. S. Appuhamy

Abstract Many reinforced concrete structures are exposed to adverse environmental conditions that lead to the corrosion of embedded steel reinforcement which causes the reduction of structural performance in the context of flexural strength, compressive strength and shear strength etc. Previous researchers mainly focused on the effects of corrosion damage on flexural behavior of reinforced concrete members and effects of corrosion on shear behaviour is not properly investigated. Finite element analysis has become a tool in analysing of reinforced concrete structures with adequate modeling assumptions. Therefore, this study was conducted to investigate the shear failure mechanism and shear capacity in longitudinally reinforced concrete beams with limited transverse reinforcement subjected to different levels of corrosion. Numerous finite element analyses were performed on concrete members with different corrosion conditions. Few concrete specimens were undergone accelerated corrosion to reduce cross sectional area of rebar thus affecting required the level of corrosion. The finite element analysis results were compared with experimental results in order to validate the developed finite element models. A parametric study was done by varying the corrosion damaged parameters and an averaged diameter with a maximum corroded pit was considered corrosion condition modelling. Residual shear capacity and percentage reduction in shear strength was analysed in accordance with corrosion damaged parameters. Empirical equations were developed to predict the residual shear capacity of corrosion damaged reinforced concrete members which can be used by structural engineers in making timely decisions.

Keywords Reinforced concrete · Corrosion · Finite element analysis · Corrosion condition modelling · Shear strength

1 Introduction

Corrosion of reinforcing steel is the predominant deterioration mechanism of reinforced concrete structures throughout the world. A study by Koch et al. [3] stated

R. A. C. G. Ranasinghe (✉) · J. M. R. S. Appuhamy
Department of Civil and Environmental Engineering, University of Ruhuna, Galle, Sri Lanka

R. Dissanayake et al. (eds.), *ICSBE 2020*, Lecture Notes in Civil Engineering 174,
https://doi.org/10.1007/978-981-16-4412-2_22

that 15% of the U.S. bridges are structurally deficient because of corroded steel. The annual direct cost of corrosion was estimated to be $8.3 billion, which includes replacement or maintenance of the deficient bridges. The indirect cost, such as traffic delays, was estimated to be 10 times that of the direct cost [3]. Predicting the residual strength capacity of the structure at the prevailing corrosion condition, with the predefined empirical equations developed by considering the geometrical change of the member at any condition is a good move towards the mitigation of hazards caused by the reduction in structural performance of concrete. However, only limited information is available for condition assessment and structural evaluation. Finite Element Analysis is an approach that can address such kind of situations. However, this requires modelling assumptions. Assessment of the sensitivity of results to the modelling assumptions requires parametric study and validation with experimental results. This paper presents the details for finite element analysis of concrete damaged reinforced concrete members subjected to shear and provides the behaviour of shear capacity of a corrosion damaged reinforced concrete member under different levels of corrosion.

2 Background

Appuhamy et al. [1] has stated two equations on corrosion condition modelling (CCM) to investigate regarding parameters in their research. It is conveyed that with these proposed analytical models with CCM parameters shows a good agreement with experimental results. Figure 1 portrays the CCM parameters that are taken into consideration.

With the experimental data, Appuhamy et al. [1] developed the graphs shown in Fig. 2 and equations for the corroded pit diameter and the corroded pit thickness were developed.

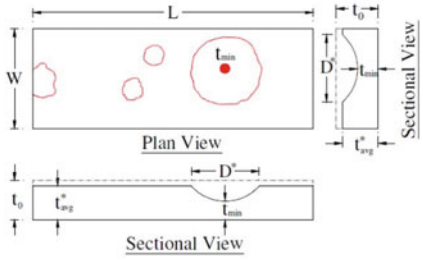

W - width of the steel plate
D - diameter of corroded pit
$t_{c,max}$ - maximum corroded depth
t_{avg} - average thickness
t_o - initial thickness
t_{min} - minimum thickness

Fig. 1 CCM parameters

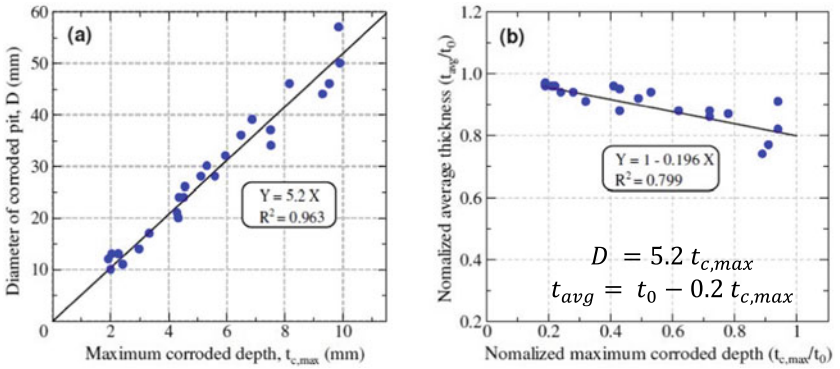

Fig. 2 Behaviour of corroded depth and diameter of corroded pit according to experimental results

3 Methodology

The methodology consists of two types of approaches namely Finite Element Analysis and the Experimental analysis as portrayed in Fig. 3.

The reduction in shear capacity of a RC beam due to the geometrical change was simulated and analysed by the Finite Element analysis software ABAQUS CAE. RC beams with different levels of corrosion were modelled as per the studies of Appuhamy et al. [1]. An experimental approach was done in order to validate the models. An accelerated corrosion was applied to the experimental RC beams as the time is a constraint for a natural corrosion. After the models were validated, a parametric study was carried out by changing the pit size and pit location in the models. Empirical equations for different parameters were derived by the results obtained.

Fig. 3 Methodology

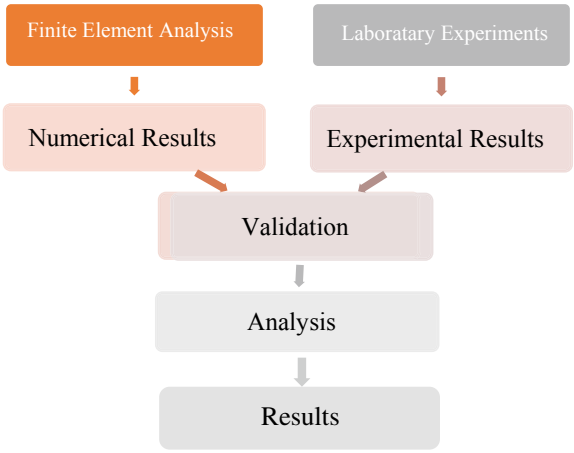

Fig. 4 Experimental r/f beam setup

Table 1 Test specimens for the experimental analysis

Experiment type	Corrosion condition	No. of beams casted	
		Corroded specimen	Control specimen
Testing of shear behaviour	Mild	3	4
	Moderate	3	
Total			10

3.1 Experimental Analysis

A shear critical beam was made with the size of 120 mm × 200 mm × 1500 mm as under reinforced beams to ensure the failure of the section of interest. Ø 10 mm deformed tension and compression bars with Ø 6 mm smooth shear links were applied. Shear links were spaced at 100 mm and 250 mm intervals as shown in Fig. 4. Table 1 portrays the combinations of the beams tested with the different levels of corrosion.

Corrosion of the embedded steel in the RC beams is a challenging task within a limited time period. To overcome this, the embedded reinforcement in the RC beams were corroded by an impressed current less than 1 A and accelerated the procedure. A DC power supply was used with 3 A and 30 V. The anode of the power supply connected to the embedded reinforcement and cathode was connected to a copper plate. The electrolyte used is NaCl solution of 5%. The time to corrode different levels were calculated with Faraday's law of estimation. So, when time of corrosion is finished the samples were taken out from the corrosion tank for testing purpose (Fig. 5).

3.2 Finite Element Analysis

The parts of concrete beam, stirrups and reinforcement bars were modelled. The materials were defined. As per Hafezolghorani et al. [2], Concrete damaged plasticity properties were conveyed and the tensile tests were done to find the material

Fig. 5 Experimental approach

properties of embedded reinforcement. Then the sections were made from the parts and the sections were assembled together to make a comprehensive RC beam. Interactions were given between the different types of sections to act them as one single component. The parts were meshed thereafter as the finite element analysis is based on discrete local approximations of the larger domains. The boundary conditions and loading were applied into the model and it was analysed. The model and the initial results are shown below (Fig. 6).

It can be seen that the maximum principle strain was developed in the shear critical side as well as the failure was occurred in the referred side.

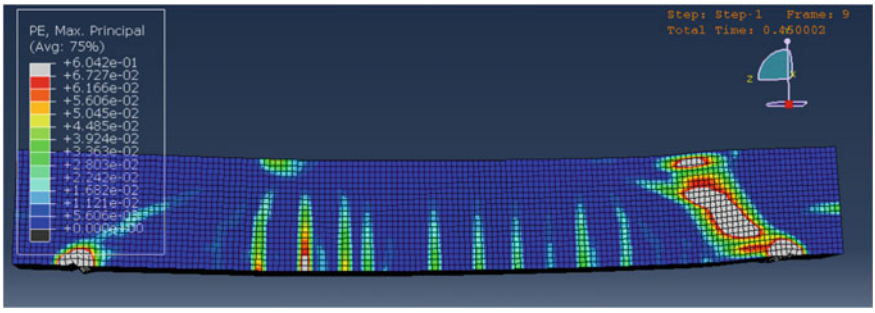

Fig. 6 The finite element analysis simulation

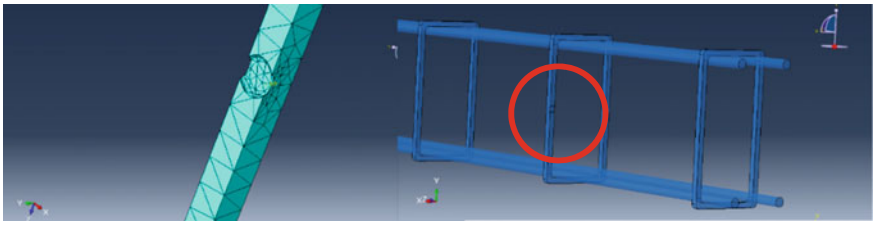

Fig. 7 Corrosion condition modelling (CCM)

3.3 Corrosion Condition Modelling (CCM)

The simulation was done according to the CCM related literature review by Appuhamy et al. [1]. The CCM review was modelled based on a corroded steel plate. By relating this theory to the reinforcement bars, the corrosion can be simulated. Corroded pits were modelled in the transverse bars of the RC beam as portrayed in Fig. 7. The simulation was done for minor, and moderate conditions of corrosion.

4 Results and Discussion

The Experimental results were obtained by testing the beams under four-point loading scheme. The ultimate shear capacity and the maximum deflection of the experimental specimens were obtained through the data loggers. The corresponding FEM data also obtained. The results were validated by the means of visual observation, ultimate shear strength and load deflection curves. Figure 8 portrays the validation by visual observation.

The validation was further done by obtaining the load–deflection curves for the FEM approach and experimental approach. The significant point of yielding and ultimate shear strength was determined from the two curves (experimental and modelled)

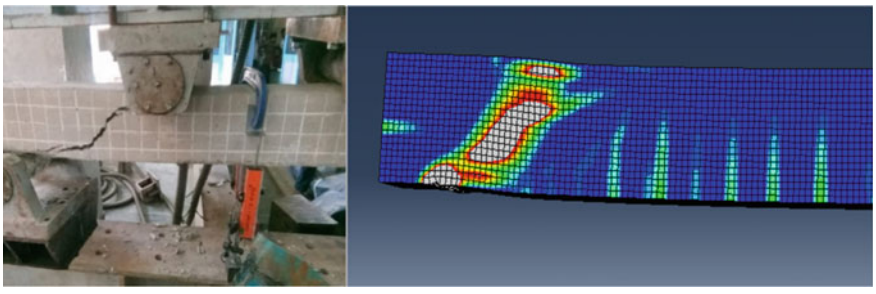

Fig. 8 Validation by visual observation

to verify the reliability of the model. The load–deflection curves for the experimental approach and the FEM approach were obtained as shown in Fig. 9.

The parametric study was done by developing corroded pits in the control beam model. The minor corrosion pits were simulated with $\mu = 0.77$, 0.82 and 0.91 as per Appuhamy et al. [1]. The maximum corrosion pit location was changed from 50 mm, 300 mm, 550 mm, and 800 mm from the free end. Only the shear critical side of the beam was subjected to the parametric study as the ultimate failure occurs at the shear critical section. The shear capacities of the corresponding models were obtained and analysed. Figure 10 interprets the Percentage reduction of shear strength in the RC beam when the corroded pit location and corrosion condition parameters changed.

The moderate corrosion condition was similarly analysed with $\mu = 0.70$, 0.60 and 0.50. The maximum corrosion pit location was changed from 50 mm, 300 mm, 550 mm, and 800 mm from the free end. The results are shown in Fig. 11.

From the parametric study it can be seen that the shear capacity of a RC beam reduces with the size of the corroded pit and also the shear capacity of a RC beam varies with the location of the corroded pit. Using bivariate linear regression analysis, an equation for the percentage reduction of Shear capacity for minor corrosion condition was developed.

For minor corrosion condition:

Shear capacity reduction percentage

$$S_{R,minor\%} = -0.06\left(\frac{L}{L_0}\right) - 28.52\mu + 26.67 \tag{1}$$

For moderate corrosion condition:

Shear capacity reduction percentage

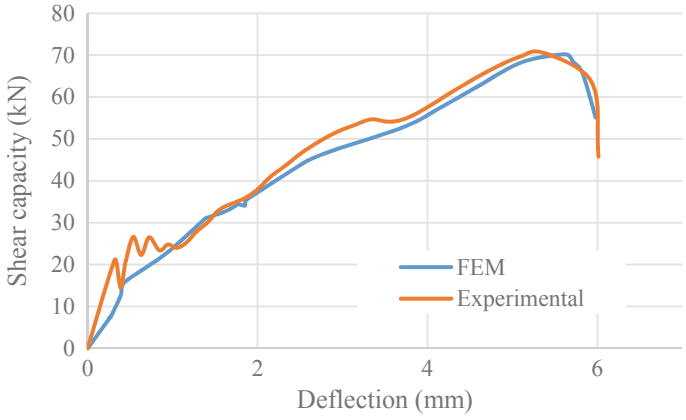

Fig. 9 Validation of finite element analysis with experimental specimens

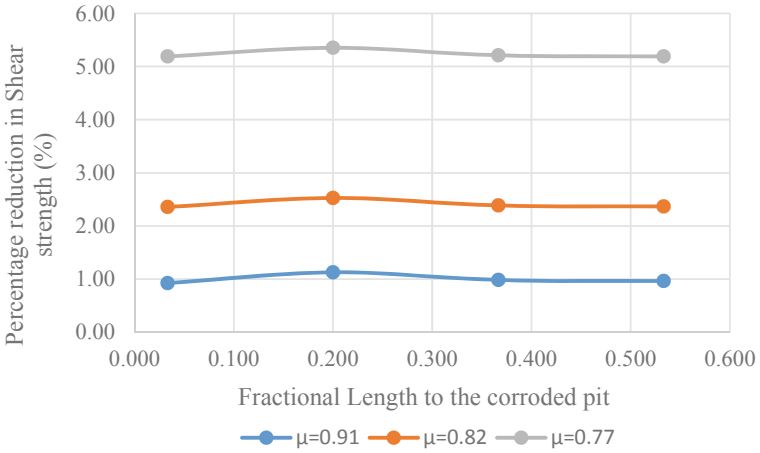

Fig. 10 Percentage reduction in shear capacity for minor corroded beams versus fractional length to the maximum corroded pit from free end

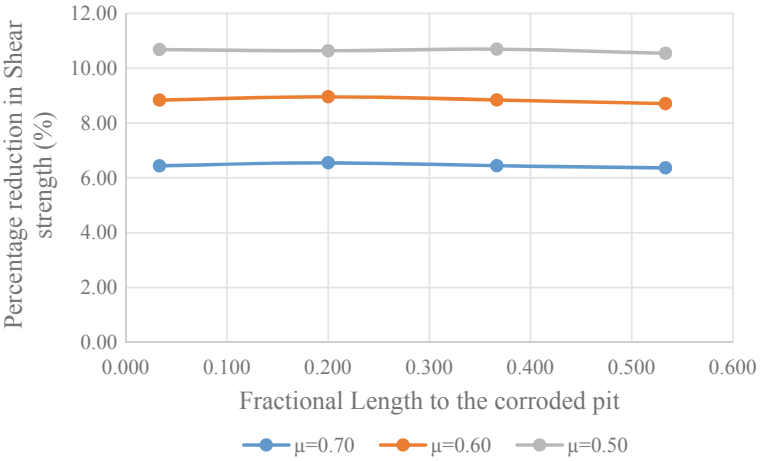

Fig. 11 Percentage reduction in shear capacity for moderate corroded beams versus fractional length to the maximum corroded pit from free end

$$S_{R,moderate\%} = -0.25\left(\frac{L}{L_0}\right) - 20.95\mu + 21.28 \tag{2}$$

$$\mu = \frac{t_{min}}{t_0} \tag{3}$$

t_o Initial thickness.
t_{min} Minimum thickness.

L Initial length of the RC beam.
L_0 Length of corroded pit from free end of the beam.

5 Conclusion

This study conveys the reduction of shear capacity of a corroded reinforced concrete beam and the prediction of strength reduction amount of the structural member, beam with similar condition for shear failure.

Based on the Finite Element analysis, simulation of minor corrosion condition reduced the shear capacity up to 5.2% and simulation of the moderate corrosion condition reduced the shear capacity up to 10.7%. With the coefficients of the linear regression analysis, it can be seen that the influence on the corrosion condition is greater than the influence on the corroded pit location for the reduction in shear strength of a RC beam.

This research only considered the reduction of area during corrosion to simulate it in ABAQUS. But there are many other factors to be considered for a good agreement of values like changes in the ductility of reinforcing steel bars due to pitting corrosion, reduction of concrete cover due to cracking or spalling, changes in strength and ductility of concrete in compression because of micro-cracking induced by corrosion of the reinforcing bars, changes in tension stiffening because of cover cracking and bond deterioration, changes in the bond between the reinforcing bars and concrete.

Moreover, with an aid of a comprehensive study, timely decisions can be made in case of corrosion damaged RC structures and the indirect costs of corrosion damage can be minimized.

References

1. Appuhamy JMRS, Kaita T, Ohga M, Fujii K (2011) Analytical study on significance of corroded surface measurement on residual strength prediction. In: Proceedings of the Twelfth East Asia-Pacific Conference on Structural Engineering and Construction. Elsevier Ltd., pp 2261–2262
2. Hafezolghorani M, Hejazi F, Vaghei R, Jaafar M, Karimzade K (2017) Simplified damage plasticity model for concrete. Struct Eng Int 27(1):68–78
3. Koch GH, Brongers PH, Thomson NG, Virmani YP, Payer JH (2002) Corrosion costs and prevention strategies in the United States. Federal Highway Administration, Washington, DC, Report No. FHWA-RD-010156

Investigation of the Best Joint Type for Combining of the Finger Jointed Timber Panel in Board Production

C. K. Muthumala, S. De Silva, P. L. A. G. Alwis, and K. K. I. U. Arunakumara

Abstract Waste sawn timber material in furniture factories and short length of sawn timber are serious problems in timber industry. To further suggest ways to minimize the waste, by applying a jointing system, this paper utilizes the finger-jointed techniques. Using this method, waste timber planks, trimmings and edgings can be used as finger-jointed boards and furniture in sustainable way. Finger joint technique is also used to eliminate wood defects which weaken the strength of sawn wood planks. Finger joint technology is used in structural and non-structural applications. Furniture mainly belongs to non-structural category. This study was conducted to **i**nvestigate the best joint type for combining of the finger-jointed timber panel in board production. Shear test was done to determine the most suitable joint type which could be employed in combining two finger-jointed timber panels. Shear test was performed for Pine—*Pinus carebaea* (soft wood) and Teak—*Tectona grandis* (Hard wood) timber types. Clear specimens, butt-jointed and tongue and groove were tested in the shearing apparatus. Eight test specimens of each timber specimens were used to obtain shear strength perpendicular to grains with 0.5 mm/min loading rate was applied using a Universal Testing Machine. Shear strength of Teak specimens with tongue and groove is higher than Teak specimens with butt joint, because bonding area of the tongue and groove specimens is higher than bonding area of the butt-jointed specimens. Specimen part with tongue of Pine is weaker than corresponding part of butt-jointed Pine specimen due to small cross-sectional area of tongue. So, Shear strength of Pine specimen with butt joint is greater than Pine specimen with tongue and groove.

C. K. Muthumala (✉)
State Timber Corporation, Rajamalwatta Road, Battaramulla, Sri Lanka

S. De Silva
Department of Civil and Environmental Engineering, Faculty of Engineering, University of Ruhuna, Hapugala, Sri Lanka

P. L. A. G. Alwis
Department of Agricultural Engineering, Faculty of Agriculture, University of Ruhuna, Mapalana, Sri Lanka

K. K. I. U. Arunakumara
Department of Crop Science, Faculty of Agriculture, University of Ruhuna, Mapalana, Sri Lanka

R. Dissanayake et al. (eds.), *ICSBE 2020*, Lecture Notes in Civil Engineering 174,
https://doi.org/10.1007/978-981-16-4412-2_23

Keywords Finger joint · Joint types · butt joint · Tongue and groove · Shear test

1 Introduction

Timber, one of the oldest and natural building materials is extensively used world-wide in furniture and construction industries. When it is employed in construction and furniture manufacturing industries, off-cut and shorter sections are unavoidable wastes which are often dumped. However due to the fact that timber is a limited resource, any sort of dumping is a matter of great concern [6]. Joining pieces of off-cuts and shorter sections together to make finger joint boards is identified as another alternative use of timber wastes.

Finger joints are described as interlocking end joints formed by machining a number of similar tapered symmetrical fingers in the ends of timber members using a finger joint cutter and then bonded together [2]. Finger joint is recognized to be sustainable, eco-friendly and economically viable technique which minimizes the waste generation in furniture manufacturing and construction activities [8]. Though the technique is relatively new to Sri Lanka the State Timber Corporation (STC) has produced finger joints worth Rs. 5.2 and 7.1 million respectively for the year 2018 and 2019 [7]. When combining finger-jointed timber panels together to make finger-jointed boards, it is important to investigate the best joint type suitable for making finger-jointed boards. Main objective of this study is to investigate the best joint type for combining of the finger jointed timber panel in finger-jointed board production.

2 Methodology

Shear test was done to determine the most suitable joint type which could be employed in combining two finger-jointed timber planks. Wood samples taken from matured Teak (*Tectona grandis*) and Pine (*Pinus carebaea*) trees (30–40-year age) were collected from Boossa timber complex of the State Timber Corporation in Sri Lanka. Specimens were prepared from defects free, heart wood pieces with straight grain in breast height portion with eight replicates for each test. The highest mean tensile strength was obtained from PVAc-SWR glue type used in finger joint production in Sri Lanka [5]. Hence PVAc-SWR glue type was used to combine two timber pieces together. Standard size of shear perpendicular to grain test specimen is 50 × 50 × 50 mm (2 × 2 × 2 inch) (with 1 inch L or T section) as shown in Fig. 1. Timber samples were seasoned to reduce moisture content down to 12%. This study was conducted at wood laboratory in State Timber Corporation, Battaramulla, Sri Lanka. All the tests were performed according to BS 373:1957 [1].

Clear specimens, butt-jointed and tongue and groove were tested in the shearing apparatus as illustrated in Fig. 2. Eight test specimens of each timber specimens were

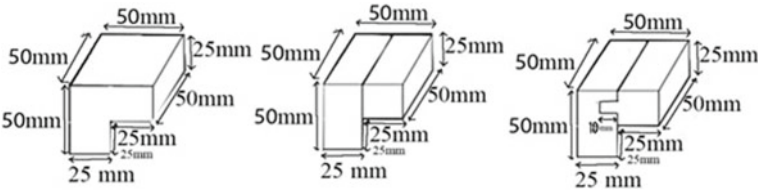

Fig. 1 Specimens for shear test

Fig. 2 Shearing tool used for the shear test

used to obtain shear strength perpendicular to grains. 0.5 mm/min loading rate was given using UTM.

The number of specimens prepared in each set (three joint types and two timber types) for shear measurements are given in Table 1 (Fig. 3).

Equation 1 was used in calculating the shear strength.

$$\text{Shear Strength Capacity} = \frac{\text{Maximum load act on sample}}{\text{Shear Area}} \tag{1}$$

Table 1 Specimen details for shear test

Joint type	Timber types	Number of specimens
Clear specimen	Teak	08
	Pine	08
Butt joint	Teak	08
	Pine	08
Tongue and groove	Teak	08
	Pine	08

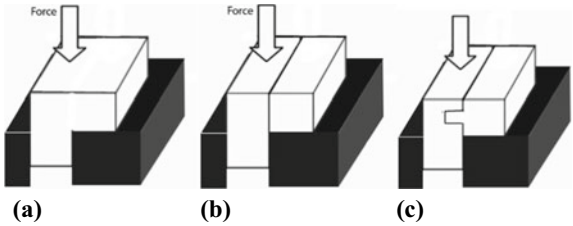

Fig. 3 Loading set-up for shear test. **a** Clear specimen. **b** Butt-jointed specimen. **c** Specimen with tongue and groove

3 Results and Discussion

Average shear strength of different joint types are shown in Table 2.

Failure modes of the Teak and Pine timber specimens are shown in Figs. 4 and 5.

Table 2 Average shear strength of different joint types (N/mm^2)

Joint type	Pine	SD	Teak	SD
Clear specimen	2.373	1.21	2.720	0.10
Butt joint	2.453	0.50	1.587	0.52
Tongue and groove	1.640	0.35	1.840	0.31

SD Standard deviation

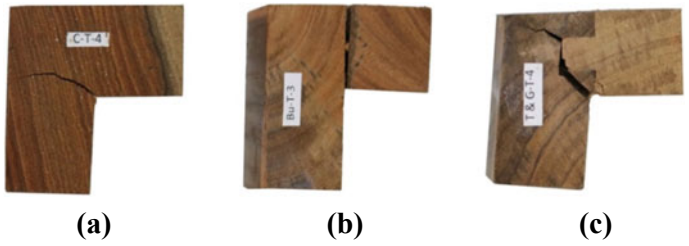

Fig. 4 Failure modes of shear test in teak **a** clear; **b** butt; **c** tongue and groove

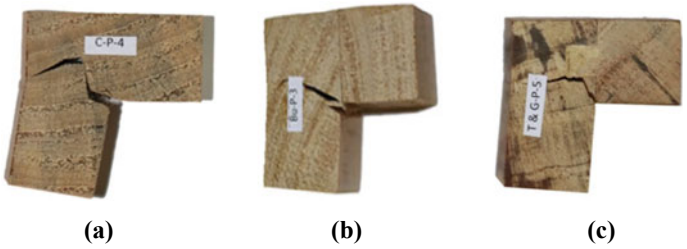

Fig. 5 Failure modes of shear test in pine **a** clear; **b** butt; **c** tongue and groove

According to Table 2, Shear strength of clear wood specimens shows the highest strength values than specimens with butt-jointed and tongue and groove jointed. Considering the butt joint and tongue and groove joint, clearly shows that, butt-jointed specimens of Pine (soft wood) has the highest shear strength rather than clear specimens and tongue and groove-jointed specimens.

Figure 6 depicts that butt-jointed Teak specimens shows the lowest shear strength. That means, when combining two timber planks of Teak, it is not suitable to use a butt joint. Mean shear strength value of Tongue and groove joint of Teak is higher than Butt joint of Teak. But Mean shear strength value of Tongue and groove joint of Pine is lesser than Butt joint of Pine. So, when two timber planks combining together, Butt joints are suitable for softwood species like Pine and tongue and grove joints are more suitable for Teak (Fig. 7).

The ability of the adhesive to penetrate into wood species dependent and is generally greater for early wood than for late wood, especially in softwoods like Pine and for vessel elements in hardwoods [3]. Frihart et al., showed that some wood species, such as teak (*Tectonia grandis*), are hard to bond because they have oily extractives that limit the ability of the adhesive to come into contact with the wood and therefore provide a chemically weak boundary layer. Frihart and Hunt [4] reported

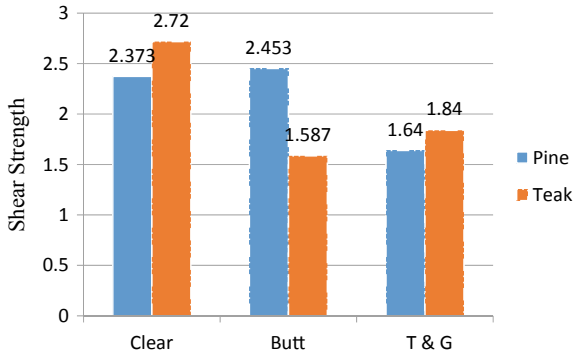

Fig. 6 Variation of shear strength versus joint types

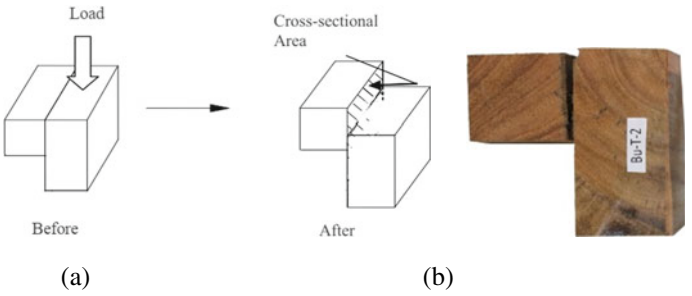

Fig. 7 Some failure mode of butt-jointed teak specimen. **a** Schematic diagram. **b** Tested teak specimen

that high-density woods are difficult to bond because the thicker cell walls and smaller diameter lumens, adhesives do not easily penetrate into the wood, limiting mechanical interlock to less than two cells deep. Much greater pressure is required to compress stronger, stiffer, high-density wood to bring contact between wood surfaces and adhesive.

Shear strength of Teak specimens with tongue and groove is higher than Teak specimens with butt joint. Because bonding area of the tongue and groove specimens are higher than bonding area of the butt-jointed specimens.

Specimen part with tongue of Pine is weaker than corresponding part of butt-jointed Pine specimen due to small cross sectional area of tongue. So Shear strength of Pine specimen with butt joint is greater than Pine specimen with tongue and groove.

4 Conclusion

Based on the results obtained from the study conducted, the following conclusions can be drawn.

Shear strength of Teak specimens with tongue and groove is higher than Teak specimens with butt joint, because bonding area of the tongue and groove specimens are higher than bonding area of the butt-jointed specimens.

Specimen part with tongue of Pine is weaker than corresponding part of butt-jointed Pine specimen due to small cross-sectional area of tongue. So, Shear strength of Pine specimen with butt joint is greater than Pine specimen with tongue and groove.

When two timber planks are combined together in finger-joint production, butt-joints are suitable for softwood species like Pine and tongue & grove-joints are more suitable for Teak.

References

1. British Standard Institution (1999) BS 373:1957, Methods of testing small clear specimens of timber. British Standards Institution, London
2. British Standard Institution (2014) BS EN 15497:2014. Structural finger-jointed solid timber—Performance requirements and minimum production requirements. European Committee for Standardization, B 1000 Brussels
3. Frihart CR, Wiedenhoeft AC, Jakes JE (2007) Wood bonding in the furniture industry and the effect of changing wood supply, In: Practical solutions for furniture and structural bonding. International workshop, Larnaka—Cyprus, 22–23 March 2007, TEI of Larissa, Department of Wood & Furniture Design & Technology, Terma Mavromichali, GR-43100 Karditsa, Greece
4. Frihart CR, Hunt CG (2010) Chapter 10: Adhesives with wood materials—bond formation and performance. In: Wood handbook—wood as an engineering material. General Technical Report, FPL-GTR-190. United States Department of Agriculture, Forest Service, Forest Products Laboratory, Madison, WI, pp 10-1–10-24

5. Muthumala CK, De Silva S, Alwis PLAG, Arunakumara KKIU (2018) Investigate the most suitable glue type for finger-joints production in Sri Lanka. Res J Agric Forestry Sci 6(11):6–9
6. Muthumala CK, De Siva S, Arunakumara KKIU, Alwis PLAG (2020) Identification of joint efficiencies in 13 mm finger jointed timber species used in Sri Lanka. In: ICSBE 2018. LNCE 44. Springer, Singapore, pp 261–267
7. Performance Report (2019) Finance Division, State Timber Corporation
8. Sandika AL, Pathirana GDPS, Muthumala CK (2017) Finger joint timber products for effective utilization of natural resources: an analysis of physical properties. Economic factors and consumers' perception. In: International symposium on agriculture and environment, University of Ruhuna, Sri Lanka, pp 109–111

Investigating the Effects of Offset Distance in CSH on Steel Plates Under Three-Point Flexural Cyclic Loads in the LCF Range

S. Abeygunasekera, J. C. P. H. Gamage, and S. Fawzia

Abstract This paper aims to investigate the effects of offset distance of crack stop hole (CSH) on steel plate with respect to its loading point. Laboratory tests and finite element simulations were performed to estimate the effect of offset distance from the midpoint of the specimens. The experimental study was performed in segments of rectangular plate stresses with a cyclic flexural load which applied through a mid-plane of the top surface of the specimen. 5 Hz frequency and 2 kN constant amplitude fatigue test were performed in the low cycle fatigue (LCF) range up to 10,000 cycles. Also, crack stop holes of 16 mm diameter were placed at the different offset distance from midpoint up to 100 mm in the range of 20 mm, and their effectiveness in Yield strength was evaluated by using laboratory test and test results were validated using a cyclic J-integral option using the ABAQUS FEM technique. The results of laboratory test as well as numerical analysis were synonymous. The offset distance of the CSH indicated a significant variation in the yield strength which in the range of 26.5–56.8% compared to the CSH at midpoint. This investigation reported a significant yield strength variation in the range of 19.3–42.1% with respect to CSH placed at mid-point of the specimen.

Keywords Location of CSH · Yield strength · 3-point flexural cyclic load · LCF · J-integral

1 Introduction

A considerable amount of research studies in the past decade highlighted the capability of delaying crack initiation by any CSH technique. However, this technique could be considered as a temporary solution and there are limitations due to the geometric constrain and the location of the crack tip. The reason is, in some cases it is impossible to drill a hole with a desired diameter as obtained from designed, due

S. Abeygunasekera (✉) · J. C. P. H. Gamage
University of Moratuwa, Katubedda, Moratuwa, Sri Lanka

S. Fawzia
Queensland University of Technology, Brisbane, Australia

R. Dissanayake et al. (eds.), *ICSBE 2020*, Lecture Notes in Civil Engineering 174,
https://doi.org/10.1007/978-981-16-4412-2_24

to the limited space in a structural member. In such situations, may be placed as an undersized CSH as a temporary solution. However, results of such an approach lead to a re-initiation of a crack (Re-cracking) from the CSH after few loading cycles. Therefore, the CSH technique is fully effective only if the diameter of the hole satisfies design requirements. However, if an appropriate CSH is placed on a particular crack tip, it would reduce cross section of the structural member.

The usual practice is attaching additional plates to the cracked member, using a welding technique. However, it was observed that in most cases cracks were re-initiated from the edges of these attached plates. Furthermore, the CSH tightened with bolts and insert pinned or mandrel is another method of controlling the re-cracking process due to continuous service loads on structural members. However, such methods are not a solution for strength losses due to discontinuity of material. CSH strengthened with CFRP material is a good alternative to overcome both issues at the same time. The aim of this work is to investigate the performance of a re-cracking of CSH with respect to offset distance from the loading point.

A limited number of research investigations related to CSH are available in literature. Lin et al. [8] explained regarding the externally bonded CFRP strips greatly reduced strain concentration of the drilled hole. Also, experimental studies conducted by Fisher et al. [6] discussed a repair technique-i.e. drilling a crack stop hole (CSH) ahead of a crack tip while authors emphasized the effectiveness of this technique to control the crack growth. The theory behind the placed CSH at the crack tip is to convert the sharp crack into a blunt notch. The size of the CSH to be drilled is governed by applying loads and material property. However, the success of this technique depends on a large number of parameters such as the length of the crack, location of CSH, type of the loads and loading frequency etc. Furthermore, Nakamura et al. showed a CFRP patching technique is an excellent first-aid technique for prolonging the fatigue life [11]. According to investigations of Miller et al. [10] Carbon Fiber Reinforced Polymer have been successfully used to replace such steel plates due to their excellent material characteristic such as light weight and better fatigue performance [10]. The combined effect of drilling holes and adhesive patches CFRP techniques should be developed as a new technique. Interestingly, the crack repairing guidelines were introduced by Indian railways manual for Indian railway bridges in 1998. The authors recommended a 7 mm diameter CSH place ahead of crack tip and welding a plate over the crack is a permanent solution to retard the crack growth. Fisher et al. [9] conducted a series of fatigue tests on steel plates strengthen by using CFRP strips. The results showed that the fatigue resistance of the joints was at least comparable with welded cover plates. Miller et al. [10] conducted two different research programs and no de-bonding was reported and the retrofit was then regarded to have good fatigue performance. Liu et al. [7] conducted a series of fatigue tests using high and medium modulus CFRP strips bonded steel plates. After the fatigue loading, tensile tests were performed to evaluate the residual bond strength capacity. The influence of the fatigue loading on bond strength was marginal and bond slip stiffness reduction was reported. Furthermore, interfacial de-bonding was observed for medium modulus CFRP and fiber breakage reported for high modulus CFRP. Similarly, Deng et al. [5] conducted an experimental program on small-scale

steel beams strengthened with CFRP strips. They reported that bonded joints crack nucleates and grows firstly in mode-I [5]. Also, Moy studied the effect of cyclic loading on epoxy curing and test results indicated a progressive stiffness, increase of the CFRP strengthen specimen as the epoxy cured. Interestingly, beams subject to higher loads during curing did not fully develop the adhesive bond. Similarly, Zhang et al. [14] beam specimens were exposed to loads varying between an upper and a lower limit throughout the curing period. Bocciarelli et al. [4] conducted fatigue tests on strengthened steel plates using CFRP strips at different loading conditions and authors recorded the stiffness degradation of the CFRP strengthened member.

However existing literature has not reported sufficient data on the repair effect achieved by combined crack stop holes with externally bonded CFRP strips [8]. For example, it has been proven that in comparison with drilled holes, the fatigue strength was greatly increased when using both drilled holes and CFRP strips on small coupon specimens of flat steel plate [13]. Therefore, in this study, the effect of repair using both drilled holes and externally bonded CFRP strips is examined experimentally using a CSH rectangular plates.

2 Specimen Preparation and Material

2.1 Overview

The specimens were designed according to the guidelines of ASTM D 790 standards [3]. The steel plates with a cross-section 40 mm (width) and 5 mm (thickness) were used for sample preparation. Also, the length of the plate member was chosen as 280 mm and the effective span was considered 240 mm. A total of twenty-four rectangular cross sectionals flat steel plates were prepared for this study. The schematic diagram of each test specimens bonded with CFRP is shown in Fig. 1.

Prior the application of the CFRP, surface preparation of the steel plate is very important to ensure effective load transfer between steel plate and the CFRP sheet. Therefore, surface preparation could be considered as the main factor when influencing bond performance; failure mechanism and the durability of the CFRP strengthening method. Various types of surface preparation techniques could be identified for pre-treatments of metallic materials. According to an investigation conducted by Baldan such techniques could be classified as chemical, mechanical, electrochemical, and thermal process [1]. The theory behind surface preparation of steel is the enhancement of the formation of chemical bonds between the metal surface and the epoxy adhesive. Therefore, when selecting a treatment method, the chemically active surface should be confirmed before the CFRP laminates while the surface should be free of any kind of contamination. In addition, the process of cleaning supports to remove weak layers, degreasing, re-cleaning and escape oil or other potential contaminants from the metal surfaces. However, the selected surface preparation technique should have the facility for practical applications and

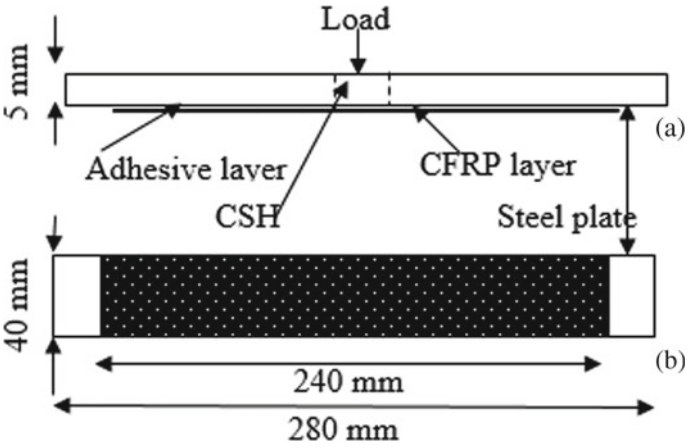

Fig. 1 Schematic diagram of CSH: **a** Side view, **b** plan view

should also be environmentally safe. The most effective way for surface preparation is recommended to be grit blasting [12]. However, the grit blasting method is not available at University of Moratuwa laboratories. Therefore, an angle grinder was used for surface preparation of samples and resulted surface is shown in Fig. 2a. Dust particles were removed using an acetone. The primer consist of two parts (base and the primer) which was mixed into weight ratios. A thin layer of primer coat was applied on the cleaned steel surface according to the manufacturer's guidelines as shown in Fig. 2b and the samples were kept for about an hour before bonding applications.

Normal modulus MBrace CF130 and Areldite 420 epoxy were selected in this strengthening process. A two-part epoxy adhesive (Araldite 420) was properly dosed with 1:2 ratios by volume and mixed until a homogeneous light gray paste was obtained. This paste was applied to the pre-treated steel surface during its pot life according to the manufacturer guidelines. Then a thin layer of adhesive was uniformly applied on top of the primed steel surfaces.

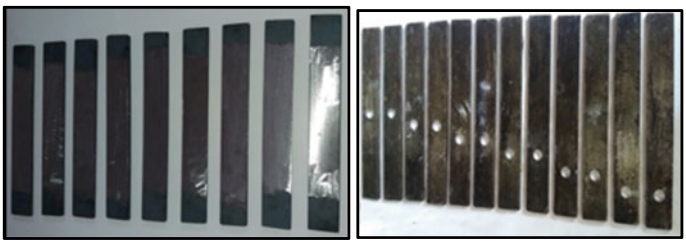

Fig. 2 Specimen preparation for laboratory test: **a** Grinded steel surface, **b** Primer coated steel surface

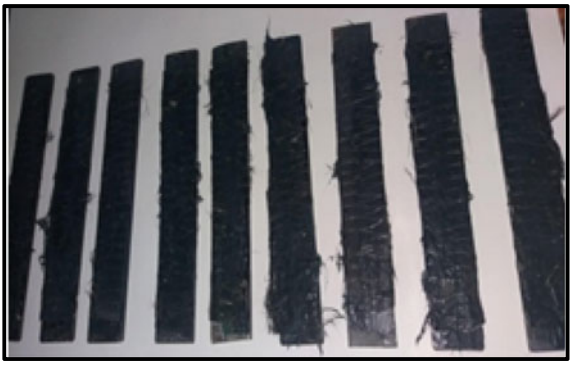

Fig. 3 The CFRP strengthened specimen

A fibre layer of CFRP fabrics (Mbrace CF 130) were cut to the explained dimensions (200 mm × 40 mm) and it was placed on top of the adhesive layer. The test specimens are shown in Fig. 3.The excess epoxy and air bubbles were removed using a ribbed roller moving in the direction of fibres. Finally, samples were kept for 72 h according to manufacturer provided guidelines.

3 The Experimental Program

The experimental program was performed at the structural testing Laboratory of the Department of Civil Engineering of the University of Moratuwa. The aim of the testing activity was to investigate the cyclic flexural behaviour of the adhesive bond offset CSH with CFRP under LCF. This test setup included two consecutive testing steps called the flexural test and axial tensile test for the same specimen. Firstly, a cyclic flexural load was applied on the specimen, then the tensile test was performed for each specimen.

3.1 Flexural Test Setup

The three-point cyclic flexural tests were conducted using a self-developed 10-kN electro-hydraulic cyclic flexural testing apparatus (see Fig. 4). The testing apparatus has the capability to control load and frequency. Specimens were kept on two cylindrical shaped, supportive rollers with 25 mm diameter each and the span length was fixed at 240 mm between centers of the rollers as shown in Fig. 4a.Each specimen was loaded up to a 10,000 cycle range of low cycle fatigue (LCF) using the developed 3-point cyclic flexural loading apparatus by actuating a spring return hydraulic actuator. The 3-point flexural cyclic load was applied on the specimen at the midplane using a loading nose with 8 mm radius as shown in Fig. 4b**.** The maximum

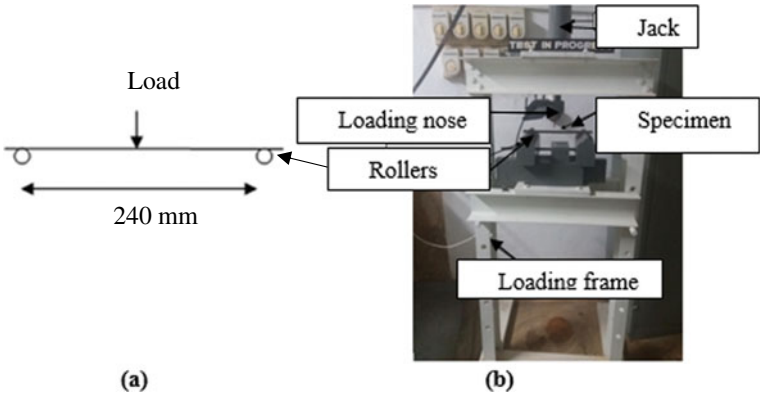

Fig. 4 Cyclic flexural load testing machine: **a** Schematic view, **b** Test setup and instrumentation

deflection in the load direction (Y-direction) at mid-plane was limited to 5 mm. The magnitude of the load and frequency were selected according to the ASTM D7774 standards. A constant amplitude 2 kN load was applied and during the testing period 5 Hz frequency was maintained. The number of cycles counted by using the digital display unit attached with an electro controller and load variation were monitored by using a load cell fixed at the midpoint of the bottom surface of the specimen.

3.2 Tensile Test Setup

After applying the 10,000 load cycles, the sample was removed from the cyclic load testing apparatus and it was attached to the tensile testing machine as shown in Fig. 5. Tensile loads were applied on specimen with 2 mm/min rate of load and measured yield value of each specimen. This procedure was repeated for each specimen within the limits of LCF. Average value of the yield load was recorded for similar specimens too.

4 Test Results

This tests series focus on estimating the average yield strength variation due to cyclic flexural effects on the offset of the CSH. Twenty four specimens were tested with control specimens as shown in Figs. 2b and 3. The yield load, crack initiation, number of cycles and failure mode were monitored during and after testing. The mechanical behaviour of the material is reflected by the yield strength of the material. The average yield strength due to the offset distance is compared with the CFRP strengthened CSH which is shown in Table 1.

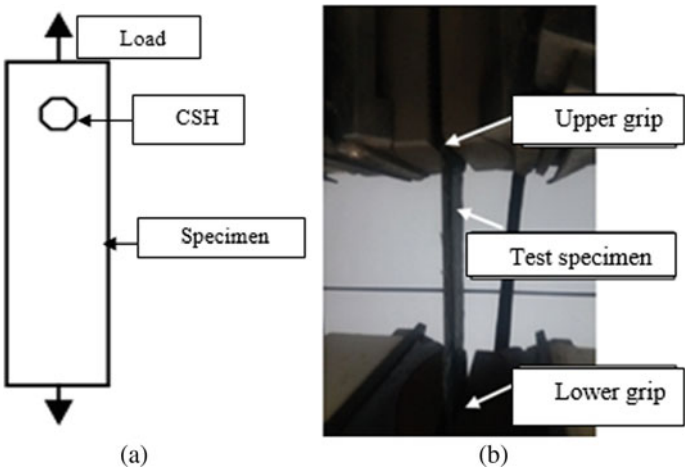

Fig. 5 Axial tensile load testing machine: **a** Schematic view, **b** Test setup and instrumentation

Table 1 Comparison of yield strength variation of unstrengthened and CFRP strengthened CSH

Offset distance (mm)	Number of specimens	Yield strength (MPa)		Strength gain by CFRP (%)
		Un strengthen CSH	CFRP strengthen CSH	
0	2	167.8	290.0	42.1
20	2	228.3	312.5	26.9
40	2	234.8	318.5	26.3
60	2	284.5	352.5	19.3
80	2	388.5	388.0	Insignificant

The comparisons of the CFRP strengthened and un-strengthened CSH shown in the Fig. 6. The common behaviour of both graphs is linear with a slightly different gradient.

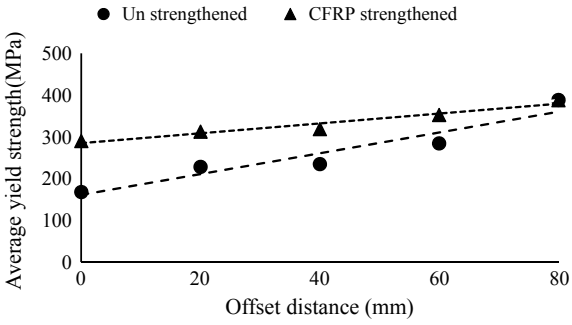

Fig. 6 Comparison of strength gains for CFRP strengthened and un-strengthened offset CSH

5 Finite Element Model

Finite element (FE) models were developed using the commercially available finite element package ABAQUS version 6.14. The models were with the same configurations of the tested plates as given in Fig. 7.The direct cyclic mode under LCF analysis method was used to determine the response of the specimens. Also, the steel plate was modeled as an elastic–plastic metal with isotropic hardening. The Young's modulus and possions ratio were considered as 200 GPa and 0.3 respectively J-integral value of the composite were adopted in FE model to represent the material behaviour.

Each specimen module was loaded with an LCF mode using the direct cyclic option. A 8 mm radius loading nose was used for loads applied and the mid-vertical span was limited to 5 mm. Furthermore, a fatigue load was applied to the specimens at the mid-plane with 5 Hz frequency as shown in Fig. 7. The static general loading method was applied from 0 to 0.02 s and the direct cyclic loading method was applied from 0.02 to 0.2 s. Then, while maintaining the fatigue load under the 2 kN constant amplitude with 5 Hz frequency. The numerical models were run several times until the best validation was achieved. Also, the required number of cycles for crack initiation (N_i) was obtained by using the results of analytical methods and the development of the Power law equation.

In this numerical analysis location of CSH were changed from 0 to 80 mm, and according to the results of the numerical analysis the minimum and maximum J-integral values were obtained. The maximum and minimum values of J integral were taken from data file of the analysis results. The cyclic J-integral value is calculated according to Eq. 1[2]. By using the Power law in Eq. 2 the required number of cycles of re cracking at the CSH is obtained [2]. The result of the CSH offsets from the center of major axis as shown in Table 2. It summarizes the maximum and minimum J-integral values together with the variation of different location from the analytical results.

$$\Delta J = \mathrm{J_{min}} + \mathrm{J_{max}} - \sqrt{\mathrm{J_{min}} + \mathrm{J_{max}}} \tag{1}$$

$$\frac{da}{dN} = 9.85 \times 10^{-4} (\Delta J)^{0.479} \tag{2}$$

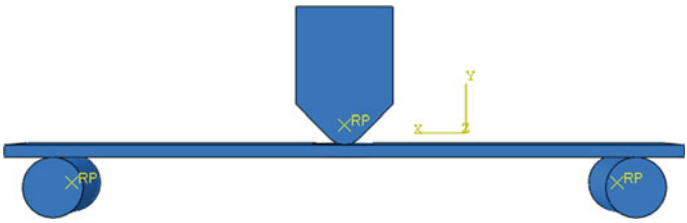

Fig. 7 The geometry for the specimen for FE model

Table 2 Properties of material

Material	Testing standards	Tensile strength (MPa)	Elastic modulus (MPa)	Poisson's ratio
Steel	ASTM A 370–02	583	200	0.3
Araldite -420	ASTM D638-02(a)	29	0.977	0.3
CFRP	ASTM D3039/D3039M	1575	175	0.3

In this analysis, offset distance of the CSH was considered as a main variable. It was changed from 20 to 80 mm and numerical modeled under the cyclic flexural loads. All other parameters except the distance of CSH with respect to the midpoint of the specimen were kept as constant during the analysis. Diameter of 16 mm CSH was placed at the relevant offset distance as explained above. The 3D model visualization of un-strengthened and CFRP strengthened is shown in Fig. 8a and b respectively.

5.1 Element Types and Mesh Density

Different types of elements are available in the finite element package, ABAQUS 6.14 software. The steel plates are modeled using 8-node 3-D solid element (C3D8H), as the three dimensional thick solid geometry leads to improve accuracy in resolving contact problems. Also, the computational time was reduced by introducing 2 mm mesh for the steel plate.

5.2 Material Properties in FE Analysis

The tensile strength and the modulus of elasticity of steel are taken from the experimental data. The steel plates had an average yield strength of 583 MPa, and the modulus of elasticity was 200 GP were reported by a coupon test. Possion's ratio value was assumed as a 0.3.The properties of three materials are listed in Table 2.

5.3 Result of FE Modeling

In this numerical analysis the location of the CSH was considered as a main variable and it varied from 0 to 80 mm respectively at the loading point. The cyclic loads were applied at the midpoint when all other parameters were kept at a constant level except the location of the CSH. Numerically modeled results have exhibited influences of

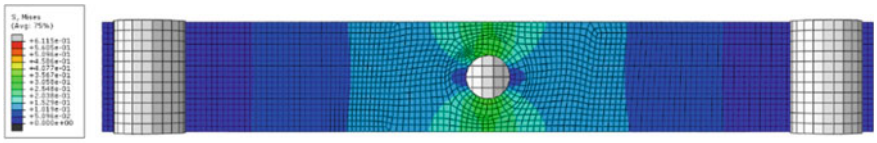

Non offset CSH

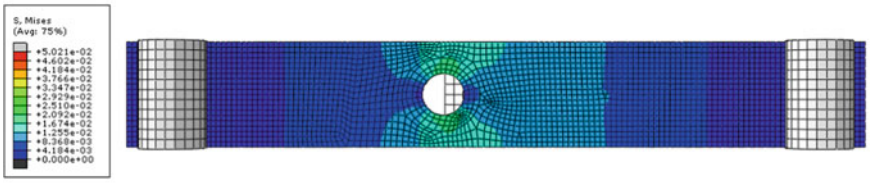

20 mm offset CSH

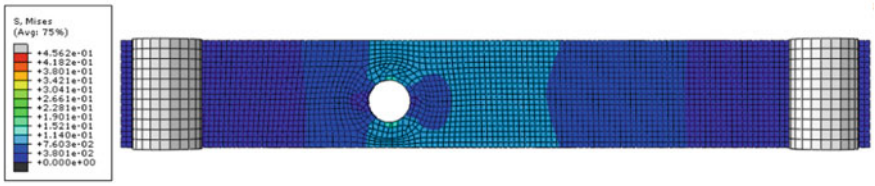

40 mm offset CSH

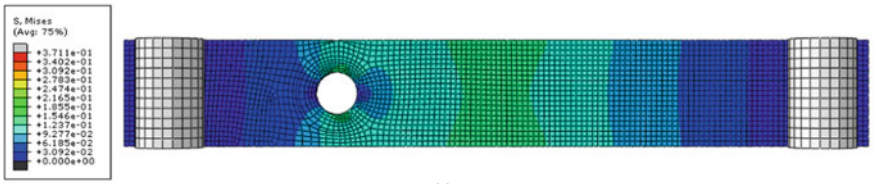

60 mm offset CSH

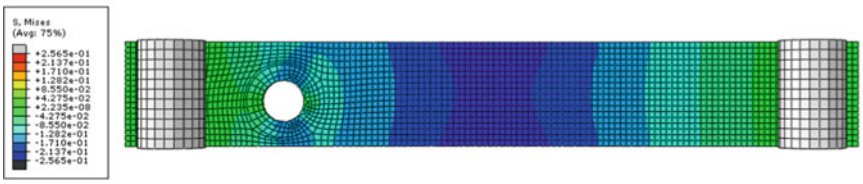

80 mm offset CSH

(a)

Fig. 8 Visualization of the bottom view under 3 points cyclic flexural load with different offset distance: **a** un-strengthened CSH, **b** CFRP strengthened CSH

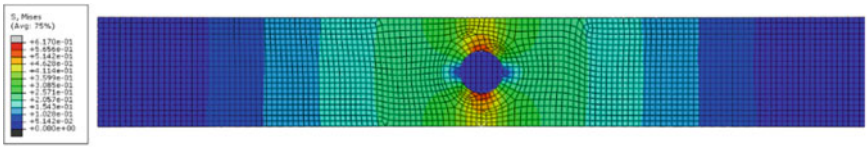

Non offset CFRP strengthened CSH

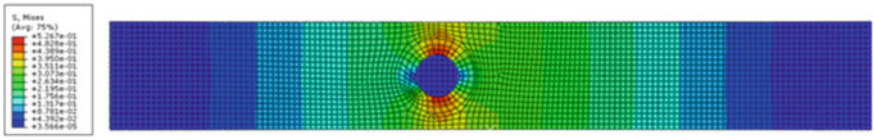

20 mm offset CFRP strengthened CSH

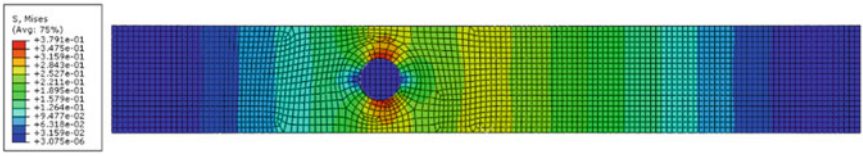

40 mm offset CFRP strengthened CSH

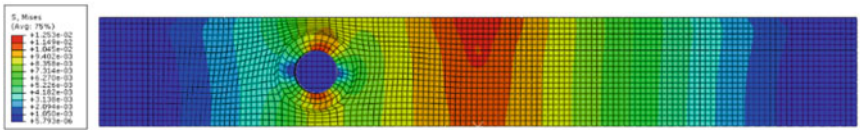

60 mm offset CFRP strengthened CSH

(b)

Fig. 8 (continued)

the location of the CSH with respect to the loading point. The results are tabulated in Table 3.

Figure 9 shows required number of cycle variation of each test series with the CSH diameter due to the effects on 3 points flexural cyclic loads with 2 kN constant amplitude load. As shown in Fig. 9, when the offset distance is increased, the number of cycles also increases in both test series. For a given load and frequency, the best-fit curves could be characterized by similar slopes.

In this numerical analysis, the location of the CSH was considered as a main variable and it varied from 0 to 100 mm respectively at the loading point. The cyclic loads were applied at the midpoint when all other parameters were kept as un-strengthened and CFRP strengthened CSH. Numerically, the modeled results agreed well with the laboratory test results with respect to the location of the CSH.The FEM results are tabulated in Table 4.

Table 3 Cyclic J-Integrals and number of cycles for crack initiation

Offset distance from mid-point (mm)	Cyclic J integral value $\times 10^{-2}$		No. of cycles for crack initiation	
	Un strengthened	CFRP strengthened	Un strengthened	CFRP strengthened
0	5.67	7.39	4011	3534
20	4.62	4.37	4423	4542
40	4.58	2.94	4440	5490
60	3.78	3.23	4868	5246
80	2.01	1.78	6589	6972

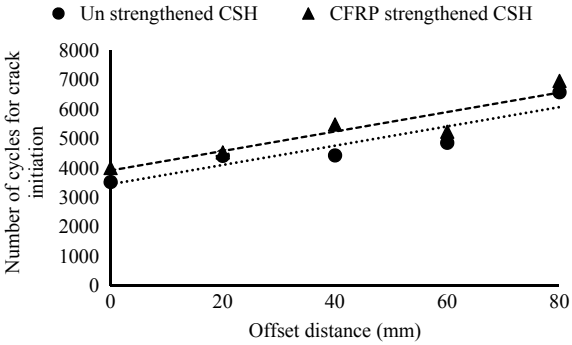

Fig. 9 No of cycles for crack initiation variation with offset distance

Table 4 Yield strength variation with offset distance according to numerical modelling results

Offset distance from mid point (mm)	Non-strengthened CSH		CFRP strengthened CSH	
	Yield load (kN)	Yield strength (Yield load × cross section) (MPa)	Yield load (kN)	Yield strength (Yield load × cross section)(MPa)
0	41.6	207.9	47.2	235.9
20	52.0	260.2	53.4	267.2
40	52.2	261.2	64.6	322.9
60	57.3	286.4	61.7	308.6
80	77.5	387.6	82.0	410.1

When offset distance is increased the Yield strength also increases as shown in Fig. 10. Reason for such behaviour is the stress concentration effect at the CSH location. On the other hand, when the offset distance of CSH increase, residual stresses and notch stress also decreases. The net effect is the increase of the yield strength. FEM results agreed well with the laboratory test results as shown in Fig. 10.

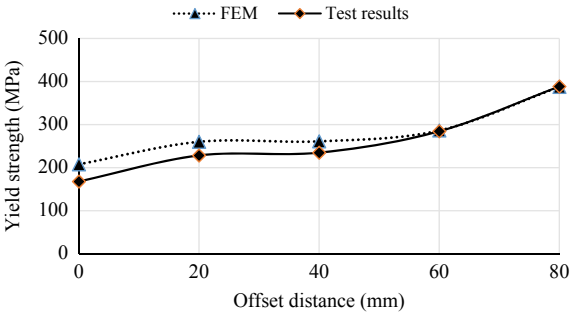

Fig. 10 Comparison of FEM and laboratory test results for un-strengthened CSH

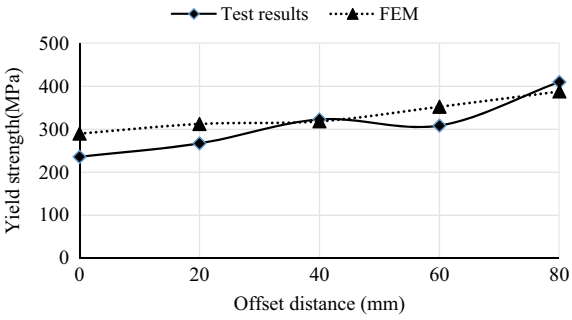

Fig. 11 Comparison of FEM and laboratory test results for CFRP strengthened CSH

When offset distance is increased the yield strength also increases as shown in Fig. 11.The reason for such behaviour is the stress concentration effect at the CSH location. On the other hand, the CFRP material added additional tensile strength and it contributes to re-distribute stress at the CSH. As a result, the overall yield strength increased when compared to non-strengthened CSH. The FEM results agreed well with the laboratory test results as shown in Fig. 11.

6 Discussion

The main purpose of this investigation was to estimate the re- cracking behaviour and yield strength variation of CSH by variation of offset distance. CSH under cyclic loading stress concentration zones are usually exposed to crack initiation. In the present case, the fatigue sensitive zone is surrounded by the CSH. Re-cracking starts at these stress concentration zones depending on the relevant stress level. However, the 3-point flexural cyclic load helps to increase the stresses at the CSH. The effect of yield stress was significant losses and it is mainly governed by the distance of the CSH, as cyclic effects convert hardening properties of material to soften. Furthermore, residual stress also significantly contributes to stress, which occurs due to the drilling and other mechanical process done on the CSH. However, magnitude of loads,

Fig. 12 Failure mode of offset hole

loading frequency; rate of loads and material properties of the parent metal also significantly effects on the results. The tendency of crack initiation is higher at the bottom surface rather than the upper side of the specimen. When offset distance increase with respect to loading point, the stress concentration reduces. As a results average yield load increases. The offset CSH strengthened with CFRP supports to reduce the stress concentration and enhances the tensile strength of the CSH specimen.

6.1 Mode of Failure and Crack Patterns

Since these specimens were prepared by using steel plates, the crack failure occurred at both side of the CSH and was perpendicular to the tensile direction which is the weakest part of the specimen. The cyclic flexural cracks started near the CSH and it appeared at the perpendicular direction of the tensile load as shown in Fig. 12. The failure mode was observed as an interface de-lamination and de-bonding of the CFRP strengthened CSH. Consequently, cyclic load causes to weaken any bond between the metal and the adhesive as well as the adhesive and CFRP sheets.

7 Conclusions

In this study, the flexural behaviour of steel fibre-reinforced CSH under cyclic loading was investigated. From the test results, the following conclusions were obtained:

(1) The fatigue resistivity of CSH with offset distance from midpoint was significantly enhanced with respect to the mid-point, even after the 3 point flexural cyclic loads.

(2) This study recorded yield load increase due to the effects of off-set distance; in the range of 26.5% to 56.8% compared to the CSH at the midpoint.
(3) The yield capacity enhancement of the offset CSH by CFRP material was in the range of 19.3–42.1% with respect to un strengthened CSH.
(4) The result of the FE model agreed well with the laboratory test results in case of un-strengthened as well as CFRP strengthened CSH.

Future Work

Further work should be performed in order to provide a larger data set of cyclic loads and then to provide a more accurate estimation of the yield strength gained by the CSH. Moreover, a parametric study should be conducted in order to investigate their effect on the overall performance while the effects of the CFRP strengthened should be compared with the results of this investigation.

Acknowledgements The authors would like to thank, University of Moratuwa (UOM) for providing support to carry out the work reported in this paper. The authors gratefully acknowledge the staff in the structural engineering and IT laboratory of the Department of Civil Engineering at the University of Moratuwa for their support in carrying out this investigation.

References

1. Baldan A (2004) Adhesively-bonded joints and repairs in metallic alloys, polymers and composite materials: adhesives, adhesion theories and surface pretreatment. J Mater Sci 39:1–49
2. Abeygunasekera S, Gamage JCPH, Fawzia S (2019) Theoritical approch to evaluate the rate of crack growth in crack stop holes using j-integral technique. ICSEM, Kandy, Sri Lanka
3. ASTM D790–10, Standard test methods for flexural properties of unreinforced and reinforced plastics and electrical insulating materials. (2011). D20 10, Ed, ASTM International, West Conshohocken, PA
4. Bocciarelli M, Colombi P, Fava G, Poggi C (2009) Fatigue performance of tensile steel members strengthened with CFRP plates. Compos Struct 87(4):334–343
5. Deng J, Lee MMK, Moy SSJ (2004) Stress analysis of steel beams reinforced with a bonded CFRP plate. Compos Struct 65:205–215
6. Fisher JW, Barthelemy BM, Mertz DR, Edinger JA (1980) Fatigue behavior of full-scale welded bridge attachments (NCHRP Report 227). Transportation Research Board, Washington, DC
7. Liu HB, Zhao XL, Al-Mahaidi R (2005) The effect of fatigue loading on bond strength of CFRP bonded steel plate joints. International Institute for FRP in Construction (BBFS)
8. Lin F, Sun JG, Nakamura H, Maeda K (2012) Fatigue crack repair using drilled holes and externally bonded CFRP strips. In: Bridge maintenance, safety, management, resilience and sustainability, Taylor & Francis, London
9. Matta F (2003) Bond between steel and CFRP laminates for rehabilitation of metallic bridges. University of Padua, Padua, Ph.D Thesi
10. Miller CT, Chajes MJ, Mertz DR, Hastings JN (2001) ASCE J Bridge Eng 6(6, November-December):514–522
11. Nakamura H, Jiang W, Suzuki H, Maeda K, Irube T (2009) Experimental study on repair of fatigue cracks at welded web gus-set joint using CFRP strips. Thin-Walled Struct 47(10):1059–1068

12. Schnerch D, Dawood MR (2006) Proposed design guidelines for strengthening of steel bridges with FRP materials. J Constr Build Mater 21:1001–1110
13. Suzuki H, Okamoto Y (2003) Repair of steel members with a fatigue crack using the carbon fiber reinforced polymer strip. J Constr Steel, JSSC 11:465–472 (in Japanese)
14. Zhang Z, Liu Y, Huang Y, Liu L, Bao J (2002) The effect of carbon-fiber surface properties on the electron-beam curing of epoxy-resin composites. Compos Sci Technol

Modification of Sequential Law for Fatigue Damage Assessment of Steel Structures Based on the Length of Stress/Strain Life Curves

M. A. V. S. G. Meegalla, P. V. D. P. L. Saparamadu, I. M. U. I. Wijayarathna, T. M. Pallewatta, and P. A. K. Karunananda

Abstract One of the main difficulties in stress/strain based fatigue damage estimation is to find a representative 'damage indicator' which can be easily connected with the stress/strain life curve (S–N curve). The mostly used damage indicator model is the Miner's rule but it does not take into account the loading sequence effect. The experimental results are higher than the Miner expectations for increasing type loading and are lower than the Miner's expectations for decreasing type of loading. Recently, a new damage indicator that is based on sequential law has been proposed to capture the load sequence effect more precisely. According to the fundamentals of the stress/strain based approach, the damage point travelling path (damage trajectory) travels along the stress/strain life curve. The obtained results of the sequential law can be further improved if the path of the actual damage trajectory is taken into consideration. This paper proposes a new damage indicator considering the movement of damage trajectory along the stress/strain life curve. Damage indicator values are obtained using MATLAB (2018a) code and confirmed the applicability of the developed new model using a numerical example. Numerical example was selected to capture the effect of multiaxial stress effect and curves based on experimental results and mathematical modes. Increasing and decreasing type loadings were applied. As shown in the numerical results, the obtained results illustrate the real trend of fatigue damage assessment. Therefore, more accurate fatigue life estimation can be predicted using newly proposed curve based fatigue damage accumulation model.

Keywords Fatigue life · Loading sequence effect · Miner's rule · Stress life approach · Sequential law

1 Introduction

Investigation of defects and failures on structural components has an important role in improving structural safety. The identification of the primary cause of failure and

M. A. V. S. G. Meegalla · P. V. D. P. L. Saparamadu · I. M. U. I. Wijayarathna · T. M. Pallewatta · P. A. K. Karunananda (✉)
The Open University of Sri Lanka, Nawala, Nugegoda, Sri Lanka
e-mail: pakar@ou.ac.lk

R. Dissanayake et al. (eds.), *ICSBE 2020*, Lecture Notes in Civil Engineering 174,
https://doi.org/10.1007/978-981-16-4412-2_25

the subsequent analysis enable recommendations for corrective action to be made that conceivably will prevent similar failures from occurring in the future. Purely static loading is rarely observed in modern engineering components of structures because of the majority of structures subjected to fluctuating or cyclic loads, rather than static loads. Those structures fail typically at stress levels significantly lower than the yield strength of the material due to this cyclic load and it is termed as fatigue. Fatigue was first recognized in 1830s. The first known fatigue failure was recorded as Versailles railway accident in 1842.

Fatigue damage is increased with the number of applied load cycles in a cumulative manner and lead to fracture and failure of the structure. When structure is loaded, a crack will be nucleated on a microscopically small scale, this crack then grows macroscopically and finally complete failure of the structure.

Deficiency of coherent theory of fatigue process of structures may be used phenomenological hypotheses on summation of damages. There are many prediction models have been proposed, but no agreed model on remaining fatigue life prediction adequately considering loading sequence effect exist because they are mostly subjected to variable amplitude loading histories in service.

Palmgren-Miner's rule is probably the simplest cumulative damage model used in fatigue analysis [1]. The major limitation of the Miner's rule is the omission of the loading sequence effect and the damage accumulation is independent of stress levels. To prevail over the shortcoming, the new damage indicator commences by sequential law with the stress/strain life curve capture the load sequence effect more precisely [2]. Based on this sequential law, researchers have shown that the results obtained by above method are more accurate than conventionally used Miner's predictions [3].

According to the fundamentals of the stress/strain based approach, the path damage point (damage trajectory) travels along the stress/strain life curve. The obtained results of the sequential law can be further improved if the path of the actual damage trajectory is taken into consideration. This paper describes a new methodology to consider the movement the damage trajectory in stress/strain life curve. Importantly, it retains the original damage transfer mechanism proposed by Mesmacque et al. [2].

2 Proposed Curved Based Damage Accumulation Model

The hypothesis behind the proposed model is that if the physical state of damage is the same, then fatigue life depends only on loading conditions. For example, if the structure is new (damage free) the life can be assessed by the stress/strain curve. This simple concept should be translated after n cycles of loading. At level i, a certain stress amplitude σ_i is applied for a number of cycles n_i, where the number of cycles to failure from the S–N curve for σ_i is N_i; thus, after n_i applied cycles, the residual life is $(N_i - n_i)$. On the stress/strain life curve, life $(N_i - n_i)$ corresponds to an admissible stress σ_{edi} at level i after n_i cycles of loading. The damage stress, σ_{edi} at level i after n_i cycles of loading [2].

Therefore, the damage stress is taken as the stress corresponding to the residual life. The introduced new damage parameter, D_i, was developed, which can be defined as the ratio of the curve length increment of number of cycles for damage stress over the curve length difference between the number of cycles for ultimate stress and the applied stress.

$$D_i = \frac{Curve\ Length((N_i - n_i)\ cycle, N_i\ cycle)}{Curve\ Length(1, N_i\ cycle)} \tag{1}$$

At the first cycle the damage stress is equal to the applied stress, i.e. $D_i = 0$ and at the last cycle the damage stress is equal to the ultimate stress and therefore, $D_i = 1$. The damage indicator is normalized to 1 at rupture. Damage is then translated to level $i + 1$ by the relations

$$\begin{aligned} D_i &= \frac{Curve\ Length((N_i - n_i)\ cycle, N_i\ cycle)}{Curve\ Length(1, N_i\ cycle)} \\ &= \frac{Curve\ Length\left(N_{equiv}\ cycle, N_{i+1}\ cycle\right)}{Curve\ Length(1, N_{i+1}\ cycle)} \end{aligned} \tag{2}$$

Then the calculations were based on the length of stress/strain life curve, the equivalent number of cycles N_{equiv} at level $i + 1$ of n_i cycles at level i. So, if the number of applied loading cycles at the level i + 1 is n_{i+1} the residual life time is then $N_{i+1} - n_{i+1}$. This procedure was continued on this way until the damage stress is equal to the ultimate stress. By this way the loading history is taken into account and the damage caused by n_i cycles at the level i depends on the previous loading. To make this procedure clear, consider the following three level example (Fig. 1).

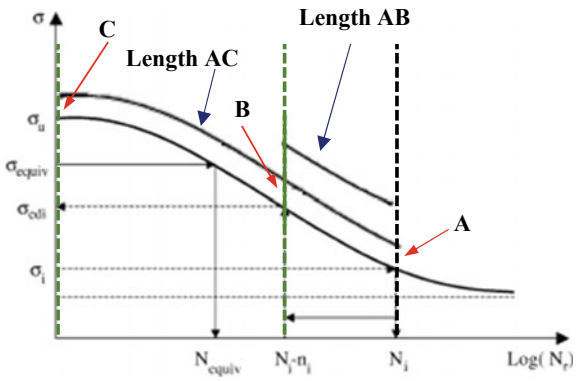

Fig. 1 The damage propagation in stress/strain life curve

2.1 Damage Propagation Over Three Stress Levels

Starting point, first level:

For a stress amplitude σ_1, the number of cycles to failure is N_1. Applying n_1 cycles with amplitude σ_1, residual life is $N_{1R} = N_1 - n_1$. Next, the admissible stress σ_1 corresponding to N_{1R} is calculated, see Figure σ_{1ed} is called damage stress.

The damage corresponding to n_1 cycles applied with amplitude σ_1 is

$$D_1 = \frac{Curve\ Length(N_{1R}\ cycle, N_i\ cycle)}{Curve\ Length(1, N_i\ cycle)} \tag{3}$$

Second level:

The damage is translated from level 1 to level 2 and the equivalent damage stress σ'_{2ed} which induces the same damage can be calculated as follows:

$$D_1 = D'_2 = \frac{Curve\ Length\left(N'_{2R}\ cycle, N_2\ cycle\right)}{Curve\ Length(1, N_2\ cycle)} \tag{4}$$

The residual number of cycles N'_{2R} can be obtained from σ'_{2ed}. For stress amplitude σ_2 the number of cycles to failure from the Wöhler curve is N_2. n_2 cycles can be applied with amplitude σ_2, and the number of residual cycles can be calculated as follows:

$$N_{2R} = N'_{2R} - n_2 \tag{5}$$

The damage stress σ_{2ed} can be calculated from N_{2R}. The cumulative damage at this level is

$$D_2 = \frac{Curve\ Length(N_{2R}\ cycle, N_2\ cycle)}{Curve\ Length(1, N_2\ cycle)} \tag{6}$$

Third level:

The damage is translated from level 2 to level 3 and the equivalent damage stress σ'_{3ed} which induces the same damage can be calculated as follows:

$$D_2 = D'_3 = \frac{Curve\ Length\left(N'_{3R}\ cycle, N_3\ cycle\right)}{Curve\ Length(1, N_3\ cycle)} \tag{7}$$

The residual number of cycles N'_{3R} can be obtained from σ'_{3ed}. For a stress amplitude σ_3 the number of cycles to failure from the Wöhler curve is N_3. n_3 cycles can be applied with amplitude σ_3, and the number of residual cycles can be calculated as follows:

$$N_{3R} = N'_{3R} - n_3 \tag{8}$$

The damage stress σ'_{3ed} can be calculated from N_{3R}. The cumulative damage at this level is

$$D_3 = \frac{Curve\ Length(N_{3R}\ cycle,\ N_3\ cycle)}{Curve\ Length(1,\ N_3\ cycle)} \tag{9}$$

The same procedure can be followed until failure, that is, when D = 1 (Fig. 2).

The above procedure is written with MATLAB code. Using this code, damage calculation is automated.

3 Validation of the Proposed Model

In the section of the validation of the proposed model is identified the failure number of cycles for the relevant applied stress using Newton Rapson code, then identified the damage stress for the applied stress and damage indicator is found by feeding the failure number of cycles as the applied number of cycles. Same procedure is applied to both Miner's rule and the sequential law [2] to find the relevant damage indicator. So as it is stated the relevant output is mentioned, so the proposed model gives the exact point where material tender to fatigue rather than the previous models.

The obtained function and the geometrical shape of new fatigue curve, which corresponds to class WI riveted connection, are illustrated in Fig. 3 (The bottom curve: UK railway assessment code given design fatigue curve). The Data to fit equation of Kohout and Vechet [4] is taken from the International Institute of Welding (IIW). Blocks of cyclic loading with increasing and decreasing amplitudes are considered. The number of cycles to failure for each load amplitude is given in Table 1. Damage Factor given by Miner's rule, sequential law and the proposed model corresponding to each stress levels are described below.

Among three stress life curves, design Wohler curve for WI riveted connections is used as the curve represents multiaxial stress states. Secondly, Wohler curve from rotating bend test data of wrought iron is used to verify the material validation. Thirdly, for mathematical model validation, Kohout and Vechet model is used.

Analysis of the calculation results showed that the better fatigue life estimations can be obtained by using the method that is sensitive to the changes of material behavior under fatigue loading in relation to the specified number of cycles of the load. Hence the actual damage trajectory travel along the curve, the proposed model gives closer values to actual failure. Note that loading conditions are in the part where the model is adjusted in high cycle fatigue.

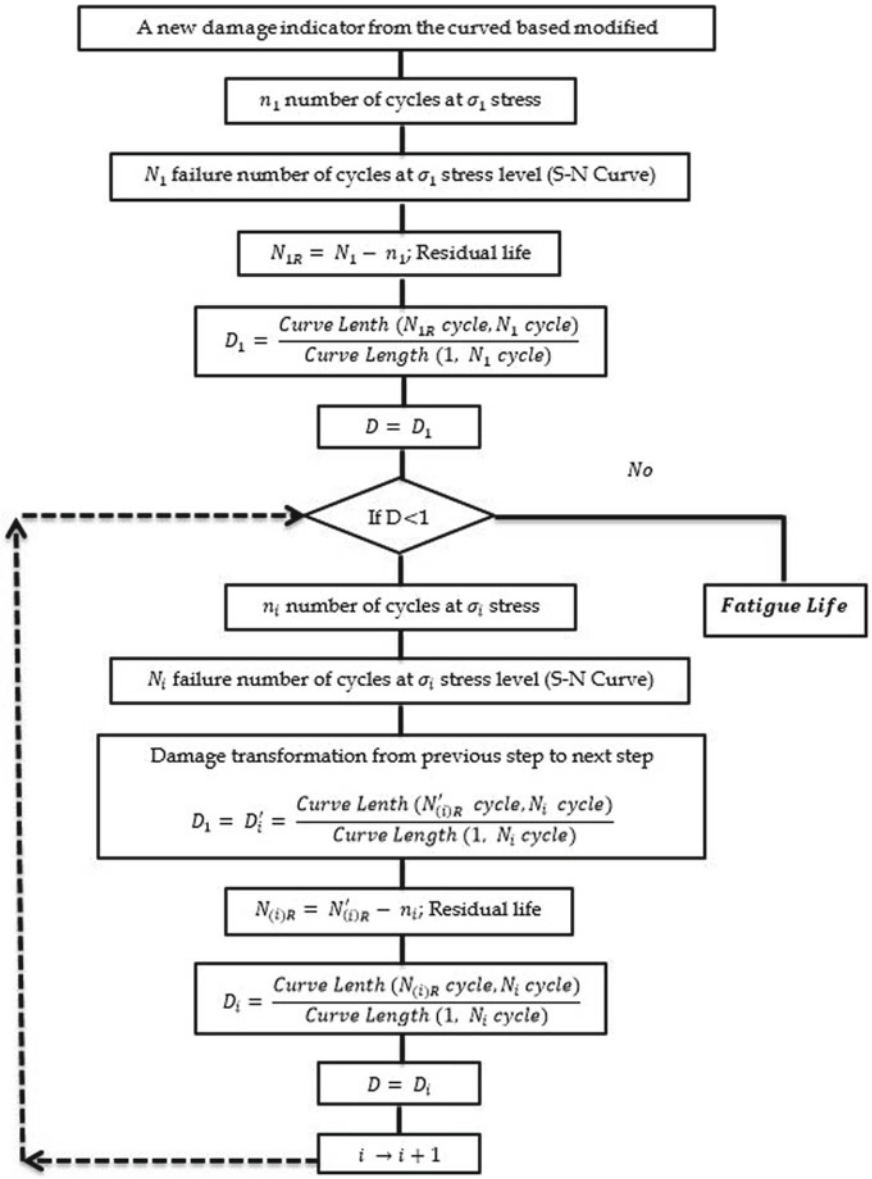

Fig. 2 Flow chart for damage stress modified curved based sequential law

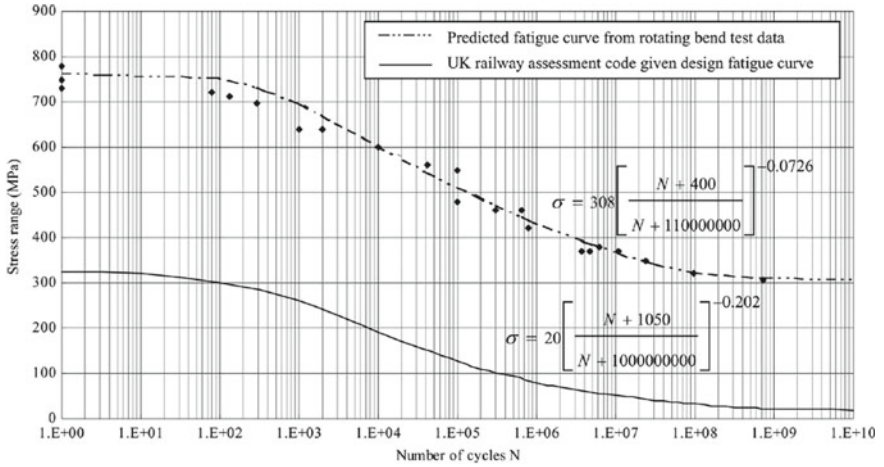

Fig. 3 Design Wohler curve for WI riveted connections (the bottom curve) and predicted Wohler curve from rotating bend test data of wrought iron material (the top curve) [3]

Table 1 Comparison of the introduced new damage parameter using uniaxial test results from literature for transformation of decreasing applied stress

S–N curve	Applied stress (MPa) (σ_1)	Applied number of cycles (n_1)	Applied stress (MPa) (σ_n)	Applied number of cycles (n_n)	Damage factor (D_n)		
					Miner rule	Sequential law	Proposed model
Design Wohler curve for WI riveted connections	200	1×10^3	100	1×10^5	0.3878	0.7695	0.7758
	100	1×10^5	200	1×10^3	0.3878	0.2638	0.2535
Wohler (stress life) curve from rotating bend test data of wrought iron material	500	7×10^4	400	1×10^5	0.5361	0.7275	0.7381
	400	1×10^5	500	7×10^4	0.5361	0.0449	0.0551
Kohout and Vechet model	300	1×10^3	200	1×10^5	0.7988	0.8129	0.8232
	200	1×10^5	300	1×10^3	0.7988	0.0524	0.0422

4 Conclusions

In this paper, a modified sequential law based fatigue life estimation procedure was introduced. It accounts the movement of damage point in the stress/strain life curve.

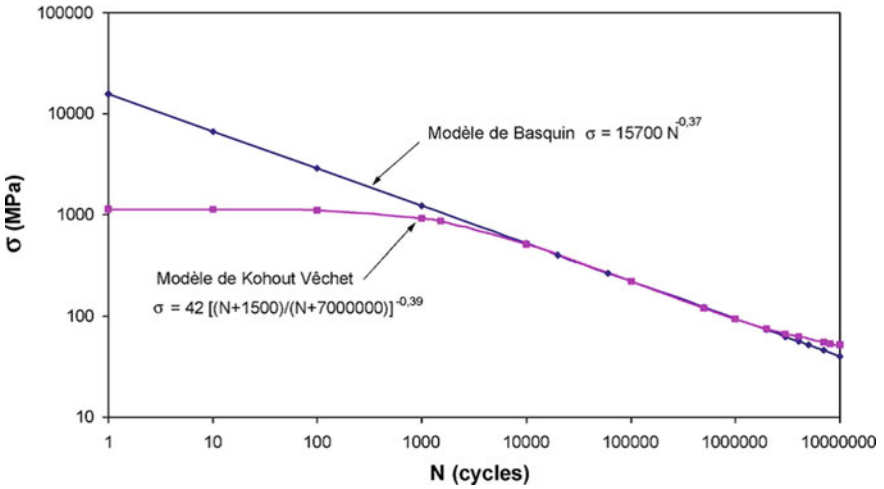

Fig. 4 Stress life curve (Kohout and Vechet) [4]

Methodology was illustrated with a numerical example. As shown there, the proposed modal predicts accurate damage estimation compared to those of Miner's rule and the sequential law. Therefore, applicability and efficiency of the proposed method is validated.

References

1. Dissanayake PBR, Siriwardane SC (2008) An accurate life estimation method for existing railway bridges. Eng J Inst Eng Sri Lanka 41(2):7
2. Mesmacque G, Garcia S, Amrouche A, Rubio-Gonzalez C (2005) Sequential law in multiaxial fatigue, a new damage indicator. Int J Fatigue [online] 27(4):461–467
3. Siriwardane S, Ohga M, Dissanayake R, Taniwaki K (2008) Application of new damage indicator-based sequential law for remaining fatigue life estimation of railway bridges. J Constr Steel Res 64(2):228–237
4. Kohout J, Vechet S (2001) A new function for fatigue curves characterization and its multiple merits. Int J Fatigue [Online] 23(2):175–183

Analysis and Design of Steel Plate Composite Beams for Shear

A. D. De Alwis, W. J. B. S. Fernando, P. Mendis, D. S. Hettiarachchi, and W. P. M. Weerasinghe

Abstract Development of tall buildings require innovative use of composite materials for optimal element sizing while ensuring structural stability. Steel composite concrete elements have widely been used when element dimensions are restricted and to ensure the structural performance of the element, where typically concrete would have imposed material restrictions. Steel I or H sections have widely been used for concrete encased composite elements and the use of steel plates have been used for coupling beams under seismic loading. This study takes into account steel plates used to withstand the induced shear in transfer beams where shear stresses are limited by the concrete shear resistance. The study shows the design process carried out for the steel composite beam element to withstand the action. An advanced finite element analysis was carried out to verify the load transfer mechanism and to illustrate the use of steel plate composite elements to transfer shear. The study shares the design process of the complex structural elements and intends to provide a guideline in designing similar complex structural elements.

Keywords Steel composite concrete elements · Steel plates · Shear in transfer beams

1 Introduction

Since the high-rise structures are built in a really limited space and under serious restrictions designers are forced to use smaller structural members with a higher resistance to fulfill the requirements. Often it is challenging to execute it with conventional design approaches so the structural engineers opt for alternatives such as composites.

A. D. De Alwis (✉) · W. J. B. S. Fernando · D. S. Hettiarachchi · W. P. M. Weerasinghe
Civil and Structural, Engineering Consultants Pvt. Ltd., No.772/A, Wijesingha Mawatha, Madinnagoda, 10100 Rajagiriya, Sri Lanka
e-mail: arthur@csec.com.lk

P. Mendis
University of Melbourne, Melbourne, Australia

R. Dissanayake et al. (eds.), *ICSBE 2020*, Lecture Notes in Civil Engineering 174,
https://doi.org/10.1007/978-981-16-4412-2_26

In this study authors illustrate the design of shear resistance of a concrete transfer element which has a design shear force exceeding the shear capacity as per the relevant codes of practices such as BS and Euro standards. As given in BS 8110-part I [1]

$$v = \frac{V}{b_v d} \tag{1}$$

But v (design shear stress at a cross section) is limited to 0.8 (fcu)1/2 or 5 N/mm^2 whichever lesser, whatever shear reinforcement is provided. Therefore the design shear stress has to be transferred via a different path to ensure the stability of the structure with the size constraints.

In the case of steel sections the shear resistance is the product of the von Misses yield criterion and the shear area. If I or H sections are considered (which are predominantly used for encased composite elements), the shear area is mainly governed by the web as shown in Eq. (2). Thus the Authors have considered to use steel plates to enhance the shear capacity of the section.

$$A_v = A_a - 2b_f t_f + (t_w + 2r)t_f \tag{2}$$

where Av is the shear area for I or H sections, Aa is the total section area, bf is the flange width, tw is the web thickness, r is the root radius and tf is the flange thickness. For composite elements the contribution of shear resistance depends on many factors such as the continuity of the section, by the cracking of the concrete and the local details of the shear connections [1], therefore the authors have considered the complete shear to be transferred through the steel plates.

2 Design Process

Shear stresses for the design were calculated by modelling the multi-story towers in ETABS [2], comprising a transfer plate and other structural elements and adding the gravity and lateral load components as per the design codes and standards.

The shear resistance is calculated by considering that the yield strength in shear is $f_{yd}/\sqrt{3}$, and that the whole of area A_v can reach this stress:

$$V_{pl,a,Rd} = A_v\left(f_{yd}/\sqrt{3}\right) \tag{3}$$

Plate dimensions and number of plates are being used depends on the space available in between two layers of reinforcement, cover to the reinforcement required etc.

Transferring the shear to the plate is ensured by providing shear studs throughout the steel section on the two faces which will act as the longitudinal complimentary shear component to the vertical shear.

Sample Calculation of Shear Plate and Studs

As per EN 1993-1-1:2005, EN 1994-1-1:2004 [3]

Design of shear plates

Design parameters

$f_y = 235$ N/mm^2,

Minimum thickness (t_w) to prevent shear buckling effects;

$$d/124\varepsilon = t_w \tag{4}$$

$$\varepsilon = \sqrt{235/f_y} \tag{5}$$

f_y	= 235 MPa
$t_{w,min}$	= 12.10 mm
Design shear force	= 26,465.4 kN
Shear plate thickness (t_w)	= 25 mm
Shear plate height, d	= 1500 mm
Shear plate resistance, $V_{pl,a,Rd}$	= $A_v(f_{yd}/\sqrt{3})$
	= 5087.9 kN
Therefore, No's of plates req.	= 6.

Design of shear studs

Design parameters

$f_{ck} = 32$ N/mm^2, Ecm = 33000 N/mm^2, $\mu = 0.5$

fu = 450 N/mm^2.

Capacity of 19 mm dia. Studs,

γ_v	= 1.25
Shear stud capacity	= $0.8 f_{cu} \pi d^2/4\gamma_v$
	= 81.66 kN
Calculation of α	= $0.2(h_{sc}/d + 1)$
Nominal height of the stud h_{sc}	= 90 mm
α	= 0.92
Shear stud capacity Pr	= $0.29\alpha d^2(f_{ck}E_{cm})^{0.5}/\gamma_v$
	= 86.07 kN
∴ Shear stud capacity	= 81.66 kN

Calculation of shear stud spacing

Min. spacing along the direction of shear, (5d)	= 80 mm
Min. spacing along the direction of transverse to shear, (4d)	= 64 mm

Shear stud distribution calculation

Section size	= PL 25 × 1500
Depth	= 1500 mm
Width	= 25 mm
Area, A	= 37,500 mm^2
Steel grade	= S235
Yield strength, p_y	= 235 N/mm^2

Max. Compression capacity of the section

$P_c = p_y xA$	=8812.5 kN
Design force for shear studs	= 8812.5 kN
Number of studs per row	= 6
Capacity of a row without friction	= 81.66 × 6
	= 490 kN
Total capacity per row	= 490 kN
Shear stud rows required	= 8812.5/490

Provide 18 rows of studs at equivalent spacing (Figs. 1 and 2).

3 Connection Design and Advanced Finite Element Analysis

In order to verify the design approach and the behavior of the connection, it was envisaged that an advanced finite element analysis had to be carried out. Analysis and design was carried out to get the von Misses stress distribution using Autodesk Fusion® [4].

Beam was modeled in Fusion with fixed end conditions and an equivalent pressure load was applied to the beam and von-Misses stresses were checked (Figs. 3 and 4).

It is evident that the von-Misses stresses are distributed evenly throughout the section. This illustrates that steel plates together with the shear studs resist the shearing actions of the section (Fig. 5).

The construction constraints such as logistics and installation difficulties causes the steel sections to be designed with splices. The splice connections were designed considering the complete shear resistance of the steel section. The splice connection was considered as a bolted connection and the bolt capacities were checked in

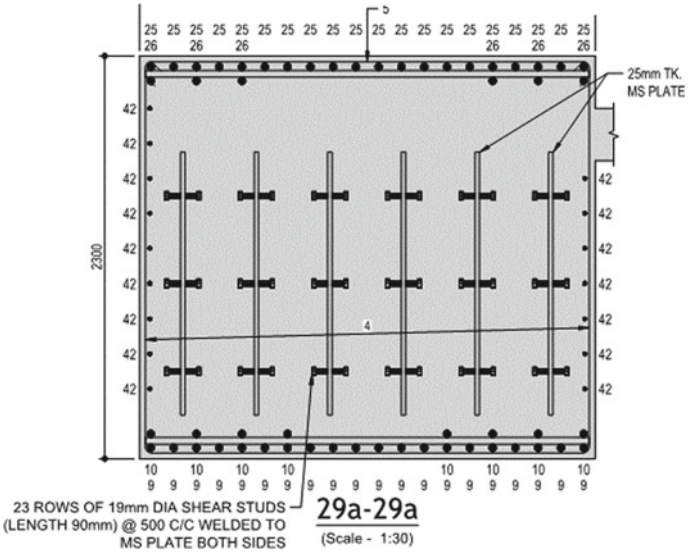

Fig. 1 Cross sectional view of composite transfer beam with steel plates

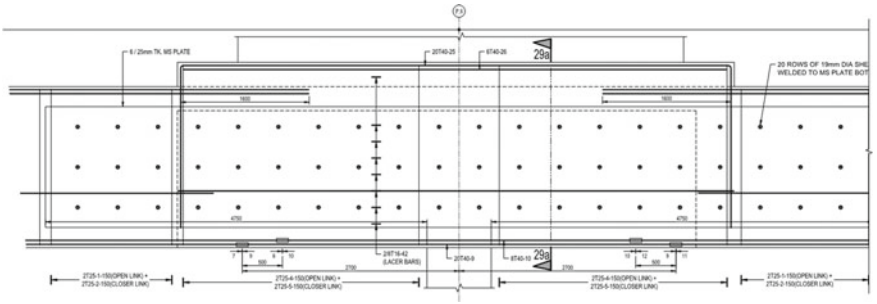

Fig. 2 Elevation view of composite transfer beam with steel plates

accordance with BS 5950 [5] to withstand the section shear capacity i.e. the applied shear for the bolt is considered to be equal to the steel plate's shear capacity. When considering the splice details for the section the connection locations were staggered taking into account the requirement for concrete workability within the element as illustrated in Fig. 6.

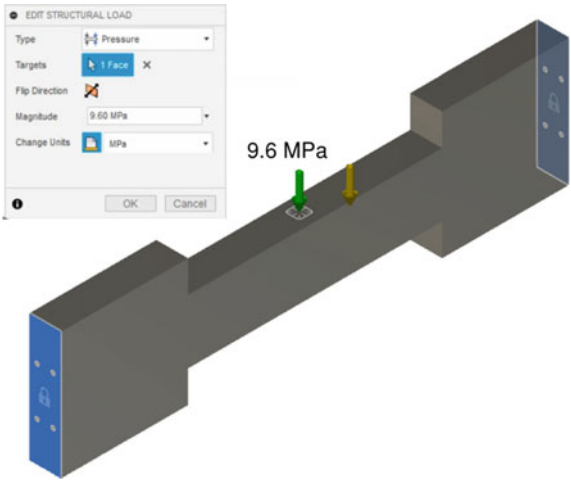

Fig. 3 Load application on model

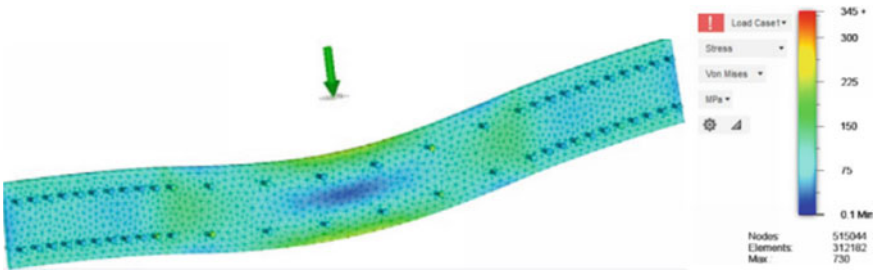

Fig. 4 Von-Misses stresses obtained

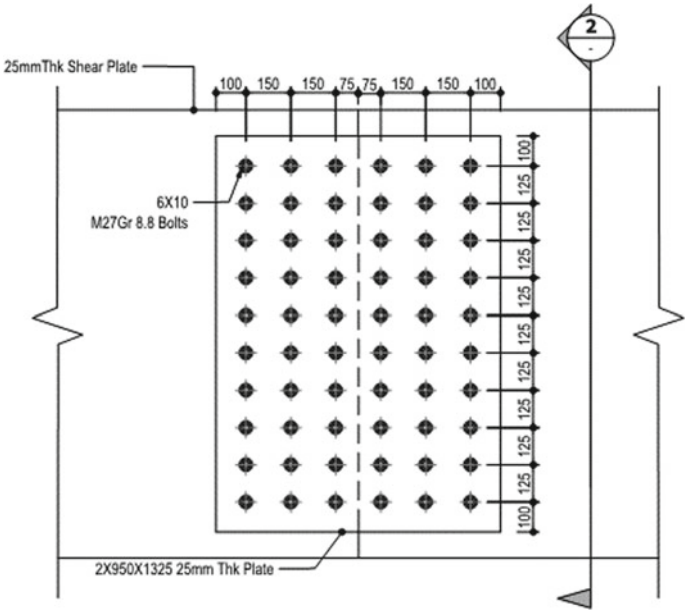

Fig. 5 Bolted splice connection detail

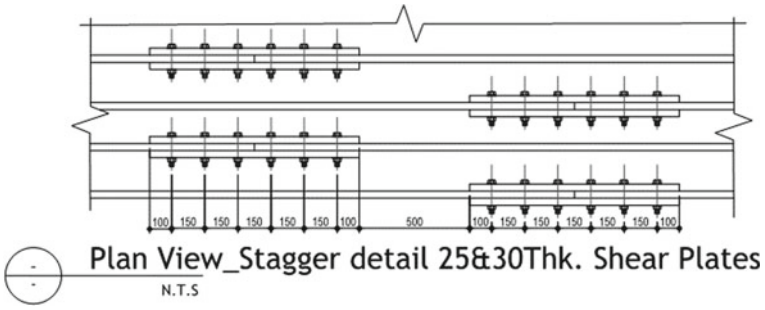

Fig. 6 Staggering detail of splice connection

4 Conclusion and Recommendations

The following conclusions and recommendations are drawn from this study

- Steel plates are capable of withstanding large shear forces in the cases where the concrete is limited in withstanding the shear.
- Due to the complex and variable nature of the contribution to shear resistance from concrete in a composite element the complete shear resistance is recommended to be resisted by the steel plate
- In order to ensure shear is transferred to the steel plate through the concrete, shear studs are introduced and the shear studs are recommended to be providing the complete vertical shear. i.e., the longitudinal complementary shear is equated to the vertical shear.
- The study provides a design guideline for steel–concrete composites to withstand shear forces, where concrete sections alone would otherwise be unable to provide the shear resistance.
- It is recommended that further insitu testing/monitoring is carried out to ascertain the behaviour of steel plate shear resisting composite beams.

References

1. BS 8110-1 (1997) Structural use of concrete—part 1: code of practice for design and construction
2. ETABS 17.0.1 software manual
3. BS EN 1994-1-1 (2004) Eurocode 4: design of composite steel concrete structures
4. Autodesk fusion structural analysis professional manual (2020)
5. BS 5950 (1990) Structural use of steelwork in building—part 1: code of practice for design in simple and continuous construction: hot rolled sections
6. BS EN 1993-1-1:2005-Eurocode 3: design of steel structures

Sustainable Material and Manufacturing

Application of Blended Cement Mix Pet Fiber High Strength Concrete for Structural Elements

A. L. M. De Silva, T. M. Shakeer, J. T. Jayawardhana, P. P. C. Saumyasiri, and M. S. T. Priyadarshana

Abstract High strength concrete (HSC) is being produced due to growing demand for taller and larger structures and due to limitation of land space. Demand for HSC in Sri Lankan construction industry is now increasing due to Sri Lanka is a developing country. However, HSC has many versatile properties, there are some drawbacks. It is noticed that HSC is relatively brittle material possessing lower tensile strength and lower flexural strength. This study focuses on the experimental investigation to improve these drawbacks of HSC by addition of PET (Polyethylene Terephthalate) fibers. PET is a polyester polymer obtained from recyclable water bottles. With the development of technology in the modern world, the production of PET bottles keeps on increasing and they are being thrown after a single use, will eventually make environmental hazards. Further the recycling capacity in Sri Lanka is very low when compared to its production. PET fiber addition was done for water cement ratio of 0.25 and PET was added in 0%, 0.5%, 1.0%, and 1.5% of total weight of the cement. Then the compressive strength, split tensile strength and flexural strength were compared with the control specimens to know the effective usage of PET fibers. The results revealed that the presence of PET fibers will increase the HSC performance. PET fibers can improve the compressive strength, tensile strength and flexural strength and also to control the cracks. It was observed that 1.0% of PET fiber content exhibit better performance among all the mixes. The results showed that 21.75% of increase in compressive strength, 25.24% of increase in split tensile strength and 42.70% of increase in flexural strength for the addition of 1.0% PET fibers to the HSC after 28 days. These recycled PET fibers introduced HSC showed better performance compared to the conventional HSC.

Keywords High strength concrete (HSC) · PET (polyethylene terephthalate) fibers · Compressive strength · Split tensile strength · Flexural strength

A. L. M. De Silva (✉) · T. M. Shakeer · J. T. Jayawardhana · M. S. T. Priyadarshana
Department of Civil Engineering, Faculty of Engineering Technology, The Open University of Sri Lanka, Nawala, Nugegoda, Sri Lanka

P. P. C. Saumyasiri
UltraTech Cement (Pvt) Ltd, New Nuge Road, Peliyagoda, Sri Lanka

R. Dissanayake et al. (eds.), *ICSBE 2020*, Lecture Notes in Civil Engineering 174,
https://doi.org/10.1007/978-981-16-4412-2_27

1 Introduction

Concrete is one of the most frequently used building material in the world nowadays. High strength concrete (HSC) is being produced due to growing demand for taller and larger structures and due to limitation of land space. In recent years, the applications of HSC have increased, and now been used in many parts of the world. Demand for HSC in Sri Lankan construction industry is now increasing due to Sri Lanka is a developing country and needs high infrastructures such as high rise buildings, dams, bridges, highways etc. The main advantage of the HSC is the reduction in size of compression elements.

Even though HSC has many advantages, there are some drawbacks. It is noticed that HSC is relatively brittle material possessing lower tensile strength and lower flexural strength. These drawbacks such as low tensile strength, low flexural strength as well as ductile property of concrete could be improved by addition of short dispersed fibers. The main fibers used as concrete reinforcing materials are steel, glass, and polymeric fiber. During recent years, steel fibers are used for reinforced concrete has gradually increased. But use of these steel fibers with concrete is more difficult due to some reasons. Higher cost, because of its production issues as well as the cost of raw material is high. And it's a well-known fact that steel reinforced concrete is vulnerable to corrosion.

This study focuses on the experimental investigation to improve these drawbacks of HSC by addition of PET (Polyethylene Terephthalate) fibers. PET is a polyester polymer obtained from recyclable water bottles. PET fiber is an eco-friendly product. With the development of technology in the modern world, the production of PET bottles keeps on increasing and they are being thrown after a single use. According to the Sirimane [1] in his article, Sri Lanka annually imports 9,600 tonnes of raw plastic virgin (PET) to produce bottles and for other requirements. Out of this, around 30% is re-exported by way of food covers, fluid containers for beverages and packaging. The balance 70% is being used in Sri Lanka and the used plastic waste remains in dump yards creating huge environmental issues. Further the recycling capacity in Sri Lanka is very low when compared to its production.

In order to improve mechanical properties of concrete, various researches are being conducted by researchers. According to the past researches, PET fibers can enhance the compressive strength of the concrete. Ochi [2] conducted uniaxial compression test and identified that compressive strength of PET fiber concrete was increased with the fiber content and this was valid up to 1% of fiber. Kim [3] observed that there was a reduction of compressive strength by 1 to 10% as the volumetric fiber percentage increase from 0 to 1% with 0.25 increments. Fraternali [4], has been identified that compressive strength was increased with the increment of PET fiber diameter. Short PET fibers give more compressive strength than the long PET fibers. Marthong [5] identified that there is a reduction of compressive strength as the volumetric fiber percentage increases beyond 0.5%. Additionally, it was declared that compressive strength also varies with the geometry and the dimensions of fibers. An

experimental study has been carried out by Saumyasiri [6] identified that compressive strength of PET fiber concrete is increasing with the fiber content up to 1% and then the compressive strength is decreasing with the increment of fiber content.

PET fibers can also enhance the tensile strength of the concrete. Marthong [5] found that the inclusion of PET fiber above 1% decreases the tensile strength. Saumyasiri [6] identified that PET fibers can improve the tensile strength when increase of PET fiber content due to the bridging action imparted by the fibers during cracking. Following objectives were achieved in this study,

- Investigate the suitability of PET fibers with blended cement high strength concrete for structural elements.
- Obtain the optimum mix proportion for blended cement mix PET fiber high strength concrete.

2 Methodology

2.1 Major Constituents Used

Portland Pozzolana Cement

For this study, main applied cement was Portland Pozzolana Cement (PPC). Because heat of hydration of PPC is lower than Ordinary Portland Cement (OPC) so that prevent the thermal cracks. Blended cement is environmentally friendly because it utilizes the product from coal fires thermal stations.

Manufactured Sand (M-Sand)

M-sand was considered as a substitute for river sand because with the fast growing of the construction industry, the demand for sand has increased and the availability of good quality river sand has depleted. Another reason for not using river sand is because of the imposing of regulations for sand mining as sand mining cause lots of environmental hazards.

Superplasticizers

In this study the main applied superplasticizer was Hypercrete R admixture. Hypercrete R is polycarboxylic ether based advanced superplasticizer which is specially developed for any type of ready-mix concreting where the slump retention is important.

Polyethylene Terephthalate (PET) Fiber

PET fibers (Fig. 1) used in this study, were collected from EURO STRONG (PVT) LTD, Sri Lanka. Table 1 shows the properties of PET fiber that used for this study.

Fig. 1 PET fibers

Table 1 Properties of PET fiber

Density	1100 kg/m^3	Absorption	Nil
Melt point	225–260 °C	Acid resistance	100%
Flash point	350 °C	Specific gravity	1.1
Thermal conductivity	Low	Fiber length	25 mm
Electrical conductivity	Low	Fiber diameter	0.19 mm

2.2 Sample Preparation

Cement, sand, PET fibers were first mixed for 10 min for avoiding bunching of PET fiber. Then water and super plasticizers were added gradually. In here Hypercrete R is used as a super plasticizer. The mixing time was 10–30 min for all mixtures due to the low w/c ratio and high binder content. Trial mix designs were carried out and a control mix design for grade 60 was selected. In here sample preparation was done for w/c ratio of 0.25. PET fiber was added in 0%, 0.5%, 1.0%, and 1.5% of the total weight of cement to investigate the properties of the concrete mix as shown in Table 2.

Table 2 PET fiber concrete sample preparation

Specimen	Cement (kg)	Water (kg)	M-Sand (kg)	Coarse aggregate (kg)	Admixture (kg)	PET %	PET (kg)
S1	600	150	650	1060	7.776	0	0
S2	600	150	650	1060	7.776	0.5	3
S3	600	150	650	1060	7.776	1.0	6
S4	600	150	650	1060	7.776	1.5	9

2.3 Experimental Procedure

Following tests are conducted to check the performances of PET mix HSC. Slump test is carried out as per procedures mentioned in BS EN 12350–2:2009 for ½ hour, 1½ hour and 2½ hour to identify how the workability change with the time. Cubes having the size of 150 mm × 150 mm × 150 mm were cast according to BS 1881-108 (1988) and cured until the testing day according to BS1881-111(1988). Concrete is poured in the mould and tempered properly so as not to have any voids. After 24 h these moulds are removed and test specimens are put in to water for curing. These specimens are tested by compression testing machine after 7 days, 28 days and 56 days curing. Cylindrical specimen which have 150 mm diameter and 300 mm height were prepared to be cast to measure the concrete's split tensile strength at 28, and 56 days of age. This test was carried out as specified in BS 1881–117. Another beam specimen (100 mm × 100 mm × 500 mm) were prepared to be cast to measure the concrete's flexural strength at 28 days, and 56 days of age. This test was carried out as specified in BS EN 12390–5:2009.

3 Results and Discussion

3.1 Variation of Concrete Workability with PET Fiber Content

To determine the workability of concrete, slump value of the concrete was measured. In this study, slump value obtained for ½ hour, 1½ hour, and 2½ hour. It was observed that there is a reduction in workability of concrete with the increases of PET fiber content as shown in Fig. 2. According to the results, concrete workability gradually decreases with the increase of the fiber content due to bunching of the PET fibers in the mix. Also, fibers with very small diameter have a much greater surface area. So

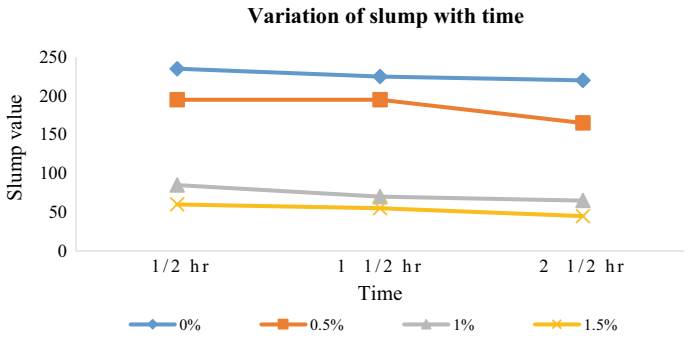

Fig. 2 Variation of slump with time

that this extra demand needs more water and mortar from the concrete mix to coat the fibers in addition to the coarse aggregate.

3.2 *Variation of Compressive Strength with PET Fiber Content*

Figure 3 shows variation of compressive strength with different PET fiber content. The comparison of the 28 days cube compressive strength results shows an increase in compressive strength of concrete contains PET fiber at 0.5% and 1.0%, then after that there is a reduction in compressive strength significantly when compared to control specimen. At 28 days, the increment of compressive strength of concrete contains PET fiber at 0.5% and 1.0% increase by 2.05% and 21.75% respectively and PET fiber at 1.5% decrease by 2.29%. The results reveal that only 0.5% and 1.0% of PET fiber increase the concrete compressive strength. PET fibers can enhance a good bonding between aggregate and cement. This difference shows in Fig. 4. Increasing of PET fiber content resulted decreasing in compressive strength because with higher fiber content, PET fibers tends to bunching together and workability of concrete start to

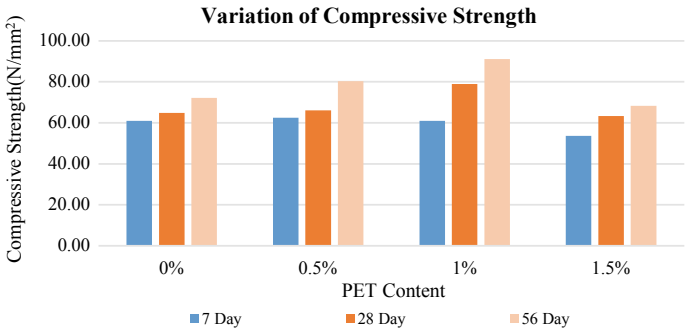

Fig. 3 Variation of compressive strength

(a) (b)

Fig. 4 After the compressive strength test **a** without PET fibers, **b** with PET fibers

reduce. Good bonding dependent upon accomplishment of a homogeneous spreading of the fibers in the concrete. Due to lack of workability compressive strength start to reduce gradually.

3.3 *Variation of Split Tensile Strength with PET Fiber Content*

Figure 5 shows variation of splitting tensile strength with PET fiber content for 28 days. It shows that PET fibers can enhance the splitting tensile strength of concrete. At 28 days the increment of splitting tensile strength of concrete contains PET fiber at 0.5%, 1.0% and 1.5% increase by 11.11%, 25.24% and 37.35% respectively. It was observed that the specimens without fibers suddenly split out once the concrete cracked. However, the PET fiber concrete specimen exhibited cracking but did not fully separated out as shown in Fig. 6.

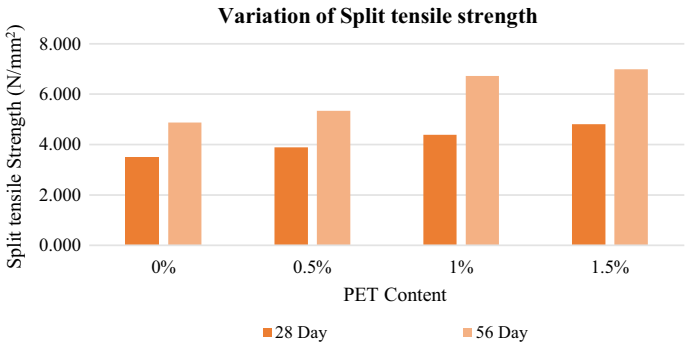

Fig. 5 Variation of split tensile strength

Fig. 6 After the split tensile test **a** without PET fibers, **b** with PET fibers

3.4 Variation of Flexural Strength with PET Fiber Content

Figure 7 shows variation of flexural strength results with PET fiber content in the reinforced concrete for 28 days. It shows that flexural strength of PET fiber introduced concrete is higher than that in the control specimen. It can be observed that there is an improvement in the flexural strength when increasing the PET fiber content. At 28 days, the increment of flexural strength of concrete contains PET fiber at 0.5%, 1.0% and 1.5% increase by 25.50%, 42.70% and 59.57% respectively. The failure of the specimen at the end of the test are shown in Fig. 8. Failure of the specimen with fiber presents better performances as compared to the reference specimens without fiber.

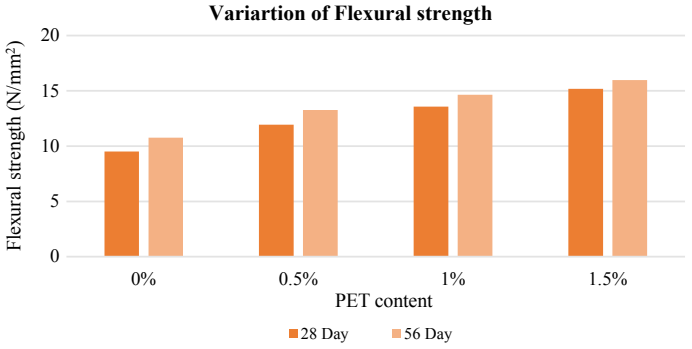

Fig. 7 Variation of flexural strength

Fig. 8 After the flexural strength test **a** without PET fibers, **b** with PET fibers

4 Conclusion

According to the study results, this production routine had successfully associated with eliminating environmental wastes and thereby switching to achieve green technology. The following conclusions can be drawn based on the outcomes of the study.

- From the slump test, it was obtained that the workability of PET fiber HSC was decreased with the increases of fiber percentage. After 1.0% of PET fiber content, fibers tend to bunch while mixing the concrete.
- 0.5% and 1.0% of PET fiber specimens are having higher compressive strengths than that for the control specimen. PET fiber can delay the unstable development of micro cracks as well as to limit the propagation of these micro cracks under load. However, a further increase in PET fiber content resulted in to reduce in the compressive strength.
- The addition of PET fibers in the HSC mix, significantly influenced the tensile strength of the concrete. Better split tensile strength was achieved with the addition of the PET fibers. Because a growing tensile crack in plain concrete can very soon lead to failure but PET fibers can increase the load carrying capacity of concrete in tension.
- The flexural strength of PET fiber introduced HSC is higher than that in the control specimen. The reason is due to the good bonding between PET fibers with the surrounding concrete which was act as confinement to the concrete and also energy absorption under flexural loading which was greatly enhanced with PET fiber reinforcement.

According to the above results, it can be concluded that for high strength concrete utilization of 1.0% PET fiber is considered to be more optimum and effectual. Also, it can be concluded that the recycled PET bottles appear to be a low cost material which would help to solve the solid waste problems and preventing environmental pollution.

Acknowledgements The authors are grateful to Dr. M.S. Thushara Priyadarshana, senior lecturer of the Department of Civil Engineering of the Open University of Sri Lanka for his great contribution and guidance to path towards success. We would like to thank Mr. Chamara Saumyasiri, Assistant manager at UltraTech cement (Pvt) Ltd and visiting lecture at Faculty of Computing and Technology of the University of Kelaniya. The authors also wish to thank for Nawaloka San Readymix for the support in preparation of specimens. Finally, thanking to every other people who were supportive by any means during our research works.

References

1. Sirimane S (2017) Recycling plastic waste the BPPL way. Availa-ble at: https://www.dailynews.lk/2017/05/02/business/114626/recy-clingplastic-waste-bppl-way

2. Ochi et al (2007) Development of recycled PET fiber and its application as concrete-reinforcing fiber. Cement Concr Compos 29(6):448–455
3. Kim et al (2010) Material and structural performance evaluation of recycled PET fiber reinforced concrete. Cement Concr Compos 32(3):232–240
4. Fraternali F et al (2011) Experimental study of the thermo-mechanical properties of recycled PET fiber-reinforced concrete. Compos Struct 93(9):2368–2374
5. Marthong C, Marthong S (2015) An experimental study on the effect of PET fibers on the behaviour of exterior RC beam-column connection subjected to reversed cyclic loading. Online Res J Inst Struct Eng
6. Saumyasiri, Sudhira (2018) Application of blended cement mix fiber concrete for road pavements. In: The 9th international conference on sustainable built environment, ICSBE2018, Kandy, Sri Lanka, 13–15 Dec 2018, p 143

Use of EPS Based Light-Weight Concrete Panels as a Roof Insulation Material for NERD Slab System

D. P. P. Meddage and M. T. R. Jayasinghe

Abstract Natural energy sources are being ceased, due to the drastic development of various industries, along with the utilization of technology. Energy, related to the building sector has accounted for almost 23–50% of the world's energy demand. Besides, reinforced concrete roof slabs have potential to contribute to this operational energy demand, acting as a heated body in the daytime. Therefore, our primary objective was to develop an energy-efficient slab system for low and middle-income families by adopting cost effective roof insulation. Accordingly, this study was directed in small scale physical models to investigate insulation characteristics of the EPS (Expanded Polystyrene) based concrete panels combined with NERD (National Engineering and Research Development) slab system. A parametric study was carried out using energy models, calibrated using the field results. Moreover, the thermal characteristics of this composite slab have displayed better results compared to prevalent roofing systems. The structural performance was assessed, in comparison to the conventional NERD slab system. This novel slab system performs well in tropical climatic conditions when it is installed with passive features. The overall decrement factor and the optimum insulation thickness were obtained as 0.6 and 75 mm respectively. Furthermore, the production of these insulation panels is an efficient way to dispose of non-biodegradable polystyrene waste.

Keywords EPS · NERD slab · Roof-insulation · Thermal-conductivity

1 Introduction

The accelerated rate of urbanization has caused land scarcity where vertical developments such as low-rise apartments should be promoted as an appropriate solution. These structures can be engaged with innovative techniques to enhance their performance. In the local context, a low-rise apartment comprised of EPS (Expanded Polystyrene) based light-weight concrete panels, has been developed recently, to enhance the energy efficiency of the envelope [8, 10]. Several studies have been

D. P. P. Meddage (✉) · M. T. R. Jayasinghe
Department of Civil Engineering, University of Moratuwa, Moratuwa, Sri Lanka

R. Dissanayake et al. (eds.), *ICSBE 2020*, Lecture Notes in Civil Engineering 174,
https://doi.org/10.1007/978-981-16-4412-2_28

already focused on the benefits of engaging EPS concrete which is manufactured of polystyrene waste [1, 3, 12, 17]. The density of conventional concrete (2400 kgm^{-3}) could be brought down to (650–750) kgm^{-3} range, reducing the dead-weight associated with a structure [7, 9]. Moreover, coarse aggregates are fully replaced using EPS beads. Thus, it leads to a significant reduction in the thermal conductivity of EPS concrete, based on EPS fraction [6].

In the study done by Gunawardana et al. [10] on low-rise apartments, they have provided NERD slab as the roof structure. This slab system is approximately 35% cost-effective compared to reinforced roof slab according to Sanjaya et al. [16]. It consists of 60 mm thick reinforced slab panels supported by precast pre-stressed NERD beams to further reduce vertical stresses at ground level.

However, the above system has poor thermal attributes in the tropical climatic zone due to the relatively low thickness of the slab. Hence, the required thermal sensation of occupants will not be achieved, especially during the daytime. Solar radiation that penetrates the roof has been a major reason that promotes air-conditioned spaces contributing to significant energy demand [13, 18]. Hence, a defensive strategy should be implemented to increase the thermal resistance of concrete roof structures to optimize energy performance [14].

Thus, several authors had progressively developed insulated slab systems in the local context. The insulated slab introduced by Halwatura et al. [11], has been installed with 25 mm thick polystyrene insulation. However, later it has been found, some durability issues due to water patches and the partial fraction of concrete in the insulation layer have affected the compound thermal conductivity. The same slab system was then developed by Nandapala et al. [14] providing discontinuous concrete strips as support. In that, the overall thermal conductivity could be increased and structural integrity was not much affected. However, the major drawback of these two studies is the utilization of pure polystyrene insulation. The manufacturing process of polystyrene is entailed with crude oil extraction, contributing to greenhouse emissions [5]. Thereby, this research was carried out to improve the thermal performance of the NERD slab system using locally manufactured EPS-based concrete panels as insulation.

2 Objective and Methodology

The objective of this study was to determine the optimum thickness of EPS insulation to be used for the NERD slab system in tropical climatic conditions. The following methodology was adopted to achieve the objective:

(a) Small scale physical models were constructed to represent the NERD composite slab system by providing different thicknesses of resistive EPS insulations.
(b) The surface temperature was recorded on top of the slab and soffit to distinguish heat flow characteristics corresponding to different thicknesses.

(c) A parametric study was performed using energy simulation to determine the optimum thickness of EPS insulation to be used in tropical climates.

3 Field Experiment

Figure 1 illustrates the arrangement of the proposed slab system. Three physical models were constructed by providing 75 mm, 100 mm, and 150 mm insulation thicknesses which were having a 1 m × 1 m plan area. 60 mm thick NERD slab consists of 50 mm × 50 mm × 3 mm welded GI mesh as reinforcement. This slab was placed on pre-stressed precast NERD beams.

Cement block-work was cast up to beam bottom level to provide adequate space to mount necessary sensors and equipment. On top of the slab, insulation panels and a 60 mm thick protective screed were laid. A sufficient number of openings are required to facilitate air movement inside a real structure. EPS insulation panels were split into 500 mm × 500 mm pieces to provide a 50 mm wide gap to support 60 mm thick top screed. Indeed, this gap will reduce the effectiveness of combined insulation when it is filled with concrete. Thus, corrections shall be applied according to Progelhofet al. [15].

Later, temperature variations of soffit and top of the slab were measured using type K thermocouples. These thermocouples are available in the range of −200 °C to + 1200 °C. Sensitivity is approximately 41 $\mu V^{\circ}C^{-1}$ [11]. The frequency of data logging was set at 5-min intervals.

Fig. 1 Proposed insulated NERD slab system

3.1 The Effect of Insulation Thickness

Diurnal variation of temperature on a typical summer day is shown in Fig. 2. Maximum soffit temperatures had been recorded as 38.4 °C, 36.4 °C, and 33.1 °C for 75 mm, 100 mm, and 150 mm EPS insulation, respectively. This indicates that at noon, the slab having the lowest thickness of insulation still transfers a substantial amount of solar radiation inside. Hence, occupants underneath will feel thermally uncomfortable due to adverse microclimatic conditions.

Besides, all models have shown a similar temperature variation at nighttime. However, the slab is becoming unnecessarily thicker due to increased insulation thickness. Further, it did not provide any significant reduction in soffit temperature. Therefore, considering practical viability, we have proceeded with the 75 mm insulation thickness for energy modeling.

4 Computer Simulation

Energy simulations were performed to optimize the thermal characteristics of the novel slab system. Design and Builder software was utilized for this purpose which is capable of simulating at any stage of construction. The energy model was calibrated according to the physical model having 75 mm insulation. It is important to notice that the calibration process depends on field conditions. Climatic data from the Rathmalana region were obtained for modeling. Later, parametric studies were carried out using a large-scale model building as shown in Fig. 3.

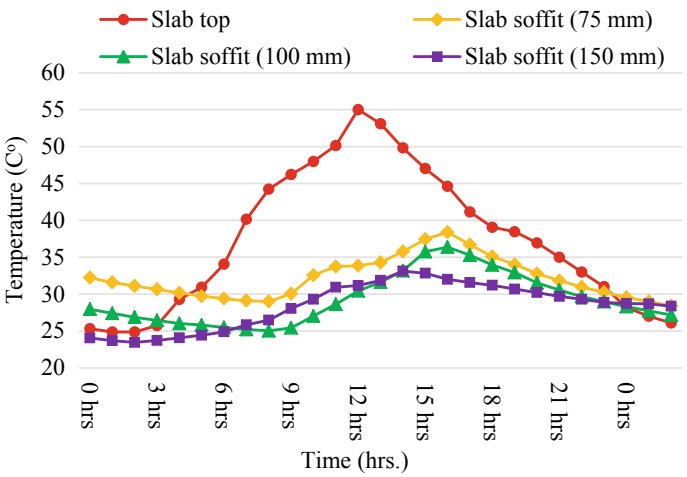

Fig. 2 Surface temperature variation of physical models

Fig. 3 Large scale energy model

4.1 The Optimum Insulation Thickness

Simulation results illustrated that 75 mm insulation could bring down soffit temperature to 37.5 °C. This value is nearly 1 °C less than the field result which is justifiable due to the supporting concrete strips in the insulation layer of physical models.

Next, the possibility of reducing insulation thickness was also examined by providing 60 mm and 50 mm of EPS layers. Corresponding maximum soffit temperature was found to be 38.5 °C and 39.2 °C. However, free-running spaces with sufficient air movement inside can tolerate temperatures up to 35 °C, according to Fig. 4. Therefore, reduced insulation thicknesses will not be effective any longer for this slab system since the required comfort levels were not met. Hence, 75 mm thickness was fairly justified as optimum insulation which needs a proper modification.

4.2 Passive Modification on the Novel Slab

Thus far, the slab did not perform as expected under tropical climatic conditions. Accordingly, the need for passive features was identified to improve the thermal performance of this novel slab. It was decided to apply a low-absorptive colour on the surface which is exposed to the sun. The mechanism of these low-absorptive colours is to reflect solar radiation while keeping the temperature of the exposed surface at a lower value. The possibility of using this slab during daytime is difficult due to

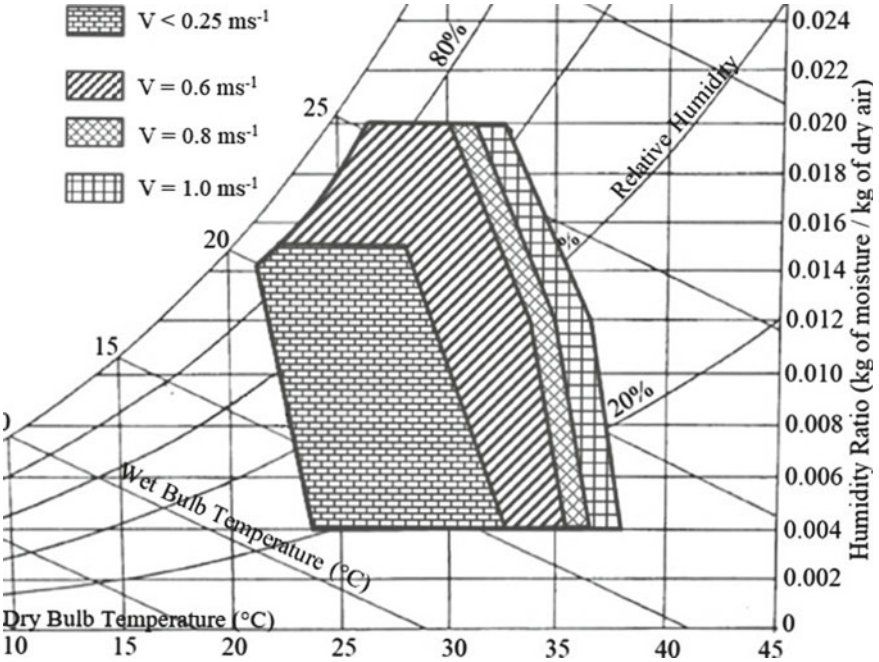

Fig. 4 Comfort zone for Colombo when air movement is available [11]

the reflected heat. After adopting this simple passive feature, the entire temperature variation satisfied the expected comfort zone. Slight discrepancies that were observed earlier also could be minimized. Above progressive steps on enhancing the NERD slab system has been summarized in Table 1.

The overall decrement factor without any insulation was 0.95 and the time lag of the peak was only 0.5 h. This explains the potential of transferring a massive amount of heat through thin concretes during the daytime in tropical climatic conditions. In particular, the utilization rate of operational energy could increase to meet the required comfort in terms of thermal sensation. Altogether, these heated envelopes form urban heat islands which can increase surrounding temperatures significantly, apart from energy utilization.

Table 1 Summary of energy modeling

Effect on the model		Peak soffit temperature (°C)	Time lag (h)	Decrement factor
Insulation	Passive feature			
Not provided	Not provided	52.5	0.5	0.95
75 mm	Not provided	37.5	3	0.68
75 mm	White colour on slab top	33	3.5	0.6

Only with EPS insulation of 75 mm, we could obtain a decrement factor of 0.68 which could later be reduced up to 0.6 by implementing the passive feature. Ultimately, this will contribute to reducing peak heat load occurring in the daytime. As well, the time lag of peak has increased up to approximately 3.5 h with this resistive insulation together with passive features. The need for passive feature can be mainly justified due to the discrepancy between thermal conductivity values of pure polystyrene (0.038 Wm^{-1} K^{-1}) [1] and EPS concrete (0.214 Wm^{-1} K^{-1}).

5 Comparison of Results

Thermal conductivity of Concrete—1.7 Wm^{-1} K^{-1} [11].

Thermal conductivity of EPS concrete—0.214 Wm^{-1} K^{-1} (from laboratory experiment).

The partial fraction of concrete in the insulation layer can be compensated as stated in Eq. (1) [15].

$$\frac{1}{K_I} = \frac{(1-\phi)}{K_P} + \frac{\phi}{K_C} \tag{1}$$

K_I—Modified Thermal conductivity of the insulation
K_P—Thermal conductivity of the insulation layer
K_C—Thermal conductivity of concrete
Φ—Partial fraction of concrete in the insulation layer (0.1 in this case)
$1/K_I = 0.9/0.214 + 0.1/1.7$
$K_I = 0.234$ Wm^{-1} K^{-1}.

Thermal resistance (R-value) can be calculated as shown in Eq. (2)

$$R = \sum\left(\frac{b_i}{k_i}\right) \tag{2}$$

b_i = Thickness of the ith layer
k_i = Thermal conductivity of the ith layer
R-value of the composite slab = $2 \times (0.06/1.7) + (0.075/0.234) = 0.39$ m^2KW^{-1}.

5.1 Comparison of Thermal Performance

The novel slab system was assessed with prevalent roofing systems in the local context. In this study, these systems were compared according to corresponding thermal characteristics. Thermal resistance (R-value) and thermal conductance (U-value) were taken as parameters for comparison. Air to air resistance ($R_{a\text{-}a}$) was

Table 2 Comparison of thermal characteristics

Roofing system	R_{Body} value (m^2KW^{-1})	U value (Wm^{-2} K^{-1})
Clay tile	0.014[a]	5.15
Asbestos sheet	0.013[a]	5.18
Cement tile	0.023[a]	4.93
Uninsulated NERD slab	0.035	4.65
Insulated NERD slab	0.39	1.75

[a]Ariyadasa et al. [2]

calculated using Eq. (3), according to surface resistance values stated by Halwatura et al. [11] to obtain thermal conductance as provided in Eq. (4).

$$R_{a-a} = R_{Si} + R_{Body} + R_{So} \tag{3}$$

R_{Si} = Surface resistance (Ceiling downward) = 0.14 m^2KW^{-1}
R_{So} = Surface resistance (Roof) = 0.04 m^2KW^{-1}
R_{Body} = Thermal resistance of the body

$$U = \frac{1}{R_{a-a}} \tag{4}$$

$R_{a\text{-}a} = R_{Si} + R_{Body} + R_{So}$
$R_{a\text{-}a}$ of composite slab = 0.14 + 0.39 + 0.04 = 0.57 m^2KW^{-1}
U-value of composite slab = 1.75 Wm^{-2} K^{-1}.

A summary of the comparison has been provided in Table 2. Accordingly, the novel slab system has indicated better thermal attributes in contrast to prevalent roofing systems. Especially, it reduces the thermal conductance value of the conventional NERD slab by approximately 62%. Thereby, the slab soffit of the novel slab with passive features, will not be considerably warm, even in the daytime, minimizing the demand for conditioned spaces. Therefore, daytime energy requirements and their adverse impacts can be further reduced. As well, potential alternate of traditional roofing systems based on thermal characteristics is justified by a 66% average reduction in thermal conductance values.

5.2 The Structural Performance

The insulation adds additional weight. The performance reduction was evaluated considering 175 mm thick NERD beams based on [4] guideline. There we could

Table 3 Effect of insulation on structural performance

Beam spacing (mm)	Maximum span allowed (m)	
	Conventional system	Novel system
650	4.5	4
600	4.6	4.1
550	4.8	4.2
500	4.9	4.4
450	5.1	4.6
400	5.4	4.8
350	5.6	5

observe, 11% of span reduction is required for the novel NERD slab system compared to the conventional NERD slab system as stated in Table 3.

On other hand, due to the compound weight of this system (3.4 kNm^{-2}), susceptibility to severe wind events can be neglected. However, bearing stresses should be evaluated in a further study to exhibit structural behavior at beam and wall connection.

6 Conclusion

The NERD slab system alone had a poor thermal performance having a small time lag (0.5 h) and a decrement factor of 0.95. Thereby, we have provided resistive insulation using EPS panels to enhance thermal performance. The reason for utilizing EPS panel insulation was that it is manufactured from non-biodegradable polystyrene waste. The main findings of this study can be stated as follows.

- The optimum EPS insulation for the NERD slab was found to be 75 mm in tropical climatic conditions, obtaining a time lag of 3 h and a decrement factor of 0.68. However, under these conditions, slab soffit was found to be fairly warm.
- When a low absorptance colour was applied on the top surface of the insulated slab, the aforementioned parameters could be altered as 3.5 h and 0.6, respectively. Consequently, maximum soffit temperature could satisfy the desired comfort range.

Hence, passive modification (white colour) of this insulated slab should be provided to ensure efficient utilization in tropical climatic conditions.

References

1. Aditya L, Mahlia TMI, Rismanchi B, Hasan MH, Metseelar HSC (2017) A review of insulation materials for energy conservation in buildings. Renew Sustain Energy Rev 73:1352–1365

2. Ariyadasa GLM, Muthurathne SSK, Adikary SU (2015) Investigating the physical, mechanical and thermal properties of common roofing materials in Sri Lanka. In: Proceedings of 6th annual national building research symposium, Sri Lanka
3. Babu KG, Babu DS (2003) Behaviour of lightweight expanded polystyrene concrete containing silica fume. Cem Concr Res 33(5):755–762
4. BS 8110-1 (1997) Structural use of concrete. Code of practice for design and construction, BS
5. Chandra MS, Nandapala K, Priyadarshana G, Halwatura RU (2019) Developing a durable thermally insulated roof slab system using bamboo insulation panels. Int J Energy Environ Eng
6. Demirboga R, Kan A (2012) Thermal conductivity and shrinkage properties of modified waste polystyrene aggregate concretes. Constr Build Mater 35:730–734
7. Dissanayake DMKW, Jayasinghe C, Jayasinghe MTR (2009) A comparative embodied energy analysis of a house with recycled expanded polystyrene (EPS) based foam concrete wall panels. Energy Build 135:85–94
8. Eric TB, Gunawardhane SGW, Damruwan HGH, Jayasinghe MTR (2019) Rapidly constructed two storey thermally comfortable houses for tropical climates with light weight loadbearing concrete panels. Presented at the ICCEA-2019–047, ResearchGate
9. Fernando PLN, Jayasinghe C, Jayasinghe MTR (2017) Structural feasibility of expanded polystyrene (EPS) based lightweight concrete sandwich wall panels. Constr Build Mater 139:45–51
10. Gunawardana SGW, Eric TB, Jayasinghe MTR (2019) Three-storied apartment buildings constructed using lightweight eps concrete panels for tropical climatic regions. Presented at the ICCEA 2019
11. Halwatura RU, Jayasinghe MTR (2008) Thermal performance of insulated roof slabs in tropical climates. Energy Build 40(7):1153–1160
12. Khatib JM, Elkordi A (2019) Characteristics of concrete containing EPS. In: Use of recycled plastics in eco-efficient concrete, pp 137–165
13. Mallik FH (1996) Thermal comfort and building designing in the tropical climates. Energy Build 23(3):161–167
14. Nandapala K, Halwatura RU (2016) Design of a durable roof slab insulation system for tropical climatic conditions. Cogent Engineering
15. Progelhof RC, Throne JL, Ruetsch RR (1976) Methods for predicting the thermal conductivity of composite systems: a review. Polym Eng Sci 16(9):615–625
16. Sanjaya BGV, Perera WWPK, Srilal WMS, Sooriyaarachchi SP (2015) Investigation on improvement of low cost NERD slab system. Presented at the international conference on structural engineering and construction management, pp 133–147
17. Sayadi AA, Tapia V, Neitzert TR (2016) Effects of expanded polystyrene (EPS) particles on fire resistance, thermal conductivity and compressive strength of foamed concrete. Constr Build Mater 112:716–724
18. Vijaykumar KCK, Srinivasan PSS, Dhandapani S (2007) A performance of hollow clay tile (HCT) laid reinforced cement concrete (RCC) roof for tropical summer climates. Energy Build 39(8):886–892

Effects of Carbon Black and Graphene Oxide Additions on Properties of Ordinary Portland Cement Composite

A. M. B. Chandima and S. P. Guluwita

Abstract Due to blooming of nanotechnology in the construction industry, various types of nanomaterials introduced to obtain 'smart cement'. For the sustainable built environment, it is required to achieve durability and increasing the compressive and tensile strength of the construction structure. This research paper aims to provide a detailed investigation of the effect of Graphene Oxide and Carbon Black nanomaterials on hardening Ordinary Portland Cement (OPC) mortar, which uses in Ultra-High Performance Concrete (UHPC). The cost of UHPC is high due to micro reinforcements and with maintenance costs. The use of Graphene oxide is the aim of making smart cement, which can avoid cracking and corrosions, and it provides better monitoring of a concrete structure. Carbon black was incorporated in the optimizing stage of to reduce the cost factor. Mechanical and morphological properties were investigated by incorporating the cement mortar with 0.01–0.1 wt.% Graphene Oxide (GO) dispersion and with 0.1–1.0 wt.% carbon black (CB) dispersion of the cement weight. The test results revealed that the addition of 0.4% of CB and 0.03% of GO by weight is the optimal quantity of the composite, showing a 43.27% increase in compressive strength for specimens evaluated at the age of 2 days and 60.61% enhancement in the flexural strength for the specimens evaluated at the age of 28 days. Interestingly, it was observed that further addition of Graphene Oxide and Carbon Black reduces the workability and efficiency of the mechanical properties due to the restacking of excess Nano particles. Morphological analysis of the Graphene Oxide Cement Composite revealed that Graphene Oxide affected the formation of cement hydration products. Carbon Black nanoparticles in the Carbon Black Cement Composite act as the reinforcing and a filling ingredient of the cement matrix.

Keywords Nanomaterials · Construction industry · Graphene oxide · Carbon black

A. M. B. Chandima · S. P. Guluwita (✉)
Department of Material Science, University of Moratuwa, Katubada, Moratuwa, Sri Lanka
e-mail: sguluwita@materials.mrt.ac.lk

R. Dissanayake et al. (eds.), *ICSBE 2020*, Lecture Notes in Civil Engineering 174,
https://doi.org/10.1007/978-981-16-4412-2_29

1 Introduction

Economic growth and enhanced urbanisation support a construction boom involving homes, infrastructure, and public buildings. As a result, cement demand is growing fast, further the requirement of high-performance concrete. Once the term "Portland Cement" had been introduced by Aspadin as a binding material, it is considered as the main ingredient use in the construction industry and it is a good composite which makes concrete along with other materials such as coarse aggregate, fine aggregate, chemical and mineral admixtures, and etc. [1]. These other ingredients contribute the enhancement of properties of the concrete. The ultimate purpose of the construction sector is to gain a higher strength within a minimal time period which helps to expedite the finishing of the project. Several admixtures (especially mineral admixtures) and blended materials (fly ash, volcanic ash, and granulated slag) are used in the present days to achieve this. Blended materials provide to increase durability and reduce heat generation during the curing process [2]. As per the research work that had been taken about the rate of consuming material, concrete is the most used material except water and numerous number of researches established which implies there are still improvements in the product required. The optimization of strength of the concrete is now in new sector which is incorporation of nanoscale binders which furthermore provides workability and durability [3].

In past few decades, the interest of researchers aroused in carbon-based nanomaterials such as graphene, carbon nanofiber (CNF), graphene oxide nano-flake (GONF) and carbon nanotubes (CNT) as composite materials for cement due to their extraordinary properties [4]. This research paper has been elaborated the nanomaterials (graphene oxide) used in cement mortar to increase the properties of composite and incorporation of carbon black contribute the reduction of cost.

1.1 Cement Composites

Ordinary Portland Cement (OPC) is still being used as a main type of cement in construction industry, interestingly, in the past few decades the trend of the usage of different composite materials as additive to cement is steeply growth. The trend is driven by demand from construction industry due to the requirement of high performance concrete with enhanced properties such as durability, temperature control, high early strength, and etc. In this scenario nano material plays a vital role as a composite material with exceptional physical properties and readily availability but the drawback is the high cost [5].

Table 1 Composition of the OPC [6]

Designation	Equivalent cement type in BS EN 197-1	Composition % (m/m)	
		Main constituent clinker	Minor additional constituents
OPC	CEM I	95–100	0–5

2 Methodology

2.1 Materials Used

Portland cement: Ordinary Portland Cement (OPC) of strength class 42.5 N, in accordance with SLS 107:2015 standard was used as a primary binding material in casting of cement composite for this study [6]. The major constituent composition of OPC is shown in Table 1 [7]. The water/cement ratio was kept in 0.5.

ISO Reference sand: The ISO standard sand (CEN standard sand) which is natural, siliceous sand and particles are rounded in shape. The silica content of this sand is at least 98%. This sand is conformed the ISO SLS 679: 2011 standard.

Graphene Oxide (GO), Carbon Black (CB): A commercially available GO (high purity grapheme oxide—start-up Graphite: Sri Lankan C99 + Vein Graphite purchased from Ceylon Graphene Technologies) and CB samples (99% high purity N330 Carbon Black—MAKROchem sp. zo.o. Lublin, Poland) were used in this study without any modifications.

2.2 Preparation and Proportioning of Cement Composite

2.2.1 Compressive and Flexural Strength

Cement-based composite materials (CBCM) were prepared from CB and from GO. The water/cement ratio of all the mixtures was kept constant at 0.5. Properly mixed GO and CB via sonication was added to cement matrix. Shenghua Lv (2016) revealed that the better sonication procedure was required to have homogenous mixture [8]. Then, the blends were mixed as the procedure mentioned in SLS ISO 679:2011 standard methods [9] for compressive strength and ASTM C348-18 standard methods [10] for flexural strength. The samples were cast into prism moulds of size 40 mm × 40 mm × 160 mm. Cement motor prisms were prepared by varying percentages of 0.01, 0.02, 0.03, 0.04, 0.05, 0.06, 0.07, 0.08, 0.09, 0.10 GO wt% and 0.1, 0.2, 0.3, 0.4, 0.5, 0.6, 0.7, 0.8, 0.9, 1.0 CB wt%. The control sample was prepared without adding additives (cement—450 g, Sand—1350 g and DI water—225 g).Composite samples which showed the optimized properties of GOCC and CBCC were taken to further analyse for investigating the co-effect of both additives.

Table 2 Composition of cement

Ingredient	CaO	SiO_2	Al_2O_3	Fe_2O_3	SO_3	MgO	Cl	IR	LOI	LSF	TiO_2/P_2O_5
Content (mass %)	62.51	19.82	5.80	5.00	3.00	0.92	0.03	0.58	1.28	0.92	0.5

2.2.2 Scanning Electron Microscopy

The microstructural changes of the hydrated cement composites and control samples were investigated by using SEM. SEM (ZEISS EVO 18 Research) was used to investigate the morphology of composite samples and the control sample.

3 Results and Discussion

3.1 Cement Characterization

The chemical composition of the OPC-42.5N strength class is given in Table 2. All the parameters of the OPC complied with the requirements of SLS 107:2015 standard.

3.2 Composition of Carbon Black

Carbon Black (N330) was examined through the scanning electron microscopy (SEM) and Fig. 1 showed the SEM image of Carbon Black. Carbon black is considered a nanostructure material which is a material contains internal or surface structure in the nanoscale [11].

3.3 Composition of Graphene Oxide

The X-ray diffraction pattern of the as-received GO is shown in Fig. 2a. It is clearly shown that the characteristic peak at 2θ of 10.1 indicates the effective oxidation of graphite and the formation of graphene oxide [12]. The graphene oxide dispersion was examined and Fig. 2b shows the SEM image. The SEM image of graphene oxide reveals that it contains several layers stacked on top of one another [12].

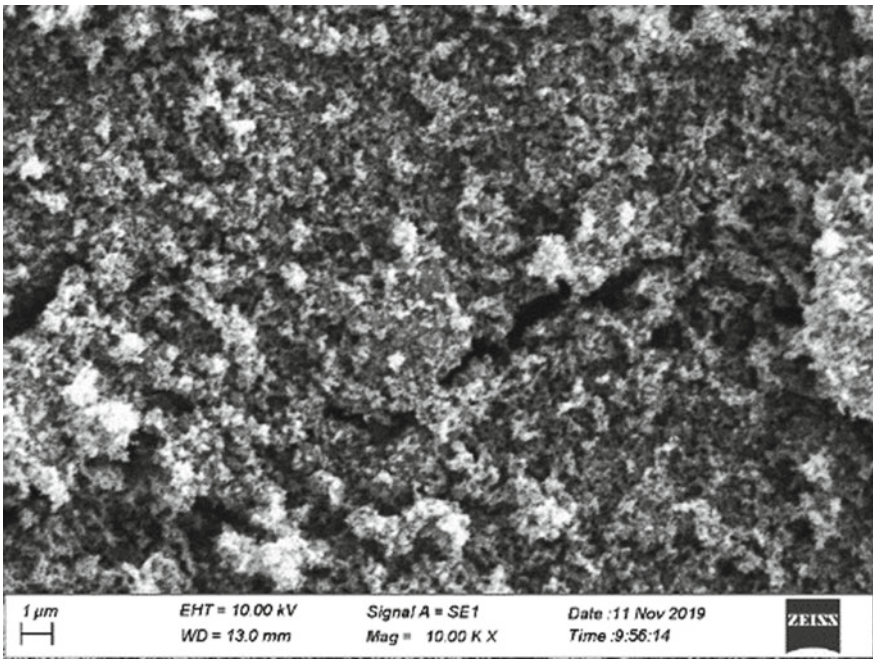

Fig. 1 The SEM image of carbon black

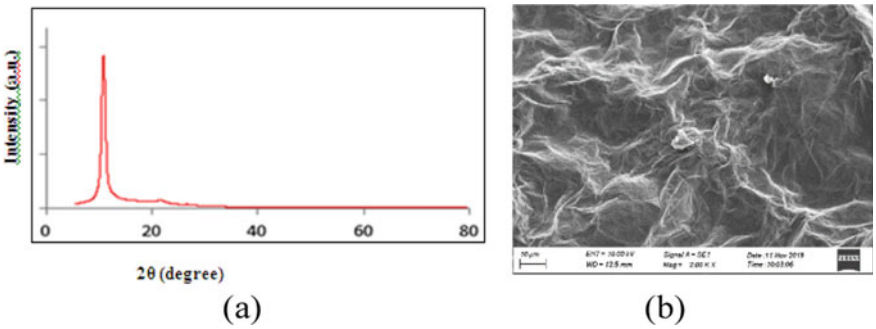

Fig. 2 **a** X-ray powder diffraction image of graphene oxide. **b** SEM image of the graphene oxide

3.4 Mechanical Properties of the Composite

Mechanical properties (compressive and flexural strength) of the hardened cement mortar composites are considered as the most vital property and the incorporation of CB and GO enhanced the mechanical properties.

3.4.1 Compressive Strength

The results of the compressive strength of samples with varying percentage of CB and GO are shown in Fig. 3a and b respectively.

It is revealed that (Fig. 3a) adding CB to the cement motor enhanced the average compressive strength of the specimens. The addition of 0.3 and 0.4% gave the maximum compressive strength; irrespective from the time period of curing and both the specimens exhibited about a 26% enhancement in compressive strength (for 2 days) with that of the control sample. However, when content of CB exceeds the 0.4% there were reduction in the compressive strength. Here, it is assumed that further addition of CB may cause excess CB which reduces the efficiency of the mechanical properties [13]. The optimal dosage of CB was 0.4% at 2 days.

The effects of the addition of GO on the compressive strength of cement mortars are illustrated in Fig. 3b. It was confirmed that, the highest compressive strengths obtained for the sample of with GO content of 0.04%, among all the specimens at 2 days and 28 days and the compressive strength were increased by 37.02% and 18.5%, respectively, in comparison with control samples. It was observed that, when the mixing amount exceeds the 0.04%, the compressive strength decreased gradually and even became lower than that of the control specimens. Krystek M. (2019) implies that there are several reasons behind this and the first reason might be water demand raised up after the addition of cementitious materials [14]. Graphene oxide has high specific surface area [15, 16] and significant adsorption capacity. Therefore, there is less water amount required for the hydration reaction of cement. Jinchang et al.

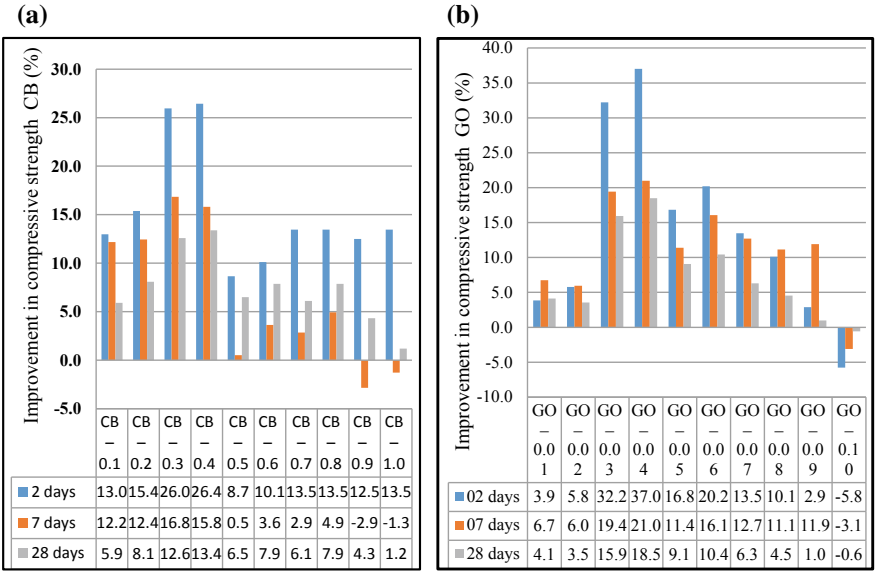

Fig. 3 **a** CB cement composite. **b** GO cement composite

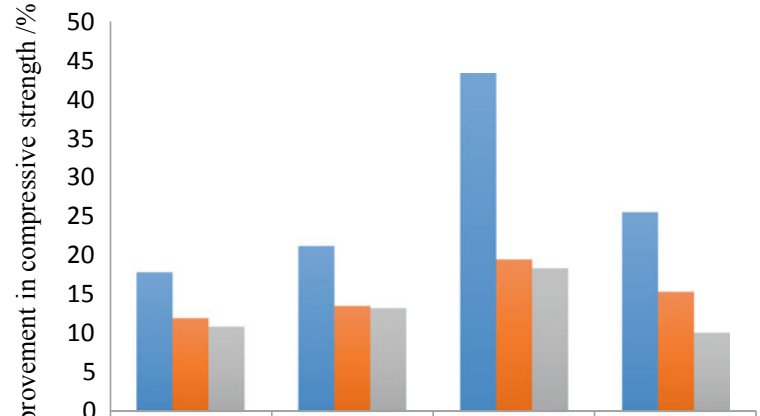

	CB-0.3% + GO-0.03%	CB-0.3% + GO-0.04%	CB-0.4% + GO-0.03%	CB-0.4% + GO-0.04%
2 days	17.79	21.15	43.27	25.48
7 days	11.92	13.47	19.43	15.28
28 days	10.83	13.19	18.31	10.04

Fig. 4 Improvement in compressive strength of carbon black + graphene oxide cement composite

[17], Cao et al. [13], and Wang et al. [18] revealed that another reason might be the agglomeration of graphene oxide due to Van der Waals attraction [13, 17, 18].

Further, the optimized bending percentages of both CB (0.3 and 0.4%) and GO (0.03 and 0.04%) were used to prepare the cement motor for the reduction of cost factor without compromising the properties. The highest increase of the strength was equal to the 43.27%, 19.43% and 18.31% for specimens evaluated at the age of 2 days, 7 days and 28 days, respectively for the cement composite specimens of 0.4% CB and 0.03% of GO. The bar chart of Fig. 4 illustrates the outcome further.

Interestingly, further comparison of the mixture of GO and CB in cement composite revealed that, additives have more effect on early strength rather than the late strength. This may be due to a high water-cement ratio; properly dispersed CB and GO were prone to in the micro-pores of the cement paste which supports to have improved structure of hydrated cement paste [19, 20]. Further, this high early compressive strength indicates that GO had an ability of accelerating the cement hydration process rather than CB [21].

3.4.2 Flexural Strength

The summary of the flexural strength of the cement mortar specimens at 28 days under the varying percentage of CB and GO are illustrated graphically in Fig. 5. It is noticeable that the incorporation of CB and GO enhances the flexural strength of

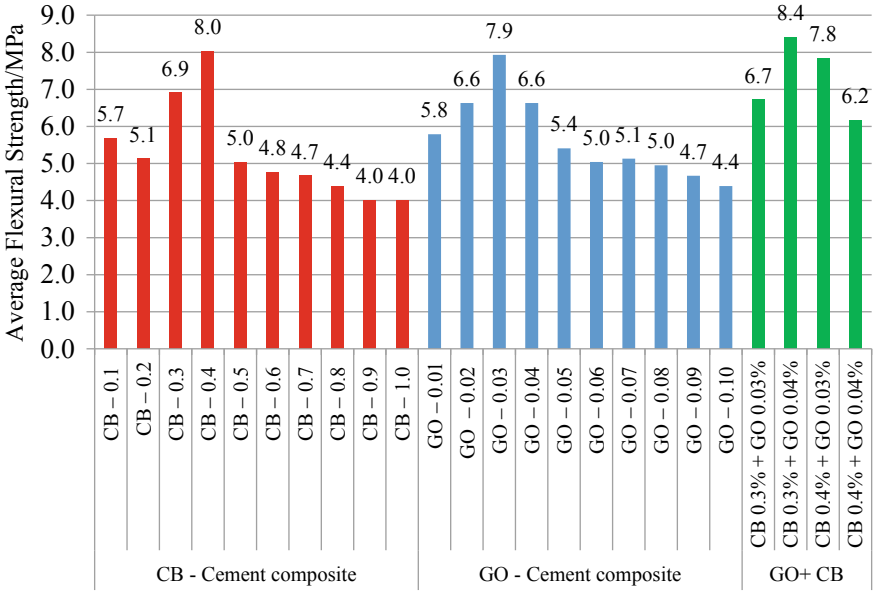

Fig. 5 Average flexural strength of the composite

all cement mortar samples (CB-GO E, CB-GO F, CB-GO G, and CB-GO H). The flexural strength increases in a range from 7.02 to 60.61% at 28 days and the highest value indicated for 0.4% CB and 0.03% GO. Even though the rate of increase in compressive strength was higher in all specimens but this pattern was difficult to see for the flexural strength. After the certain value of the addition of CB and GO flexural strength was decreased than the control sample.

3.5 Microstructure Characterization

Scanning Electron Microscope was widely used by the researchers to elucidate the microstructure of cement composite mortar. The variation of the mechanical strength of hardened cement mortar with variation of additives basically depends on its microstructure mainly, solid phases, pore structure and quantity, and distribution of pore structure. SEM images correspond to the cement composite were studied to determine the relationship of mechanical strength with microstructure.

Figure 6 of control specimens of cement motor samples without any additives, revealed several needle-shaped ettringite projecting into the pores and the amorphous morphology of the calcium silicate hydrate (C-S-H) gel. There were several pores structure in the cement mortar composite and ettringite formation (AFt) was insufficient inside the pores which lead to the low strength than other samples [4]. Figure 7 shows the images of SEM analysis of CBCC with 0.4% CB at 07 days. It is clearly

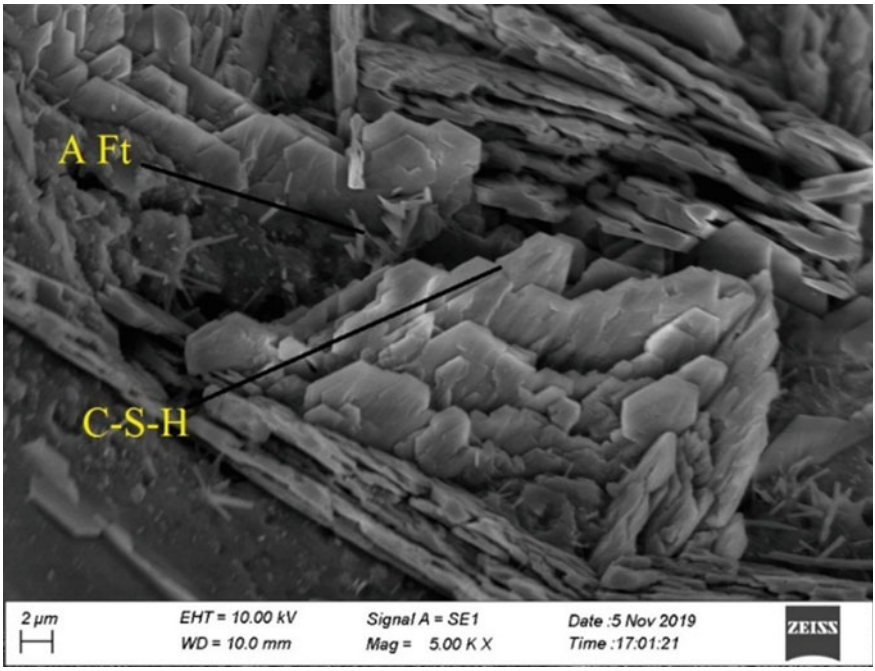

Fig. 6 The images of SEM analysis (control cement motor for 07 days)

visible that CB was not affected the hydration products of the cement motor and it acts as a reinforcing and filling ingredient of the cement matrix. Figure 8 shows the images of SEM analysis of GOCC with 0.04% GO at 07 days. Interestingly, it is found that GO affect the formation of cement hydration product (flower-like hydration crystals) which confirms the GO contributes to the hydration process and further its nucleation effect and it provided better filling effect [22]. GO has a large specific surface area which provides better growth space for the hydration products. Since GO reduces the porosity it results in high strength and ductility cement motor [23].

SEM images of the cement composite which were mixed with 0.4% CB and 0.03% GO contents after curing for 07 days is shown in Fig. 9. The structure of the control cement mortar indicates the formation of many disorganized stacked bar shaped crystals and needle shapes crystals in Fig. 6. These can be considered as products of cement hydrations crystals such as ettringite and calcium hydroxide.

As per the previous studies of the influence of GO in the cement hydration process revealed that the cement hydration process rate is not enhanced by GO and they found the morphology of GOCC is almost similar to that of the cement mortar without GO. However, recent research work [24] revealed that the GO is strongly influenced the hydration structure of the cement mortar which regulated the formation of flower-like hydration crystals [24].

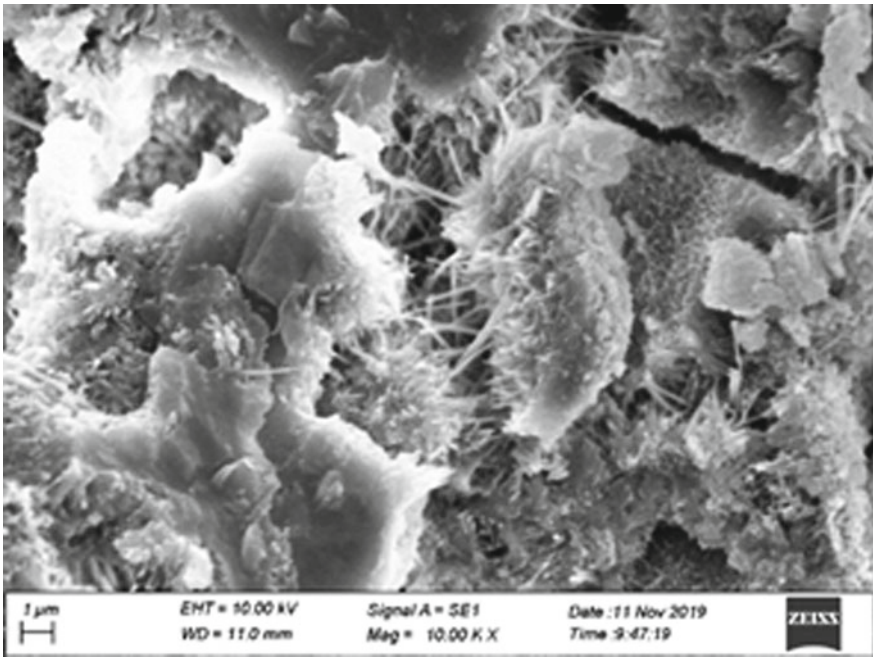

Fig. 7 The images of SEM analysis of CBCC with 0.4% CB at 07 days

4 Conclusion

Incorporate of Graphene Oxide and Carbon Black in cement motor showed an interested modification in mechanical and microstructural properties. It is confirmed that CB was acted as reinforcement filler which strengthens the structure of the cement composites. It is found that the high bond strength is resulted due to the influence of GO on the hydration process of cement at the molecular level. It is required to have better disperse GO to react with the cement matrix. Therefore, advanced dispersion methods are required to achieve this target.

Addition of 0.03% and 0.04% GO accelerate the process of cement hydration which helps to the formation of hydrated product and provided proper reinforcing of the structure resulted from the increase the mechanical strength (compressive strength and flexural strength) of the hardened cement motor.

For the mixture of CB and GO cement composite the highest compressive strength showed by 0.4% CB and 0.03% GO combination. This should be attributed to the fact that a properly dispersed CB and GO enhanced the mechanical properties of the composite which also improved the microstructure of the composite.

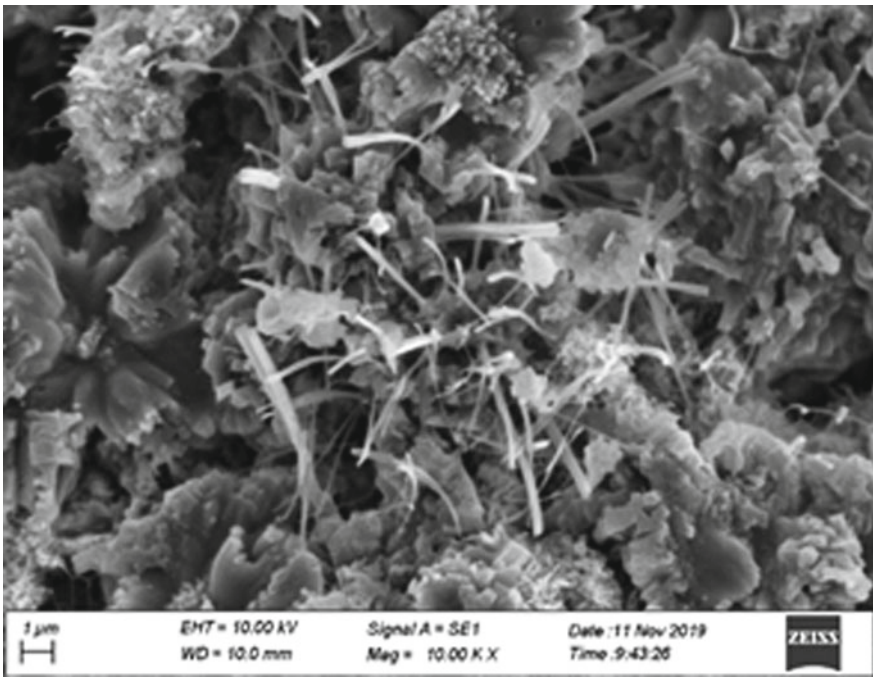

Fig. 8 The images of SEM analysis of GOCC with 0.04% GO at 07 days

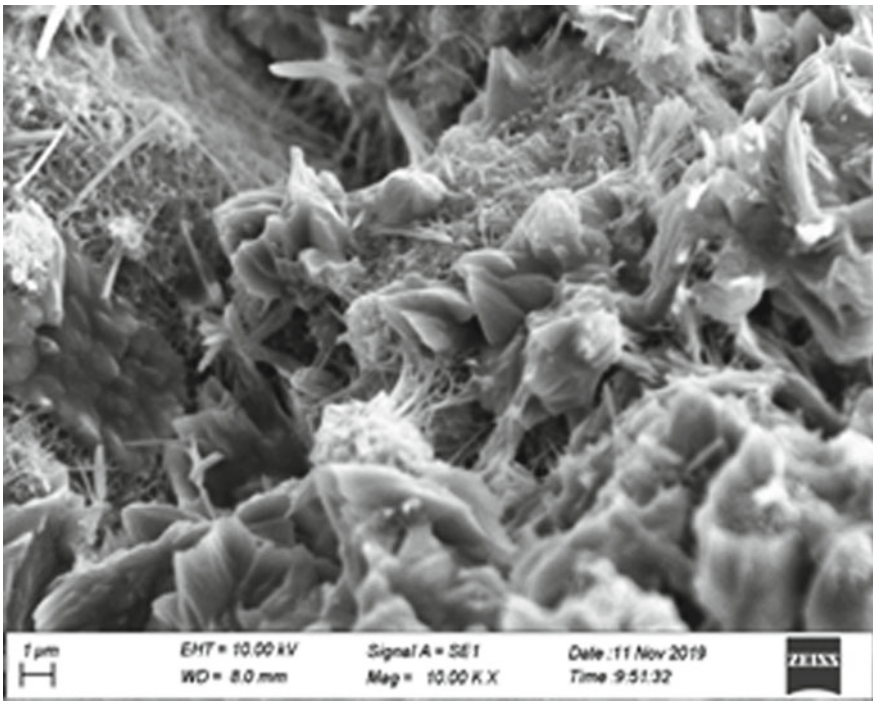

Fig. 9 The images of SEM analysis of CB 0.4% and GO 0.03% cement composite at 07 days

References

1. Mindess S, Young JF, Darwin D (2003) Concrete, 2nd edn. Prentice-Hall, Upper Saddle River
2. Odler I (1998) Lea's chemistry of cement and concrete, 4th edn. Arnold Publishers, London, pp 241–297
3. Uttamkumar HP, Suthar JB (2017) Feasibility of nano graphene oxide powder with concrete—a review. IJSART 3(5)
4. Jinwoo A, Matthew M, Wonseok C, Boo H (2018) Feasibility of using graphene oxide nanoflake (GONF) as additive of cement composite; admixture (additive) for cement composites. Appl Sci 8:419
5. Schindler AK (2002) Concrete hydration, temperature development, and setting at early-ages. Ph.D. Dissertation, University of Texas at Austin, Austin
6. SLS 107:2015, Specification for ordinary Portland cements (second revision), pp 10–29
7. BS EN 197-1:2011, Cement Part 1: Composition, Specifications and conformity criteria for common cements, pp 7–43
8. Lv S, Zhang J, Zhu L, Jia C (2016) Preparation of cement composites with ordered microstructures via doping with graphene oxide nanosheets and an investigation of their strength and durability. Materials
9. Test method for cement—determination of strength, ISO SLS 679 (2011)
10. Test method for flexural strength of hydraulic cement mortars. ASTM C348-18
11. Nanotechnologies—Vocabulary—Part 3: Carbon nano-objects, ISO/TS 80004-1:2015
12. Gurunathan S, Han JW, Eppakayala V, Kim J (2013) Green synthesis of graphene and its cytotoxic effects in human breast cancer cells. Int J Nanomed

13. Cao ML, Zhang HX, Zhang C (2016) Effect of graphene on mechanical properties of cement mortars. J Cent South Univ 23:919−925
14. Kim B, Taylor L, Troy A, McArthur M, Ptaszynska M (2018) The effects of graphene oxide flakes on the mechanical properties of cement mortar. Comput Concre 21(3):261–267
15. Zhu Y, Murali S, Cai W et al (2010) Graphene and graphene oxide: synthesis, properties, and applications. Adv Mater 22:3906–3924
16. Krystek M (2019) Mechanical properties of cement motor with graphene oxide. Archit Civ Eng Environ
17. Jinchang P, Yeming W (2018) Graphene oxide on the microstructure and mechanical properties of cement based composite material
18. Wang Y, Yang J, Ouyang D (2019) Effect of graphene oxide on mechanical properties of cement mortar and its strengthening mechanism. Materials 12:3753
19. Wang Q, Wang J, Lu CX, Liu BW, Zhang K, Li CZ (2015) Influence of graphene oxide additions on the microstructure and mechanical strength of cement. New Carbon Mater 30(4):349–356
20. Anwar A, Mohammed SB, Wahab AM, Liew SM (2020) Enhanced properties of cementitious composite tailored with graphene oxide nanomaterials—a review. Development in the built environment
21. Fakhim B, Hassani A, Rashidi A, Ghodousi P (2014) Preparation and mechanical properties of graphene oxide. Sci World J
22. Chandima AMB (2019) Effects of carbon black and graphene oxide additions on properties of ordinary Portland cement composite. Unpublished MSc thesis, University of Moratuwa
23. Wang B, Zhao R, Zhang T (2018) Pore structure and durability of cement-based composites doped with graphene nanoplatelets. Mater Express 8(2)
24. Lv S, Ma Y, Qiu C, Sun T, Liu J, Zhou Q (2013) Effect of graphene oxide nanosheets of microstructure and mechanical properties of cement composites. Constr Build Mater 49:121–127

Tensile Characteristics of Waste Based Natural Fibre Composites from Rice Husk and Low Density Polythene Waste

P. M. I. B. Abesinghe, S. N. B. M. W. Y. S. Narayana, and H. M. C. C. Somarathna

Abstract Manufacturing new products with waste material has exposed a tremendous contribute to sustainable waste management globally. Recently, natural fibres have gained attention among researchers, engineers and scientists as an alternative reinforcement for synthetic fibre-reinforced polymer composites due to low cost, fairly good mechanical properties, high specific strength, bio-degradability and eco-friendly characteristics. This project was carried out to investigate the tensile properties of waste based Natural Fibre Composite (NFCs) with the use of Rice Husk (RH) as the reinforcement material and the low-density polythene (LDPE) as the matrix. five types of waste based NFCs were developed by varying the weight fraction of fibre to LDPE weight, and weight fractions considered in this study are 10, 20, 30, 40 and 50%. Simple techniques were used to manufacture NFCs, such as shredder machine and hot press machine which do not need high expertise. Uniaxial tensile test was carried out according to the ASTM D3039, using universal tensile testing machine with displacement control loading method. Load, displacement and time histories were obtained and further analyses were undertaken by obtaining Young's modulus, yield stress, yield strain, ultimate tensile stress, failure strain, resilience modulus and toughness modulus for each variation. All types of NFCs with varying RH content show behaviour of materials having typical nonlinear elastic–plastic region. Research findings indicated that addition of 20–40% RH content provide better overall performance under universal tensile behaviour, by mainly considering the behaviour under elastic region and ultimate tensile strength.

Keywords Natural fibre composites · Rise husk · Low-density polythene · Tensile characteristics · Sustainability · Waste management

P. M. I. B. Abesinghe · S. N. B. M. W. Y. S. Narayana · H. M. C. C. Somarathna (✉)
Department of Civil Engineering, Faculty of Engineering, University of Jaffna, Ariviyal Nagar, Killinochchi 44000, Sri Lanka
e-mail: hmccsomarathna@eng.jfn.ac.lk

R. Dissanayake et al. (eds.), *ICSBE 2020*, Lecture Notes in Civil Engineering 174,
https://doi.org/10.1007/978-981-16-4412-2_30

1 Introduction

In last few decades, composite materials, especially those reinforced with different synthetic and natural fibre have been used as materials to accomplish the required demands for several application in many fields including civil and mechanical engineering [3]. Generally during the manufacturing process of synthetic fibres and their composites, huge amount of toxic gas mainly CO_2 is released to the environment, which cause global warming [6]. Therefore, tremendous attention was paid to seek alternatives for these synthetic fibres and, particularly replace these synthetic fibres with natural fibres. Vast varieties of natural fibres have been explored to use as reinforcement in composites. The production of natural fibres has been progressively increasing, since, they are easy to handle and present numerous benefits in terms of eco-friendliness [3].

Disposal of plastic waste in to the environment is considered to be a severe problem due to its non-biodegradability and presence in large quantities. Hence, finding alternative ways of disposing plastic waste by reusing in eco-friendly means are becoming a major research area in the present as well. In order to that reuse plastic as a binder for Natural Fibre Composites (NFCs) is a sustainable engineering approach to reduce the impact on the environment [4]. Polymeric materials are widely used as a matrices for NFCs as they are light weight and can be processed at low temperature. Both thermoplastic and thermoset polymers have been used for matrices with natural fibres. Most of natural fibres are thermally unstable above 200 °C, and hence proper thermal control is essential during the manufacturing [7]. Because of this restriction, only thermoplastics that soften below this temperature such as Polypropylene, Polyethylene, Polyvinyl Chloride, Polyolefin, Polystyrene and thermosets (which can be cured below this temperature) are useable as a matrix [7].

Advantages of NFCs are low processing cost, low density, high modulus, corrosion resistance, high creep resistance, high toughness and higher strength to weight ratio, as well as contain renewable and enhanced biodegradable properties [1, 2, 5]. However, compared to synthetic fibre composites, NFCs show some adverse characteristics such as low durability, high moisture absorption, low strength, greater variability of properties etc. [3]. Sri Lanka is an agricultural based country where high quantity of agricultural waste is produced annually, and not been used effectively which are dumped or burned. Compared to the natural fibre waste at different industries, Rice Husk (RH) is one of the agro-industrial waste product which is most accumulated in Sri Lanka and most of Asian countries. About 700 million tonnes of rice produced annually and the RH contain 20% of total paddy weight [1]. Mostly RH waste ends up in landfill or burnt without any uses in the south Asian region [1].

The purpose of this research is to investigate feasibility of NFCs which are manufactured using RH and thermoplastic waste through simple techniques. Therefore comprehensive understanding on the NFCs is essential in terms of their physical, mechanical, durable and chemical characteristics in detail. This paper discusses the findings of the universal tensile test which was carried out with different NFCs with varying RH content.

Fig. 1 Material used for manufacturing of NFCs **a** RH; **b** LDPE

2 Materials and Methods

2.1 Materials

The materials used in the study are RH and Low Density Poly Ethylene (LDPE). RH was obtained from Iranamadu, Kilinochchi which was nearly 2 months old from the harvesting (Fig. 1a). LDPE was obtained from MAS kreeda, Vaanavil, which was used for packing purposes (Fig. 1b).

2.2 Preparation of NFC Sheets

The NFC sheets were manufactured by compression moulding. The hot press machine and cold press machine were used to prepare the NFC sheets. RH and LDPE serve as the reinforcement and matrix respectively, and additional adhesive was not used. The fibre or reinforcement content is the main factor that decides the mechanical properties of any fibre composites [7]. Five types of waste based NFCs were developed by varying the weight fraction of fibre to LDPE weight, and weight fractions considered in this study are 10, 20, 30, 40 and 50%. Simple techniques were used to manufacture NFCs. Initially, a layer of LDPE was laid and then RH was hand laid in a random fashion which forms another layer on top of LDPE layer. This layering process was repeated several times depending on the fraction of reinforcement required for different reinforcement weight fractions considered. Then the layers were pressed using hot press and the sheets were shredded in to small pieces. Subsequently shredded particles put in to a mould and pressed again using hot press machine under 135 °C, 100 psi (689 kPa) temperature and pressure respectively, and

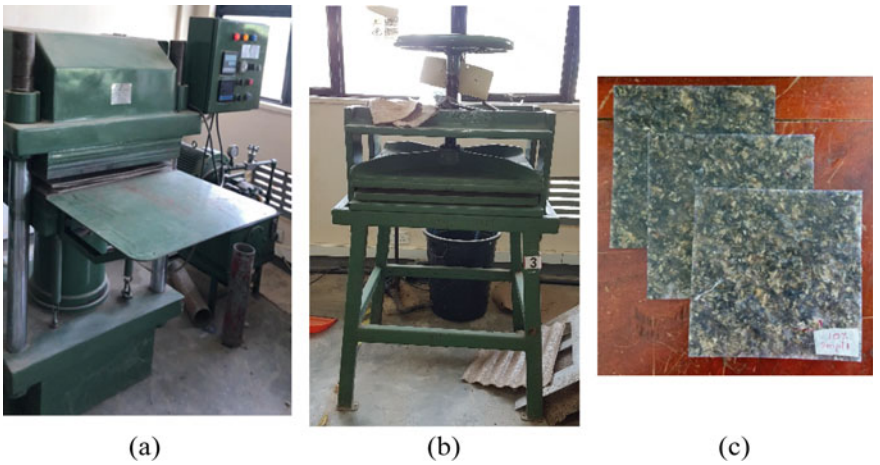

Fig. 2 Machine used for manufacturing **a** hot press machine; **b** cool press machine, **c** 2 mm thick NFCs specimen

2 mm thick NFC sheets were produced. Subsequently, the mould was kept 5 min in the hot press moulding machine. Then, the mould was removed from the hot press moulding machine and it was put in to the cold press machine for another 10 min. The mould was removed after 10 min and the NFC sheets were cut and separated from the mould (Fig. 2).

2.3 Universal Tensile Test

According to ASTM D3039, rectangular shaped specimens were used which cut from the pre-cast NFC sheets. The width for a random-discontinuous composite was 25 mm and the overall length was 150 mm according to ASTM D3039. Twenty (20) specimens were cut in the same direction from each reinforcement weight fraction provided. Universal tensile testing machine was used with displacement control method, and the standard head displacement rate of 2 mm/min was used. Strain gauges were used to obtain the displacement which avoid the inaccuracy due to the slipping of specimens through grips. All the test specimens were tested at ambient condition. Load vs displacement histories were obtained and the average of three measurements were used for each dimension of the test specimens for further analysis.

3 Results and Discussion

The load versus displacement histories were converted in to stress vs strain (engineering) curves and the average stress vs strain relationships for RH content are displayed in Fig. 3, which were obtained by considering all test specimens for each type. All types of NFCs with varying RH content show behaviour of materials having typical nonlinear elastic–plastic region. Young's Modulus, Yield stress, Yield strain, Resilience Modulus and Toughness modulus were obtained using the individual stress vs strain graph which were plotted for each specimen. Young's modulus, yield stress and yield strain was obtained from the strain offset method with 0.005 strain offset. The variation Young's module of the NFCs with the increasing content of RH is shown in Fig. 4. Results shows that Young's module was increased with the RH content, where the highest was obtained with 50% of RH content. Addition of RH acts as a reinforcement material which results stiffness to the NFCs. The variation of yield strength with varying RH content is displayed in Fig. 5. Nearly gradual increment of the yield strength was exhibited up to 40% of RH content showing maximum at 40%, and sudden reduction of the yield strength was shown from 40 to 50% content of RH. Even though the addition of RH as fibre increases the initial stiffness, LDPE content is insufficient as the matrix to bond RH fibre effectively when RH content is 50%, which reduces the yield strength. The addition of 40% of

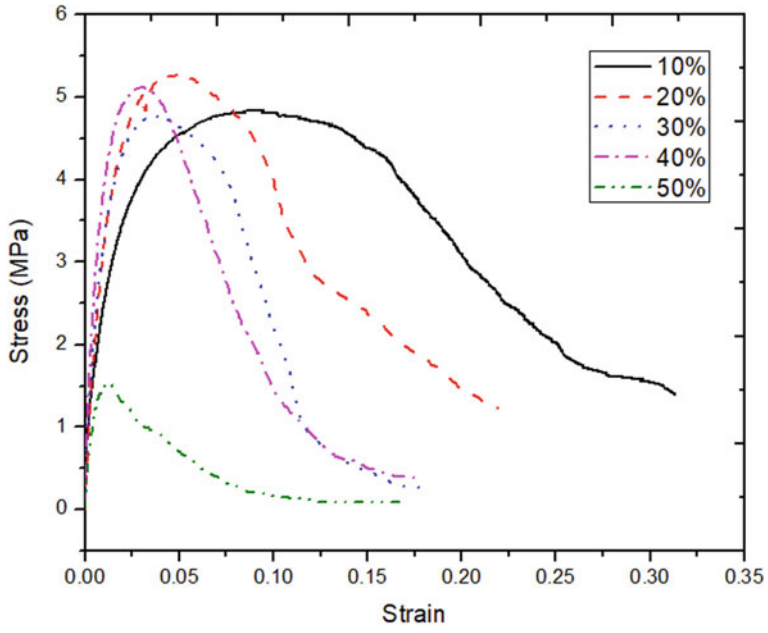

Fig. 3 Average stress versus strain histories for varying RH content

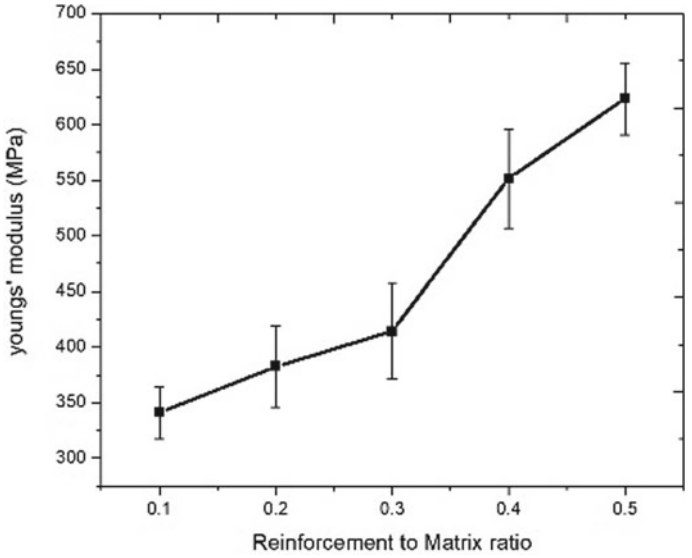

Fig. 4 Variation of Young's modules with RH content

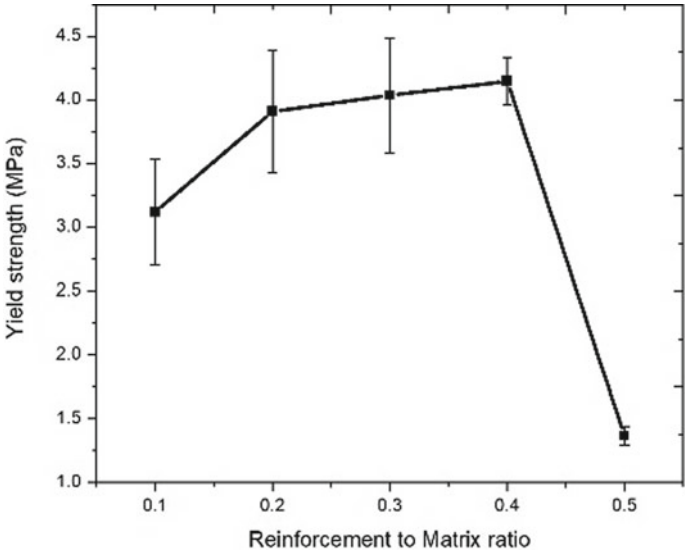

Fig. 5 Variation of yield strength with RH content

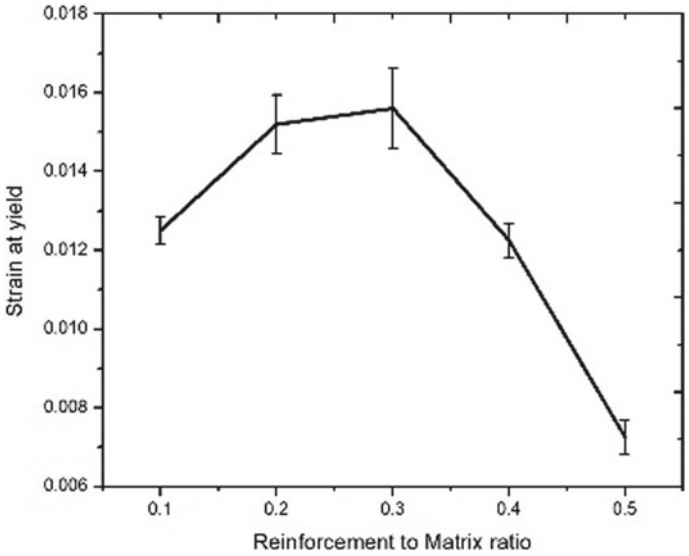

Fig. 6 Variation of yield strain with RH content

RH as the reinforcement material enhances the yield stress by 33% compared to the fully LDPE specimen.

Figure 6 displays the variation of yield strain with RH content, and it shows highest yield strain at 30% of RH content. Yield strain depends on the initial stiffness and elongation capability. Addition of RH fibre increases the initial stiffness while reducing elongation capability, where the highest was observed at 30%.

Yield point is a salient point in the stress–strain response of materials, since it replicate the reversible capability of the material when unloading. Therefore special attention is essential to be paid until the yield point. The ultimate tensile strength variation of the NFCs with the increasing content of fibre is shown in Fig. 7. Results shows that ultimate tensile strength was slightly fluctuating with the fibre content up to 40%, and sudden reduction was observed at 50%, which is same as the response in yield stress.

Cumulative strain energy was calculated by integrating the area under the stress versus strain curve and resilience and toughness modules were obtained. Resilience modules and toughness modules represent the cumulative strain energy up to elastic limit, and fracture point respectively. The variation of resilience modulus along with the increasing content of RH is plotted in Fig. 8. It shows that resilience modulus was increased with the fibre content up to 30%. Because combine effects of enhancement of the yield strength and reduction of the yield strain with the increasing content of RH has resulted its maximum at 30%. This highlights the capability of energy absorption capacity during the elastic deformation which is optimum at 30% of RH content.

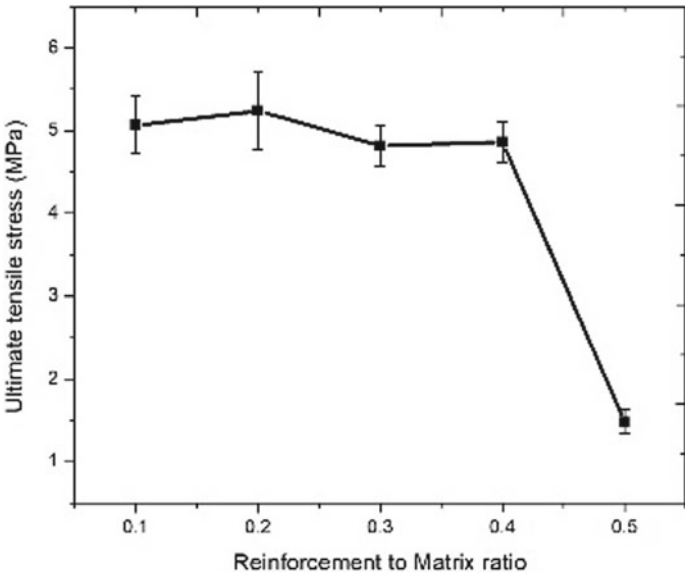

Fig. 7 Variation of ultimate tensile strength with RH content

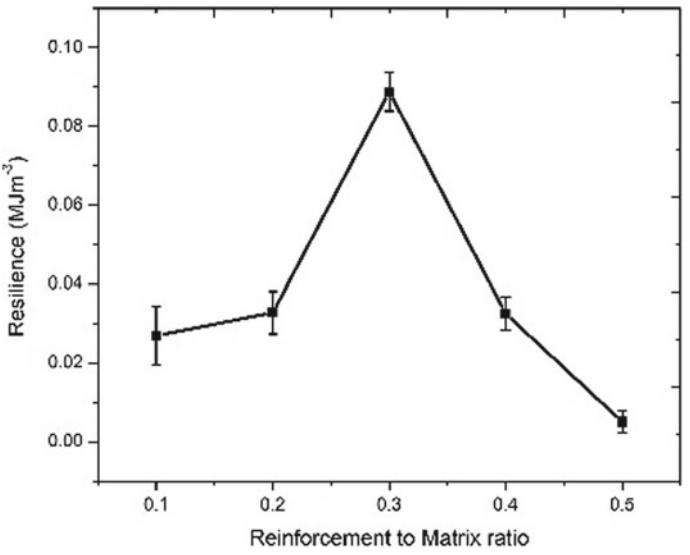

Fig. 8 Variation of resilience modules with RH content

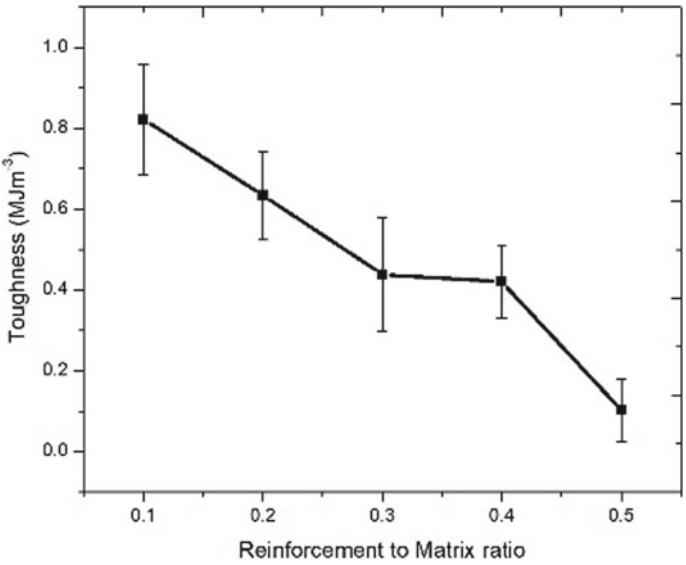

Fig. 9 Variation of toughness modules with RH content

The variation of the Toughness modulus of the NFCs with the varying content of RH is shown in Fig. 9, which shows that toughness modulus was reduced when the RH content is increased. Reduction of the toughness modules was caused by the reduction of the strain capacity due to the addition of RH. This signify the total strain energy that can be absorbed up to its ultimate failure.

4 Conclusion

Evidence of the present study demonstrates the feasibility of manufacturing NFCs with RH and LDPE waste. Findings show that RH can be used as a reinforcing material and the varying content (weight fraction) of RH influence the tensile properties of developed NFCs. The stress–strain relationship shows that all types follow the typical behaviour of an elastic–plastic material. Enhancement in Young's modulus, yield strength, and ultimate tensile strength are noted up to 40%, which show gradual reduction in the Yield strain, and toughness modules. Resilience modules was optimum at 30% of RH content which implies the highest energy absorption capacity under elastic behaviour. This behaviour was mainly due to increment in interfacial bond and adhesion between matrix and reinforcement phases. By considering the overall findings, it can be concluded that the 20–40% RH content provide better overall performance under universal tensile behaviour.

Acknowledgements The authors would like to extend their gratitude to University of Jaffna for providing the necessary funding for this research through URG/2018/SEIT/09, and to the Department of Civil Engineering for the generous supply of materials and laboratory facilities.

References

1. António J, Tadeu A, Marques B, Almeida JAS, Pinto V (2018) Application of rice husk in the development of new composite boards. Constr Build Mater 176:432–439. https://doi.org/10.1016/j.conbuildmat.2018.05.028
2. Dan-Mallam Y, Hong TW, Abdul Majid MS (2015) Mechanical characterization and water absorption behaviour of interwoven kenaf/PET fibre reinforced epoxy hybrid composite. Int J Polym Sci 2015. https://doi.org/10.1155/2015/371958
3. Dittenber DB, Gangarao HVS (2012) Critical review of recent publications on use of natural composites in infrastructure. Compos Part A Appl Sci Manuf 43:1419–1429. https://doi.org/10.1016/j.compositesa.2011.11.019
4. Jayaraman K, Bhattacharyya D (2004) Mechanical performance of woodfibre-waste plastic composite materials. Resour Conserv Recycl 41:307–319. https://doi.org/10.1016/j.resconrec.2003.12.001
5. Kumar PSS, Allamraju KV (2019) A review of natural fiber composites [Jute, Sisal, Kenaf]. Mater Today Proc 18:2556–2562. https://doi.org/10.1016/j.matpr.2019.07.113
6. Maciel NDOR, Ferreira JB, Vieira JDS, Ribeiro CGD, Lopes FPD, Margem FM, Monteiro SN, Vieira CMF, Silva LCD (2018) Comparative tensile strength analysis between epoxy composites reinforced with curaua fiber and glass fiber. J Mater Res Technol 7:561–565. https://doi.org/10.1016/j.jmrt.2018.03.009
7. Pickering KL, Efendy MGA, Le TM (2016) A review of recent developments in natural fibre composites and their mechanical performance. Compos Part A Appl Sci Manuf 83:98–112. https://doi.org/10.1016/j.compositesa.2015.08.038

Development of Pervious Concrete by Using Bottom Ash as Supplementary Cementious Material

L. C. G. De Silva, W. A. N. Dilrukshi, A. S. J. M. U. D. Jayasekara, T. Priyadarshana, and M. K. Samantha

Abstract Urbanization has reduced ground water level and flooding of roads due to extensive use of non-permeable paving method. To continue urbanization while preserving ground water and to mitigate street flooding will require a pervious concrete (PC). Although the pervious concrete has lot of environmental and economic benefits, its uses are still limiting in Sri Lanka. This research provides a background for developing a mix design using BA as a supplementary material and also achieving optimum balance between porosity and strength is essential with use of locally available materials. This study investigated the potential of using coal BA, waste product of coal combustion, as a substitute for sand which is scarce, in an optimum PC mix design. Concrete cubes 150 mm × 150 mm × 150 mm were manufactured in both mix design 1 (MD1) and 2 (MD2). In MD1 coarse aggregate replaced in 5–10 mm and 5–12.5 mm aggregate sizes with BA. In MD2 aggregate sizes of 5–12.5 mm and 14-20 mm studied in two separate arms by serial replacement of cement 0%, 7%, 12%, 15%, 20% and 30%. Compressive strengths were measured in day 7, 14 and 28. Effective porosity, permeability, flexural strength and abrasion have been measured. Cost analysis performed with the selected mix design versus conventional methods. Both 5–12.5 mm and 14–20 mm coarse aggregate mix designs—28-day percentage increase in compressive strength show linear increase and effective porosity inversely proportionate with the percentage replacement of cement with BA. In series replacement with BA both arms showed compressive strength inversely proportionate to percentage increase in effective porosity. Although it decreases the effective porosity with the percentage of BA, the effect on porosity is relatively lesser compared to the increase compressive strength. Optimum mix design of this study was concluded for PC as a paving method is 5–12.5 mm aggregate size with 12% BA replacement. When compared with the conventional paving methods, proposed PC mix design was cost-effective.

L. C. G. De Silva (✉) · W. A. N. Dilrukshi · A. S. J. M. U. D. Jayasekara · T. Priyadarshana
Department of Civil Engineering, Faculty of Engineering Technology, The Open University of Sri Lanka, Nawala, Nugegoda, Sri Lanka

M. K. Samantha
Incee Cement, 413, R. A. De Mel Mawatha, Colombo, Sri Lanka

R. Dissanayake et al. (eds.), *ICSBE 2020*, Lecture Notes in Civil Engineering 174,
https://doi.org/10.1007/978-981-16-4412-2_31

Keywords Pervious concrete (PC) · Bottom ash (BA) · Mix design (MD)

1 Introduction

Pervious concrete (PC) is a pore structure which allows water to percolate through it while maintaining its structural performance. It is a mixture of cement, coarse aggregate and water. The main difference between pervious concrete and conventional concrete is, containing little or no fi-ne aggregates (sand) in mix. Generally, it is comprised of single size coarse aggregates to achieve a continuous void network.

Sometimes admixtures and supplementary cementitious materials are also used to get the desired output. In conventional concrete, mainly the voids between the coarse aggregates are filled with fine aggregates. Cementitious materials are used only to provide a sufficient coating around the aggregates to ensure the durability and bonding [1]. So, the bond between coarse aggregates and cement paste with absence of fine aggregates creates voids. Due to these voids, it has high porosity usually in the range of 15–30% from the total concrete volume. Due to this pore structure allows water to percolate through while maintaining its structural performance.

By using conventional concrete as a paving material, the natural pervious ground is converting in to an impervious land cover. The impervious nature of the conventional concrete pavements causes several adverse effects on the environment. It increases the storm water runoff quantity which results in occurring of flash floods, pollution of natural waterways due to adding of first flush which contains large amount of pollutants, decrease ground water recharge and also it creates thermal discomfort for urban dwellers, tree roots will not get enough water and air etc.

Pervious concrete is an eco-friendly strategy to decrease the impact due to the above reasons. Therefore, the pervious concrete is mainly use as a sustainable paving material for parking areas, pedestrian walk ways, low volume road pavements, tennis courts, as a sound proofing material to reduce traffic induced noise levels and also for partition walls. But it should not use for load bearing structural elements due to low strength characteristics.

Strength and permeability characteristics are the most significant properties of pervious concrete that should concern. Under strength properties, mainly to be consider about compressive strength and flexural strength. When using this as paving material, flexural strength is more significant than compressive strength. Permeability characteristics give an idea about the water passing through it. Permeability is depending on porosity or inter particle void content. When void content is increasing, the permeability is also increasing. But it resulted in decreasing the strength characteristics. These porosity and strength characteristics of pervious concrete is depending on various factors such as aggregate type, aggregate size and gradation, paste content, water/cement ratio, aggregate/cement ratio, compaction method etc.

In lot of countries pervious concrete is widely used as a paving material in the construction field. But in Sri Lanka, use of pervious concrete is not in use due to various reasons such as,

1. Due to absence of proper mix design method suitable for Sri Lankan conditions.
2. Due to rapidly clogging of mud and fine dust particles in voids of pervious concrete.
3. Due to difficulty in achieving required strength and permeability characteristics at same time.

There is a great requirement of developing a simple mix design method for pervious concrete which can be used in Sri Lanka. Another to investigate properties of BA which is a by-product of Norochcholai Coal power plant. This research is intended to simulate and promote effectively recycling of coal BA in construction field and also provide a solution for environmental and social problems related to its disposal. This is the first time in world using BA as a supplementary material for pervious concrete.

This study is carried out to achieve the following objectives.

- To identify the most appropriate mix proportion with suitable aggregate size, gradation and bottom ash composition, which achieve required permeability, based on both strength and porosity.
- To determine the environmental & economic benefits of pervious concrete in Sri Lanka.

2 Methodology

2.1 Materials Used

Aggregates: Locally available coarse aggregates with the size ranges of 5–12.5 mm and 14–20 mm to be used to studied this research.

All aggregate ranges were tested to determined specific gravity, bulk density, absorption and inter particle void content using test methods accordance with BS 812-2-1995 (Aggregate testing).

Grade 42.5 Portland Fly Ash Cement (PPC) was used for all pervious concrete mixes which is having density of 3150 kg/m^3.

2.2 Mix Design Method Used

Proposing simplified mix design methods considering basic principle of inter particle void (IPV) content of aggregates. The basic assumption is that inter particle voids in tamped aggregates are filled with paste volume and air void content in pervious concrete. Figure 1 shows the arrangement of compacted aggregates inside the vessel and shows the IPV values obtained for each combination.

When considering aggregate size range 5–12.5 mm the average IPV content of all aggregate combinations was determined as 0.35 by aggregate test results. Design

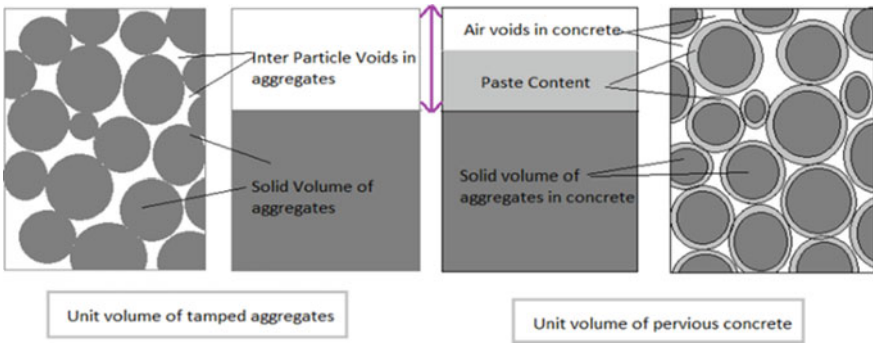

Fig. 1 Simplified proposed mix design method

porosity and paste volume were selected as 0.15 and 0.20 respectively, such that addition of those two values are equal to average IPV content (i.e. 0.35). These values are in the typical ranges in literature.

Water/cement ratio was kept at 0.29 for all concrete mixes which is optimum water/cement ratio for pervious concrete according to literature [2]. Adjustments of mix proportions were made to account absorption and moisture content of course aggregates.

A size of 150 mm × 150 mm × 150 mm moulds were used to determine compressive strength. For each concrete mix 9 cubes were casted in order to check compressive strengths after 7 day, 14 days and 28 days. Effective porosity, permeability, flexural strength and abrasion measured. Cost analysis performed with the selected mix design versus conventional methods.

2.3 Mixing and Compaction Procedure Used

To improve the bond between cement paste and aggregates, mixing and compaction procedure introduced by Wang et al.

2.4 Consistency of Pervious Concrete

As the pervious concrete does not produce significant slump, consistency of pervious concrete was assessed by the ball-in-hand consistency test according to ASTM C860-15. Test is conducted to ensure the fresh mixes attained sufficient wetness to form the aggregate paste bonding. The workability of pervious concrete is assumed to be satisfactory when a handful sample of the mixture is squeezed and released resulting in a mixture that neither crumbles nor becomes void free. Figure 2 shows the consistency of a pervious concrete sample.

Fig. 2 Consistency of pervious concrete

2.5 Laboratory Testing

(a) Compressive strength test
Three cubes which are having a standard dimension of 150 × 150 × 150 mm were used to determine the uniaxial compressive strength of pervious concrete at 28 days according to the test method given in BS1881-117. "200 Ton Amsler testing machine" was used to test the specimens, in which the upper bearing block is stationary while the lower bearing block moves upwards to compress the specimen.

(b) Permeability test
Since pervious concrete has relatively high permeability values, constant head method was used to determine the coefficient of permeability of pervious concrete. Cube specimens which are having (150 × 150 × 150) mm cast inside and Steel and PVC apparatus were used for this test.

(c) Porosity test
Porosity was determined by using basic principles of Archimedes'. The sample which was taken out from the curing tank after 28 days was kept aside for about 20–30 min to drain out pore water. The mass of dry sample was measured (ml). A container was partly filled with water and the weight of container with water was recorded. Scale was set to zero. The specimen was submerged in water and the reading of the scale was recorded (M).

(d) Flexural strength test
Three-point bending test was performed to find the flexural strength of pervious concrete. Beam which is having a standard size of 150 × 150 × 750 mm was used as the specimen.

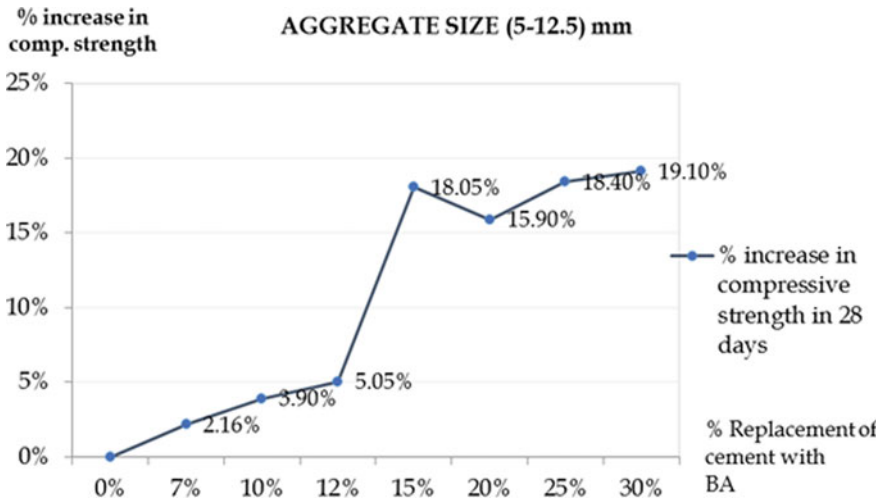

Fig. 3 Percentage increase in compressive strength in 28 days (5–12.5 mm)

3 Results and Discussion

3.1 Compressive Strength

According to the results, observed percentage increasing with compressive strength in 28 days for range (5–12.5) mm getting maximum compressive strength in 15% replacement of bottom ash (BA) and drop with 20% replacement of BA. For range (14–20) mm maximum compressive strength in 25% replacement of BA and started to drop (Figs. 3 and 4).

3.2 Porosity Test

According to the test results shown in above graphs, effective porosity in 28 days for aggregate size range (5–12.5) mm and (14–20) mm were linearly decreases with the percentage increase of replacement of cement with bottom ash.

Graphical representation of variation of porosity with bottom ash replacements are shown in Fig. 5 for range (5–12.5) mm and Fig. 6 for range (14–20) mm.

Variation between effective porosity and compressive strength in 28 days for aggregate range (5–12.5) mm shows in Fig. 7 and aggregate range (14–20) mm shows in Fig. 8.

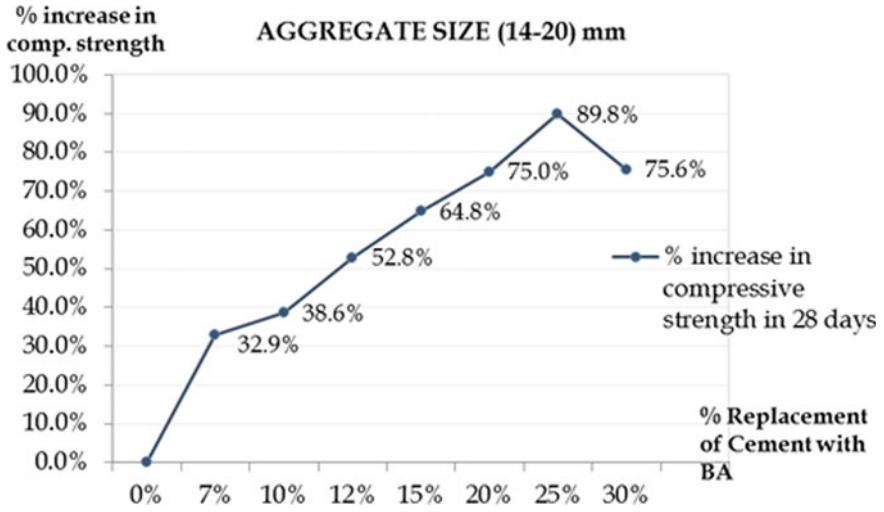

Fig. 4 Percentage increase in compressive strength in 28 days (14–20 mm)

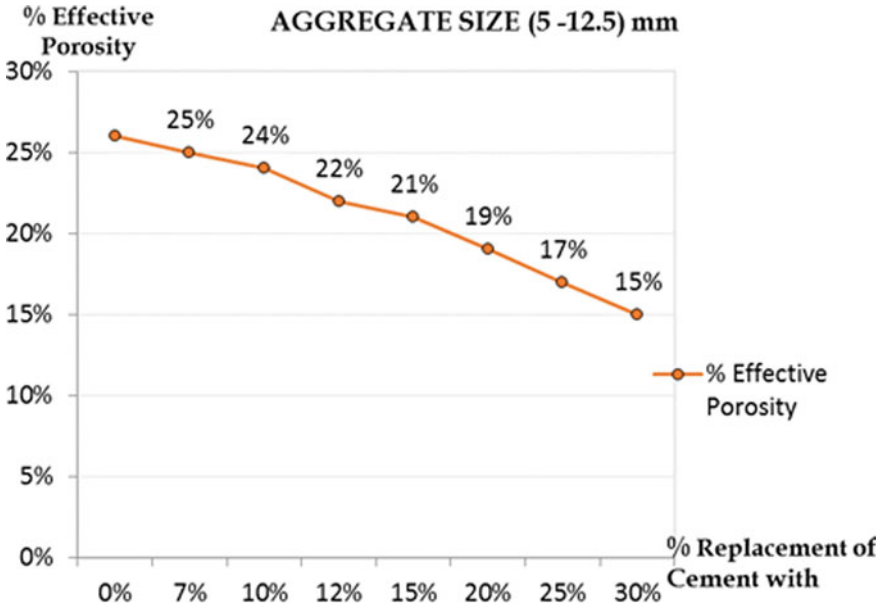

Fig. 5 Percentage of effective porosity (5–12.5) mm

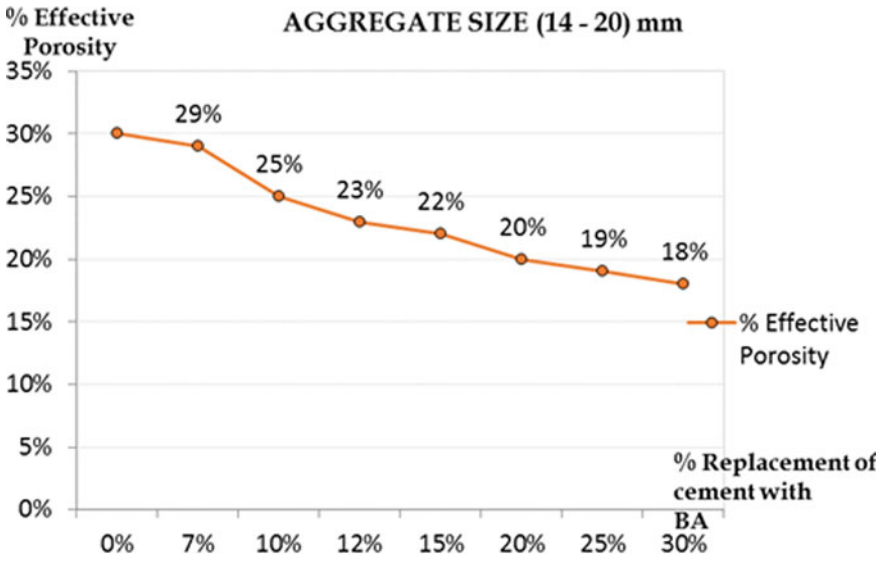

Fig. 6 Percentage of effective porosity (14–20) mm

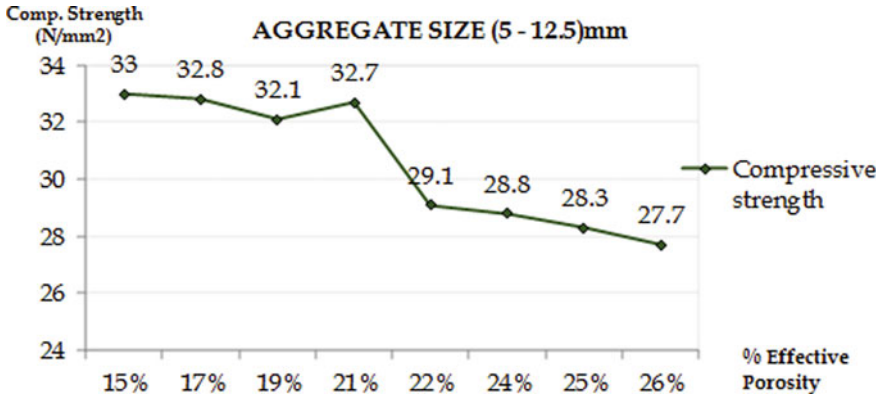

Fig. 7 Effective porosity & compressive strength in 28 days (5–12.5 mm)

3.3 Permeability Test

Void content (air voids) in a previous concrete sample consists of both isolated pores as well as interconnected pores. Interconnected pores mainly contribute for the water percolation through pervious concrete. Generally, the permeability of pervious concrete is varying within the range of 0.2–5.4 mm/s. According to the obtained results, it was observed that most of the permeability values are higher than and

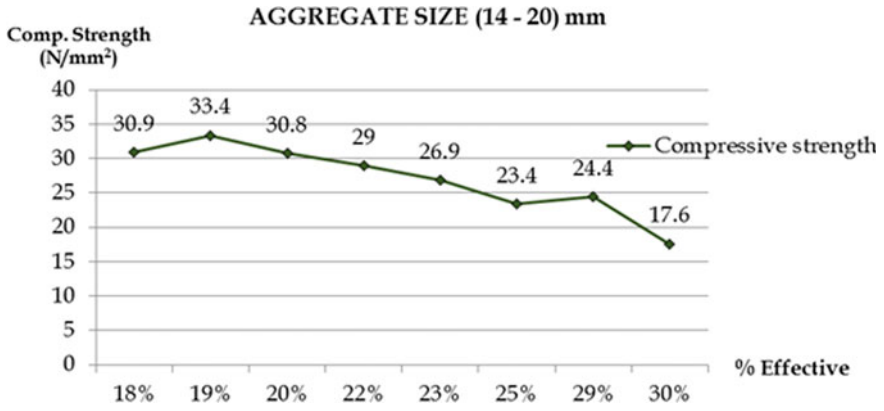

Fig. 8 Effective porosity & compressive strength in 28 days (14–20 mm)

very close to this range and also higher than the permeability value of clean sand (1–0.01 mm/s).

Permeability with bottom ash replacement, the graphs shown in Fig. 9 for range (5–12.5) mm and Fig. 10 for range (14–20) mm in below.

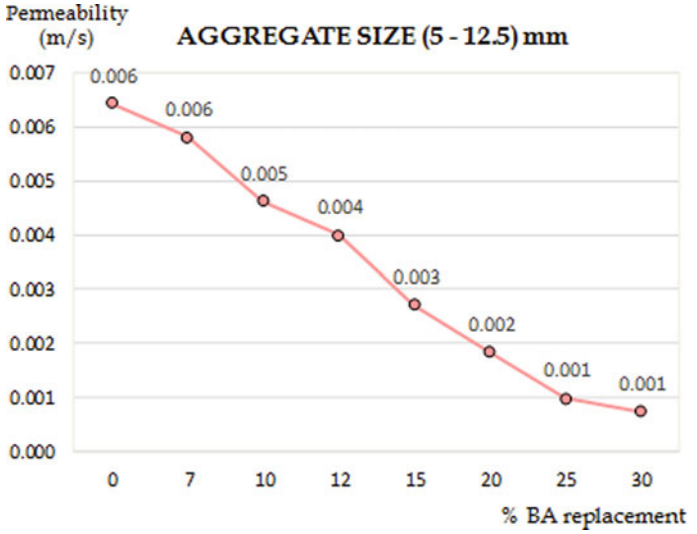

Fig. 9 Permeability of range (5–12.5 mm)

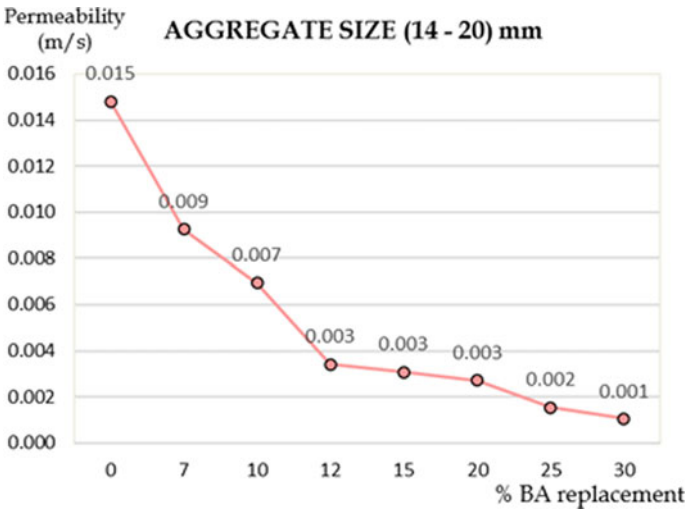

Fig. 10 Permeability of range (14–20 mm)

3.4 Flexural Strength

When using pervious concrete as a paving material, flexural strength is also important as same as the compressive strength. Flexural strength values of pervious concrete are generally ranging between 2 N/mm^2 and 5 N/mm^2. Obtained flexural strength values for tested samples are within this range. Among them range (5–12.5) mm shows the flexural strength value of 3.27 N/mm^2 and range (14–20) mm shows flexural strength value 3.02 N/mm^2.

3.5 Practical Application

According to the results we gathered from testing for Compressive strength, porosity, permeability and also flexural strength for performance evaluation of pervious concrete with bottom ash replacements, we selected most suitable range for our practical application (Figs. 11 and 12; Table 1).

3.6 Cost Analysis

Cost of the developed mix design of pervious concrete using bottom ash compared with conventional paving methods as our main objective to apply proposed pervious concrete as a paving method.

Fig. 11 Practical application of range (5–12.5 mm)

Fig. 12 Practical application of range (14–20 mm)

In this study cost of machinery and skilled labour were not considered. Only cost of material per square meter was compared.

Material cost per 01-meter cube is shown in Table 2 (Fig. 13).

4 Conclusions and Recommendations

The following conclusions can be made from the outcomes of the study.

- Results obtained for physical and chemical properties of Bottom ash (BA) are within the acceptable limits.
- Accordingly, the engineering properties archived from different composition of bottom ash mixes, 12% of cement replacement with bottom ash in both (14–20) mm and (5–12.5) mm aggregate size range showed the best results.
- Results showed adding of bottom ash increases the compressive strength of Pervious concrete.

Table 1 Property details of selected ranges (5–12.5) mm & (14–20) mm

Selected design details for final practical application		
Ref. No	(14–20)–12%	(5–12.5)–12%
Size of aggregate	(14–20) mm	(5–12.5) mm
Cement replacement % with BA	12%	12%
Mix design (considering $1m^3$)	Cement—484 kg	Cement—484 kg
	B/Ash—66 kg	B/Ash—66 kg
	Aggregate—1654 kg	Aggregate—1656.6 kg
	Water—140 kg (W/C = 0.29)	Water—140.3 kg (W/C = 0.29)
	Admixture—2.2 l	Admixture—2.2 l
Days	28	28
Avg. compressive strength (N/mm^2)	26.9	29.1
Porosity (%)	23	22
Actual concrete density for 1 m^3 with results (kg)	2035.8	1809.8
Permeability (mm/s)	3.419	3.527
Flexural strength	3.02	3.27

Table 2 Material cost per 01-m cube

Material	Rates (Rs.)
Aggregate (5–12.5 mm)	1,890.00 per m^3
Aggregate (14–20 mm)	1,890.00 per m^3
Sand	10,000.00 per m^3
Bottom ash	3.85 per kg
Cement	16.96 per kg
Admixture	405.00 per L

- There is good linear relationship between effective porosity and compressive strength.
- Optimum mix design we propose for pervious concrete as a paving method is (5–12.5) mm design 12% BA and (14–20) mm design 12% BA.
- The proposed mix design has permeability within range (3.4–4) mm/s and flexural strength (3.27 N/mm^2) for range (5–12.5) mm and (3.02 N/mm^2) for range (14–20) mm. Hence if it used in pavement and carparks the need for expensive drainage system could be minimized and could prevent city flooding and increase ground water level. So, it could be regarded as green solution for car parks pavement and jogging tracks come with urbanization.
- Bottom ash is a cost-effective secondary material in developing pervious concrete in Sri Lankan set up.

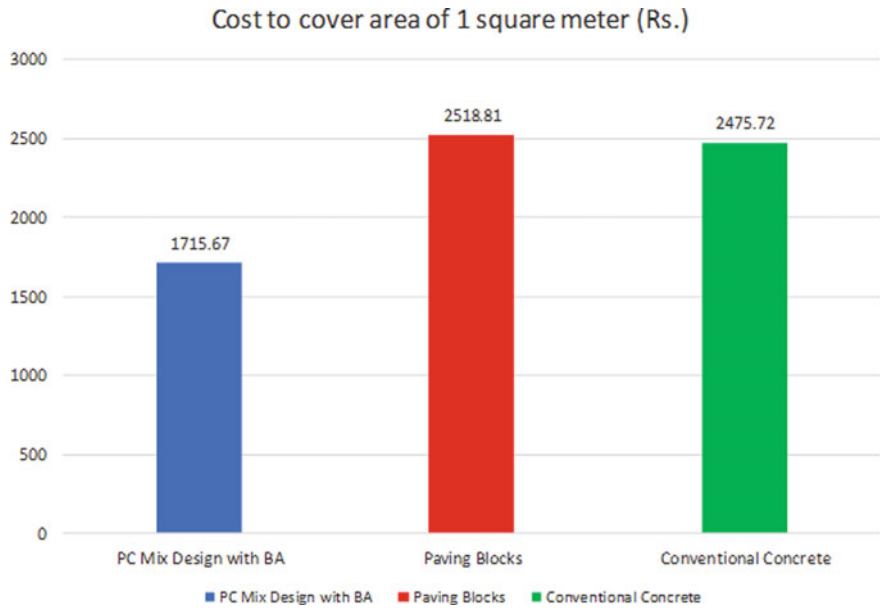

Fig. 13 Graphical representation of cost analysis

- Further studies are suggested.
- It is recommended to investigate on properties of pervious concrete made by using fiber mix supplementary cementitious material as partial replacement for cement or use bonding agent, which will enhance the mechanical properties of pervious concrete.

Acknowledgements We would like to acknowledge Dr. Thushara Priyadarshana, senior lecturer of the Department of Civil Engineering of the Open University of Sri Lanka, our project supervisor, for his patient guidance, enthusiastic encouragement and useful critiques of this project work and also to our research assistant, Engineer Samantha, who is in INSEE for his guidance, comments and support made it possible for us to work on the topic which is of great interest.

Thanks to the Project engineer and Technical and Laboratory staff of Research lab of ICC Precast research lab, Piliyandala, for their help in offering us the resources in running this project from the beginning.

References

1. Chandrappa AK, Biligiri KP (2016) Previous concrete as a sustainable pavement material—research finding and future prospects: a state-of-the-art review. Constr Build Mater 111:262–274
2. Yahia A, Kabagire KD (2014) New approach to proportion pervious concrete. In: Construction and Building Materials. s.l.:s.n., pp 38–46.

Effect of Nano-$Mg(OH)_2$ on the Mechanical and Flame Retardant Properties of Nano-$Mg(OH)_2$-Ribbed Smoked Sheet Rubber Composite

K. M. G. C. Bandara, M. R. Abeywardena, and D. G. G. P. Karunaratne

Abstract Polymeric composites incorporated with inorganic nanofillers have become a greater attraction in the modern field of material chemistry due to their improved properties. Yet flammability is a major drawback as the polymer materials burn easily. Nonflammable polymers made incorporating halogenated fire retardants cause several negative impacts such as emission of corrosive, toxic, and, smoky halogenated compounds. Magnesium hydroxide can be considered as a halogen free fire retardant. In this work, nano-$Mg(OH)_2$ was synthesized using the in-situ deposition method. Ribbed Smoked Sheet (RSS) rubber composites were made incorporating nanofiller in 5–12.5 phr loadings by compounding in the two-roll mill. The composites were tested for tensile strength, hardness, rebound resilience, compression, swelling index and, flame retardancy. Incorporation of nanofiller showed improved mechanical and flame retardant properties.

Keywords Nano-$Mg(OH)_2$ · Fire retardant · Tensile strength · Nano-$Mg(OH)_2$–ribbed smoked sheet rubber composite

1 Introduction

Polymeric-inorganic nano-composites have gained a greater attraction in the modern field of material chemistry. Carbon nanotumes in epoxy resins and polyvinyl alchohol layered silicate nanocomposite are some examples [12]. Studying about nanocomposites has expanded in many fields such as superconductivity, magnetism, nonlinear optics and, thermal stability [12]. Application of nano-composites in flame retardant materials is one of the promising studies among those. Polymers are often filled with fillers and fabricate as composites to improve its stiffness, enhance barrier properties, enhance resistance to fire and ignition and, reduce cost. But it causes drawbacks

K. M. G. C. Bandara (✉) · M. R. Abeywardena · D. G. G. P. Karunaratne
Department of Chemical and Process Engineering, University of Peradeniya, Peradeniya 20400, Sri Lanka

M. R. Abeywardena
Postgraduate Institute of Science, University of Peradeniya, Peradeniya 20400, Sri Lanka

R. Dissanayake et al. (eds.), *ICSBE 2020*, Lecture Notes in Civil Engineering 174,
https://doi.org/10.1007/978-981-16-4412-2_32

such as opacity and brittleness. To overcome these weaknesses nanocomposites with fillers in nanometric range are used [11].

Though the use of polymeric materials is increasing, most of the polymer materials burn easily. Hence flammability is an obstacle. Nonflammable polymers are made by using halogen type flame retardants and antimony trioxide which fulfills the fire-retardant need to a certain extent. But these types of flame retardants have many negative impacts such as emission of corrosive, toxic, and, smoky halogenated compounds. Magnesium hydroxide and aluminium hydroxide are halogen free fire retardants that avoid these drawbacks [4]. Synthesis of nano-$Mg(OH)_2$ with different morphological structures and different particle sizes are done in many methods and their applications as a fire retardant material have been analyzed by many researchers. When heat is applied $Mg(OH)_2$ undergoes an endothermic decomposition leaving MgO which acts as a barrier to protect composite from burning and water which dilutes the concentration of oxygen reducing the burning rate [4]. Positive results have been obtained by them in decreasing the flammability with the use of nano-$Mg(OH)_2$ than conventional $Mg(OH)_2$. This is due to the improved properties of nanoparticles because of their higher surface to volume ratio.

Sri Lanka owns a large dolomite deposition where it mainly contains carbonates of Calcium and Magnesium [1]. Therefore, dolomite can be used as a source to synthesize $Mg(OH)_2$. Magnesite and brucite are some other sources of Mg. Currently, dolomite is mined and powdered and directly used as a fertilizer in cultivation to supply Mg. It is also used in construction industry. If nano-$Mg(OH)_2$ synthesized from dolomite is successfully utilized in a product as a fire retardant material it will be a value addition to a locally available raw material.

Several types of research have been done in incorporating nano-$Mg(OH)_2$ as a filler material in different composites to improve properties. In a study done by Lv et al. [9] have observed that the effect of different morphological structures of magnesium hydroxide nanoparticles on flame retardant properties in ethylene–vinyl acetate blends. It was found that nanocomposites blended with the lamellar-like nanoparticles possess higher flame-retardant efficiency and mechanical reinforcing effect by comparison with common micrometer grade magnesium hydroxide particles through their study. Similarly, Huang et al. [4] have studied about the effect of particle size on flame retardancy of $Mg(OH)_2$ filled ethylene–vinyl acetate copolymer composites and suggested that smaller particle size should be chosen as flame retardants and good dispersion of particles also should be assured. Mechanical and flame retarding properties of nano-$Mg(OH)_2$-polypropylene composites have been observed by Mishra et al. [10] and investigated that the time required to burn nanofilled composite was greater than that of virgin polypropylene. Also, studies have been done incorporating nano-$Mg(OH)_2$ as a filler in different rubber composites such as Styrene-butadiene rubber (SBR), polybutadiene rubber (PBR) and, Ethylene–propylene–diene monomer rubber (EPDM). The effect of nano-$Mg(OH)_2$ in rubber composites has been studied by Zhang et al. [15], Gui et al. [2] and, Patil et al. [11] and observed the improved properties after incorporating the nanofiller.

Though there is a great need in developing flame retardant rubber composites for applications such as electric cables, there are few researches done on this. In

this study surface modified hydrophobic nano-$Mg(OH)_2$ particles were mixed with ribbed smoked sheet (RSS) rubber to fabricate nano-$Mg(OH)_2$-RSS composite with improved mechanical and fire retarding properties. The effect of the nanofiller loading amount on the properties of the final composite was investigated in this work. Nano-$Mg(OH)_2$ was synthesized with an in situ deposition method and the nanoparticle size was confirmed by scanning electron microscopy (SEM).

2 Experimental

2.1 Materials

Ribbed smoked sheet (RSS) rubber was purchased from Dipped Products Pvt. (Ltd.). Magnesium chloride ($MgCl_2$) (70%), sodium hydroxide (NaOH) (98%), urea (CH_4N_2O) (94%), zinc oxide (ZnO) (91%), stearic acid (98%) and, toluene (99.5%) analytical grade were obtained from Sigma Aldrich were used. Sulfur (S) (99%) and 2-Mercaptobenzothiazole (MBT) industrial grade were used.

2.2 Synthesis of Nano-$Mg(OH)_2$

Lamella type nano-$Mg(OH)_2$ particles were synthesized using an in-situ deposition method [6, 10]. Initially, a solution was prepared by dissolving 163 g of NaOH and 10 g of urea in 750 ml of distilled water. 600 ml of the second solution was made by mixing 272 g of $MgCl_2$ and distilled water. $MgCl_2$ solution was filtered using a vacuum filter. $Mg(OH)_2$ mixture was made by mixing $MgCl_2$ solution dropwise with the initial solution while stirring. Then the mixture was stirred for 2 h and kept 24 h for aging. The precipitate was separated using a continuous centrifuge (KOKUSAN H-660) at 10,000 rpm. Separated particles were dried at 90 °C for 48 h.

2.3 Surface Modification of Nano-$Mg(OH)_2$

$Mg(OH)_2$ tends to congregate due to its own chemical property. The dispersion quality of $Mg(OH)_2$ can be improved by modifying the interfacial region between the $Mg(OH)_2$ and polymer matrix. This was achieved by making nano-$Mg(OH)_2$ particles hydrophobic [14]. 0.2 g of stearic acid and 0.22 g of NaOH were added to 125 ml of distilled water and the mixture was stirred using a magnetic stirrer while heating. After the temperature reached to 70 °C, 10 g of nano-$Mg(OH)_2$ particles were added. Then the mixture was stirred for 2 h. The precipitate was washed two

Table 1 Compounding formulation

Ingredient	Amount/phr
RSS rubber	100.0
ZnO	6.0
Stearic acid	0.5
MBT	0.5
Sulphur	3.5
Nano-$Mg(OH)_2$	Variable (0–12.5%)

times with distilled water and two times with ethanol respectively and dried 3 h at 80 °C.

2.4 Compounding and Composite Preparation

For the preparation of nano-$Mg(OH)_2$-rubber composite compounding was done by adding zinc oxide, stearic acid, MBT and, Sulphur to RSS rubber as given in Table 1. Compounding was carried out in a two-roll mill.

Initially RSS rubber was fed into a two-roll mill and ground for 1 min. Then zinc oxide, stearic acid and, MBT were added. After one minute of the milling process, nano-$Mg(OH)_2$ particles were added and milling was continued for another minute. Then Sulphur was added and milled for one minute. After another one minute of dumping the sample was taken out of the mill and kept for 24 h at 20 °C. Then the samples were tested for cure characteristics and rheo graphs using Rubber Process Analyzer (D-RpA3000; monTech, Germany) at 150 °C. After that test sheets were made by vulcanizing the samples at 150 °C and 10 MPa according to the obtained optimum cure time (t_{90}). Finally test specimens were cut from test sheets after 24 h which were kept at 20 °C.

2.5 Characterization of the Vulcanizates

2.5.1 Mechanical Properties

Tensile strength was measured by subjecting dumb-bell shaped specimen to Instron 3365 Universal Testing Machine (Instron Ltd., Buckinghamshire, UK) at a cross head speed of 500 $mm.min^{-1}$. The test was conducted according to the ISO 37: 2005(E) procedure at 27 °C. The hardness of the samples was measured using a Durometer type A (INSTRUMENT and MFG.CO., INC., NEW YORK, USA) according to ASTM D 2240 procedure. Wallace Lupke Pendulum was used to measure rebound resilience according to ISO 46625: 1986(E) procedure. All the results were averaged using five measurements. Compression test was done according to the ISO

815: 1991(E) procedure at room temperature. Percentage compression values were calculated using Eq. (1)

$$Compression = \frac{(t_0 - t_i)}{(t_0 - t_n)} \times 100 \quad (1)$$

where, t_0 = original sample thickness (mm), t_i = final sample thickness after recovery (mm), t_n = thickness of spacers between compression plates (9.54 mm).

2.5.2 Swelling Index

The swelling index is an indirect measurement of total cross-link density. It was determined by immersing the samples in toluene according to ASTM D 471-12a. Initially the weight of 30 mm × 5 mm × 2 mm test pieces were measured and dipped in toluene at 25 °C. The test pieces were kept in a dark environment for 72 h. Then the pieces were dried at 70 °C for 15 min and allowed to cool at room temperature for another 15 min. Finally, the weight was measured in the swelled samples. Swelling index was calculated using Eq. (2) [11]

$$Swelling\ index = \frac{X - Y}{Y} \quad (2)$$

where, X = mass of samples after swelling and Y = mass of samples before swelling.

2.5.3 Flame Retardancy and Thermal Stability

A vertical fire test was carried out similar to the ASTM D 3801 procedures. Width of 10 mm, length of 50 mm and thickness of 2 mm samples hung vertically on a metal wire using metal hooks were fired using liquid petroleum gas flame at the bottom. The time taken to ignite and the time taken to burn the sample completely was measured. Thermogravimetry analysis (TGA) was done using SDTQ600 Thermo Gravimetric Analyzer.

3 Results and Discussion

3.1 Synthesized Nano-$Mg(OH)_2$

Figure 1 shows the SEM images of nano-$Mg(OH)_2$ particles. Lamellar shaped particles were in the range of 50 × 150 nm. Figure 2a, b shows the FTIR spectra of not modified nano-$Mg(OH)_2$ particles and surface modified hydrophobic nano-$Mg(OH)_2$ particles respectively. FTIR spectrum gives evidence for the surfactants adsorbed on

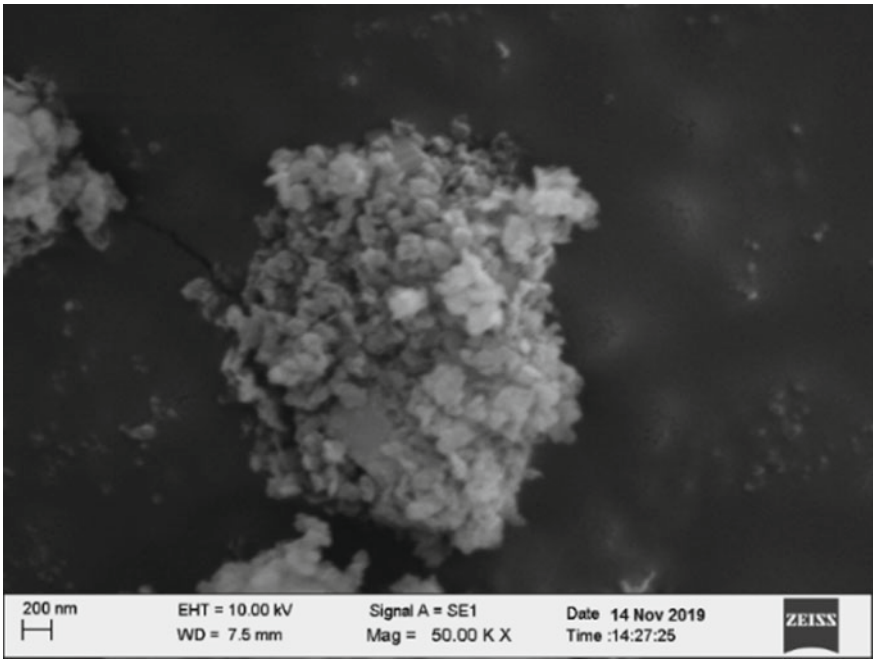

Fig. 1 SEM images of nano-$Mg(OH)_2$ particles

the surface of the nano-$Mg(OH)_2$ particles and functional groups. The sharp peak at 3694 cm^{-1} is due to the O–H stretch in the magnesium hydroxide crystal structure [8]. The adsorption peaks between 1444 and 1623 cm^{-1} can be attributed to the O–H stretching mode in water and the CH_2/NH scissoring mode. The peaks at 2920 and 2850 cm^{-1} are the symmetric vibrations of aliphatic groups $(–CH_2–)_n$, which indicates that the surfactants with the aliphatic groups are adsorbed on the surface of the $Mg(OH)_2$ nanoparticles [9]. Moreover, the absorption of C=O stretching vibration of carboxylate in the surface modified nano-$Mg(OH)_2$ is found at around 1569 and 1462 cm^{-1} [5].

3.2 Vulcanizate

Figure 3 depicts the SEM image of the vulcanizate. It is clear from the images that the particles are properly distributed throughout the rubber matrix.

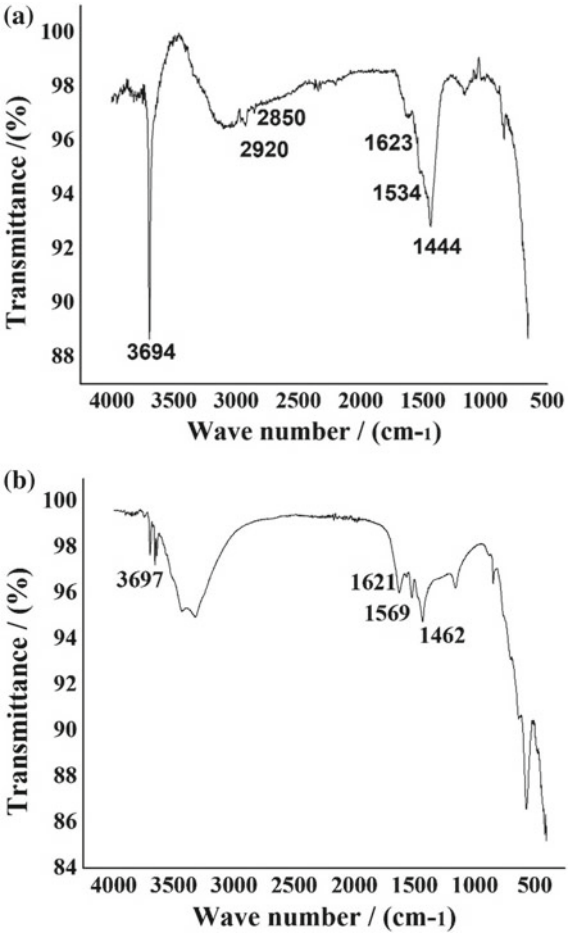

Fig. 2 **a** FTIR spectrum of not modified nano-$Mg(OH)_2$ particles. **b** FTIR spectrum of modified nano-$Mg(OH)_2$ particles

3.3 Mechanical Properties

Curing times of the compounds containing different filler loadings are given in Fig. 4. Curing time is lower up to the 10% filler loading composite. The reason for the lower curing time is the reduced particle size and increased surface area of the filler material. It also increases the surface reaction. Further increment of the filler will drastically increase the curing time with the decreased interaction between rubber and filler matrix due to agglomeration.

Figure 5 demonstrates the tensile strength of the vulcanizates with different filler loadings. Tensile strength has been increased with the increase of filler loading up to 5% and it has been significantly decreased upon further addition of the filler. Usually, nanoparticles are capable of forming a large number of interactions with the polymer matrix due to its high surface area compared to conventional fillers.

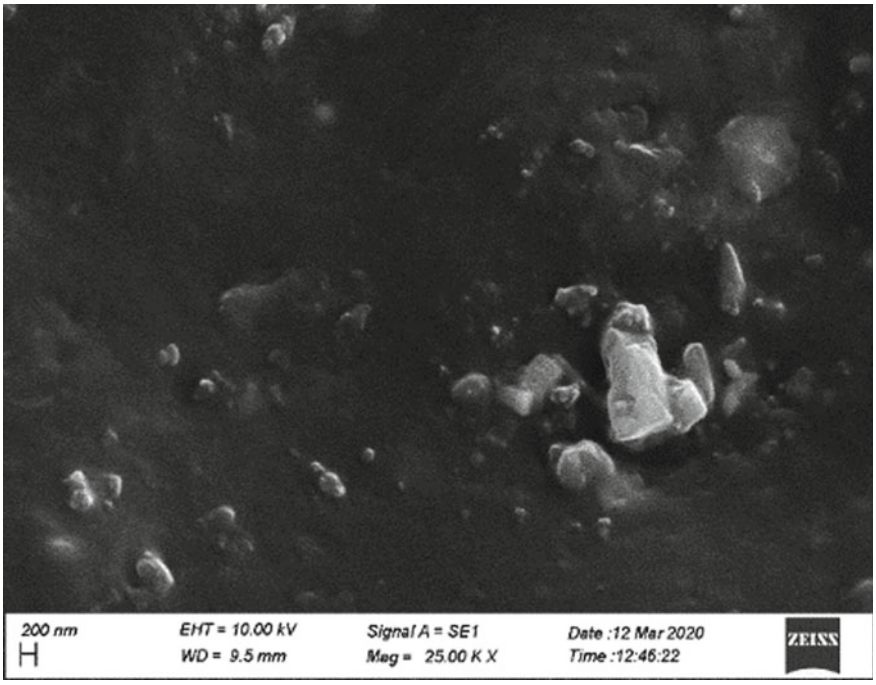

Fig. 3 SEM image of the vulcanizate

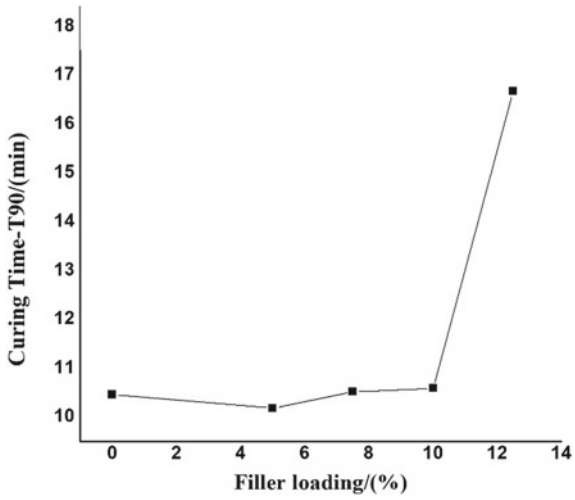

Fig. 4 Curing times of the composites

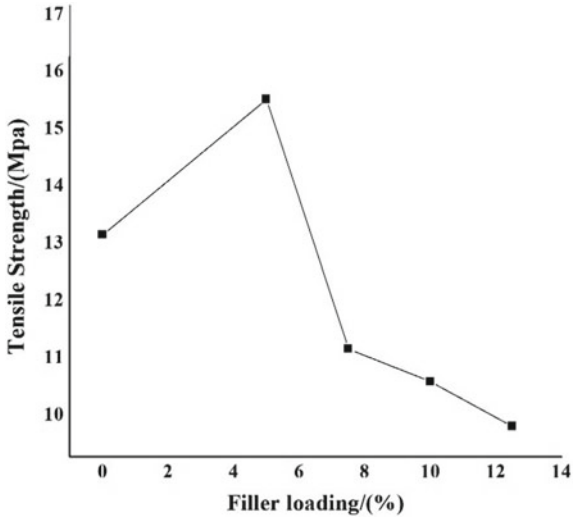

Fig. 5 Tensile strength of the composites

Therefore, existence of the nanofiller may increase the cross-link density within the composite and thus, facilitate the stress transfer into the reinforcement. These factors can cause an increase in the tensile strength of the nanocomposite. However, the reduction of tensile properties after 5 phr may be due to the non-homogeneous dispersion and high agglomeration of the filler particles inside the rubber matrix. It can result in stress concentration on the NR matrix when it is subjected to extension and disturb the steadiness of the composite.

Hardness variation of the vulcanizate is illustrated in Fig. 6. Hardness curve has an upward trend with the increase of filler loading amount. This is due to the strong interactions with the polymer matrix due to the increment of cross-link density.

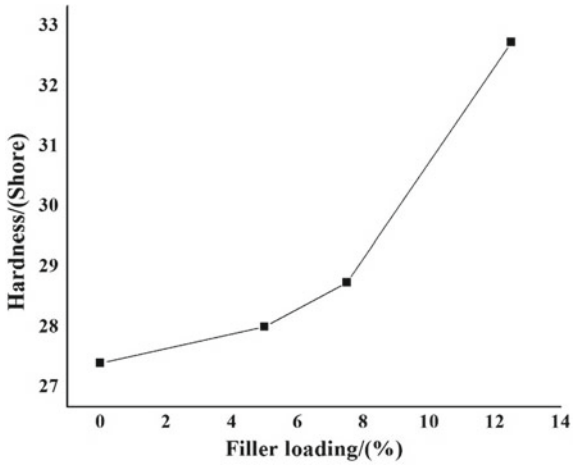

Fig. 6 Hardness of the composites

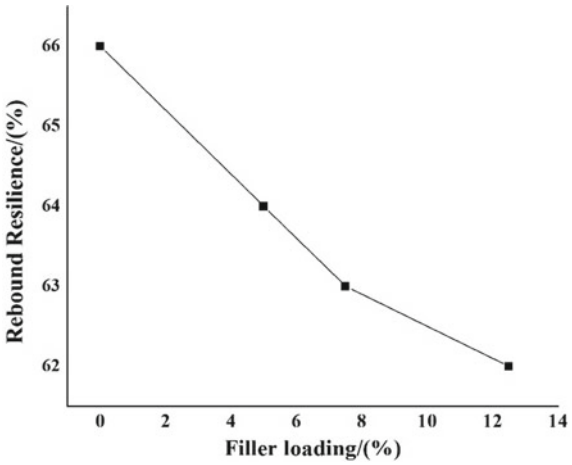

Fig. 7 Rebound resilience of the composites

Figure 7 depicts the rebound resilience variation of the vulcanizates. With the increase of nanofiller loading, the rebound resilience values have behaved in a downward trend. The increase in the filler loading has reduced the molecular mobility while declining the elasticity. Therefore, rebound resilience decreases as the introduction of filler loading facilitates stiffness.

Compression values of nano-$Mg(OH)_2$-RSS rubber composite with different filler loadings are given in Fig. 8. It is seen from the figure that the compression has risen to a peak value at 7.5% filler loading along with the increase of nanofiller. Cross-link density increases with the introduction of nanofiller. As a result, the molecular mobility decreases. When a force is applied these cross-links get damaged and do not get recovered after removing the force. As a result, molecular mobility decreases while increasing the compression [13]. Further increment of filler has reduced the

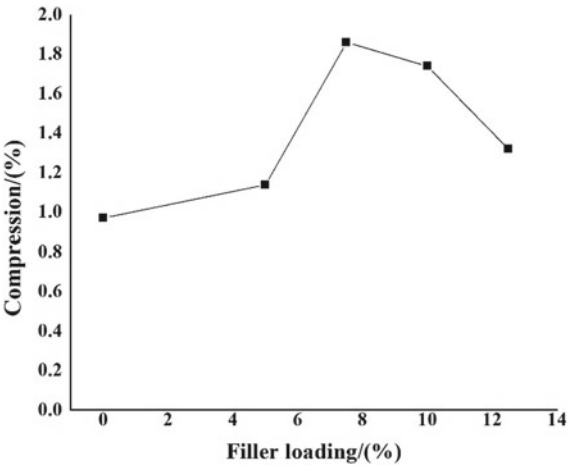

Fig. 8 Compression of the composites

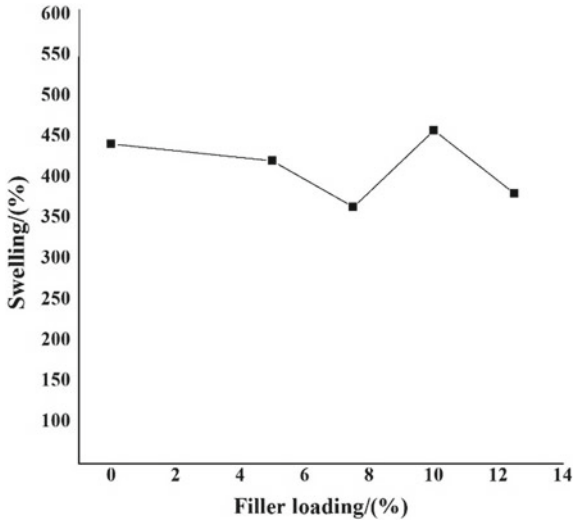

Fig. 9 Swelling index of the composites

compression. This is due to the less damage caused to cross-links due to particle shape change from sharp edged lamellar structure to smooth spherical structure with agglomeration.

Swelling indices of the nano-$Mg(OH)_2$-RSS rubber composite samples are represented in Fig. 9. It is clear from the diagram that there are no significant fluctuations in the swelling indices along with the incorporation of nanofiller. Swelling percentage has been slightly decreased up to 7.5% filler loading with the increase of nanofiller. The resistance to swelling due to cross-links is the reason for this behaviour. This in return decreases the toluene absorption. Further increment of filler has been slightly increased the swelling percentage. This is due to the higher toluene absorption into the pores formed by agglomeration.

3.4 Thermal Stability and Flammability

The decomposition characteristics of the $Mg(OH)_2$ are very important and related to the flame retardancy of the composite [4]. When heat is supplied $Mg(OH)_2$ decomposes endothermically into MgO while releasing water. This process absorbs a lot of heat. Released water can reduce the concentration of oxygen on the surface of the material and MgO acts as a barrier protecting the composite from burning.

Figure 10 depicts the TGA curves of composites with different filler loadings. It can be seen that the first weight loss which accounts for the decomposition of nano-$Mg(OH)_2$ and rubber started at 380 °C and ended at 500 °C in all the samples. It can be stated that incorporation of nanofiller has not affected the thermal stability of the composite. The second weight loss which is very slight is due to the firing of MgO

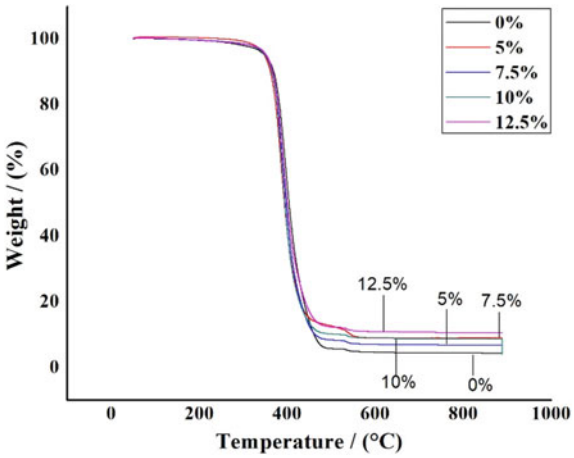

Fig. 10 TGA graphs of the composites

[3, 7]. The residue amount has been increased with the increase of nanofiller. That is because of the more formation of the MgO.

Time taken for the ignition and time taken for the complete combustion of the composites with different nanofiller concentrations are given in Figs. 11 and 12 respectively. Both the times have been increased with the increased incorporation of filler. This is due to the high heat absorption caused by the endothermic decomposition of nano-$Mg(OH)_2$. Through the figures, it is clear that nano-$Mg(OH)_2$ is appropriate qualitatively and quantitatively in improving flame retardancy.

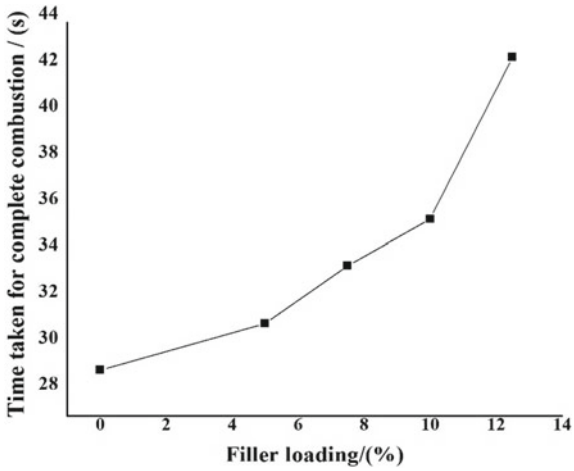

Fig. 11 Time taken for complete combustion of the composites

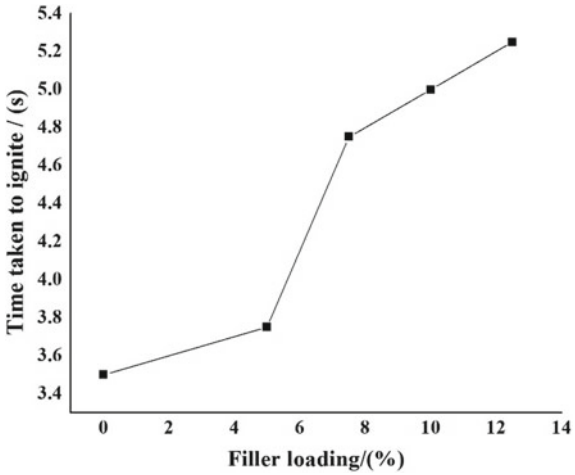

Fig. 12 Time taken to ignite the composites

4 Conclusions

Nano-$Mg(OH)_2$-RSS rubber composites were successfully prepared by mechanical compounding and curing. The synthesized composites were compared with virgin RSS. The Nano-$Mg(OH)_2$ filler showed improved mechanical and flame retardant properties. Flame retardancy improved significantly with the increase of nanofiller loading proving nano-$Mg(OH)_2$ as a promising flame retardant. The highest tensile strength was observed in the sample with optimum filler loading of 5%. Furthermore, it has a lower swelling index and better curing along with improved mechanical properties.

References

1. Abeywardena MR et al (2020) 'Surfactant assisted synthesis of precipitated calcium carbonate nanoparticles using dolomite: effect of pH on morphology and particle size. Adv Powder Technol Soc Powder Technol Jpn 31(1):269–278. https://doi.org/10.1016/j.apt.2019.10.018
2. Gui H et al (2007) Flame retardant synergism of rubber and $Mg(OH)_2$ in EVA composites. Polymer 48(9):2537–2541. https://doi.org/10.1016/j.polymer.2007.03.019
3. Hanna AA, Abdelmoaty AS, Sherief MA (2019) Synthesis, characterization, and thermal behavior of nanoparticles of $Mg(OH)_2$ to be used as flame retardants. J Chem. https://doi.org/10.1155/2019/1805280
4. Huang H et al (2006) Effect of particle size on flame retardancy of $Mg(OH)_2$-filled ethylene vinyl acetate copolymer composites. J Appl Polym Sci 100(6):4461–4469. https://doi.org/10.1002/app.22677
5. Huang H et al (2007) Stearic acid surface modifying $Mg(OH)_2$: mechanism and its effect on properties of ethylene vinyl acetate/$Mg(OH)_2$ composites. https://doi.org/10.1002/app
6. Jiang W et al (2009) Preparation of lamellar magnesium hydroxide nanoparticles via precipitation method. Powder Technol 191(3):227–230. https://doi.org/10.1016/j.powtec.2008.10.023

7. Kandola BK, Campus D (2009) Study of the relationship between flammability and melt rheological properties of flame retarded poly (butylene terephthalate) containing nanoclays, pp 1–24. https://doi.org/10.1039/9781847559210-00168
8. Liu P, Guo J (2007) Organo-modified magnesium hydroxide nano-needle and its polystyrene nanocomposite. J Nanopart Res 9(4):669–673. https://doi.org/10.1007/s11051-006-9079-4
9. Lv J, Qiu L, Qu B (2004) Controlled synthesis of magnesium hydroxide nanoparticles with different morphological structures and related properties in flame retardant ethylene-vinyl acetate blends. Nanotechnology 15(11):1576–1581. https://doi.org/10.1088/0957-4484/15/11/035
10. Mishra S et al (2004) Effect of nano-$Mg(OH)_2$ on the mechanical and flame-retarding properties of polypropylene composites. J Appl Polym Sci 94(1):116–122. https://doi.org/10.1002/app.20750
11. Patil CB et al (2008) Effect of nano-magnesium hydroxide on mechanical and flame-retarding properties of SBR and PBR: a comparative study. Polym Plast Technol Eng 47(11):1174–1178. https://doi.org/10.1080/03602550802391987
12. Qiu L et al (2003) Preparation and characterization of $Mg(OH)_2$ nanoparticles and flame-retardant property of its nanocomposites with EVA. Compos Struct 62(3–4):391–395. https://doi.org/10.1016/j.compstruct.2003.09.010
13. Wypych G (2017) Microscopic mechanisms of damage caused by degradants. Atlas Mater Damage 113–305. https://doi.org/10.1016/b978-1-927885-25-3.50007-0
14. Zhang F, Zhang H, Su Z (2007) Surface treatment of magnesium hydroxide to improve its dispersion in organic phase by the ultrasonic technique. Appl Surf Sci 253, 7393–7397. https://doi.org/10.1016/j.apsusc.2007.03.022.
15. Zhang Q et al (2004) Effect of particle size on the properties of $Mg(OH)_2$-filled rubber composites. J Appl Polym Sci 94(6):2341–2346. https://doi.org/10.1002/app.21037

Utilization of Coal Fly Ash and Bottom Ash as Raw Materials in Synthesis of Zeolites

H. M. R. S. Herath, C. S. Kalpage, and A. Manipura

Abstract Continuous production and accumulation of coal ash in coal boilers has become a major economic and environmental concern. Transport of ash offsite for cement and concrete production seems economically unattractive. On-site value addition can be done if coal ashes could be converted to zeolites that possess high environmental applications. The present study was done to evaluate the possibility of converting coal ashes to zeolites. Coal ashes were subjected to chemical treatments to study the effect on material characteristics. X-ray fluorescence spectrophotometry results evidenced extraction of Al with alkaline treatment and extraction of Si with acid treatment proving the possibility of synthesizing zeolite X with alkaline treatment. Alkaline treatment followed by hydrothermal crystallization yielded 62% and 54% of zeolite from fly ash and bottom ash respectively. X-ray diffraction and Fourier transformation-infrared spectroscopy patterns of synthesized zeolites showed characteristics of standard zeolite X, verifying the formation of Zeolite X.

Keywords Coal fly ash · Coal bottom ash · Zeolite X · Alkaline fusion · Alkaline treatment · Acid treatment

1 Introduction

Coal ash is a byproduct of coal combustion mainly in coal boilers and power plants and has a very low commercial value. These coal combustion byproducts can be described as inorganic residues which also contain unburned carbon. Coal fly ash, which is finer and rises with flue gases, and coal bottom ash, which is heavier and remains at the bottom are mainly categorized as coal ashes. Continuous generation and accumulation of these coal ashes in production facilities and power generation processes have become a huge economic and environmental problem mainly due to the filling up of land space and unsafe disposal methods. Coal ash waste from power plants has been used as a raw material in the production of cement over some time

H. M. R. S. Herath (✉) · C. S. Kalpage · A. Manipura
Department of Chemical and Process Engineering, Faculty of Engineering, University of Peradeniya, Peradeniya, Sri Lanka

R. Dissanayake et al. (eds.), *ICSBE 2020*, Lecture Notes in Civil Engineering 174,
https://doi.org/10.1007/978-981-16-4412-2_33

[10] and currently, the manufacturing of Autoclaved Aerated Concrete (AAC) blocks using coal ash has become trending in most of the countries including Sri Lanka. AAC production paves the path to managing coal ash generated not only in power plants but also in boilers in process industry. But, there can be more economical solutions that lead to proper management of coal ash on-site other than transporting tons of material to AAC production facilities or cement kilns. Utilization of daily produced fly ash and bottom ash for on-site synthesis of zeolites seems an appealing solution.

Coal ash itself is used in water purification applications but, applications are limited due to low adsorption capacity [4]. Coal ashes mainly consist of Si and Al and offer great potential for converting into zeolites which are generally known as alumino-silicates (AlO_4^{5-}, SiO_4^{4-}) with three dimensional tetrahedral frameworks. Having a repetitive uniform structure, zeolites offer a large surface area with high porosity for many adsorption applications. Charge imbalance in the framework makes it hold cations like heavy metals, ammonia, toxins, odors, petrochemicals, and other gases. Conversion of coal ash to zeolites is simply a value addition by going through a simple process. So it can be hypothesized that, a value addition can be done to coal fly ash and bottom ash by converting them to zeolites due to the high content of oxides of Si and Al present.

This study is aimed to evaluate the possibility of synthesizing zeolite X from coal fly ash and bottom ash obtained from fluidized bed boiler, Brandix Textiles Ltd., Pannala, Sri Lanka. The first stage of the study is aimed to evaluate the effect of pretreatments with alkaline and acid solutions while the second stage of the study is aimed to synthesize zeolite X from alkaline fusion method and evaluate the characteristics of products and raw materials.

2 Materials and Methods

This study was done in two stages where in the first stage, fly ash and bottom ash were treated with NaOH and HCl to study the effect of those treatments on material properties and then, with the conclusions of stage 1, stage 2 was conducted to synthesize and characterize zeolites synthesized from coal fly ash and bottom ash. Characterization results of raw materials and treated samples in stage 1 were analyzed to identify significant effects on the material properties. Characterization results of raw materials and synthesized zeolites were analyzed to verify the formation of zeolite X with the help of characteristics of standard zeolite X.

2.1 Materials

The samples of coal fly ash and coal bottom ash were collected from fluidized bed boiler, Brandix Textiles Ltd., Pannala, Sri Lanka. 98% NaOH and HCl were used for

pretreatments and analytical grade NaOH pallets were used as the activation agent in zeolite synthesis.

2.2 Material Characterization

The ashes and products were characterized by X-ray fluorescence spectrophotometer (XRF) to determine elemental compositions by using HORIBA Scientific XGT- 5200 X-ray Analytical Microscope. Surface morphology of products was analyzed by scanning electron microscopy (SEM), Hitachi SU6600 Analytical Variable Pressure FE-SEM (Field Emission Scanning Electron Microscope). X-ray diffraction (XRD) patterns were obtained to observe crystalline phases from X-Ray Diffractometer: Bruker D8 Focus under the conditions, Cu-Kα radiation (1.54 Å), a voltage of 40 kV, a current of 40 mA, 2θ range from 5° to 80°, an increment of 0.5° and a scan speed of 10.0 s/step. Functional groups of raw materials and products were observed by Fourier transformation infrared spectroscopy (FTIR) using the Bruker Vertex80 FT-IR Spectrometer.

To evaluate the zeolite synthesis process, percent yield of zeolite produced was calculated using Eq. (1).

$$\%\ \text{yield} = \frac{W_{Zeolite}}{W_{Coal\ ash}} \times 100 \tag{1}$$

where, $W_{zeolite}$ is the weight of the zeolite product (g), and $W_{Coal\ ash}$ is the weight of the raw material (g), either fly ash or bottom ash.

2.3 Pretreatments of Raw Materials

Coal fly ash and bottom ash were subjected to two types of treatments to enhance the content of Si and Al and study the effect of pretreatment methods [3]. Coal ashes were treated with NaOH where 10 g of ash was dissolved in 100 mL of NaOH solution at 2 mol/L followed by heat treatment at 90 °C for 24 h. Next coal ashes were treated with HCl where 80 g of ash was dissolved in 100 mL of HCl solution at 2 mol/L followed by drying at 90 °C for 48 h. Raw materials and treated samples were characterized by XRF, XRD, and FT-IR.

2.4 Zeolite Synthesis

Alkaline fusion method [8] was used to convert coal ashes to zeolite X. Fly ash or bottom ash was mixed with ground NaOH at 1:1.2 ratio. The solid mixture was

placed in muffle furnace at 600 °C for one and a half hours. The heat-treated product was ground and mixed with deionized water at 0.2:1 ratio and stirred for 24 h. The formed hydrogel was placed in the oven at 100 °C for 24 h. The dried product was washed with deionized water until the pH reduces to 10–11. It was then centrifuged at 200 rpm and dried in the oven at 110 °C for 24 h. Products were characterized by XRF, SEM, XRD, and FT-IR.

3 Results and Discussion

3.1 Effect of Pretreatments

Elemental compositions of coal fly ash and bottom ash obtained from XRF are shown in Table 1. Silicon and aluminum show highest percentages compared to other elements like Fe, Ca, Mg and K. These elements are generally present as oxides in coal ash and presence of high amounts of oxides of Si and Al verify the potential of coal ashes to convert into zeolites which have three-dimensional tetrahedral frameworks of Si and Al in which two tetrahedra are connected with an oxygen atom.

Si/Al ratio of raw materials used for zeolite synthesis is very important as it directly affects the yield and purity of the product [3]. Therefore Si/Al ratio of raw materials should be adjusted by performing necessary pretreatments to remove impurities and extract more Si and Al. According to Table 1, NaOH treated ash samples show reduced percentage of Si and increased percentage of Al resulting extraction of Al while HCl treated ash samples show increased percentage of Si and reduced percentage of Al resulting in extraction of Si. During the treatment process a decrease in Ca, Fe and other impurities can be observed. Reduction of impurities acts favorably in the synthesis of zeolites as they tend to inhibit the growth of zeolite crystals in certain planes [2, 9].

The next stage of this study was aimed to synthesize zeolite X which has Si/Al ratio between 2 and 3 [6]. Coal fly ash and bottom ash show Si/Al ratios of 3.4 and

Table 1 Chemical composition of coal ashes and treated samples obtained by XRF

Element	Coal fly ash (Mass %)			Coal bottom ash (Mass %)		
	Raw	NaOH treated	HCl treated	Raw	NaOH treated	HCl treated
Si	50.4	48.79	56.12	39.81	38.01	44.21
Al	14.84	17.77	13.24	15.3	18.02	14.32
Fe	16.77	14.32	13.07	24.45	20.34	19.84
Ca	6.38	4.65	4.03	8.28	8.02	8.22
Mg	4.48	4.32	4.31	5.42	4.92	5.02
K	3.73	4.34	3.91	3.37	4.21	4.04
Si/Al	3.4	2.7	4.2	2.6	2.1	3.1

2.6 respectively. So to obtain zeolite X, Si/Al ratio should be reduced. This can be achieved by extracting more of Al by treating with NaOH. Therefore, activation with NaOH is recommended for synthesis zeolite X using these raw materials.

Figure 1 shows X-ray diffraction spectrums obtained for fly ash and alkaline and acid treated fly ash samples. Peaks appeared at 2θ values; 20.9°, 26.6°, 50.1° and 67.9° correspond to crystalline phase quartz (SiO_2) while peaks appeared at 2θ values; 16.7°, 26.2° and 60.1° correspond to crystalline phase mullite ($Al_6Si_2O_{13}$) [7]. These XRD results also prove the presence of Si and Al in coal ash and support the conclusion that coal ash is a potential raw material for synthesis of zeolites. According to Fig. 1, the X-ray diffraction of raw sample and treated samples have the same pattern, giving the idea that pretreatments with either alkaline or acid did not affect the crystalline phases present in the raw sample.

FT-IR spectrums for raw fly ash and treated ash samples are shown in Fig. 2. FT-IR spectroscopy is used to identify functional groups present in a certain sample by recording vibrations that occurred due to bond stretching and bending moments when subjected to infra-red radiation. Vibrations at wavenumbers 3451 and 1639 cm^{-1} correspond to stretching and bending of bonds of hydroxyl groups adsorbed on the surface of the ashes. The band at 1078 cm^{-1} corresponds to asymmetric stretching vibration of Si–O(Al) while the band at 794 cm^{-1} corresponds to asymmetric stretching of O–T–O groups (T can be either Si or Al). At 462 cm^{-1}, bending vibration of O–Si–O is present [5]. FT-IR results also prove the presence of high contents of Si and Al. Raw sample and treated samples show bond vibrations at almost the

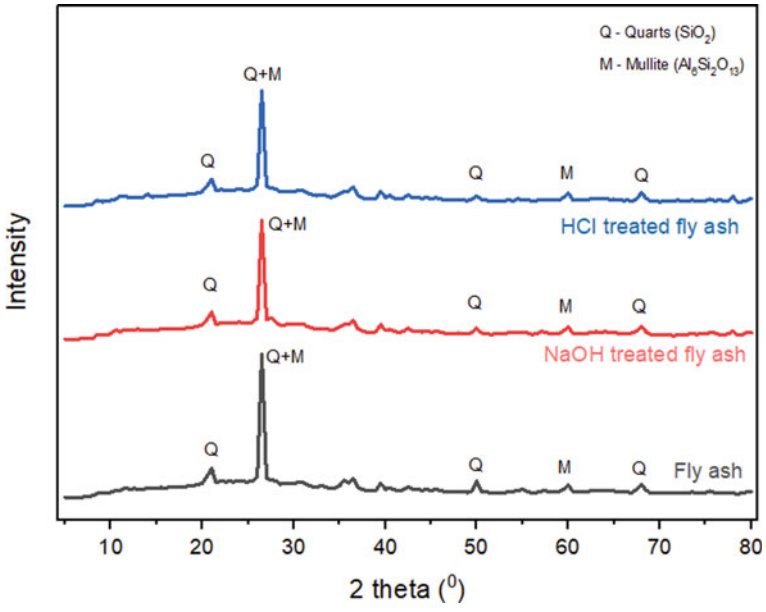

Fig. 1 X-ray diffraction of fly ash and treated ash samples

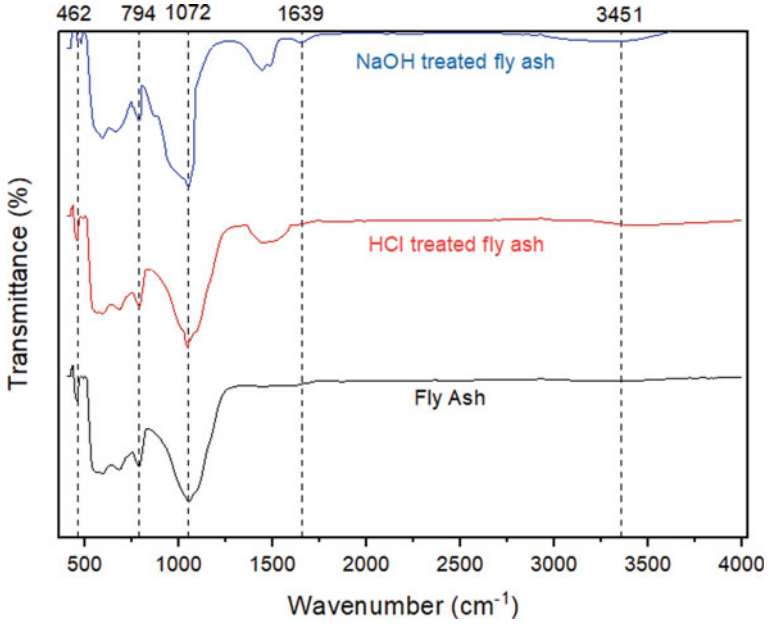

Fig. 2 FT-IR spectrum of fly ash and treated ash samples

same wavenumbers giving the idea that pretreatments had not affected the original bonds present in raw ash. In addition to that, the intensity of bands especially at 3451 and 1639 cm^{-1} has increased due to pretreatments suggesting an increase in the concentration of more hydrated products.

3.2 Zeolite Yield and Elemental Compositions

Zeolite yield was obtained considering the total mass of zeolite synthesized by the alkaline fusion method. Table 2 shows percent yields of zeolites obtained from fly ash and bottom ash considering 3 trials with the same NaOH/Ash ratio. Fly ash yielded 62% of zeolite while bottom ash yielded 54% of zeolite under the same conditions. As shown in Table 3, bottom ash possesses more impurities (components other than Si and Al) than fly ash. Presence of unburned carbon in coal ash is very common in industrial boilers and power generation processes. Among fly ash and bottom

Table 2 Percent yield of zeolites synthesized from coal fly ash and bottom ash

	Si/Al	NaOH/Ash	Yield percent (%)
Zeolite-fly ash	3.4	1.2	62
Zeolite-bottom ash	2.6	1.2	54

Table 3 Elemental compositions of raw materials and synthesized zeolites

Element	Mass %			
	Fly ash	Zeolite-FA	Bottom ash	Zeolite-BA
Si	50.4	46.34	39.81	33.54
Al	14.84	16.3	15.3	16.9
Na	–	14.72	–	20
Fe	16.77	13.2	24.45	17.5
Ca	6.38	3.22	8.28	4.58
Mg	4.48	4.82	5.42	1.67
Si/Al	3.4	2.8	2.6	2.0

ash, bottom ash has more tendency to contain unburned carbon resulting in low percentages of Si and Al. During the process of converting coal ash to zeolites, the raw materials undergo many treatments including heat treatments. These treatments may result in evaporation of volatile carbon or other compounds and formation of gases like CO and CO_2 reducing the mass of the final product [2]. Other impurities like CaO and Fe_3O_3 also reduce during the process. So, the presence of more impurities results in the reduction of final product yield.

As shown in Table 3, alkaline fusion of coal ash resulted in products with Si/Al ratios lie in the range of standard zeolite X (which is 2–3).

3.3 Morphological Analysis of Synthesized Products

Standard zeolite X has an octagonal crystal shape [8]. Micrograms of zeolites synthesized by coal fly ash and bottom ash are represented in Figs. 3 and 4 respectively. Octagonal crystal shape cannot be observed in both cases. The presence of impurities interfere the growth of zeolite crystal. Impurities like CaO, Fe_2O_3 and unburned carbon restrict the growth of crystal lattice in certain planes resulting in distorted shapes [2]. The shape of zeolite synthesized from bottom ash deviates more from octagonal shape than that of the zeolite synthesized from fly ash due to the presence of more impurities in bottom ash.

3.4 Analysis of Crystalline Phases

Figures 5 and 6 show X-ray diffraction patterns obtained from XRD for fly ash and its zeolite, and bottom ash and its zeolite respectively. As discussed in Sect. 3.1, fly ash and bottom ash shows characteristic peaks mainly for quarts (SiO_2) and mullite ($Al_6Si_2O_{13}$). After going through the alkaline fusion process, new peaks

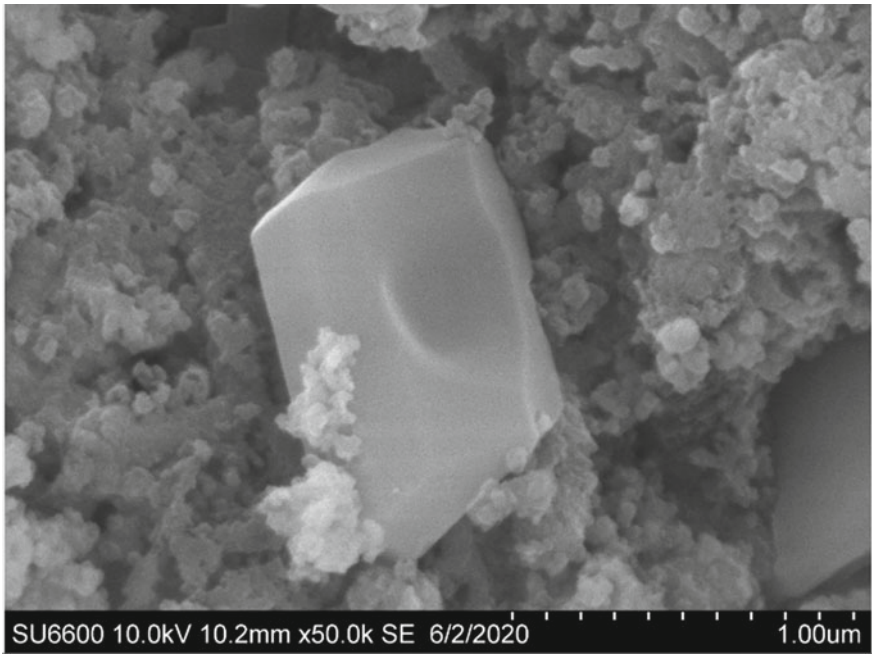

Fig. 3 SEM image of zeolite synthesized from fly ash

have appeared whilst disappearing peaks correspond to quarts and mullite. Most of the newly appeared peaks correspond to peaks of standard zeolite X at 2θ values of 6.10°, 9.97°, 15.39°, 23.24°, 30.85°, and 33.49° [7]. So, it proves the formation of zeolite X from both fly ash and bottom ash.

Presence of the peak for quarts and mullite at 26.6° in the synthesized zeolite with less intensity interprets that, those crystalline phases are not fully converted to zeolite X and presence of unidentified peaks in both raw material and product shows the existence of impurities and formation of other unwanted compounds during the synthesis process.

Figure 7 shows the comparison of X-ray diffraction patterns of zeolites synthesized from fly ash and bottom ash. The intensity of a peak represents the purity and the extent of the formation of zeolite crystal. According to the diffraction patterns of two types of zeolites, zeolite from fly ash shows high intensities compared to zeolite from bottom ash. This is due to the variations in crystal growth. As bottom ash has a high content of impurities, the resistance to crystal growth is high in some planes resulting in reduced purity. Most of the peaks correspond to standard zeolite X are not present in both synthesized zeolite types, because crystals have not grown in some planes those responsible to give reflections at some 2θ values.

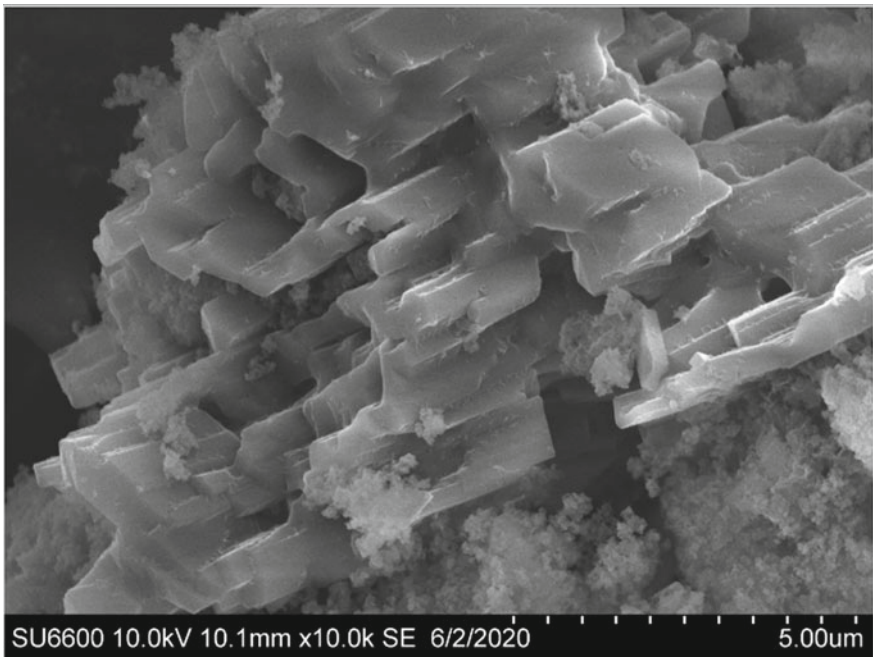

Fig. 4 SEM image of zeolite synthesized from bottom ash

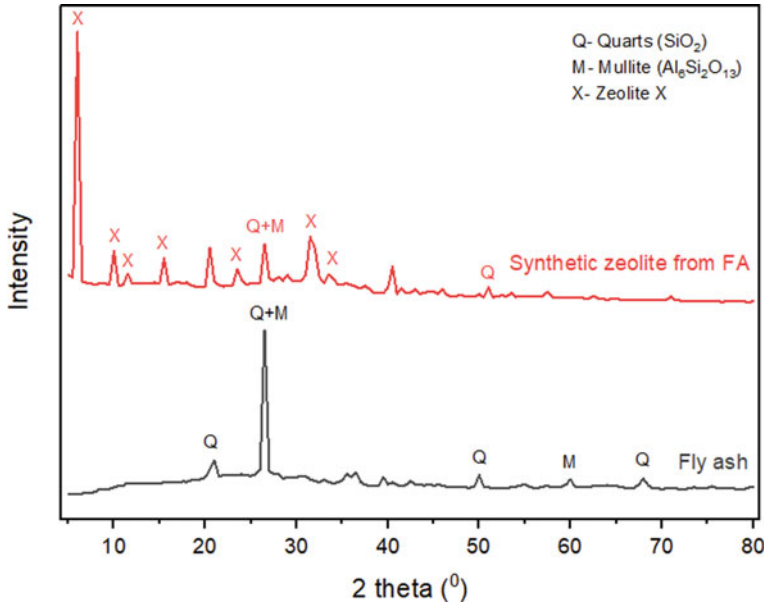

Fig. 5 X-ray diffraction patterns for fly ash and its zeolite

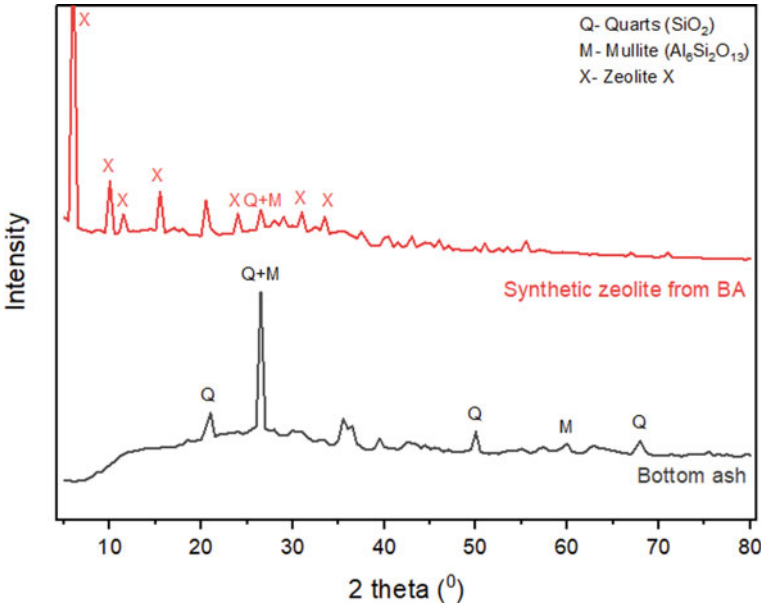

Fig. 6 X-ray diffraction patterns for bottom ash and its zeolite

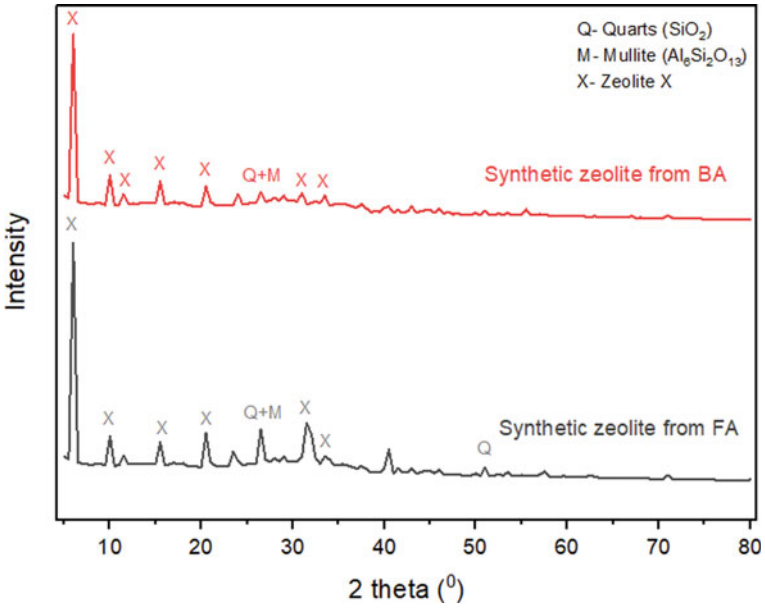

Fig. 7 X-ray diffraction patterns for zeolites synthesized from fly ash and bottom ash

3.5 Analysis of Functional Groups

FT-IR spectrums of raw material and zeolite products for fly ash and bottom ash are represented in Figs. 8 and 9 respectively. Fly ash and bottom ash show significant bands at 1078, 794, and 462 cm^{-1} wavenumbers that correspond to Si–O(Al) asymmetric stretching, T–O–T asymmetric stretching (T can be either Si or Al) and symmetric bending of O–Si–O respectively [7]. In FT-IR spectrums of zeolites, the broad band at 3451 cm^{-1} and the band at 1639 cm^{-1} correspond to OH stretching and bending vibrations of water molecules that are absorbed during the synthesis process. An asymmetric stretching of Si–O(Al) can be seen at 978 cm^{-1} and other significant bands at 646 and 460 cm^{-1} attribute to asymmetric T–O–T stretching and symmetric bending of O–T–O modes (T can be either Si or Al) [1]. These bands correspond to the bands of standard zeolite X proving the formation of zeolite X from both fly ash and bottom ash.

The positions of the bands of asymmetric stretching of T–O–T and O–T–O have changed in the raw sample and the product. Substitution of Al atoms in tetrahedral positions during the synthesis process results in a change of the position of the band and wavenumber of the stretching vibration band decreases with an increase of Al content in the structure [5]. As the alkaline activation extracts more of Al and with the substitution of Al atoms in the lattice framework, the wavenumber of stretching vibration bands have been decreased in the synthesized zeolite. These FT-IR results

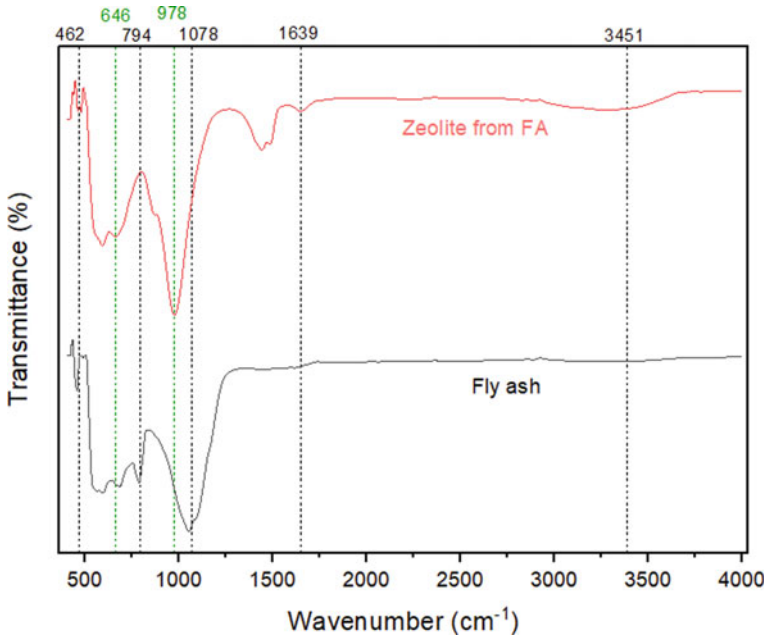

Fig. 8 FT-IR spectrums of fly ash and its zeolite

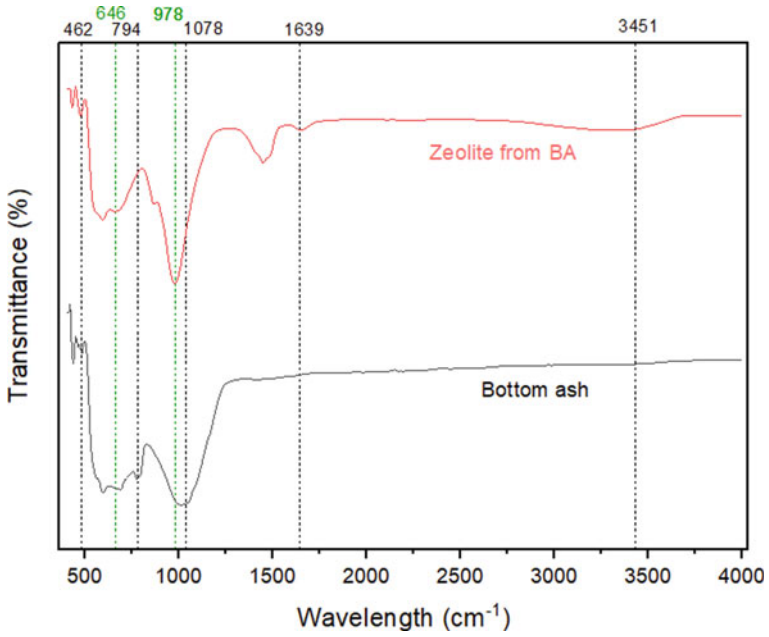

Fig. 9 FT-IR spectrums of bottom ash and its zeolite

support the conclusions drawn from XRD analysis, proving the formation of zeolite X once again.

Figure 10 shows the comparison of FT-IR spectrums of zeolites synthesized from fly ash and bottom ash. Both show vibrations for the same bond modes. Intensities of vibrations slightly vary due to the difference in Si/Al ratios of raw materials.

4 Conclusions

Coal ash is mainly composed of Si and Al. It demonstrates the potential of coal fly ash and bottom ash to convert into zeolites, which are interlinked tetrahedra of Si and Al. Pretreatments with NaOH and HCl help in the extraction of silicon and aluminum, without compromising the crystalline arrangement and functional groups present in pure ash. Acid treatment is efficient for silicon extraction while alkaline treatment is efficient for the extraction of aluminum from the ash. Activation with alkaline is more suitable for synthesis of zeolite X as zeolite X should have a lower Si/Al ratio (2–3) than in raw materials used in this study.

Characterization of synthesized products reveals that Zeolite X can be synthesized by alkaline treatment followed by hydrothermal crystallization. The presence of impurities (components other than Si and Al) restricts the growth of zeolite crystal in certain planes resulting in distorted crystal shapes. Zeolite synthesized from fly

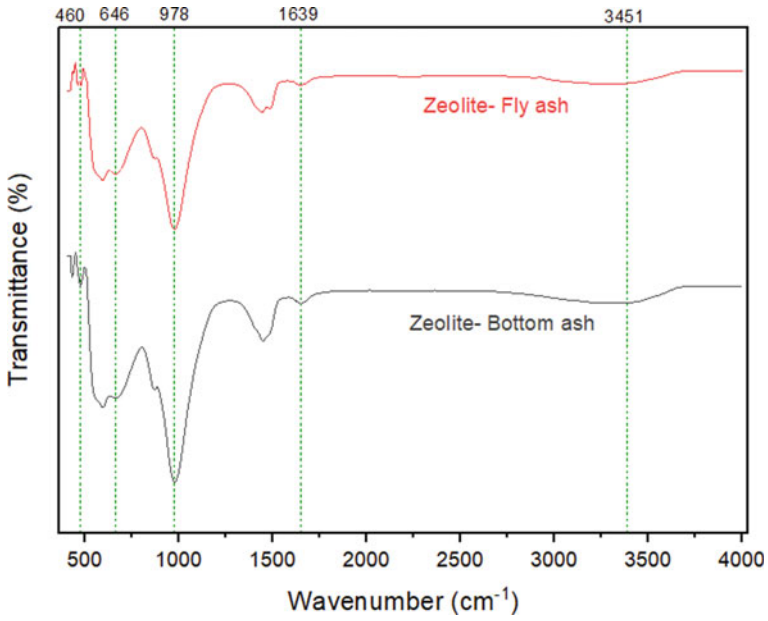

Fig. 10 FT-IR spectrums of zeolites synthesized from fly ash and bottom ash

ash shows higher yield and purity than that of zeolite synthesized from bottom ash, due to the lower content of unburned carbon and other impurities present in fly ash. Characteristics of the final product vary with the Si/Al ratio of the raw materials.

This study can be extended to obtain zeolites with high purity by performing pretreatments to reduce the content of impurities significantly and altering the synthesis conditions in order to find optimum synthesis conditions.

Acknowledgements Authors sincerely acknowledge the encouragement and guidance provided by Dr. A. Illangasinghe, course coordinator and all the members of the academic and non-academic staff members of Department of Chemical and Process Engineering, University of Peradeniya, Mr. Manoj Dassanayake, Engineering Manager, Brandix Textiles Ltd., Sri Lanka, Prof. Ranjith Dissanayake, Mr. Selvakumar and Ms. Rashmi Kumarasinghe, Assistant Manager Analytical Services, Sri Lanka Institute of Nanotechnology.

References

1. Abidin AZ, Abu Bakar NHH, Ng EP, Tan WL (2017) Rapid degradation of methyl orange by Ag doped zeolite X in the presence of borohydride. J Taibah Univ Sci 11(6):1070–1079. https://doi.org/10.1016/j.jtusci.2017.06.004
2. Fansuri H, Yanti Y, Londar E, Widiastuti N (2010) Synthesis of zeolite-A from coal bottom ash: the influence of unburned carbon to the zeolite quality. Chem Eng 1–9

3. Gomes ACC, de Vasconcelos Ferraz A, da Rocha LPG (2018) Characterization of coal fly ash for use in synthesis of zeolites. Mater Sci Forum (MSF) 930:578–583. https://doi.org/10.4028/www.scientific.net/MSF.930.578
4. Mohan S, Gandhimathi R (2009) Removal of heavy metal ions from municipal solid waste leachate using coal fly ash as an adsorbent. J Hazard Mater 169:351–359
5. Mozgawa W, Krol M, Dyczek J, Deja J (2014) Investigation of the coal fly ashes using IR spectroscopy. Spectrochim Acta Part A Mol Biomol Spectrosc 132:889–894. https://doi.org/10.1016/j.saa.2014.05.052
6. Scherzer and Julius (1989) Octane-enhancing, zeolite FCC catalysts: scientific and technical aspects. Catal Rev 31(3):215. https://doi.org/10.1080/01614948909349934
7. Treacy MMJ, Higgins JB (2007) Collection of simulated XRD powder patterns for zeolites, 5th revised edn. https://doi.org/10.1016/B978-0-444-53067-7.X5470-7.
8. Wang H et al (2016) Synthetic zeolite from coal bottom ash and its application in cadmium and nickel removal from acidic wastewater. Desalin Water Treat 57(54):26089–26100. https://doi.org/10.1080/19443994.2016.1160438
9. Wang S, Zhu ZH (2007) Effects of acidic treatment of activated carbons on dye adsorption. Dyes Pigm 75:306–314
10. Wu Z, Naik RT (2002) Properties of concrete produced from multicomponent blended cements. Cem Concr Res 32:1937–1942

Modification of a Bottom Ash Based Insulation Material Using Saw Dust, EPS and Aggregate Chips

K. A. D. Y. T. Kahandawa Arachchi, J. C. P. H. Gamage, and G. I. P. de Silva

Abstract Bottom ash shows moderate properties of thermal resistivity when incorporated with conventional cement-sand plasters. This paper investigates the possibility of incorporating other commonly used insulation materials to develop a superior blend as cementitious insulation. Recycled EPS, sawdust, and aggregate chips were blended with a developed bottom ash based mix proportion and mechanical properties of the mortar were analyzed. Compressive strength, workability, and thermal conductivity were tested. The results indicated a 26% increment in thermal performance when EPS was introduced and a 33% increment when sawdust was introduced. On the contrary, their strengths reduced drastically. The aggregate chips had an inverse effect where thermal conductivity increased along with the strength. However, the compressive strength increased up to 75%.

Keyword Bottom ash · EPS · Cementitious mortar · Saw dust · Aggregate chips

1 Introduction

Thermal comfort has been one of the key areas that are being researched worldwide over the past decades [2]. With the rising global temperatures, the comfort inside a building is often paid more concentrated attention. From a sustainable point of view, utilizing waste material in building engineering is also a trending research area [13], [9]. Thereby, bottom ash, a waste by-product of the coal power generation process, was investigated on its usability as a thermal insulation material.

As of 2020, about 40% of the world's power generation is made through coal power generation [8]. Although the developed countries focus more on rather cleaner sources of power, third world countries are often bound to use coal energy for the foreseeable future [8]. In that case, the generation of coal power would create two main by-products; fly ash and bottom ash [11]. Fly ash is currently used in the cement

K. A. D. Y. T. Kahandawa Arachchi (✉) · J. C. P. H. Gamage
Department of Civil Engineering, University of Moratuwa, Moratuwa, Sri Lanka

G. I. P. de Silva
Department of Material Science and Engineering, University of Moratuwa, Moratuwa, Sri Lanka

R. Dissanayake et al. (eds.), *ICSBE 2020*, Lecture Notes in Civil Engineering 174,
https://doi.org/10.1007/978-981-16-4412-2_34

industry as a blend in or a replacement for cement [7]. The continued research on bottom ash shows that it is capable to be utilized as an insulation material [11, 12]. However, no attempts have been made to commercialize such a product as per the author's knowledge.

The coarse nature of bottom ash would make it impossible to use it as a replacement for cement as fly ash is often used [15]. On the contrary, bottom ash could be used as an efficient replacement for fine aggregates.

The available research on bottom ash suggests that the thermal conductivity of a mortar would decrease if the percentage of bottom ash would increase [18]. Meanwhile, bottom ash has been identified as a porous material in nature which indicates that the introduction of bottom ash to a cementitious mortar would severely affect the mechanical properties of the mix [1]. Moreover, at an oven-dried state, bottom ash would demand more water than normal river sand which would implicate that the water/cement ratio for the mortar mix would increase than the accepted norms [14].

When insulation materials for thermal comfort are concerned, the most commonly, used materials can be expanded polystyrene (EPS) [10], fiberglass [3], vermiculite [16], and natural fibers [20], etc. However, no research has been conducted by incorporating one or more of these existing insulation materials with bottom ash. This paper presents an experimental process where a mortar mixture with bottom ash is further modified with EPS, sawdust, and aggregate chips to identify the possibility of developing a superior mix.

2 Methodology

Figure 1 shows a detailed description of the test series carried out during the course of research.

2.1 Materials

Figure 2 shows the materials used in the experimental program. Ordinary Portland Cement (OPC) of with a 28-day compressive strength of more than 42.5 MPa, River sand passing through 2.36 mm sieve, bottom ash passing through 2.36 mm sieve and Millennium Hypercrete [17] as the superplasticizer was used. Recycled EPS passing through 800 μm seive, saw dust passing through 2 mm sieve and aggregate chips passing through 800 μm sieve was used for the modification of the plaster.

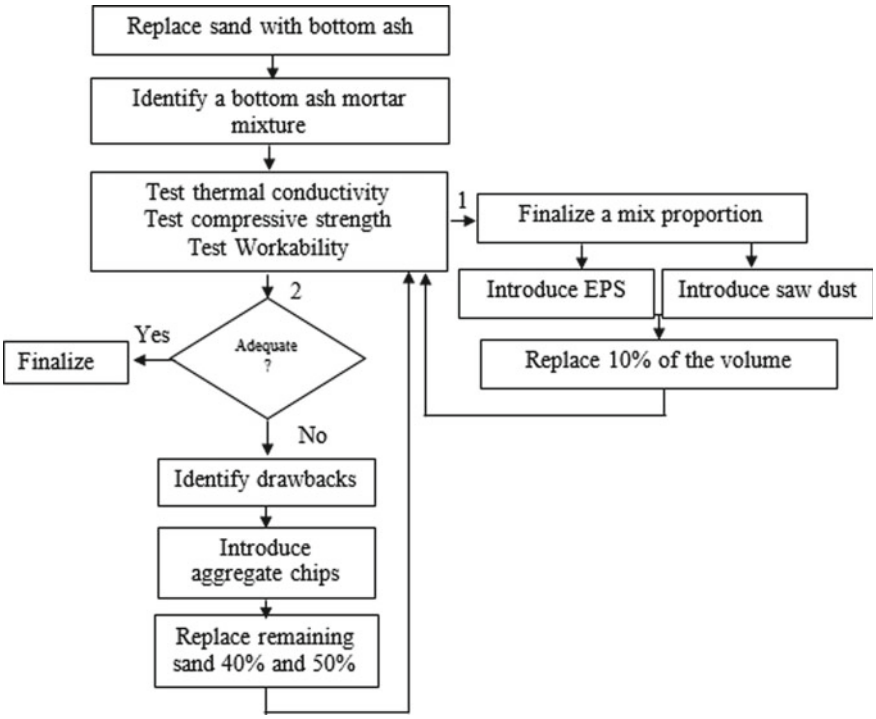

Fig. 1 Overview of the test program

Fig. 2 **a** Cement, **b** River sand, **c** Bottom ash, **d** Aggregate chips, **e** Saw dust, **f** EPS

2.2 Procedure

A 1:3, cement:sand mixture was selected and the fine aggregates were replaced with bottom ash in 10% intervals. Table 1 gives the mix proportions for the samples. Thermal conductivity of the mixtures were analyzed using Lee's disc method [5] and the compressive strength was tested as per BS EN 1015-11:1999 [6] (Fig. 3).

The results of thermal conductivity testing and compressive strength testing (Fig. 4) indicated that both conductivity and strength would reduce with the

Table 1 Mix proportions

Sample	% of Bottom Ash to Wt	Cement (g)	Sand (g)	Bottom Ash (g)
BA0	0	50	150	0
BA10	10	50	135	15
BA20	20	50	120	30
BA30	30	50	105	45
BA40	40	50	90	60
BA50	50	50	75	75
BA60	60	50	60	90
BA70	70	50	45	105
BA80	80	50	30	120
BA90	90	50	15	135
BA100	100	50	0	150

(a) (b)

Fig. 3 Testing: **a** Thermal conductivity, **b** Compressive strength testing

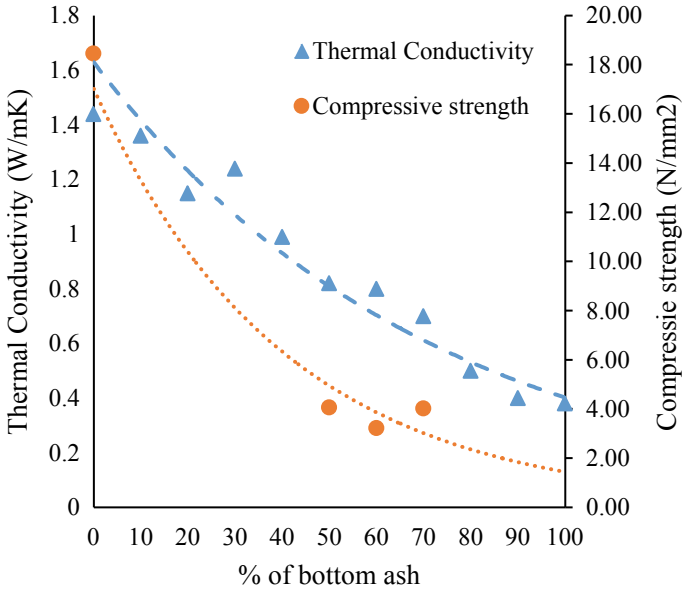

Fig. 4 Results of Thermal conductivity and Compressive strength testing

percentage of bottom ash as predicted. Thereby, a reasonable percentage (60%) was selected to continue with the modification process.

60% replacement of fine aggregates with bottom ash was modified with 10 ml of superplasticizer per a kilogram of cement, along with a water/cement (w/c) ratio of 1.2 or better workability and strength enhancement.

In the first part of the test series, EPS was blendered using a mechanical blender, and saw dust was added to the mix 10% per volume as they are light weight and the mix proportions are given in Table 2.

The results indicated in Fig. 5 dictates the fact that addition of a more porous material to an already porous compound might reduce the compressive strength more drastically. As per the workability of the modified mortars, Fig. 6 shows that the sample with saw dust had a better consistency when compared to EPS mixture.

Table 2 Modified mix proportions part 1

Sample	Cement (kg)	Sand (kg)	Bottom ash (kg)	Other (weight/volume) (m^3)	w/c ratio	Superplasticizer (ml)
BA60-EPS	1	1.4	1.6	0.002058	1.2	10
BA60-Saw dust	1	1.4	1.6	0.002058	1.2	10

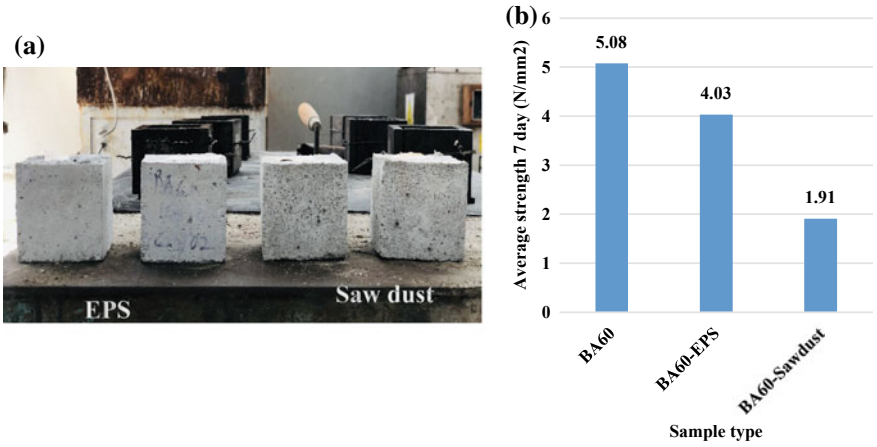

Fig. 5 Compressive strength testing: **a** Samples, **b** Results

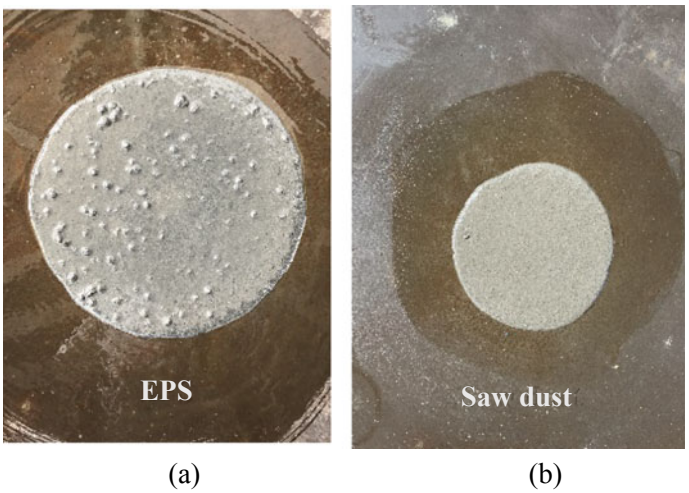

Fig. 6 Flow table test

If the modified mortar to adhere to N-type mortar standards [4], which require a minimum compressive strength of 5 MPa, the mixture is severely lacking in compressive strength. Thereby, by identifying the major drawback of the process and the previous results of inadequate compressive strength of BA60 itself, the test series was diverted to part 2 of the flow diagram.

The BA60 mixture had 40% of its fine aggregates remaining compared to a conventional 1:3 cement:sand plaster. Considering the fact that fine aggregates contribute largely toward the early strength of a mortar [19], the remaining fine aggregates were completely replaced with aggregate chips. i.e. 40% of aggregate chips against 60%

Table 3 Modified mix proportions part 2

Sample	Cement (kg)	Aggregate chips (kg)	Bottom ash (kg)	w/c ratio	Superplasticizer (ml)
BA60-chip	1	1.4	1.6	1.2	10
BA50-chip	1	1.5	1.5	1.2	10

Fig. 7 Compressive strength cubes for chip samples

Table 4 Test results

Sample	Avg. strength (N/mm^2)	Avg. flow (mm)	Avg. thermal conductivity (W/m °C)
BA60	5.08	175	0.75
BA60-EPS	4.03	135	0.55
BA60-Sawdust	1.91	137	0.50
BA60-chip (40%)	6.13	200	0.82
BA60-chip (50%)	8.84	180	0.86

of bottom ash. Further expanding the research BA50 mixture was also modified with aggregate chips as per mix proportions given in Table 3.

Figure 7 shows the compressive strength samples for BA60-chip samples while Table 4 gives the results from the thermal conductivity, compressive strength and workability testing for all samples.

3 Results and Discussion

The overall results obtained at each phase of the test series was compared to understand the correlation between the results (Fig. 8).

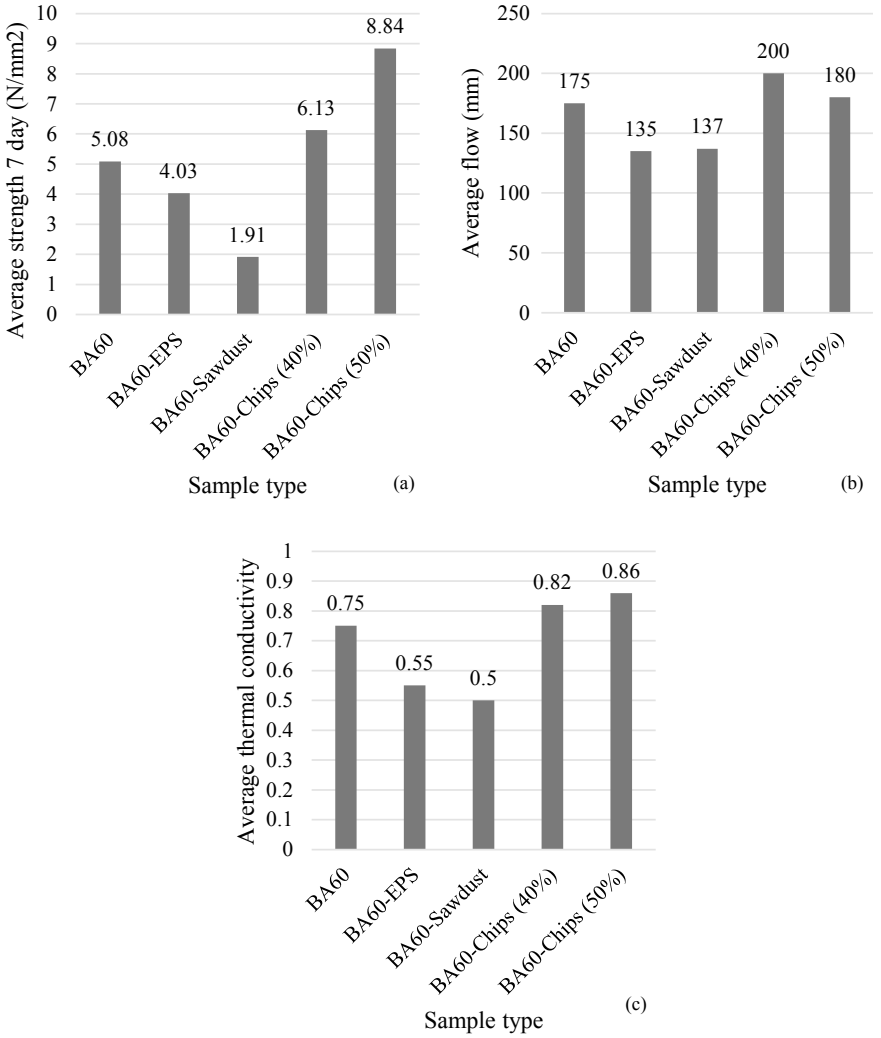

Fig. 8 Results comparison: **a** Compressive strength, **b** Flow, **c** Thermal conductivity

The porosity of bottom ash makes the original mixture more thermal resistive. However, the resistivity could be increased if more porous materials as saw dust or EPS entered the mixture. However, that would increase the exiting drawbacks on the mechanical properties of the mortar. If the said mortar was applied on a structural element as a wall, a light impact would damage the finishing of the wall rendering the insulation compromised. Thereby, the introduction of aggregate chips which could increase the mechanical properties would be useful. However, the results indicate that chips could conduct heat at a higher rate affecting the thermal resistivity of the material.

4 Conclusion

This paper presents an experimental program to understand the behaviour of a bottom ash based cementitious material when other insulation materials were introduced. The following conclusions were made.

- Introduction of bottom ash to a cement:sand mortar would increase its thermal performance by while decreasing its mechanical performance.
- The results indicated a 26% increment in thermal performance when EPS was introduced and a 33% increment when sawdust was introduced. However, their strengths reduced drastically.
- Introduction of the aggregate chips have increased the compressive strength up to 75%.

Acknowledgements The financial support from National Research Council, Sri Lanka is greatly appreciated (Grant no: PPP18-01).

References

1. Ahn YB, Jang JG, Lee HK (2016) Mechanical properties of lightweight concrete made with coal ashes after exposure to elevated temperatures. Cement Concr Compos 72:27–38. https://doi.org/10.1016/j.cemconcomp.2016.05.028
2. Antoniadou P et al (2015) Integrated evaluation of the performance of composite cool thermal insulation materials. Energy Procedia 78:1581–1586. https://doi.org/10.1016/j.egypro.2015.11.214
3. Asdrubali F, D'Alessandro F, Schiavoni S (2015) A review of unconventional sustainable building insulation materials. Sustain Mater Technol 4(2015):1–17. https://doi.org/10.1016/j.susmat.2015.05.002.
4. ASTM International (2007) ASTM C 270–07. Standard specification for mortar for unit masonry. https://doi.org/10.1520/C0270-10
5. ASTM International (2018) ASTM D7340-07, Standard practice for thermal conductivity of leather. West Conshohocken, PA. Available at: www.astm.org
6. British Standards (1999) BS EN 1015-11:1999: Methods of test for mortar for masonry
7. Demirbog R (2003) Influence of mineral admixtures on thermal conductivity and compressive strength of mortar. Energy Build 35:189–192
8. Evans S, Pearce R (2020) Mapped: the world's coal power plants. Available at: https://www.carbonbrief.org/mapped-worlds-coal-power-plants. Accessed: 20 April 2020
9. Kahandawa Arachchi KADYT, Gamage JCPH, De Silva GIP (2019) Thermal insulaltion systems for CFRP/concrete composites: a review. In: International conference on structural engineering and construction management, Kandy, Sri Lanka
10. Kaya A, Kar F (2016) Properties of concrete containing waste expanded polystyrene and natural resin. Constr Build Mater 105:572–578. https://doi.org/10.1016/j.conbuildmat.2015.12.177
11. Mandal AK, Sinha OP (2014) Review on current research status on bottom ash: an Indian prospective. J Inst Eng (India): Ser A **95**(4):277–297. https://doi.org/10.1007/s40030-014-0100-0
12. Mandal AK, Sinha OP (2017) Production of thermal insulation blocks from bottom ash of fluidized bed combustion system. Waste Manage Res 35(8):810–819. https://doi.org/10.1177/0734242X17707575

13. Meyer C (2009) Cement & concrete composites: the greening of the concrete industry. Cement Concr Compos 31(8):601–605. https://doi.org/10.1016/j.cemconcomp.2008.12.010
14. Piyarathne RMIE, Udamulla KMLA (2013) Use of bottom ash in replacement of river sand in making cement mortar. In: International symposium on advances in civil and environmental engineering practices for sustainable development, pp 191–197
15. Ramzi Hannan NIR et al (2017) A comprehensive review on the properties of coal bottom ash in concrete as sound absorption material. MATEC Web Conf. 103:01005.https://doi.org/10.1051/matecconf/201710301005
16. Ranasinghe R et al (2011) Bond performance of CFRP strengthened concrete subjected to fire. In: Civil Engineering Research for Industry, pp 37–42
17. Technical datasheet, Millennium Hypercrete (no date) Available at: http://mctlk.com/. Accessed: 9 Nov 2019
18. Torkittikul P et al (2017) Utilization of coal bottom ash to improve thermal insulation of construction material. J Mater Cycles Waste Manag 19(1):305–317. https://doi.org/10.1007/s10163-015-0419-2
19. Yalley PP, Sam A (2018) Effect of sand fines and water/cement ratio on concrete properties. Civil Eng Res J 4(3). https://doi.org/10.19080/cerj.2018.04.555636
20. Zach J et al (2013) Development of thermal insulating materials on natural base for thermal insulation systems. Procedia Eng 57:1288–1294. https://doi.org/10.1016/j.proeng.2013.04.162

Modification of Engineered Cementitious Composite Mortar to Use as an Adhesive for CFRP/Concrete Bond

M. W. C. Himasha, J. C. P. H. Gamage, G. I. P. De Silva, and V. Attanayaka

Abstract This study focuses on the development of a thermally insulative cementitious adhesive for bonding Carbon Fiber Reinforced Polymer (CFRP) fabrics with concrete using Engineered Cementitious Composite (ECC) mortar. The poor thermal performance of epoxy adhesive encouraged the development of a new cementitious adhesive which could resist elevated temperature. The ECC adhesive was developed using locally available materials. The developed adhesive has a low thermal conductivity between 0.145 and 0.18 W/(mK) which shows its resistance to elevated temperature. The developed adhesive showed an average bond strength of 570.28 N/mm^2 for an effective bond length of 150 mm. When compared with epoxy adhesive, ECC adhesive showed a 15% reduction in bond strength. However, under elevated temperature, the bond strength reduction in ECC adhesive is very low compared to the bond strength reduction in epoxy. When the bondline temperature was incremented up to 100 °C, the strength reduction evident in modified ECC adhesive was 5.21%, while it was 69% for epoxy adhesive. It shows that the developed ECC adhesive resist high temperature better than epoxy. The average 28 days tensile strength of the adhesive was 3.83 N/mm^2 and the average 28 days compressive strength was 52.77 N/mm^2. A finite element model was developed and validated for the pullout test to predict the bond performance of ECC adhesive. The parametric study conducted varying the adhesive thickness concluded that the bond strength enhanced with the increment of adhesive thickness up to 20 mm.

Keywords Engineered cementitious composite · Cementitious adhesive · Carbon fibre reinforced polymer · Thermal performance · Finite element modelling

M. W. C. Himasha (✉) · J. C. P. H. Gamage
Department of Civil Engineering, University of Moratuwa, Moratuwa, Sri Lanka

G. I. P. De Silva
Department of Materials Science and Engineering, University of Moratuwa, Moratuwa, Sri Lanka

V. Attanayaka
Airow Solutions (Pvt) Ltd, Maharagama, Sri Lanka

R. Dissanayake et al. (eds.), *ICSBE 2020*, Lecture Notes in Civil Engineering 174,
https://doi.org/10.1007/978-981-16-4412-2_35

1 Introduction

Carbon Fiber Reinforced Polymer (CFRP) is a generally used retrofitting material in structural applications. The epoxy is a commonly used commercially available polymeric adhesive which is used to bond CFRP with concrete. It is used widely due to its higher bonding strength. However, the bond strength of epoxy is susceptible to deteriorate when exposed to a higher temperature beyond its glass transition temperature [12]. The glass transition temperature is the temperature around which a polymeric adhesive undergoes a sudden drop in its adhering properties [5]. For epoxy adhesive, the glass transition temperature is around 60–70 °C [11]. The high cost of materials [16], emission of toxic fumes [25] and flammability [25] are other disadvantages of epoxy adhesives. Therefore, a lot of researchers suggested replacing epoxy with a cementitious adhesive to resist high temperature [12, 13]. Cementitious adhesives show better performance under elevated temperatures and good consistency with concrete [16]. Researches have been conducted on introducing cementitious insulations to overcome this issue [15, 24]. However, those attempts introduced an extra dead load to the structure and their bonding with CFRP/epoxy composite is questionable.

Most of the cementitious adhesives developed for CFRP-concrete bond are brittle in nature [12, 28]. Brittleness reduces the effective transferring of the load from concrete to CFRP [12, 28]. ECC is a cementitious mortar reinforced with dispersed multidirectional fibres. Fibres contribute to creating ductility in ECC [20]. ECC comprises Portland cement, silica sand, fly ash, water and fibres. Higher fly ash content in ECC increases the ductility and reduces the compressive strength [30]. ECC can be developed by using different fibres such as Poly Vinyl Alcohol (PVA), Polyethylene terephthalate (PET), Polyethylene (PE) and Polypropylene (PP). Sathishkumar et al. [23] conducted tests on ECC developed with the above-mentioned fibre types to analyze changes in mechanical properties. Results suggested that PVA is the ideal fibre type among them [23]. PET fibres showed better results than PE and PP fibres [23]. ECC with fibre content as 2% of cement content showed the highest tensile, compressive and flexural strengths for all the 4 types of fibres [23]. The 2% fibre content is the suggested fibre proportion to be used in developing ECC since it is closer to the critical fibre content needed to attain the strain hardening stage [19]. The microcracks develop in the strain hardening stage, further enhanced the ductile nature in ECC [22]. Fly ash content lowers the thermal conductivity of ECC [14, 30]. The mix proportion defined as ECC-M45 is tailored to attain multiple cracking and to maintain a controlled crack width [19].

Approximately 75% of the total cost of ECC developed with PVA fibres (ECC-PVA) is spent on PVA fibres [31]. Therefore it is not an economically feasible product. PET is a solid waste and recycled PET fibres can be used to develop ECC with PET fibres (ECC-PET). ECC can be modified to use in a wide range of purposes [18]. Therefore, the authors focus on developing ECC-PET as a thermally insulative cementitious adhesive for CFRP-concrete bond. The ECC-M45 mix proportion was modified to develop the cementitious adhesive. The adhesive was developed using

locally available materials. A lot of researchers have successfully developed the local versions of ECC [7, 19]. The developed adhesive was tested for its mechanical properties, bond performance and thermal effect on bond strength. A finite element model was developed and validated to perform a parametric study on the performance of ECC-PET adhesive.

2 Test Program

The authors have used the locally available materials in developing ECC as a thermally insulative adhesive for CFRP-concrete bond. The initial phase of the test program was to decide a fibre proportion to develop the adhesive depending on its thermal conductivity. The next phase was to determine the mechanical properties of the developed cementitious adhesive. The feasibility of the adhesive was evaluated depending on its bond strength and thermal performance.

2.1 Material Properties and ECC Adhesive Preparation

The materials used to develop ECC adhesive are Portland cement, silica sand, fly ash, water and Polyethylene Terephthalate (PET) fibres (Fig. 1). The required silica sand was obtained from Piramal Glass Ceylon PLC, Naththandiya, Sri Lanka and fly ash was obtained from the Norochcholi power plant, Sri Lanka. A chemical analysis was conducted on fly ash at the Geological Survey and Mines Bureau of Sri Lanka to find the chemical composition of the material (Table 1). The chemical composition of fly ash drastically differs depending on the source from where it is obtained. This change can be seen when comparing with the chemical composition of fly ash used by [28] to develop ECC as an adhesive (Table 1).

The fly ash obtained from Norochcholai power plant can be categorized as class F type as per STM C618-19 [1]. The CaO content in fly ash collected from Norochcholai plant is below 10%. The fly ash with a CaO content lower than 10% shows more pozzolanic characteristics [9]. The pozzolanic materials need the presence of Calcium hydroxide for the formation of solid matter [9]. Therefore water requirement might be high for hydration. The PET fibres have a thickness of 0.4 mm and a length of

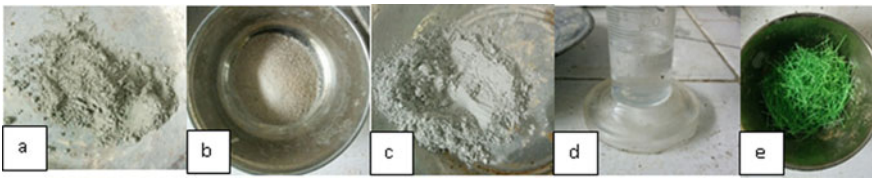

Fig. 1 **a** Cement, **b** Silica sand, **c** Fly ash, **d** Water, **e** PET fibers

Table 1 Chemical composition of fly ash

	Norochcholai power plant, Sri Lanka	DTE Monroe Power Plant, State of Michigan, USA [28]
SiO_2 (%)	46.89	42.20
Al_2O_3 (%)	30.69	22.51
MgO (%)	1.56	3.20
CaO (%)	7.56	15.66
Na_2O (%)	0.23	0.98
K_2O (%)	0.64	1.53
P_2O_5 (%)	2.67	–
Fe_2O_3 (%)	1.88	9.20
SO_3	–	1.85
Loss on ignition	5.59	1.34

Table 2 Manufacturer-provided material properties of CFRP fabric [29]

Parameter	Value
Sheet weight	300 g/m^3
Carbon content	95%
Net effective thickness	0.166 mm
Modulus of elasticity	240 GPa
Tensile strength	4000 MPa
Elongation at break	2%

10 mm. The manufacturer provided properties of CFRP fabric is given in Table 2 [29].

Sample preparation was done in accordance with ASTM C305 [3]. Portland cement, silica sand, fly ash and PET fibres were mixed in a mechanical mixer initially and then water was added to the paste gradually. The whole paste was kept for mixing in the mechanical mixer for 10 min with an angular velocity of 50 rpm, to get a homogenous mixture. The mix proportion of ECC-M45 self-consolidating mortar [19] was used to develop the ECC adhesive. Water cement ratio of this particular mix design is 0.56 which resulted in a dry mortar with poor adhering qualities. Therefore, the water-cement ratio was increased to 0.85 to achieve the desired sticky nature. Cement:fly ash:silica sand:water mix proportion ratio of modified ECC adhesive is 1:1.2:0.8:0.85.

2.2 Thermal Conductivity

The thermal conductivity test was conducted to check how the deviation of the fibre content affects the thermal conductivity of the mortar. Thermal conductivity is the property which indicates the ability of a material to conduct heat [4]. Lee's disc method is commonly used to determine the thermal conductivity of bad heat conductors [4]. Circular samples with a diameter of 60 mm and a thickness of 5 mm were cast to test for the thermal conductivity. Figure 2 shows Lee's disc apparatus and the samples. The samples were cast deviating the fibre volume in the mix proportion as 1%, 2%, 3%, 4% and 5% of cement volume and for each fibre volume, 3 circular samples were cast.

Prepared samples were demoulded after 1 day of curing and then the samples were cured in a water bath for 27 days. Then these samples were dried for a day in the air (27 ± 3 °C; 74 ± 5%) before testing for thermal conductivity. The silicone heat sink compound was applied on both sides of the sample to obtain an even surface. The test was conducted in accordance with ASTM D7340-07 [3]. Figure 3 shows the test results.

According to Fig. 3, thermal conductivity increased with the increase of fibre content in a relatively linear manner. Thus, the mix designs with lower fibre contents show better resistance to elevated temperature. ECC achieves its optimum tensile ductility when the fibre content is 2% of cement content [19]. Further, the experiments conducted by [23] highlighted the fact that ECC-PET reached its highest tensile, compressive and flexural strengths at 2% fibre content. The thermal conductivity corresponding to this fibre content ranged in between 0.145 and 0.18 W/(mK).

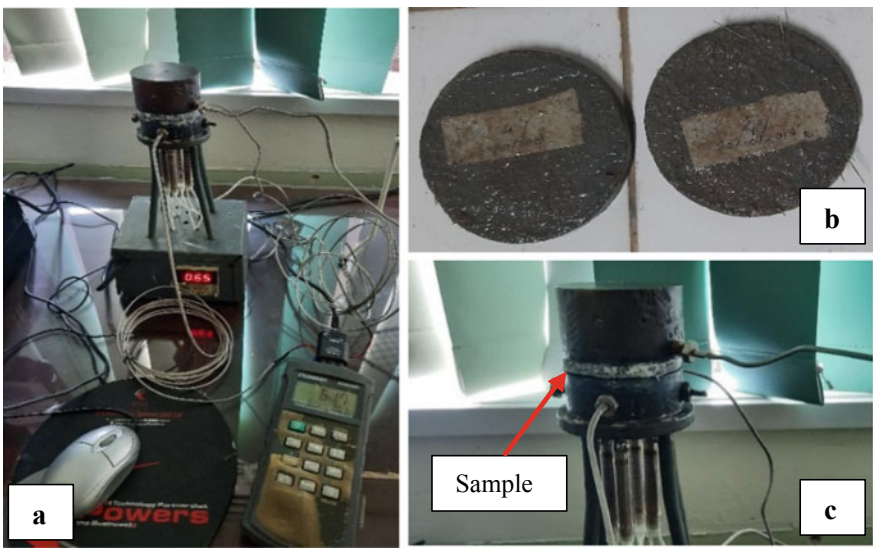

Fig. 2 **a** Lee's disc apparatus, **b** Samples, **c** Sample mounted in the apparatus

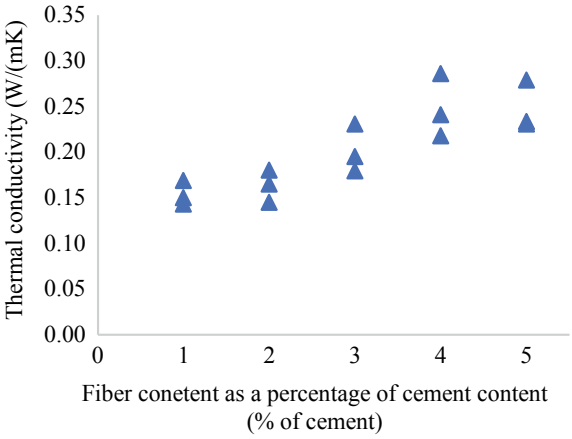

Fig. 3 Thermal conductivity—fiber content graph

Therefore, depending on both experimental results and literature data, 2% of fibre content was selected as the optimum fibre content to develop ECC adhesive. The density of fly ash is less than one third of the cement. Since the lowering of density reduces the thermal conductivity, the fly ash content also affected in lower thermal conductivity in this adhesive [6].

2.3 Developed Adhesive Properties

The developed adhesive was tested for its mechanical properties. Samples with the dimensions of 70 mm × 70 mm × 70 mm were cast for compressive strength test in accordance with ASTM C109 [2]. Average 7 days and 28 days compressive strengths of cementitious adhesive were 16.97 N/mm^2 and 52.77 N/mm^2, respectively. The dumbell shaped samples were cast to conduct the uniaxial tensile test in accordance with CRD-C 260-01 [26]. The average tensile strength was 3.83 N/mm^2 and the average tensile strain was 5.86%. The density of developed ECC adhesive was 1895.04 kg/m^3.

2.4 Bond Strength and Effective Bond Length

A series of direct pull out tests were conducted to find the effective bond length of the developed adhesive. Grade 25 concrete blocks with the dimension of 100 mm × 100 mm × 250 mm were used as the concrete substrate to bond CFRP fabric. The bond surface of the concrete block was grinded and wiped using a wet cloth to remove the week layer on top of the concrete block. After drying the surface, the developed ECC adhesive was applied on top of the bonding surface to a thickness of

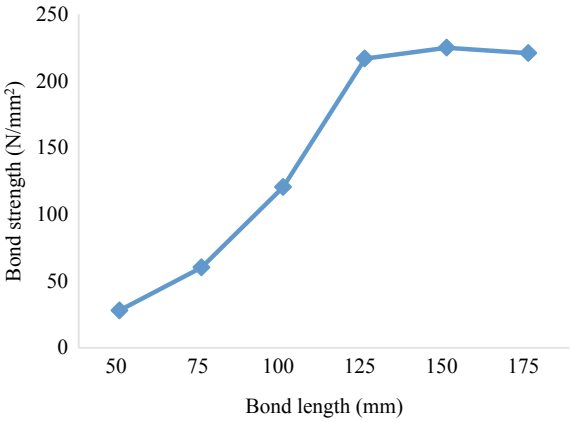

Fig. 4 Bond strength—Bond length graph

5 mm. A CFRP fabric strip with a width of 75 mm was laid on top of ECC adhesive layer maintaining a part of CFRP fabric strip (100 mm length) outside the bonding region to fix the grip to pull the CFRP strip during testing. The grip was fabricated by fixing 2 aluminium sheets, each with the dimension 75 mm × 100 mm on either side of the CFRP fabric strip part left for the grip, using epoxy adhesive. Samples were fabricated with 6 different bond lengths; 50 mm, 75 mm, 100 mm, 125 mm, 150 mm and 175 mm. Samples were cured for 28 days before testing.

Samples were mounted on the universal testing machine using a setup fabricated to conduct the pullout test (Fig. 5). The CFRP strip was pulled with a rate of 2 mm/min. Figure 4 shows the test results.

The bond strength increased up to 150 mm bond length. The bond strength deviation between two bond lengths; 150 mm and 175 mm was very low. Therefore, 150 mm was selected as the effective bond length for the developed ECC adhesive. The corresponding bond strength for effective bond length was 224.9 N/mm^2. However, the bond strength of epoxy-bonded sample for the same bond length is 670.68 N/mm^2. Therefore, the bond strength reduction in developed ECC adhesive compared with the epoxy-bonded sample was 66.47%. An interface bond between CFRP and ECC adhesive was evident in all the samples. Therefore, measures were taken to avoid this bond interface failure and to enhance the bond strength in the next phase of the test program.

2.5 Enhancement of Bond Strength

To avoid the interface failure between CFRP and ECC adhesive, approaches were taken to increase surface free energies. One approach was to increase the surface friction and the other approach was to change the nature of adhesive by using ECC slurry over ECC mortar. Therefore the first technique implemented was sticking

Fig. 5 Testing the sample

silica sand on top of CFRP fabric using epoxy adhesive before bonding it using ECC adhesive (E-M-SS-1/2). The second technique was to replace the silica sand in the first technique with sand sieved through 1.7 mm sieve (E-M-S-1/2). The third option was to remove silica sand in ECC adhesive mix and produce the ECC slurry to use as the adhesive for CFRP (E-S-N-1/2). The fabricated samples were tested for their pull out strength and the obtained results are given in Table 3.

Apart from E-M-S-1/2, all the other approaches failed in the CFRP-ECC adhesive interface failure. Samples E-M-S-1 and E-M-S-2 failed due to interface failure between ECC adhesive and concrete substrate. Therefore, sticking sand on CFRP fabric have avoided the CFRP-ECC adhesive interface failure. Moreover, these samples achieved the highest bond strength of 570.25 N/mm^2 which showed a 158% of bond strength enhancement when compared with the previous bond strength of ECC adhesive without strength enhancement techniques. Further, it can be seen that the bond strength of ECC adhesive has reached a value closer to epoxy adhesive bond strength. In all these instances, the effective bond length was maintained. Hence, depending on these results it can be concluded that sticking sand on CFRP

Table 3 Test results of bond strength enhancing techniques

Sample code	Average failure load (kN)	Bond strength (N/mm^2)	Percentage strength enhancement compared to the sample without strength enhancement (%)
E-M-SS-1	5.60	449.80	100
E-M-SS-2			
E-M-S-1	7.10	570.28	158
E-M-S-2			
E-S-N-1	1.55	124.50	−45
E-S-N-2			

using epoxy is a successful method of enhancing surface free energy in CFRP-ECC adhesive interface.

2.6 Thermal Performance of the ECC Adhesive

Cementitious adhesives were suggested to use over epoxy adhesives because of their thermal resisting nature. Therefore, the developed ECC adhesive and epoxy adhesive were tested for their thermal performance by conducting the pullout test under elevated temperature. The bondline temperature of samples was elevated up to 100 °C using a 1000 W flashlight while conducting the pullout test. Two K-type stainless steel shield thermocouples were fixed to the bondline while fabricating the samples to monitor the temperature rise. A data logger was used to read the bondline temperature. Figure 6 shows how the bond strength has deviated when both adhesive types were exposed to 100 °C.

Bond strength reduction at elevated temperature was comparatively low in ECC adhesive compared to the epoxy adhesive. The failure occurred in the ECC adhesive-concrete interface, even under high-temperature exposure. It showed that the ECC adhesive-concrete interface is sensitive to temperature. The glass transition temperature of epoxy exceeded when exposing the sample to 100 °C. It resulted in a drastic bond strength drop as indicated in Fig. 6.

3 Numerical Model

To assess the behaviour of direct pullout test, a three-dimensional Finite Element model was developed [10]. The model was analysed in a computer with an Intel(R) Core(TM) i5-4200U processor and an 8 GB RAM.

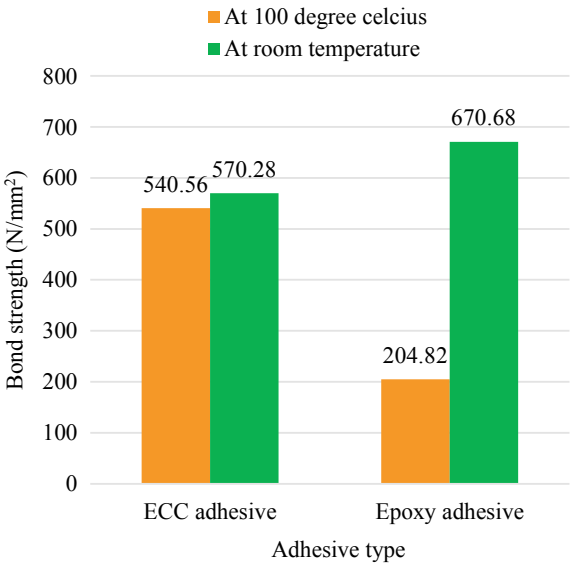

Fig. 6 Effect of elevating bondline temperature

3.1 Material Models, Defining of Elements and Mesh Analysis

The Concrete Damage Plasticity (CDP) model was used to assign the nonlinear behaviour of concrete [27]. Nehdi et al. [21] simulated ECC using both the CDP model and Drucker/Prager (DP) model. Li and Zhang [17] have highlighted the effectiveness of modelling dynamic actions of cementitious materials using the CDP model. Therefore the CDP model was used in damage modelling for both ECC adhesive and concrete block. CFRP fabric was modelled as a Lamina element.

The eight-node linear hexahedral solid element with reduced integration (C3D8R) was used to model both concrete block and ECC adhesive layers. The four-node quadrilateral membrane shell element with reduced integration (M3D4R) was used to model CFRP fabric. Mesh convergence analysis was carried out to determine the optimal mesh size. According to the results, the element size of 5 mm was used for ECC adhesive layer, 2.5 mm elements were used for meshing CFRP fabric and 10 mm elements were used for concrete block. The aspect ratio of elements was kept between 0.5 and 1. Figure 7a shows the meshed setup.

3.2 Boundary Conditions and Bond-Slip Behaviour

The same boundary conditions provided in the experimental setup were modelled. Loading was simulated as a displacement in CFRP fabric. Figure 7b presents the

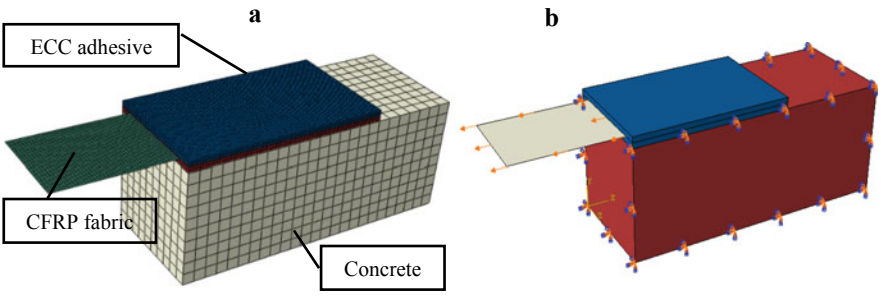

Fig. 7 **a** Meshed model, **b** Boundary conditions and loading

applied boundary conditions and loading. Bond-slip was observed in both ECC-concrete and ECC–CFRP interfaces. Therefore, it was necessary to accompany the bond-slip behaviour with the adhering properties of ECC adhesive. This was simulated by defining a cohesive contact interaction for the mentioned contact surfaces along with damage initiation and damage evolution criteria. It follows the traction–separation law proposed by Camanho et al. [8] which defines that once the damage initiation is reached the bond will undergo progressive damage.

3.3 Validation of the Model

The experiment and predicted load vs displacement graphs are given in Fig. 8. Both graphs follow a comparatively similar path. But the predicted load versus displacement graph showed slightly higher loading values compared to the experiment loading values for a particular displacement. The ultimate failure load of the

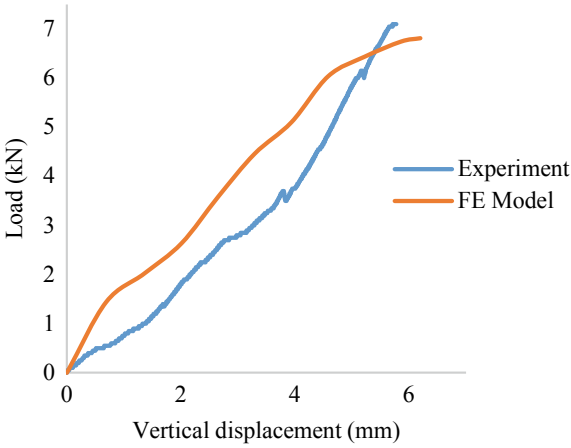

Fig. 8 Load–Vertical displacement graph

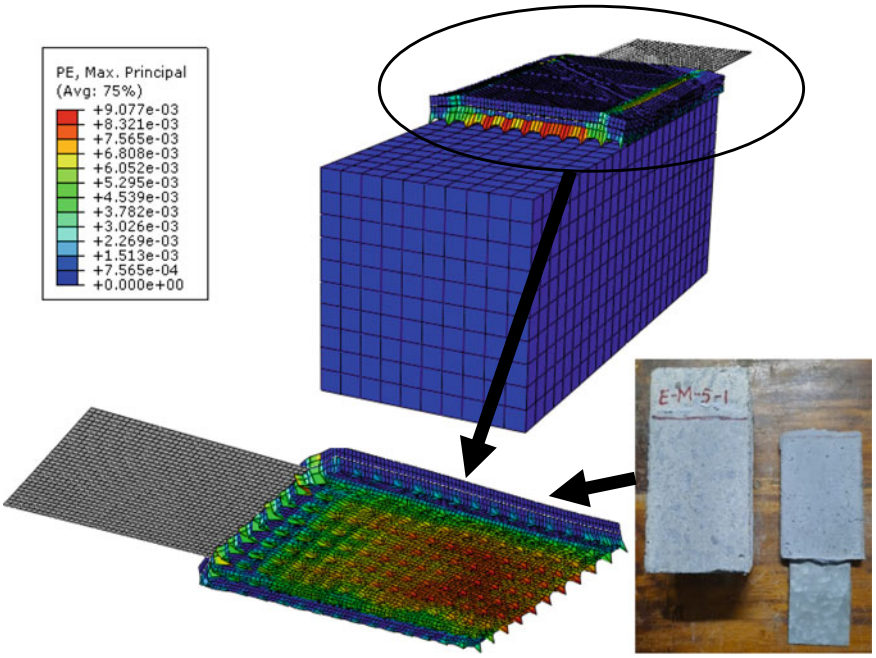

Fig. 9 ECC–Concrete interface bond failure

FE model was 6.81 kN whereas the failure load of the experimental setup was 7.1 kN. Therefore, the predicted value showed a 4.08% deviation from the actual value. Displacement at failure load in the experimental setup was 5.78 mm while it was 6.2 mm in the FE model. Thus, the predicted displacement showed 7.27% of increment from the actual displacement. This is fairly a good prediction for the actual scenario. Figure 9 shows how the evolved ECC adhesive-concrete interface failure was predicted in the FE model.

3.4 Parametric Study

A parametric study was performed to check the effect of adhesive thickness on bond strength. Therefore, models were developed for different adhesive thicknesses where two equivalent adhesive layers are applied on the top and bottom of CFRP fabric. Hence, the adhesive thickness is the overall thickness which includes both top and bottom adhesive layers. Failure loads for adhesive thickness 2.5 mm, 5 mm, 10 mm and 20 mm were 0.37 kN, 2.45 kN, 7.10 kN and 9.40 kN respectively (Fig. 10). The corresponding bond slip at failure loads were 1.87 mm, 2.90 mm, 5.71 mm and 9.55 mm (Fig. 10).

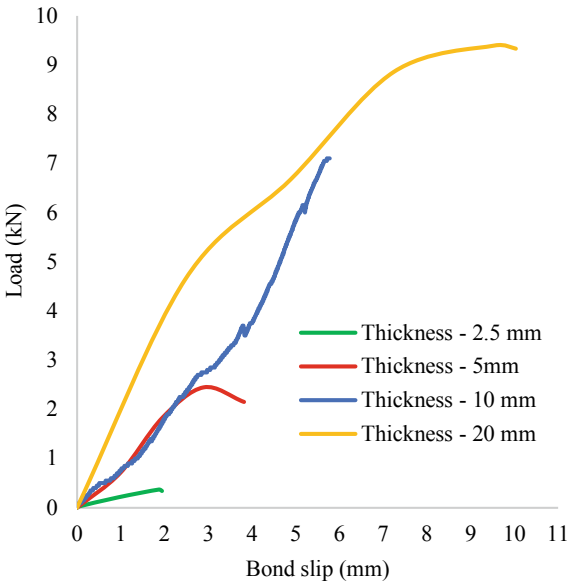

Fig. 10 Effect of ECC adhesive thickness

Failure load at 5 mm adhesive thickness is nearly equivalent to 7 times the failure load corresponding to 2.5 mm adhesive thickness. Thus, the failure load enhancement is 562% of the failure load for 2.5 mm adhesive thickness. Percentage failure load enhancement for 10 mm adhesive thickness is 190% of the failure load for 5 mm adhesive thickness. This percentage increment further reduces to 32%, when the adhesive thickness increment from 10 to 20 mm. Therefore it is clear that the percentage increment of failure load gradually decreases with the increment of adhesive thickness, even though failure load keeps on increasing gradually.

When bond-slip at failure load is concerned, with the increment of adhesive layer thickness, bond-slip at failure increases gradually. But unlike the behaviour in failure load, here the percentage increment of failure load bond-slip between two consecutive adhesive thicknesses keeps on increasing as 55% of bond-slip enhancement from adhesive thickness 2.5 mm to 5 mm, 97% for adhesive thickness from 5 to 10 mm. But this slightly reduced to 67% when adhesive thickness incremented from 10 to 20 mm. Hence, it is clear that the enhancement of ECC adhesive layer thickness will enhance the bond strength. But this enhancement gradually decreases as the percentage increment between 2 consecutive adhesive thicknesses.

4 Conclusions

The following conclusions were made from the experimental and numerical study.

1. Thermal conductivity of ECC-PET adhesive with PET fibre content as 2% of cement content ranged between 0.145 and 0.18 W/mK. Thus, the adhesive shows thermal resisting nature.
2. The developed ECC-PET adhesive showed 7 days compressive strength of 16.97 N/mm^2, 28 days compressive strength of 52.77 N/mm^2 and tensile strength of 3.83 N/mm^2.
3. The effective bond length of developed adhesive is 150 mm and the corresponding average bond strength is 224.9 N/mm^2. The failure occurred in CFRP-ECC interface.
4. The CFRP-ECC interface failure can be avoided by sticking sand on top of CFRP fabric using epoxy adhesive before adhering it to a concrete substrate using ECC-PET adhesive.
5. This approach enhanced the average bond strength to 570.28 N/mm^2. The percentage of bond strength enhancement was 158%. The failure occurred in ECC-concrete bond interface.
6. The average bond strength was reduced by 5.21% when the bondline temperature of samples adhered using ECC-PET adhesive was incremented to 100 °C, whereas for epoxy adhesive this reduction was around 69%.
7. The ECC-concrete bond is sensitive to temperature increment.
8. From the parametric study, it was found that the increment of developed ECC adhesive thickness increases the failure load. However, the percentage failure load enhancement between 2 consecutive adhesive thicknesses reduces gradually.

Acknowledgements Authors would like to highly acknowledge the financial support provided by the National Research Council grant No: PPP 18-01. Furthermore, the help given by the laboratory technicians in the Department of Civil Engineering, University of Moratuwa during the experimental work is highly appreciated.

References

1. American Society for Testing and Materials (2005) ASTM C618-19-standard specification for coal fly ash and raw or calcined natural pozzolan for use in concrete. ASTM International
2. American Society for Testing and Materials (2009) ASTM C 109/C 109M—standard test method for compressive strength of hydraulic cement mortars. ASTM International, pp 29–31. https://doi.org/10.1201/9781420091175-c5
3. American Society for Testing and Materials (2018) ASTM D7340 - 07(2018) standard practice for thermal conductivity of leather. ASTM International, West Conshohocken, PA, 15.04. https://doi.org/10.1520/D7340-07R18
4. Bapat B (2020) Measurement of thermal conductivity by Lee's method. Available at: http://www.iiserpune.ac.in/~bhasbapat/phy221_files/Lee%27sMethod.pdf
5. Barnes R, Fidell J (2006) Performance in fire of small-scale CFRP strengthened concrete beams. J Compos Constr 10(December):503–508. https://doi.org/10.1061/(ASCE)1090-0268(2006)10:6(503)

6. Bentz DP, Peltz Mu, Durán-Herrera A, Valdez P, Juárez C (2011) Thermal properties of high-volume fly ash mortars and concretes. J Build Phys 34(3):263–275. https://doi.org/10.1177/1744259110376613
7. Boshoff WP, Van Zijl (2007) Tensile creep of SHCC. In: Fifth international RILEM conference on high performance fibre reinforced cement composites (HPFRCC), Mainz, pp 87–96
8. Camanho PP, Dávila CG, De Moura MF (2003) Mixed-mode progressive delamination in composite materials. J Compos Mater 37(May 2014):1415–1438. https://doi.org/10.1177/0021998034505
9. Ćojbašić L, Stefanović G, Sekulić Ž (2005) Influence of the fly ash chemical composition on the portland cement and fly ash mixture hydration mechanism. FACTA UNIVERSITATIS Ser Mech Eng 3(1):117–125
10. Dassault Systemes Simulia and Corporation (2014) ABAQUS Standard user's manual, Version 6.14, ABAQUS. Rhode Island, USA.
11. Gamage JCPH, Al-Mahaidi R, Wong MB (2006) Bond characteristics of CFRP plated concrete members under elevated temperatures. Compos Struct 75:199–205. https://doi.org/10.1016/j.compstruct.2006.04.068
12. Hashemi S, Al-mahaidi R (2012) Flexural performance of CFRP textile-retrofitted RC beams using cement-based adhesives at high temperature. Constr Build Mater 28(1):791–797. https://doi.org/10.1016/j.conbuildmat.2011.09.015
13. Himasha MWC, Gamage JCPH (2019) A review on cementitious adhesives used to bond CFRP with concrete. In: 10th international conference on structural engineering and construction management, Kandy, p 93
14. Huang X, Ranade R, Zhang Q, Ni W, Li VC (2013) Mechanical and thermal properties of green lightweight engineered cementitious composites. Constr Build Mater 48:954–960. https://doi.org/10.1016/j.conbuildmat.2013.07.104
15. Kahandawa Arachchi KADYT, Gamage JCPH , De Silva GIP (2019) Thermal insulation systems for CFRP/concrete composites: a review. In: 10th international conference on structural engineering and construction management, p 94
16. Koisch BB (1998) Carbon fiber cement matrix (CFCM) overlay system for Masonry Strengthening. J Compos Constr 2(May):105–109. https://doi.org/10.1061/(ASCE)1090-0268(1998)2:2(105)
17. Li J, Zhang YX (2012) Evaluation of constitutive models of hybrid-fibre engineered cementitious composites under dynamic loadings. Constr Build Mater 30:149–160. https://doi.org/10.1016/j.conbuildmat.2011.11.031
18. Li V (2008) Engineered Cementitious Composites (ECC)—material, structural, and durability performance engineered cementitious. In: Concrete construction engineering handbook. CRC Press
19. Li VC (2007) Engineered cementitious composites (ECC)—material , structural , and durability performance. In: Nawy E (ed) Concrete construction engineering handbook. CRC Press
20. Makwana JJ, Rathod DJD (2017) Interface characterization of different types of fibers in engineered cementitious composites (ECC). IOSR J Mech Civil Eng 14(01):08–14. https://doi.org/10.9790/1684-1401020814
21. Nehdi ML, Ali MAEM (2019) Experimental and numerical study of engineered cementitious composite with strain recovery under impact loading. Appl Sci 9(5):994. https://doi.org/10.3390/app9050994
22. Sahmaran M, Li VC (2008) Durability of mechanically loaded engineered cementitious composites under highly alkaline environments. Cement Concr Compos 30:72–81. https://doi.org/10.1016/j.cemconcomp.2007.09.004
23. Sathishkumar P, Sampathkumar P, Karthik M, Vignesh C (2016) Significance of various fibres on engineered cementitious concrete. Int J Sci Eng Technol 4(1):284–290. Available at: http://www.ijset.in/wp-content/uploads/2016/02/10.2348.ijset0116284.pdf
24. Selvaranjan K, Gamage JCPH, De Silva GIP, Attanayaka V (2020) Thermal performance of rice husk ash mixed mortar in concrete and masonry buildings. Budownictwo i Architektura 19(4):43–52. https://doi.org/10.35784/bud-arch.2121

25. Täljsten B, Blanksvärd T (2007) Mineral-based bonding of carbon FRP to strengthen concrete structures. J Compos Constr 11(April):120–128. https://doi.org/10.1061/(ASCE)1090-0268(2007)11:2(120)
26. US Army Corps of Engineers (2001) CRD-C260–01 standard test method for tensile strength of hydraulic cement mortars. COE Standards, pp 1–8. Available at: https://www.wbdg.org/FFC/ARMYCOE/STANDARDS/crd_c260.pdf
27. Wahalathantri BL, Thambiratnam DP, Chan THT, Fawzia S (2011) A material model for flexural crack simulation in reinforced concrete elements using Abaqus. In: First international conference on engineering, designing and developing the built environment for sustainable wellbeing, pp 260–264. Available at: http://eprints.qut.edu.au/41712/
28. Wu C, Li VC (2017) CFRP-ECC hybrid for strengthening of the concrete structures. Compos Struct 178:372–382. https://doi.org/10.1016/j.compstruct.2017.07.034
29. X-Calibur Structural Systems (2020) X-Wrap C300 technical data sheet. Available at: https://www.x-calibur.us/files/X-WrapC300.pdf
30. Yang EH, Yang Y, Li VC (2007) Use of high volumes of fly ash to improve ECC mechanical properties and material greenness. ACI Mater J 104(6):620–628. https://doi.org/10.14359/18966
31. Yu J, Leung CKY (2017) 'Strength improvement of strain-hardening cementitious composites with ultrahigh-volume fly ash. J Mater Civil Eng 29(9):5017003. https://doi.org/10.1061/(ASCE)MT.1943-5533.0001987

Assessment of Wood Properties in Lesser-Known *Shorea* spp. in Sri Lanka

C. K. Muthumala, W. V. T. D. Amarasinghe, and T. S. Mudalige

Abstract Timber species, Beraliya dun (*Shorea disticha*), Navada dun *(Shorea stupularis),* Dun (*Shorea zeylanica*), Yakahalu dun (*Shorea trapezifolia*), Yakal dun (*Shorea astylosa*) and Thiniya dun (*Shorea congestiflora*) are lesser-known timber species belongs to Dipterocarpaceae family in Sri Lanka. Therefore it is important to identify these species and classify according to their timber properties to popularize among people engaged in the timber industry and forest management. In this study wood density, modulus of rupture (MOR), modulus of elasticity (MOE), compression parallel to grain (CNP) and compression perpendicular to the grain (CPG) of six *Shorea* timber species grown in Rathnapura district in Sri Lanka were investigated. The tests for mechanical properties were performed through the Universal Testing Machine (UTM 100 PC). Determination of the wood anatomical features especially vessels, rays and parenchyma with related to wood physical properties and density also investigated. To study the anatomical features, slides were prepared with small wood section and observed through the microscope using SE premium software and vessel diameter and ray measurements were measured. Six *Shorea* spp. were identified by using a prepared dichotomous key. The wood density was grouped into four classes as very high, high, medium and low respectively. Out of the six *Shorea* species, *Shorea disticha* shows the highest values for MOR and MOE tests and the *Shorea trapezifolia* was reported as the second highest values for MOR and MOE. *Shorea trapezifolia* has reported the highest values for CNP, CPG and Tensile strength values. According to the density values, the highest value shown by the *Shorea trapezifolia* and lowest was from *Shorea zeylanica.*

Keywords *Shorea* · Strength properties · Anatomical features · Density

1 Introduction

The rapid growth of the population and expansion of the constructions of Sri Lanka, the timber demand is increasing annually. Historically, Sri Lanka is rich in timber

C. K. Muthumala · W. V. T. D. Amarasinghe (✉) · T. S. Mudalige
State Timber Corporation, Battaramulla, Sri Lanka

R. Dissanayake et al. (eds.), *ICSBE 2020*, Lecture Notes in Civil Engineering 174,
https://doi.org/10.1007/978-981-16-4412-2_36

resource; nearly 300 local timber species are available in Sri Lanka however only 30 species are commonly available in the market. Since banning of logging from natural forests and shrinkage of the extent of forest plantations; Sri Lanka cannot fulfil the country's industrial timber demand, which tends to increase timber importation. For instance, according to statistics of the Food and Agriculture Organization [3], the sawn wood quantity imported in 2017 has increased by approximately 192% or 48,000 m^3 compared to the sawn wood quantity imported in 2013 (from 25,000 m^3 in 2013 to 73,000 m^3 in 2017). Therefore, it is vital to popular lesser-known timber species of Sri Lanka to the local market to cut the foreign exchange via dropping the wood importation.

The genus *Shorea* (Dipterocarpaceae) is rich in species diversity with 194 species distributed in Bangladesh, Borneo, India, Indonesia, Java, Malaysia, Moluccas, Malaya, Nepal, Philippines and Sri Lanka [2]. The timber of many of these species is valued commercially as important timber. Species of Dipterocarpaceae is identified as valuable contraction timber in Sri Lankan timber market and ten Species of *Shorea* are endemic to the wet zone of Sri Lanka. In recent years, their distributions have been drastically reduced through clear-cutting of the forests and selective logging operations, which are classified as the rate in the IUCN Red Data Book. Thus, the popularity of these species and their timber uses are vital to get attention from public and policymakers to upsurge population of *Shorea* species. Nevertheless, no identified of anatomical and physical properties of these species in Sri Lanka, those properties are essential to popular for commercial uses. Because, timber is a natural structural material, unlike steel and concrete, which are synthesized under controlled environments, then their structural properties can have fixed to the desired values. However, strength properties and other characters of timber vary within the same species even from tree to tree due to the effects of certain growth characteristics [4]. Therefore, in practice, a classification system of strength classes is used.

Strength property means the ultimate resistance on species, loading condition, load duration, and many assorted material and environmental factors. Because wood is anisotropic, mechanical properties also vary in the three principal axes. Property values in the longitudinal axis are generally significantly higher than those in the tangential or radial axes. Flexural (bending) properties are critical; bending stresses are induced when a material is used as a beam, such as an in a floor or rafter system. These collective factors show the importance of discovering anatomical and physical properties of the *Shorea* species to expand their population in Sri Lanka. The general objective of this study is the identification of suitability of six Shorea species for various timber purposes; specifically about their anatomical properties, mechanical properties and physical properties.

Table 1 Selected timber species for the experiment

Common Name	Scientific name
Beraliya dun	*Shorea disticha*
Navada dun	*Shorea stipularis*
Yakal dun	*Shorea astylosa*
Dun	*Shorea zeylanica*
Yakahalu dun	*Shorea trapezifolia*
Thiniya dun	*Shorea congestiflora*

2 Materials and Methods

2.1 Sample Selection

In this investigation, six timber species available in Rathnapura District in Wet zone: low land, in Sri Lanka were selected. Along with six *Shorea* spp., a randomized sample is used for the stand selection. The sample testing was conducted in a wood laboratory in the State Timber Corporation, Battaramulla, Sri Lanka. Following are the selected species. The samples were selected above from the heartwood portion of diameter at breast height (DBH) in mature trees (Table 1).

2.2 Observation of Wood Anatomical Characters

Woodblock of 2 cm × 2 cm × 2 cm was obtained for the slide preparation. Anatomical observations on qualitative and quantitative parameters were made under the light microscope at 4 × 10 magnifications. Measurements were obtained using anatomical photos and Micrometrics SE Premium 4 software. Quantitative wood anatomical features; the mean tangential diameter of vessel Lumina, mean tangential diameter of vessels were measured. Qualitative parameters such as the shape of vessel, deposits availability in vessels, parenchyma arrangement were identified. One of the set of slides from each species was prepared and measurements were taken for each sample [6] available at Research Division of the State Timber Corporation. Wood samples were studied using handheld microscope Toontor—TE013 to observe vessel number and Ray number accommodated in 25 mm^2. Anatomical observations were taken at 20 magnifications within 25 mm^2 area by using a photo. Following features were used for Construction of Identification keys following IAWA [6]: Vessels,Rays; Parenchyma; Intercellular canal; Physical properties. Ray cells are derived from the cambium, spread in the radial direction through the xylem from bark towards the pith and right angle to the annual rings.

Table 2 Classification of density

Density class	Density at 12% MC (kg m^3)
Very high density	840 <
High density	641–840
Medium density	500–640
Low density	500 >

2.3 Determination of Physical Properties

2.3.1 Determination of Moisture Content

Specimens of 20 × 20 × 20 mm were weighed and oven-dried at 103 ^{0}C until specimens reach a constant weight. The moisture content (r) was determined using Eq. 1 [1].

$$r = \frac{M_r - M_0}{M_0} \times 100 \tag{1}$$

where: r is the moisture content of specimen (%), M_r is the moist weight of the specimen, M_0 is the fully dried specimen mass before impregnation.

2.3.2 Determination of Mean Wood Density

The wood density was calculated by using Eq. 2.

$$\text{Density} = \frac{\text{Weight of ovendry wood (kg)}}{\text{Volume of wood } (m^3)} \tag{2}$$

Determination of density was calculated based on the oven-dry weight and green volume using the water displacement method. Table 2 shows the density categorization.

2.4 Determination of Mechanical Properties

The wood species were machined and trimmed to obtain the standard size of 20 mm × 20 mm × 300 mm for Three-point bending test; 20 mm × 20 mm × 60 mm for Compression parallel to grain; 50 mm × 50 mm × 50 mm for Compression perpendicular to Grain; 20 mm × 3mm × 5 mm Tensile test. Samples were replicated four times for each test. All tests were conducted using Universal Testing Machine (UTM 100 PC). Following Eq. (3)–(5) were used to calculate mechanical strengths.

Modulus of Rupture;

$$\text{MOR} = \frac{3\text{FL}}{2\ \text{bd2}} \tag{3}$$

where: MOR = Modulus of Rupture (Nmm^2); F = Maximum force (N); L = Length of the specimen (mm); b = Width of the specimen; d = Depth/Thickness of specimen (mm).

Modulus of elasticity;

$$\text{MOE} = \frac{\text{FL3}}{4\delta\text{bd3}} \tag{4}$$

where: MOE = Modulus of Elasticity (Nmm^2); F = Maximum load at proportionate stage (N); L = Length of the beam between supports (mm); b = width of the specimen; d = Depth/Thickness of the specimen (mm); δ = Maximum deflection.

Compression parallel to grain;

$$\text{Compressive strength of the Specimen} = \frac{\text{Maximum Load act on the specimen at Serviceabiity state (N)}}{\text{Load acting area (mm}^2\text{)}} \tag{5}$$

3 Results and Discussion

3.1 Anatomical Properties

In this study, it represents the number of vessels that accommodates in 25 mm^2 areas. *S. trapezifolia* shows the highest no of vessels among the species while *S. stipularis* represents the lowest vessels amount. *S. disticha* and *S. astylosa* accommodate a similar amount of vessels. *S. congestiflora* and *S. zeylanica* species possess the second and third highest amount of vessels respectively. Table 3 shows a summary of the results on anatomical features.

Table 3 Summary of the anatomical features *Shorea* spp.

Species name	Vessel (nos.)	Rays (nos.)	Vessel diameter (mm)
S. disticha	116	46	151.8
S. stipularis	99	35	155.5
S. astylosa	115	35	168.5
S. zeylanica	154	37	100.4
S. trapezifolia	187	27	171.7
S. congestiflora	161	33	230.9

However, when considering the vessel diameters, it does not represent the same pattern of the number of vessels distributed in the selected species. It shows the highest value for the vessel diameter for the *S. congestiflora* and the lowest for the *S. zeylanica.* The rays of *S. disticha* show the highest number and *S. trapezifolia* shows the lowest. According to the results, *S. stipularis* and *S. astylosa* species represent the same amount of rays.

3.2 Dichotomous Key for Six Shorea *spp.*

Following are the Dichotomous key for six *Shorea* spp. These keys are vital for species identification.

1. (a) Axial parenchyma absent or rare—*S. congestiflora*
   (b) Axial parenchyma Present—(2)
2. (a) Intercellular canals not present—*S. stipularis*
   (b) Intercellular canals present—(3)
3. (a) Axial parenchyma pattern is Aliform/confluent—(4)
   (b) Axial parenchyma pattern is not Aliform/ confluent—(5)
4. (a) Vessels exclusively solitary—*S. trapezifolia*
   (b) Vessel radial multiples—*S. zeylanica*
5. (a) Homogenous ray cells—*S. trapezifolia*
   (b) Heterogeneous ray cells—*S. disticha*

3.3 Physical and Mechanical Properties

Summary of the tested physical and mechanical properties are shown in Fig. 1. The tests results show that the highest MOE and MOR reported by *S. disticha*, followed by *S. trapezifolia.* The lowest MOE and MOR were reported by *S. zeylanica. S. trapezifolia* has shown the highest values of CNP, CGP and Tensile, second-highest CNP is recorded by *S. congestiflora* and second-highest CGP is recorded by *S. astylosa* while the second-highest Tensile is recorded by *S. disticha.* The lowest CNP is reported by SZ and the lowest CGP is reported by *S. disticha.* The lowest tensile value is reported by *S. astylosa.* When comparing with wood densities, the highest showing by *S. trapezifolia* (1044 kg m^3), following *S. astylosa.* The lowest wood density is shown by *S. zeylanica* (517 kg m^3) while *S. disticha* and *S. stipularis* have reported similar wood density. The categorization of species based on wood density is in Table 4.

S. trapezifolia and *S. astylosa* can be classified as Very High Density while other all tested *Shorea* spp are classified under Medium Density. It is clear the relationship between wood density and physical and mechanical properties [5, 7]. Thus, it can be described the higher CNP, CGP and Tensile of *S. trapezifolia*, while it cannot be described higher values in MOE and MOR of *S. disticha.* However, wood density is

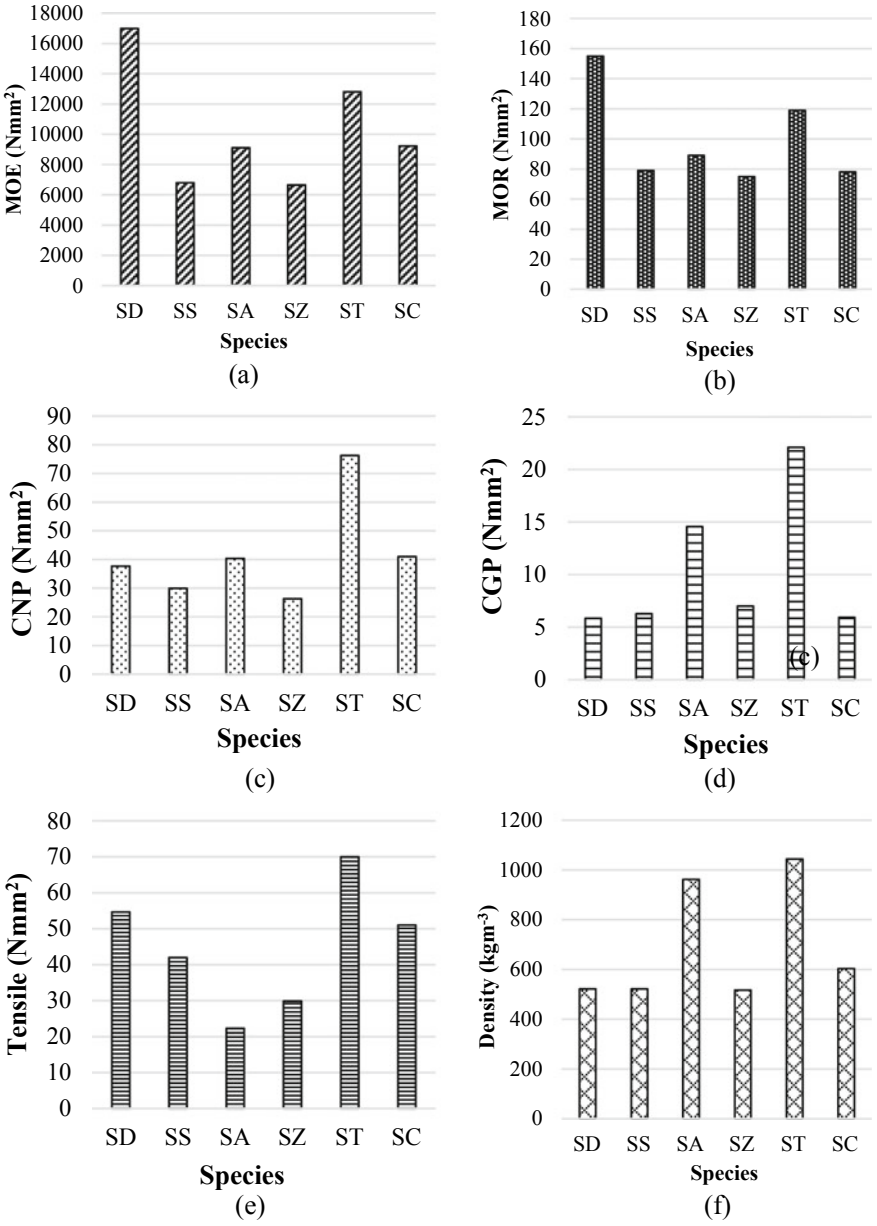

Fig. 1 Compression of the mechanical and physical properties of *Shorea* spp.; **a** MOE (N mm^{-2}); **b** MOR (N mm^{-2}); **c** CNP (N mm^{-2}); **d** CPG (N mm^{-2}); **e** Tensile (N mm^{-2}); (**a**) Wood density (kg m^{-3}). *SD* (*S. disticha*), *SS* (*S. stipularis*), *SA* (*S. astylosa*), *SZ* (*S. zeylanica*), *ST* (*S. trapezifolia*), SC (*S. congestiflora*)

Table 4 The categorization of species based on wood density

Species	Classification of density
S. disticha	Medium density
S. stipularis	Medium density
S. astylosa	Very high density
S. zeylanica	Medium density
S. trapezifolia	Very high density
S. congestiflora	Medium density

not the only factor that affects wood mechanical properties; variations of anatomical features among species significantly influence the variation of mechanical properties.

These results show a clear guiding to use of *Shorea* species for construction, however, their application should be developed based on the design of any building structure. Thus, in accordance with the construction design, the proper *Shorea* species should be selected. However, it is vital to understand the strength values of the species are varying from tree to tree, even within the same tree. Moreover, this study has limited to the *Shorea* grown in Rathnapura District, however, the selected species have distributed in some other districts of the wet zone. Studying the strength properties of *Shorea* in other parts of the wet zone is essential to develop a more constructive guideline for their application. Consequently, it is important to obtain a valid strength report of the *Shorea* timber before practical applications to maximize their utilization.

4 Conclusions

This study aims to explore anatomical, physical and mechanical properties of the lesser-known six *Shorea* spp. The results of the anatomical investigation of the selected species show that the highest number of the vessel reported in *Shorea trapezifolia* while *Shorea stipularis* represents the lowest. *Shorea disticha* and *Shorea astylosa* accommodate a similar amount of vessels. According to the vessel diameter, *Shorea congestiflora* consists of the largest vessels and the smallest vessels are in *Shorea zeylanica.* The rays of *Shorea disticha* show the highest number and *Shorea trapezifolia* shows the lowest.

According to test results of mechanical properties, *Shorea disticha* shows the highest MOE and MOR while the lowest was recorded by *Shorea zeylanica. Shorea trapezifolia* has shown the highest values of CNP, CGP and Tensile strengths. Moreover, *Shorea trapezifolia* shows the highest wood density and both *Shorea trapezifolia* and *Shorea astylosa* were classified as Very High Density. The lowest wood density is reported by *Shorea zeylanica*, however, including *Shorea zeylanica* all other species are classified as Medium Density.

Acknowledgements Authors wish to acknowledge the staff of wood science laboratory of State Timber Corporation for their technical support and all field officers who supported for the sampling.

References

1. BS (1999) BS 373:1957. Methods of testing small clear specimens of timber. British Standards Institution, BSI 07
2. Dayanandan S, Ashton PS, Williams SM, Primark RB (1999) Phylogeny of the tropical tree family dipterocarpaceae based on nucleotide sequences of the chloroplast rbcL gene. Am J Bot 86:1182–1190
3. FAO (2019) Forest products, FAO statistics, yearbook, food and agriculture organization of the United Nations, Rome
4. Forde CM (2009) Introduction to timber as an engineering material. In: ICE manual of construction materials. ICE Publishing, London
5. Horáček P, Fajstavr M, Stojanović M (2017) The variability of wood density and compression strength of Norway spruce (*Picea abies* /L./Karst.) within the stem. Beskydy 10(1,2):17–26
6. IAWA (1989) Iawa list of microscopic features for hardwood identification. Leiden International Association of Wood Anatomists at the National Herbarium of the Netherlands, Leiden
7. Missanjo E, Matsumura J (2016) Wood Density and mechanical properties of *Pinus kesiya* Royle ex Gordon in Malawi. Forests 7:135

Assessment of Hydrophobicity/Oleophilicity and Hydrophilicity/Oleophobicity for Autoclave Aerated Concrete Grains Coated with Stearic and Oleic Acids

M. J. Zafar, A. Matsuno, H. T. T. Dang, P. T. Huyen, T. T. V. Nga, and K. Kawamoto

Abstract Oily wastewater is produced by the rapid urbanization, industrialization and economic growth in developing countries. At present, many oily wastewater treatment practices such as flotation, chemical coagulation, adsorption, filtration and membrane separation are available. Among them, oil/water separation techniques using natural hydrophobic/oleophilic (vice versa) and artificially modified solid grains have been paid much attention due to their cost effectiveness, quick treatment and sustainability but the potential use of hydrophobized porous grains has not been fully studied. This study aims to assess porous grains of autoclave aerated concrete (AAC) grains coated by hydrophobic agents (HAs) and discuss the applicability to oil/water separation technique. The AAC grains (0.106–0.250 mm) was prepared from waste scrap in Vietnam and were coated with two types of HAs, Oleic acid (OA) and Stearic acid (SA), at different concentrations. The degree of hydrophobicity/oleophilicity was assessed by measuring contact angles of water in air (CA_a) and oil in water (CA_o) in the laboratory. Results showed that the measured CA_a for both OA–and SA–coated AAC grains rapidly increased with increasing HA concentrations and reached the maximum of 140°–145° at HA $\geq$ 100 g/kg while CA_o decreased with increasing HA concentrations and the maximum CA_o values were 137°–140° at HA $\leq$ 10 g/kg. The correlations between CA_a and/or CA_o with organic carbon content (OC) and A/B ratio (ratio of hydrophobic groups to hydrophilic groups determined from FT-IR spectra) indicated that the measured CA_a for both OA- and SA-coated AAC grains increased with the increase in OC and A/B ratio and became a plateau (almost constant), while the measured CA_o showed a monotonic decrease with increase in OC and A/B ratio. In next phase, column filtration experiments shall be conducted for examining the oil/water separation efficiency and capacity based on the tested results of this study.

M. J. Zafar (✉) · A. Matsuno · K. Kawamoto
Saitama Univeristy, 255 Shimo-Okubo, Saitama 338-8570, Japan

H. T. T. Dang · T. T. V. Nga
National University of Civil Engineering, 55 Giai Phong Road, Hanoi 84-024, Vietnam

P. T. Huyen
Hanoi University of Science and Technology, Dai Co Viet Road, Hanoi 84-024, Vietnam

R. Dissanayake et al. (eds.), *ICSBE 2020*, Lecture Notes in Civil Engineering 174,
https://doi.org/10.1007/978-981-16-4412-2_37

Keywords Oily wastewater · Oil/water separation · Autoclave aerated concrete · Hydrophobicity/oleophilicity · Contact angle (°)

1 Introduction

In the last few years, the unplanned urbanization and industrialization has produced several challenges like massive discharge of untreated oily wastewater and oil-spill accidents [11]. In most of developing countries, the treatment facilities of oily wastewater are limited due economic and technical constraints. The generated untreated oily wastewater from domestic sources and industries such as petrochemicals, food, textiles, and metal industries, biopharmaceutical and oil/gas refineries are being directly discharged into natural environment and serious water pollution and endangering aquatic life which ultimately affect human health, living nature, destruct natural landscape [3].

Many techniques such as flotation, coagulation, chemical treatment, gravity separation, biological treatment, filtration, and membrane separation have been used to treat and remediate oily wastewater. Among them, oil/water separation techniques based on adsorption and filtration using hydrophobized and/or oleophilized membrane, mesh, porous media, and grains have been progressed in recent years [14, 19]. For example, Bigui et al. [1] tested the hydrophobized quartz sand (solid grains) as filter media and concluded that oil water separation efficiency can be further improved by increasing the hydrophobicity of filter beds. Recently, natural and artificially modified solid grains (sand), porous meshes and membranes with improved surface hydrophobicity/oleophilicity (vice versa, hydrophilicity/oleophobicity) have also been developed for oil/water separation [17, 20]. Previous studies showed high efficiency and capacity in the oil/water separation but the cost of material preparation and secondary pollutant generation still remained as a great challenge [16]. Therefore, one of a unique approach to overcome those problems is to utilize safety and inert waste and industrial by-products with low-cost and unwanted generated from industrial and constriction/demolition activities. The utilization of those materials would contribute to promote the reuse/recycling of waste. For example, Kumara et al. [5, 6] studied the adsorption capacities of heavy metals e.g., Cd^{2+} and Pb^{2+} in high concentrated wastewater using various types scrap waste obtained from industrial by-products (IBPs) and construction-demolition waste (CDW). They revealed that Autoclaved Aerated Concrete (AAC) had a high potential for effective and low-cost treatment of wastewater due to its high porosity and low alkalinity compared to other cementitious materials.

In this study, to examine further the application of AAC waste/scrap to the wastewater treatment, especially for the applicability to oil/water separation technique, we assessed the hydrophobicity/oleophilicity and oleophobicity/hydrophilicity of AAC grains coated with low-cost hydrophobic agents such as Oleic acid (OA) and Stearic acid (SA) in the laboratory. This would provide basic information for our column tests in the next experiments.

Table 1 Basic physical and chemical properties of AAC grains

Tested material	Air-dried water content	BET specific surface area	Specific gravity	LOI	pH	EC
AAC (size: 106–0.250 mm)	(%)	(m^2/g)	–	(%)	–	(mS/cm)
	2.0	14.6 ± 0.1	2.57	9.4 ± 0.3	9.01	0.9
	Chemical composition (%)					
	SiO_2	CaO	Al_2O_3	Fe_2O_3	H_2O	Others
	55.18	28.89	2.76	1.72	7.63	3.82

2 Materials and Methods

2.1 Autoclave Aerated Concrete

In this study, Autoclave Aerated Concrete (AAC) was taken from a stocking yard of waste scrap at a AAC block manufacturing factory in Vietnam. To prepare clean and uniform grains (0.106–0.250 mm) for the laboratory tests, the AAC was crushed, washed with a low foaming neutral cleansing agent, and rinsed thoroughly with distilled water following the procedure of Subedi et al. [12]. The AAC grains has highly porous property rich in both micropores ($d < 10$ μm) and meso- and macropores of $d \geq 10$ μm. The tobermorite (crystalline calcium silicate hydrate; $Ca_5Si_6(O, OH, F)_{18}5H_2O$) is one of major components of AAC [8–10, 13]. The basic physical and chemical properties of AAC grain used in this study were shown in Table 1.

2.2 Hydrophobic Agents

The commercially available OA (molar mass 282.46; Kanto Chemical Co., Japan) and SA (molar mass 284.47; Fujifilm Wako Pure Chemical Corporation, Japan) were used as hydrophobic agents (HAs) in this study because of low-cost, easy to handle, and environmental friendly. OA is a monounsaturated omega-9 fatty acid with a chemical formula of $CH_3(CH_2)_7CH{:}CH(CH_2)_7COOH$ and density is 0.895 g/ml at 20 °C. SA is a saturated fatty acid with chemical formula of ($CH_3(CH_2)_{16}COOH$). Different concentrations of HAs (OA and SA) were used ranging from 5 to 750 (g of HA/kg of AAC grains; hereafter, g/kg) based on a solvent-aided method for assessment of hydrophobicity/oleophilicity and oleophobicity/hydrophilicity. The ethanol (C_2H_5OH; molar mass 46.07) and diethyl ether ($C_2H_5OC_2H_5$; molar mass 74.12) were used as solvents for coating OA and SA, respectively [12, 15].

Table 2 Basic composition of Soybean oil

Material	Flash point	Specific gravity (at 25 °C)	Linoleic acid	Linolenic acid	Oleic acid	Other saturated and unsaturated fatty acids
	(°C)	–	(%)	(%)	(%)	(%)
Soybean oil	331	0.920	53.5	6.9	23.7	15.9

2.3 Soybean Oil

In our test, the commercially available soybean oil (Wako 1st grade; Fujifilm Wako Pure Chemical Corporation, Japan) was used. The appearance is colourless to pale yellow. The composition of soybean oil was shown in Table 2 [2, 4]. Linoleic acid and linolenic acid are the main component of soybean oil. The molecular formula of linoleic acid is

$$CH_3(CH_2)_3(CH_2CH{:}CH)_2(CH_2)_7COOH \text{ (molecular weight: 280.45)}$$

while the molecular formula of linolenic acid is

$$CH_3(CH_2CH{:}CH)_3(CH_2)_7COOH \text{ (Molar: 278.43)}.$$

2.4 Chemical Characterization of AAC Grains Coated with HAs

The organic carbon (OC) content for tested samples was measured by an automatic organic element analyser (FLASH 2000 elemental Analyzer, Thermo Fisher Scientific, Inc., USA). Fourier-transform infrared (FT-IR) spectroscopy technique was used to evaluate the hydrophobic to hydrophilic ratio (hereafter A/B ratio) by using FT-IR spectrometer (Tensor II FT-IR spectrometer, Bruker, UK). The obtained FT-IR spectra was analysed at two absorption bands i.e., hydrophobic (CH–), and the hydrophilic (CO–) functional groups. The CH– (Band-A) and CO– (Band-B) happens at the 3020–2800 cm^{-1} and 1740–1615 cm^{-1} signal area (see Fig. 3; [7, 12]).

2.5 Measurement of Contact Angles in Air and Water

To assess the degree of hydrophobicity/oleophilicity at 'solid-air interface' (CA_a) and hydrophilicity/oleophobicity at 'solid–liquid interface' (CA_o), a simple and common

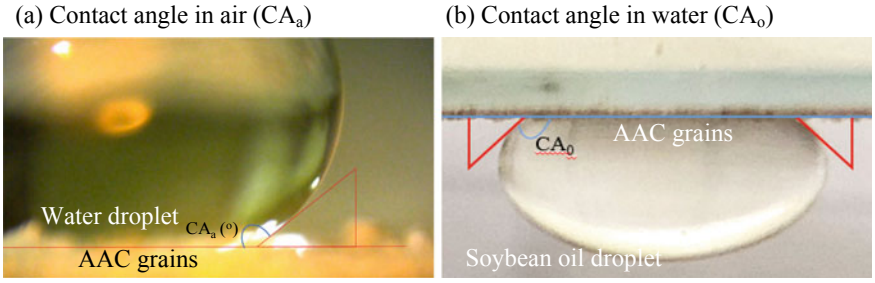

Fig. 1 Examples of captured camera image to determine **a** CA_a and **b** CA_o for a tested sample of OA-coated AAC grain

laboratory testing was performed. The CA_a was measured by sessile drop method using the contact angle analyser (Digital microscope VHX-900 series, Keyence, Japan) following the procedure of Subedi et al. [12] and Zafar et al. [18]. The CA_o was assessed by simple experiment in which the adhesive tape was pasted on glass slide and the OA- and SA-coated AAC grains were carefully sprinkled covering all the tape surface. The glass slide was tapped gently to remove the excessive grains and was carefully placed in a beaker filled with distilled water. In a beaker, it is again gently tapped to remove trapped air bubbles. A small drop of soybean oil (0.1 mL) was carefully placed on the sample with micro syringe and camera image was captured periodically to measure CA_o. Examples of contact angles, CA_a and CA_o, are shown in Fig. 1.

3 Results and Discussion

3.1 Organic Carbon

The measured and calculated OC for both OA- and SA-coated AAC grains are summarized in Fig. 2.

It should be noted that the OC and inorganic content of non-coated samples were less than ~1% and after eliminating this, the OC of coated samples with HAs were calculated. It can be seen clearly from Fig. 2 that for both OA- and SA-coated AAC grains, the measured values became lower than the added OC (calculated from chemical compound and added HA amount) i.e., all the points were above the straight line. This might be due to loss in HA during mixing or handling or may be volatilization in draft chamber. Similar results have been reported for Toyoura sand by Subedi et al. [12].

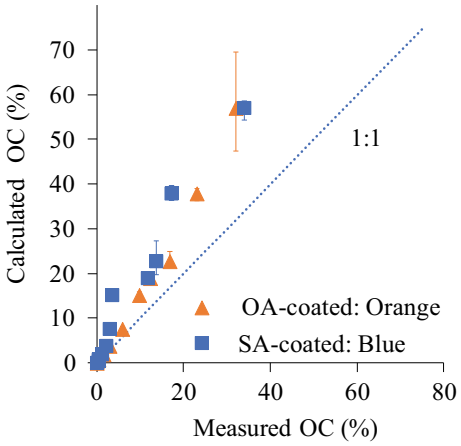

Fig. 2 Comparison between measured and calculated OC for OA- and SA-coated AAC grains

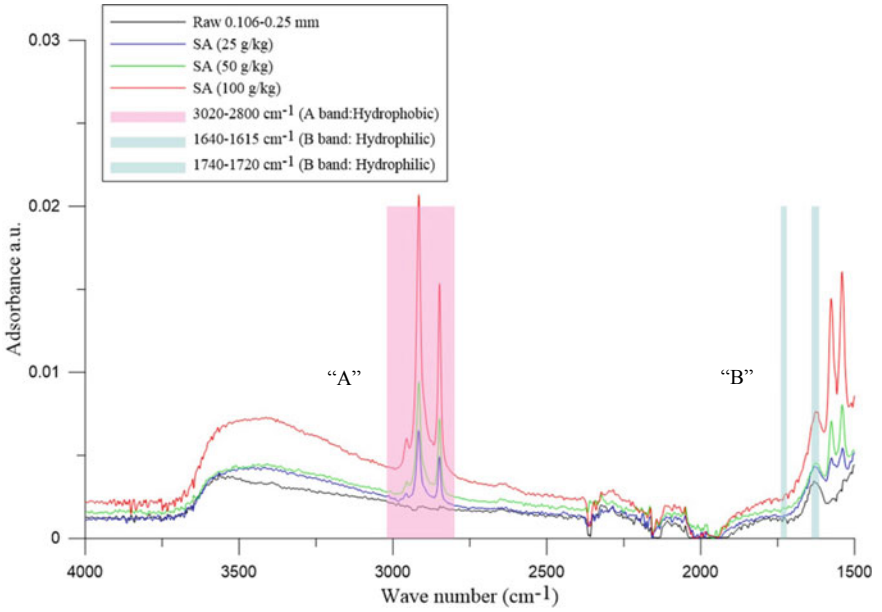

Fig. 3 Example of FT-IR spectrum for tested sample

3.2 FT-IR Analysis

Figure 3 showed an example of FT-IR spectra. In the FT-IR spectra, two bands of hydrophobic functional group (CH– of 3020–2800 cm^{-1}; A band) and hydrophilic functional groups (CO– of 1740–1720 and 1640–1615 cm^{-1}; B band) were detected

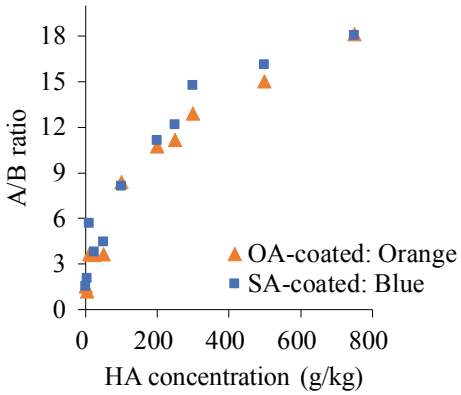

Fig. 4 Relation between measured A/B ratio and HA (g/kg) for OA- and SA-coated AAC grains

and the areas were calculated. Then, the ratio of A and B bands were calculated (hereafter A/B ratio).

The A/B ratio is one of indicators to represent the hydrophobicity of tested samples and higher A/B ratio indicates that higher hydrophobicity [7, 12]. Relationships between measured A/B ratio and HA (g/kg) were shown in Fig. 4. For OA- and SA-coated AAC grains, measured A/B ratio monotonically increased with increasing in HA content.

3.3 Contact Angles as a Function of HA

Figure 5a, b showed measured CA_a and/or CA_o as a function of HA (g/kg) for OA- and SA-coated AAC grains.

For both OA- and SA-coated AAC grains, the measured CA_a increased with increasing HA concentrations and reached the maximum (136°–143°) at HA $\geq$ 100 g/kg and maintained the values (plateau). On the other hand, CA_o decreases rather monotonically with increasing in HA. The maximum CA_o was recorded as 137°–140° at HA $\leq$ 10 g/kg. For further assessment of hydrophobicity/oleophobicity and oleophobicity/hydrophilicity, the measured CA_a and CA_o were compared with A/B ratio and measured OC (%) as shown in Fig. 6. The CA_a gave a rapid increase with the increase in A/B ratio and OC and then kept almost constant. On other hand, the CA_o decreases with the increase in A/B ratio and OC (%). Further studies are needed to examine the mechanism of hydrophobicity/oleophilicity and hydrophilicity/oleophobicity of tested samples but A/B ratio and OC would be good indicators to understand the quantitative understanding of coating characteristics of hydrophobic agents on the porous grain surface.

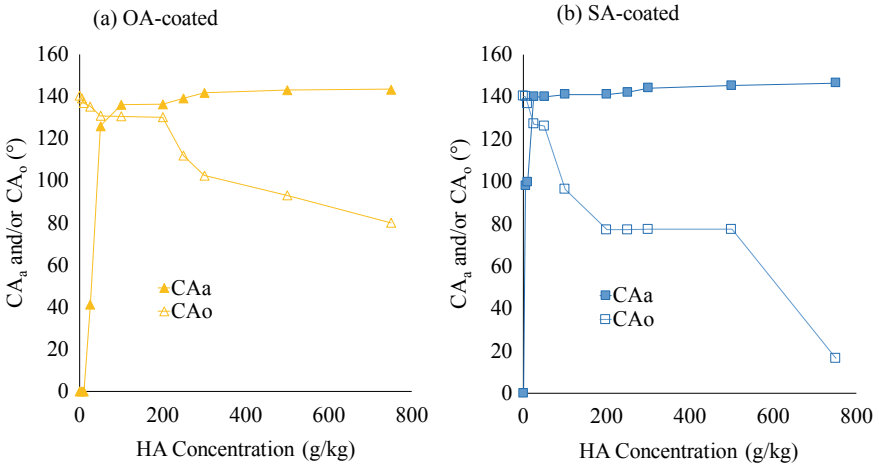

Fig. 5 Measured CA_a and/or CA_o as a function of HA (g/kg). **a** OA-coated and **b** SA-coated AAC grains

4 Conclusions

The hydrophobicity/oleophilicity and hydrophilicity/oleophobicity for artificially hydrophobized AAC grains with two types of hydrophobic agents were assessed based on the contact angle measurements in the laboratory testing. The measured CA_a increased with the increase in HA content while CA_o decreased with the increase in HA content. The maximum CA_a and CA_o for both OA- and SA-coated AAC grains reached high values of ~140°, indicating that the AAC grains coated with HAs have a high potential for fabricating the hydrophobicity/oleophilicity and hydrophilicity/oleophobicity and a high applicability to the oil/water separation technique to treat oily wastewater.

With regard to practical applications, harmless scrap waste should be encouraged for effective utilization in the field of oil/water separation from the viewpoints of reuse and recycling of waste, sustainability, and green development. Therefore, future tests involving column filtration experiments, with the modified AAC grains developed at the optimized conditions obtained from this study, will be conducted to evaluate the oil/water separation efficiency and capacity.

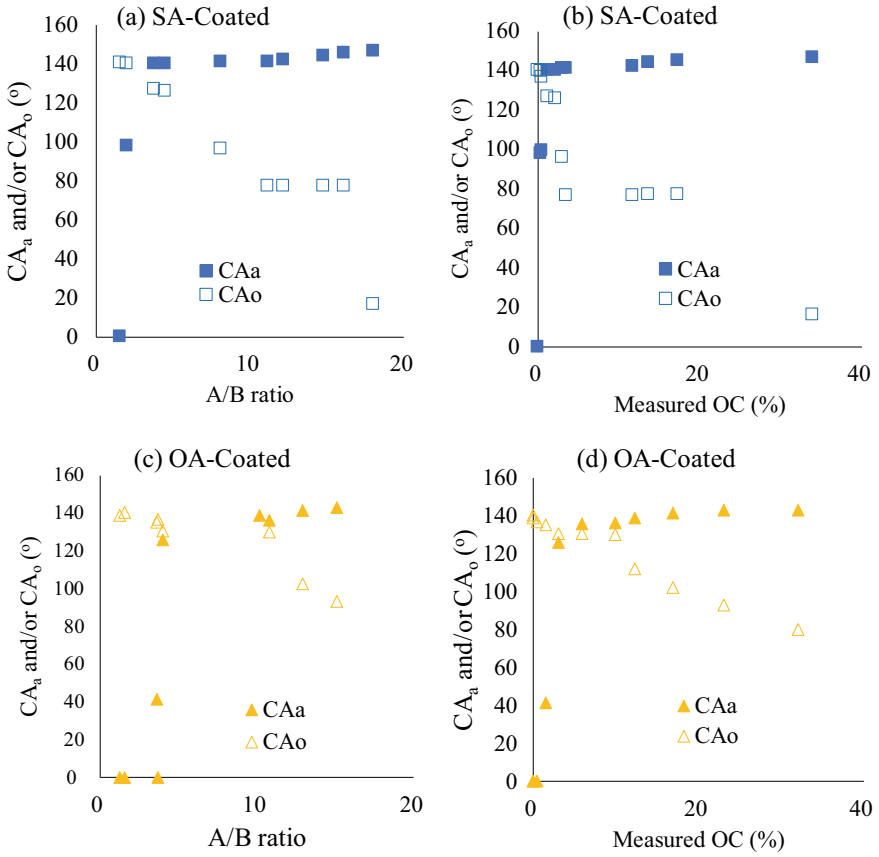

Fig. 6 Comparisons between measured CA_a and/or CA_o with A/B ratio and OC for SA- and OA-coated AAC grains

Acknowledgements This research was supported by JST-JICA Science and Technology Research Partnership for Sustainable Development (SATREPS) project (No. JPMJSA1701).

References

1. Bigui W, Jianlin L, Gang W, Qing C (2018) Filtration of oil from oily wastewater via hydrophobic modified quartz sand filter medium. J Water Reuse Desalin 8(4):544–552
2. Gerde JA, Hammond EG, Johnson LA, Su C, Wanf T, White PJ (2020) Soybean oil. Bailey's Ind Oil Fat Product. https://doi.org/10.1002/047167849x.bio041.pub2
3. Gupta RK, Dunderdale GJ, England MW, Hozumi A (2017) Oil/water separation techniques: a review of recent progresses and future directions. J Mater Chem A 5(31):16025–16058
4. Japan Association for Inspection and Investigation of Foods Including Fats and Oils (2020). Available at: https://www.syken.or.jp/publics/index/73. Accessed: Nov 2020

5. Kumara GMP, Kawamoto K, Saito T, Hamamoto S, Asamoto S (2019) Evaluation of autoclaved aerated concrete fines for removal of Cd(II) and Pb(II) from wastewater. J Environ Eng (U S) 145(11)
6. Kumara GMP, Matsuno A, Nga TTV, Giang NH, Kawamoto K, (2019) Simultaneous removal of Pb(II) and Cd(II) from binary and multi-metals solutions using autoclaved aerated concrete and steel slag grains as low-cost adsorbents. Retrieved from www.cisapublisher.com
7. Matejkova S, Simon T (2012) Application of FTIR spectroscopy for evaluation of hydrophobic/hydrophilic organic components in arable soil. Plant Soil Environ 58(4):192–195
8. Matsuno A, Ishizuka S, Nguyen TL, Dung NT, Nguyen VT, Nguyen HG, Kawamoto K (2020) Comparison of macropore structures and networks of autoclaved aerated concrete blocks using micro-focus X-ray computed tomography. Int J GEOMATE 19(71):160–165
9. Matsushite F, Aono Y, Shibata S (1999) Durability of building materials and components, vol 8, pp 159–169
10. Narayanan N, Ramamurthy K (2000) Structure and properties of aerated concrete: a review. Cem Concr Compos 22(5):321–329
11. Shao S, Li Y, Li T, Qi D, Zhang D, Zhao H (2019) Removal of emulsified oil from aqueous environment by using polyvinylpyrrolidone-coated magnetic nanoparticles. Water (Switzerland) 11(10)
12. Subedi S, Kawamoto K, Jayarathna L, Vithanage M, Moldrup P, Jonge LWD, Komatsu T (2012) Characterizing time-dependent contact angles for sands hydrophobized with oleic and stearic acids. Vadose Zone J 11(1)
13. Trong LN, Asamoto S, Matsui K (2017) Sorption isotherm and length change behavior of autoclaved aerated concrete. Cem Concr Compos 94:136–144
14. Wang B, Liang W, Guo Z, Liu W (2015) Biomimetic super-lyophobic and super-lyophilic materials applied for oil/water separation: a new strategy beyond nature. Chem Soc Rev 44(1):336–361
15. Wijewardana NS, Kawamoto K, Moldrup P, Komatsu T, Kurukulasuriya LC, Priyankara NH (2015) Characterization of water repellency for hydrophobized grains with different geometries and sizes. Environ Earth Sci 74(7):5525–5539
16. Xue Z, Cao Y, Liu N, Feng L, Jiang L (2014) Special wettable materials for oil/water separation. J Mater Chem A 2(8):2445–2460
17. Young J, Huo J, Chen F, Yang Q, Hou X (2018) Oil/water separation based on natural materials with super-wettability: recent advances. Phys Chem Chem Phys 20(39):25140–25163
18. Zafar MJ, Matsuno A, Saito T, Dang HTT, Huyen PT, Kawamoto K (2020) Characterization of hydrophobicity for artificially hydrophobized autoclave aerated concrete grains. In: 3rd international symposium on coupled phenomena in environmental geotechnics (CPEG), CPEG2020-124-2020 (in press)
19. Zhang Y, Zhang Y, Cao Q, Wang C, Yang C, Li Y, Zhou J (2020) Novel porous oil-water separation material with super-hydrophobicity and super-oleophilicity prepared from Beeswax, Lignin, and Cotton. Sci Total Environ 706:135807
20. Zhao B, Ren L, Du Y, Wang J, (2020) Eco-friendly separation layers based on waste peanut shell for gravity-driven water-in-oil emulsion separation. J Clean Product 255:120184

Characterization of Water Retention and Unsaturated Hydraulic Conductivity for Recycled Road-Base Materials

Ryohei Ito, Akira Kato, Akihiro Matsuno, and Ken Kawamoto

Abstract Not only characterization of saturated hydraulic property but also unsaturated hydraulic properties such as water retention and unsaturated hydraulic conductivity are necessary to evaluate an accurate water movement process and the design of water drainage in the road pavement system. Till now, only limited data is available for the unsaturated hydraulic properties for unbound roadbed materials due to the difficulty of measurement. This study carried out the measurements of water retention capacity (WRC) and unsaturated hydraulic conductivity for recycled concrete aggregates (RCA) that typically used for the road base and subbase materials. After grading particle size distribution of RCA adjusted to Japanese technical specification, the tested sample was compacted in a cylindrical mould following the modified Proctor method and then used to measure WRCs and unsaturated hydraulic conductivity. The WRC was measured under the main drying process by a combinational technique with a hanging water, pressure chamber, and a dew-point potentiometer and the unsaturated hydraulic conductivity was measured by an evaporation method. Besides, Toyoura sand was used as a reference material. Results showed the graded RCA gave a smaller water retention capacity compared to Toyoura sand at saturation, however, its water retention became higher than Toyoura sand at the suction range exceeding 10 kPa. As well as water retention property, the saturated hydraulic conductivity of graded RCA became smaller than Toyoura sand at saturation, however, the measured unsaturated hydraulic conductivities of graded RCA at the suction range of 10–100 kPa ranged in the orders of 10^{-6}–10^{-8} cm/s and became higher than those of Toyoura sand.

Keywords Recycled concrete aggregates (RCA) · Road-base and subbase · Water retention curves (WRCs) · Unsaturated hydraulic conductivity

R. Ito · A. Matsuno · K. Kawamoto (✉)
Graduate School of Science and Engineering, Saitama University, 255 Shimo-okubo, Sakura-ku, Saitama 338-8570, Japan
e-mail: kawamoto@mail.saitama-u.ac.jp

A. Kato
Division of Civil Engineering, National Institute of Technology, Tomakomai College, 443 Nishikioka, Tomakomai, Hokkaido 0591275, Japan

R. Dissanayake et al. (eds.), *ICSBE 2020*, Lecture Notes in Civil Engineering 174,
https://doi.org/10.1007/978-981-16-4412-2_38

1 Introduction

Due to rapid urbanization and industrialisation, the generation of construction and demolition waste (CDW) have increased especially at urban areas in developing countries. On the other hand, the recycling of CDW is popular in developed countries and recycled concrete aggregates (RCA) from CDW are commonly used as unbound roadbed materials (i.e., base and subbase in the road pavement system), contributing the save of a natural resources such as natural rock, gravel, and sand. Presently, several technical and engineering specifications such as bearing capacity and packed condition are required for satisfying the application of RCA as a roadbed material (e.g., [4]). Not only those technical specifications but also water retention and hydraulic properties are also important to evaluate an accurate water movement process and the design of water drainage in the road pavement system. Till now, many studies focused on the water capacity at saturation and saturated hydraulic conductivity, however, very limited studies that investigated the unsaturated hydraulic properties for unbound roadbed materials. Rahardjo et al. [7] and Kato et al. [5] measured the water retention curve (WRC) of RCA, but, did not report the unsaturated hydraulic conductivities of tested materials.

One of the reasons to determine the unsaturated hydraulic conductivity of RCA is supposed to be the difficulty of measurement in the laboratory. The RCA contains the coarse fraction (typically, >9.5 mm) and it is difficult to apply a suction-controlled method that is commonly applied to measure the unsaturated hydraulic conductivity in the fields of Soil Science and Geotechnical Engineering because of the contact problem of porous cup with tested samples. Nowadays, on behalf of the suction-controlled method, an evaporation method becomes popular to determine the unsaturated hydraulic properties (e.g., [3]). The evaporation method is applicable to determine both WRCs and unsaturated hydraulic conductivities based on van Genucthen-Mualem model [6, 10], it can be expected to be a useful tool for measuring unsaturated hydraulic property of RCA. As a preliminary measurement, therefore, this study carried out the measurement of WRC and unsaturated hydraulic conductivity of RCA by using the evaporation method and reported the results comparing to a reference data of Toyoura sand.

2 Materials and Methods

2.1 Materials

A commercially available recycled concrete aggregate (RCA), as a roadbed material in Japan, was used in this study. The RCA was sieved and graded under 31.5 mm following a Japanese technical standard [4]. Besides, Toyoura sand with the average diameter of 0.2 mm was used as a reference material. Measured particle size distributions for graded RCA and Toyoura sand were shown in Fig. 1. Basic physical and

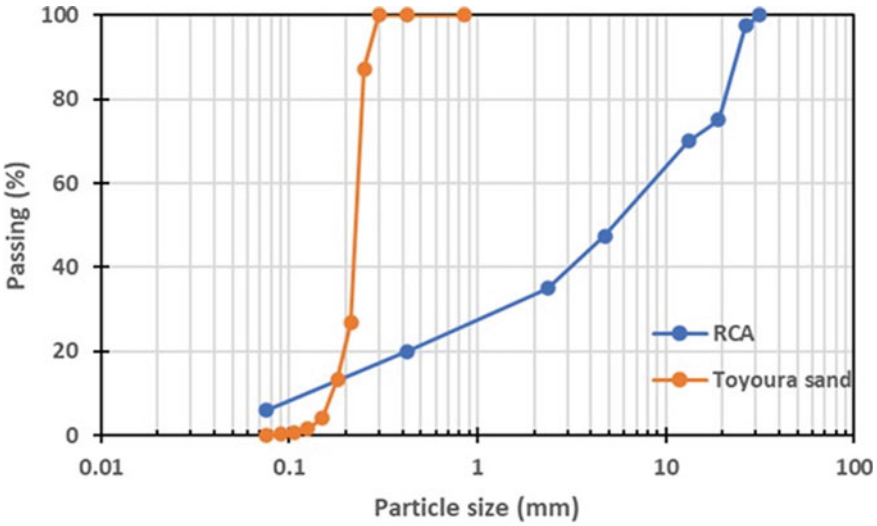

Fig. 1 Particle size distributions (PSDs) for RCA and Toyoura sand

chemical properties for tested samples were summarized in Table 1. The photos of tested samples and multi planer reconstruction (MPR) and binarized images taken by a micro-focus X-ray CT system were shown in Fig. 2.

To decide the packing density of graded RCA, a compaction test was carried out to determine the maximum dry density, $\rho_{d\max}$, and optimum moisture content by a modified Proctor method [1]. The measured compaction curve was shown in Fig. 3. The $\rho_{d\max}$ and optimum moisture content became 1.81 g cm^{-3} and 11.0%, respectively.

Table 1 Physical and chemical properties for tested samples

Samples	Particle size (mm)	$\rho_{d\max}$ (g cm^{-3})	Wopt (%)	G_s	EC (mS cm^{-1})	pH
Graded recycled concrete aggregate (RCA)	0–31.5	1.81	11.0	2.59	1.8	10.7
Toyoura sand	0.075–2	–	–	2.65	–	–

$\rho_{d\max}$ the maximum dry density, G_s specific gravity, *EC* electrical conductivity

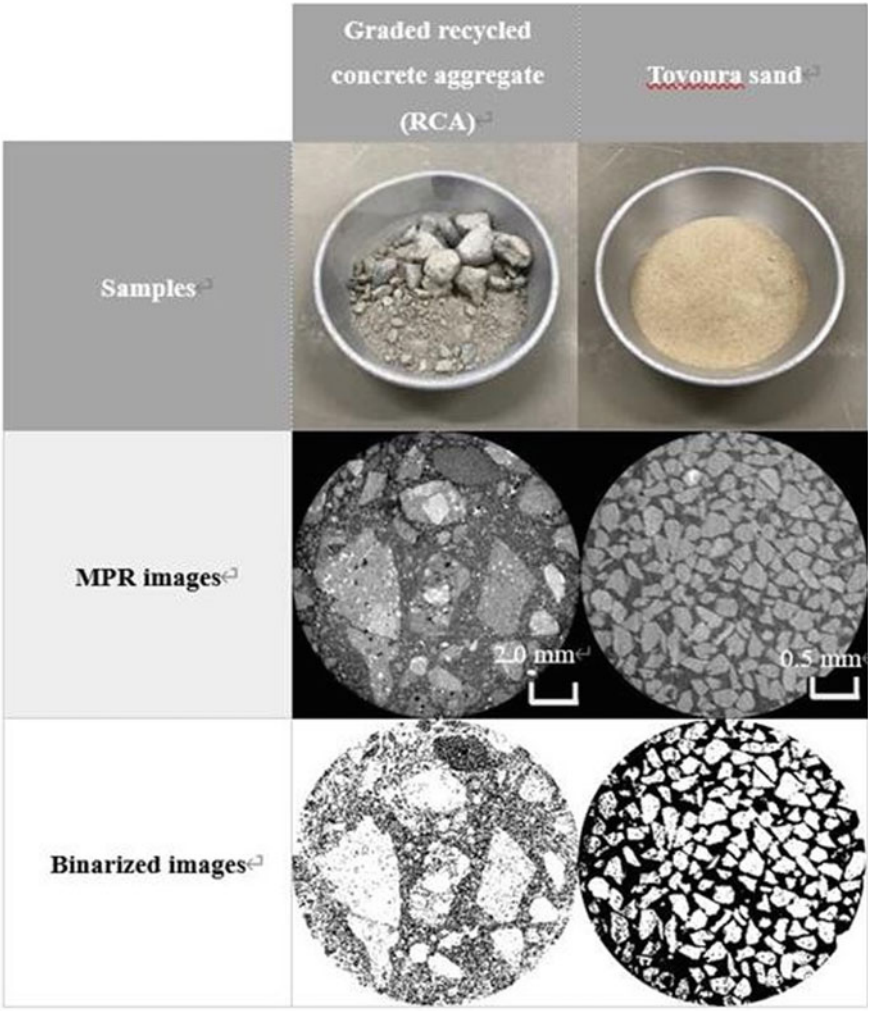

Fig. 2 Sample photos, multi planar reconstruction (MPR) and binarized images taken by a micro-focus X-ray CT for RCA (Hand packing, porosity: 23%. Scanning resolution: 30 μm) and Toyoura sand (Hand packing, porosity: 40%. Scanning resolution: 5 μm)

2.2 Measurement of Water Retention Curve and Unsaturated Hydraulic Conductivity

A series of measurements of water retention curve (WRC), saturated and unsaturated hydraulic conductivities were summarized in Table 2. For the measurement of WRC, graded RCA was packed in a stainless mould with 12 cm height and 15 cm diameter by a modified Proctor method [1] to achieve ~100% of degree of compaction (i.e.,

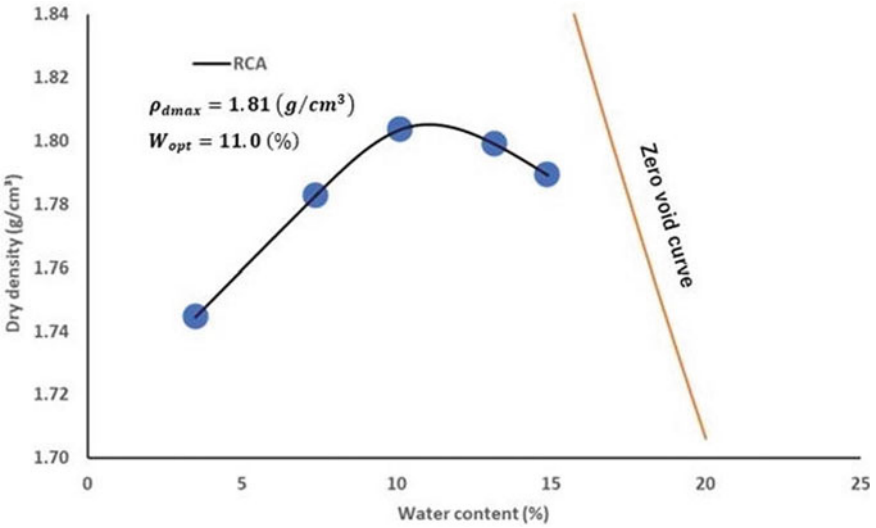

Fig. 3 Compaction curve for graded RCA

Table 2 Measured properties and parameters for tested samples

Measured	Measured parameters	Equipment/standards
Water retention	(1) Water retention curve (Main drying process)	[Modified Proctor (MP) Compaction] – Hanging water (Sand box 08.01, Eijkelkamp Soil and Water, Netherland) – Pressure chamber (1600 extractor, Soilmoisture Equipment Corp., USA) – Dew-point potentiometer (WP4, METER Group, Inc., USA) (Hand compaction) – Evaporation method (HYPROP2 METER Group, Inc., USA)
Hydraulic property	(1) Saturated hydraulic conductivity (2) Unsaturated hydraulic conductivity	– Constant head method [2] – Evaporation method (HYPROP2 METER Group, Inc., USA)

Note that two RCA samples were compacted by modified Proctor (MP) compaction and hand packing. Toyoura sand was compacted by hand packing only

$\rho_{d\max}$). First the packed sample was fully saturated in water for 1 week. Then, the WRC was measured using the combinational technique of a hanging water method (Sand box 08.01, Eijkelkamp soil and water, Netherland) at desired suction values (P, kPa) of 3, 10, and 100 kPa, a pressure chamber (1600 Extractor, soil moisture Equipment corp., USA) at $P = 1000$ kPa, and a dew-point potentiometer (WP4, METER Group, Inc., USA) at $P > 1000$ kPa.

Saturated hydraulic conductivities (k_s, cm s^{-1}) of tested samples were measured using a constant head method [2].

Unsaturated hydraulic conductivities of the tested samples were measured by an evaporation method using HYPROP2 (METER Group, lnc., USA) (Fig. 3). For the evaporation method, graded RCA sample was packed by the modified Proctor method [1], and Toyoura sand was packed with a small rammer (hand packing), respectively. First, the tested sample was fully saturated with water and placed on the weigh balance, and then monitor the internal suction change at two tensiometers and weight change during the continuous evaporation stage [8]. It is noted that the evaporation method can measure both WRCs and unsaturated hydraulic conductivity (k, cm s^{-1}) based on van Genuchten (VG)-Mualem model [6, 10]:

$$S_e = \left[\frac{1}{1+(\alpha h)^n}\right]^m \tag{1}$$

$$k = k_s \cdot S_e^{0.5} \cdot \left\{1 - \left(1 - S_e^{1/m}\right)^m\right\}^2 \tag{2}$$

where α (cm^{-1}), n and m ($m = 1–1/n$) are fitting parameters, Se is effective saturation [$Se = (\theta - \theta r)/(\theta s - \theta r)$], θ is volumetric water content (cm^{-3} cm^{-3}), θs and θr are saturated and residual volumetric water contents (cm^{-3} cm^{-3}), and ks (cm s^{-1}) is saturated hydraulic conductivity.

3 Results and Discussion

3.1 Water Retention Curve

Measured WRCs for graded RCA and Toyoura sand were shown in Fig. 4 and the VG parameters were fitted by using SWRC-Fit program [9] and were summarized in Table 4. Compared to the WRC of Toyoura sand, those for the graded RCA samples measured by a combinational technique and evaporation method gave smaller water retention capacities at saturation (i.e., θ_s). For the graded RCA, however, the decrease in water content with increasing of P became small (represented by n in VG parameter) and water retention of graded RCA became higher than Toyoura sand at the P range exceeding 10 kPa. This implies that the water retention capacity of graded RCA can be expected compared to sand materials at the unsaturated condition.

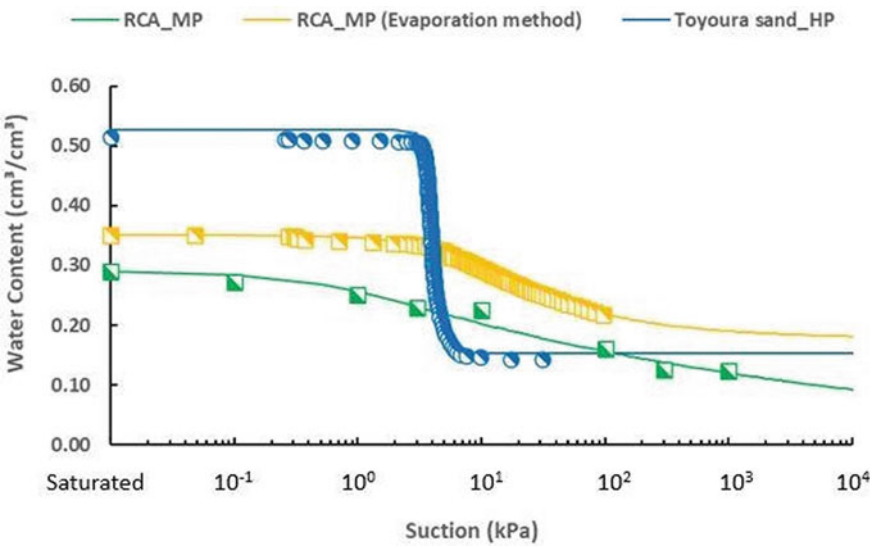

Fig. 4 Water retention curves (WRCs) for RCA and Toyoura sand. RCA: Graded recycled concrete aggregates, MP: Modified Proctor compaction, HP: Hand compaction

Table 4 VG parameters for tested samples

Samples	θr (cm^3 cm^{-3})	θs (cm^3 cm^3)	α (1/kPa)	n
RCA_MP	0.044	0.290	0.061	1.117
RCA_MP (evaporation method)	0.177	0.351	0.165	1.513
Toyoura sand_HP	0.163	0.515	0.255	15.77

3.2 Unsaturated Hydraulic Conductivity

Measured unsaturated hydraulic conductivities for graded RCA and Toyoura sand were shown in Fig. 5. As well as the water retention, the saturated hydraulic conductivity of graded RCA became around 2 orders smaller than Toyoura sand at saturation. However, the measured unsaturated hydraulic conductivities of graded RCA at the P range of 10–100 kPa ranged in the orders of 10^{-6}–10^{-8} cm/s and became higher than those of Toyoura sand. This can be understood that the connected water networks existed at even though the unsaturated condition of $P = 10$–100 kPa for graded RCA and contributed to the water movement. On the other hand, the water networks were disconnected in Toyoura sand and resulted in the very small unsaturated hydraulic conductivities (almost zero) at the P range exceeding 10 kPa.

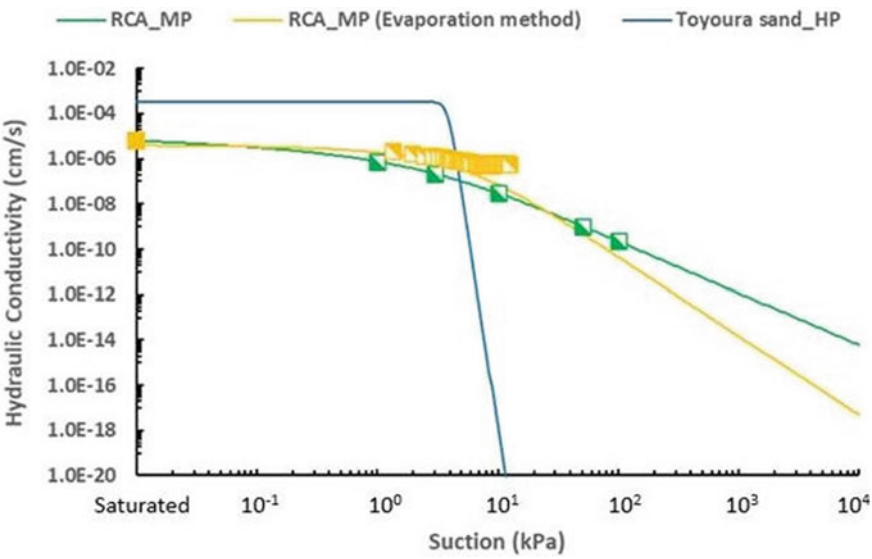

Fig. 5 Saturated and unsaturated hydraulic conductivities for RCA and Toyoura sand. RCA: Graded recycled concrete aggregates, MP: Modified Proctor compaction, HP: Hand compaction

4 Conclusions

In this study, we carried out the measurements of WRC and unsaturated hydraulic conductivity for graded RCA and compared the measured results to those of Toyoura sand. The tested results can be understood as a preliminary measurement, however, the evaporation method (that is applicable to have a simultaneous measurement of WRC and unsaturated hydraulic conductivity) is likely to be a useful tool to determine unsaturated hydraulic property of graded RCA samples containing a coarse fraction with >9.5 mm. Further studies are needed to increase the number of measurements and to improve the accuracy of measured unsaturated hydraulic property.

Acknowledgements This research was partially supported by a JST-JICA Science and Technology Research Partnership for Sustainable Development (SATREPS) project and graded recycled concrete aggregate (RCA) is also provided by MASUO GROUP company.

References

1. ASTM D1557 (2012) Standard test methods for laboratory compaction characteristics of soil using modified effort (56,000 ft-lbf/ft^3 (2,700 kN-m/m^3)). ASTM International, USA
2. ASTM D5856 (2015) Standard test method for measurement of hydraulic conductivity of porous material using a rigid-wall, compaction-mold permeameter. ASTM International, USA

3. Geistlinger H, Leuther F (2018) Evaporation study for real soils based on HYPROP hydraulic functions and micro-CT-measured pore-size distribution. Vadose Zone J 17:180041
4. Japan Road Association (2007) Pavement survey & test methods handbook. Japan Road Association, Japan
5. Kato A, Ito R, Matsuno A, Uchimura T, Tuan NV, Nguyen HG, Kawamoto K (2019) Water retention and gas transport characteristics of recycled graded roadbed materials blended with AAC grains. In: Proceedings of seventeenth international waste management and landfill symposium (Sardinia 2019), vol 218
6. Mualem Y (1976) A new model for predicting the hydraulic conductivity of unsaturated porous media. Water Resour Res 12:513–522
7. Rahardjo H, Vilayvong K, Leong EC (2011) Water characteristic curves of recycled materials. Geotechn Test J 34(1):89–96
8. Schindler U, Durner W, von Unold G, Muller L (2010) Evaporation method for measuring unsaturated hydraulic properties of soils: extending the measurement range. SSSAJ 74(4):1071–1083
9. Seki K (2007) SWRC fit—a nonlinear fitting program with a water retention curve for soils having unimodal and bimodal pore structure. In: Hydrology and earth system sciences discussions. Available at: Cited by 228. Related articles all 14 versions
10. van Genuchten MT (1980) A closed-form equation for predicting the hydraulic conductivity of unsaturated soils. Soil Sci Soc Am J 44:892–898

Proposing a Methodology to Identify the Optimum Mix Design of Autoclaved Aerated Concrete Blocks in the Context of Sri Lanka

H. M. U. R. Herath and P. B. R. Dissanayake

Abstract Introduction of Green Building Materials and Products (GBMP) results in a reduction of energy consumption over the lifetime of a building thus leading to a reduction in toxic, environmental pollution as well as ensuring the security of energy and raw resources as appropriate. The building construction industry has widely used fly ash based products as GBMP. Fly ash is a waste material generated from electricity power plants and is used in cement production with special properties such as workability and durability as well as in the production of concrete. However, in Sri Lanka, the industrial usage of fly ash is very low as compared to the high volume generated from the Coal Power Plant located in Norochcholai, Sri Lanka. This very wasteful, fly ash can be effectively used as a fundamental raw material in the manufacturing of Autoclaved Aerated Concrete (AAC) blocks—which are popular as light weight building materials. Using Autoclaved Aerated Concrete in Sri Lanka, facilitates two major aspects: Firstly, unused waste fly ash can be removed from the Norachcholai power plant premises in a sustainable way; Secondly, the Sri Lankan construction industry gains a sustainable building material. Nevertheless, there are certain issues in using fly ash based AAC in construction sites, such as its problem of drying shrinkage in the block which leads to cracks in constructed walls. The AAC manufacturing process is done in accordance with IS: 2185 (Part 3)—1984, but raw material sources are not providing the required qualities according to the code. Although the raw materials are not providing the required qualities for the production process it is a must to use available sources in Sri Lanka. This question can be addressed by optimizing the mixture design for the available materials in Sri Lanka, considering its drying shrinkage and compressive strength, stays within the limits given in BS EN 771-4:2011+A1:2015 Specification masonry units Part 4. Eleven different mixture designs were prepared by varying fly ash, cement and lime, subsequently tested and thereafter, an equation to calculate drying shrinkage and compressive strength was formulated as a function of fly ash cement and lime. Using the results of this research, optimization of the mixture design can be done in the AAC manufacturing plant.

H. M. U. R. Herath (✉) · P. B. R. Dissanayake
Department of Civil Engineering, Faculty of Engineering, University of Peradeniya, Peradeniya, Sri Lanka

R. Dissanayake et al. (eds.), *ICSBE 2020*, Lecture Notes in Civil Engineering 174,
https://doi.org/10.1007/978-981-16-4412-2_39

Keywords Autoclaved aerated concrete · Compressive strength · Drying shrinkage · Response surface methodology

1 Introduction

Green Building materials are introduced to the construction industry to reduce the usage of energy and to minimize the raw material extraction from nature. Furthermore, according to Spiegel and Meadows [1], green building materials are environmentally responsible materials which are aligned with that of renewable materials.

This emphasis on conserving natural resources and energy, in addition to tackling GHG emissions have led to innovative uses of building materials produced from waste. Waste materials possess less embodied energy and thus their use in construction means that the embodied energy of buildings (and building associated materials and services) is greatly reduced. Thus, with green building materials—overall energy consumption in buildings (and the industry as well) can be reduced [2].

Autoclaved aerated concrete (AAC) wall constructing material is manufactured using quartz rich sand, Fly ash, cement and lime as the main ingredients, and using Aluminum powder as the aerating agent. Slurry is made using Fly ash/Sand, cement and lime mixed with water and after the slurry is produced and Aluminum powder is added to the slurry to react with alkali, which thus causes the AAC's porous structure. The AAC is thereafter cut to its required shapes and sent to the Autoclave to get its unique crystal structure.

Autoclaved aerated concrete (AAC) wall constructing material has been identified as a green building material with a very low embodied energy and the use of Autoclaved Aerated Concrete reduces the cost of the construction [3]. According to Wittmann [4], energy consumption in the manufacturing process of AAC is much less than that of Clay Bricks. According to Drochytka et al. [5], energyuse can be reduced by 7% in residential buildings if Autoclaved Aerated Concrete materials are utilized for wall constructions, furthermore it was mentioned that from one square meter of an AAC wall—almost 350 kg of CO_2 emission can be saved, considering its life cycle. All these Better properties of AAC material relies on its specific physical structure.

Properties and the Physical structure of the AAC material is highly dependent on its mix design, and these properties that arise, vary according to the quality of the materials and manufacturing process [6]. Due to these reasons, it is a must to optimize the mixture design according to the context of where it is manufactured since the material qualities and manufacturing process can be varied from region to region. In a publication by Herath et al. [7] cracks were identified, through the wall panels along construction joints, at local construction sites, where AAC blocks were used. And according to them High Drying shrinkage and Lesser compressive strength was the reason for cracks. The mixture design used in manufacturing is the mixture design given in the manufacturing plant manual, however, despite being

Table 1 Compression between available lime and required lime according to IS: 712-1984

Characteristics	Limitations according to IS: 712—1984 for quicklime type "C"	Quicklime used in Sri Lanka
Calcium and magnesium oxide, present, Min (on ignited basis)	85	79
Magnesium oxide percent (on ignited basis), Max	–	–
Silica alumina and ferric oxide, present, Min (on ignited basis)	–	–
Anhydrate magnesium oxide, percent, Max	–	–
Insoluble residue in dilute acid and alkali, percent, Max on ignited basis)	2	6
Carbon dioxide, percent, max (on oven dry basis)	5	11
Free moisture content, percent, Max	–	–
Available lime as CaO, percent, Min (dry basis)	75	50

manufactured in accordance with these mixture designs defects of AAC material was found in construction sites.

Due to this reason, this study was started to investigate the reasons for above mentioned defects and to mitigate or reduce the defects by optimizing the mixture design and the manufacturing process. In the study it was decided to test raw materials used in manufacturing for its quality as according to IS: 2185 (Part 3)—1984, from these tests it was found that lime sources in Sri Lanka does not have the adequate qualities as specified in IS: 2185 (Part 3)—1984, and as mentioned in the Table 1.

2 Research Question

When it comes to the manufacturing—there is a lack of optimum mix design for Autoclaved Aerated Concrete (AAC), as raw materials have different chemical compositions from region to region, and especially in Sri Lanka, the quality of lime used for manufacturing is not satisfying the qualities according to the IS: 2185 (Part 3)—1984. Due to this reason, optimizing the mixture design for the available materials in Sri Lanka is a hard task. AAC material acquires its required compressive strength and lower drying shrinkage from its mixture design and the manufacturing process. In this study, optimizing the mixture design is focused for: firstly, the available materials

in Sri Lanka, and secondly, in doing so while the AAC material obtains its required compressive strength and a lower drying shrinkage.

3 Methodology

In order to get a correlation between the mixture design and Physical parameters it is a must to design a mixture design experiment. For that purpose, Extreme vertices mixture design method was used according to ReliaSoft, 2017, Minitab 19 software package was used to do the Extreme vertices design. According to the Lanka AAC Pvt. Ltd. plant manuals, in the mixture design, the following ranges have been given for raw material as per Table 2.

The Minitab19 software was used to perform the calculations of the mixture design. The following mixture design was derived using the analysis results given by mintab19 software as shown in Fig. 1. When the points in the triangle are

Table 2 Range of raw materials to be used in mixture design. (percentage by weight)

Bound	Component		
	Fly ash (%) (X1)	Cement (%) (X2)	Lime (%) (X3)
Lower	55	20	10
Upper	70	30	15

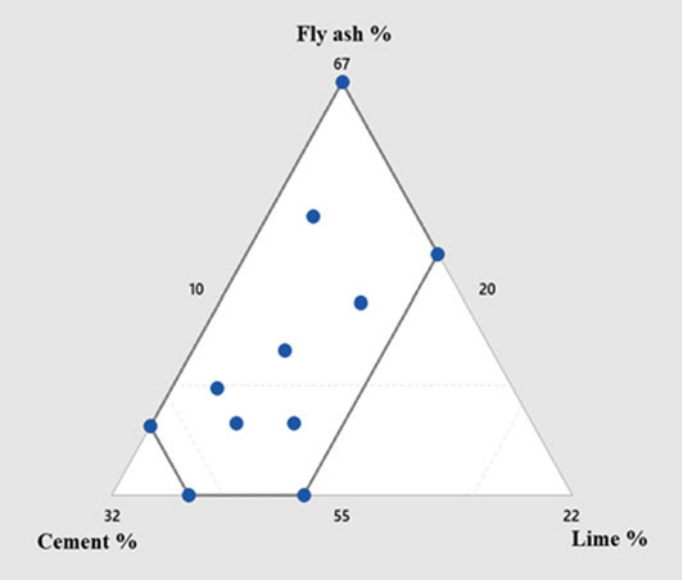

Fig. 1 Plot of mixture design constraints and samples

Table 3 Mixture design derived for the research (percentage by weigh)

Sample number	Fly-ash (%)	Lime (%)	Cement (%)	Gypsum (%)
S1	57.1	12.2	27.7	3
S2	55	12	30	3
S3	62	15	20	3
S4	57.1	13.7	26.2	3
S5	67	10	20	3
S6	59.2	12.4	25.4	3
S7	57	10	30	3
S8	55	15	27	3
S9	58.1	11.2	27.7	3
S10	63.1	11.2	22.7	3
S11	60.6	13.7	22.7	3

observed, mixture proportions for different samples can be tabulated in Table 3, for the continuation of the research.

Response Surface Methodology (RSM) is a collection of statistical and mathematical techniques useful for developing, improving, and optimizing processes. The most extensive applications of RSM are in the particular situations where several input variables potentially influence some performance measure or quality characteristic of the process. Thus, performance measure or the quality characteristic is called the response. The input variables are called independent variables, and they are subjected to the control of the scientist or engineer. The field of RSM consists of the experimental strategy for exploring the space of the process or independent variables, empirical statistical modeling to develop an appropriate approximating relationship between the yield and the process variables, and optimization methods for finding the values of the process variables that produce desirable values of the response [8].

Samples were made manually as the process is compatible to the original process used in the manufacturing plant under the supervision of the plant manager as the number of samples are adequate to conduct Drying Shrinkage tests and compressive strength tests as showed in Fig. 2.

Prepared samples were tested for the Drying Shrinkage and compressive strength. In National Building Research Organization Laboratory, Jawatta, Colombo and Compressive strength teste were carried out at Faculty of Engineering University of Peradeniya. Drying shrinkage tests were done according to SLS 855: 1989 + AMD 1994: Specifications for cement block and Compressive strength tests were done according to ASTM C 1386-07. Results obtained from the laboratory testing are tabulated in Table 4.

Fig. 2 Preparation of samples

Table 4 Experiment results

Sample number	Fly ash %	Cement %	Lime %	Experimented drying shrinkage %	Compressive strength (N/mm^2)
1	57.1	27.7	12.2	0.009	2.96
2	55	30	12	*	2.33
3	62	20	15	*	1.96
4	57.1	26.2	13.7	0.020	3.59
5	67	20	10	0.024	1.92
6	59.2	25.4	12.4	0.017	2.35
7	57	30	10	0.024	1.05
8	55	27	15	0.014	5.54
9	58.1	27.7	11.2	0.008	1.08
10	63.1	22.7	11.2	0.023	1.25
11	60.6	22.7	13.7	*	0.83

4 Statistical Analysis

Developing the Correlation (Regression Model) between Mixture Design versus Drying shrinkage and Compressive Strength using Response surface methodology (RSM) was done using Response surface methodology and minitab1 software package was used to perform the RSM approach.

Regression model derived for Drying Shrinkage is shown in Eq. (1). And the graphical interpretation of the regression model is shown in Fig. 3 (Table 5).

$$\begin{aligned} Drying\ Shrinkage\,\% = {} & (\text{Fly ash}\,\%) * (-0.0021107) + (\text{Cement}\,\%) * 0.081697 \\ & + (\text{Lime}\,\%) * 0.0313892 + (\text{Fly ash}\,\%) \\ & * (\text{Cement}\,\%) * (-0.0011577) \\ & + (\text{Fly ash}\,\%) * (\text{Lime}\,\%) * 0.0006742 \\ & + (\text{Cement}\,\%) * (\text{Lime}\,\%) * (-0.0034169) \end{aligned} \quad (1)$$

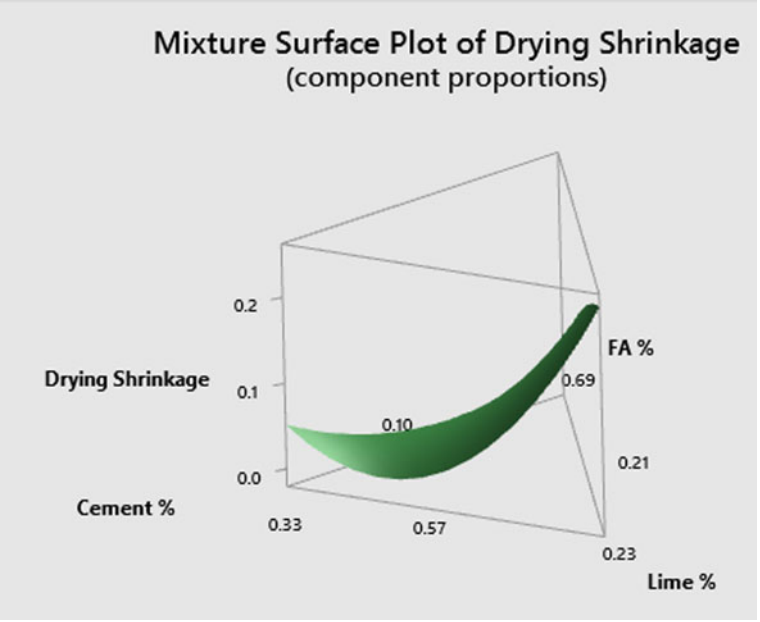

Fig. 3 Mixture surface plot of drying shrinkage

Table 5 Model summary for drying shrinkage

S	R-sq	R-sq(adj)	PRESS	R-sq(pred)
0.0031675	85.06%	77.60%	0.0002734	59.30%

Regression model derived for Compressive Strength is shown in Eq. (2). And the graphical interpretation of the regression model is shown in Fig. 4 (Table 6)

$$\begin{aligned} Compressive\ Strength\ \left(\mathrm{N/mm^2}\right) = {} & (\text{Fly ash }\%) * (0.5124) \\ & + (\text{Cement }\%) * (-0.2567) \\ & + (\text{Lime }\%) * 5.5596 \\ & + (\text{Fly ash }\%) * (\text{Cement }\%) * (-0.0107) \\ & + (\text{Fly ash }\%) * (\text{Lime }\%) * (-0.1037) \\ & + (\text{Cement }\%) * (\text{Lime }\%) * (0.0041) \end{aligned} \quad (2)$$

R squared and the adjusted R squared values are closer to 1 indicating the predicted values are closer to the actual values and the models has a higher accuracy.

The Predicted R squared values are 59.30% and 57.60%, for regression models derived for Drying Shrinkage and compressive strength, respectively, which indicates that the fitted model has an adequate predictive accuracy. Which means that the model

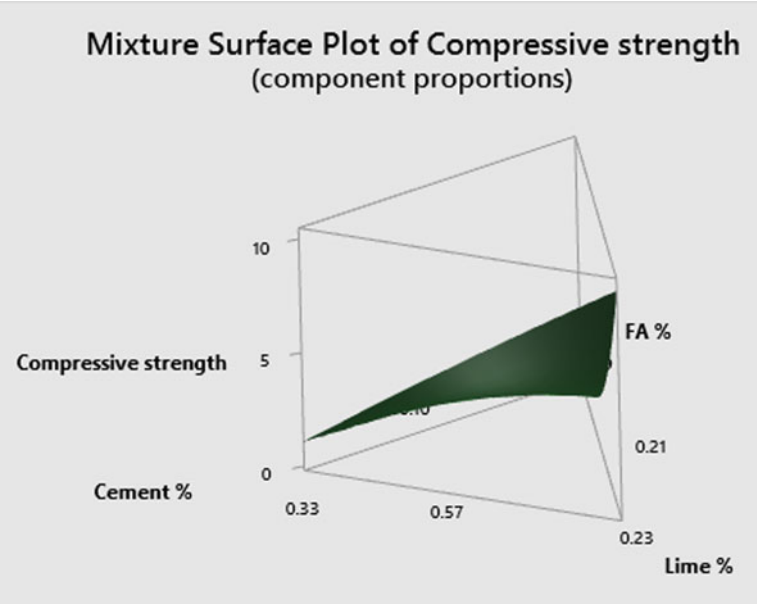

Fig. 4 Mixture surface plot of compressive strength

Table 6 Model summary for compressive strength

S	R-sq	R-sq(adj)	PRESS	R-sq(pred)
0.697875	72.95%	67.94%	20.6118	57.60%

is predicting the dry shrinkage when applying a new set of values of explanatory variables, with 59.3% and 57.60% of accuracy for regression models derived for Drying Shrinkage and compressive strength, respectively. But with further experiments it is obvious that the accuracy can be increased.

In order to use a Regression Model following conditions should be satisfied.

- Residuals are normally distributed (Normal Probability plot/histogram)
- Residuals must have constant variance with mean zero (fitted vs. Residuals plot)
- No correlation among the residuals (Observation order vs. Residual plot).
- Multicollinearity should not exist.

According to Figs. 5 and 6, Derived regression models satisfy the abovementioned conditions.

Normal probability shows that the residuals are normally distributed. Regression Model Assumptions 1 is satisfied for both regression models. The fitted values vs. residual plots shows whether the residuals are randomly bounced roughly from a horizontal band around the 0 line. Regression Model Assumptions 2 is satisfied for

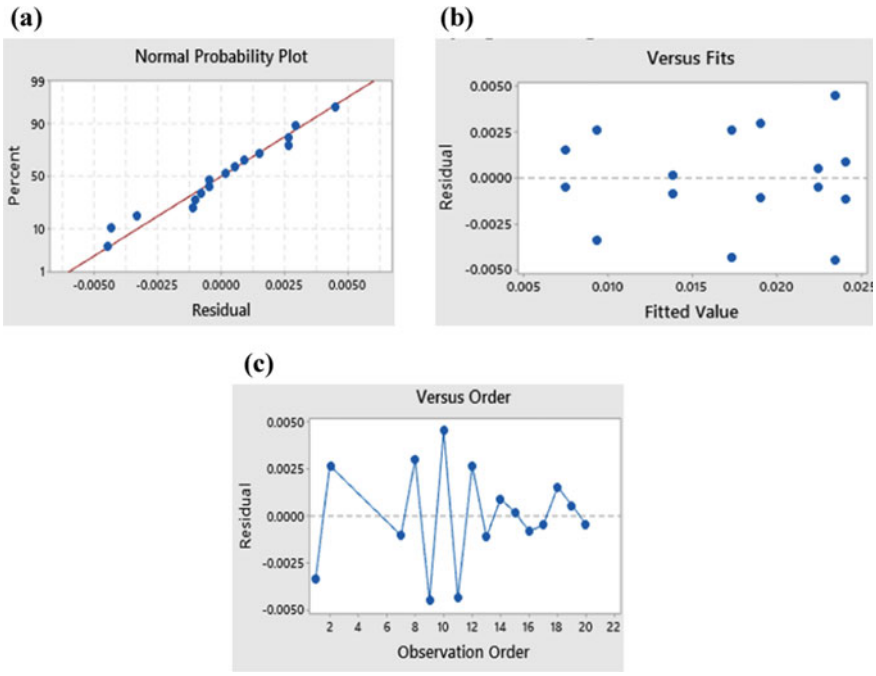

Fig. 5 **a** Normal probability plot. **b** The fitted values versus residual plot. **c** Observation order plot for drying shrinkage

both regression models. Observation order versus residual plot indicates that there is no serial correlation among the error terms.

Regression Model Assumptions 3 is satisfied for both regression models. Regression Model Assumptions 4 (Multicollinearity should not exist) can be safely ignored since the independent variables are manually controlled, for both regression models.

Since all four Assumptions are satisfied for both Regression Models developed, for Drying Shrinkage and Compressive strength, they are valid to be used.

5 Conclusions and Recommendations

Along with the changing environmental factors affecting the entire world—the need to utilize sustainable building construction materials in the construction industry, is dire—this is also the case in Sri Lanka. But when introducing highly technical construction materials, in place of the traditional building materials, as sustainable materials it is a must to check for sustainable features. It is imperative to find out whether those materials will behave as they are meant to behave. Autoclaved Aerated Concrete has been identified as a sustainable building construction material in the

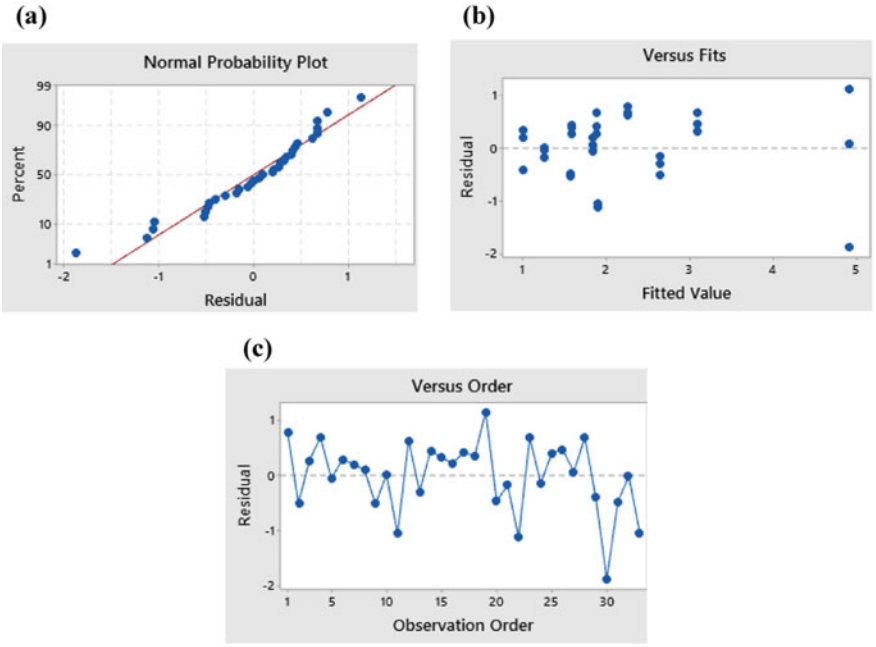

Fig. 6 **a** Normal probability plot. **b** The fitted values versus residual plot. **c** Observation order plot for compressive strength

Sri Lankan context. But there were problems in its High Drying Shrinkage and Low Compressive Strength. This study has been done to optimize the mixture design of the AAC material so as to ensure that AAC obtains adequate Compressive strength and low Drying Shrinkage.

In this study, a broad discussion was done on the literature of how mixture design affects the physical parameters of the final product. In Sri Lankan construction sites, propagation of cracks on constructed walls were found, due to drying shrinkage of the AAC block material. Using Response Surface Methodology, an eleven mixture design experiment was designed in order to obtain a correlation between the mixture design versus drying shrinkage and compressive strength. The samples were then prepared and laboratory tests were carried out. Using the obtained laboratory data, statistical analysis was done, and two equations were derived (Regression models)—derived as the results of the research for drying shrinkage and compressive strength, in terms of the mixture design which can be used to optimize the mixture design.

- Further experiments for more samples should be done in order to optimize the equations proposed in the research.
- The mixture design must be developed, while Keeping the drying shrinkage and compressive strength According to the "BS EN 771-4:2011+A1:2015 Specification masonry units Part 4: Autoclaved Aerated Concrete masonry units"

and obtain its other required physical parameters according to the BS EN 771-4:2011+A1:2015. The same mixture experimental design and response surface methodology can be used.

- Quality of lime in Sri Lanka doesn't satisfy the requirements according to the IS: 712-1973. Further experiments should be done to realize the effect of using lime having high impurity levels, to the properties of the AAC material.
- Using coal bottom ash to reduce the drying shrinkage as a replacement to the mixture design—in order to do this more research should be done.

References

1. Spiegel R, Meadows D (1999) Green building materials: a guide to product selection and specification. Wiley, New York
2. Bakhoum ES, Garas GL, Allam ME (2015) Sustainability analysis of conventional and ecofriendly materials: a step towards green building. ARPN J Eng Appl Sci 10(2):788–796
3. Rathi SO, Khandve PV (2016) Cost effectiveness of using AAC blocks for building construction in residential building and public buildings. Int J Res Eng Technol 5(05):517–520
4. Wittmann FH (ed) (1992) Advances in autoclaved aerated concrete. AA Balkema, pp 11–34
5. Drochytka R, Zach J, Korjenic A, Hroudová J (2013) Improving the energy efficiency in buildings while reducing the waste using autoclaved aerated concrete made from power industry waste. Energy Build 58:319–323
6. Jani SN, Shah DS (2014) Analysis of microstructure and properties of AAC block with its manufacturing process. J Int Acad Res Multidiscip 2:278–285
7. Herath H, Sylva K, Dissanayake P (2018) A case study on selection of green building material related to contextual considerations. In: ICSBE 2018, 96
8. Kathleen MC, Natalia YK, Jeff R (2004) Response surface methodology. Center for computational analysis of social and organizational systems (CASOS), Tech Rep
9. Reliawiki.org (2020) Mixture design—Reliawiki [Online]. Available at: http://reliawiki.org/index.php/Mixture_Design. Accessed 29 Sept 2020

Water Treatment and Pollution Control

A Model for Management of Sivalakulama Tank Cascade System

K. A. C. K. H. Gunasekara, K. D. W. Nandalal, and U. S. Imbulana

Abstract From ancient times Sri Lanka was considered as a water rich country. But recently people, specially living in dry zone, are facing many issues without having adequate amount of water resources for their daily use. Many water management practices consider availability of water resources and demand for water only without taking interactions between them. For management of a tank cascade system it is important to incorporate dynamic interactions among different sectors that comprise a water resource system, such as, physical components (tanks, canals, etc.), economical aspect, agricultural sector, etc. A model was developed for the optimal management of Sivalakulama cascade system, which comprises of 20 tanks and situated in Galenbindunuwewa DS division in Anuradhapura district. The study was limited to a sub-system of the Sivalakulama tank cascade system comprising 10 tanks, which are connected in series and parallel. The model is based on System Dynamics Modeling approach, which enables incorporation of different sectors such as physical aspects, economic sector and agriculture sector. The model was calibrated using observed water levels in three tanks in the sub system. The model showed the reliability of each tank in the system in supplying the Yala and Maha irrigation requirements and the possibility to study the impact of having other field crops requiring less water.

Keywords Tank cascade systems · System dynamics modeling · Vensim PLE

1 Introduction

Sri Lanka was reputed for her hydraulic civilization having more than 10,000 small tanks in the dry zone of Sri Lanka, which are connected in series and parallel forming into tank cascade systems. However, people living in the dry zone are presently facing many issues as an adequate amount of water resources are not available for their day to day works. Besides the rapid increase in population and economic growth, improper

K. A. C. K. H. Gunasekara (✉) · K. D. W. Nandalal
Faculty of Engineering, University of Peradeniya, Peradeniya, Sri Lanka

U. S. Imbulana
CRIWMP, UN Compound 202-204, Baudhaloka Mawatha, Colombo, Sri Lanka

R. Dissanayake et al. (eds.), *ICSBE 2020*, Lecture Notes in Civil Engineering 174,
https://doi.org/10.1007/978-981-16-4412-2_40

water resource management systems may be responsible for these prevailing problems. Thus, it is very important to investigate the possibility to manage these tank cascade systems optimally to satisfy present water demands.

Many studies reviewing ancient practices adopted in the management of tank cascade systems have been carried out. However, studies on modeling of tank cascade systems for their optimal management are scarce or not available at all. This paper presents an attempt made towards filling that gap through the use of a simulation model developed for a tank cascade system for deriving an optimal management strategy for it.

Sivalakulama tank cascade system in Malawathu Oya basin in Sri Lanka is used as the case study system. A simulation model was developed to facilitate management decisions related to irrigation scheduling and water allocation among tanks of a subsystem of the Sivalakulama tank cascade system. The model uses System Dynamics Simulation Modelling approach, which is cost effective, user-friendly and facilitates in taking effective management decisions.

2 Literature Review

A tank cascade system is a series of tanks connected in series and parallel within a catchment. These tanks are meant to store water from seasonal streams and used for multiple uses including irrigation as the major use. Also, tanks in the system convey water to hydraulically connected tanks located downstream. Perera [4] presented evolution of tank cascade studies in Sri Lanka comprehensively including study periods on different perspectives in relation to tank cascades. Tank cascade based studies have become more complex in recent years, with the understanding of tank cascades as "hydro-ecological units" rather than "hydrological units".

System Dynamics was developed as a system level model tool for business managers to analyze complex issues in stocks and flows of goods and services in 1950s [5]. It has been used in various sectors to identify complex interrelationships and feedbacks between components of various systems. The System Dynamics concept has been used as a methodology and tool to address dynamically complex problems in water resources management [7]. Kaushalya and Nandalal [2] developed a System Dynamics based simulation model that helps in making decisions for managing Nachchaduwa Reservoir for fulfilling the water requirements of its irrigation area. System Dynamics modelling has been applied for assessment of water resources at country scale as well as global scale. Nandalal and Semasinghe [3] used a System Dynamics based simulation model to predict water resources in Sri Lanka.

2.1 Study Area

The Sivalakulama tank cascade system, which comprises of 20 tanks, is located in Galenbindunuwewa Divisional Secretariat Division of the Anuradhapura District, which is within the dry zone of the country. It is in the DL1b agroecological zone, where 75% expectancy value of annual rainfall is greater than 900 mm. Soil in the area is mainly Reddish Brown Earth and Low Humic Gley soils and the terrain is undulating terrain. Aquifer in the area is Shallow Regolith aquifer region under-laying deep Factures Zone aquifer region.

Only ten tanks in the Sivalakulama tank cascade system shown in Fig. 1 and given in Table 1 are considered in the study. Salient features of selected tanks are shown in Table 2. Figure 2 shows the locations of Huruluwewa rainfall gauging station and Mahailluppallama agro-meteorological station used in the study.

Rainfall gauging station at Huruluwewa, which is located at about 6 km from the study area, is the closest rainfall gauging station. Daily rainfall data from January

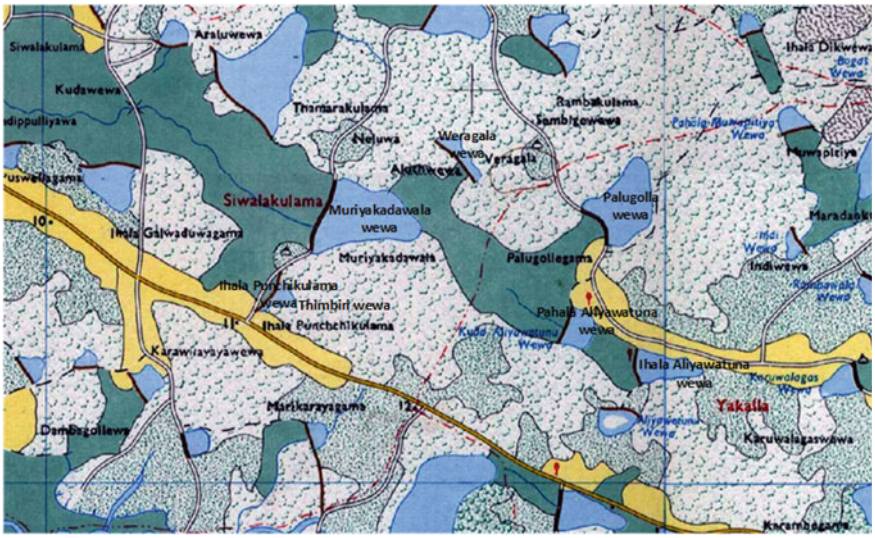

Fig. 1 Study tank cascade system

Table 1 Tanks in the study cascade system

	Tank		Tank
1	Palugolle wewa	6	Veragala wewa
2	Ihala Aliya Watunu wewa	7	Aluth wewa
3	Pahala Aliya Watunu wewa	8	Thimbiri wewa
4	Batala wewa	9	Ihala Punchikulama wewa
5	Moragoda wewa	10	Muriyakadawala wewa

Table 2 Salient features of tanks

	Tank	Sluice sill (MASL)	FSL (MASL)	HFL (MASL)	BTL (MASL)
1	Palugolle wewa	138.12	141.88	142.40	143.38
2	Ihala Aliya Watunu wewa	140.49	142.73	143.10	144.24
3	Pahala Aliya Watunu wewa	136.74	140.00	140.50	141.50
4	Batala wewa	142.25	143.37	143.57	144.28
5	Moragoda wewa	142.00	143.73	143.85	144.68
6	Veragala wewa	138.45	139.73	140.50	141.50
7	Aluth wewa	137.01	139.93	140.50	141.27
8	Thimbiri wewa	137.00	137.93	138.50	139.27
9	Ihala Punchikulama wewa	132.92	135.10	135.70	136.58
10	Muriyakadawala wewa	129.82	133.46	133.96	134.72

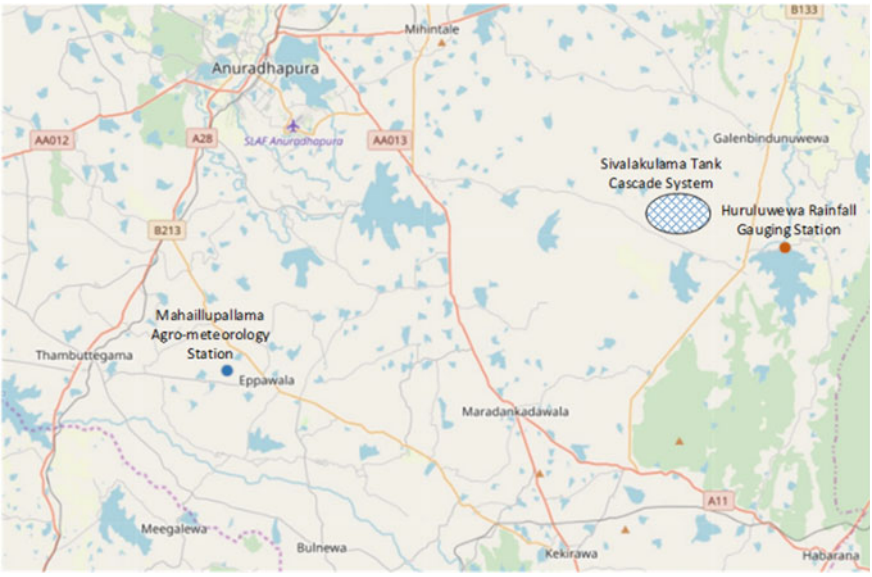

Fig. 2 Sivalakulama tank cascade system and hydrometeorology stations

2018 to Aug 2020 were used for the development of the model. Figure 3 shows daily rainfall distribution from January 2018 to August 2020. Data at Mahailluppallama agro-meteorology station, which is located about 25 km from the Sivalakulama tank cascade system, were used in the study. Daily pan evaporation data from 2013–2017 were used for the development of the model.

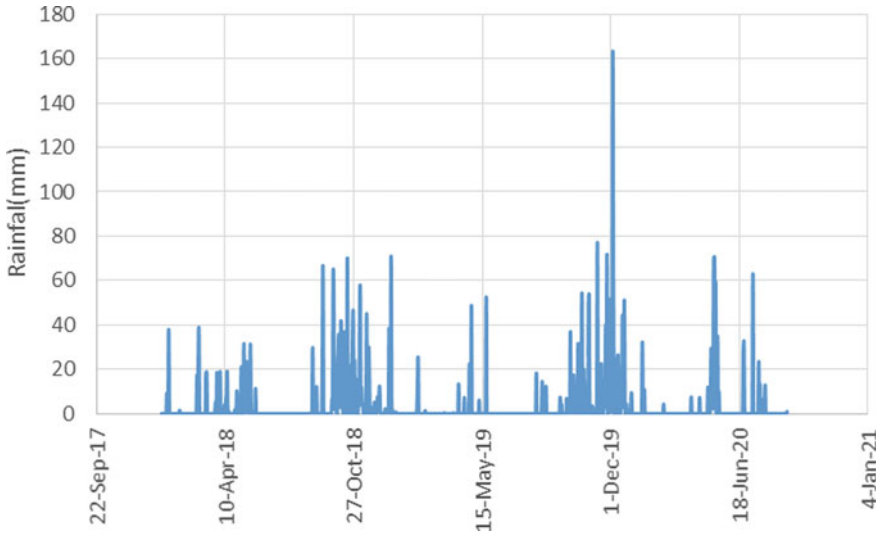

Fig. 3 Daily rainfall at Huruluwewa from 2018 to 2020

3 Methodology

Configuration of the part of Sivalakulama tank cascade system moelled in the study, which comprises of ten tanks linked in series and parallel, is presented in Fig. 4.

As it indicates, Batala wewa, Ihala Aliya Wetuna wewa, Moragoda wewa, Thimbiri wewa, Ihala Punchikulama wewa, Aluth wewa and Veragala wewa are upstream end tanks. They receive water from their catchments only. The other tanks, viz., Palugolle wewa, Pahala Aliya Wetunu wewa and Muriyakadawala wewa receive

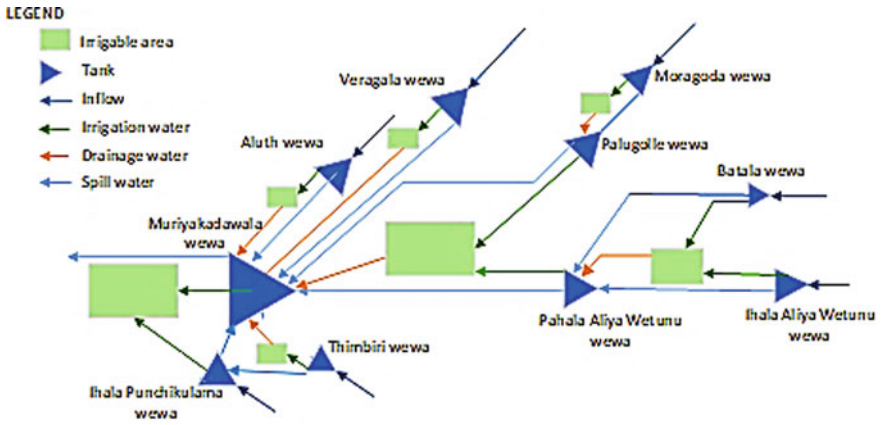

Fig. 4 Configuration and connectivity of study tank cascade system

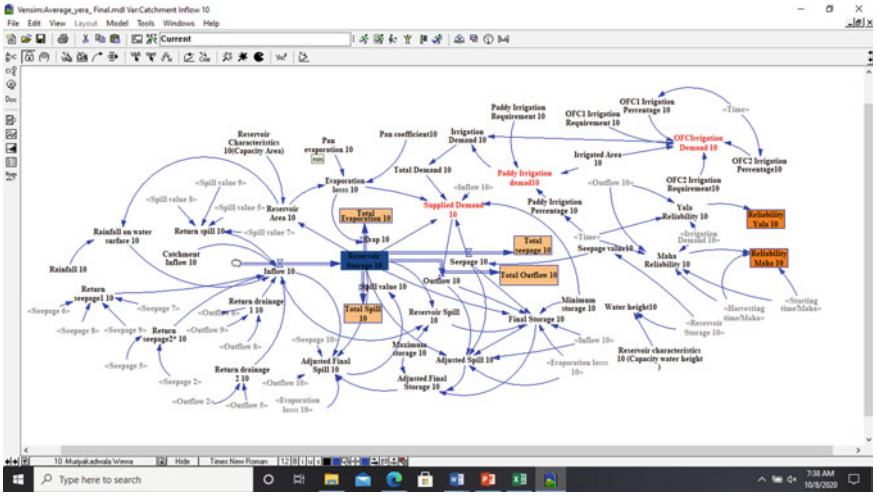

Fig. 5 Model for a tank in Vensim Environment

water from their own incremental catchment and spillage and drainages water from upstream tanks.

The simulation model is developed using the Vensim Simulation Environment (Version 8), which facilitates use of the system dynamics modeling objects such as stocks, flows, feedback mechanisms and delays. Figure 5 shows layout diagram for one tank of the tank cascade system in the Vensim Environment. This view consists of physical component, agricultural component and economic component of one tank. Similarly, all the tanks are configured in different views, one view for each tank, and those were connected based on the hydraulic connections among them. Thus, the model consists of 10 views for the 10 tanks.

Physical component (Water balance component)

In this component, tank inflow, outflow, seepage, spill, evaporation and tank storage were considered. Tanks located at the upstream end of the tank cascade system receive runoff from the catchment and rainfall on the tank water surface as 'inflow' components. The 'outflow' components include, evaporation from tank, seepage through tank bed, water issue for irrigation, and spillway discharge.

All other tanks in the tank cascade system receive a fraction of the outflow from the immediately upstream tank(s) besides the runoff generated in their incremental catchments and the rainfall on tank water surface. This additional inflow comprises of two different components: return flow due to seepage and irrigation water issues and a fraction of spillway discharge.

The outflow components of these tanks are same as those of most upstream tanks. In all these tanks, only a fraction of outflow can reach the immediately downstream tank as return flow.

Observed inflow data are not available for the tanks in the cascade system. Therefore, daily rainfall over catchments was used to generate inflows to the tanks using rainfall-runoff models. Rainfall-runoff models were developed using HEC-HMS software [6] to determine inflows from catchments. Out of the methods available in the software, initial and constant loss rate method was used for estimating loss. Clark Unit Hydrograph method was used for the transformation while Recession method was used as the baseflow method.

Part of irrigation water issued to a command area drains to a downstream tank and it is estimated as a fraction of irrigation water issue. Additionally, the water that is lost due to seepage and percolation at an upstream tank reaches the downstream tank. Determination of the fraction of the water reaching downstream tank due to seepage (tank bed) and percolation (tank bund) from the upstream tank is very difficult and thus, fractions in the range 0.1 to 0.4 were used in the model as suggested by [1].

Return flow due to spillway discharge at upstream tanks is estimated as a fraction of it. Though this fraction could vary from tank to tank, the value of 0.5 was used in the absence of field measurements as suggested by [1].

Irrigation water requirements of the irrigable area below tanks are estimated using the software CROPWAT (Version 8.0). These are determined for paddy and many other field crops for both Yala and Maha seasons.

The water requirements are estimated for different crop stages. Reference evapotranspirations are calculated based on the modified penman method using daily climate data at Mahailluppallama agro-meteorological station. The model calculates crop evapotranspirations at different stages using relevant crop factors and compares with effective rainfall, which is about 80% of the observed rainfall, and computes the irrigation water requirements. A field application efficiency of 70% and conveyance efficiency of 30% are assumed to determine water issues needed from the tank.

During the system simulation water is released to satisfy irrigation water requirement if sufficient volume of water is available in the tank. If the water volume available in the tank is less than the required amount the tank releases the available amount only, thus not satisfying the demand totally.

Agricultural component

Under agricultural component paddy and other field crop types, their irrigation percentages and irrigation schedules were analyzed.

Economic component

Under economic component cost and income for paddy and other field crops were incorporated. As a final parameter, the model computes profits from different crops.

4 Results

Data available for calibration were minimum and variation of water level in three tanks, viz., Pahala Aliya Wetuna Wewa and Ihala Aliya Wetuna Wewa,

Muriyakadawala Wewa, were only available for the period March to May 2020. However, these levels are not referred to mean sea level, too. Therefore, only the variation of water levels were compared at the calibration stage. Figures 6, 7 and 8 show the comparisons of water levels recorded and the resulted from the model.

Model can give results as a graph or a table for all the variables defined in a view. Graphical representations of tank storage, inflow, outflow, evaporation, seepage and

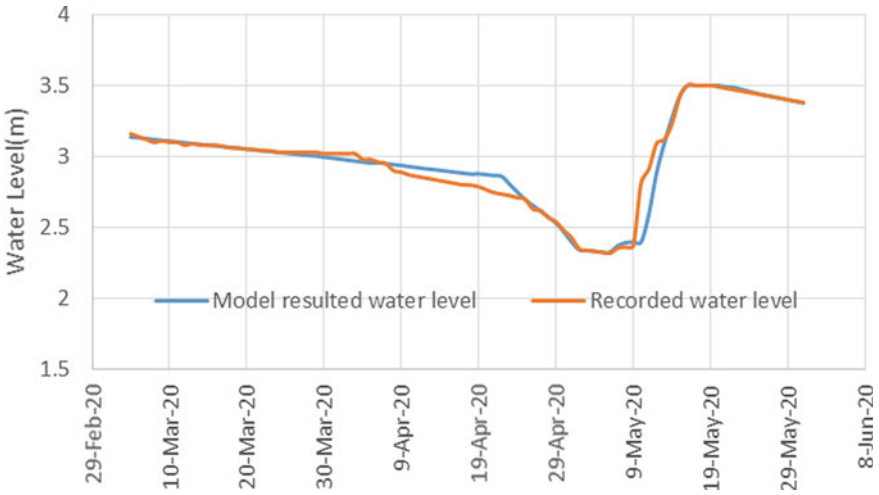

Fig. 6 Comparison of water levels: Pahala Aliya Wetuna Wewa

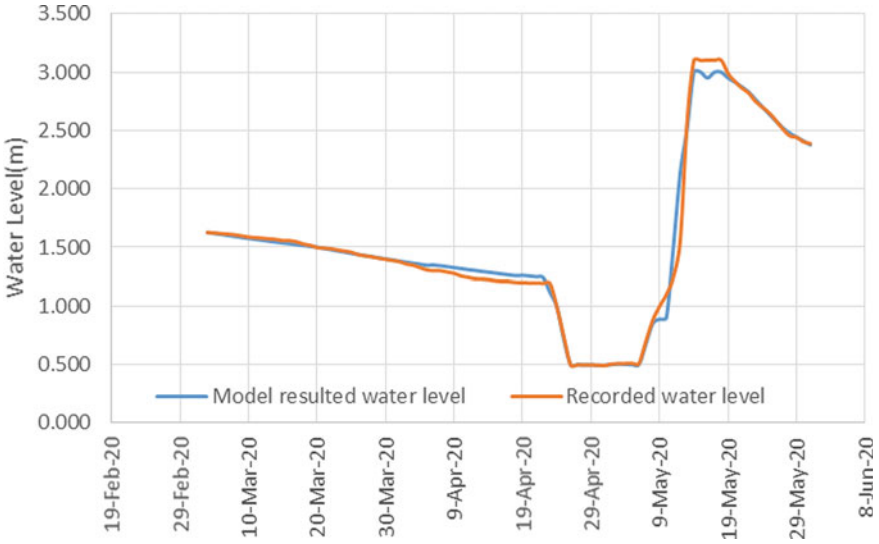

Fig. 7 Comparison of water levels: Ihala Aliya Wetuna Wewa

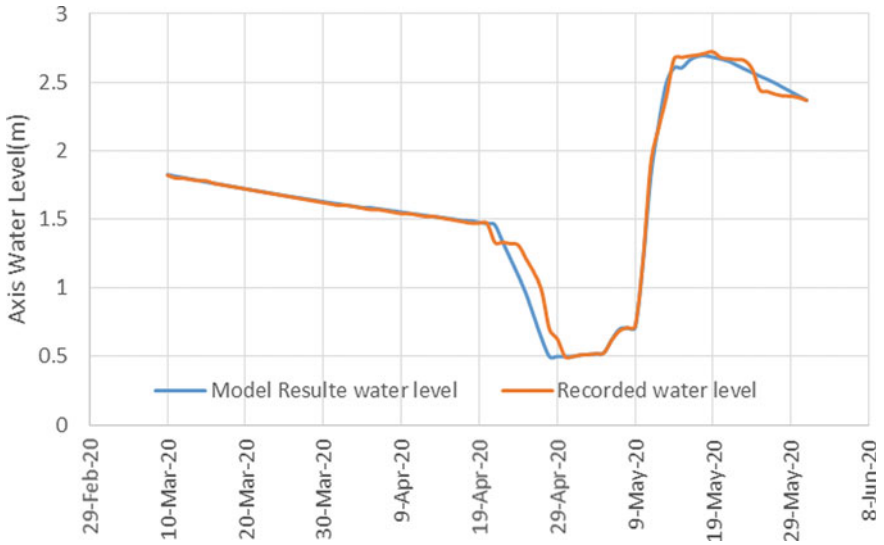

Fig. 8 Comparison of water levels: Muriyakadawala tank

spills of Ihala Aliya Wetuna Wewa, Pahala Aliya Wetuna Wewa and Muriyakadwala Wewa are shown in Fig. 9.

In agricultural component, the important variables are Yala water reliability and Maha water reliability. Those variables represent the percentage by which a tank is capable of supplying daily irrigation water requirement for paddy in the Yala and Maha seasons. For this analysis, paddy variety which is harvested in 3½ months was used for both Yala and Maha season. Tables 3 and 4 represent paddy irrigation water demand, tank water release and water reliability of the 10 tanks for both the Yala and Maha seasons.

5 Conclusions

The model carries out a water balance for the tank cascade system at a daily time step. The irrigation water requirements are totally satisfied when sufficient water is available in the supply tank. In the case where water available in the tank is less than the irrigation water requirement, only the available water is issued satisfying the irrigation requirement partially. This affects the reliability of the system. The results indicate that seven tanks out of the 10 tanks in the Sivalakulama Tank Cascade sub-system studied are capable of supplying the Maha season irrigation water requirement totally. Three small tanks are not having sufficient water in the Maha season. For the Yala season all the tanks do not have sufficient water for irrigation. For the Yala season, it is important to give attention for other field crops which consume less

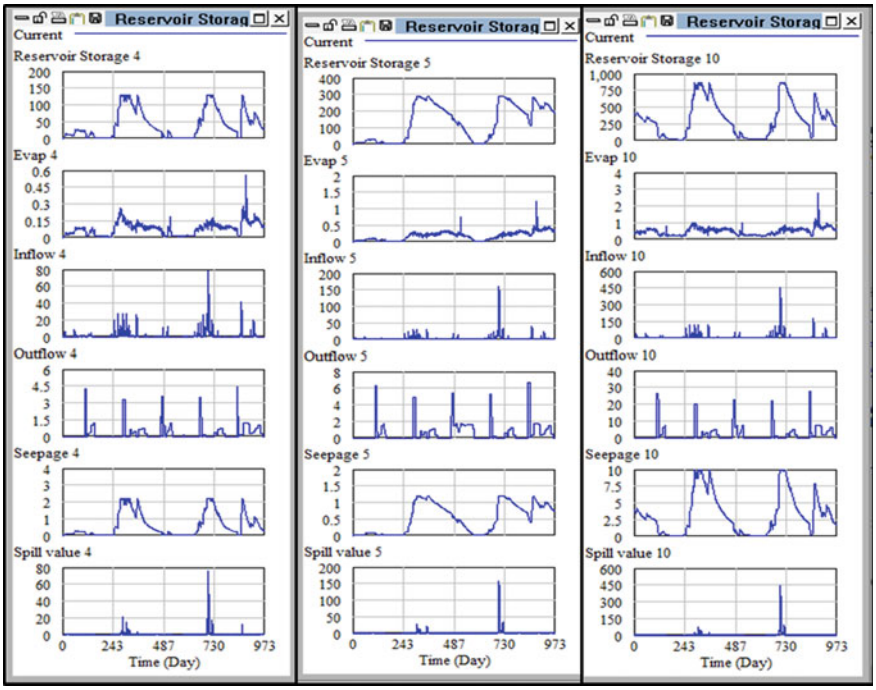

Fig. 9 Tank water balance components of Ihala Aliya Wetuan Wewa, Pahala Aliya Wetuna Wewa and Muriyakadawala Wewa

Table 3 Irrigation water demand, tank water release and water reliability for Maha season

Tank name	Irrigation water demand (1000 m^3)	Water release (1000 m^3)	Water reliability (%)
Moragoda wewa	47.2	47.2	100
Palugolle wewa	306.6	306.6	100
Batala wewa	35.6	31.6	87
Ihala Aliya Watunu wewa	70.5	70.5	100
Pahala Aliya Watunu wewa	106.1	106.1	100
Thimbiri wewa	23.3	11.9	56
Ihala Punchikulama wewa	94.4	94.4	100
Veragala wewa	58.9	48.2	86
Aluth wewa	58.9	58.9	100
Muriyakadawala wewa	441.2	441.2	100

Table 4 Irrigation water demand, tank water release and water reliability for Yala season

Tank name	Irrigation water demand (1000 m^3)	Water release (1000 m^3)	Water reliability (%)
Moragoda wewa	90.0	52.0	56
Palugolle wewa	584.6	147.7	30
Batala wewa	67.8	7.8	26
Ihala Aliya Watunu wewa	134.5	59.1	90
Pahala Aliya Watunu wewa	202.3	198.7	95
Thimbiri wewa	44.5	6.0	1
Ihala Punchikulama wewa	180.1	49.1	30
Veragala wewa	112.2	11.0	24
Aluth wewa	112.2	45.4	39
Muriyakadawala wewa	841.3	405.1	46

water during cultivation period. The model can be used to study the most suitable crop types for the Yala season and also their cropping calendars. An important feature of the model is that it provides output at the end of each day including the tank water height, tank storage, and other required information, for decision making regarding tank management.

Further the developed model could be used by tank cascade system managers in making diverse decisions including the following.

1. Decide areas that could be supplied with irrigation water under each tank in a cascade system along with the type of crop that could to be used.
2. Investigate the type of crop that may be cultivated under each tank in a cascade system.
3. Decide best cropping calendars for different types of paddy varieties and other field crops.
4. Investigate the impact of changes done to system components such as tank capacity, sluice capacity, etc., which may be useful during system rehabilitation work.
5. Investigate the possibility to add new structures such as diversion weirs, canals, etc., into the cascade system and study their impacts.

Acknowledgements The study was supported by Climate Resilient Integrated Water Management Project funded by the Green Climate Fund and implemented by the Ministry of Irrigation (formerly the Ministry of Mahaweli Development and Environment) with the technical support of the UNDP.

References

1. Jayathilaka C, Sakthivadivel R, Shinogi YMI, Witharana P (2001) Predicting water availability in irrigation cascade systems: the cascade water balance model. Research Report 48, International Water Management Institute, Colombo, Sri Lanka
2. Kaushalya RDT, Nandalal KDW (2017) System dynamics based model for the Nachchaduwa Reservoir in the Malwathu Oya Basin, Sri Lanka. J Inst Eng Sri Lanka L(4):31–40
3. Nandalal KDW, Semasinghe BAD (2006) System dynamics simulation model for the assessment of water resources in Sri Lanka. In: Proceedings of 32nd WEDC international conference, Colombo
4. Perera MP (2017) Evolution of tank cascade studies of Sri Lanka. Saudi J Hum Soc Sci 2(7):597–610
5. Tidwell VC, Passell HD, Conrad SH (2004) System dynamics modeling for community-based water planning: application to the Middle Rio Grande. Aquat Sci 66:357–372
6. US Army Corps of Engineers (2013) Hydrologic modeling system HEC-HMS. Hydrologic Engineering Centre, USA
7. Winz I, Brierley G (2007) The use of system dynamics simulation in integrated water resources management. School of Geography, Geology and Environmental Science, University of Auckland, New Zealand

Study of Coagulant Dosage Variation According to the Design G Value of Coagulation and Flocculation Processes in a Water Treatment Plant

R. M. M. C. Dassanayake, N. S. Jayasinghe, A. P. K. Wickramage, K. B. K. D. K. Kandeyaya, W. B. M. L. I. Weerasekara, and S. K. Weragoda

Abstract There are several treatment processes in conventional water treatment plants (WTP). The coagulation and flocculation processes (CFP) are conducted to remove the turbidity of raw water (RW). CFP has become critical in the water treatment process due to impacts from overdosing and underdosing of coagulant on the public health and treatment efficiency. Most of the WTPs in Sri Lanka perform the jar test considering only the RW pH and turbidity in order to determine the optimum coagulant dose. However, there is no concern over the velocity gradient (G) value in WTP design when conducting the jar test. Therefore, this study was conducted to compare the optimum coagulant doses obtained from a general jar test method (M1) and a WTP design G value considered method (M2) for the same RW sample. The rapid mixing, slow mixing speeds, and settling times for M1; 2 min in 150 rpm, 20 min in 30 rpm, and 30 min respectively. The rapid mixing, slow mixing speeds, and settling times for M2; 3 min in 71 rpm, 30 min in 40 rpm, and 30 min respectively. Two trials were carried out for each method using Poly aluminium chloride as the coagulant (PAC). The optimum coagulant dose of M1 is 0.62 mg/L in trial one and 3.95 mg/L in trial two. The optimum coagulant dose of M2 is 0.70 mg/L in trial one and 4.05 mg/L in trial two. Hence the optimum coagulant dose of M1 is greater than that of M2. Therefore, it is recommended to consider the design G value of the WTP to obtain a more accurate optimum coagulant dose.

Keywords Coagulation · Flocculation · Velocity gradient · Rapid mixing · Slow mixing · Optimum coagulant dose

R. M. M. C. Dassanayake
Faculty of Engineering, University of Peradeniya, Peradeniya, Sri Lanka

N. S. Jayasinghe · A. P. K. Wickramage · K. B. K. D. K. Kandeyaya · W. B. M. L. I. Weerasekara · S. K. Weragoda (✉)
China Sri Lanka Research Grant Project, 90/3, Pahala Kondadeniya, Katugasthota, Sri Lanka

R. Dissanayake et al. (eds.), *ICSBE 2020*, Lecture Notes in Civil Engineering 174,
https://doi.org/10.1007/978-981-16-4412-2_41

1 Introduction

Advancements of water purification processes are attracting more attention in recent years, with the aspects of the lack of safe and readily available drinking water, and adverse health and environmental effects. Therefore, any water treatment plant (WTP) functionally plays a fundamental role in enhancing the quality of water to standard levels, by reducing the hazardousness due to the facts of microbial contamination and the presence of unnecessary chemical constituents. However, in the interest of optimizing water treatment processes in WTPs, it is mandatory to incorporate an adaptive approach in technical and operational aspects through regular performance assessments of each unit process.

In Sri Lanka, WTP designs are based on a conventional approach that applies the combination of coagulation, sedimentation, filtration, and disinfection processes [1]. Amongst coagulation and flocculation processes are crucial steps which usually done to remove the turbidity of raw water. Coagulation is the destabilization of colloidal particles present in raw water by the application of particular coagulants like Alum and Poly Aluminium chloride [2]. Flocculation promotes the growth of the floc formation by aggregation of destabilized particles. The optimization of the coagulant dosage is crucial since it impacts on public health and the environment, and the low treatment efficiencies [3, 4].

However, the success of the coagulation process depends on the rapid and thorough dispersion of chemicals by rapid mix and it has become critical due to the availability of several types of coagulants [4]. Whereas the chemical demand is directly affected by the settling velocities of water in Coagulation and Flocculation Process (CFP). Apart from that, the dosage of coagulant is determined based on pH; but the chemicals are still not properly dosed as there is no concern over alkalinity, time of mixing (t), and velocity gradient (G). Furthermore, the flocculation process is important in precipitation where the mixture is gently stirred to promote the growth of the floc.

These facts reflect the chemical, physical and mechanical parameters associated with rapid mixing and flocculation are extremely important in the optimization of CFP in the water treatment process [5]. Reactions of coagulation chemicals are rapid; softening reactions occur more slowly. In either case, it is desirable to disperse the chemicals quickly, before reactions are complete. To homogenize the coagulant, the rapid mixture is designed to provide a short period of violent agitation. Traditionally, in water treatment, the degree of agitation in the mixing unit is measured by G value and t.

Considering all these consequences, the performance assessment of these steps, based on monitoring, process parameter control, and experimental tests, is a viable tool for process optimization. In this case, the jar test is the laboratory scale experiment of ruling out and quantifying the optimum treatment program for the removal of suspended substances in raw water in a particular WTP. In Sri Lanka, the chemical dosage controlling and CFP optimization by conducting jar tests is not properly practicing even in large scale water treatment plants. Since the raw water qualities of the water sources in WTPs can be varied unpredictably with high peaks of turbidity,

the sudden peaks of high turbidity made difficulties in the water treatment process, especially in coagulation and flocculation. Therefore, it is a necessity to address this problem to optimize the water treatment process to meet the SLS 614:2013 drinking water standards. Thus, the need has always been existed to optimize G and t parameters for the purpose of plant design, upgrading, and in-plant performance evaluations [6].

In this context, the objective of this study was to optimize the coagulation and flocculation process by taking the G value into consideration while developing a method to find the G value of the jar test apparatus and to archive the plant G value to the jar test in order to find if there is a difference between the chemical dosages by conducting the jar test according to the G values thus get the most economical way of chemical dosing in the water purification process.

2 Methodology

2.1 Mathematical Model Development

In the water treatment process, the degree of agitation in the mixing unit is measured by velocity gradient (G) and time of mixing (t). For mixing equipment, the G is given by Eq. (1), [7].

$$G = \sqrt{(P/V\mu)} \tag{1}$$

where

G = velocity gradient, l/s
P = power imparted to the water in the mixing chamber, N m/s
V = volume of the basin, m^3
μ = absolute viscosity of the water, N s/m^2

The G value for static mixers can be calculated by using the following Eq. (2).

$$G = \sqrt{\frac{\rho.g.\Delta H}{\mu.\tau_c}} \tag{2}$$

where

G = velocity gradient, l/s
ρ = density of water, kg/m^3
ΔH = Head loss over mixing tank (m)
μ = Absolute viscosity of the water, N s/m^2
τ_c = Residence time in the mixing zone (s).

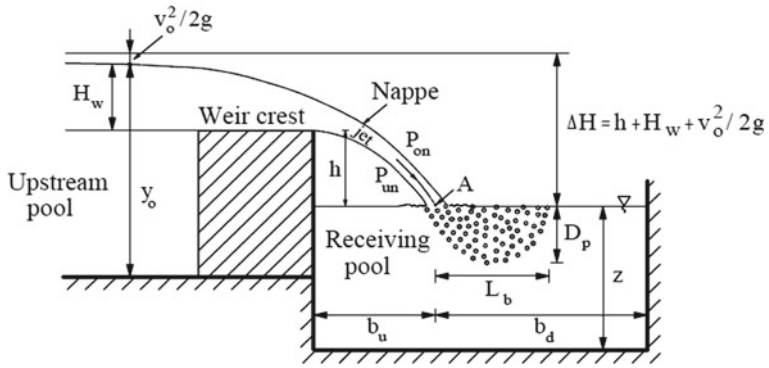

Fig. 1 Cross section of free over fall from a weir [8]

***Note** The $\Delta H = h + H_w + v_o^2/2g$ (Fig. 1) [8].
Where

h = Vertical height of the weir crest with respect to the water surface level in the receiving pool (i.e., drop height)
H_w = Vertical difference between the water surface in the upstream pool and the weir crest
v_o = average flow velocity in the upstream pool.

It is well known that if H_w is measured at a distance sufficiently for upstream of the weir (i.e., more than 4 H_w), $v_o^2/2g$ is generally negligible.
Therefore, ΔH can be taken as follows;

$$\Delta H = h + H_w$$

The flocculation process always deals with two parameters: Speed of stirring (n) and time of mixing. As Eq. (3), the time of mixing is multiplied by the velocity gradient to obtain Camp number (Gt).

$$Gt = V/Q\sqrt{(P/(V\mu))} = 1/Q\sqrt{(P/(V\mu))} \quad (3)$$

where

t = time of mixing, s
Q = flowrate, m^3/s
P = power requirement, W
l = dynamic viscosity, $N\,S/m^2$
V = flocculator volume, m^3.

Table 1 Calculated rpm and t parameters for GKWTP design G value

Parameter	Rapid mix	Slow mix
Average G value of the plant /(s^{-1})	330	40
Rpm	1.4823 * G2/3 = 71	1.4823 * G2/3 = 17
t/(min)	2.5	30

The residual turbidity initially decreases with increasing Camp number; it reaches a minimum value and then starts increasing again with further increases in Camp number [9].

2.2 Laboratory Analysis

Past jar test results of the Greater Kandy (GKWTP) were studied. 10L Raw water samples were collected from GKWTP for jar test. The initial turbidity and pH of the samples were measured with the aid of a Turbidity meter (ThermoScientific, ECTN 100IR) and Multiparameter (WTW Multi 3630 IDS) respectively at the laboratory. Then the jar test was conducted for the raw water samples by using PAC as the coagulant.

Initial tests were conducted by varying the pH of the samples (5–8) using H_2SO_4 or NaOH while keeping the dosage of PAC constant (usually between 1.1 and 1.5 mg/L). Initial mixing was conducted for a standard jar test prodcedure (M1) at a speed of 150 rpm for 2 min and after 2 min the speed was reduced to 30 rpm and further mixing was done for further 20 min. After 30 min settling turbidity and pH was measured using the turbidity meter and the Multiparameter respectively and a graph was plotted showing the relationship between turbidity to obtain the optimum pH. The same procedure was carried out by keeping the pH constant at the optimum value and altering the dosage of PAC and the correlation between PAC dosage and the turbidity was formulated.

Then the jar test was conducted again considering the plant design G values (M2) (Table 1), rapid mixing was done at a speed of 71 rpm for 3 min and after 3 min the speed was reduced to 40 rpm and further mixing was done for further 30 min. A graph was plotted for the relationship between the pH and turbidity and a correlation was developed between pH and turbidity with considering plant G value and without considering the plant G value.

2.3 Statistical Analysis

G value of the jar test apparatus is calculated by (Fig. 2) Eq. (4) [10].

Fig. 2 The jar test apparatus

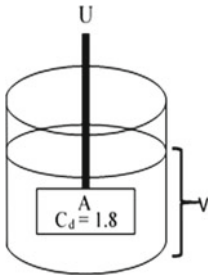

$$G = \left(C_d A U^3 / 2vV\right)^{1/2} \tag{4}$$

where

$C_d = 1.8$, Drag coefficient of the paddle; jar-test apparatus (Model #3461 made by Phipps and Bird, Inc., Richmond, VA).
$A = 0.001875\ m^2$ (=0.025 × 0.075 m), Area of the paddle;
U = rpm * 0.34 m/60 s, Velocity of the paddles relative to that of the water, the circumference of the jar test container was 0.34 m,
rpm = Rotational speed of the paddle
$v = 10^{-6}\ m^2/s$, Kinematic viscosity of water;
V = 1000 mL, Water volume in the beaker
$G = (V C_d A U^3/2vV)^{1/2}$
$U = G^{2/3} (2vV/C_d A)^{1/3}$
By substitute values, $U = G^{2/3} (8.3998 \times 10^{-3})$
But; U = rpm * 0.34 m/60 s
Therefore; rpm * 0.34 m/60 s $= G^{2/3} (8.3998 \times 10^{-3})$
rpm $= 1.4823 * G^{2/3}$.

Table 1 shows the calculated rpm and mixing time (t) for jar test apparatus according to the design G values of the GKWTP.

3 Results and Discussion

Figure 3 shows the graph of pH versus turbidity for two trials.

Initial pH of water

First trial = 7.01 second trial = 7.24.

Initial Turbidity of water

First trial = 7.15 NTU Second trial = 6.32 NTU
Temperature = 27 °C.
PACL concentration = 1%

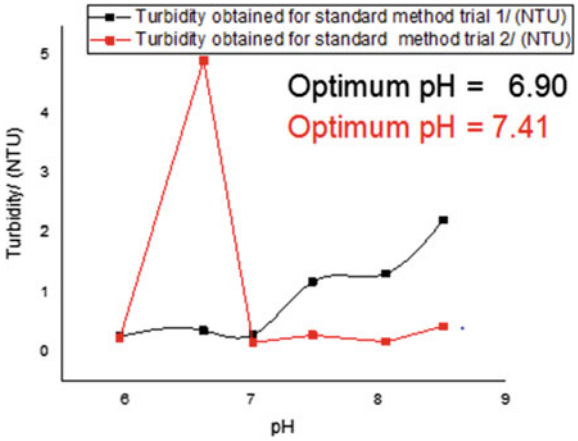

Fig. 3 pH versus turbidity of two trial

According Fig. 3, optimum pH was recorded as 6.90 and 7.41 for the first trial and second trial respectively. It is almost the raw water pH. PAC generally consumes less alkalinity than alum. PAC is effective over pH range 5.0– to 8.0 [11]. Therefore, pH correction was not needed.

Figure 4 shows the PAC dose vs turbidity for jar test conducted according to M1 and M2 (Trial 1).

According to Fig. 4 optimum PAC doses were recorded as 0.62 and 0.70 ppm in for method M1 and M2 respectively.

Figure 5 shows the PACL dose vs turbidity for jar test conducted according to M1 and M2 (Trial 2).

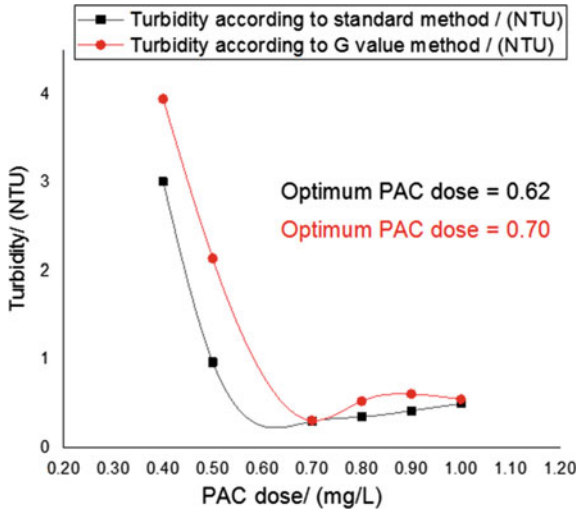

Fig. 4 PACL dose vs turbidity for jar test conducted according to M1 and M2 M1 and M2 (Trial 1)

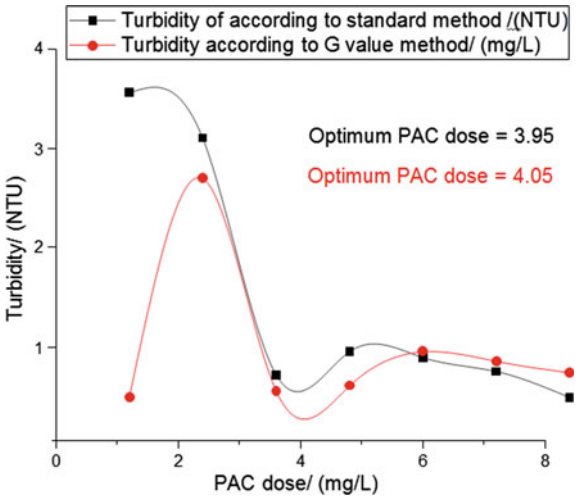

Fig. 5 PAC dose vs turbidity for standard jar test method and G value considered method (Trial 2)

Table 2 The summary of PAC doses of two trials

Trial	Method	pH	Turbidity/(NTU)	PAC dose/(mg/L)
1	M1	7.01	7.15	0.62
	M2			0.70
2	M1	7.24	6.32	3.95
	M2			4.05

According to Fig. 5 optimum PAC doses were recorded as 3.95 and 4.05 ppm in for method M1 and M2 respectively. The destabilization of the particulate matter in water resulted by adding PAC. Subsequently, a microfloc is formed which cause to reduce the turbidity of water [12].

Table 2 shows the summary of PAC doses of two trials conducted for M1 and M2 methods.

According to Table 2, the PAC differs slightly in M1 and M2. The difference of the rpm and the G values of the M1 and M2 could be the reason for the difference of the PAC dose [6].

4 Conclusion

Optimum PAC dose is slightly high when considered the G value of the plant design. The PAC dose required to the plant CFP also increased accordingly. Therefore, it is recommended to consider the design G values of the treatment plants to obtain an optimum coagulant dose. However, Coagulation and flocculation depends on many factors, as characteristics of the water source, flocculation time, added chemicals etc.

Therefore, further studies will be conducted, considering all the effecting factors to optimize the coagulation and flocculation process of WTPs.

References

1. Amarasooriya AAGD, Weragoda SK (2015) New tap project. Japan Water Research Center. Available at: http://www.jwrc-net.or.jp/aswin/en/newtap
2. Koohestanian A, Hosseini M, Abbasian Z (2008) The separation method for removing of colloidal particles from raw water. Eur J Agric Environ Sci 4(2):266–273. Available at: http://idosi.org/aejaes/jaes4(2)/20.pdf
3. Bouyer D, Line A, Cockxi A, Do-Quang Z (2001) Experimental analysis of floc size distribution and hydrodynamics in a jar-test. Chem Eng Res Des 79(8):1017–1024. https://doi.org/10.1205/02638760152721587
4. Dentel SK (1991) Coagulant control in water treatment. Crit Rev Environ Control 21(Feb 2015):41–135. https://doi.org/10.1080/10643389109388409
5. Rossini M, Garrido JG, Galluzzo M (1999) Optimization of the coagulation ± flocculation treatment: influence of rapid mix parameters. Water Res 33(8):1817–1826
6. Cornwell DA, Bishop MM (1983) Determining velocity gradients in laboratory and full-scale systems. J Am Water Works Assoc 75(9):470–475. https://doi.org/10.1002/j.1551-8833.1983.tb05197.x
7. Quasim SR, Motley EM, Zhu G (2011) Water works engineering- planning, design and operation, pp 246–257
8. Emiroglu ME (2010) Estimating flow characteristics of different weir types and optimum dimensions of downstream receiving pool. J Hydrol Hydromech 245–260
9. Mohammed TJ, Shakir E (2017) Effect of settling time, velocity gradient, and camp number on turbidity removal for oilfield produced water. Egypt J Pet. https://doi.org/10.1016/j.ejpe.2016.12.006
10. Zhang TC, Emary SC (1999) Jar tests for evaluation of atrazine removal at drinking water treatment plants. Environ Eng Sci. https://doi.org/10.1089/ees.1999.16.417
11. Gebbie P (2001) Using polyaluminum coagulants in water treatment. In: 64th annual water industry engineers and operators' conference, Bendigo, 5–6 September 2001, 39–47. Available at: http://wioa.org.au/conference_papers/2001/pdf/paper6.pdf
12. Febrina W, Mesra T, Hendra (2020) Optimum dosage of coagulant and flocculant on sea water purification process. In: International conference on environment and technology. IOP conference series: earth and environmental science, vol 469. https://doi.org/10.1088/1755-1315/469/1/012023

Clarification Efficiency of Plate Settlers Analyzed by CFD Modelling

W. M. L. K. Abeyratne, S. B. Weerakoon, and N. G. P. B. Neluwala

Abstract Sedimentation is a crucial process of water treatment facilities, where the gravity settling of suspended solids occur. The sedimentation tanks in conventional water treatment plants occupy a large area and consume up to 30% of the total construction cost. The use of plate settlers is an economical technology which increase the efficiency and capacity of sedimentation tanks. This study investigated the effectiveness of plate settlers compared to the plain settlers using the rectangular tanks in a water treatment plant. The ANSYS CRX 17.2 software was used as the CFD tool for meshing and calculating the results. Four cases including a plain settler and three plate settlers with plates installed at 3, 1 and 0.5 m spacing were analyzed in this study for the comparison of performances. The length, thickness and inclination angle of plates were kept constant. Installing plates reduced the large vortex zones and created a more up-flow distribution of streamlines allowing particles to settle easily compared to the plain settling tank. The efficiency of sedimentation was improved by increasing the number of plates in plate settlers. This is due to the increasing effective settling area of tanks. The inclined plates had different effects on the suspended solid removal efficiency in solids with different diameters, which might be difficult to characterize by experimental studies. The sedimentation efficiency of the particles with larger diameters have higher efficiency than the small diameter particles. The Computational Fluid Dynamics modelling can be used to accurately predict the suspended particle removal efficiency in plain settling and plate settling tanks, and therefore can be used to optimize their design.

Keywords Sedimentation · Plate settlers · Clarification efficiency · Computational fluid dynamics

W. M. L. K. Abeyratne (✉) · S. B. Weerakoon · N. G. P. B. Neluwala
Faculty of Engineering, University of Peradeniya, Peradeniya, Sri Lanka
e-mail: abeyratnelka@eng.pdn.ac.lk

R. Dissanayake et al. (eds.), *ICSBE 2020*, Lecture Notes in Civil Engineering 174,
https://doi.org/10.1007/978-981-16-4412-2_42

1 Introduction

Sedimentation or clarification is based on the gravitational force due to the difference in density between particles and fluid [2]. This is one of the most essential components in water and wastewater treatment plants. In this process, a considerable percentage of suspended solids like clay and silt which are present in the source or coagulation units are settled by gravity and thereby affects the treatment efficiency of the secondary and/or tertiary treatment processes and subsequently the efficiency of the overall treatment plant.

The sedimentation tanks in conventional water treatment plants occupy a large area and consume up to 30% of the total construction cost. The use of plate settlers is an economical technology which can increase the efficiency and capacity of sedimentation tanks by greatly reducing the retention time and total operation cost. The plate settlers are settlers with inclined parallel plates sloped at an angle which increase the effective settling area and decrease the particle settling depth. It also reduces the eddy effect at tank inlet and prevent dead spaces by producing more uniform flow. It prevents unsettled influent mixing with partially settled liquid [4].

Inclined plate settlers are used in treating wastewater due to their low space requirement and high removal rates. The prediction of sedimentation efficiency of these settlers is essential for their performance evaluation. The main objective of this study is to investigate the effectiveness of plate settlers compared to the plain settlers using the rectangular tanks in a water treatment plant. The ANSYS CFX 17.2 software was used as the Computational Fluid Dynamics tool for meshing and calculating the results. Four cases including a plain settler and three plate settlers with plates installed at 3, 1 and 0.5 m spacing were analyzed in this study for the comparison of performances. The length, thickness and inclination angle of plates were kept constant.

2 Computational Modelling

2.1 Governing Equations of the Model

The commercial software ANSYS CFX 17.2 was used for the numerical simulations of this multiphase flow phenomena. Multiphase flow is a flow with presence of different phases (solids, liquid, and gases). Flow in a sedimentation tank is defined as a liquid–solid multiphase dispersed flow where sediment particles (Dispersed phase) is mixed with water (Continuous phase) forming a continuous medium mixture with a varying composition and density.

This mixture density is affected by presence of solids in different locations. ‘Mixture model’, which is a simplified version of Euler-Euler approach and in which all the phases are considered as continuous is used for the simulations because the overall motion of particle is of interest rather than tracking individual particles.

The 'Mixture model' which is used in ANSYS CFX is the 'Algebraic slip model (ASM)'. This model is appropriate to calculate velocity of dispersed phase if the time scale to reach the equilibrium slip velocity is very small [1]. In ASM one fluid with a variable composition is used (Water with suspended solids of different diameters and densities). The governing equations of the model are,

$$\frac{\partial \rho_m}{\partial t} + \frac{\partial \left(\rho_m U_m^i\right)}{\partial x_i} = 0 \tag{1}$$

$$\frac{\partial \rho_m U_m^i}{\partial t} + \frac{\partial \rho_m U_m^j U_m^i}{\partial x^j} = -\frac{\partial P}{\partial x^i} + \frac{\partial \left(\tau_m^{ij} + \tau_{Tm}^{ij} + \tau_{Dm}^{ij}\right)}{\partial x^j} + g^i \rho_m \tag{2}$$

where, x^i is Cartesian coordinate in i-direction, U_m^i is mixture flow velocity in i-direction, P is the pressure, t is time, g^i is acceleration of gravity, τ_m^{ij} is the mixture viscous diffusion stress, τ_{Tm}^{ij} is the mixture turbulent diffusion stress and τ_{Dm}^{ij} is the mixture apparent diffusion stress.

Concentration field for each class of solids in the tank is determined by the mass balance equation. For each class of mass fractions ($Y_{n,s}$) after using Bussinesq approximation,

$$\frac{\partial \left(\rho_m Y_{s,n}\right)}{\partial t} + \frac{\partial \left(\rho_m Y_{s,n}\left(U_m^j + U_{Ss,n}^j\right)\right)}{\partial x^j} = \frac{\partial}{\partial x^j}\left(\mu_m \frac{\partial Y_{s,n}}{\partial x^j} + \frac{\mu_{tm}}{0.09}\frac{\partial Y_{s,n}}{\partial x^j}\right) \tag{3}$$

The subscript "s, n" for class of solids, μt_m is eddy viscosity of mixture, Y is mass fraction and $U_{S\,s,n}$ is the slip velocity of particles.

2.2 Calibration of the Model

The model was calibrated by using the study Stamou and Gkesouli [5] on the settling tanks of the water treatment plant of Aharnes, Athens, Greece. The plan view of the tank (Fig. 1) is approximately symmetrical and therefore only one half was modeled. Tanks has four inlet openings near the bottom of the tank (Fig. 2). The effluent exits through a series of V notch weirs installed at outlet channels.

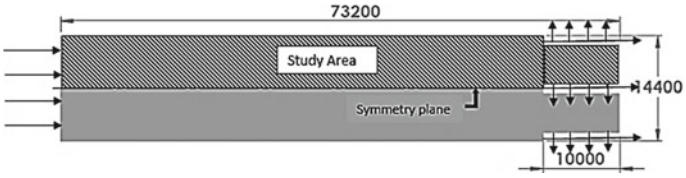

Fig. 1 Plan view of the tank (all dimensions are in millimeters) [3]

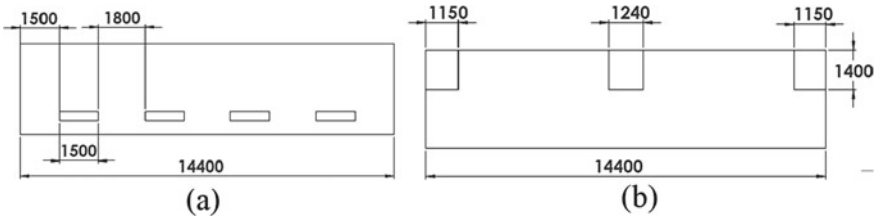

Fig. 2 Dimensions of the **a** Inlet **b** Outlet (all dimensions are in millimeters) [3]

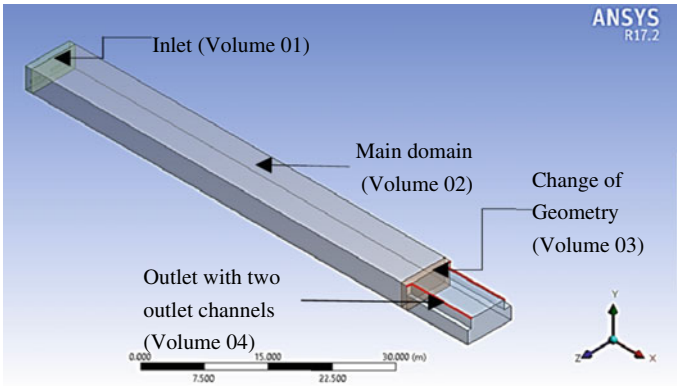

Fig. 3 Tank geometry developed in the ANSYS CFX 17.2 Design Modeler

The model calibration was done for two scenarios S-1 and S-2 with inlet mass flow rates 0.25 m^3/s and 0.31 m^3/s respectively. The geometry was created as realistically as possible to match the dimensions of the sedimentation tanks using Design Modeler in ANSYS-CFX 17.2 (Fig. 3).

The geometry was developed in four volumes (Fig. 3): The main domain and the outlet volume where the geometry is simple were meshed using structures grids with hexahedral elements. The regions of complex geometries like, inlet, change of geometry were meshed using unstructured grids. The mesh at the inlet openings and outlet channels were refined.

Boundary conditions were applied to all faces of the fluid domain. At the two inlet openings, parallel flow was imposed with a uniform horizontal velocity and turbulence intensity was set at 5%. Inlet solid concentration was assumed to be uniformly distributed as in Table 1. Sum of the inlet mass flow rates was set as the outlet boundary condition. The bottom of the tank was set as a no-slip smooth wall, solids were assumed to be deposited and removed from the domain. The top surface (free surface) of the domain was treated as a free-slip wall, thereby the normal velocity component and normal gradients of other variables were set to zero. All the vertical walls except the right side of domain, at which symmetry condition was used

Table 1 Details of inlet solid classes

Solid class	Solid diameter (μm)	Inlet mass fraction for S-1	Inlet solid concentration for S-1 S_{in} (mg/l)	Inlet mass fraction for S-2	Inlet solid concentration for S-2 (S_{in}) (mg/l)
S1	41	0.45	3.15	0.45	3.15
S2	17	0.17	1.19	0.36	2.52
S3	9.5	0.23	1.61	0.04	0.28
S4	5	0.15	1.05	0.15	1.05
Total		1.00	7.00	1.00	7.00

were treated as smooth walls and no-slip conditions were applied. For the numerical method, the advection scheme was upwind.

In model calibration, streamline pattern on a xy plane at z = − 1.9 m and on an xz plane at y = 0.7 m was compared for the scenario S-1. The eddy V1 which is approximately 20 m long (Fig. 4) was observed in the calculated streamline pattern on the plane z = − 1.9 m similar to the Stamou and Gkesouli [5]. A very large, 40 m length and anticlockwise eddy H1, which is formed in on the xy plane close to the bottom of the tank was observed in the calculated streamline pattern for y = 0.7 m (Fig. 5). According to Stamou and Gkesouli [5] this eddy forms due to the interaction of V1 with the solid wall of the tank.

The suspended solid concentration at x = 63 m at the plane 0.1 m away from the left wall of the tank (Fig. 6) was compared for the scenario S-2. Furthermore, the SS removal efficiency of tank in scenario S-2 in Stamou and Gkesouli [5] was 67.43% and the value obtained in this study was, 66.57%.

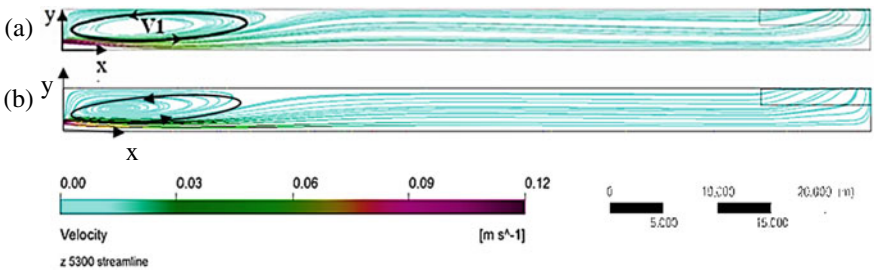

Fig. 4 Streamline pattern on a xy plane at z = − 1.9 m **a** Results of Stamou and Gkesouli [5] **b** Calculated results in this study

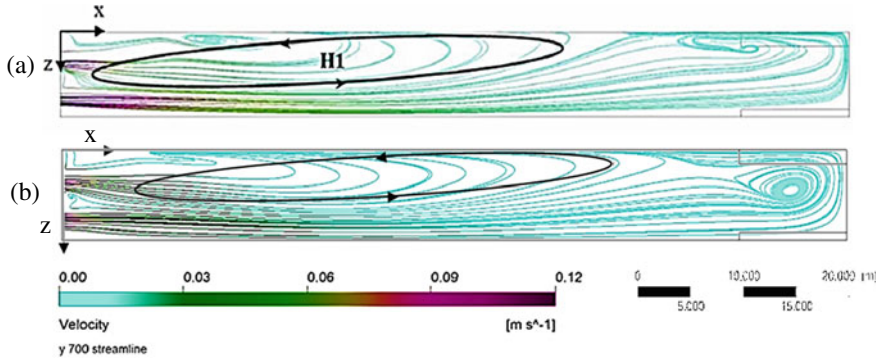

Fig. 5 Streamline pattern on an xz plane at y = 0.7 m **a** Results of Stamou and Gkesouli [5] **b** Calculated results in this study

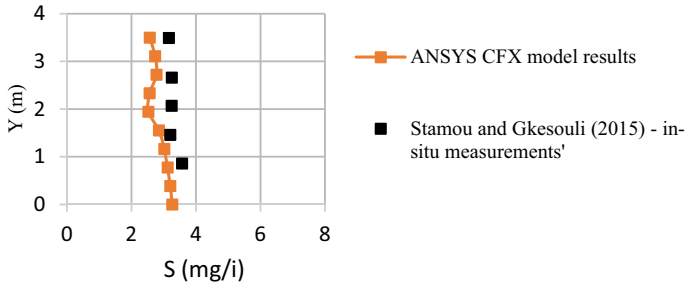

Fig. 6 Variation of suspended solid concentrations at x = 63 m along the tank depth (y) for the scenario S-2

2.3 *Model Application*

In this study, three cases were analyzed and compared with plain sedimentation tank for the comparison of performances. The plates were installed at 3 m, 1 m and 0.5 m spacing in case PS-1 (Fig. 7), PS-2 and PS-3 respectively. The plate thickness, length and inclination angle were kept constant at 0.02 m, 1.5 m and 60° respectively. The

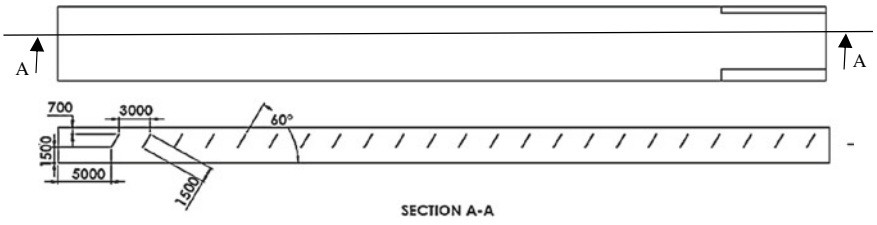

Fig. 7 Longitudinal section of simulated plate settler configuration of PS-1

ratios of increased settling areas in simulated plate settlers are 0.24, 0.61 and 1.38 in PS-1, PS-2, and PS-3 respectively.

The domains were meshed using Hex-Dominant mesh of 0.2 m size. The major locations of interest like, inlet, outlet and plates were refined in order to obtain precise results. The simulations were run with the similar boundary conditions and solid characteristics used in the model calibration for scenario S-2 under the Sect. 2.3. Transient state simulations were selected to better visualize the flow characteristics and removal efficiencies of different configurations. For the numerical method, the advection scheme was upwind, and the transient scheme was set as second-order backward Euler.

The flow field and velocity contour plots at a plane z = − 1.9 m are compared in the Figs. 8 and 9. In the Plane sedimentation tank, large recirculation eddy area was observed as in Fig. 8a. However, the vortex zones were reduced in the plate settlers, and were located between the inclined plates. The reduction of the vortex zone area has indicated an improvement in the hydraulic regime as well as a more even up flow distribution in between the inclined plates allowing more space for particle settling.

According to Fig. 9, the velocity in the tanks range from 0 to 0.145 m/s and the recirculation areas in-between plates in the plate settlers generate more low velocity areas than the plain sedimentation tank providing favorable hydraulic conditions for particle settling. Therefore, the treatment efficiency is enhanced in the plate settlers.

The variation of overall tank solids removal efficiency (R %) of plate settlers were compared with the plain settler (Fig. 10). In PS-1 the removal efficiency of solid class S2 and S3 has been increased by 8.4% and 4.3% respectively. In PS-2, the removal efficiency of solid class S2 and S3 has been increased by 11.9% and

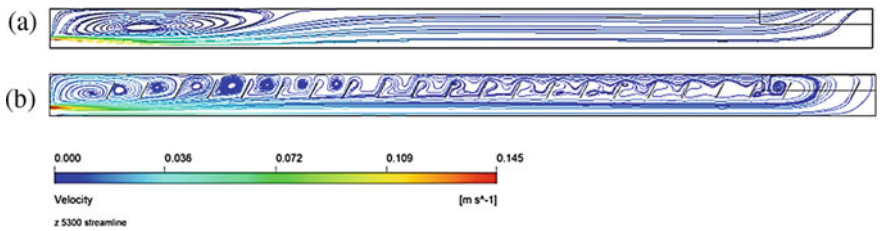

Fig. 8 Velocity streamline pattern at the plane z = − 1.9 m **a** Plain settler **b** PS-1

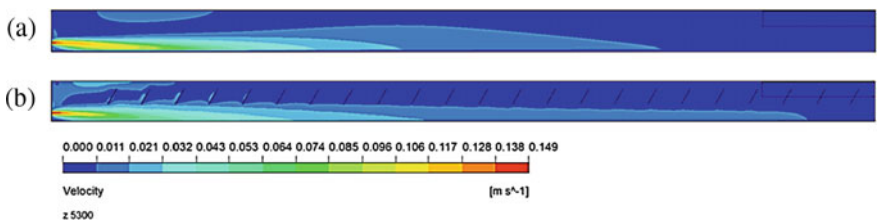

Fig. 9 Velocity contour plots at z = − 1.9 m **a** Plain settler **b** PS-1

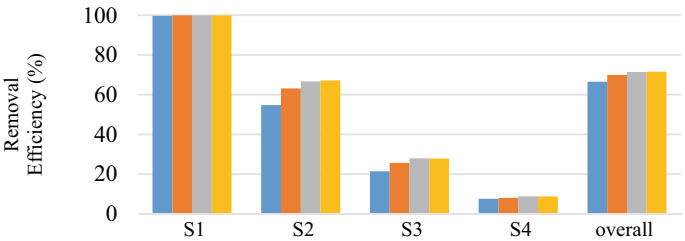

	S1	S2	S3	S4	overall
Plain settler	99.68	54.76	21.43	7.62	66.57
PS-1	99.98	63.13	25.69	8.09	69.96
PS-2	99.97	66.68	27.92	8.84	71.43
PS-3	99.97	67.14	27.86	8.81	71.59

Fig. 10 Comparison of removal efficiencies in plain settler and plate settlers

6.49% respectively. In PS-3, the removal efficiency of solid class S2 and S3 has been increased by 12.38% and 6.43% respectively after 8.3 h while the deposition of solid classes S1 and S4 is almost similar in all simulations of plate settlers.

3 Conclusions

1. Although the plain sedimentation tank does not show the short circuiting of the flow, installing plates reduced the large vortex zones and created a more up-flow distribution of streamlined allowing particles to settle easily.
2. The inclined plates had different effects on the SS removal efficiency in each solid group. Although the sedimentation efficiency was enhanced by plates, the smallest diameter particle group still remains unsettled inside the tank.
3. The efficiency of sedimentation was improved by increasing the number of plates in lamella settlers, due to the increase in settling area, and reducing the settling depth.
4. The CFD tools can be used to analyse the suspended particle removal efficiency in plain settling tanks and plate settlers.

Acknowledgements We thank NORAD WaSo-Asia Project for providing financial assistance for this research.

References

1. ANSYS CFX-Solver Theory Guide, Release 14.0. Available at: http://read.pudn.com/downloads500/ebook/2077964/cfx_thry.pdf [Accessed 10 July 2019]

2. Carlsson B (1998) An introduction to sedimentation theory in wastewater treatment
3. Gkesouli A (2018) CFD modeling of wind effect on the hydrodynamic behavior and removal efficiency of settling tanks. Ph.D. Thesis, Athens, Greece
4. Schroepfer GJ (1933) Factors affecting the efficiency of sewage sedimentation. Sewage Works J 5
5. Stamou A, Gkesouli A (2015) Modelling settling tanks for water treatment using computational fluid dynamics. J Hydroinf 17(2):742–765

Removal of Fluoride in Water and Wastewater Using Electrodialysis/Electrodialysis Reverse Process: A Review

T. P. Malalagama, T. Binghui, K. B. S. N. Jinadasa, D. R. Samaraweera, and F. Yang

Abstract Fluoride enriched water has a profound effect on human health. Therefore, maximum allowable fluoride concentration in drinking water is limited to 1.5 mg/L in World Health Organization (WHO) standards. Not only drinking water, but also several types of wastewater are contaminated with fluoride. Therefore, untreated fluoride enriched wastewater can be created serious issues on environmental health and aquatic lives. Many methods have been used to remove excessive fluoride present in water and wastewater such as Adsorption, ion exchange, chemical precipitation, electrodialysis, electrocoagulation, reverse osmosis, nanofiltration etc. Many organizations and industries focused on their interest on electrodialysis process to remove excessive fluoride in water due to simplicity and low operational cost of the process. Whilst there are a number of reviews that have attempted to optimize ED performance for fluoride removal from water/wastewater, ED technology still has limitations involving scaling, membrane fouling, and permselectivity. In this paper, an extensive review of current studies on the process, principles, and setups of ED technology on fluoride removal is given to deliver a comprehensive collection of all the main findings published so far. Finally economic feasibility also described.

Keywords Electrodialysis · Electrodialysis reverse · Fluoride removal · Water treatment · Wastewater treatment

1 Introduction

Literature reported that fluoride ions are presented in water as well as wastewater in different concentrations [36]. Fluoride in drinking water can be beneficial or harmful depending on its concentration. Health benefits such as prevention of skeleton and

T. P. Malalagama (✉) · T. Binghui · F. Yang
State Key Laboratory of Environmental Aquatic Chemistry, Research Center for Eco-Environmental Sciences, University of Chinese Academy of Sciences, Chinese Academy of Sciences, Beijing 100085, China

K. B. S. N. Jinadasa · D. R. Samaraweera
University of Peradeniya, Sri Lanka, India

R. Dissanayake et al. (eds.), *ICSBE 2020*, Lecture Notes in Civil Engineering 174,
https://doi.org/10.1007/978-981-16-4412-2_43

Table 1 Effects of prolonged use of drinking water on human health related to fluoride content [2]

Fluoride ion concentration, mg/L	Health outcome
< 0.5	Dental caries
0.5–1.5	Optimum dental health
1.5–4.0	Dental fluorosis
4.0–1.0	Dental and skeletal fluorosis
> 10.0	Crippling fluorosis

dental problems can be obtained when the fluoride intake is maintained below 0.4–1 mg/L. However, when the concentration is above this level, it may causes dental and skeleton fluorosis and lesions of the endocrine glands, thyroid and lever [1]. Therefore, maximum allowable fluoride concentration in drinking water is limited to 1.5 mg/L in World Health Organization (WHO) standards. If fluoride concentration is larger than the allowable concentration, excessive fluoride should be removed [2] otherwise it may causes severe health hazards [3]. Some of the health hazards related to high fluoride intake is shown in Table 1.

Not only drinking water, also several types of wastewater are contaminated with fluoride. Fertilizer industries discharge wastewater into the environment which are enriched in fluoride and such wastewater can contain up to approximately 9720 mg/L fluoride in them which can create serious issues on environmental health and aquatic lives [4].

Several methods such as, adsorption [5], ion exchange [6], chemical precipitation [7], electrodialysis [8], electrocoagulation [9], reverse osmosis [10], nanofiltration [11], ultrafiltration [12] and Donnan dialysis [13] have been tested to remove excessive fluoride in water as well as wastewater.

Chemical methods such as precipitation have been used to treat high fluoride concentrated water [7]. Therefore, these methods can be used to remove excessive fluoride present in industrial wastewater.

Adsorption is one of the economical and useful technique which can be used in low pollutant concentration of fluoride. Activated carbon is the most common material used for adsorption process even though it is expensive [5], Therefore, different types of economical and low cost materials have been used for fluoride removal in recent past such as bleaching earths, red mud, alum sludge, Bauxite, carbon etc. [14–16]. But low purity of treated water was provided from these methods [3].

Ion exchange resins are used in industries to remove fluoride from industrial wastewater. However this technology can be applied only for small volume of water and it requires long reaction time to separate fluoride from wastewater [6].

Reverse osmosis is another technology which can be applied to remove fluoride from water. Sometimes it removes 90% of fluoride from wastewater. But there is a contrast between removal efficiency in obtained results in conducted researches [10].

Nanofiltration also remove fluoride satisfactorily where pH level is lower (less than 4.5). But ultrafiltration is unable to remove fluoride in water due to its lower molecular size [12].

Electrocoagulation is gained much interest recently to remove fluoride in water. This technology is easy to operate at both scales (batch and continuous flow), it is inexpensive as it does not require any addition of chemicals and it does not produce a large quantity of sludge that would require subsequent post treatment. A recent study has reported that the electrocoagulation unit which was built with Al and Fe electrodes can achieved 77.7% removal for fluoride [9].

Donnan dialysis (DD) with anion exchange membranes is an attractive membrane process to remove fluoride from the water. Few studies have been carried out using this method and found out that the DD process also an efficient method for defluoridation. However this method have few operational problems such as electrolyte leakages occur from the receiver to the feed compartment [13].

Studies have been conducted to identify feasibility of fluoride removal using electrodialysis treatment in recent past. Not only for fluoride, electrodialysis has been tested worldwide for various contaminants such as Nitrate (NO_3^-), Bromide (Br^-), Sodium (Na^+), Salinity and hardness (Ca^{2+} and Mg^{2+}) etc. [4]. Interest has been increased using ED for treating fluoride enriched water because of its simplicity and its ability to avoid many defects associated with chemical processes [17]. This may happen due to permselective membranes used in ED which is control fluoride concentration by acceptable pH and chemicals additives for human health [7]. Many researchers conducted their studies on ED process to remove fluoride from groundwater [8], brackish water [7], seawater [18], industrial wastewater [4], municipal wastewater [19] etc.

2 ED Process to Removal Anions

Electrodialysis (ED) or electrodialysis reversal (EDR) is an electrochemical charge-driven separation process where dissolved ions are separated through ion permeable membranes under the influence of an electrical potential gradient [20]. This process can be used to remove excessive fluoride present in water or wastewater. Ion exchange membranes, fabricated from ion exchange polymers, have the ability to selectively transport ions with a positive or negative charge and reject ions of the opposite charge.

An ED stack consists of a series of anion exchange membranes (AEM) and cation-exchange membranes (CEM) arranged in an alternating mode between an anode and a cathode. The positively charged cations migrate toward the cathode, pass through the cation-exchange membrane and are rejected by the anion-exchange membrane, and vice versa for negatively charged anions that migrate to the anode [18]. Therefore, negatively charged fluoride ions are moved to the anode as shown in Fig. 1. This result in an alternating fluoride enriched ion concentrated one compartment (concentrate) and depleted concentrated in the other (dilute) ([21, 37, 20]). Figure 1 shows a summary of the fluoride removal process in an ED system (X-ions describes the behavior of the fluoride ions).

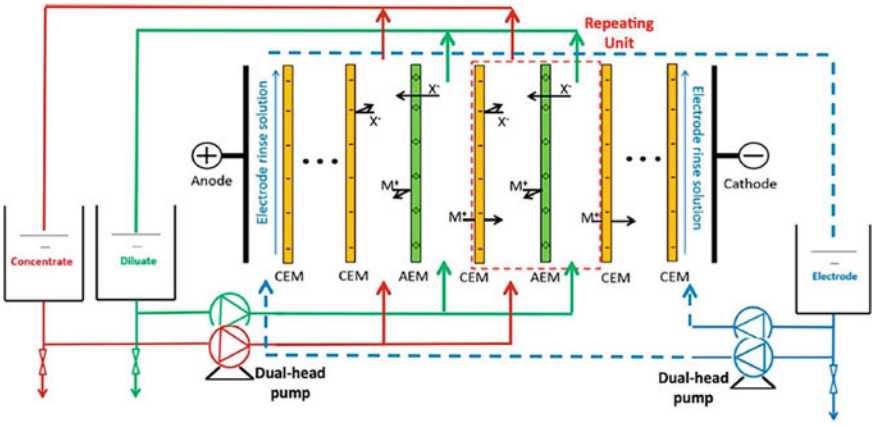

Fig. 1 A detailed scheme of the ED system. X− and M+ refer to negatively and positively charged ions passed through AEM and CEM [22]

3 Factors Affecting Fluoride Removal in Electrodialysis

Fluoride removal efficiency of ED depends on many factors associated with the operational setup, feed water behavior, and membrane properties [23].

3.1 Effect of Voltage and Current Density

Electrodialysis is an electrochemical process which use ion exchange membrane to separate ions from transferring ions through ion exchange membrane under applied current. Therefore, applied voltage to ED is directly proportional to the current and it is a governing factor of fluoride removal from the water [24]. When current increased gradually fluoride ion pass through the ion exchange membrane increased proportionately. This happens possibly because more driving force was provided to drive fluoride ion transport across the anion membrane when the voltage was high [25]. Therefore ion present in dilute chamber decrease and same amount increased in concentrate chambers. So high fluoride removal efficiency can be obtained in maximum applied current density [1]. This was proven by Fadila Djouadi et al. [26] in his research. Three values of current intensities (0.05, 0.07 and 0.1 A) were tested for electrodialysis which has initial fluoride concentration of the feed solution was 100 mg/L. Most elimination of fluoride has been obtained at highest current intensity (0.1 A). The increase in voltage can greatly shorten the operation time and improve work efficiency. Electro diffusion due to the electrical potential gradient is the dominant ion migration mechanism in this process, so a higher voltage promotes the migration of ions [27].

3.2 Effect of Temperature

Temperature affect the flowing characteristics as well as dissolved ions characteristics too. Since the dehydration and activation of ions are highly temperature-correlated, the increase in solution temperature is favorable for F^- to migrate through the membrane matrix [27]. This may happen due to increase of ion mobilization as well as dilatation of membrane network. Reference [28] has been tested the influence of temperature in fluoride removal by changing temperature for 16, 25 and 40 °C by fixing applied voltage of the ED to10 V and flow rate to 180 l/h. The maximum removal of fluoride ions have been shown in highest temperature of 40 °C. However the temperature cannot be increased drastically due to operating conditions of the ion exchange membranes. Sometime it may damage the ion membrane matrix and fail to complete the desired task of the membrane [27].

3.3 Effect of the Composition, Concentration of Solutions

Effect of Composition—High fluoride efficiency is shown where fluoride ions are the only available ions otherwise it is decreased where any other monovalent or bivalent ions are presented. This can be explained by activity co-efficient of the ions, Stokes radius and hydration free energy of these anions [27]. This has been clearly shown in Ergun et al. by using NaF-only, NaF–NaCl (monovalent-monovalent) and NaF–$NaSO_4$ (monovalent-bivalent) as feed ions to ED setup. Then result shows a least removal efficiency in bivalent mixture. Further it has observed that the activity coefficient of the fluoride ions in the 10 mm in NaF-only, NaF–NaCl (monovalent-monovalent) and NaF–$NaSO_4$ ions sets are 0.900, 0.874 and 0.838 respectively. Same observation has revealed by Kabay et al. [18] in his research too. In [18] research conducted with 100 mg/L fluoride solution containing both Chloride and Sulfate ions. The ratios of concentration of ion have been maintained 1:1 in binary mixtures (F:Cl and F:SO_4) and 1:1:1 in tertiary mixture (F:Cl:SO_4). This can be explained in an ion exchanger, the monovalent ion needs only one fixed charged ion that is corresponding to a half set of a bivalent ion. In the presence of monovalent and bivalent ions together in the IEM, a monovalent ion can transfer along with a usual fixed ion, thus it can moves more easily from one fixed ion to next. In contrast bivalent ion don't move more easily because their motion is interfered with by the coexistence of monovalent ions [1].

Effect of concentration—Comparatively high fluoride efficiency can be seen where the concentration of fluoride ion is low. Ergun et al. have been conduct an experiment by introducing concentration of fluoride is 100 mg/L and decreases it to 0.1 mg/L in feed phase. Then the fluoride removal efficiency of the solution is increased from 5 to 78%.

3.4 Effect of Input Flow Rate

Flow input rate is directly correlated with ion exchange rate through the membranes. Therefore there is a high involvement in flow rate to remove fluoride in ED process. This has been observed in several studies. Reference [27] study has clearly shown that amount of migrated fluoride increased with increasing flow rate from 100 to 200 L/h. To evaluate the influence of the input flow rate, experiment was conducted in 100, 150, 200 l/h flow rates. And highest fluoride removal efficiency was shown at the flow rate of 200 L/h. As the flow rate increases, the boundary layer becomes thinner and the internal resistance smaller, which enhances the migration rate of ions. However, an excessive flow rates, decreases the residence time of ions on the surface of the membrane, may resulting in decreased mass transfer [27].

But in [18] research shows a contrasting observation that there is no contribute in flow rate on removing fluoride from water where experiment was carried out in different flow rates of 0.8, 1.2 and 1.6 L/min with fixing concentration of the fluoride is 100 F/L in the solution. Voltage of the ED was maintained 10 V at room temperature.

3.5 Effect of Operation Time

Operation time of the ED affected much in fluoride removal rate. It was shown in [25] experiment where tea infusion fed to short term ED to identify optimal process duration for deflouridation performance by varying ED duration from 1 to 15 min for 10 g/kg initial concentration. The highest fluoride removal rate was shown in the longest (10 min) ED operation time. Therefore it is required to provide sufficient time to remove fluoride from the solution when it is flowing through the membranes to increase the rejection capacity. The concentration of the fluoride amount is high, it is required to provide long operation period to remove fluoride vise-versa short operation period is sufficient to removal of low fluoride concentrated solutions. The time inside the ED/EDR setup is decided by the flux required to transport through the IEM to obtain required efficiency of the system [17].

3.6 Effect of Initial Fluoride Concentration

Concentration of the influent is a highly involved factor with the removal efficiency of any kind of ion removal process. This concept applied to ED process too. When considering technologies which can be used to remove higher IFC, ED process is one of the effective process. The removal efficiency of fluoride has increased where ion concentration is low. Reference [1] has shown this relationship by introducing 0.1, 10 and 100 mM fluoride concentrated feed water to ED where maintaining

Table 2 Gibbs hydration energies and stroke energies

Anion species	Gibbs hydration energy (kJ mol^{-1})	Stroke radii (nm)
Fluoride	472	0.164
Chlorine	347	0.119

constant applied current (1.41 mA/cm^2) and other factors of the ED. Results of the experiment shows that the removal of fluoride increased from 5 to 78% with decreasing the concentration of fluoride from 100 to 0.1 mM in the feed phase. Meantime it shows that flux of fluoride ion increased with increasing the fluoride ion concentration because transported amount of fluoride increased with increasing the fluoride concentration.

3.7 Effect of Feed Water Nature and Concentration

Feeding water nature, it's composition as well as ionic strength of each contaminated ions are dominant parameters of removing fluoride in electrodialysis process. When high salt concentration is available in feed water the energy efficiency of the system increase accordingly vise-versa when concentration of salt is low the process of the system slowdown.

Number of studies have been conducted to identify the removal pattern of the fluoride where other anion are presented. Effect of Cl^- and $(NH_4)_2SO_4$ to fluoride ions have been studied by Luo et al. [27]. This experiment was discovered that, Fluoride ion migration has been decreased from 3.5 to 1.5 g when Cl^- ion presents in the solution increase from 10,000 to 30,000 mg/L. This effect can be explained by stroke energy and Gibbs hydration free energy in these two anions. Effect of fluoride removal efficiency when presence of SO_4^{2-} ions also studied by Luo et al. [27] and same pattern of the presence of Cl^- was observed due to same reason (Table 2).

Further studies have been conducted to identify the impact of organic matters on fluoride removal by Banasiak and Schäfer [29]. It shows that fluoride removal efficiency was enhanced by the presence of organic matters in the solution while the flux decreased indicating mutual dependence of inorganic and organic contaminations in the ED. The mechanism for this involves the possible territorial binding and/or complexation of the inorganic contaminants to the negatively charged organic matters.

3.8 Effect of pH

Many researchers reported that optimum pH value to remove fluoride from the water is 5.5 to 6. However optimum value has changed according to type of the anion

exchange membranes. In lower pH values fluoride ion is not a dominant species due to formation of weakly ionized hydrofluoric acid [1]. When increasing pH value beyond the optimum value in anion membrane types show a significant decrease of fluoride through the membrane. This may be a result of competition between fluoride ions and hydroxide ions [4]. Influence of pH was tested by Fadila Djouadi et al. [26] by adding Na_2SO_4 and NaOH in adjusting pH value of the feed solution to acid pH of 4, neutral one to 7 and base pH to 10. Previously selected parameters that are initial fluoride concentration and current density were maintained at 140 mg/L and 0.1 A respectively. The result was shown that neutral and acidic solutions give best removal of fluoride from solutions.

3.9 Type of Membrane

Broadly membrane can be classified as Anion Exchange Membrane (AEM) and Cation Exchange Membrane (CEM) depending on the ion permitted to transfer through it. Fluoride is considered as a negatively charged ion. So fluoride is permitted to transfer through AEMs. Reference [1] AEM further can be classified as homogeneous and heterogeneous according to polymer contain in functional group [30]. Both these types can be used to remove fluoride. But membrane characteristics also affected to fluoride removal efficiency [1].

Water content—low water content of the membrane indicates that its structure contains more cross link agents. Therefore low water content causes low conductivity. That's why high fluoride transportation efficiency can be seen in high water content membranes. This can be clearly shown in Table 3 [1].

Ion Exchange Capacity—transport rate increased with increasing of ion exchange capacity. Ion exchange capacity in SB-6407 membrane is higher than the ACM and Poly (2-chloroaniline) membranes as at Table 3. That's why SB-6407 membrane shows higher ion transport rate [1].

Thickness and cross sectional area—when increasing the thickness of the membrane transport of ion decreased proportionally. However there is no relationship between cross sectional area and the ion transport efficiency. This was clearly shown in [4] research by two membrane surface area sizes of 100 and 200 cm^3.

Table 3 Comparison of nature of different membranes and the flux of fluoride ions [1]

Membrane	Water content (%)	Ion exchange capacity (meq/g)	Thickness (mm)	Flux (mol/cm^3 s
ACM	13–18	1.4–1.7	0.15	1.48×10^{-8}
Poly (2-chloroaniline)	20	0.55	0.05	0.03×10^{-8}
SB-6407	42	2.1–2.5	0.15	1.62×10^{-8}

4 Analysis of Real Water/Wastewater for Defluoridation in ED Process

Number of pilot scale models have been run to identify the applicability of ED to remove fluoride from water as well as wastewater in recent past across the world. Two of them have been described below for water and wastewater and other few examples are shown in Table 3.

Dental fluorosis is widely spread in Morocco due to high fluoride content in many regions. Therefore, ONEP Co. in collaboration with Eurodia Cooperation and Ibn Tofail University has conducted a study to remove excessive fluoride from water using electrodialysis plant with 1 m^3/h. and…?? The electrodialysis operations were conducted to groundwater in N'zalat Laadem. This study showed that desired water quality including fluoride concentration can be achieved with predetermined optimized operation conditions [31].

Not only for portable water, wastewater also have been tested to remove excessive fluoride using ED pilot models. The treated effluent of the sewage treatment plant located in Novo Hamburgo, Southern Brazil is one of an example which has been used as a feeding water to pilot scale ED. It was revealed that ED can be applied as a tertiary treatment for domestic sewage, and it can be provided reusable standardized quality water for industrial use [19] (Table 4).

Table 4 Summary of fluoride removal from real water and wastewater using ED/EDR processes

Location	Source type/study scale	Capacity	Initial feed fluoride concentration (IFF), removal efficiency (η)	References
Cachoeira, City of Santana-Bahia	Groundwater/Labscale	0.6 m^3/h	IFF—7.49 mg/L, η—80%	[32]
City of Benguerier, Moroccan	Groundwater/Continuous ED	2200 m^3/d	IFF—2.32 ppm, R—94%, η—40%	[33]
N'zalat Laadem, Morocco	Ground water/Pilot plant	1 m^3/h	IFF—1.8 ppm, R—90%, η—10%	[31]
Novo, Hamburgo, Southern Brazil	Domestic wastewater/Pilot batch plant	80 L/h	IFF—0.6 mg/L, R—, η—72%	[19]
Kizidere, Kutahya, Turkey	Ground water/Lab scale	40 mL/min	IFF—20.6 mg/L, R—, η—95%	[1]

5 Cost of Using EDR for Fluoride Removal

Generally the capital and operating costs of an ED plant strongly depends on the quality of the influent water as well as the treated effluent, membrane type and membrane area, capacity of the plant and other plant components, their effective life span under operating conditions. Therefore analyzing and comparing the cost of different electrodialysis is difficult [34].

However, economic study has been conducted to evaluate the cost of fluoride removal by electrodialysis on the basis of industrial and economic data by Lahnid et al. [33]. This plant has been designed to provide water to average consumption for domestic use in rural area for 50,000 people according to the Morroccan standards of 50 L/day per capita (plant capacity—2200 m^3/d). Then investment cost and operating cost have been considered to evaluate the cost of the produced cubic meter of water after removing fluoride. The capital costs have been calculated by including the process (pre-treatment and treatment), building construction and auxiliary equipment. The operating costs have been calculated by including consumables, energy and the installations maintenance (membrane replacement, electrode replacement etc.). Capital cost for the plant was estimated to be € 833,207. The calculated operating cost was € 0.154/m^3in 2008 [33].

The PV-EDR system found through conventional design method in the research of Bian et al. [35] have been predicted to be $40,138 (€ 33,729.4) for 24 m^3/day EDR system in 2017 at India [35].

6 Conclusion

According to available literature, electrodialysis gives promising performances of removing fluoride from both water and wastewater. Though it may difficult to achieve higher fluoride removal efficiencies, it can remove excessive fluoride to provide desired standards of drinking water as well as discharge standards of wastewater. For that purpose, associated factors of ED process such as ED setup, feed water characteristics and membrane properties should be optimized. Applied current can be increased to maximize the removal efficiency of fluoride from the solution. Temperature should be maintained less than 40 °C and pH should be maintained between 5.5 and 6.0 for optimum performances. Flow rate also can be varied considering the impact of residence time of fluoride ions on the membrane surface. Because increased flow rates can reduce the removal efficiency due to low residence time. There has been only few studies carried out to identify the effects of membrane types on removal efficiency. Low cost of operation has been the most favorable point for the full scale implementation of ED/EDR systems.

Acknowledgements This study was financially supported by National Natural Science Joint Foundation of China-Sri Lanka (218611422020) and International Partnership Program of Chinese Academy of Sciences, Grant No. 121311KYSB20190071. The authors appreciated the program

of China-Sri Lanka Joint Research and Demonstration Center for Water Technology and China-Sri Lanka Joint Center for Education and Research in Sri Lanka by the Chinese Academy of Sci-ences. The reviewers' comments enhanced manuscript quality.

References

1. Ergun E et al (2008) Electrodialytic removal of fluoride from water: effects of process parameters and accompanying anions. Sep Purif Technol 147–153. https://doi.org/10.1016/j.seppur.2008.09.009
2. Mohapatra M et al (2009) Review of fluoride removal from drinking water. J Environ Manage 91(1):67–77. https://doi.org/10.1016/j.jenvman.2009.08.015
3. Arahman N et al (2016) The removal of fluoride from water based on applied current and membrane types in electrodialyis. J Fluorine Chem 97–102. https://doi.org/10.1016/j.jfluchem.2016.10.002
4. Bagastyo AY et al (2017) Electrodialytic removal of fluoride and calcium ions to recover phosphate from fertilizer industry wastewater. Sustain Environ Res 27(5):230–237. https://doi.org/10.1016/j.serj.2017.06.002
5. Menkouchi Sahli MA et al (2007) Fluoride removal for underground brackish water by adsorption on the natural chitosan and by electrodialysis. Desalination 212(1–3):37–45. https://doi.org/10.1016/j.desal.2006.09.018
6. Yadav KK et al (2019) Fluoride contamination, health problems and remediation methods in Asian groundwater: a comprehensive review. Ecotoxicol Environ Saf 182:109362. https://doi.org/10.1016/j.ecoenv.2019.06.045
7. Zeni M et al (2005) Study on fluoride reduction in artesian well—water from electrodialysis process. Desalination 185(1–3):241–244. https://doi.org/10.1016/j.desal.2005.03.080
8. Clímaco Patrocínio D et al (2019a) Concentration effect and operational parameters on electrodialysis reversal efficiency applied for fluoride removal in groundwater. J Environ Chem Eng 7(6). https://doi.org/10.1016/j.jece.2019.103491
9. López-Guzmán M et al (2019) Simultaneous removal of fluoride and arsenic from well water by electrocoagulation. Sci Total Environ 678:181–187. https://doi.org/10.1016/j.scitotenv.2019.04.400
10. Shen J, Schäfer A (2014) Removal of fluoride and uranium by nanofiltration and reverse osmosis: a review. Chemosphere 117:679–691. https://doi.org/10.1016/j.chemosphere.2014.09.090
11. Chakrabortty S, Roy M, Pal P (2013) Removal of fluoride from contaminated groundwater by cross flow nanofiltration: transport modeling and economic evaluation. Desalination 313:115–124. https://doi.org/10.1016/j.desal.2012.12.021
12. Mondal S, Chatterjee S, De S (2015) Theoretical investigation of cross flow ultrafiltration by mixed matrix membrane: a case study on fluoride removal. Desalination 365:347–354. https://doi.org/10.1016/j.desal.2015.03.017
13. Hichour M et al (1999) Fluoride removal from diluted solutions by Donnan dialysis with anion-exchange membranes. Desalination 53–62. https://doi.org/10.1016/S0011-9164(99)00027-2
14. Bhatnagar A, Kumar E, Sillanpää M (2011) Fluoride removal from water by adsorption—a review. Chem Eng J 171(3):811–840. https://doi.org/10.1016/j.cej.2011.05.028
15. Khandare D, Mukherjee S (2019) A review of metal oxide nanomaterials for fluoride decontamination from water environment. Mater Today Proc 1146–1155. https://doi.org/10.1016/j.matpr.2019.06.575
16. Singh J, Singh P, Singh A (2016) Fluoride ions vs removal technologies: a study. Arab J Chem 9(6):815–824. https://doi.org/10.1016/j.arabjc.2014.06.005

17. Amof Z et al (2005) Fluoride removal Corn brackish water by electrodialysis. Elsevier, pp 215–223
18. Kabay N et al (2008) Separation of fluoride from aqueous solution by electrodialysis: effect of process parameters and other ionic species. J Hazard Mater 153(1–2):107–113. https://doi.org/10.1016/j.jhazmat.2007.08.024
19. Gally CR et al (2018) Electrodialysis for the tertiary treatment of municipal wastewater: efficiency of ion removal and ageing of ion exchange membranes. J Environ Chem Eng 6(5):5855–5869. https://doi.org/10.1016/j.jece.2018.07.052
20. Van der Bruggen B (2018) Ion-exchange membrane systems-electrodialysis and other electromembrane processes. In: Fundamental modeling of membrane systems: membrane and process performance. Elsevier Inc. https://doi.org/10.1016/B978-0-12-813483-2.00007-1
21. Al-Amshawee S et al (2020) Electrodialysis desalination for water and wastewater: a review. Chem Eng J 380:122231. https://doi.org/10.1016/j.cej.2019.122231
22. Al-Amshawee S et al (2020b) Electrodialysis desalination for water and wastewater: a review. Chem Eng J 380(March 2019). https://doi.org/10.1016/j.cej.2019.122231
23. Damtie MM et al (2019) Removal of fluoride in membrane-based water and wastewater treatment technologies: Performance review. J Environ Manag 251(August). https://doi.org/10.1016/j.jenvman.2019.109524
24. Tanaka Y (2015) Electrodialysis, progress in filtration and separation. Elsevier Ltd. https://doi.org/10.1016/B978-0-12-384746-1.00006-9
25. Peng C et al (2020) Evaluation of the feasibility of short-term electrodialysis for separating naturally occurring fluoride from instant brick tea infusion. J Sci Food Agric 100(1):168–176. https://doi.org/10.1002/jsfa.10011
26. Fadila Djouadi B et al (2018) Electrodialysis for fluoride and nitrate removal from synthesized photovoltaic industry wastewater. Sep Purif Technol 204(2):108–115
27. Luo Z et al (2019) Selective separation and recovery of fluoride ion from ammonia-based flue gas desulfurization slurry using electrodialysis. J Chem Technol Biotechnol 94(8):2561–2568. https://doi.org/10.1002/jctb.6052
28. Amor Z et al (1998) Optimization of fluoride removal from brackish water by electrodialysis. Desalination 263–271. https://doi.org/10.1016/S0011-9164(98)00223-9
29. Banasiak LJ, Schäfer AI (2009) Removal of boron, fluoride and nitrate by electrodialysis in the presence of organic matter. J Membr Sci 334(1–2):101–109. https://doi.org/10.1016/j.memsci.2009.02.020
30. Scarazzato T et al (2020) Achievements in electrodialysis processes for wastewater and water treatment. Curr Trends Future Dev (Bio-) Membr 128–160. https://doi.org/10.1016/B978-0-12-917378-7.00005-7
31. Tahaikt M et al (2006) Defluoridation of Moroccan groundwater by electrodialysis: continuous operation. Desalination 215–220. https://doi.org/10.1016/j.desal.2005.06.027
32. Clímaco Patrocínio D et al (2019) Concentration effect and operational parameters on electrodialysis reversal efficiency applied for fluoride removal in groundwater. J Environ Chem Eng 7(6):103491. https://doi.org/10.1016/j.jece.2019.103491
33. Lahnid S et al (2008) Economic evaluation of fluoride removal by electrodialysis. Desalination 230(1–3):213–219. https://doi.org/10.1016/j.desal.2007.11.027
34. He W et al (2020) Field demonstration of a cost-optimized solar powered electrodialysis reversal desalination system in rural India. Desalination 476:114217. https://doi.org/10.1016/j.desal.2019.114217
35. Bian DW et al (2019) Optimization and design of a low-cost, village-scale, photovoltaic-powered, electrodialysis reversal desalination system for rural India. Desalination 452:265–278. https://doi.org/10.1016/j.desal.2018.09.004 Elsevier (August 2018)
36. Singh J, Singh P, Singh A (2016) Fluoride ions vs removal technologies: a study. Arabian J Chem 9(6):815–824. https://doi.org/10.1016/j.arabjc.2014.06.005
37. Zeni M, Riveros R, Melo K, Primieri R, Lorenzini S (2005) Study on fluoride reduction in artesian well—water from electrodialysis process. Desalination 185(1–3):241–244. https://doi.org/10.1016/j.desal.2005.03.080

Development of an Adsorbent Material for Removing Natural Organic Materials from Water

H. K. T. M. Herath, M. K. D. D. S. Meegoda, and K. G. N. Nanayakkara

Abstract Humic acid (HA) is the most prevailing component of Humic substances in total organic carbon (TOC) which is the main fraction of natural organic matter (NOM) in water sources. Studies in many regions of Sri Lanka showed that the TOC levels are higher than the desirable level of 2 mg/l. Even though the presence of NOM higher than the tolerable level may affect the quality of water, there is no treatment procedure carried out other than the conventional treatment process. Due to the low efficiency of conventional treatment processes in removing NOM, adsorption is proposed as a cost-effective, efficient, and simple technique that overcomes the drawbacks of other techniques. Chitosan is an excellent natural, biodegradable, and abundant adsorbent material. In this research, raw chitosan beads and chitosan/hydroxyapatite (Hap) composite beads made with chitosan powder, eggshells, and poly-ethylene–glycol (PEG), were used to investigate and compare the removal efficiencies of the adsorbent and performance in removing HA. A zero-point charge (pH_{zpc}) study was conducted to characterize the adsorbent materials. Further, the behaviour of the materials with humic acid at neutral pH was investigated using the effect of the contact time, the adsorbent dosage on the removal efficiencies of raw and modified chitosan adsorbents. Moreover, Kinetic studies and isotherm studies were conducted for adsorbents by using a synthetic wastewater sample at neutral pH. A removal efficiency of 74, 60%, and removal capacity of 1.37 mg/g, 1.11 mg/g was achieved for raw and modified chitosan materials, respectively.

Keywords Adsorption · Chitosan · Humic Acid · Hydroxyapatite

1 Introduction

Groundwater is increasingly utilized for potable water supply especially in smaller towns and rural areas of Sri Lanka since groundwater is considered as the cheapest and the safest source of water supply. However, Large quantities of dissolved Natural

H. K. T. M. Herath (✉) · M. K. D. D. S. Meegoda · K. G. N. Nanayakkara
Department of Civil Engineering, Faculty of Engineering, University of Peradeniya, Peradeniya, Sri Lanka

R. Dissanayake et al. (eds.), *ICSBE 2020*, Lecture Notes in Civil Engineering 174,
https://doi.org/10.1007/978-981-16-4412-2_44

Organic Matter (NOM) are present in groundwater due to the decomposition of organic compounds and metabolic reactions [7]. It is also identified that the dissolved potion of (NOM) exists in surface water even after purification of water applying conventional treatment processes [14]. However, the SLS 614:2013 standards have not introduced a tolerable level of Total Organic Carbon (TOC) to be presented after drinking water treatment.

When NOM present in drinking water sources, it has a significant impact to the quality of water. For instance, the presence of NOM in high concentrations causes the formation of halogenated disinfectant by-products which is potentially carcinogen to human health at the disinfection stage and the complication of aesthetic drinking water quality [13]. Therefore, the Environmental Protection Agency (EPA) for drinking water suggest to maintain the TOC concentration below 2.0 mg/l [12] before disinfection by chlorine.

Among all the components of NOM, Humic acid (HA) is one of the predominant constituents. Therefore, several treatment methods have been followed to remove HA from drinking water sources such as coagulation and flocculation, ion exchange, adsorption and reverse osmosis. However, among them, adsorption is being drawn a particular attention because of the merits it contains. It is a mass transfer operation [4] in which substances (adsorbate) present in a liquid phase are accumulated onto a solid phase (adsorbent) and thus removed from the liquid [3] Activated carbon, chitosan, zeolite, rice husk ash and palm oil are some of the common adsorbents found in studies for the removal of HA from water [2].

Chitosan is an excellent natural adsorbent due to the presence of the amine ($–NH_2$) and hydroxyl (–OH) groups [5]. It is commonly obtained by de-acetylation of chitin where generally found in the shells of arthropods. It is an abundant low-cost material that is renewable, biodegradable and non-toxic. Therefore, it is more applicable in removing HA from water.

Even though many studies have been carried out using different techniques to increase the adsorption capacity of raw chitosan, the studies to remove HA in water using chitosan-based adsorbent materials are rather limited. Hence, in this study, our ultimate objectives are to develop an adsorbent material using chitosan as the base material and to investigate the efficiency of both materials in removing humic substances from synthetic wastewater.

2 Materials and Methods

2.1 Materials

Chitosan was obtained from Norwegian University of Life Science. Sample of Hap was prepared from egg shells collected from food courts. Humic acid was purchased from Aldrich Chemical Company, USA. All the other material used were analytical Grade Purity. Deionized water was used to prepare all the aqueous solutions.

2.2 Preparation of Raw Chitosan Beads (Raw Adsorbent)

The raw chitosan was dissolved in a 2.5 wt% acetic acid solution by stirring it for 5 h at 25 °C. The obtained gel was added dropwise to 1.0 M NaOH solution. Then, the formed beads were dried at 37 °C for three days and next, it had been washed with distilled water until a constant pH reading and a zero TOC reading are obtained. Finally, the washed beads were dried at 37 °C for 24 h. [1].

2.3 Preparation of Chitosan/Hydroxyapatite Composite Beads (Modified Adsorbent)

The preparation of Hap was done according to the method followed by Hamzah and Salleh [6]. First, the eggshells were washed using distilled water and dried at 40 °C temperature. Then, the powder passing through 250 μm sieve was extracted by crushing. The sieved powder was diluted in HCl and a 0.125 M di-potassium hydrogen phosphate (K_2HPO_4) solution had been added to the above mixture and left for 7 days at 37 °C temperature until a white precipitate was gained. The precipitate was filtered (7 μm). Finally, Hap was obtained by drying the washed precipitate at 80 °C for 2 h. Then, the same procedure of preparing raw beads was followed by adding Hap (20%) and PEG (10%) to chitosan (3 g) solution.

2.4 Experimental Studies for Adsorption

A sample of synthetic HA solution with initial TOC level of 4 mg/l which is around the identified mean TOC level by Indrashanthi et al. [8] was prepared by dissolving 15 mg of HA powder in a 9 pH NaOH solution. All the laboratory scale experimental studies were conducted as batch studies at 7 pH in room temperature (25 °C) in order represent the physical parameters of groundwater. The samples were shaken at 250 rpm using a mechanical shaker for all the studies conducted. For both raw chitosan and modified chitosan/Hap composite beads, the influencing factors on removal efficiency of HA were investigated by accomplishing effect of adsorbent dosage study, effect of contact time study. For further understanding of solute uptake rate and the adsorption mechanisms, kinetic and isotherm models were analysed.

3 Results and Discussion

3.1 Characterization of Adsorbents

The characterization of raw chitosan and modified chitosan/Hap composite adsorbents was conducted using pH_{zpc} study. The pH_{zpc} of raw chitosan beads and modified chitosan beads was around 7. Hence, at the neutral pH, the charge of the surface could be determined as neutral for both materials. Since the sorption studies also conducted at neutral pH, the removal efficiency of both adsorbent materials was lower than expected.

3.2 Effect of Adsorbent Dosage

The effect of contact time study was evaluated for raw and modified adsorbent dosage ranging from 1 to 4.5 g/l for a contact time of 3 h and 24 h by using a synthetic HA solution with initial concentration of 4 mg/l at 7 pH in 25 °C.

As shown in Fig. 1a and b, for both adsorbents, the removal efficiency increased with the adsorbent dosage up to 3 g/l, due to the availability of active sites for adsorbing particles. The removal efficiency decreased with the increment of adsorbent dosage after 3 g/l since, a fixed-dose of beads can only adsorb a certain amount of humic acid depending on the active sites available in the material. Further, the decrease in the amount of humic acid adsorbed on to the adsorbent with increasing

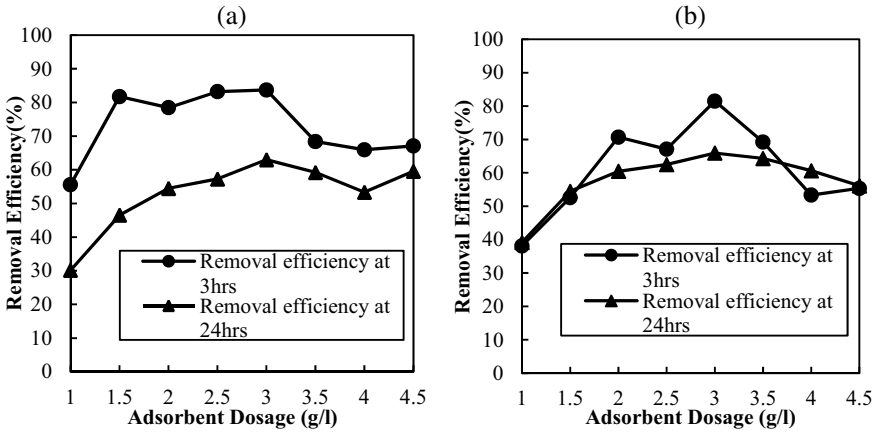

Fig. 1 Effect of adsorbent dosage for filtered HA sample (Initial HA concentration = 4 mg/l; Temperature = 25 °C; pH 7) **a** raw beads 3 h and 24 h of contact time **b** modified beads with 3 h and 24 h of contact time

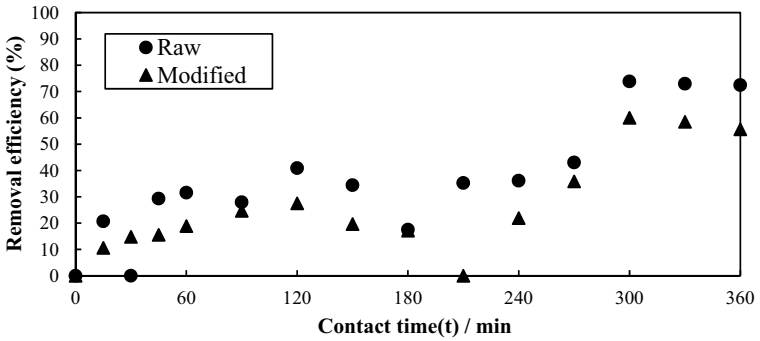

Fig. 2 Effect of contact time for the removal of humic acid by raw and modified materials sample (Initial HA concentration = 4 mg/l; Temperature = 25 °C; Adsorbent dosage = 3 g/L; pH 7)

raw and modified bead dose is due to the reduction in the concentration gradient between humic acid concentration in the solution surface of the beads [11].

3.3 Effect of Contact Time

According to the Fig. 2, the removal efficiencies were varying dramatically for each test run conducted with the same procedure due to the reason of structural heterogeneity of humic substances [17].

According to the results obtained, Optimum contact time was given as 300 min and the removal efficiency of 74%, 60%, and removal capacity of 1.37 mg/g, 1.11 mg/g was achieved for raw and modified chitosan materials, respectively. Raw chitosan beads have a higher adsorption capacity compared to modified chitosan beads for the removal of humic acid. According to [15], the introduction of Hap with low concentrations, the Hap will be occupied in some NH_2 sites of chitosan. Moreover, introduction of lower concentrations of PEG tends to attach to the active sites of chitosan while the porosity is getting lower [15]. As a result of both phenomenon the removal efficiency and removal capacity of modified chitosan/Hap composite adsorbent were lower than expected.

3.4 Kinetic Study

Adsorption kinetics has prime importance in describing the solute uptake rate and time required for the adsorption process. Initially, the kinetic studies carried out considering pseudo-first-order and pseudo-second-order kinetic models.

According to the results obtained, the coefficient of correlation (R^2), showed lower values interpreting that the data does not fit with any of these models. Therefore, the

order of the reaction was tried to obtain by modelling the experimental data using the fundamental kinetic equation shown in Eq. (1).

$$\frac{dC}{dt} = -KC^n \tag{1}$$

where C is the concentration at time t, K is the kinetic constant and n is the order of the reaction.

A MATLAB code was developed and validated the code with known data set to find the optimum order of reaction which fits best for the kinetic study data. However, the results which give the optimum order of the reaction also had a low coefficient of correlation (R^2). The heterogeneity of the humic acid solution and the adsorbent surface [9] may have caused due to the increasing of dissolution of humic acid particles with time. Therefore, it is needed to carry out the Elovich model and Intra particle diffusion model for further understanding of the kinetic behaviour of the system [9].

3.5 Isotherm Study

The adsorption isotherm describes the transmission of adsorbate from the solution phase to the adsorbent phase at equilibrium condition. The experimental data of adsorbent dosage study conducted for optimum contact time (300 min) was modelled with Langmuir and Freundlich isotherm models. Based on results obtained, the Langmuir plot as shown in Fig. 3 was found to be best fitted for both raw and modified material and the value of maximum adsorption capacity was 3.22 mg/g and 3.04 mg/g respectively which advocated that adsorption occurs on a homogeneous surface with no interaction between adsorbed molecules by monolayer sorption [10].

However, the value of the correlation coefficient obtained from the Freundlich model for both materials also indicates that the adsorption of humic acid fitted well the

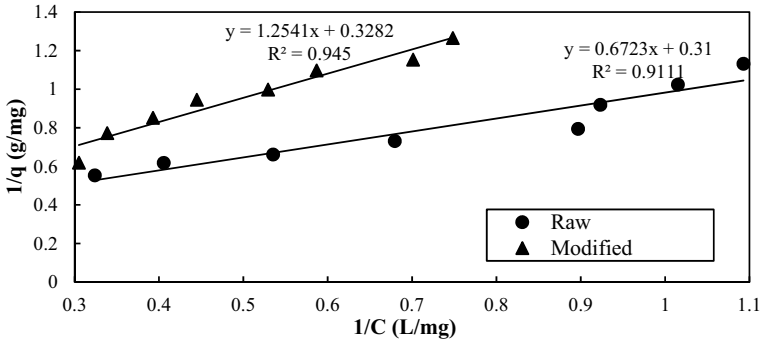

Fig. 3 Linearized Langmuir model for raw and modified chitosan beads

Freundlich isotherm. The exponent n was greater than unity, hence it is an indication of a favourable physical adsorption process [16].

4 Conclusion

In this study, the applicability of raw chitosan beads and modified chitosan/Hap composite beads for removing HA was investigated. The experimental studies were conducted at Neutral pH in room temperature. Indication of neutral surface charge of both adsorbents at 7 pH and heterogeneity behaviour of the adsorbate affected to the performance of the both materials. The maximum adsorption capacity was obtained as 1.4 mg/g and 1.1 mg/g for raw and modified materials respectively.

Acknowledgements The authors sincerely acknowledge the financial support given by the Tokyo Cement Company (Lanka) PLC and WaSo Asia grant.

References

1. Barreiro-Iglesias R, Coronilla R, Concheiro A, Alvarez-Lorenzo C (2005) Preparation of chitosan beads by simultaneous cross-linking/insolubilisation in basic pH: rheological optimisation and drug loading/release behaviour. Eur J Pharm Sci 24(1):77–84
2. Bhatnagar A, Sillanpää M (2017) Removal of natural organic matter (NOM) and its constituents from water by adsorption–a review. Chemosphere 166:497–510
3. Crittenden JC, Trussell RR, Hand DW, Howe KJ, Tchobanoglous G (2012) MWH's water treatment: principles and design. Wiley, Hoboken, New Jersey
4. Dąbrowski A (2001) Adsorption—from theory to practice. Adv Coll Interface Sci 93(1–3):135–224
5. Dong C, Chen W, Liu C (2014) Preparation of novel magnetic chitosan nanoparticle and its application for removal of humic acid from aqueous solution. Appl Surface Sci 292:1067–1076
6. Hamzah S, Salleh MFM (2015) Hydroxyapatite/chitosan biocomposite for Remazol blue dyes removal. In: Applied Mechanics and Materials, vol 695, pp 106–109. Trans Tech Publications Ltd.
7. Ibrahim N, Aziz HA (2014) Trends on natural organic matter in drinking water sources and its treatment. Int J Sci Res Environ Sci 2(3):94
8. Indrashanthi SANT, Rajasinghe RMCA, Nanayakkara KGN (2017) Research on investigating the reverse osmosis membrane performance in CKDu affected areas. Peradeniya, Sri Lanka: Department of Civil Engineering, University of Peradeniya
9. Kajjumba GW, Emik S, Öngen A, Özcan HK, Aydın S (2018) Modelling of adsorption kinetic processes—errors, theory and application. In: Advanced sorption process applications, pp 187–206
10. Kalavathy MH, Karthikeyan T, Rajgopal S, Miranda LR (2005) Kinetic and isotherm studies of Cu (II) adsorption onto H_3PO_4-activated rubber wood sawdust. J Colloid Interface Sci 292(2):354–362
11. Kumar PS, Ramalingam S, Senthamarai C, Niranjanaa M, Vijayalakshmi P, Sivanesan S (2010) Adsorption of dye from aqueous solution by cashew nut shell: studies on equilibrium isotherm, kinetics and thermodynamics of interactions. Desalination 261(1–2):52–60

12. Mayer BK, Ryan DR (2017) Impact on disinfection byproducts using advanced oxidation processes for drinking water treatment. In: Applications of advanced oxidation processes (AOPs) in drinking water treatment. Springer, Cham, pp 345–386
13. Niri MV, Mahvi AH, Alimohammadi M, Shirmardi M, Golas-tanifar H, Mohammadi MJ, Naeimabadi A, Khishdost M (2015) Removal of natural organic matter (NOM) from an aqueous solution by NaCl and surfactant-modified clinoptilolite. J Water Health 13(2):394–405
14. Senavirathene BWHR, Thilakarathne DGLC, Nanayakkara KGN (2019) Water quality analysis of surface water sources in Anuradhapura district. Department of Civil Enginering, University of Peradeniya, Peradeniya, Sri Lanka
15. Shi C, Lv C, Wu L, Hou X (2017) Porous chitosan/hydroxyapatite composite membrane for dyes static and dynamic removal from aqueous solution. J Hazard Mater 338:241–249
16. Sun Y, Chen JL, Li AM, Liu FQ, Zhang QX (2005) Adsorption of phenol from aqueous solution by aminated hypercrosslinked polymers. Adsorpt Sci Technol 23(4):335–346
17. Swietlik J, Sikorska E (2006) Characterization of natural organic matter fractions by high pressure size-exclusion chromatography, specific UV absorbance and total luminescence spectroscopy. Pol J Environ Stud 15(1):145

Synthesis of Zeolites from Rice Husk Ash for Removal of Dyes in Wastewater

M. C. Welagedara, D. G. G. P. Karunarathne, and A. Manipura

Abstract Rice husk is an agricultural waste which contains high amount of silica. This silica can be extracted from rice husk by burning at higher temperatures. Therefore, rice husk ash (RHA) can be used as the silica source when synthesizing zeolites. Zeolites are three-dimensional microporous aluminosilicate which are widely used in industrial applications. In this study, potential of using zeolites synthesized from RHA for the adsorption of dye in polluted water was tested. RHA was obtained by burning rice husk at 700 °C and zeolites were synthesized by using RHA and sodium aluminate in alkali media. Synthesized zeolites were yielded as 75.4% (w/w) and classified as Zeolite A (LTA) based on the XRD analysis. Adsorption capacity and adsorption rate of synthesized zeolites were tested for Methylene Blue (MB) solution through equilibrium and kinetic studies. The adsorption of MB onto RHA was also studied for comparison. Langmuir model and Pseudo second order kinetic model were well fitted with the experimental data with higher coefficient of determination. The monolayer adsorption capacities of the synthesized zeolites and RHA were 16.89 mg/g, 17.42 mg/g and 12.19 mg/g respectively. Synthesized zeolites show higher adsorption capacity than the RHA revealing that Zeolite A synthesized using RHA can use to adsorb dye in polluted water. This study also can be extended to obtain the best zeolite which has a greater adsorption capacity by adjusting synthesis conditions.

Keywords Rice husk ash · Adsorption · Zeolites · Equilibrium study · Kinetic study · Dye removal

1 Introduction

Rice husk is an agricultural waste which is a by-product of rice milling. In Sri Lanka, the annual amount of discharge rice husk is about 572,000 MT [1]. Rice husk is used as a fuel, animal feed, brick making, and as a fertilizer but still causes

M. C. Welagedara (✉) · D. G. G. P. Karunarathne · A. Manipura
Department of Chemical and Process Engineering, Faculty of Engineering, University of Peradeniya, Kandy 20400, Sri Lanka

R. Dissanayake et al. (eds.), *ICSBE 2020*, Lecture Notes in Civil Engineering 174,
https://doi.org/10.1007/978-981-16-4412-2_45

disposal problems. Natural rice husk contains higher amount of silica and extract highly pure silica from rice husk and make an efficient use of it has recently received more attention [2]. The ash obtained from burning of rice husk contains 70–99% silica [3] making it economically attractive. But in Sri Lanka, still rice husk ash is an agricultural waste which required high storage facilities. When burning rice husk at high temperatures, crystalline silica is formed and it cause damages to respiratory tract and other tissues, and cancer according to the International Agency for Research on Cancer (IARC) [4, 5]. In order to protect the environment and reduce the rice husk waste, appropriate rice husk ash utilization strategies must be found.

Though most of the silica sources used in commercial zeolite synthesis are available as solutions, gels, fumed solids, colloids and organic derivatives which are highly expensive, several researchers have found that, producing zeolites from rice husk ash is commercially beneficial [3]. White colour ash, rich with silica considered as unreactive in normal conditions, but amorphous silica is highly reactive in alkali media when synthesizing some zeolites [6]. Amorphous silica can be obtained from burning of rice husk at 550–800 °C, and at higher temperatures crystalline silica is formed [7].

Zeolites are microporous aluminosilicate minerals with three dimensional structures, comprising a SiO_4^{4-} and AlO_4^{5-} tetrahedral linked by a shared oxygen atom. Most of the zeolites are hydrated and crystalline [3]. International Zeolites Association have identified around 175 unique zeolites and over 40 naturally occurring zeolites. Zeolites are widely used in industrial applications such as catalysts, ion exchangers, adsorption agents and water softeners [3] because of its useful properties such as strong hydrophobicity, excellent shape selectivity, good catalytic activity and, high thermal stability [8]. Because of the less purity, uneven pore size, natural zeolites cannot meet the huge demands in industry. Therefore, use of synthesized zeolites becomes very popular besides the natural ones. Zeolites have many synthesized forms such as zeolite A (Na, Ca, K), zeolite X (Na, K, Ba), zeolite Y (Na, Ca, NH_4), zeolite L (K, NH_4), zeolite Ω (Na, H), zeolon (MOR-H, Na), ZSM-5, zeolite F (K) and zeolite W (K), and natural forms such as mordenite, chabazite, erionite and clinoptilolite [9]. Since zeolites has hydrophilic properties, can be used as adsorbents which is mostly in water purification purposes. The studies [10, 11] reveals that the synthesized zeolites can be used as an adsorbent for the removal of dyes from aqueous solution. Therefore, there is much interest in synthesizing zeolites from using low cost silica source like rice husk.

The objective of this study is to extract amorphous silica from rice husk by chemical leaching and synthesize zeolite A from rice husk ash and test the ability of synthesized zeolites from rice husk ash in the removal of dyes in polluted water.

2 Materials and Method

2.1 Chemicals and Materials

Rice husk which is used to prepare rice husk ash was taken from a local rice mill near the University of Peradeniya, Sri Lanka. The chemical leaching of rice husk was done using HCl (36.46%, Sigma Aldrich). Sodium hydroxide (98% NaOH anhydrous pellets) and analytical grade $NaAlO_2$ were used to synthesize Zeolite A.

2.2 Preparation of Rice Husk Ash

First, the rice husk was washed with deionized water and dried in the oven at 110 °C for 8 h. Then, the dried rice husk was digested with HCl (1M) for 3 h with boiling at 80 °C. The digested rice husk was repeatedly washed with deionized water until it becomes neutral and again dried in the oven at 110 °C for 8 h. After that, the chemical treated rice husk was burned in the muffle furnace at 700 °C for 4 h until it becomes pure white ash. Then, the obtained rice husk ash was ground and sieved before the analysis [8].

2.3 Synthesis of Zeolite A

Sodium hydroxide solution (100 mL, 3M) was prepared and divided it into two parts. Sodium aluminate solution was prepared by mixing $NaAlO_2$ into one sodium hydroxide solution and other part is mixed with ash. Then above two solutions were mixed together and kept in room temperature for 48 h while stirring. After that time, the solid product obtained in the synthesis was separated by centrifugation (2500 rpm, 15 min). Then, the solid was washed with distilled water and dried in the oven at 110 °C for 5 h before the analysis.

2.4 Characterization

Synthesized rice husk ash and zeolites were analysed using X-ray power diffraction (XRD) analysis and Fourier transform infrared (FTIR) analysis. The morphologies of the samples were identified by scanning electron microscope (SEM) after performing the platinum coating.

2.5 Adsorption Tests

The equilibrium and kinetic studies were conducted to test the extent of their ability to adsorb die (Methylene Blue) in polluted water. The adsorption capacity of the synthesized zeolites was measured with respect to rice husk ash and zeolites synthesized using commercial silica.

2.6 Adsorption Isotherms

Equilibrium study was performed 50 mL samples of Methylene blue solutions with different concentrations ranging from 20 to 100 ppm. The solutions were stirred for 3 h placing 50 mg of adsorbents in each. The concentrations of the filtered solutions were determined by using UV–Vis spectrophotometer.

Two adsorption isotherms which are Langmuir model and Freundlich model were developed and using coefficient of determination of each model, the most suitable model was chosen.

Langmuir equation,

$$q_e = \frac{K_L C_e q_m}{(1 + K_L C_e)} \tag{1}$$

where, K_L is the Langmuir constant, C_e is the equilibrium concentration (mg/L), q_m is the maximum amount of adsorbate per unit weight of adsorbent to form a complete monolayer on the surface (mg/g) and q_e is the solid phase adsorbate concentration at equilibrium (mg/g).

Freundlich equation,

$$q_e = K C_e^{1/n} \tag{2}$$

where, q_e is the equilibrium adsorbed capacity in mg/g, Ce is the equilibrium concentration in mg/L, K is the adsorption capacity and 1/n are the adsorption intensity.

2.7 Adsorption Kinetics

The kinetic behaviour of the adsorbents was determined by stirring 60 ppm of MB solution with 50 mg of adsorbent and 0.2 mL samples were collected at 30 min of time intervals for 150 min. After each time interval, the collected samples were filtered and concentrations were measured using UV–Vis spectrophotometer.

The adsorption kinetic data were also analysed by using Pseudo first order and Pseudo second order kinetic models. The most suitable model for the adsorbents were determined comparing the coefficient of determinations of each model.

Pseudo first order kinetic model,

$$\frac{dq_t}{dt} = K_1(q_e - q_t) \tag{3}$$

where, q_e and q_t are the amount of adsorbed dye at the equilibrium and time t in mg/g, K_1 is the Pseudo first order adsorption rate in g/mg min.

Pseudo second order kinetic model,

$$\frac{dq_t}{dt} = K_2(q_e - q_t)^2 \tag{4}$$

where, K_2 is the Pseudo second order rate constant in g/mg min.

The adsorbed dye amount per unit mass of adsorbent at equilibrium (q_e) and the amount of adsorbed dye per unit mass of adsorbent at time t (q_t) was determined using following equation.

$$q_e = \frac{(C_o - C_e)V}{m} \tag{5}$$

where, C_o is the initial concentration of MB solution in mg/L, C_e is the equilibrium concentration determined by UV–Vis spectrophotometer in mg/L, V is the volume of the MB solution in l and m is the mass of the adsorbent in mg.

3 Results and Discussion

3.1 Characterization

The rice husk burned at 700 °C, gave pure white color. Phase analysis of RHA was determined by XRD, verifying the presence of silica phase in RHA. The XRD patten of RHA was confirmed as a broad peak from 15° to 40° with a centered peak at 21° as shown in Fig. 1. This is the typical type of amorphous silica [12].

The FTIR spectrum of RHA is given in Fig. 2, which consists bands at 456, 805 and 1083 cm^{-1}. The vibration in 1083 cm^{-1} is assigned to the Si–O–Si [13]. According to Pongdong et al. [14] the peaks at wave numbers 458 and 805 cm^{-1}, may be represents the characteristic bands of amorphous silica.

The SEM image of RHA shown in Fig. 3, determines that ash particles contain porous physical nature with irregular shapes.

In this study, two samples of zeolites were synthesized by changing the silica source to compare, the characteristics of zeolite made from RHA and commercial

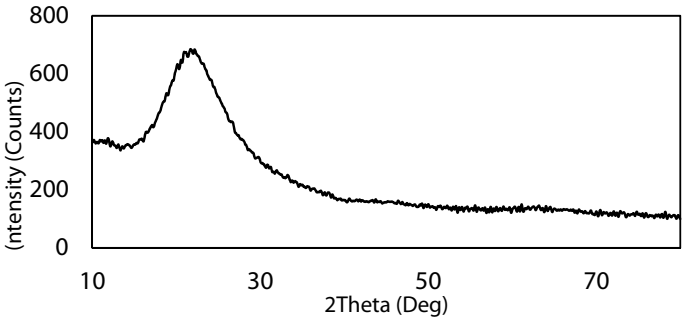

Fig. 1 XRD pattern of RHA

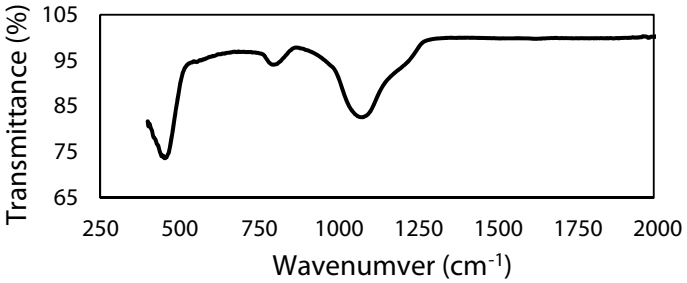

Fig. 2 FTIR spectrum of RHA

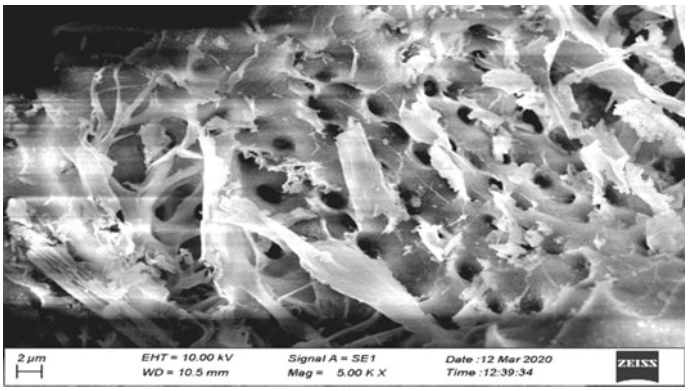

Fig. 3 SEM micrograph of RHA

silica Two experiments were conducted maintaining same conditions while only changing the silica source. Zeolite 1 was synthesized from RHA as the silica source and Zeolite 2 was synthesized from commercial silica. The XRD patterns of two samples are shown in Fig. 4. Based on XRD analysis of two samples were classified

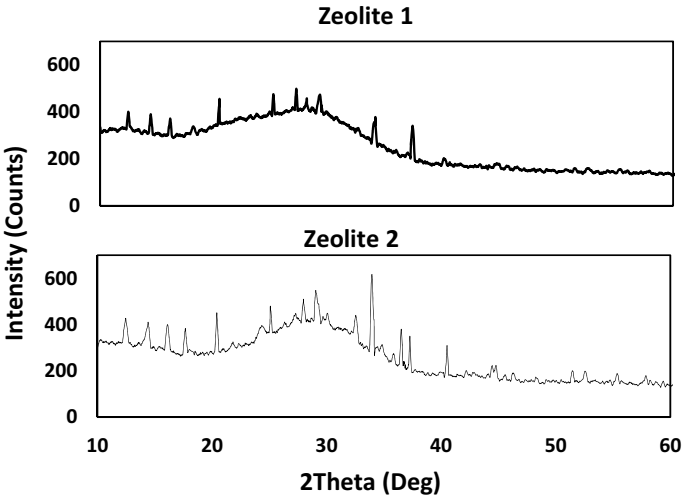

Fig. 4 XRD patterns of Zeolite 1 and Zeolite 2

as Zeolite A (LTA) with a chemical formula $Na_{96}Al_{96}Si_{96}O_{384}.216H_2O$. This was confirmed by its characteristics X-ray peaks at two theta angles about 12.46°, 14.40°, 16.11°, 17.65°, 21.36°, 26.11°, 27.11°, 29.03°, 32.54°, 34.18°, 36.51°, 37.26° and 40.14° [15]. There are more peaks observed in zeolite 2 are detected as Zeolite A and less peaks in zeolite 1 detected as Zeolite A. This is because of the silica source in zeolite 1. The impurities present in RHA including unburned C and some other inorganic impurities may cause to formation of Zeolite A.

Figure 5 is an illustration of FTIR spectrum of synthesized samples which are quite similar. The bands are observed in the range of 300–1000 cm^{-1} with different

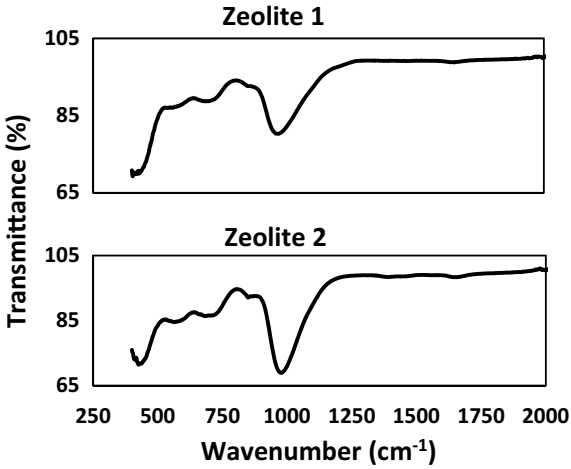

Fig. 5 FTIR spectrum of synthesized samples

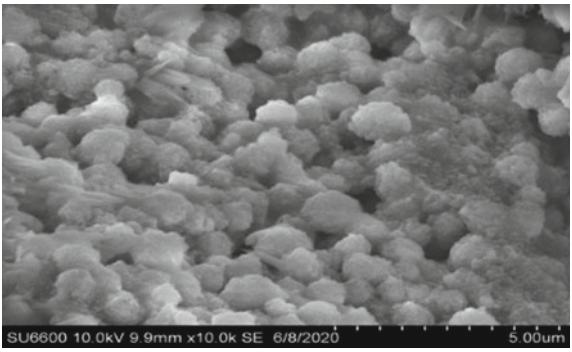

Fig. 6 SEM micrograph of Zeolite 1

contributions at 438, 563, 719, 844 and 985 cm^{-1}. According to Mozgawa et al. [16], the vibration at each wave numbers can be assigned as;

- 985 cm^{-1}—asymmetric stretching vibrations of bridge bonds—ν_{as} Si–O (Si) and ν_{as} Si–O (Al)
- 719 cm^{-1}—symmetric stretching vibrations of bridge bonds—ν_s Si–O–Si
- 555 cm^{-1}—(complex band) symmetric stretching vibrations of bridge bonds—ν_s Si–O–Si and bending vibrations—δ O–Si–O
- 468 cm^{-1}—bending vibrations—δ O–Si–O, occurring in "antiphase".

The vibration at wave number 844 cm^{-1} can be assigned to the OH group which can easily link with water molecules and also reveals that the synthesized samples have hydrophilic characteristics.

The SEM image shows the morphology of the synthesized samples as illustrated in Fig. 6. Zeolite A possesses the LTA-type framework and the morphology of zeolite A generally exhibits cubic particles [11, 3]. According to Fig. 6, the exact shape was not formed, because of the presence of impurities restrict growth of zeolite crystals in certain planes.

The yields of the synthesized samples were calculated as follows and resulted yields are shown in Table 1.

$$\text{Yield} = \frac{W_{\text{Zeolite}}}{W_{\text{Silica source}}} \times 100\% \tag{6}$$

A lower yield shows the zeolite 1, which was synthesized using RHA than that of zeolite 2 which was synthesized using commercial silica. This may be caused by

Table 1 Yields of synthesized Zeolites

Sample	Silica source	Yield (%)
Zeolite 1	Rice husk ash	75.4
Zeolite 2	Commercial silica	87.3

the impurities presents in RHA. Some unburned carbon can be released as gasses in the synthesis process which may contribute to the low yield of zeolite 1.

3.2 *Equilibrium Isotherms*

Equilibrium isotherms was investigated using two models, Langmuir and Freundlich isotherms for the dye adsorption considering three adsorbents which are RHA, Zeolite 1 and Zeolite 2. Figure 7 shows the adsorption of MB dye initially increases with increasing dye concentration and then levels off which might be due to the presence of more vacant sites at the beginning.

The higher coefficient of determination value confirms that the adsorption process follows the Langmuir model and linearized Langmuir model is shown in Fig. 8. The resulted Langmuir constants and maximum adsorbed quantities are indicated in Table

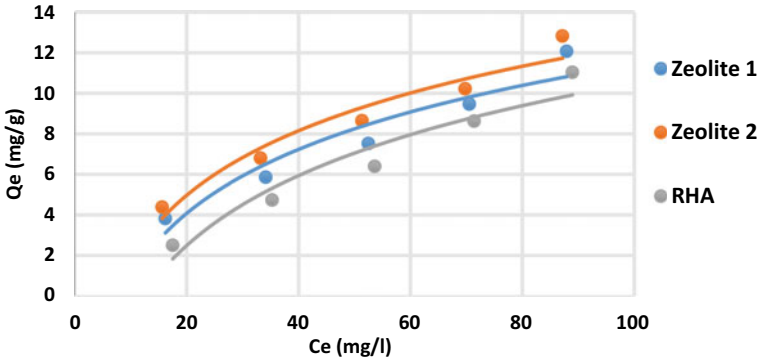

Fig. 7 MB adsorption into RHA and synthesized samples

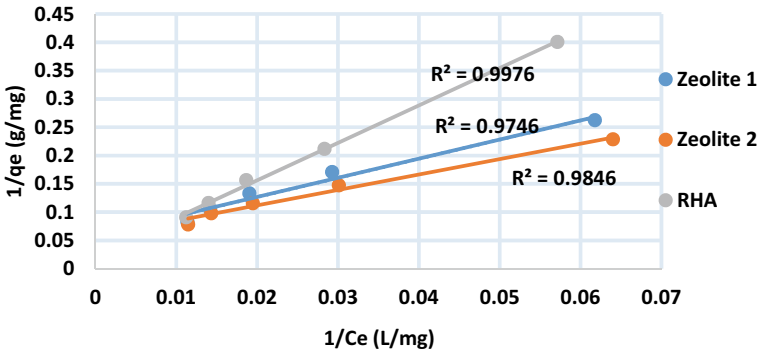

Fig. 8 Linearized Langmuir model for RHA and synthesized samples

Table 2 Estimated parameters for linearized Langmuir model

Material	Q_m (mg/g)	K_L (L/mg)	R^2
RHA	12.19	3.58×10^{-3}	0.93
Zeolite 1	16.89	17.50×10^{-3}	0.91
Zeolite 2	17.42	21.03×10^{-3}	0.94

2. According to the results, higher Q_m and K_L values are given by synthesized samples than RHA, which reveals that Zeolite A has a higher adsorption capacity than the RHA. Also, when comparing the Q_m, values, suggested that the required number of adsorbents to remove given amount dye is high in RHA than the synthesized zeolites. It is implied in the study [10] the enhancement in adsorption can be attributed to increase in surface area. Therefore, Zeolite A synthesized using RHA can be used to remove dyes in polluted water because of its higher adsorption capacity. According to the study of Wang et al. [17] reveals higher Q_m and K_L than the current study in adsorption of MB dye using Zeolite A. By optimizing the synthesis process can be obtained a higher adsorption capacity than this study.

3.3 Adsorption Kinetics

Kinetic study was also investigated using two models, Pseudo first order and Pseudo second order kinetic model considering above mentioned three adsorbents. The time dependence of the adsorption of MB by three adsorbents are shown in Fig. 9. As the contact time increases, the amount of dye adsorbed into the adsorbents are increased significantly. During initial 125 min, the rate of removal of dye was to be found rapid and it remained constant thereafter. After a lapse of time, the remaining surface sites are difficult to occupied because of the repulsion between the solute molecules

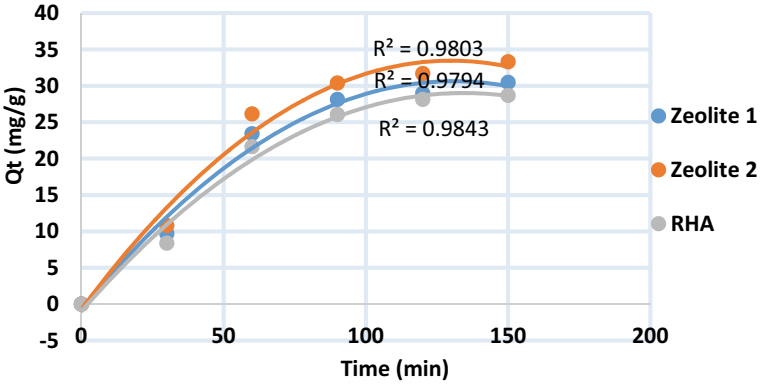

Fig. 9 MB adsorption kinetics for RHA and synthesized zeolites

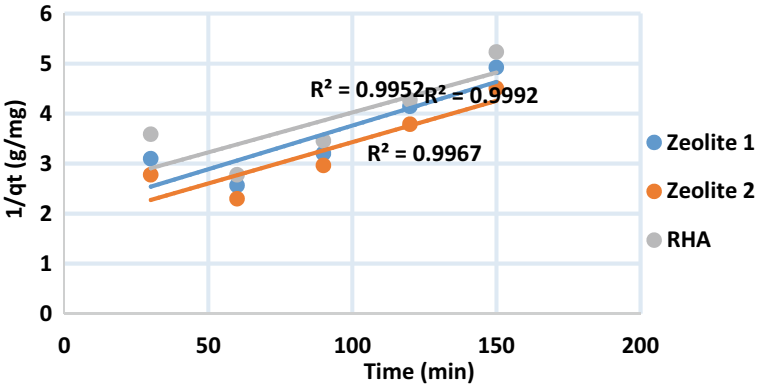

Fig. 10 Linearized Pseudo second kinetic model for RHA and synthesized zeolites

Table 3 Estimated parameters for linearized Pseudo second order kinetic model

Material	K_2 (g/mg min)	Q_e (mg/g)	R^2
RHA	8.44×10^{-4}	34.97	0.99
Zeolite 1	9.58×10^{-4}	36.23	0.99
Zeolite 2	8.99×10^{-4}	39.84	0.99

of the solid and bulk phases [18]. The validity of the two models were determined using correlation coefficient (R^2) for each adsorbent. The experimental data were well fitted with the Pseudo second order kinetic model and linearized Pseudo second order kinetic model for three adsorbents were shown in Fig. 10. The resulted equilibrium adsorbed quantities and Pseudo second order adsorption rate are indicated in Table 3. Three adsorbents show somewhat similar kinetics but synthesized zeolite A samples show slightly higher values than the RHA.

4 Conclusions

Burning rice husk ash at 700 °C, pure white amorphous silica can be obtained with a porous structure. Using this RHA as the silica source, Zeolite A can be synthesized in alkali media. Preparation of RHA must take into account when synthesizing zeolites, because the impurities like, inorganic compounds and unburned carbon may restrict the growth of zeolite crystals in certain planes and also contribute to the lower yield.

According to the equilibrium and kinetic study, synthesized zeolites show a better adsorption capacity than the RHA and also the zeolite synthesized from the commercial silica shows higher adsorption capacity than that of zeolite synthesized using RHA. Zeolites synthesized using RHA can be used as an adsorbent in removal of dyes

in polluted water. This study can be extended to obtain Zeolite A with better adsorption capacity by changing the synthesis conditions. Even though zeolite has higher adsorption capacity, in terms of cost, RHA may better. Therefore, better applications of zeolite, other than dye adsorption, must be investigated.

Acknowledgements I sincerely acknowledge the encouragement and guidance provided by Prof. D. G. G. P. Karunarathne and Dr. A. Manipura, project supervisors, Dr. A. Elangasinghe, Head, Department of Chemical and Process Engineering, University of Peradeniya, and all the members of the academic and non-academic staff members of Department of Chemical and Process Engineering, University of Peradeniya.

References

1. Rathnayaka RPKCS, Ariyaratne AR (no date) Paddy husk fuel block. Trop Agric Res 18
2. Xiong L, Sekiya EH, Sujaridworakan P, Wada S, Saito K (2009) Burning temperature dependence of rice husk ashes in structure and property. J Met Mater Min 19(2):95–99
3. Wajima T, Kiguchi O, Sugawara K, Sugawara T (2009) Synthesis of zeolite-A using silica from rice husk ash. J Chem Eng Jpn 42(SUPPL. 1):61–66. https://doi.org/10.1252/jcej.08we139
4. Jaroonvechatam N, Sansuksom P, Worathanakul P, Kongkachuichay P (2013) Suz-4 zeolite synthesis derived from rice husk ash. Chiang Mai J Sci 40(1):109–116
5. Worathanakul P, Trisuwan D, Phatruk A, Kongkachuichay P (2011) Effect of sol-gel synthesis parameters and Cu loading on the physicochemical properties of a new SUZ-4 zeolite. Colloids Surf A: Physicochem Eng Aspects 377(1–3):187–194. https://doi.org/10.1016/j.colsurfa.2010.12.034
6. Younesi H, Ghasemi Z (2011) Preparation and characterization of nanozeolite NaA from rice husk at room temperature without organic additives. J Nanomater. https://doi.org/10.1155/2011/858961
7. Jaya RP, Amin ZM, Ahmad ZA (2013) Properties of mortar containing rice husk ash at different temperature and exposed to aggressive environment. Adv Mater Res 620:87–93. https://doi.org/10.4028/www.scientific.net/AMR.620.87
8. Kongmanklang C, Rangsriwatananon K (2015) Hydrothermal synthesis of high crystalline silicalite from rice husk ash. J Spectrosc 2015:2–7. https://doi.org/10.1155/2015/696513
9. Pang W, Xu R, Yu J, Huo Q, Chen J (2010) Chemistry of zeolites and related porous materials. Chem Zeolites Related Porous Mater. https://doi.org/10.1002/9780470822371
10. Fungaro DA, Bruno M, Grosche LC (2009) Adsorption and kinetic studies of methylene blue on zeolite synthesized from fly ash. Desalin Water Treat 2(1–3):231–239. https://doi.org/10.5004/dwt.2009.305
11. Nyankson E, Adjasoo J, Efavi JK, Yaya A, Manu G, Kingsford A, Abrokwah RY (2020) Synthesis and kinetic adsorption characteristics of Zeolite/CeO2 nanocomposite. Sci Afr 7:e00257. https://doi.org/10.1016/j.sciaf.2019.e00257
12. Ban G, Song S, Lee HW, Kim HT (2019) Effect of acidity levels and feed rate on the porosity of aerogel extracted from rice husk under ambient pressure. Nanomaterials 9(2). https://doi.org/10.3390/nano9020300
13. Yu LY, Huang ZX, Shi MX (2014) Synthesis and characterization of silica by sol-gel method. Adv Mater Res 1030–1032:189–192. https://doi.org/10.4028/www.scientific.net/AMR.1030-1032.189
14. Pongdong W, Yu J, Huo Q, Chen J (2015) Influence of filler from a renewable resource and silane coupling agent on the properties of epoxidized natural rubber vulcanizates. J Chem. https://doi.org/10.1155/2015/796459

15. Treacy MMJ, Higgins JB (2007) Collection of Simulated XRD powder Patterns for Zeolites Fifth (5th) Revised Edition. https://doi.org/10.1016/B978-0-444-53067-7.X5470-7
16. Mozgawa W, Barczyk K, Krol M (2014) Investigation of the coal fly ashes using IR spectroscopy, spectrochimica acta-part a: molecular and biomolecular spectroscopy. Elsevier B. 132:889–894. https://doi.org/10.1016/j.saa.2014.05.052
17. Wang C, Li J, Sun X, Wang L, Sun X (2009) Evaluation of zeolites synthesized from fly ash as potential adsorbents for wastewater containing heavy metals. J Environ Sci. Res Centre Eco-Environ Sci, Chinese Acad Sci 21(1):127–136. https://doi.org/10.1016/S1001-0742(09)60022-X
18. Benmaamar Z, Hamitouche H, Boutoumi H, Benmaamar H, Ould Baba Ali S, Benmaamar A, Aggoun A (2017) A batch study of adsorption equilibrium and kinetic for methylene blue onto synthesized zeolite. J Mater Environ Sci 8(2):539–550

A Comparison Study of Removing Rhodamine B from Wastewater by Nitric Acid Functionalized Rice Husk, Coconut Husk and Synthetic Porous Carbon

Charitha Thambiliyagodage, Sulakshini Ranchagoda, and Shanitha Mirihana

Abstract The present comparison study describes the effectiveness of different carbon based adsorbents for the successful removal of Rhodamine B (RhB) from wastewater. Selected adsorbents are rice husk (RH) and coconut husk (CH) as the agricultural waste products and porous carbon synthesized by resorcinol formaldehyde polymerization via sol gel method (SC). Such porous materials were functionalized using nitric acid. Morphology of the materials were examined by the Scanning electron microscope (SEM) and the surface functionalities were determined by FT-IR spectroscopy. Adsorption of all functionalized and raw porous materials was determined by varying parameters such as pH of the medium, adsorbent dosage, dye concentration and contact time. Generally, all the selected adsorbents were capable of removing RhB and functionalized adsorbents were much effective than the untreated adsorbents. Among all the adsorbents selected for the comparison, functionalized rice husk (FRH) showed highest activity compared to other adsorbents as it consists of both carbon and silica, while others have only carbon. Interestingly adsorbents prepared by natural waste materials were more effective than the synthetic carbon suggesting that these tested materials could be used in novel water purification systems to decontaminate waste and drinking water.

Keywords Rice husk · Coconut husk · Resorcinol–formaldehyde · Nitric acid · Rhodamine B · Wastewater

Charitha Thambiliyagodage and Sulakshini Ranchagoda—are contributed equally.

C. Thambiliyagodage (✉) · S. Mirihana
Faculty of Humanities and Sciences, Sri Lanka Institute of Information Technology, Malabe, Sri Lanka
e-mail: charitha.t@sliit.lk

S. Ranchagoda
Institute of Chemistry Ceylon, Adamantane House, 341/22, Kotte Road, Rajagiriya, Sri Lanka

R. Dissanayake et al. (eds.), *ICSBE 2020*, Lecture Notes in Civil Engineering 174,
https://doi.org/10.1007/978-981-16-4412-2_46

1 Introduction

Synthetic dyes are extensively used in industrial applications including textile [24], paper [22], food [11] and paint [1] industries. Such dyes are classified into different groups depending on their chemical structure as azo, anthraquinone, sulphur, phthalocyanine, and triarylmethane [32]. Azo dyes consisting of two nitrogen groups are quantitatively the most important group and being the most problematic pollutant of wastewater originated by dye discharging sources. The release of dye contaminated wastewater to natural habitats is hazardous not only to the aquatic life disturbing the natural equilibrium but also to the human beings causing allergies, dermatitis, skin irritations [5, 6, 20]. Hence, the removal of dyes from effluents before they are released to the natural water reservoirs is of great importance. Many methods have been reported to remove such dyes from wastewater by adsorption [18, 26, 44], photocatalytic degradation [7, 14, 17], electrochemical methods [42] and coagulation-flocculation [25], of which adsorption has been found to be the most promising method. Decoloration of wastewater by adsorption of dyes by Activated carbon has been found to be very efficient due to its high surface area, porous structure, high degree of surface functionality and high adsorption capacity [4, 13, 28]. However, commercially available activated carbon is very expensive and has high regeneration cost. Hence, researchers are interested in finding alternative materials which are efficient, inexpensive and easily available [4]. Different adsorbents such as alumina [3], silica [2, 21], zeolites [43], which have been reported as other alternatives and naturally available waste materials like orange peel [37], rice husk [29], saw dust [12], coir pith [31], straw [23] have been used to produce functionalized activated carbon as potential candidates to remove dyes from wastewater. It is vital to use low cost waste materials as adsorbents to remove dyes from contaminated water basically due to two reasons. Disposal of such waste materials generated by agriculture, industry or any other means is problematic and regeneration of spent materials as adsorbents is unnecessary due to the low cost and abundance. Hence, it is important to develop an inexpensive, abundant and efficient adsorbent from waste materials for the removal of industrial pollutants. From our previous study we have shown that non-functionalized rice husk is capable of removing methylene blue, methyl orange and metal ions like Pb^{2+}, Cu^{2+}, Cd^{2+} and Ni^{2+} [41]. Continuing such interest, a comparative study was carried out using nitric acid treated porous carbon originated by paddy husk and coconut husk as the agricultural waste materials and carbon synthesized by resorcinol–formaldehyde polymerization to remove RhB from artificial wastewater.

2 Materials and Methods

2.1 Materials

Rhodamine B was supplied by Prym Intimates Lanka (Pvt.) Ltd., Lot 16–17. Biyagama EPZ, Walgama, Malwana, Sri Lanka. Rice husk was collected from Nawagamuwa area and coconut husk was collected from Kuliyapitiya area, Sri Lanka country. Polyethylene glycol 20,000 (PEG), and Cetyl triammonium bromide (CTAB), HCl, HNO_3, NaOH, Formalin, Ethylenediamine were procured from Sisco Research Laboratories (Pvt.) Ltd, India.

2.2 Instrumentation

Fluorescence emissions were recorded on a Fluorescence spectrophotometer (Model: HITACHI F-2700) and the FT-IR spectra were collected by a ABB MB3000, Canada FTIR using ATR device. Scanning electron microscopic images were taken by Hitachi SU6600 Analytical Variable Pressure FE-SEM.

2.3 Methods

2.3.1 Preparation of Carbonaceous Materials

RH from paddy that are harvested in Sri Lanka were employed as the raw material. The soil and dust in the rice husks were washed with distilled water and ethanol and dried at 80 °C. Then the purified RH was separately treated with 2 mol dm^{-3} HCl acid at 60 °C for 2 h with regular stirring. Acid leached RH was rinsed with distilled water until the pH of the filtrate reaches ~ 6 and was dried at 80 °C. Then RH was placed in a muffle furnace and heated at 400 °C for 2 h to obtain acid leached RHA. CH obtained from Sri Lanka was used to produce the coconut based porous carbon adsorbent. CH was washed with distilled water and ethanol many times to remove all the dust and solid particles followed by drying at 80 °C and a portion of it was carbonized as mentioned above.

Hierarchically porous monolithic carbon was synthesized by dissolving resorcinol (3 g) in a solvent mixture of ethanol (11.5 mL) and distilled water (9 mL) followed by addition of 1.5 g of PEG with constant stirring at room temperature. Mixture was stirred until all PEG dissolves and 1.5 g of CTAB was added to the mixture. Once all the CTAB dissolves in the solvent mixture 0.1 g of ethylenediamine was added and the mixture was stirred for 30 min. Formalin containing formaldehyde (4.5 g, 35 wt%) was quickly added to the mixture. The reaction mixture was stirred further for 10 min and the resulting homogeneous emulsion in closed vessels were transferred

to an oven and were heated at 80 °C for 4 h. Resulting gels were dried at 50 °C for 2 days and were carbonized at 400 °C for 2 h.

All the prepared carbon based porous adsorbents were functionalized with 6 M HNO_3 acid at 60 °C for 6 h with regular stirring. After the treatment, adsorbents were rinsed with distilled water until the pH of the washings reached ~ 6 and was dried at 80 °C. The dried samples was sifted through sieves of 0.5 mm pore size and stored in a desiccator until further use. Hereafter, all functionalized RH, CH and SC adsorbents will be labeled in the text as FRH, FCH and FSC, respectively.

2.3.2 Preparation of RhB Solutions

A stock solution of 100 mg/L was prepared by dissolving accurately weighed sample of dye in a 250 mL of distilled water. The desired experimental concentrations of dye solutions were prepared by the appropriate dilutions of the stock solution in distilled water. The pH of each solution was adjusted by adding diluted HCl or NaOH solution and measured with a benchtop meter.

2.3.3 Batch Study

The effect of experimental parameters of pH (2–10, step size: 2), initial dye concentration (5–20 mg/L, step size: 5 mg/L), and adsorbent dosage (5–30 mg, step size: 5 mg) were studied in the batch mode for a total of 60 min. RH was incubated for 2 h and as the equilibrium reached in 60 min, other two adsorbents were incubated only for one hour to be consistent with RH to compare their results. pH of the medium was not changed and kept that of distilled water for all the experiments except at the pH optimization. In each adsorption experiment, 25 mL sample of RB solution with known concentration was transferred to a 50 mL centrifuge tube, and known weight of the adsorbent was added into the tube and they were shaken for 1 h at 200 rpm in the orbital shaker. Except for the experiments of which effect of RB concentration was supposed to determine, concentration was kept constant at 5 mg/L. Similarly, the weight of porous carbon material was kept constant at 25 mg in all experiments, where it was only varied at mass optimization experiment. The concentration of RB solution was determined by using a Fluorescence spectrophotometer of which the wavelength range was adjusted to 564–574 nm. The adsorption capacity was calculated by using the following equation:

$$qt = V\frac{C_o - \mathrm{Ct}}{m}$$

where C_o and C_t were the initial concentration and the concentration at time t in mg/L respectively, m was the mass of the adsorbent in g, and v was the volume of the solution in L. The removal efficiency was calculated using the following equation:

$$E = \frac{C_o - Ct}{C_o} 100\%$$

2.3.4 Reusability of the Adsorbent

Functionalized adsorbent (30 mg) was dispersed in 25 mL of 5 mg/L RhB solution was shaken for 1 h. The used adsorbent was isolated and was washed with distilled water and ethanol until the washings had no pink colour. Washed adsorbent was used again with the same experimental conditions. After each run the concentration of the remaining RB in the solution was determined.

3 Results and Discussion

3.1 Material Characterization

3.1.1 Material Synthesis

Hierarchically porous carbon was synthesized by a modified procedure [19, 41]. Resorcinol and formaldehyde are the precursors of the polymerization while PEG is the macropore directing agent and CTAB is the mesopore directing agent. Ethylenediamine provides the required basicity to the reaction medium acting as a catalyst for the polymerization. In addition it act as a crosslinking agent and provides N based functional groups to the carbon structure as well [19].

3.1.2 SEM Analysis

Scanning electron microscopic images of the adsorbents were taken in order to study the morphology. RH has a naturally available irregular shaped macropore structure which lead to macropore channels as shown in the Fig. 1a. CH also show irregular shaped macropores which are much oriented. Further they have formed ordered macropore tubes as shown in the Fig. 1b. SEM images of SC (Fig. 1c) show spherical, eclipse shaped, and irregular shaped macropores with a wide variation in size are scattered in the matrix of carbon without interconnectivity. These macropores also form macropore channels but they are disordered. The solvent to polymer ratio affect the morphology of the macropores, the size of the macropores and the skeleton and the interconnectivity of the macropores. The observed macropore structure of SC resulted due to the small ratio of solvent to polymer used in the synthesis [27]. Macropores are formed during the spinodal decomposition. When resorcinol is mixed with

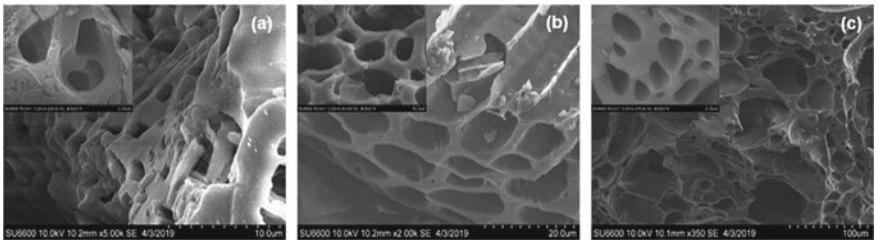

Fig. 1 SEM images of **a** RH, **b** CH, **c** SC

PEG, they form H bonds with each other. During the prepolymerization formaldehyde copolymerized with resorcinol and form oligomers and the solubility of the polymer mixture in the alcoholic solution decreases separating polymer phase from the alcoholic solvent. After prepolymerization, the solution was heated and hence the immiscibility progress with concomitant polymerization. This is known as polymerization induced phase separation. The phase separation could develop from either spinodal decomposition or bimodal decomposition. Bimodal decomposition causes the appearance of isolated spherical domains as resulted in this synthesis as shown in the Fig. 1c. Bicontinuous microstructures are developed by spinodal decomposition and such system has not developed in this work as shown by the SEM images [27]. Mesopores should be originated from the soft template method where CTAB form a micelle structure and resorcinol interacts with CTAB via electrostatic interactions [8]. During the carbonization these CTAB molecules are burnt off resulting mesopores. Micropores are generated during the carbonization process where small molecules are removed from the carbon matrix and resulting small voids create micropores if the diameter is less than 2 nm and mesopores if the diameter is greater than 2 nm.

3.1.3 FT-IR Analysis

Adsorption capacity of an adsorbent depends on the porosity of the adsorbent and the density of the surface functional groups present. Generally, carbon based adsorbents have functional groups based on heteroatoms such as carbon, oxygen, nitrogen and sulfur. FT-IR analysis was performed for all the samples and the acquired FT-IR spectra are given in the Fig. 2. FT-IR spectra of RH and FRH are given in Fig. 2a. The band at 1095 cm^{-1} can be assigned to the Si–O–Si stretching, the shoulder band around 800 cm^{-1} to Si–O bending and Si–OH stretching collectively and the band at 465 cm^{-1} to Si–O out of plane deformation [36]. FT-IR spectra of CH and FCH, and SC and FSC are given in Fig. 2b, c respectively. The broad peak appeared 3300–3500 cm^{-1} which is more apparent in the functionalized adsorbents can be attributed to the OH stretching [39]. The wide peak at (1540–1650 cm^{-1}) shows the presence of asymmetric stretch of the COO^- group [38] and the peak at 1046 cm^{-1} shows the presence of C–O–C functional group [30, 39]. The peaks correspond to the above functional groups which are related to the COOH are high in intensity in

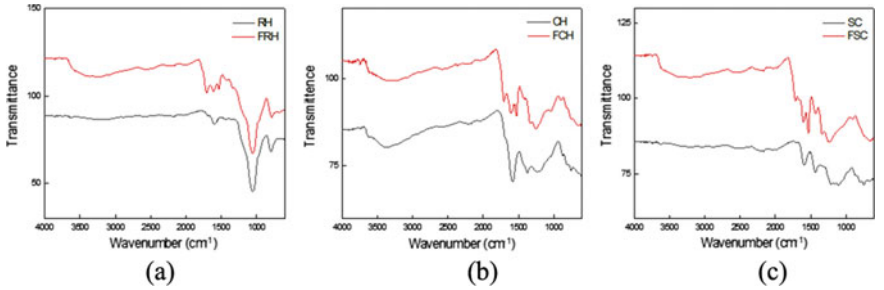

Fig. 2 FT-IR Spectra of **a** RH and FRH, **b** CH and FCH, **c** SC and FSC

the functionalized adsorbents clearly suggest that the surface of the adsorbents have oxidized by concentrated nitric acid treatment agreeing with the mechanism proposed by Zhang et al. that HNO_3 acid oxidize the surface of the carbon introducing COOH groups [46].

3.1.4 Effect of pH

pH is one of the main parameter that controls the adsorption of adsorbates to adsorbents. The pH of the solution was adjusted by the addition of HCl and NaOH. Variation of adsorption capacity with pH is shown in Fig. 3. The structure of RhB changes with changes in the pH. At low pH values where the medium is highly acidic RhB exists in the cationic and monomeric form [10, 34]. Thus, RhB molecule can penetrate the porous structure of the adsorbents. At pH values higher than 4 the zwitterion form exists and upon alkalization the zwitterion form predominates and it may increase the aggregation of the RhB molecules. RhB molecules aggregated due to the attractive electrostatic interactions between the carboxyl group and the xanthene groups of the monomer. Hence, aggregated RhB molecules or dimers of RhB will not easily penetrate through the porous structure of the adsorbents. At high pH, abundantly available OH^- creates a competition between the $–N^+$ and COO^-

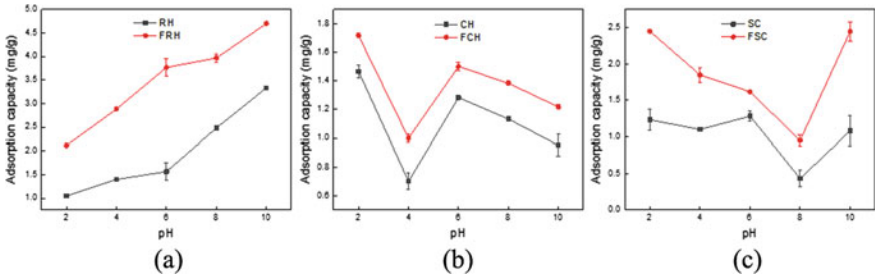

Fig. 3 Effect of pH on adsorption of RhB on **a** RH and FRH, **b** CH and FCH, **c** SC and FSC

and decreases the aggregation of RhB increasing the adsorption RhB to the adsorbate surface [10, 34].

Nitric acid was used to functionalize the adsorbate surface. Highly concentrated nitric acid oxidize the surface of the adsorbents FRH, FCH, and FSC introducing –COOH and lactone groups to the adsorbent surface. In addition carbon surfaces consist of Nitrogen based functional groups especially in synthetic carbon where nitrogen was introduced by ethylenediamine. These functional groups get protonated at lower pH values and get deprotonated at high pH values. However, the net charge of the adsorbent surface and the attraction or repulsion interactions between the adsorbent and RB cannot explain the adsorption behavior of RB with varying pH values. Adsorption capacity of RH and FRH increases from 1.05 mg/g and 2.12 mg/g respectively, at pH 2 to 3.33 mg/g and 4.70 mg/g respectively, at pH 10. RH mainly consists of carbon and silica where silica provides additional negative charge to the adsorbent compare with CH and SC. At acidic pH of 2, and 4 and even at pH 6 where the cationic form of RhB is predominant, RhB molecules have interacted with the RH and FRH surface though the charge of the adsorbent surface is not a principal factor that determines the adsorbent adsorbate interactions. Moreover, as carbon and silica both components of RH contain pores of different sizes, different size of RhB as monomers and aggregates could still get into the porous structure. Since silica tend to dissolve at higher pH values, diameter of the pores of silica tend to increase with the dissolution of the pore walls facilitating larger molecules to migrate through the pores. Hence the adsorption capacity of both RH and FRH increases with increasing pH. Adsorption capacity of FRH is higher than that of RH due to the new functional groups introduced to the adsorbent surface such COOH, lactone as indicated by the FT-IR spectra as given in the Fig. 2a.

Adsorption capacity of SC and FSC decreases generally with increasing pH up to 8 and increases to a maximum of 1.23 mg/g and 2.45 and mg/g respectively, at pH 10. Adsorption capacity of SC and FSC at pH 2 shows highest adsorption capacity as the cationic RhB molecules can easily pass through the porous system and get adsorb to the carbon surface. As the pH increases to pH 8 the monomeric cationic RhB gradually converts to its zwitterion form and results in aggregated (dimer like) RhB molecules. The macropores present in SC are large in size and have only few in a given area compared with RH and CH where the amount of macropores is high in a given area. Presence of mesopores and micropores does not affect the adsorption of aggregated RhB molecules as they cannot enter such small pores. Thus, the limiting factor is the amount of macropores and hence, when the pH increases the resulting penetration and adsorption of aggregated RhB molecules is comparatively low. But when the pH increases to 10 due to alkalinity the aggregation of RhB molecules is prevented and adsorption of RhB increases. CH and FCH show a different behaviour where the adsorption capacity decreases from pH 2–4 and then increases at pH 6 and again decreases gradually to pH 10. It is evident that the adsorption capacity of RhB by CH and FCH is high at pH as the cationic monomeric RhB easily adsorb to the adsorbent surface. However, that has drastically reduced at pH 4 and again increases to pH 6 which reduces till pH 10. pKa of RhB is 3.7 and transformation of the cationic form to zwitterionic form starts at pH greater than the pKa [30]. As the pH

increases from 2 to 4 the availability of OH^- groups increase and may have initiated the aggregation of RhB resulting lower adsorption capacity. When the pH increases to pH = 6, medium is almost neutral and dimeric form of RhB molecules may exist in addition to the monomeric RhB resulting high adsorption capacity relative to pH 4. Meanwhile beyond pH 6 adsorption capacity again decreases which could be due to the surface charge of the material. Surface become more negatively charged as the pH increases and the zwitterion form and the lactone form of RhB which predominates at high pH values would have been repelled by the surface of the adsorbent. Further as described above as the RhB aggregates entrance of the molecules to the porous structure become difficult resulting low adsorption capacities at high pH values. Interestingly, the adsorption capacity of CH is higher than FCH only when the pH of the medium is changed indicating the H^+ and OH^- concentrations of the medium and hence the surface charge of the adsorbent have significant influence in adsorption. However, the surface charge of the adsorbent has played a crucial role in adsorbing RhB to CH being different from RH and SC. Moreover, the adsorption capacity of RH species (RH and FRH) is higher than both CH and SC species, which could be attributed to the presence of two different main components, carbon and silica in the same adsorbent while others are single component adsorbents (carbon only). RH has carbon and silica as the components and in both low and high pH silica tend to dissolve [45]. The dissolution of the adsorbent in such conditions is a problem and hence all the rest of studies were performed at neutral pH though the three different adsorbents showed three different optimum pH values of maximum adsorption.

3.1.5 Effect of Adsorbent Dosage

The effect of adsorbent dosage on adsorption have been determined by adding varying weights of adsorbents to a fixed volume and initial concentration of RhB and by shaking for a fixed time. The efficiency of RhB removal by RH and FRH increases with increasing mass of the adsorbent as shown in the Fig. 4a. The removal efficiency

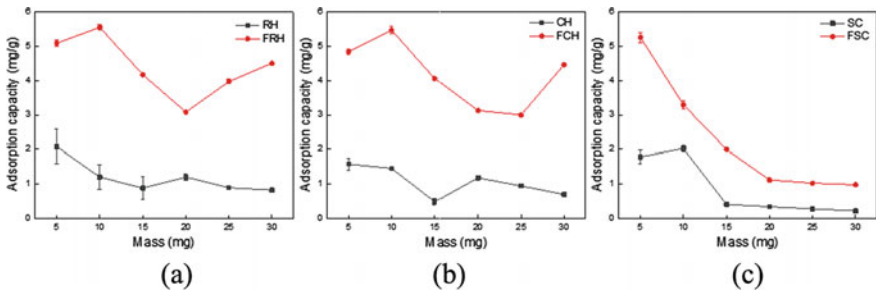

Fig. 4 Effect of adsorbent dosage on adsorption of RhB on **a** RH and FRH, **b** CH and FCH, **c** SC and FSC

is comparatively high in FRH than RH at all the adsorbent dosages. At higher adsorbent weights like 20, 25, 30 mg, efficiency drastically increases in FRH compared to RH of which efficiency is almost the same. This could be attributed to the fact that high concentration of functional groups have been created on the adsorbent surface during functionalization exposing enough adsorption sites to the adsorbates. But in RH only the weight of the mass was increased and the functionalities has not proportionally increased resulting same removal efficiencies. However, the adsorbent capacity of both RH and FRH do not have a particular trend. The increase in adsorption capacity of FRH from 5 to 10 mg resulted due to the strong driving force and high surface area. Adsorption capacity of FRH decreases with increasing adsorbent dosage from 10 to 20 mg because there is a less commensurate increase in adsorption with the rise in the adsorbent dosage. On further increment of adsorbent weight from 20 to 30 mg adsorption capacity increases slowly due to the available high concentration of functional groups introduced and due to the predominant adsorption, and intraparticle diffusion taking place simultaneously [16, 33]. Above described net behavior of removal efficiency and adsorption capacity was also observed with CH and FCH as given in the Fig. 4b. However, in SC and FSC a different behavior was observed as shown in the Fig. 4c. Adsorption capacity of SC increases from 5 to 10 mg but drastically decreases from 10 to 15 mg and then gradually decreases. Rise of adsorption capacity initially of SC could be attributed to the available high surface area and the strong driving force of RhB molecules as described with FRH. Decrease of adsorption capacity of SC afterwards and totally in FSC with increasing weight of the adsorbent could be due to the agglomeration of the adsorbent particles reducing the surface area and covering of the adsorption sites [9]. Efficiency of both FSC and SC initially increases when weight of the adsorbent increase from 5 to 10 mg and then decreases from 10 to 20 mg. Efficiency of SC generally remain constant afterwards while that of FSC increases again. A clear increasing trend of efficiency with increasing weight of both SC and FSC was not observed because the reduction in the concentration of RhB in the solution varies which could be due to the irregularity of the functional groups distribution on the adsorbent surface, adsorbent particles agglomeration, disordered nature of the porous system, challenges in transport of RhB to the adsorbate surface etc.

3.1.6 Effect of Initial Dye Concentration

The effect of variation in the initial dye concentration of RhB (5–20 mg/L) was carried out using 30 mg of the adsorbent for 60 min. The data indicate that the adsorption capacity decreases with increasing concentration of RhB in all adsorbents as given in the Fig. 5. At lower concentrations, the ratios of RhB molecules to the available adsorption sites and the surface area were low, resulting high adsorption capacity [35, 40]. But at higher concentration available adsorption sites become limited reducing the adsorption. Adsorption capacity decreases with increasing RhB concentration because with increasing concentration the amount of RhB adsorbed decreases though the weight of the adsorbent is constant.

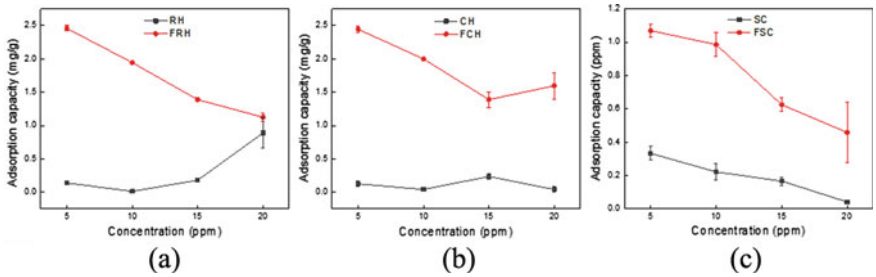

Fig. 5 Effect of initial dye concentration on adsorption of RhB on **a** RH and FRH, **b** CH and FCH, **c** SC and FSC

Adsorption capacity of RH increased at higher concentrations. It is only the carbon component get functionalized with nitric acid treatment and not the silica component of RH normally. So introduced adsorption sites to carbon become the limiting factor in RhB adsorption at increasing concentrations of RhB on FRH only and not in RH. Once the RhB molecules adsorb to the surface of the FRH the surface get crowded from the bulky RhB molecules restricting the penetration of unadsorbed RhB molecules to the deep active sites present in the porous structure. However, in RH as the surface is not functionalized the surface will be much available facilitating the penetration of RhB molecules to the porous structure of both carbon and silica. At increasing RhB concentrations comparatively high amount of RhB get adsorbed to the adsorbent than the lower concentrations in RH than FRH due to easy access of the mesoporous structure of silica. So with increasing RhB concentrations studied, adsorption capacity of FRH decreases but that of RH increases. This behavior was only observed in RH/FRH adsorbent system because they are two component systems. In single component adsorbents studied, adsorbents of which the surface is not functionalized, CH and SC also behave in the same way that their functionalized counterpart, FCH and FSC. It is important to note that the micropore structure mainly contributes to the adsorption process but the adsorbate molecule should be small enough to reach the micropores. The molecule size of RB is about 1.8 nm and the micropore diameter is less than 2 nm [15]. Therefore, micropore structure is not accessible to RhB molecules and they tend to adsorb to mesopore structure. When the porous structure of RH is considered as it has two components, carbon and silica, micropores are present only in the carbon matrix and mesopores are present in both components. As CH and SC are single component adsorbents the micropores and mesorpores of carbon contribute to the adsorption process. But for a constant weight, carbon and silica of RH contributes while only carbon is accountable for the weight of CH and SC. So all together the porous structure naturally available and introduced functional groups contribute to the adsorption process.

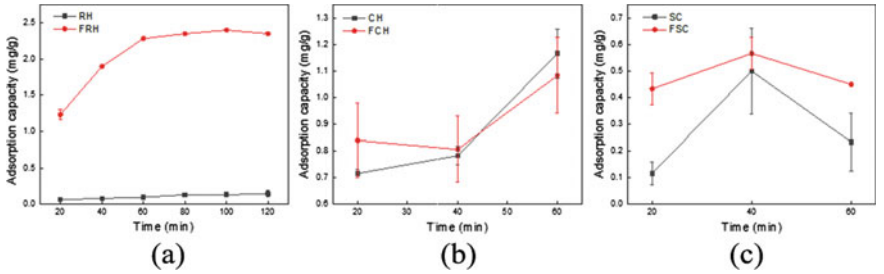

Fig. 6 Effect of initial dye concentration on adsorption of RhB on **a** RH and FRH, **b** CH and FCH, **c** SC and FSC

3.1.7 Effect of Contact Time

RH and FRH were subjected to determine the effect of time on adorption. As shown in the Fig. 6 adsorption capacity of FRH increases with time up to 60 min followed by constant behavior after that. Behaviour of RH is similar to FRH though the adsorption capacity is very low compared to FRH. As the equilibrium of adsorption has reached in 60 min in FRH and RH, other porous materials were also subjected to the same conditions for one hour. FCH and CH and FSC and SC showed fluctuating adsorption during this time period.

3.1.8 Reusability Study

The reusability of the functionalized adsorbents (FRH, FCH and FSC) were evaluated by using the same amount of functionalized adsorbent for three cycles of adsorbtion of RhB at the same experimental conditions. Adsorbent was washed with ethanol and distilled water to remove any loosely bound RhB molecules. Figure 7 shows the reusability of the functionalized adsorbents. It could be clearly seen that the adsorption capacity decreases with the number of the cycle used. This could

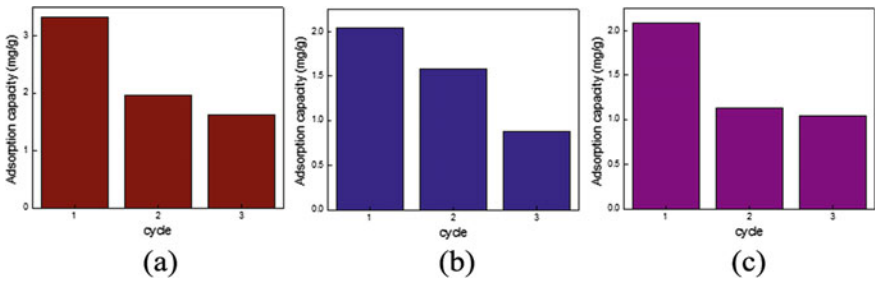

Fig. 7 Reusability of adsorbents on adsorption of RhB on **a** RH and FRH, **b** CH and FCH, **c** SC and FSC

be due to the fact that the adsorption has occur through both chemisorption and physisorption where monolayer of RhB molecules have adsorb to the adsorbent surface through chemisorption and subsequently monolayers of RhB molecules adsorb onto the existing layers via physisorption. Upon washing with distilled water and ethanol physisorbed RhB molcules have washed off. Adsorption capacity has dramatically dropped in the second cycle of all three functionalized adsorbents. This could be because physisorbed RhB molecules remove when the adsorbents are washed with distilled water and ethanol and the chemisorbed molecules are not. So the chemisorbed molecules from the first cycle remains on the adsorbent and on subsequent cycles RhB molecules adsorb only via physisorption. Especially in FRH and FSC the adsorption capacity at the second and third cycles is almost the same with a slight reduction supporting the hypothesis. However, in FCH adsorption capacity keep decreasing.

4 Conclusions

This work compared the adsorption of a dye RhB onto different carbon based adsorbents originated from two different waste materials, rice husk and coconut husk, and porous carbon synthesized by resorcinol formaldehyde polymerization. All the adsorbents were functionalized with nitric acid. Adsorption was determined as a function of pH, amount of adsorbent dose, concentration and contact time. From the results it has been concluded that, all the natural and synthetic adsorbents were effective in removing RhB, while the functionalized adsorbents were much more effective compared to the untreated adsorbents. Functionalized rice husk was much more effective than all other adsorbents and adsorbents derived from natural waste materials were comparatively more effective than the synthetic porous carbon.

Acknowledgements The authors are grateful to Sri Lanka Institute of Nanotechnology for performing the Scanning electron microscopic analysis.

Declaration of Interest The authors declare that they have no competing interests.

References

1. Aboulhassan MA et al (2006) Improvement of paint effluents coagulation using natural and synthetic coagulant aids. J Hazard Mater 138(1):40–45. https://doi.org/10.1016/J.JHAZMAT.2006.05.040
2. Ahmed MN, Ram RN (1992) Removal of basic dye from waste-water using silica as adsorbent. Environ Pollut 77(1):79–86. https://doi.org/10.1016/0269-7491(92)90161-3
3. Banerjee S et al (2017) Adsorption characteristics of alumina nanoparticles for the removal of hazardous dye, orange G from aqueous solutions. Arab J Chem. https://doi.org/10.1016/J.ARABJC.2016.12.016

4. Bharathi KS, Ramesh ST (2013) Removal of dyes using agricultural waste as low-cost adsorbents: a review. Appl Water Sci 3(4):773–790. https://doi.org/10.1007/s13201-013-0117-y
5. Bhatnagar A, Jain AK (2005) A comparative adsorption study with different industrial wastes as adsorbents for the removal of cationic dyes from water. J Colloid Interface Sci 281(1):49–55. https://doi.org/10.1016/J.JCIS.2004.08.076
6. Bhattacharyya KG, Sharma A (2004) Azadirachta indica leaf powder as an effective biosorbent for dyes: a case study with aqueous Congo Red solutions. J Environ Manage 71(3):217–229. https://doi.org/10.1016/J.JENVMAN.2004.03.002
7. Chakrabarti S, Dutta BK (2004) Photocatalytic degradation of model textile dyes in wastewater using ZnO as semiconductor catalyst. J Hazard Mater 112(3):269–278. https://doi.org/10.1016/J.JHAZMAT.2004.05.013
8. Chen A et al (2016) Synthesis of mesoporous carbon nanospheres for highly efficient adsorption of bulky dye molecules. J Mater Sci 51(14):7016–7028. https://doi.org/10.1007/s10853-016-9991-7
9. Crundwell FK (2014) The mechanism of dissolution of minerals in acidic and alkaline solutions: Part II application of a new theory to silicates, aluminosilicates and quartz. Hydrometallurgy 149:265–275. https://doi.org/10.1016/J.HYDROMET.2014.07.003
10. Deshpande AV, Kumar U (2002) Effect of method of preparation on photophysical properties of Rh-B impregnated sol–gel hosts. J Non-Cryst Solids 306(2):149–159. https://doi.org/10.1016/S0022-3093(02)01054-2
11. Dotto GL, Pinto LAA (2011) Adsorption of food dyes onto chitosan: optimization process and kinetic. Carbohyd Polym 84(1):231–238. https://doi.org/10.1016/J.CARBPOL.2010.11.028
12. Garg V et al (2003) Dye removal from aqueous solution by adsorption on treated sawdust. Biores Technol 89(2):121–124. https://doi.org/10.1016/S0960-8524(03)00058-0
13. Geçgel Ü, Özcan G, Gürpınar GÇ (2013) Removal of methylene blue from aqueous solution by activated carbon prepared from pea shells (*Pisum sativum*). J Chem 2013:1–9. https://doi.org/10.1155/2013/614083
14. Gümüş D, Akbal F (2011) Photocatalytic degradation of textile dye and wastewater. Water Air Soil Pollut 216(1–4):117–124. https://doi.org/10.1007/s11270-010-0520-z
15. Guo Y et al (2005) Use of rice husk-based porous carbon for adsorption of Rhodamine B from aqueous solutions. Dyes Pigm 66(2):123–128. https://doi.org/10.1016/J.DYEPIG.2004.09.014
16. Gupta VK et al (2010) Equilibrium and thermodynamic studies on the adsorption of the dye tartrazine onto waste "coconut husks" carbon and activated carbon. J Chem Eng Data 55(11):5083–5090. https://doi.org/10.1021/je100649h
17. Gupta VK et al (2012) Photo-catalytic degradation of toxic dye amaranth on TiO2/UV in aqueous suspensions. Mater Sci Eng, C 32(1):12–17. https://doi.org/10.1016/J.MSEC.2011.08.018
18. Han R et al (2010) Characterization of modified wheat straw, kinetic and equilibrium study about copper ion and methylene blue adsorption in batch mode. Carbohyd Polym 79(4):1140–1149. https://doi.org/10.1016/J.CARBPOL.2009.10.054
19. Hao G-P et al (2011) Structurally designed synthesis of mechanically stable Poly(benzoxazine-co-resol)-based porous carbon monoliths and their application as high-performance CO_2 capture sorbents. J Am Chem Soc 133(29):11378–11388. https://doi.org/10.1021/ja203857g
20. Hao OJ, Kim H, Chiang P-C (2000) Decolorization of wastewater. Crit Rev Environ Sci Technol 30(4):449–505. https://doi.org/10.1080/10643380091184237
21. Huang C-H et al (2011) Adsorption of cationic dyes onto mesoporous silica. Microporous Mesoporous Mater 141(1–3):102–109. https://doi.org/10.1016/J.MICROMESO.2010.11.002
22. Hunger K, Gregory P, Miederer P, Berneth H, Heid C, Mennicke W (2002) Important chemical chromophores of dye classes. Ind Dye 13–112. https://doi.org/10.1002/3527602011.ch2
23. Kannan N, Sundaram MM (2001) Kinetics and mechanism of removal of methylene blue by adsorption on various carbons—a comparative study. Dyes Pigm 51(1):25–40. https://doi.org/10.1016/S0143-7208(01)00056-0

24. Kant R, Kant R (2012) Textile dyeing industry an environmental hazard. Nat Sci 04(01):22–26. https://doi.org/10.4236/ns.2012.41004
25. Kasperchik VP, Yaskevich AL, Bil'dyukevich AV (2012) Wastewater treatment for removal of dyes by coagulation and membrane processes. Pet Chem 52:545–556. https://doi.org/10.1134/S0965544112070079
26. Khodaie M et al (2013) Removal of methylene blue from wastewater by adsorption onto $ZnCl_2$ activated corn husk carbon equilibrium studies. J Chem 2013:1–6. https://doi.org/10.1155/2013/383985
27. Liang C, Dai S (2009) Dual phase separation for synthesis of bimodal meso-/macroporous carbon monoliths. Chem Mater 21(10):2115–2124. https://doi.org/10.1021/cm900344h
28. Malik PK (2004) Dye removal from wastewater using activated carbon developed from sawdust: adsorption equilibrium and kinetics. J Hazard Mater 113(1–3):81–88. https://doi.org/10.1016/J.JHAZMAT.2004.05.022
29. Mane VS, Deo Mall I, Chandra Srivastava V (2007) Kinetic and equilibrium isotherm studies for the adsorptive removal of Brilliant Green dye from aqueous solution by rice husk ash. J Environ Manage 84(4):390–400. https://doi.org/10.1016/J.JENVMAN.2006.06.024
30. Mohammadi M et al (2010) Removal of Rhodamine B from aqueous solution using palm shell-based activated carbon: adsorption and kinetic studies. J Chem Eng Data 55(12):5777–5785. https://doi.org/10.1021/je100730a
31. Namasivayam C, Kavitha D (2002) Removal of congo red from water by adsorption onto activated carbon prepared from coir pith, an agricultural solid waste. Dyes Pigm 54(1):47–58. https://doi.org/10.1016/S0143-7208(02)00025-6
32. Popli S, Patel UD (2015) Destruction of azo dyes by anaerobic–aerobic sequential biological treatment: a review. Int J Environ Sci Technol 12(1):405–420. https://doi.org/10.1007/s13762-014-0499-x
33. Raghuvanshi S, Singh R, Kaushik CP, Raghav A (2004) Kinetics study of methylene blue dye bioadsorption on baggase, Epa.Niif.Hu. (n.d.). http://epa.niif.hu/02500/02583/00003/pdf/EPA02583_applied_ecology_2004_02_035-043.pdf (accessed October 6, 2019)
34. Ramuthai S et al (2009) Rhodamine B adsorption-kinetic, mechanistic and thermodynamic studies. E-J Chem 6(s1):S363–S373. https://doi.org/10.1155/2009/470704
35. Rangabhashiyam S et al (2015) Biosorption potential of a novel powder, prepared from *Ficus auriculata* leaves, for sequestration of hexavalent chromium from aqueous solutions. Res Chem Intermed 41(11):8405–8424. https://doi.org/10.1007/s11164-014-1900-6
36. Shokri B, Firouzjah MA, Hosseini SI (2009) FTIR analysis of silicon dioxide thin film deposited by metal organic-based PECVD. In: Proceeding 19th International Plasma Chemical Society 1–4. https://www.ispc-conference.org/
37. Sivaraj R, Namasivayam C, Kadirvelu K (2001) Orange peel as an adsorbent in the removal of Acid violet 17 (acid dye) from aqueous solutions. Waste Manage 21(1):105–110. https://doi.org/10.1016/S0956-053X(00)00076-3
38. Smith B (2018) Infrared spectral interpretation: a systematic approach. https://content.taylorfrancis.com/books/download?dac=C2006-0-03642-5isbn=9780203750841format=googlePreviewPdf (accessed October 15, 2019)
39. Sumathi S et al (2010) Selection of best impregnated palm shell activated carbon (PSAC) for simultaneous removal of SO_2 and NOx. J Hazard Mater 176(1–3):1093–1096. https://doi.org/10.1016/J.JHAZMAT.2009.11.037
40. Thakur A, Kaur H (2017) Response surface optimization of Rhodamine B dye removal using paper industry waste as adsorbent. Int J Ind Chem 8(2):175–186. https://doi.org/10.1007/s40090-017-0113-4
41. Thambiliyagodage CJ, Cooray VY, Perera IN, Wijesekera RD (2020) Eco-friendly porous carbon materials for wastewater treatment. In: Springer, Singapore, pp. 252–260. https://doi.org/10.1007/978-981-13-9749-3_23
42. Vlyssides A et al (2000) Testing an electrochemical method for treatment of textile dye wastewater. Waste Manage 20(7):569–574. https://doi.org/10.1016/S0956-053X(00)00028-3

43. Wang S, Li H, Xu L (2006) Application of zeolite MCM-22 for basic dye removal from wastewater. J Colloid Interface Sci 295(1):71–78. https://doi.org/10.1016/J.JCIS.2005.08.006
44. Yagub MT et al (2014) Dye and its removal from aqueous solution by adsorption: a review. Adv Coll Interface Sci 209:172–184. https://doi.org/10.1016/J.CIS.2014.04.002
45. Yu J-X et al (2009) Polymer modified biomass of baker's yeast for enhancement adsorption of methylene blue, rhodamine B and basic magenta. J Hazard Mater 168(2–3):1147–1154. https://doi.org/10.1016/J.JHAZMAT.2009.02.144
46. Zhang G et al (2008) The surface analytical characterization of carbon fibers functionalized by H_2SO_4/HNO_3 treatment. Carbon 46(2):196–205. https://doi.org/10.1016/J.CARBON.2007.11.002

Modified Sawdust in Adsorption of Heavy Metals from Textile Effluent

W. A. G. T. N. Gunawardhana, W. S. M. S. K. Wijerathna, W. C. T. K. Gunawardana, and K. Kawamoto

Abstract Cr(III) adsorption from textile industrial effluent was studied with the aim of contributing towards achieving targets of SDG 6 (Sustainable Development Goals). Highly toxic effluent discharge from textile industries cause the majority of the pollution of waterways which is due to the unaffordability of the existing effluent treatment techniques. Proven efficiency of modified sawdust to adsorb heavy metals could be a sustainable solution as an abundantly available industrial byproduct of sawdust. Biochar derived from sawdust by pyrolizing at 400 °C was further modified using 0.1M KOH or 0.1M H_2O_2 solutions separately. Batch experiments conducted using synthetic Cr(III) aqueous solution in neutral pH condition indicated an equilibrium contact time of 1 h with optimum initial Cr(III) concentration of 5 mg/L with 1 and 2 g of adsorbent dosages for KOH and H_2O_2 modified biochars respectively under single solute system. Further competitive Cr(III) adsorption with the presence of Cu(II) and Zn(II) were examined through batch studies. Results indicated that Cr(III) adsorption was favored in pH base range when examined under multi-metal system along with Cu(II) and Zn(II). Adsorption capacities were increased with the physical and chemical modifications. The physical characterization carried out using Specific Surface Area (SSA) analysis showed a 97.9% increase of SSA when raw sawdust was modified into biochar. KOH and H_2O_2 modifications had further increased the SSA of biochar by 37.8% and 51.5% respectively. X-ray Powder Diffraction (XRD) analysis confirmed the removal of impurities in adsorbents after physical and chemical modifications while the Point of Zero Charge (pH_{pzc}) analysis established the favorability of using a neutral pH in the solution media. Heavy metal removal percentages were observed as 97.5 and 94.1% for KOH modified biochar and H_2O_2 modified biochar under optimum conditions. Findings suggest that the higher SSA and stability of the added functional groups lead the KOH modification to sawdust derived biochar to be an efficient, environmental friendly adsorbent which could be used in treatment of heavy metals in industrial effluent. Further chemical

W. A. G. T. N. Gunawardhana · W. S. M. S. K. Wijerathna · W. C. T. K. Gunawardana (✉)
Department of Civil Engineering, Faculty of Engineering, University of Peradeniya, Peradeniya, Sri Lanka
e-mail: chandimag@pdn.ac.lk

K. Kawamoto
Graduate School of Science and Engineering, Saitama University, Saitama, Japan

R. Dissanayake et al. (eds.), *ICSBE 2020*, Lecture Notes in Civil Engineering 174,
https://doi.org/10.1007/978-981-16-4412-2_47

characterizations using SEM and FTIR analyses could be recommended to evaluate the surface properties of the adsorbents.

Keywords Adsorption · Sawdust · Biochar · Physical and chemical modification · Heavy metal

1 Introduction

Due to the evolvement of industries all over the world, contamination of receiving water bodies by industrial wastewater discharges has become a serious issue. Among the various types of toxic compounds released by the industries, heavy metals cause significant threat to the living beings as well as to the environment because of their non-biodegradability. At higher concentrations, Cr(III) is a potential toxic metal. Industrial effluent from metal plating, tanning, rubber, photography, pigment manufacturing, textile and electro plating industries contain high concentrations of Cr(III) and other heavy metal compounds [5], which need to be treated before releasing to the environment. Among the available technologies to treat heavy metal contaminated wastewater, adsorption process has gained much attention recently due to its economic viability as well as the high affinity of heavy metal ions to available organic adsorbents [1]. Bio adsorbents such as sawdust and biochar can be used as effective adsorbents due to their proven efficiency.

In order to enhance the adsorption ability of biochar, it can be modified chemically using acids, bases, chemical oxidation, organic solvents and surfactants [6, 7]. Though there are lots of studies carried out to investigate the efficiency of low-cost adsorbents to treat heavy metal contaminated wastewater, most of them have used either raw adsorbents or physically/chemically modified adsorbent. Only a limited number of researches have been carried out using both physico-chemical modifications to adsorbents. Therefore, in present study a series of modifications were done to sawdust to develop different adsorbent materials. In this context, raw sawdust was used as an adsorbent and a physical modification to sawdust (biochar) was carried out followed by a chemical modification to biochar (KOH/H_2O_2). Moreover, Cr(III) is not widely studied for single and competitive metal adsorption with the presence of Zn(II) and Cu(II). Therefore, it was also intended to study in this research. Hence, the objectives of this research were to modify and characterize sawdust as an adsorbent, to investigate the efficiency of raw and modified sawdust in removal of Cr(III) from aqueous solutions and to investigate the efficiency of competitive adsorption of Cr(III) with presence of Zn(II) and Cu(II).

2 Materials and Methods

Locally available sawdust was collected from a saw mill, was sieved, and the particle size under 1.18 mm was used for experiments after washing several times with distilled water and drying at 44 °C for 24 h (RSD).

Pre-processed sawdust was pyrolized in a muffle furnace with presence of N_2 at 400 °C for 2 h to produce biochar. The pyrolized material was then washed thoroughly with distilled water, was dried and sieved to obtain biochar with particle size smaller than 150 μm (BC).

Biochar was then chemically modified using KOH base solution [9]. 25 g of prepared biochar was mixed with 250 ml of 0.1 M KOH solution and was stirred at 150 rpm for 5 h at 65 °C. Then, the base modified biochar (BBC) was obtained by filtering, washing and finally drying the residue for 24 h at 60 °C.

The oxidation modification was done by mixing 37.5 g of prepared biochar with 250 mL of 0.1M H_2O_2 solution. Then, it was stirred at 110 rpm for 2 h at room temperature. After that, the mixture was filtered and rinsed several times with distilled water and oven dried overnight at 80 ºC to obtain oxidation modified biochar (OBC). A similar method was used by Xue et al. [11] in their study.

The stock solutions of 500 mg/L were prepared for Cr(III), Cu(II) and Zn(II) by dissolving the $Cr(NO_3)_3 \cdot 3H_2O$, $Cu(NO_3)_2 \cdot 3H_2O$ and $Zn(NO_3)_2 \cdot 6H_2O$ solutions in distilled water. Required adsorbate samples for batch experiments were then prepared by dilution of stock solutions with distilled water. pH of the solution was adjusted to desired values by adding 0.1M NaOH and 0.1M HNO_3. All the chemical compounds used in the study were of analytic grade.

Batch experiments were carried out to investigate the metal sorption behaviour of the four adsorbents in a single solute system with Cr(III) and in a competitive solute system having Cr(III), Cu(II) and Zn(II).

First, effect of contact time for adsorption behavior was investigated for all the four adsorbents namely: RSD, BC, BBC and OBC for 2 h. Synthetic wastewater samples were mixed with adsorbent samples and shaken for 2 h. BBC and OBC were further investigated by varying pH (2–10), initial Cr(III) concentration (0.5–20 mg/L) and adsorbent dosage (0.5–5 g/L). All the experiments were carried out at room temperature and after the experiments supernatants were analyzed for final heavy metal concentrations using Atomic Adsorption Spectrometer (AAS) after filtering by 0.45 μm filter papers. Removal efficiencies were obtained using Eq. (1) and the adsorption capacities were obtained using Eq. (2).

$$Removal\ Efficiency(\%) = \frac{(C_i - C_f) * 100}{C_i} \tag{1}$$

$$Adsorption\ capacity(\mathrm{mg/g})q = \left(C_i - C_f\right) * \frac{V}{m} \tag{2}$$

where C_i and C_f are the initial and final Cr(III) concentrations (mg/l), V is the volume of the solution (L) and m is the weight (g) of the adsorbent used in experiment respectively.

Physical properties of adsorbents were analyzed using Brunauer–Emmett–Teller (BET) analyzer and X-Ray Powder Diffraction (XRD) method. Point of zero charge (pH_{PZC}) values of adsorbents were identified using the method described in Bakatula et al. [2].

3 Results and Discussion

3.1 Physical and Chemical Characterization of Adsorbents

Specific surface area (SSA) analysis of all the adsorbents were done using Brunauer–Emmett–Teller theory. SSA values of 0.859, 1.700, 2.343 and 2.575 m^2/g were obtained for RSD, BC, BBC and OBC respectively. It was observed that the SSA of RSD nearly doubled when transforming into biochar. Chemical modification to biochar by KOH had increased the specific surface area by 38% and H_2O_2 modification had increased surface area by 51%. Thus as expected, the pyrolysis process would have improved pore structure and textural features of the biochar and further surface chemical modifications would have increased SSA of biochar through oxidation and base modification.

X-Ray diffraction analysis showed (Fig. 1), considerable number of peaks were disappeared and/or reduced by the physical and chemical modifications. BBC shows only two peaks ($2\theta = 14.901°, 24.273°$) and OBC showed three peaks ($2\theta = 14.899°$, 24.302°, 38.167°). It was observed that 14.9° and 24.3° peaks were common in all adsorbent surfaces which could be due to impurities such as SiO_2 and $CaCO_3$ [8]. Moreover, it was observed that chemical modifications reduced the number of peaks in the XRD patterns which could be a result of the reduction of impurities in biochar [4] while parts of impurities such as SiO_2 and $CaCO_3$ were still left.

The pH of the point of zero charge of the adsorbent depends on the properties of functional groups on the adsorbent surface. In this study, point of zero charge

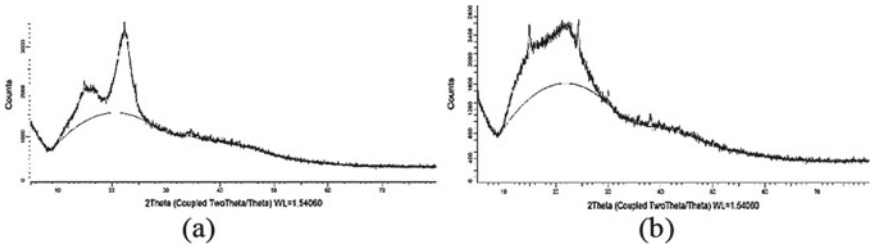

Fig. 1 X-ray diffractogram of **a** RSD, **b** OBC

determination experiments were carried out for all the four adsorbents within 2–11 pH range. Obtained results for the point of zero charge values were 5.32, 5.06, 6.19, 5.30 for RSD, BC, BBC and OBC respectively. Therefore, the batch experiments were conducted at neutral pH (which is a higher pH value than the pH_{PZC} values) to ensure a negatively charged surface of adsorbent to favor adsorption by electrostatic attraction between adsorbent and the cationic ions in the solution.

3.2 Batch Experiments for Single Heavy Metal System

3.2.1 Effect of Contact Time on Cr(III) Adsorption

Figure 2 shows the profiles obtained for four adsorbents namely; RSD, BC, BBC and OBC for adsorption of Cr(III). All the experiments were carried out for a 5 mg/L concentration of Cr(III) and 2 g/L adsorbent mass and in neutral pH. The adsorption of Cr(III) was increased with increasing contact time.

As shown in Fig. 2, the adsorption rate initially increased rapidly, and the optimum removal was reached around 60 min for all the adsorbents with removal efficiencies of 87, 83, 71 and 70% for OBC, BC, RSD and BBC respectively. The higher removal efficiencies obtained for BC and OBC mainly related with the increase in specific surface area due to the physical modification and the surface chemical characteristics improvement due to the chemically modified biochars.

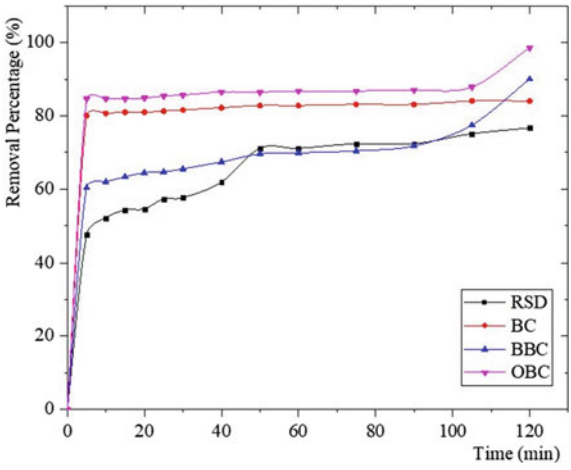

Fig. 2 Effect of contact time on Cr(III) adsorption [adsorbent dosage 2 g/L, initial Cr(III) concentration 5 mg/L, pH 7]

3.2.2 Effect of pH on Cr(III) Adsorption

The effect of pH on the adsorption of Cr(III) by the chemically modified biochars (BBC and OBC) were investigated at initial pH ranging from 2 to 10. The pH of the solution was clearly an important parameter that affects the adsorption process. The maximum Cr(III) removal percentage of 96.2% for BBC was observed within 6–8 pH. For OBC, the maximum removal percentage of 97.7% was obtained within 7–8 pH. This indicates that at neutral pH range, both BBC and OBC are effective in removing Cr(III).

3.2.3 Effect of Initial Concentration on Cr^{3+} Adsorption

For BBC and OBC, the maximum Cr(III) removal percentages of 87 and 96% were observed at 5 mg/L initial concentration respectively. Reduction in adsorption was identified with further increase in the initial concentration. This can be explained by the fact that at higher concentrations, when the number of competing ions to adsorb into the available charge sites increase, lack of active sites on the adsorbent surface lead to a decreased adsorption [3].

3.2.4 Effect of Adsorbent Dosage on Cr(III) Adsorption

Figure 3 shows that adsorption increases with increasing adsorbent dosage, to a maximum at 1 g/L (removal percentage 97.5%) for BBC and at 2 g/L (removal percentage 94.1%) for OBC. These results suggest that the relationship between adsorbent dosage and removal efficiency was related to increases in the specific surface area and number of adsorption sites with increasing adsorbent dosage.

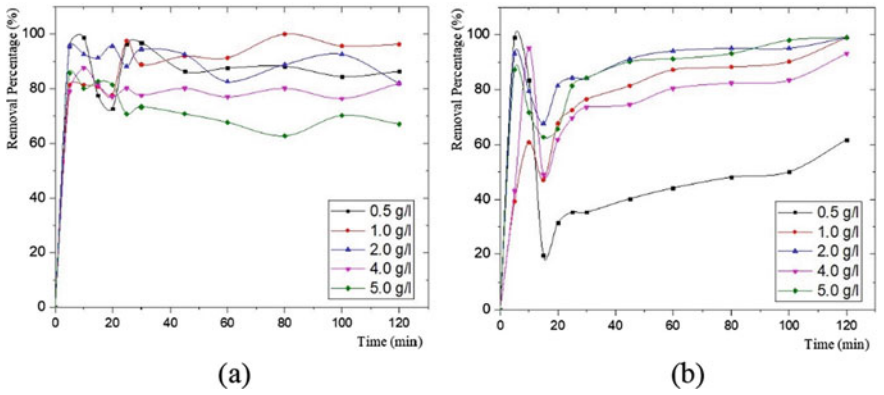

Fig. 3 Effect of adsorbent dose on Cr(III) adsorption [For **a** BBC, **b** OBC; Initial Cr(III) concentration 5 mg/L, pH 7]

Table 1 Optimum contact time, removal efficiency and adsorption capacities of the adsorbents in competitive metal adsorption experiment

Adsorbent	Optimum contact time (min)	Removal efficiency (%)		Adsorption capacity, q (mg/g)
Raw sawdust (RSD)	60	Cr(III)	80.0	0.77
		Cu(II)	88.4	0.55
		Zn(II)	91.6	0.97
Biochar (BC)	120	Cr(III)	10.3	0.03
		Cu(II)	18.8	0.04
		Zn(II)	6.80	0.01
KOH modified biochar (BBC)	120	Cr(III)	23.4	0.09
		Cu(II)	61.8	0.07
		Zn(II)	78.7	0.14
H_2O_2 modified biochar (OBC)	120	Cr(III)	9.8	0.04
		Cu(II)	9.7	0.02
		Zn(II)	55.7	0.14

3.3 Batch Experiments for Competitive Heavy Metal System

The behavior of Cr(III) adsorption in a competitive system was investigated using a solution containing Cu(II) and Zn(II). In these experiments fixed values of initial concentrations of all the heavy metals, adsorbent dosage and the initial pH were maintained, at 5 mg/L, 2 g/L and 7 respectively. The obtained results are presented in Table 1.

Except for RSD, heavy metal adsorption reached the equilibrium within the first 120 min while RSD showed an optimum contact time of 60 min. Though the removal of three different heavy metals vary significantly, majority of adsorbents showed high selectivity for Zn(II) adsorption. This may be due to the difference in ion selectivity for various adsorbents. As investigated by Wang and Qin [10], the ion selectivity of various adsorbents depends on the properties of ions such as hydrated radius, electronegativity and softness.

4 Conclusion

This study was mainly focused on identifying the efficiency of Cr(III) removal by sawdust and sawdust derived biochars. Experiments were conducted in single heavy metal solution and competitive heavy metal condition where Cu(II) and Zn(II) were present in the solution.

According to the obtained results, the removal of Cr(III) was increased significantly for chemically modified biochar, especially in BBC. Physical modifications

had increased the specific surface area of biochar by 97.9% and KOH and H_2O_2 modifications further increased the specific surface area by 37.8% and 51.5% respectively. Point of zero charge of values of all the adsorbents were below 7 providing favorable negatively charged surface of adsorbent to attract cationic ions in the solution at neutral pH.

Considering competitive heavy metal removal by adsorbents, almost all the adsorbents showed a high selectivity for Zn(II), when it was tested in competitive metal conditions with Cr(III), Zn(II) and Cu(II) are present in the solution. Results indicate that BBC could be used effectively to remove heavy metals from textile industry effluent. Further investigations could be carried out for physical characterizations of adsorbents using FTIR and SEM analyzes.

Acknowledgements This work was supported by the Department of Civil Engineering, University of Peradeniya. We also acknowledge the Water and Society (WaSo-Asia) Project for the financial assistance provided.

References

1. Argun ME, Dursun S, Ozdemir C, Karatas M (2007) Heavy metal adsorption by modified oak sawdust: thermodynamics and Kinetics. J Hazard Mater 141:77–85
2. Bakatula EN, Richard D, Neculita CM, Zagury GJ (2017) Determination of point of zero charge of natural organic materials. Environ Sci Pollut Res 25(29)
3. Gunatilake SK (2016) Removal of Cr(III) Ions from wastewater using sawdust and rice husk bio char pyrolyzed at low temperature. Int Educ Res Found Publ 4(4):44–54
4. Huang H, Tang J, Gao K, He R, Zhao H, Werner D (2017) Characterization of KOH modified biochars from different pyrolysis temperatures and enhanced adsorption of antibiotics. R Soc Chem 7:14640–14648
5. Li Q, Zhai J, Zhang W, Wang M, Zhou J (2007) Kinetic studies of adsorption of Pb(II), Cr(IIII) and Cu(II) from aqueous solution by sawdust and modified peanut husk. J Hazard Mater 141:163–167
6. Ouafi R, Rais Z, Taleb M, Benabbou M, Asri M (2017) Sawdust in the treatment of heavy metals-contaminated wastewater. Environ Res 11(1):111–132
7. Rajapaksha AU, Chen SS, Tsang DCW, Zhang M, Vithanage M, Mandal S, Gao B, Bolan NS, Ok YS (2016) Engineered/designer biochar for contaminant removal/immobilization from soil and water: potential and implication of biochar modification. Chemosphere 148:276–291
8. Sousa FW, Sousa MJ, Oliveira IRN, Oliveira AG, Cavalcante RM, Fechine PBA, Neto VOS, de Keukeleire D, Nascimento RF (2009) Evaluation of a low-cost adsorbent for removal of toxic metal ions from wastewater of an electroplating factory. J Environ Manage 90:3340–3344
9. Trakal L, Sigut R, Sillerova H, Faturikova D, Komarek M (2014) Copper removal from aqueous solution using biochar: effect of chemical activation. Arab J Chem 7:43–52
10. Wang X, Qin Y (2005) Equilibrium sorption isotherms for of Cu^{2+}on rice bran. Process Biochem 40:677–680
11. Xue Y, Gao B, Inyang M, Zhang M, Zimmerman AR, Ro KS (2012) Hydrogen peroxide modification enhances the ability of biochar (hydrochar) produces from hydrothermal carbonization of peanut hull to remove aqueous heavy metals: batch and column tests. Chem Eng J 200(202):673–680

Assessment of Land Use/Land Cover (LULC) Changes and Urban Growth Dynamics Using Remote Sensing in Dhaka City, Bangladesh

Md. Sajib Hossain and Mafizur Rahman

Abstract Dhaka, the capital city of Bangladesh is considered one of the main economic drivers of the country that contributes a significant amount to the nation's economy. Consequently, the city failed to cope with the increasing demand for accommodation, industrial and infrastructure development, which caused rapid and haphazard development in and around the city. As land is considered a finite resource, the proper use of it should not be underestimated. As a result, understanding the growth pattern of urban areas is of immense importance in urban planning. By applying remote sensing techniques, a series of spatiotemporal changes can be observed to identify possible ecologically sensitive areas. The study identified the spatiotemporal LULC pattern and measured the built-up dynamics and the growth intensity index of Dhaka and its nearby areas within 5 km using remote sensing techniques. The supervised classification technique was applied to classify the images into six different classes namely built-up, sandfill/barren land, water-body, vegetation, wetland and agricultural land. The study suggests that over the study period the built-up and sandfill/barren land have increased by 67% and 679%. As a result of vast demand for accommodation, primarily lowlands and agricultural land around the city are sand-filled to facilitate building new satellite towns like Purbachal, Uttara 3rd phase, Jhilmil and Jalshiri. In terms of the degree of dynamism and annual intensity index, peripheral cities like Kaliganj and Bandar showed the highest degree of change in the study period, which signifies faster urbanization in those areas. This study, therefore, will help us understand the built-up dynamics especially in the peripheral regions of Dhaka city and will also help planners to make better decisions.

Keywords Remote sensing · Land use/land cover (LULC) change · Dhaka · Urbanization

Md. S. Hossain (✉) · M. Rahman
Department of Civil Engineering, Bangladesh University of Engineering and Technology, Dhaka 1000, Bangladesh

R. Dissanayake et al. (eds.), *ICSBE 2020*, Lecture Notes in Civil Engineering 174,
https://doi.org/10.1007/978-981-16-4412-2_48

1 Introduction

Bangladesh is one of the fastest-growing economies in the world and the main economic hub of the country is its capital, Dhaka. Consequently, the city has flourished as a political, educational, and cultural center that leads to high population growth, rapid urbanization and unplanned industrialization [13]. Moreover, the city produces more than one- third of the nation's GDP [14]. Currently, Dhaka is the 11th largest megacity in the world and is expected to be the 6th largest in 2030 [18]. Dhaka's urban population is growing at an estimated 4 percent each year since independence in 1971, at a time when national population growth was 2.2% [4]. This phenomenal growth is partly driven by the reclassification of rural areas into urban areas and natural urban population growth but also partly by considerable rural to urban migration [14]. In recent years, there has been an increasing number of development projects taken to solve the accommodation problem in the Dhaka City area. However, due to the lack of available lands in the central region, most of the development projects are now located at the peripheral and connecting cities like Keraniganj, Rupganj, Kaliganj, Savar etc. However, the quick-urbanized areas, which are highly influenced by human activities, have the most severe land-use changes in developing countries, and their climatic impact cannot be ignored [19]. Consequently, Land use can disrupt the surface water balance and the partitioning of precipitation into evapotranspiration, runoff, and groundwater flow [6]. So, the assessment of land use and land cover change in Dhaka city and its nearby areas have major importance for sustainable development and environmental protection. Remote sensing-the science, technology and art of obtaining information about objects from a distance—takes us well beyond the limits of human capabilities [3]. Conventional survey and mapping methods do not provide the necessary information in a timely and cost-effective manner [17]. Remotely sensed data, with their advantages in spectral, spatial, and temporal resolution, have demonstrated their power in providing information about the physical characteristics of urban areas, including size, shape, and rates of change, and have been used widely for mapping and monitoring of urban biophysical features [11]. So, the main goal of the study is to assess land use/land cover change in Dhaka and its nearby 5 km areas using remote sensing technique to find out the critical areas that need further attention.

2 Materials and Methods

2.1 Study Area

The Dhaka city area is located at the center of Bangladesh and is surrounded by four major river systems, namely the Buriganga, Turag, Tongi and Balu, which are flowing to the south, west, north and east sides, respectively [10]. The study area is located between 23° 37′ N to 23° 57′ N and 90° 17′ E to 90° 34′ E. The area is

topographically flat and the surface elevation ranges between 0 and 33 m with a mean of 9.1 m. Additionally, most urban areas are located at elevations ranging from 6 to 8 m [5]. Dhaka enjoys a fairly equitable tropical monsoon climate, with an annual average temperature of 25 °C (77°F) and monthly means varying between 18 °C (64 °F) in January and 29 °C (84 °F) in August [7] (Fig. 1).

The annual rainfall of Dhaka City varies from 1169 to 3028 mm and the annual average rainfall of 2076 mm [1]. Nearly 80% of the rainfall occurs during the monsoon season, which lasts from May to the end of September [7]. The study area is characterized by Quaternary alluvial sequences of the Madhupur tract, which is an elevated Pleistocene terrace that surrounds floodplains of the Jamuna, Ganges and Meghna rivers [2, 8].

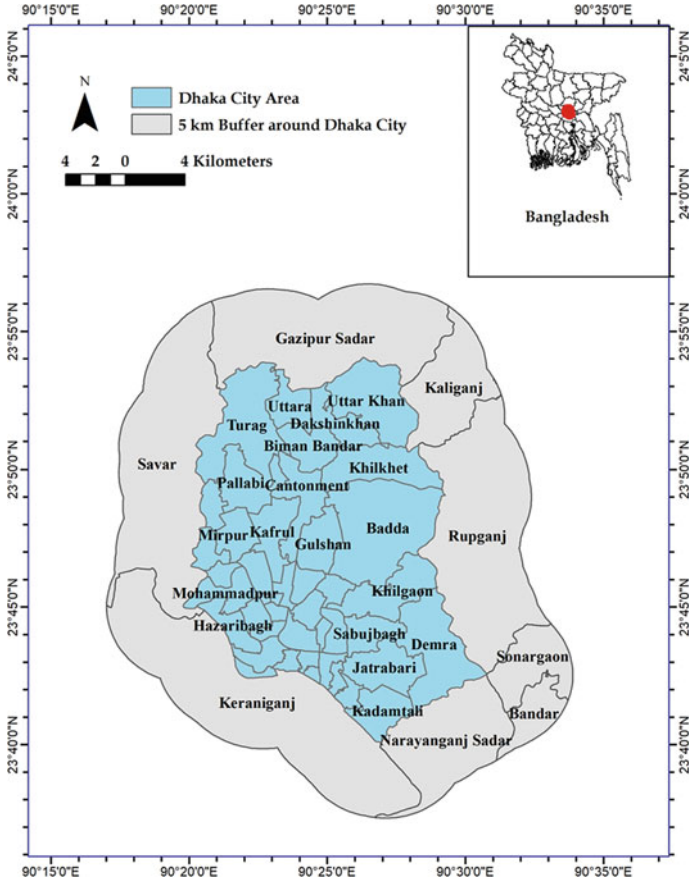

Fig. 1 Study area

Table 1 Different data used in the study

Data type	Data source
Landsat-5 TM (2000, 2010)	USGS online
Sentinel-2A (2019)	USGS online
City boundaries	UNOCHA
Digital elevation data	USGS online
Google earth image (2000–2019)	Online resource

2.2 Data Source and Method

2.2.1 Data

The study analyzed the LULC dynamics of the Dhaka city and its connecting city areas within 5 km from the periphery by remote sensing technique (Table 1).

The satellite data used for the study were downloaded from the United States Geological Survey (USGS) website that is freely available. The Landsat 2000 and 2010 data have a spatial resolution of 30 m and were acquired by the satellite on 19th January 2000 and 30th January 2010 respectively. On the other hand, the Sentinel-2A data was acquired on 19th September 2019 that has a spatial resolution of 10 m. In terms of the Dhaka city and its connecting cities shapefiles, acquired from the United Nations Office for the Coordination of Humanitarian Affairs (UNOCHA) website. To assist the LULC classification surface elevation map of 30 m resolution of the area was generated using Shuttle Radar Topography Mission (SRTM) data, acquired from the same site. Furthermore, high-resolution Google Earth images from 2000 to 2019 were considered for GPS point extraction, identifying seasonal variation, and accuracy assessment.

2.2.2 Methodology

Dhaka city area map was created from administrative data downloaded from the United Nations Office for the Coordination of Humanitarian Affairs (UNOCHA) website. Later the map was projected to Bangladesh Transverse Mercator System (BTM) coordinate system and a 5 km buffer was generated using the ArcMap 10.5 software. Data processing including geometric rectification, radiometric enhancement, image classification, class recoding and accuracy assessment were performed by Erdas Imagine 2015 software When image data is recorded by sensors on satellites it can contain errors in geometry and in the measured brightness values of the pixels [15]. Consequently, geometrical rectification was performed by 30 control points, which were evenly spread throughout the images. The first-order polynomial was applied to reproject the images into the Bangladesh Transverse Mercator System (BTM) coordinate system and the resampling was done using the nearest neighbour method. In all three cases, the root means square error (RMSE) were under 0.5 pixel.

LULC classification heavily depends on identifying objects of different classes so the brightness level and contrast of the images were adjusted. The supervised classification method was applied to classify the images into six different classes namely built-up, sandfill/barren land, water-body, vegetation, wetland and agricultural land. However, due to similar spectral response and seasonal variation, some of the pixels were misclassified. To improve the overall accuracy, the misclassified pixels were reclassified using the recode tool in ERDAS Imagine 2015 software. The kappa coefficient of the agreement is frequently used to summarize the results of an accuracy assessment used to evaluate land-use or land-cover classifications obtained by remote sensing [16]. The calculation for the kappa coefficient was executed in R open-source statistical computing and graphics software (https://www.rproject.org/).

The dynamic LULC change index compares the given LULC classes thus the index helps to detect the most dynamic LULC type and shows the degree of dynamism of each class [12]. As proposed by Zhao et al. [20] the index calculation is shown in the formula Eq. (1).

$$K = \frac{U_a - U_b}{U_a} \times \frac{1}{t} \times 100 \tag{1}$$

where, K is the rate of LULC change

U_a is area of a certain LULC type at the beginning

U_b is area of a certain LULC type at the end

t is length of time.

At the same time, the annual expansion intensity index has been calculated to find out the built- up dynamics. According to Hu et al. [9] the index value was calculated by,

$$B_{i,t+n} = \frac{U_{i,t+n} - U_{i,t}}{T} \times 100 \tag{2}$$

$B_{i,t+n}$ is the annual expansion intensity of spatial unit i

$U_{i,t+n}$ is urban area at the spatial unit i at time t + n

$U_{i,t}$ is urban area at the spatial unit i at time t

T is the land area of at the spatial unit i.

Based on Hu et al. [9] the index value classified as:

1.92—high-speed expansion,

1.05–1.92—fast speed expansion,

0.59–1.05—medium expansion,

0.59–0.28—slow speed expansion and

< 0.28 slow expansion.

3 Result and Discussion

3.1 Result

The LULC classification map for Dhaka city and its nearby areas for 2000, 2010 and 2019 were produced. The overall accuracy measured for the classification in 2000, 2010 and 2019 was 90.3%, 89.8% and 92.3% respectively and the kappa coefficient was 88.3%, 87.7% and 90.7% for those years. The spatial pattern of urban expansion reveals that notable expansion in the Dhaka city and its peripheral areas. It can be seen from Fig. 2 that the expansion is not uniform in all direction and the built-up area is expanding in the north, north-western, south and south eastern part of the study area. However core part remained unchanged as the part has seen earlier urbanization. In addition, the increase in built-up area is observed on the banks of the rivers around the city. As the rivers work a transportation network, the agricultural and wetland near the banks are converted at a faster rate.

Moreover, from the analysis, it has been observed major sandfill area in the eastern, north-western and south-eastern part of the study area. The areas can be divided into four main zone namely northern and north -eastern Dhaka city, Rupganj-Kaliganj, Keraniganj and Savar sandfill zones. Previously, the expansion happened in the northwards direction from the old Dhaka situated on the bank of Buriganga river. However, the low lands in eastern, north-eastern parts worked as a barrier to the urban expansion and the main target for the expansion was the agricultural and relatively higher elevation lands in the north. But in recent years the trend has been altered due to higher demand for land for residential projects in Dhaka city. Consequently, the low lands in Dhaka city especially in Dakshin Khan, Uttar Khan, Turag, Khilkhet, Khilgaon are converted into sand fill areas. As revealed from Fig. 2, another major landfill zone is observed in Rupganj-Kaliganj area where several satellite town namely Purbachal and Jalshiri are expected to be built-up. The same situation goes for Keraniganj as Jhilmil satellite town is one of the main reasons for landfill in the area. In addition, level of development in the area has been seen higher due to close proximity from the old Dhaka region.

However, Savar sandfill zone shows a very different kind of result. The area was heavily industrialized due to the establishment of textile industries in between 2000 and 2010 but the city lacked accommodation for middle and higher-class people. Thus, it created a vast demand for residential land, which led to the encroachment of wetland and agricultural to sand fill area (Table 2).

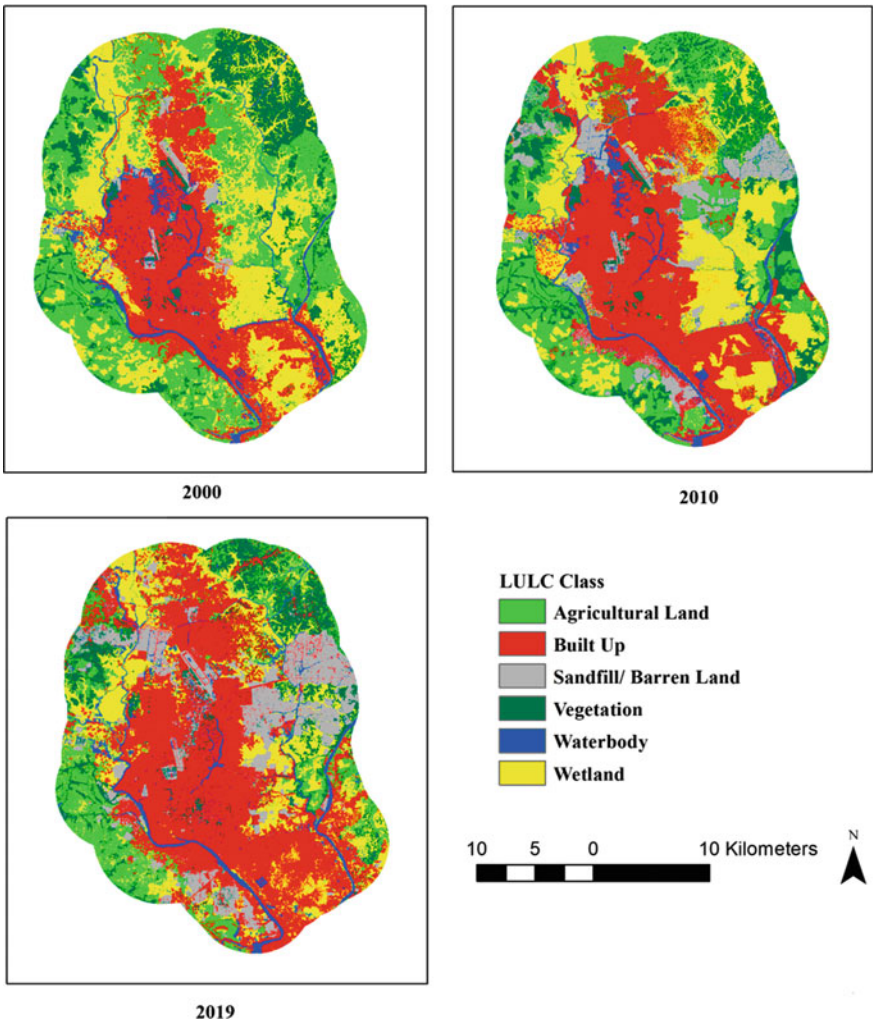

Fig. 2 Land use/land cover maps for 2000, 2010 and 2019

Table 2 Land use-land cover of the study area by year of investigation

LULC class	Area (ha)		
	2000	2010	2019
Agricultural land	18,848.79	13,623.12	7296.88
Built up	18,251.37	24,083.46	30,488.16
Water-body	3959.55	4536.54	4105.61
Sandfill/barren land	1397.43	7041.51	10,881.5
Vegetation	9660.87	9043.65	8853.77
Wetland	24,288.12	18,075.78	14,778.76

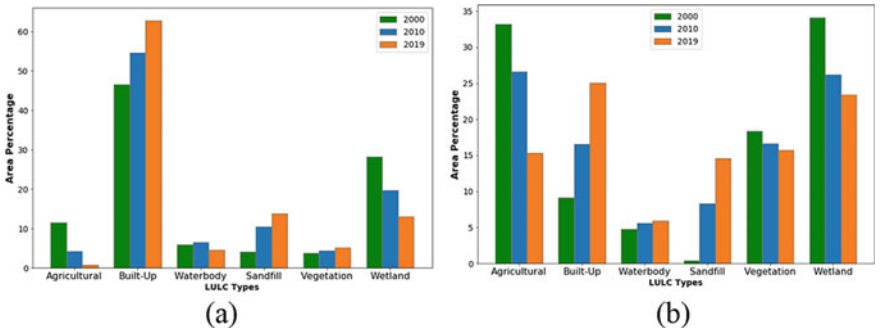

Fig. 3 LULC classification of **a** Dhaka city area, **b** Dhaka city connecting areas

It is evident from the LULC analysis that the built-up area has become the dominant land use pattern in the past nineteen years while there is a significant decrease in agricultural and lower lands. The percentage share of the built-up area was increased from 23.9% in 2000 to 31.5% in 2010 and 39.9% in 2019. In contrast, agricultural land's percentage decreased from 24.7% in 2000 to 17.8% in 2010and to only 9.6% in 2019. Additionally, the percentage of wetland decreased from 2000 to 2010 was 8.1% and from 2010 to 2019 was 4.4% (Fig. 3).

The most obvious finding to emerge from the analysis is that the built-up has become the dominant LULC pattern in 2019 in Dhaka City connecting areas whereas there is a significant reduction in agricultural and wetland.

Contrary to expectations, this study found a slight increase in vegetation in Dhaka city. This result may be explained by the fact that the LULC classification of 2019 was performed by Sentinel-2 data of 10 m pixel size, which has better accuracy in detecting vegetation cover in comparison to previous yearly Landsat data of 30 m pixel size.

3.1.1 Built-Up Dynamism and Annual Growth Intensity

The degree of urban growth dynamism and annual growth intensity index is not uniformly distributed throughout the study area. Though in the past 19 years the degree of dynamism remained the same for Dhaka city, in other peri-urban areas except Savar are very high especially in areas like Kaliganj and Bandar (Table 3).

The a typical increase in the built-up area in Kaliganj happened due to the infrastructure development and recent settlement in the Purbachal residential model town. In addition, the paved road contributes to industrial development in the area. In the case of Bandar, the transformation of low lands into brick fields has contributed to a sudden increase in the degree of dynamics and annual growth intensity index in the area. In terms of Savar, the development occurred due to the establishment of textile industries in the northern part of the area by converting mainly the area near the highway in between 2000 and 2010. However, the area was mostly developed prior

Table 3 Degree of dynamism in Dhaka city and its nearby areas

Area name	Expansion in between 2000 and 2010 (in ha)	Expansion in between 2010 and 2019 (in ha)	Degree of dynamism in 2010	Degree of dynamism in 2019
Sonargaon	132.7	146.3	10.9	6.4
Savar	886.7	185.9	20.2	1.6
Rupganj	348.3	587.2	23.9	13.2
Narayanganj	632.6	617.6	4.1	3.1
Keraniganj	700.9	1321	7.6	9.1
Kaliganj	1.7	165.8	3.8	296.5
Gazipur Sadar	747.2	645.4	7.6	4.2
Bandar	16.1	236.6	2.6	33.5
Dhaka city	2410.2	2471.9	1.7	1.7

to the year 2010, as a result the dynamism and the intensity index both are reduced significantly in recent years.

Besides, from Table 4, it can be observed that the annual growth index is quite high in all other areas. Particularly in Narayanganj where several industrial zones like Fatullah, Adamje, Kachpur were established. These industrial zones have caused a large influx of work seeker people around the country. Sonargaon, Gazipur Sadar, Rupganj and Keraniganj show similar kinds of urbanization trend.

Table 4 Annual growth intensity index for Dhaka city and its nearby areas

Area name	Annual growth intensity index in 2010	Graded intensity index in between 2000 and 2010	Annual growth intensity index in 2019	Graded intensity index in between 2010 and 2019
Sonargaon	7.9	HSE	8.8	HSE
Savar	9.4	HSE	2	HSE
Rupganj	4.3	HSE	7.2	HSE
Narayanganj	16.2	HSE	15.8	HSE
Keraniganj	6.1	HSE	11.4	HSE
Kaliganj	0.1	SE	5.9	HSE
Gazipur Sadar	9.5	HSE	8.2	HSE
Bandar	1.8	FSE	25.9	HSE
Dhaka City	8	HSE	8.2	HSE

HSE (high speed expansion), *SE* (slow expansion), *FSE* (fast speed expansion)

3.2 Discussion

The urban expansion in Dhaka city is highly influenced by the growing demand for accommodation. The rate of urbanization did not decrease in the study period, which shows a greater threat to the lowlands in the city. In recent years, the city has experienced a few urban floods and further degradation of lowlands will certainly make the current situation worse. Similarly, the peripheral cities are facing growing demands for residential and industrial development. But, if sustainable development is not ensured in these regions, in the future this may lead to a serious ecological problem in the area.

The sub-urban areas around Dhaka are largely covered with homestead vegetation. As a result, mainly in the Landsat image of 30 m spatial resolution, the small buildings could not be identified properly. Besides, the agricultural lands between them sometimes are misclassified to vegetation. Another important factor was the presence of water hyacinth and other aquatic plants in wetland and water bodies that lead to misclassifying them to vegetation. One of the major challenges to the study was to discriminate between agricultural lands and wetland also between water body and wetland as both classes pose quite similar spectral signature. Though the recode tool was used to minimize the error, in several locations, the classes may be misclassified.

4 Conclusion

To get a clear picture of urban dynamics and environmental impacts, the evaluation of urban growth and spatiotemporal changes has become increasingly important. The study examined the spatiotemporal LULC pattern and measured the built-up dynamics and the growth intensity index of Dhaka and its connected cities by remote sensing techniques. The results of this study indicate a rapid urbanization process where wetland and agricultural land are being converted to built-up land. Consequently, built-up area will emerge as the main feature of LULC in the coming days in the peripheral urban areas of Dhaka city. The built-up area increased from 23.9 to 31.5% from 2000 to 2010 and 39.9% in 2019. Besides, there is a substantial increase in the sandfill area in the study area as a 7.4% area has increased between 2000 to 2010 and 5% between 2010 to 2019. Moreover, the study found a serious reduction in ecologically sensitive wetland areas in the region. The total reduction in the wetland was 39.15% in just 19 years. In the case of agricultural land, the loss was much higher as nearly as 61.3% of land converted to other land cover classes in the same time series. This study can contribute to urban planning and proper management of land and other resources to protect the environment from further degradation by providing quantitative information for stakeholders.

References

1. Ahammed F, Hewa GA, Argue JR (2014) Variability of annual daily maximum rainfall of Dhaka, Bangladesh. Atmosp Res 137:176–182
2. Ahmed KM (1999) Dupi Tila aquifer of Dhaka: hydraulic and hydrochemical response to extensive exploitation. In: Groundwater in the urban environment: selected city profiles
3. Aronoff S (2004) Remote sensing for GIS managers
4. Baker JL (2007) Dhaka: improving living conditions for the urban poor. In: Bangladesh development series, vol 17. Available at: https://openknowledge.worldbank.org/handle/10986/2201
5. Flood Action Plan (1991) 8A (1991) Master plan study for greater Dhaka protection project. Japan International Cooperation Agency, Dhaka. Available at: https://openjicareport.jica.go.jp/pdf/11702909_06.-pdf
6. Foley JA et al (2005) Global consequences of land use. Science 309(5734):570–574
7. Hassan MM, Southworth J (2018) Analyzing land cover change and urban growth trajectories of the mega-urban region of Dhaka using remotely sensed data and an ensemble classifier. Sustainability 10(1):10
8. Hoque MM, Bala SK (2004) Vulnerability of Dhaka metropolitan area aquifer. In: Proceedings of the second APHW conference, APHW-the Asia Pacific association of hydrology and water resources, pp 419–426
9. Hu ZL, Du PJ, Guo DZ (2007) Analysis of urban expansion and driving forces in Xuzhou city based on remote sensing. J China Univ Min Technol 17(2):267–271. https://doi.org/10.1016/S1006-1266(07)60086-8
10. Ishtiaque A, Mahmud MS, Rafi MH (2015) Encroachment of canals of Dhaka City, Bangladesh: an investigative approach. GeoScape 8(2):48–64. https://doi.org/10.2478/geosc-2014-0006
11. Jensen JR, Cowen DC (1999) Remote sensing of urban/suburban infrastructure and socio-economic attributes. Photogramm Eng Remote Sens 65:611–622
12. Mohamed A, Worku H (2019) Quantification of the land use/land cover dynamics and the degree of urban growth goodness for sustainable urban land use planning in Addis Ababa and the surrounding Oromia special zone. J Urban Manag 8(1):145–158
13. Naziruzzaman M (1999) Performance of the existing sewerage system of Dhaka city and Pagla sewage treatment plant. Available at: http://lib.buet.ac.bd:8080/xmlui/handle/123456789/1873
14. Rajuk (2015) Dhaka structure plan 2016–2035. Available at: http://www.rajukdhaka.gov.bd/rajuk/image/slideshow/1./Draft/Dhaka/Structure/Plan/Report/2016-2035(Full//Volume).pdf
15. Richards JA, Jia X (1999) Remote sensing digital image analysis. Springer, Berlin
16. Stehman S (1996) Estimating the kappa coefficient and its variance under stratified random sampling. Photogramm Eng Remote Sens 62(4):401–407
17. Weng Q (2010) Remote sensing and GIS integration: theories, methods, and applications. McGraw-Hill, New York
18. World Bank (2012) Bangladesh: towards accelerated, inclusive and sustainable growth—opportunities and challenges. In: Bangladesh development series, vol 1. Available at: http://hdl.handle.net/10986/12288
19. Yao X, Wang Z, Wang H (2015) Impact of urbanization and land-use change on surface climate in middle and lower reaches of the Yangtze River, 1988–2008. Adv Meteorol
20. Zhao Y et al (2012) Examining land-use/land-cover change in the lake dianchi watershed of the Yunnan-Guizhou plateau of Southwest China with remote sensing and GIS techniques: 1974–2008. Int J Environ Res Public Health 9(11):3843–3865. https://doi.org/10.3390/ijerph9113843

Development of a Combined Electrocoagulation and Electrochemical Oxidation Reactor for Treating Service Station Effluent

B. U. Kaushalya, R. Inthushan, M. A. C. R. Mallikaarachchi, and K. G. N. Nanayakkara

Abstract Effluents generated from service stations contain several categories of pollutants such as detergents, oil and grease, organic materials, and heavy metals. Most of the literature suggests the electrochemical methods as effective and sustainable methods to treat such wastewater. This research focuses on removing total suspended solids (TSS), oil and grease (O&G), and chemical oxygen demand (COD) from both synthetic and actual service station wastewater samples by using an electrochemical cell carrying a novel anode. An aluminium anode was used to support electrocoagulation (EC), while a copper-plated graphite anode was used to support electrochemical oxidation (EO). Two separate batch reactors were tested initially for individual EC and EO efficiencies of treating the targeted pollutants for 40 min of reaction time under a current density of 30 mA/cm^2. The EO efficiencies of removing TSS, O&G, and COD were increased by 21%, 56.3%, and 29.2%, respectively, from the modification of graphite by copper-plating. The efficiency study of the combined reactor with both EC and EO anodes was carried out under two approaches, i.e., the constant current study and constant time study, in order to investigate the optimum operating conditions. TSS, O&G, and COD removal efficiencies of 100%, 100%, and 99.4% were achieved respectively under a reaction time of 60 min at a constant current density of 20 mA/cm^2 for synthetic wastewater. The efficiency study of the electrochemical cell carried out under the optimum operating conditions for actual service station effluent resulted in TSS and O&G removal of 100% and COD removal of > 99%. Therefore, the developed combined reactor carrying novel electrodes can be suggested as an efficient treatment method for the treatment of service station effluent.

Keywords Advanced oxidation · Electrochemical oxidation · Electrocoagulation · Oil and grease · Service station wastewater

B. U. Kaushalya · R. Inthushan · M. A. C. R. Mallikaarachchi · K. G. N. Nanayakkara (✉)
Department of Civil Engineering, Faculty of Engineering, University of Peradeniya, Peradeniya 20400, Sri Lanka
e-mail: kgnn@pdn.ac.lk

R. Dissanayake et al. (eds.), *ICSBE 2020*, Lecture Notes in Civil Engineering 174,
https://doi.org/10.1007/978-981-16-4412-2_49

1 Introduction

Rapid urbanisation and industrialisation have influenced the excessive waste generation all over the world in the past few decades. The water quality of surface and groundwater bodies have been adversely affected by the contamination causing due to industrial waste. These wastewaters have the potential of creating a high impact on the environment when proper treatment and management methods are not practised.

Wastewater generated from service stations contains several categories of pollutants such as detergents, oil and grease, gasoline residue, organic materials, heavy metals, acids and suspended solids which may cause severe health risks and environmental impacts [3, 6]. Several methods such as dissolved air floatation, ultrafiltration, constructed wetland and chemical treatment have been practised to treat service station effluent, and most of these methods have been reported complex, less economical, consuming larger footprint and less efficient [6, 10]. Most of the literature suggests the electrochemical treatment as a promising alternative for wastewater treatment due to its environmental compatibility, versatility, energy efficiency and cost-effectiveness.

Electrochemical water treatment consists of two main mechanisms, i.e. electrocoagulation (EC) and electrochemical oxidation (EO). An electrochemical reactor is a simple arrangement of two electrodes named anode and cathode and a current supply. EC process can be explained as the electro-dissolution of the anode, creating metallic hydroxide flocs that agglomerate within the medium to be treated [8]. The formed flocs can be removed by either sedimentation or floatation. In the EO process, either pollutant are oxidised by diffusing to the anode surface or by an oxidant generated at the anode surface [1]. Usually, aluminium, iron and stainless steel are used as sacrificial electrodes in EC processes (Kuokkanen et al. 2013) while materials such as graphite, lead dioxide, and boron-doped diamond are used for EO processes [2, 4, 7].

The majority of the previous studies on service station wastewater treatment have been incorporated with the EC process. Harinarayanan Nampoothiri et al. [5] developed a reactor setup with five parallel anodes and five parallel cathodes for the EC process. The materials used for the reactor were mild steel and aluminium, which resulted in 89 and 80.05% oil removal efficiency. A significant observation of the mentioned study was the simultaneous decrease of the chemical oxygen demand (COD) along with oil removal. In most of the studies, the EC process was focused on removing oils and COD in service station wastewater but lacked in studies related to simultaneous EC and EO processes. The focus of this research was to develop an efficient and economical reactor to remove oil and grease (O&G), total suspended solids (TSS) and COD in service station effluent.

2 Materials and Methods

2.1 Materials

In this study, aluminium (Al) plates with dimensions 50 mm × 30 mm × 1 mm were used as anodes for the EC process. Graphite rods extracted from size C alkaline batteries were used as the substrate material for anodes in the EO process. For the modification of graphite anodes, analytical grade copper sulphate and sulphuric acid and for the preparation of synthetic wastewater, distilled water, kerosene, sodium dodecyl sulphate (surfactant), analytical grade sodium chloride and grease were used. Analytical grade sodium hydroxide and sodium carbonate were used for cleaning of electrodes.

2.2 Modification of EO Anode

Initially, the graphite rods were cleaned by soaking in a 5% aqueous sodium hydroxide and 5% sodium carbonate. Subsequently, the rods were subjected to reverse current at a temperature of 70 °C to remove any impurity present on the surface. Treated graphite rods were electroplated using a 250 g/L $CuSO_4.5H_2O$ and 50 g/L H_2SO_4 solution while using a copper electrode as the anode. A cathode current density of 25 mA/cm^2 was provided for 1 h for the electroplating process while keeping 1 cm electrode distance. After that, the surface morphology of the modified and non-modified graphite electrodes were compared and analysed by scanning electron microscopy (SEM) and energy-dispersive x-ray spectroscopy (EDX) methods.

2.3 Preparation of Synthetic Wastewater

Synthetic service station wastewater was prepared using kerosine and distilled water. 50 mL of kerosene, 3 mL of sodium dodecyl sulphate and 3 g of grease were added to 1 L of distilled water which was then agitated at 300 rpm in a rotary shaker (GFL 3005 Analogue Orbital Shaker) for 15 min. Initial pH, TSS, COD and O&G were measured by portable pH meter (Sension + PH1), gravimetric determination using vacuum filtration (AMBL-105-D), dichromate COD method (HACH DR 900) and hexane gravimetry method respectively.

2.4 Experimentation

Initially, two separate reactors for EC and EO processes were tested for the removal of targeted pollutants. In the EC reactor, aluminium plates with the previously specified dimensions were used as both anode and cathode. Both modified and non-modified graphite anodes were tested for the comparison in the EO reactor while using an uncoated graphite rod as the cathode. For both EC and EO reactors, the reactor volume was 100 mL and all the experiments were carried out for 40 min reaction time at a current density of 30 mA/cm^2.

In the combined EC and EO reactor, two anodes (i.e. Al plate and modified graphite rod) were used while a non-modified graphite rod was used as the cathode. Experiments in the combined reactor were carried out considering two parameters; reaction time and current density. Initially, the current density was kept at a constant value of 20 mA/cm^2, and experiments were carried out for 30, 60, 90 and 120 min reaction times. In the second series of experiments, the reaction time was set to 60 min and carried out the reactions at different current densities of 5, 10, 15 and 20 mA/cm^2. The reactor volume was 150 mL. Finally, the developed combined reactor was tested for actual service station wastewater samples.

For EO reactor and the combined reactor, 30 mg of NaCl was added to the electrolyte to support the oxidation process. A standard laboratory DC power supply (TENMA 72-10495, 0–30 V 5 A with twin outputs) was used to supply the required current. After all the reactions, final pH, TSS, COD and O&G were measured using the previously mentioned method in Sect. 2.3.

3 Results and Discussions

3.1 SEM and EDX Analysis

SEM images of non-modified and modified graphite samples with 5000 magnification are shown in Figs. 1 and 2, respectively. Comparison of two images clearly shows that the copper particles are agglomerated on the surface, and the pore density has been reduced in the modified sample.

From the EDX spectrums, the compositions of the modified and non-modified electrodes with respect to weight and atomic percentages are compared in Table 1. It could be seen that a significant amount of copper (11.12% w/w) was deposited on the substrate surface after modification. The deposited copper was expected to support the EO process.

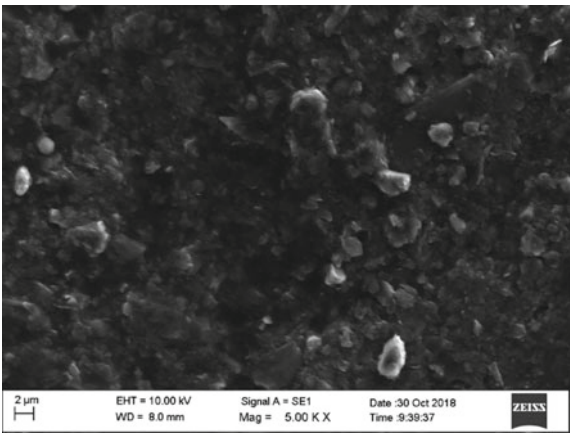

Fig. 1 SEM image of the non-modified graphite electrode

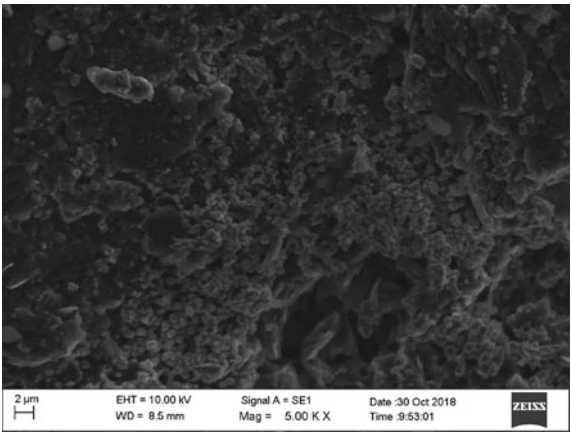

Fig. 2 SEM image of the modified graphite electrode

Table 1 Composition of the non-modified and modified graphite electrodes

Element	Non-modified graphite electrode		Modified graphite electrode	
	% w/w	% Atomic	% w/w	% Atomic
C	89.97	93.18	82.18	92.71
O	7.43	5.78	4.95	4.19
Cu	–	–	11.12	2.37
Other	2.60	1.04	1.75	0.73

3.2 Separate Reactor Study

When comparing final TSS, COD and O&G concentrations after the treatment under the conditions specified in Sect. 2.4 with the initial concentrations, all three reactors

(i.e. EO reactor with the non-modified electrode, EO reactor with the modified electrode and EC electrode) exhibited the potential of reducing the targeted parameters. However, the EC reactor alone could achieve 80.8% TSS removal, 97% of COD removal and 100% O&G removal. It could be seen that the aluminium anodes are efficient in removing the mentioned pollutants in water. It can be explained that the hydroxide complexes of Al^{3+} ions released from the anode to the medium could perform efficiently as coagulants.

When the two scenarios of EO reactor was compared, it could be clearly observed that the modified graphite anode performed better than the non-modified one. The reactor with non-modified anode could achieve removal efficiencies of 38.2%, 46.8% and 36.4% for TSS, COD and O&G respectively. With the modification of copper coating on graphite anode, a significant increment of pollutant removal was achieved, resulting 59.2% of TSS removal, 76% COD removal and 92.7% of O&G removal. The copper coating may have released copper ions which could act as oxidants and further supported EO process. The Cu^{2+} ions have the potential to reduce gaining electrons and oxidise the pollutants in the medium as per the Eq. (1). Therefore, the modification could enhance the EO performance of the anode.

$$Cu^{2+}_{(aq)} + 2e^{-} \rightarrow Cu_{(s)} \tag{1}$$

3.3 Combined Reactor Studies

The combined reactor studies were carried out in two series of experiments which were described in Sect. 2.4. From the results obtained from the separate reactor study, it could be predicted that combining the two reactors would further enhance the performance due to the integration of both EC and EO processes.

Figure 3 illustrates the variation of the removal efficiencies for targeted parameters with the reaction time at a constant current density of 20 mA/cm^2. It could be seen an enhanced removal efficiency for all the pollutants in the combined reactor when compared to the separate reactor studies. When considering O&G, it could be seen that there was no significant variation in removal efficiency with the increase of time. However, the TSS and COD removal efficiency was increased up to 60 min of reaction time, and a decrease could be observed with the increase of reaction time. As the reaction time increases, the energy supplied to the medium increases. Beyond a specific reaction time, the energy may have been sufficient to break the bonds in the flocs. Therefore, the flocs may have been dissolved back to the medium, increasing the TSS quantity. In addition, a previous study carried out by Swain et al. [9], a similar behaviour could be observed for the TSS removal with the increase of reaction time. Excessive generation of micro-bubbles with the increase of reaction time may also destabilise the flocs and reduce the removal efficiency.

Since the maximum efficiency in the constant current density study could be achieved at 60 min of reaction time, it was taken as the optimum reaction time for the

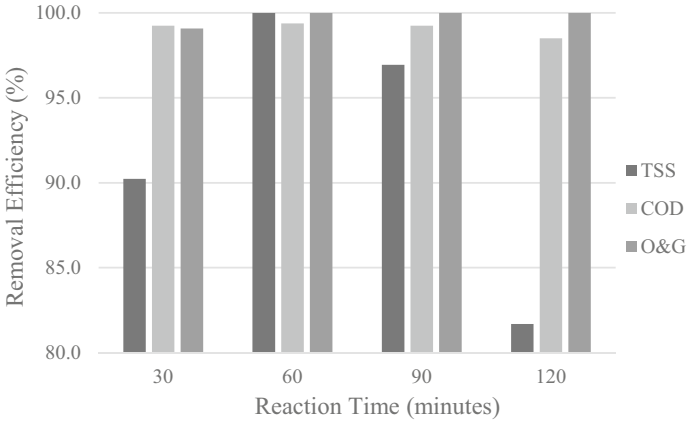

Fig. 3 TSS, COD and O&G removal efficiencies of the combined reactor with the reaction time at a constant current density of 20 mA/cm^2

constant time study. It could be seen in Fig. 4 that a less current density as 5 mA/cm^2 is sufficient to remove TSS entirely from the medium. However, COD removal efficiency was decreased with the increase of current density. That phenomenon could also be explained by the breakage of flocs due to the electric field. As per Swain et al. [9], increasing the electricity may also result in the rapid generation of microbubbles and create excessive floatation process, which may break the flocs. Although the efficiencies were high, it is essential to check the treated water quality against the discharge standards. The results of the constant current density study and the constant time study are summarised in Tables 2 and 3, respectively. The guidelines

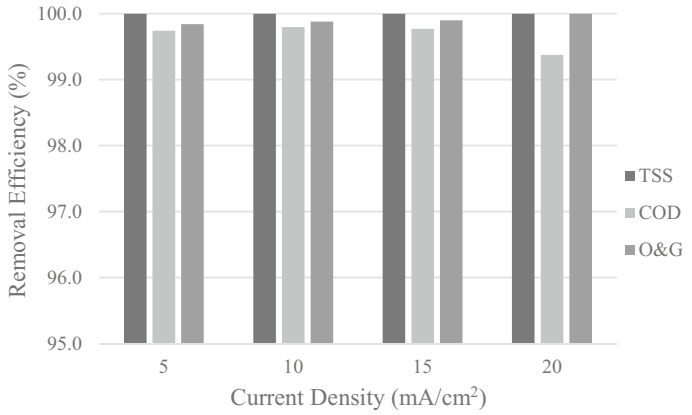

Fig. 4 TSS, COD and O&G removal efficiencies of the combined reactor with the current density at a constant reaction time of 60 min

Table 2 Summary of the results of constant current density study

Parameter	CEA tolerance limit	Initial value	Final value			
			30 min	60 min	90 min	120 min
pH	6.0–8.5	8.08	6.17	9.97	9.17	11.01
TSS (mg/L)	< 50	1638	160	0	50	100
COD (mg/L)	< 250	40,050	300	250	300	600
O&G (mg/L)	< 10	35,701	328	0	0	0

Table 3 Summary of the results of constant time study

Parameter	CEA tolerance limit	Initial value	Final value			
			5 mA/cm^2	10 mA/cm^2	15 mA/cm^2	20 mA/cm^2
pH	6.0–8.5	8.08	8.64	8.15	5.00	9.97
TSS (mg/L)	< 50	1638	0	0	0	0
COD (mg/L)	< 250	40,050	103	81	91	250
O&G (mg/L)	< 10	35,701	56	42	36	0

imposed by the central environmental authority (CEA) were used to compare the values.

In order to comply with the CEA discharge standards for all the parameters, the optimum operating conditions for the combined reactor were selected as 60 min of reaction time under a current density of 20 mA/cm^2. In addition, the pH value was observed to be increased after the reactions. In the EC process, hydroxide complexes of aluminium are generated, and it may have created additional alkalinity to the effluent. Therefore, pH should be adequately adjusted to be in the tolerance limits before discharge or reuse.

3.4 Testing for Actual Service Station Wastewater

From the judgements derived from the two studies carried out for the synthetic wastewater samples, actual service station wastewater samples were tested at optimum operating conditions. The samples were randomly obtained from a service station in *Vavuniya*. It could be observed that the TSS and O&G were removed entirely under the optimum conditions and the COD values of the treated samples were below the detection limit (< 20 mg/L) of the equipment. Since the synthetic wastewater samples were higher in strength, the observed optimum operating conditions were able to eliminate TSS and O&G entirely and COD more than 99% from the lower strength actual service station wastewater samples. The experimental results for the actual wastewater treatment are shown in Table 4.

Table 4 Results from the actual wastewater samples under optimum operating conditions

Parameter	CEA tolerance limit	Initial value	Final value
pH	6.0–8.5	7.71	8.34
TSS (mg/L)	< 50	176	0
COD (mg/L)	< 250	2170	< 20
O&G (mg/L)	< 10	227	0

4 Conclusion

From the EO reactor study, it could be seen that the copper plating on the graphite substrate could significantly increase the treatment efficiency by 55%, 62.4%, and 54.7% for TSS, COD, and O&G, respectively in synthetic wastewater. Therefore, copper-plated graphite could be suggested as an economical alternative to be used as anodes for the EO process.

The suitability of aluminium electrodes for the EC process is verified through the results observed in the experiments. EC reactor alone could remove the TSS by 80.8%, COD by 97%, and O&G by 100% in synthetic wastewater. However, combining both EC and EO processes could enhance all the targeted pollutants' treatment efficiency and extents below the CEA maximum permissible limits. The combined reactor could remove TSS and O&G entirely and COD to > 99% from the actual service station wastewater. Hence the developed combined reactor could be suggested as an economical and efficient method of treating service station wastewater.

The optimum operating conditions decided through the experiments were 60 min of reaction time with 20 mA/cm^2 anodic current density. Increasing reaction time and current density may decrease treatment efficiency. However, it could be observed that the pH of the treated samples was in the alkaline range. Therefore, pH adjustment is recommended prior to the discharge of the effluent. Further optimisation of the operating conditions, development of a single anode to support both EC and EO processes, improving the reactor for continuous flow scenario, and further studies of leaching chemicals to the effluents could be recommended for future studies.

Acknowledgements Authors acknowledge the funds received by the International Foundation for Science, Sweden (W5336-2) and NORAD WaSo Asia project.

References

1. Anglada Á, Urtiaga A, Ortiz I (2009) Contributions of electrochemical oxidation to waste-water treatment: fundamentals and review of applications. J Chem Technol Biotechnol 84(12):1747–1755
2. Anglada Á, Urtiaga A, Ortiz I, Mantzavinos D, Diamadopoulos E (2011) Boron-doped diamond anodic treatment of landfill leachate: evaluation of operating variables and formation of oxidation by-products. Water Res 45(2):828–838
3. Banchon C, Castillo A, Posligua P (2017) Chemical interactions to cleanup highly polluted automobile service station wastewater by bioadsorption-coagulation-flocculation. J Ecol Eng 18(1):1–10
4. Flox C, Arias C, Brillas E, Savall A, Groenen-Serrano K (2009) Electrochemical incineration of cresols: a comparative study between PbO_2 and boron-doped diamond anodes. Chemosphere 74(10):1340–1347
5. Harinarayanan Nampoothiri M, Manilal A, Soloman P (2016) Control of electrocoagulation batch reactor for oil removal from automobile garage wastewater. Procedia Technol 24:603–610
6. Mazumder D, Mukherjee S (2011) Treatment of automobile service station wastewater by coagulation and activated sludge process. Int J Env Sci Dev, 64–69
7. Patel U, Suresh S (2008) Electrochemical treatment of pentachlorophenol in water and pulp bleaching effluent. Sep Purif Technol 61(2):115–122
8. Pouet M, Grasmick A (1995) Urban wastewater treatment by electrocoagulation and flotation. Water Sci Technol 31(3–4)
9. Swain K, Abbassi B, Kinsley C (2020) Combined electrocoagulation and chemical coagulation in treating brewery wastewater. Water 12(3):726
10. Zaneti R, Etchepare R, Rubio J (2011) Car wash wastewater reclamation. full-scale application and upcoming features. Resour Conserv Recycl 55(11):953–959

Variation of Copper Adsorption with Initial pH and Pyrolysis Temperature by Saw Dust and Paddy Husk Biochar Made in an Industrial Type Pyrolizer

H. M. P. Wijeyawardana, Biplob Pramanik, A. K. Karunarathna, Chamila Gunasekara, David Law, and K. G. N. Nanayakkara

Abstract Copper (II) ions (Cu^{2+}) are one of the widely spread heavy metals in the environment causing ecological and human health risk. Among the conventional methods of Cu^{2+} removal, adsorption is observed as the most favorable. Biochar, a product of pyrolysis, has a relatively structured carbon matrix with high degree of porosity and extensive surface area, like activated carbon suggesting its suitability to be used as an adsorbent material. In this study, biochar was synthesized using an industrial type pyrolyzer and low-cost agricultural waste materials; saw dust and paddy husk as feedstocks. Six sets of biochar were made adhering to three temperature ranges: 350–450, 450–550 and 550–650 °C with a resident time of 30 min. Further, the effect of solution pH on the adsorption of Cu was tested. All the biochar materials exhibit similar trend of maximizing adsorptive removal at pH = 6. At lower pH values the surface charge of the biochar materials is positive creating unfavorable grounds for Cu^{2+} removal. As pH increases above 6.5, Cu^{2+} precipitates as $Cu(OH)_2$ lowering the amount of soluble Cu^{2+} in the solution. Thus, the negative adsorptive removal efficiencies can be observed at the pH values above 6. The trend followed the shape of a maximum graph for almost all biochar materials where the removal maximizes at 450–550 °C pyrolysis temperature as lower temperatures favor more functional groups while the higher temperatures favor the development of higher specific surface area. At most pH values, the saw dust biochar shows higher removal percentage compared to the paddy husk biochar. Hence, a positive indication of Cu removal is present at lower pH values. The kinetics follow the pseudo-second order model suggesting that chemisorption is dominant. However, isotherms of adsorption, surface characterization of the materials, tests for leaching of adsorbed pollutants

H. M. P. Wijeyawardana · B. Pramanik · C. Gunasekara · D. Law
School of Engineering, Royal Melbourne Institute of Technology, Melbourne, Australia

H. M. P. Wijeyawardana · K. G. N. Nanayakkara (✉)
Faculty of Engineering, University of Peradeniya, Kandy, Sri Lanka
e-mail: kgnn@pdn.ac.lk

A. K. Karunarathna
Faculty of Agriculture, University of Peradeniya, Kandy, Sri Lanka

R. Dissanayake et al. (eds.), *ICSBE 2020*, Lecture Notes in Civil Engineering 174,
https://doi.org/10.1007/978-981-16-4412-2_50

must be performed before field applications are done with the developed biochar materials.

Keywords Adsorption · Biochar · Copper · Slow pyrolysis · Saw dust · Paddy husk

1 Introduction

Water pollution is identified as a major cause of water insecurity [17]. This has resulted in large fraction of the world's population not having access to safe drinking water. Hence, consumption of polluted water has been suggested to be a leading cause of deaths worldwide [11]. In recent decades, heavy metal pollution has become a global environmental issue and the prime focus of environmental security [9]. The main reason for heavy metal toxicity is that heavy metals are non-biodegradable, toxic, and easy to accumulate at low concentrations in living organisms [5]. Copper (Cu) is a micronutrient that is essential to plants, animals and humans [4, 1]. Excess exposure to Cu by humans could result in health problems such as temporary and permanent disorders and damages of digestive system, kidney or liver and in plants it can damage cell membranes leading to death of plants [4, 1]. Therefore, controlling the levels of pollutant concentrations in water is important to maintain water quality in the environment.

To date, the common techniques used to sequester heavy metals from water are cementation, precipitation, coagulation–flocculation, ionic exchange and membrane separation [4, 5]. However, the major drawbacks in practicing these methods are high initial capital cost, operational and maintenance costs [12]. However, adsorption is observed as a favorable process for heavy metal mainly due to its cost-effectiveness [4]. Also it allows the easy regeneration and recovery of the separation medium (adsorbent) as well [1]. However, conventional adsorbent materials like activated carbon are costly and the high costs discourages the use of adsorption process in water treatment [5].

Biochar can be identified as a good alternative to costly adsorbents which has large specific surface area, porous structure, enriched functional groups and mineral components which make it suitable to be used as a good adsorbent material [3, 19, 20]. Further, Tan et al. [18] and Dai et al. [3] states that biochar has a similar porous structure compared with activated carbon. Further, considering the adsorption of heavy metals Shen et al. [15] reports that the environmental impacts of using biochar as the functional unit are lower that of than activated carbon. Biochar is a product of pyrolysis of biomass [18]. In pyrolysis process, thermal degradation of the chemical constituent of the biomass is done keeping the reaction atmosphere inert to obtain the energy [19]. Biochar is among the three main products of the pyrolysis process alongside bio oil and syngas [19]. The slow pyrolysis is mainly used for the biochar production as it yields more biochar compared with other pyrolysis techniques [3, 8]. The general temperature ranges used for slow pyrolysis ranges from 350 to 750 °C.

Past studies have identified that, properties of biochar depends upon the feedstock properties and pyrolysis temperature mainly [3, 18].

Among the feedstocks used for biochar production, agricultural biomass is identified as one of the most abundant renewable resources on the earth, mainly including crop residues, wood biomass [3]. The ability of producing low cost biochar with the utilization agricultural residuals and wastes as inputs for biochar production has been explored by many studies [18]. The properties of agricultural feedstocks change mainly due to presence of different fractions of cellulose, hemicellulose and lignin [15, 16]. The lignin, hemicellulose and cellulose also thermally decompose at different temperatures and the different degrees of thermal decomposition of feedstocks result significantly different properties and consequently different adsorption capacities for heavy metals [15, 16]. Generally, high temperatures result in biochar with high surface area. However, the availability of surface functional groups decline with high temperatures. The adsorption of metal ions on the carbonaceous materials is said to be dependent on both surface chemistry, porosity and its distribution [16]. Therefore, optimization of pyrolysis temperature selection depending on the sorptive removal has to be carefully evaluated in order to develop and efficient biochar material. In literature most biochar production has been done in laboratory scale using specialized finance commonly with N_2 gas supplied to maintain an oxygen depleted environment. But now, interest has grown for working to produce efficient and cost-effective biochar production stoves [3]. Compared with the laboratory methods, biochar production furnace has many advantages such as; potentially much cleaner, with lower emissions of carbon monoxide, hydrocarbons, and fine particles and have lower greenhouse gas (carbon dioxide and methane) [3].

2 Materials and Methods

2.1 Materials

Rice milling generates a by-product know as husk where about 22% of the weight of paddy is received as husk. In most of the rice processing areas located in Sri Lanka, the surplus paddy husk is considered as a waste material creating environmental problems and often available free of charge [14]. Furthermore, the estimated saw dust output in 2010 was estimated to be 212 kt in Sri Lanka and most of it is freely available in large heaps around the sawmills creating disposal and environmental problems [14]. Hence, utilization of these two underutilized waste products were considered in this study. The feedstocks used were paddy husk (PH) obtained from Anuradhapura, Sri lanka and saw dust (SD) obtained from Gelioya, Sri lanka. All the chemical reagents used were of analytical grade and distilled water was used in all the experiments. In the adsorption studies the stock solutions of Cu^{2+} were prepared by using $Cu(NO_3)_2 \cdot 2H_2O$. The adjustments for pH were done by using HCl and NaOH. All the chemical reagents used were of analytical grade.

Table 1 Abbreviations of the biochar materials

Feed stock	350–450 °C	450–550 °C	550–650 °C
Paddy husk	PH1	PH2	PH3
Saw dust	SD1	SD2	SD3

2.2 Methods

Six sets of biochar were made adhering to three temperature ranges: 350–450, 450–550 and 550–650 °C with a resident time of 30 min. Then, biochar was quenched with water to cool it to room temperature. The abbreviations used for the biochar materials are given in Table 1.

The effect of initial solution pH and contact time in the removal of Cu^{2+} were analysed based on the removal efficiencies. In all the experiments, the initial concentrations of Cu^{2+} was 10 mg/L. All the experiments were conducted at room temperature (25 °C). An adsorbent dosage of 1 g/L was used in all the adsorption studies. The batch adsorption experiments were done by shaking biochar suspensions in a shaking incubator shaker at room temperature (25 °C) at 120 rpm for 24 h. After this, residual Cu concentration was measured by filtering the suspension mixtures with AISIMO membrane filter paper of pore size 0.45 μm and preserved with HNO_3 and analyzed using Shimadzu AA-7000 Atomic Absorption Spectrophotometer (AAS).

3 Results and Discussion

3.1 Variation of Removal of Cu with pH

Figure 1 shows the variation of the adsorptive removal of all the six biochar materials. The removal efficiency was calculate using Eq. 1 where E-percentage removal, %; C final-the final concentration Cu in the solution after sorption, mg/L; C initial-the initial concentration Cu in the solution, mg/L;

$$E = \left(1 - \left(\frac{Cfinal}{Cinitial}\right)\right) \times 100\% \tag{1}$$

All the biochar materials exhibit similar trend of maximizing adsorptive removal at pH = 6. Comparable results can be observed in the study of [2] where hardwood biochar showed a optimum removal at initial solution pH of 5.

Table 2 illustrates the changes to the pH value of the solution after adsorption equilibrium was reached. Final pH values increase when the initial pH value is 3–6 whereas it decreases when initial pH is 7–9 and similar changes has been observed in literature [7]. As pH increases above 6, Cu^{2+} precipitates as $Cu(OH)_2$ occur lowering the amount of soluble Cu in the solution and lowers the sorption efficiency [7].

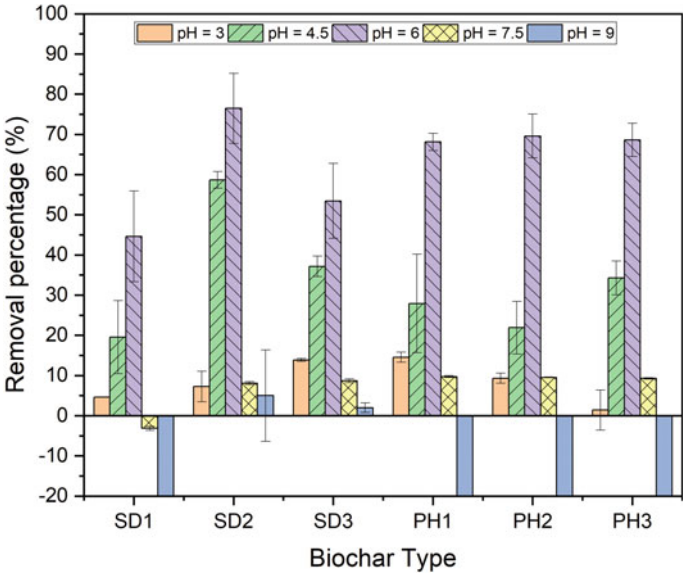

Fig. 1 Variation of adsorptive removal with initial pH of the solution for each type of biochar (Temperature = 25 °C; Contact Time = 24 h; Adsorbent dosage = 1 g/L; Initial Cu concentration = 10 mg/L)

Table 2 Variation of solution pH value after 24 h of contact time

Biochar type	Initial pH = 9	Initial pH = 7.5	Initial pH = 6	Initial pH = 4.5	Initial pH = 3
SD1	7.36	7.59	6.40	3.41	3.21
SD2	7.58	7.71	6.50	4.52	3.24
SD3	7.63	7.58	6.45	4.72	3.25
PH1	7.60	8.01	6.25	3.20	3.12
PH2	7.55	7.85	6.23	4.60	3.11
PH3	7.51	7.70	6.18	4.70	3.11

Measuring the pH values after 24 h of contact time, drift of final pH values of the solution can be observed. Thus, the negative adsorptive removal efficiencies can be observed at the pH values above 6.

3.2 Variation of Removal with Time

The variation of adsorption with time was studied using the SD2 and PH1 as they showed the highest removal efficiency for Cu removal. The results are shown in Fig. 2 where about 70% of the removal occurred within 2–3 h and then the equilibrium was

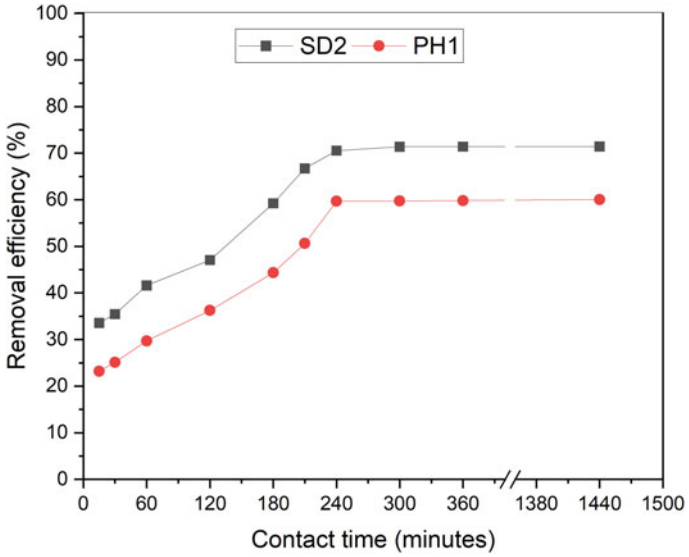

Fig. 2 Variation of adsorptive removal with time of the SD2 and PH1 (Initial pH = 6.0; Temperature = 25 °C; Adsorbent dosage = 1 g/L; Initial Cu concentration = 10 mg/L)

reached around 6 h. Similar observations have been made by previous studies in Cu removal which employed wood biomass and rice husks as feedstock for biochar production [2, 13].

The pseudo-first order model (equation of Lagergreen), the pseudo-second order model and the intraparticle diffusion model were applied to study the kinetics of biochar sorption [13]. The analysis indicated that the pseudo-second order model best described the Cu adsorption kinetics for both SD2 and PH1 with correlation coefficient values of 0.9914 and 0.9723 respectively. Therefore, the pseudo-second order model indicates that the rate-limiting step is chemical sorption (chemisorption) between the adsorbents and the Cu ions. This is on par with the observations in literature which states that biochar made with wood and rice husk follow pseudo-second order model for Cu sorption [6, 10, 13].

3.3 Variation of Removal with Pyrolysis Temperature and Feedstock

The trend follows the shape of a maximum graph for almost all biochar materials where the removal maximizes at 450–550 °C pyrolysis condition. However, at pH = 4.5 for paddy husk biochar the removal shows an increasing trend. Similar observation can be seen for saw dust biochar at pH = 3. In contrast the paddy husk biochar shows decreasing trend of removal at pH = 3.

Table 3 Optimum conditions obtained through adsorption studies

Property	Selection made
Feedstock material	Saw dust
Pyrolysis temperature	450–550 °C
Optimum pH	6.0
Sorption capacity	8.3 mg/g

At most of the studied pH values, the SD2 shows higher removal percentage compared to the paddy husk biochar. However, at pH = 6, the paddy husk biochar performs better than saw dust biochar at temperature ranges except 450–550 °C, where the saw dust biochar displays more removal percentage. The optimum conditions obtained during the study is shown in Table 3.

4 Conclusions and Recommendations

With the results obtained a positive indication of Cu^{2+} removal is present at lower pH values. Therefore, the biochar made in this study has the potential to be used in treatment of water with lower pH values like in acid mine drainage. The kinetics follow the pseudo-second order model suggesting that chemisorption is dominant. However, isotherms of adsorption, surface characterization of the materials, tests for leaching of adsorbed pollutants must be performed before field applications are done with the developed biochar materials.

Acknowledgements Authors would like to acknowledge the NORAD WaSo-Asia Project for the financial support given to conduct this research.

References

1. Abd Hamid S, Azha SF, Sellaoui L, Bonilla-Petriciolet A, Ismail S (2020) Adsorption of copper (II) cation on polysulfone/zeolite blend sheet membrane: synthesis, characterization, experiments and adsorption modelling. Colloids Surf 601. https://doi.org/10.1016/j.colsurfa.2020.124980
2. Chen X, Chen G, Chen L, Chen Y, Lehmann J, Mcbride MB, Hay AG (2011) Adsorption of copper and zinc by biochars produced from pyrolysis of hardwood and corn straw in aqueous solution. Bioresour Technol 102:8877–8884
3. Dai Y, Zhang N, Xing C, Cui Q, Sun Q (2019) The adsorption, regeneration and engineering applications of biochar for removal organic pollutants: a review. Chemosphere 223:12–27
4. Gong J-L, Wang X-Y, Zeng G-M, Chen L, Deng J-H, Zhang X-R, Niu Q-Y (2012) Copper (II) removal by pectin–iron oxide magnetic nanocomposite adsorbent. Chem Eng J 185–186:100–107
5. Hegazi HA (2019) Removal of heavy metals from wastewater using agricultural and industrial wastes as adsorbents. HBRC J 9:276–282

6. Inyang MI, Gao B, Yao Y, Xue Y, Zimmerman A, Mosa A, Pullammanappallil P, Ok YS, Cao X (2015) A review of biochar as a low-cost adsorbent for aqueous heavy metal removal. Crit Rev Environ Sci Technol 46:406–433
7. Kołodyńska D, Wnętrzak R, Leahy JJ, Hayes MHB, Kwapiński W, Hubicki Z (2012) Kinetic and adsorptive characterization of biochar in metal ions removal. Chem Eng J 197:295–305
8. Li H, Dong X, Da Silva EB, De Oliveira LM, Chen Y, Ma LQ (2017) Mechanisms of metal sorption by biochars: biochar characteristics and modifications. Chemosphere 178:466–478
9. Li Y, Zhou Q, Ren B, Luo J, Yuan J, Ding X, Bian H, Yao X (2020) Trends and health risks of dissolved heavy metal pollution in global river and lake water from 1970 to 2017. Rev Environ Contam Toxicol 251:1–24
10. Mohan D, Pittman CU Jr, Bricka M, Smith F, Yancey B, Mohammad J, Steele PH, Alexandre-Franco MF, Gomez-Serrano V, Gong H (2007) Sorption of arsenic, cadmium, and lead by chars produced from fast pyrolysis of wood and bark during bio-oil production. J Colloid Interface Sci 310:57–73
11. Mullaney J, Lucke T (2014) Practical review of pervious pavement designs. CLEAN Soil, Air, Water 42:111–124
12. Muthu M, Santhanam M, Kumar M (2018) Pb removal in pervious concrete filter: effects of accelerated carbonation and hydraulic retention time. Constr Build Mater 174:224–232
13. Pellera FM, Giannis A, Kalderis D, Anastasiadou K, Stegmann R, Wang JY, Gidarakos E (2012) Adsorption of Cu(II) ions from aqueous solutions on biochars prepared from agricultural by-products. J Environ Manage 96:35–42
14. Perera KKCK, Rathnasiri PG, Senarath SAS, Sugathapala AGT, Bhattacharya SC (2005) Assessment of sustainable energy potential of non-plantation biomass resources in Sri Lanka. Biomass Bioenerg 29:199–213
15. Shen Z, Zhang Y, Jin F, Mcmillan O, Al-Tabbaa A (2017) Qualitative and quantitative characterisation of adsorption mechanisms of lead on four biochars. Sci Total Environ 609:1401–1410
16. Štefelová J, Zelenka T, Slovák V (2017) Biosorption (removing) of Cd(II), Cu(II) and methylene blue using biochar produced by different pyrolysis conditions of beech and spruce sawdust. Wood Sci Technol 51:1321–1338
17. Stets EG, Sprague LA, Oelsner GP, Johnson HM, Murphy JC, Ryberg K, Vecchia AV, Zuellig RE, Falcone JA, Riskin ML (2020) Landscape Drivers of Dynamic Change in Water Quality of U.S. Rivers. Environ Sci Technol 54:4336–4343
18. Tan X, Liu Y, Zeng G, Wang X, Hu X, Gu Y, Yang Z (2015) Application of biochar for the removal of pollutants from aqueous solutions. Chemosphere 125:70–85
19. Tripathi M, Sahu JN, Ganesan P (2016) Effect of process parameters on production of biochar from biomass waste through pyrolysis: a review. Renew Sustain Energy Rev 55:467–481
20. Zhang C, Liu L, Zhao M, Rong H, Xu Y (2018) The environmental characteristics and applications of biochar. Environ Sci Pollut Res Int 25:21525–21534

Three-Dimensional Modelling of Flow in a Vertical Slot Fishway

H. M. P. M. Hitihamu, D. M. Pananwala, and S. B. Weerakoon

Abstract The flow characteristics of fishways constructed to facilitate fish migration bypassing barriers in rivers, depend on the fishway geometry and the layout. Hence, the selection of the baffles and pools arrangement within the channel is essential for an optimum design of a fishway. In this study, the suitability of flow characteristics of vertical slot fishway (VSF) with selected geometric design was assessed by both experimental study and numerical modelling. Three—dimensional computational fluid dynamic model was developed by using ANSYS CFX 17.2 software. Model validation was done based on the water depth and velocity measurements obtained from laboratory experiments. Suitability of flow characteristics were assessed for increasing slopes by developing CFD models for 7, 9, 11 and 13% slope cases. It was found that the maximum values of velocity, turbulent kinetic energy and energy dissipation rate in the fishway occur at the slots and they increase with the increasing slope. The low velocity pool volumes corresponding to each slope were computed to assess the adequacy of the resting zones for fish. The study concludes that the pool length of the VSF could be 43% larger than the recommended values with the fishway slope up to 13%, while ensuring favourable flow conditions for fish passage to economize the VSF design.

Keywords Vertical slot fishway · CFD model · Velocity · Low velocity pool volume

1 Introduction

Migration of fish is one of the main natural phenomena taking place in the riverine environment. The upstream and downstream movement of the fish has been highly affected due to both natural and artificial barriers such as dams, weirs and waterfalls, as they restrict the free movement of fish. This leads to severe environmental problems causing the imbalance of the riverine ecology. Therefore, fishways are introduced in

H. M. P. M. Hitihamu (✉) · D. M. Pananwala · S. B. Weerakoon
Department of Civil Engineering, University of Peradeniya, Peradeniya, Sri Lanka
e-mail: prasadi.hitihamu@eng.pdn.ac.lk

R. Dissanayake et al. (eds.), *ICSBE 2020*, Lecture Notes in Civil Engineering 174,
https://doi.org/10.1007/978-981-16-4412-2_51

such environments for the purpose of maintenance of longitudinal connectivity for fish in riverine systems [2]. Fishways are comprised of sloping channels and with the use of weirs, baffles, or vanes they have been partitioned in to pools with openings for fish to swim through. Fishways have been classified in to several types such as: pool and weir, vertical slot, culvert and Denil fishways based on the in-channel device arrangement [3].

Vertical slot fishways are considered as the most efficient type of fishways due to their ability to function effectively even with significant fluctuations of upstream and downstream water levels [8]. The baffle wall opening in VSF allows fish to ascend the fishway at any preferred swimming depth [4]. This is a benefit of VSF compared to overflow fishways such as pool and weir type, which needs fish to jump over the weirs. In vertical slot fishways, the height to be passed has been divided into several small drops forming a series of pools and the water passes from one pool to another through the deep slots located in the cross-walls separating two pools. It is recommended that, in vertical slot fishways, pool width shall be 5–9 times and the pool length shall be 7–12 times of the slot width [9]. Using $8b_0$ as pool width and $10b_0$ as pool length where b_0 is the width of the slot, gives satisfactory flow characteristics [3]. However, hydraulically suitable conditions for a fish passage have been achieved with different dimensions by adopting low overall fishway slope [5].

Reference [6] recommends that the maximum flow velocity of a fishway be less than the maximum attainable swimming speed of fish for a successful migration. It is also recommended that the velocity in a pool of a fishway be kept under 0.30 ms^{-1} in 30–50% of the pool's volume (referred to as low velocity pool volume), as the resting zones of the fish accommodating them to remain for short periods without excessive fatigue [1].

The slope of a fishway determines the total length of the facility, hence slope is a key element in its cost [9]. The main objective of this study is to assess the suitability of flow characteristics of VSF with selected geometric design for different channel slopes, viz.: 7, 9, 11 and 13%. Three-dimensional flow modelling was done for all the slope cases adapting same boundary conditions using ANSYS-CFX CFD software. The simulated results of velocity and depths were verified using experimental observations. The maximum velocities, turbulent kinetic energy (TKE) values and energy dissipation rates, and water profiles and low velocity pool volumes corresponding to each slope were analyzed.

2 Materials and Methods

2.1 Experimental Data Collection

The laboratory setups of the VSF consists of 6 pools created by cross walls with vertical slots placed in staggered manner along the channel as indicated in Fig. 1a.

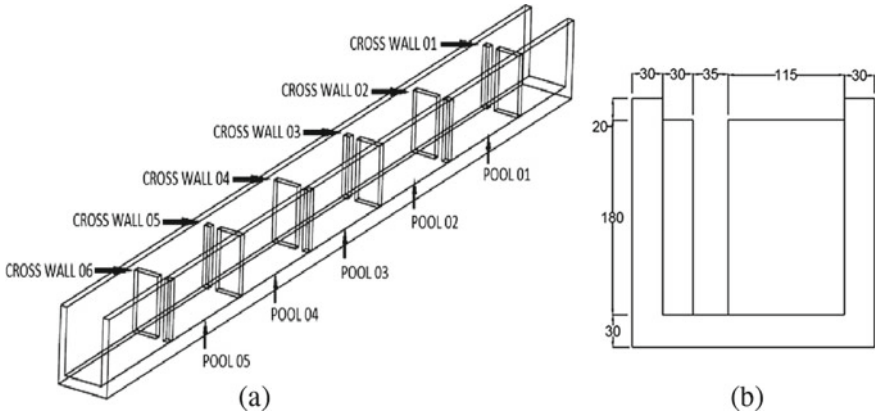

Fig. 1 **a** Slot arrangement and **b** slot dimensions (in mm) of VSF model

Slot dimensions are indicated in Fig. 1b. The pool length was 43% larger than the recommended pool length [3, 9].

With the aid of a constant head tank, a discharge of 3.75 kg/s was maintained at the inlet. Downstream water depth was set to 180 mm by using a wooden plate with clamps fixed at the outlet. Experimental data collection was done for 9% and 11% channel slopes. Fully developed flows independent from the upstream water levels could be observed from the pool No. 2 downstream. Water depth values along the center line of the channel were measured by means of a Vernier scaled depth gauge with an accuracy of 0.1 mm. Directional water velocities along pool 2 were measured by using an electromagnetic flow meter. Velocity measurements were taken in three planes parallel to the pool floor at h = 2 cm, 6 cm and 10 cm where h is the height above the pool floor level. A total of 96 point velocities were recorded within the pool, with 32 measurements in each of these planes.

2.2 Numerical Modelling

Numerical simulations were carried out for fluid domains of 7, 9, 11 and 13% slopes. The geometry was developed using SOLID WORKS 2016 to match the dimensions of the experimental setup and was imported to ANSYS-CFX. It resolves three dimensional Reynolds-averaged Navier—Stokes equation using the finite volume method. Hex- dominant mesh of size 0.01 m was selected as the mesh, after conducting a mesh independency test for 0.008 m, 0.01 m and 0.012 m mesh sizes.

Mass flow rate of 3.75 kg/s and the turbulence intensity of 5% were set at the inlet. Outlet boundary was a pressure boundary and the downstream depth was set as 180 mm in all the simulations. Top surface of the fluid domain was set as an open

boundary which is a pressure boundary. The walls were considered as smooth walls and no-slip condition was applied.

$K - \varepsilon$ turbulence model was used and the simulation was carried out under steady state conditions as a standard free surface model. High resolution was used as the model advection scheme. Model convergence criterion was defined as 0.0001 and therefore the iterations were continued until the non-dimensional residual of each of velocity, TKE, energy dissipation and mass was less than 0.0001. This convergence criteria could be achieved in less than 1000 iterations.

3 Results and Discussion

3.1 Model Validation

Figure 2 compares the water depth profiles along the mid vertical plane obtained from the simulation and the measurements of the laboratory VSF with 9% slope. In Fig. 3 compares the velocities along the pool width at h = 2 cm plane, at a distance of 2 cm from the upstream baffle in pool 2 of 11% slope case. The comparisons of measured and simulated water depths and velocities along other locations in the pool too showed a good agreement.

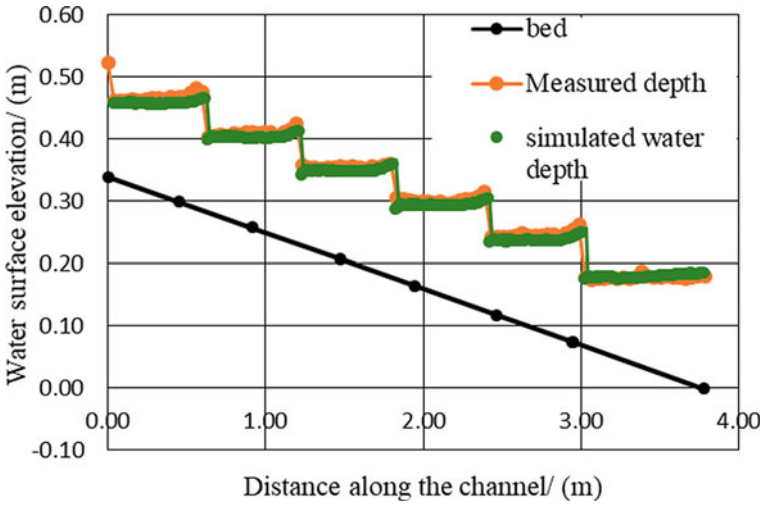

Fig. 2 Measured and simulated water depth profiles along the mid vertical plane of 9% slope VSF

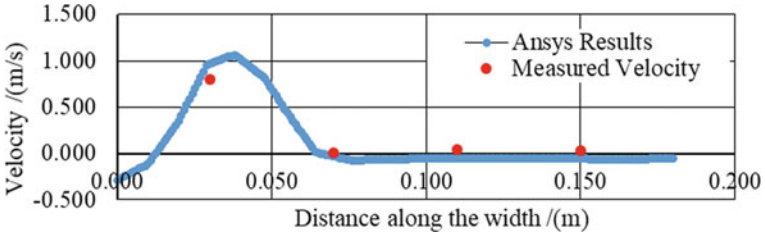

Fig. 3 X-directional velocity comparison at h = 2 cm plane, at a distance of 2 cm from the upstream baffle in pool 2 of 11% slope case

3.2 Model Simulation Results

Velocity contour plots and vectors generated from the simulations of VSFs with 7, 9, 11 and 13% slopes at h = 2 cm plane in pool 2, 3 and 4 are shown in Fig. 4. The maximum flow velocities occur at the slots and these maximum velocity at the slot increases with the increase of the flow and the slope as expected. Accordingly, Table 1 shows the maximum velocities at each planes in different VSF slopes, and the maximum velocities were observed in the 13% slope VSF.

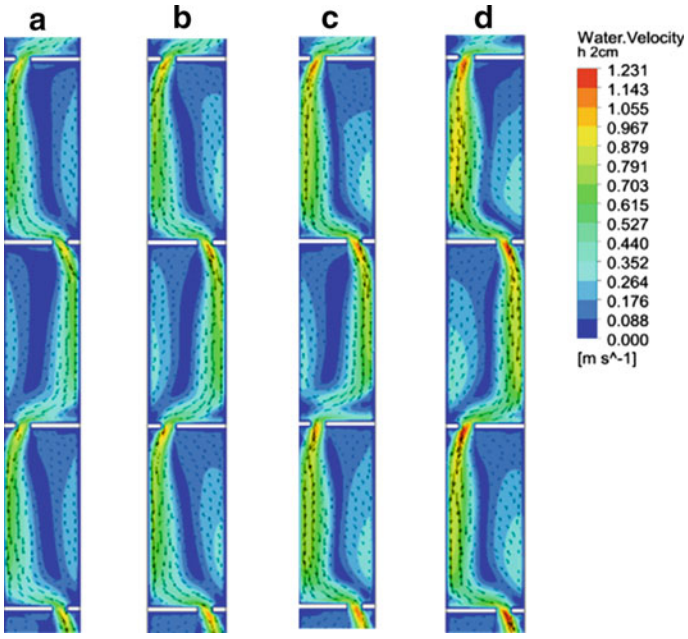

Fig. 4 Velocity contour plots at a plane 2 cm above pool floor of **a** 7% **b** 9% **c** 11% and **d** 13% slope VSF simulations

Table 1 Vertical distribution of the maximum velocities in VSFs of different slopes

Height (h) above the pool floor/(cm)	Maximum velocity/(m/s)			
	S = 7%	S = 9%	S = 11%	S = 13%
2	0.965	1.074	1.129	1.231
4	0.937	1.038	1.118	1.168
6	0.929	1.021	1.096	1.229
8	0.922	1.005	1.129	1.308
10	0.903	1.052	1.182	1.277
12	0.938	1.061	1.159	1.177

TKE and turbulence eddy dissipation distributions were also analyzed in the pools. TKE is high in and around the slots but starts to dissipate rapidly inside the pool. TKE is negligible in some areas within the flow recirculation zones. The maximums of TKE and turbulence eddy dissipation also increase with the flow and the channel slope. A large volume of the pool occupies with the lower values of energy dissipation in VSFs with all the slopes. It is a favourable condition for fish as they usually avoid higher energy dissipation areas [9]. The maximum values of TKEs, turbulence eddy dissipations and low velocity pool volumes in VSFs of each slope case are tabulated in Table 2.

The low velocity pool volume was calculated using the velocity limit of 0.11 m/s which is equivalent to the recommended velocity limit of 0.3 m/s [1], based on Froude similarity with actual fishways [6, 7]. Low velocity pool volume was in a satisfactory level up to 13% slope simulation. Therefore, VSF analyzed in this study is an economized design to facilitate favourable flow conditions for fish passage up to 13% slope even for pool lengths 43% larger than the recommended values [3, 9].

The water surface profiles obtained in the VSFs of all the slopes for the same discharge and same downstream control depth were compared. When the slope increases, the difference in water level between two adjacent pools (Δh) increases and the average water depth in the pools decreases. The increasing of Δh is accompanied with the increase in the velocities.

Table 2 Maximum TKEs, maximum turbulent eddy dissipations and low velocity pool volumes in VSFs of different slopes

VSF slope (%)	Maximum TKE/(m^2/s^2)	Maximum turbulent eddy dissipation/(m^2/s^3)	Low velocity pool volume in pool 2/(%)
7	0.078	1.366	37
9	0.091	1.931	33
11	0.101	2.263	32
13	0.122	2.828	29

4 Conclusion

The study presents experimental and three-dimensional numerical model simulated flow properties for VSFs of different slopes with staggered baffle walls. Simulated water depths and velocities were validated using measurements carried out.

The maximum velocities, TKEs and energy dissipation rates occur at the slots and increase with the increasing slope. As the slope increases the difference in water level between two adjacent pools (Δh) increases and the average water depth in the pools decreases. Low velocity pool volume was in a satisfactory level up to 13% slope simulation.

VSF layout given is an economized design to facilitate favourable flow conditions for fish passage up to 13% slope.

Acknowledgements Authors are thankful to NORAD WaSo-Asia Project for providing the financial support for this study.

References

1. Bell MC, United States. Army. Corps of Engineers. North Pacific Division (1986) Fisheries handbook of engineering requirements and biological criteria. Portland, Or. Fish Passage Development and Evaluation Program, Corps of Engineers, North Pacific Division, p 290
2. Clay CH (1995) Design of fishways and other fish facilities, 2nd edn. Lewis Publishers, Ann Arbor, MI
3. Katopodis C (1992) Introduction to fishway design. Freshwater Institute, Department of Fisheries and Oceans—Central and Arctic Region, Winnipeg, Man
4. Liu M, Rajaratnam N, Zhu DZ (2006) Mean flow and turbulence structure in vertical slot fishways. J Hydraul Eng 132(8):765–777
5. Marriner BA, Baki ABM, Zhu DZ, Cooke SJ, Katopodis C (2016) The hydraulics of a vertical slot fishway: a case study on the multi-species Vianney-Legendre fishway in Quebec, Canada. Ecol Eng 90:190–202
6. Marriner BA, Baki ABM, Zhu DZ, Thiem JD, Cooke SJ, Katopodis C (2014) Field and numerical assessment of turning pool hydraulics in a vertical slot fishway. Ecol Eng 63:88–101
7. Nippon Koei, Fichtner (2017) Fish ladder, Moragolla hydropower project. Ministry of Power and Renewable Energy, Ceylon Electricity Board, Democratic Socialist Republic of Sri Lanka
8. Quaranta E, Katopodis C, Revelli R, Comoglio C (2017) Turbulent flow field comparison and related suitability for fish passage of a standard and a simplified low-gradient vertical slot fishway. River Res Appl 33(8):1295–1305
9. Wang RW, David L, Larinier M (2010) Contribution of experimental fluid mechanics to the design of vertical slot fish passes. Knowl Manag Aquat Ecosyst 396:02

Two—Dimensional Modelling of Flow in Rantambe Reservoir for Sediment Management

W. M. D. M. Wasala, R. M. C. B. Rathnasiri, and S. B. Weerakoon

Abstract Sediment accumulation in reservoirs reduces reservoir capacities and expected benefits from reservoir projects. This is especially prominent in small reservoirs built across rivers carrying high sediment loads. Rantambe reservoir built across the Mahaweli river just downstream of the Randenigala reservoir is one of the reservoirs severely affected by sedimentation. The original capacity of the reservoir was 11.5 MCM in 1990 and in 2014 the capacity was 6.14 MCM. Randenigala reservoir releases and the flow of the Uma-Oya tributary are the main sources of the Rantambe reservoir, and the Uma-Oya tributary carries large sediment load to the reservoir annually. Flushing of sediment is carried out using the two bottom outlets each with an area of 9.7 m^2 during the flood season, though it is not adequate to restore the reservoir capacity. This study focuses on investigating the potential of reducing the sediment entering into the reservoir from the Uma-Oya during the flood season using a sediment bypass tunnel which originates from a low weir built across the Uma-Oya. A two-dimensional hydrodynamic model was set up, flow patterns and bed shear stress were analyzed. For calibration of the model, simulated velocities were compared with the measured velocities. The model was validated with Manning's roughness coefficient of 0.03. The model was then applied introducing a low weir and a bypass tunnel. The bed shear and velocities increase in Uma-Oya, and the flow is directed towards to the tunnel. There is a 18% increment in the area of high bed shear stress to erode the deposited sediments compared to the condition under current practice of flushing under same conditions. This proposed sediment bypass tunnel is an effective technique to control the sediment management of the Rantambe reservoir.

Keywords Reservoir sedimentation · Sediment bypass tunnel · Rantambe reservoir

W. M. D. M. Wasala (✉) · R. M. C. B. Rathnasiri · S. B. Weerakoon
Department of Civil Engineering, University of Peradeniya, Srilanka, India

R. Dissanayake et al. (eds.), *ICSBE 2020*, Lecture Notes in Civil Engineering 174,
https://doi.org/10.1007/978-981-16-4412-2_52

1 Introduction

Reservoirs impounded by dam construction across the rivers face the issue of sediment accumulation resulting in loss of the effective storage and operational problems. Sediment management strategies mainly divided into 3 parts (ICOLD 1989, 1999, 2009, Morris & Fan 1998, Kantoush & Sumi 2010, Annandale 2011, 2013, [1], 2012, [2]): (1) sediment yield reduction, (2) routing sediments around or through the reservoir, and (3) recover volume by sediment removal or dam heightening. It is often possible to bypass sediment around the reservoir which avoids reservoir sedimentation and supplies sediment to the downstream reaches.

Rantambe reservoir built across the Mahaweli River in 1990, is one of the major reservoirs in Sri Lanka. It is a shallow reservoir with a capacity of 11.5 MCM, and with a surface area of 1.3 km^2 and an average depth of 8.6 m. It has faced this sedimentation problem and already 45% of its effective storage has reduced. Due to sediment accumulation, it reduced its original capacity of 11.5 MCM to 6.14 MCM within 34 years from 1980 to 2014 (NBRO 2014). Flushing of sediment is carried out using the two bottom outlets, each with an area of 9.7 m^2, through the dam during the flood season, though it is not adequate to restore the reservoir capacity.

The main sources of water for the Rantambe reservoir are the Uma-Oya tributary discharging to the reservoir and the Mahaweli River flow which is the release from the Randenigala reservoir built across the river at the upstream (Fig. 1).

The Uma-Oya discharge carries a huge sediment load into the Rantambe reservoir. The sediment load is deposited on the reservoir bed in the region downstream of the discharge point of the Uma-Oya into the reservoir. The particle size distribution at the reservoir bed shows that D50 is 0.0156 mm. Although regular flushing is carried out using the bottom outlets provided in the dam, it has not been effective to efficiently restore the reservoir capacity. The soil erosion rate in the Uma-Oya watershed varies widely from 0 to 1493.1 t/ha/yr, reflecting different land use practices in the area. Because of existing land use, around 195,000 tons of sediment are deposited in the Ranatambe reservoir every year, contributing to around 0.0203 GWHs of electricity loss per year. This loss could be avoided by dredging the sediments with an annual dredging cost of 0.260 million LKR [3].

Fig. 1 Rantambe reservoir area

The main purpose of this research is to investigate efficiency of sediment removal by a sediment bypass tunnel from the Uma-Oya with a low weir constructed across the Uma-Oya. A computational model is applied to analys the flow patterns and bed shear stresses in the reservoir and the Uma-Oya. Rantembe reservoir and the Uma-Oya can be considered as shallow water flows and hence a two-dimensional depth averaged hydrodynamic computational model could be used for the analysis (Weerakoon and Tamai 2001). Accordingly, Sedimentation and River Hydraulics Two-Dimensional Model (SRH-2D model) of the United States Bureau of Reclamation with the Surface Water Modelling System (SMS) interface is used here. In terms of modeling capabilities, SRH-2D is comparable to many existing models [4].

2 SRH 2D Model

SRH-2D is a two-dimensional hydraulic and sediment transport model for river systems under continuous development (Lai 2018). Details can be found in USBR website (https://www.usbr.gov). This 2D dynamic wave model is based on the Shallow Water equations:

Continuity Equation

$$\frac{\partial h}{\partial t} + \frac{\partial hU}{\partial x} + \frac{\partial hV}{\partial y} = e \tag{1}$$

2D Momentum equation

$$\frac{\partial hU}{\partial t} + \frac{\partial hUU}{\partial x} + \frac{\partial hVU}{\partial y} = \frac{\partial hT_{xx}}{\partial x} + \frac{\partial hT_{xy}}{\partial y} - gh\frac{\partial z}{\partial x} - \frac{\tau_{bx}}{\rho} + D_{xx} + D_{xy} \tag{2}$$

$$\frac{\partial hV}{\partial t} + \frac{\partial hUV}{\partial x} + \frac{\partial hVV}{\partial y} = \frac{\partial hT_{xy}}{\partial x} + \frac{\partial hT_{yy}}{\partial y} - gh\frac{\partial z}{\partial y} - \frac{\tau_{by}}{\rho} + D_{yx} + D_{yy} \tag{3}$$

where,

t	time
x, y	horizontal Cartesian coordinates
h	water depth
U, V	depth-averaged velocity components in x and y directions
e	excess rainfall rate
g	gravitational acceleration
T_{xx}, T_{xy}, Tyy	depth-averaged turbulent stresses
D_{xx}, D_{xy}, D_{yx}, Dyy	dispersion terms due to depth averaging
ρ	water density
z	water surface elevation.

3 Methodology

Contour maps in the area and bathymetry maps of the reservoir were used to identify the topography of study area and to identify the bed topography of reservoir. Mesh was generated, using the scatter module and Arc GIS, to cover the computational domain which includes the entire reservoir from the downstream of the Randenigala dam and part of the Uma-Oya. The model was applied to analyze sediment bypassing and flushing during flood flow of the Uma-Oya. Three flow boundaries, namely, inflows from Randenigala reservoir release and the Uma-Oya, and outflow through the bottom outlet of Rantambe reservoir were used. The release for the power house was not considered during flushing. The particles that have particle diameter less than 0.0156 mm would be mobile if the critical bed shear stress is above 0.0378 N/m^2 [5].

4 Model Calibration and Validation

The model was calibrated using the field observations taken along the two cross-sections given in previous research (Herath et al. 2017) (Fig. 2).

The calibration was done by adjusting the Manning's roughness coefficient of the reservoir bed until the model output velocities match with the observed velocities. Figure 3 shows the comparison of simulated and measured velocities at Section 1A. The computed results were found to be acceptable with the measured values for the Manning's roughness coefficient of 0.030.

The model was validated using the velocities under different boundary conditions at two cross sections shown in Fig. 4 (Gunasinghe et al. 2018). Figure 5 shows the comparison of velocities at Section 2A.

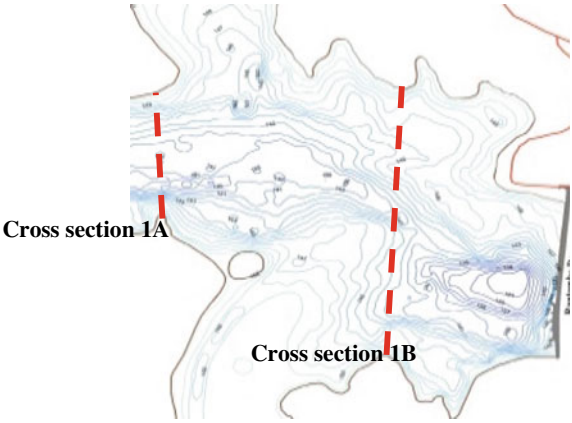

Fig. 2 Locations of cross section 1A and 1B

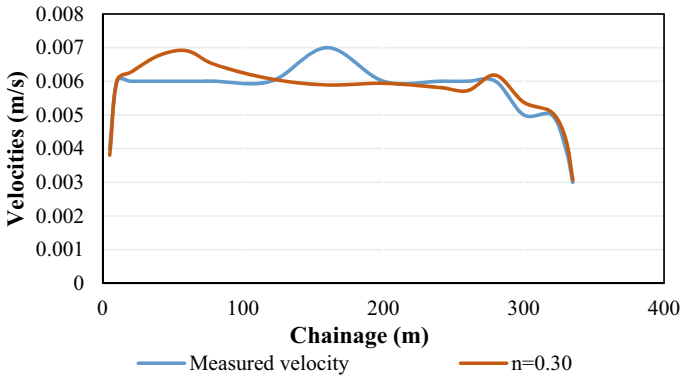

Fig. 3 Stream wise velocities at Section 1A

Fig. 4 Locations of cross section 2A and 2B

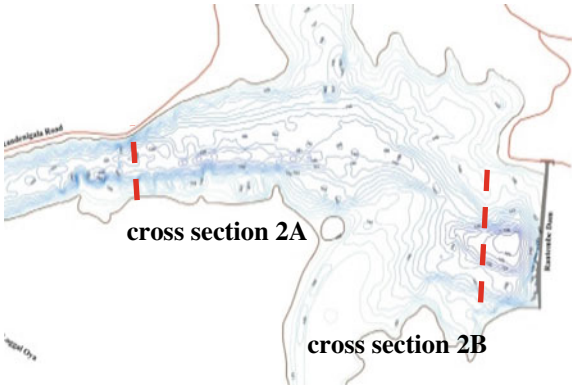

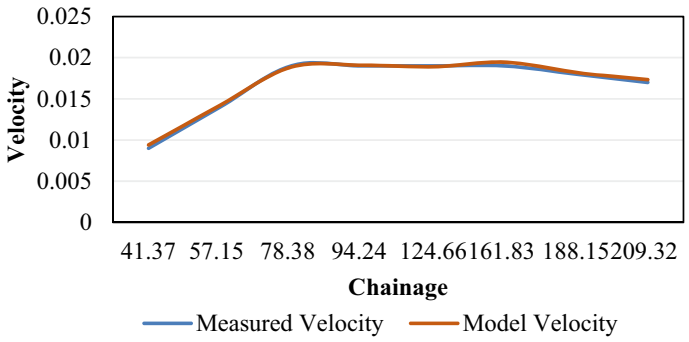

Fig. 5 Comparison of velocity at Section 2A

Table 1 Boundary conditions of the considered cases

	Case 01 Existing conditions		Case 02 With bypass layout	
	01-a	01-b	02-a	02-b
Randenigala (m^3/s)	355	158	355	158
Uma-Oya (m^3/s)	45	20	85	60
Rantambe (m^3/s)	200 × 2	89 × 2	200 × 2	89 × 2
Tunnel (m^3/s)			40	40
Water surface elevation (m)	155	132	155	132

5 Model Application

The analysis of the flow patterns and bed shear stresses in the reservoir and the Uma-Oya under different inflow and layout of the tunnel inlet with the weir was carried out while the bottom outlet gates were open.

Two cases were considered:

- Case 01—Flow patterns for the existing conditions
- Case 02—Flow patterns for the weir with bypass tunnel layout (Table 1).

6 Results and Discussion

Under existing conditions, a diminutive increment of bed shear stresses and velocity patterns could be identified when flushing with low water surface elevation and low discharge corresponding to Case 1-b than higher water surface elevation and greater discharge corresponding to Case 1-a. But under both conditions, bed shear stress and velocity magnitudes were very low. The velocities larger than 0.1 m/s and bed shear stresses larger than 0.04 N/m^2 were distributed in a relatively small area of the reservoir as shown in Fig. 6.

A different flow pattern appears with the introduction of the weir with 131 m crest level across the Uma-Oya and the bypass tunnel inlet just upstream of it at the right bank (Fig. 7). Increased velocities and bed shear stress could be identified when flushing with the low reservoir water surface elevation and a low discharge (Case 02-b). Bed shear stress for Case 02-b is shown in Fig. 7, where an increment of 18% of erodible area was observed.

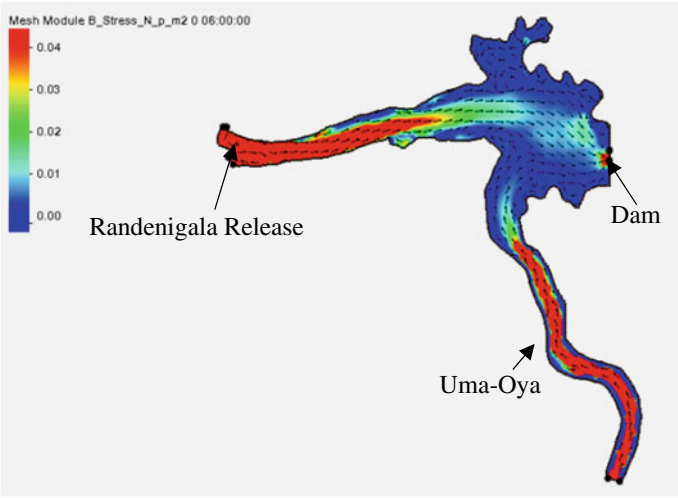

Fig. 6 Bed shear profile for Case 01-b

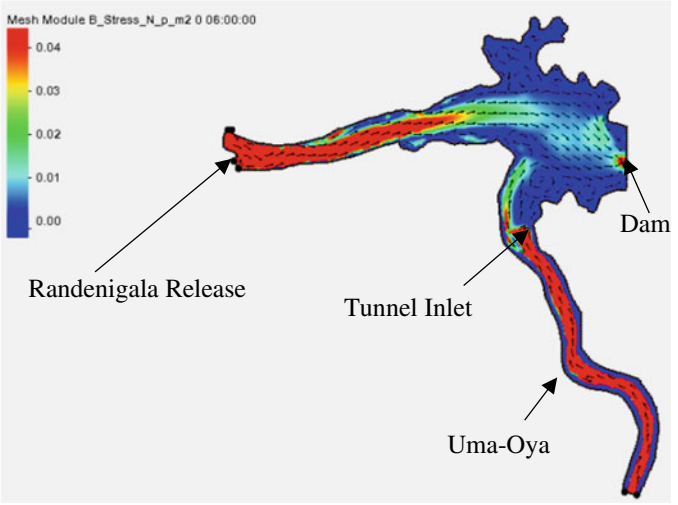

Fig. 7 Bed shear stress for position 01 in Case 02-b

7 Conclusion

Two-dimensional computational model was set up for Rantambe reservoir for its sediment management.

In can be concluded that,

- The proposed bypass tunnel with a low weir across the Uma-Oya is a potential sediment management strategy for the Rantambe Reservoir.
- The Uma-Oya flow is directed to the tunnel creating high shear stresses along the river bed to bypass sediment through the tunnel.

Acknowledgements Authors acknowledge the assistance given by the Director of HAO & M Division, Mahaweli Authority Sri Lanka and Engineer-in-charge Randenigala and Rantambe reservoirs, Eng. K.K.T.B. Rajarathne by providing necessary data and at field work.

References

1. Auel C, Boes R (2011) Sediment bypass tunnel design—review and outlook. Laboratory of Hydraulics, Hydrology and Glaciology (VAW), ETH Zurich, Switzerland
2. Kondolf GM, Gao Y, Annandale GW, Morris GL, Jiang E, Zhang J, Cao Y, Carling P, Fu K, Guo Q, Hotchkiss R, Peteuil C, Sumi T, Wang WH, Wang Z, Wei Z, Wu B, Wu C, Yang CT (2014) Sustainable sediment management in reservoirs and regulated rivers: experiences from five continents. Earth's Future Res Art 2:256–280
3. Udayakumara EPN, Gunawardena UADP (2016) Reducing siltation and increasing hydropower generation from the Rantambe reservoir, Sri Lanka, SANDEE Working Paper No 113–16
4. Habtamu G (2008) Comparison of 2D Hydrodynamic models in river reaches of ecological importance, Hydro_AS-2D and SRH-W, Master of Science Program Water Resources Engineering and Management—WAREM, pp 10–92
5. Berenbrock C, Tranmer A (2008) Simulation of flow, sediment transport, and sediment mobility of the lower Coeur d'Alene River, Idaho. Geol Surv (U.S.), viii
6. Morris GL (2020) Classification of management alternatives to combat reservoir sedimentation. Water 12(3):861
7. Moussa AMA (2013) Predicting the deposition in the Aswan High Dam Reservoir using a 2-D model. Ain Shams Eng J 4(2):143–153
8. Ratnayesuraj CR, Rifas KM, Risly S, Weerakoon SB (2015) Model study of sediment flushing in Rantambe reservoir. In: 3rd international symposium on advances in civil and environmental engineering
9. Weerakoon S, Tamai N, Kawahara Y (2003) Averaged flow computation at a river confluence. In: Proceedings of the institution of civil engineers water and maritime engineering
10. Lai YG (2009) Two-dimensional depth-averaged flow modeling with an unstructured hybrid mesh. J Hydraul Eng
11. Weerakoon SB, Herath HMSS, Hettiarachchi HATT (2017) Two-dimensional computational modeling of river flow—case study of Rantembe reservoir
12. Weerakoon SB, Gunasinghe ARP, Weerasinghe HPDA (2018) Different sediment flushing arrangements for Rantambe reservoir analyzed by two-dimensional hydrodynamic model

Investigation on the Performance of Multi-stacked Floating Wetlands for Leachate Treatment in a Controlled Environment

M. A. I. A. Moragoda, K. D. A. N. Kumarage, G. M. P. R. Weerakoon, and M. I. M. Mowjood

Abstract Leachate releasing from solid waste dump sites or sanitary landfills, is rich in organic pollutants and heavy metals, contributes heavily in contamination of water bodies. Therefore, it is necessary to treat the landfill leachate appropriately up to the effluent standards, before releasing them in to the environment. Constructed wetlands have been identified as an appropriate technology for wastewater treatment in tropical developing countries. However, despite many advantages the large land area requirement and the impacts of outdoor environmental conditions have been identified as major limitations for application of this technology at many places. Therefore, this study has been focused on reducing the land area requirement by designing a multi-stacked floating wetland system. The experimental set-up had three multi-stacked wetland systems, each containing 3 units of 32 cm × 52 cm × 28 cm (length:width:height) in size stacked one over the other and planted with *Eichhornia crassipes* (common water hyacinth). Two of them were placed inside a greenhouse, while the remaining system was kept outside the greenhouse in open environment. One of the system kept inside the greenhouse was set with a supplementary lighting arrangement. All three units were fed with synthetic leachate to achieve a 60 cm/day hydraulic loading rate (HLR). Results showed that the wetland system kept inside the greenhouse with supplementary lighting had a significant positive impact in removing BOD_5, COD, TOC, Pb, Cu and Zn with average removal efficiencies of 77.4%, 79.1%, 97.9%, 89%, 89.3% and 87.7%, respectively.

Keywords Artificial red lights · Floating constructed wetlands · Heavy metals · Greenhouse conditions · Leachate treatment

M. A. I. A. Moragoda · K. D. A. N. Kumarage · G. M. P. R. Weerakoon (✉)
Faculty of Engineering, University of Peradeniya, Peradeniya, Sri Lanka
e-mail: prabhaw@eng.pdn.ac

M. I. M. Mowjood
Faculty of Agriculture, University of Peradeniya, Peradeniya, Sri Lanka

R. Dissanayake et al. (eds.), *ICSBE 2020*, Lecture Notes in Civil Engineering 174,
https://doi.org/10.1007/978-981-16-4412-2_53

1 Introduction

Water scarcity has become a growing issue worldwide. Along with increasing population, urbanization and industrial development fresh water bodies are getting polluted with improper waste discharges, which further intensifies the prevailing water scarcity. Contamination of freshwater resources can be resulted by the release of untreated or partly treated wastewater into the water bodies from households, industries, agricultural lands, sanitary landfills etc. In developing countries like Sri Lanka, releasing of leachate from solid waste dump sites to fresh water resources is inevitable due to the practice of open dumping. Therefore, implementation of appropriate and adaptable treatment technologies is important to mitigate these environmental impacts.

Constructed Wetlands (CWs), which are artificially developed to mimic processes found in natural wetlands, have been identified as an appropriate technique for leachate treatment in tropical developing countries, with simple technology and low cost of installation, operation and maintenance. However, the large land area requirement and the impact of outdoor environmental conditions have been identified as major limitations for application of CWs for wastewater treatment at many places, due to the rising demand for land particularly in densely populated areas.

Basically, CWs are categorized according to their flow patterns as surface flow or subsurface flow wetlands. Technological development of CWs are in three main hydrological regimes, whose mode of action is different even though they are based on the same biological principle. Accordingly, there are free water surface (FWS) wetlands, subsurface flow (SSF) wetlands and floating wetlands. In floating wetlands species float on the water surface [11], which contain floating macrophytes such as water hyacinth (*Eichornia crassipes*), duckweed (*Lemna spp.*) etc., or use of emerging other species that are made to float. Buta et al. [4], has reported that *Eichhornia crassipes*, which is commonly available in tropical environments has been used in floating wetlands with successful results.

In CWs, pollutants in wastewater are removed by various physical, chemical and biological processes such as sedimentation, adsorption, assimilation by plants and microbial transformations [11]. Consequently, vegetation plays an important role in pollutant removal in floating wetlands and sunlight is a major factor for the macrophyte growth. Therefore, provision of an artificial light for additional hours, could make an impact in the macrophyte growth which in turn would ultimately enhance the performance of floating wetlands. The present study evaluated the leachate treatment performance using multi-stacked floating wetlands by providing a controlled environment by means of a greenhouse. Further, this study investigated the impact of artificial light for additional hours during the day on performance of multi-stacked floating wetlands.

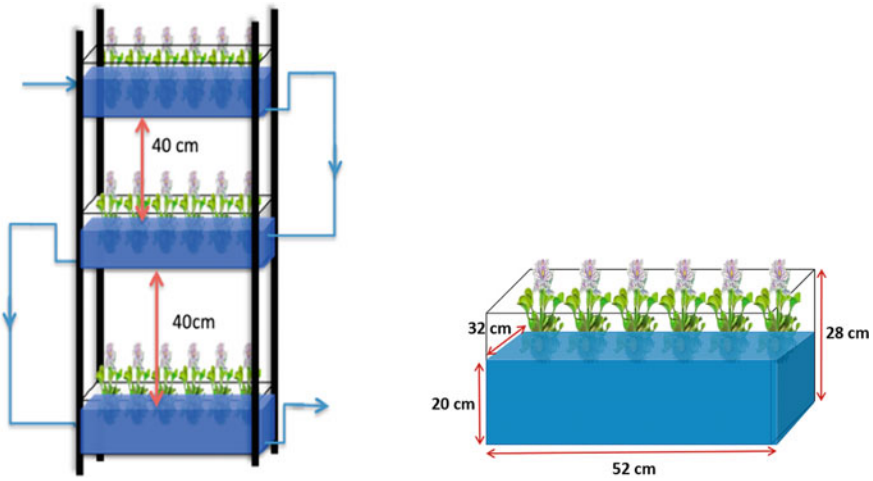

Fig. 1 Dimensions and spacing between multi-stacked floating wetland units system and flow arrangement

2 Methodology

2.1 Experimental Setup

This study was conducted in Meewathura farm in University of Peradeniya, Sri Lanka (80°35′32″ E, 70°15′16″ N). The experimental set-up had three multi-stacked floating wetland (MSFW) systems, each containing 3 units of floating wetlands of 32 cm × 52 cm × 28 cm (length:width:height) in size stacked one over the other and planted with *Eichhornia Crassipes* (common water hyacinth) as shown in Fig. 1. Two of them (System 01 and System 02) were placed inside a greenhouse (GH), while the remaining system (System 03) was kept at outside the greenhouse. A supplementary lighting system had introduced to a system (System 02) inside the greenhouse. All three MSFW systems were fed with synthetic leachate, to achieve 60 cm/day hydraulic loading rate (HLR) (theoretical hydraulic retention time (HRT): 3-days), using an overhead tank and a constant head tank as shown in Fig. 2.

2.2 Arrangement of Supplementary Lighting

The daylight hours are observed to last up to 12 h on average throughout the year in Sri Lanka. Thus, a supplementary light was provided using 10 W red flood lights from 4–6 am and from 6–8 pm to increase the daylight hours up to 16 h for System 02 using a timer. It is necessary to consider the quality of light to meet the requirements of plant photosynthesis and photo morphogenesis for successful growth as plant

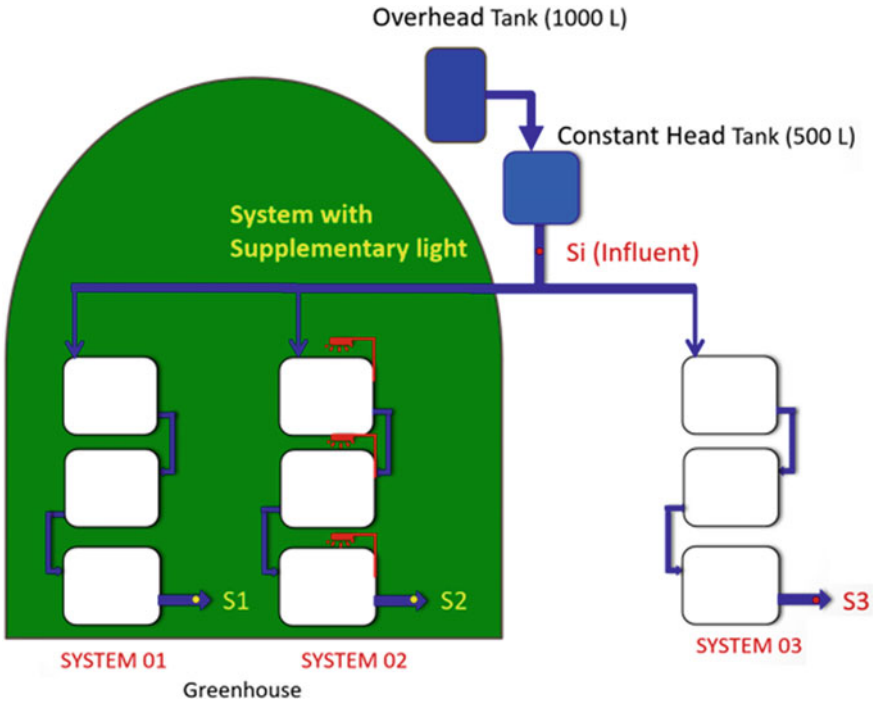

Fig. 2 Experimental setup (Si, S1, S2 and S3 are sample points)

physiology strongly depends on the light spectrum [9]. Chlorophyll in plants has a distinct light absorption peak in the red-light region at the wavelength of 660 nm [7]. Red light is usually defined as radiation with wavelengths between 600 and 700 nm as shown in Fig. 3 [8] and therefore, 10 W red flood lights were selected for the provision of supplementary light in this study.

2.3 System Operation

Initially, all three MSFW systems were fed with tap water for one week to flush and rid the system from existing pollutants. Then, synthetic leachate prepared as explained in the following section was fed to the systems and left to acclimatize for another two weeks. At the end of 3rd week, heavy metals; lead (Pb), copper (Cu) and zinc (Zn) were spiked along with synthetic leachate. Samples from the influent and effluent of each system were collected at the influent and effluent of all three systems with a sampling frequency of 4-days interval.

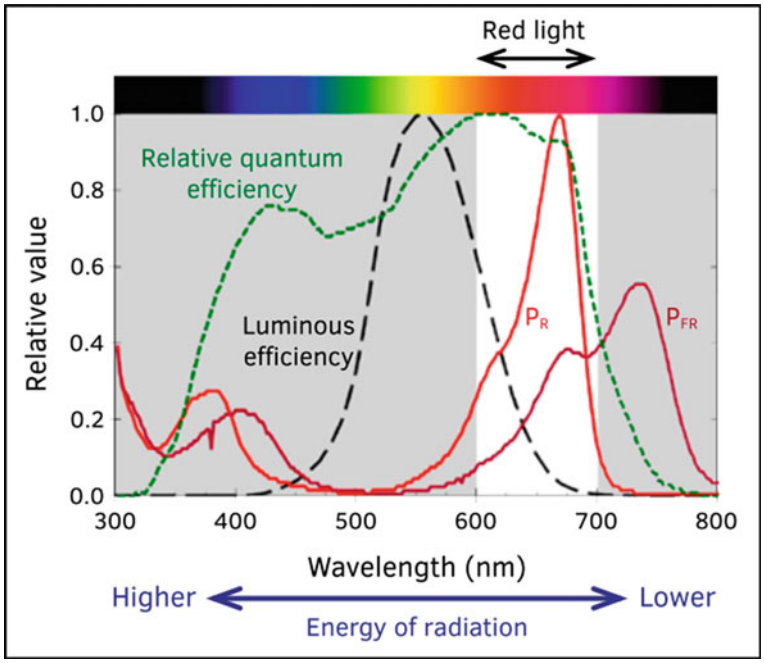

Fig. 3 Relative quantum efficiency curve

2.4 Synthetic Leachate Preparation

Synthetic leachate was prepared mixing 500 g of granular sugar, 50 g of sodium acetate (CH_3COONa), 1.5 g of di-potassium phosphate (K_2HPO_4), 18 g of sodium bicarbonate ($NaHCO_3$), 18 g of potassium carbonate (K_2CO_3), 2.5 g sodium chloride (NaCl), 8 g of calcium chloride ($CaCl_2$), 8 g of magnesium chloride hexahydrate ($MgCl_2{\cdot}0.6H_2O$), 4 g of magnesium sulfate heptahydrate ($MgSO_4{\cdot}7H_2O$) and 500 g of urea ($CO(NH_2)_2$) in 1000 L of tap water. Heavy metals, 5 g of lead nitrate ($Pb(NO_3)_2$), 5 g of copper sulfate pentahydrate ($CuSO_4{\cdot}5H_2O$) and 5 g of zinc sulfate heptahydrate ($ZnSO_4{\cdot}7H_2O$), were added into the 1000 L of synthetic water.

2.5 Wastewater Analysis

Water quality parameters such as pH, electrical conductivity (EC), dissolved oxygen (DO), five-day biochemical oxygen demand (BOD_5), chemical oxygen demand (COD), total organic carbon (TOC) and heavy metals; lead (Pb), copper (Cu) and zinc (Zn) were measured in all collected samples, following the standard methods for water and wastewater analysis [1] in the Environmental Laboratory, Faculty of

Engineering, University of Peradeniya. The removal efficiencies (RE) of these pollutants were estimated using Eq. 1, in each wetland system, where C_i is the influent pollutant concentration and C_o is the effluent pollutant concentration.

$$\text{Removal Efficiency} = \frac{Ci - Co}{Ci} \times 100\% \quad (1)$$

2.6 Plant Growth Measurements

The plant growth was monitored during the study period, with respect to non-destructive measurements of wet weight of each plant and number of leaves corresponding to each unit and each system.

2.7 Statistical Analysis

All the statistical analysis in this study were performed using "MINITAB 15" statistical software. The normality of measured wastewater parameters was determined by 'Anderson Darling' test and 'one-way ANOVA' test was used to determine the significant treatment differences between two wetland systems.

3 Results and Discussion

3.1 Wastewater Characteristics

The average wastewater characteristics at the influent and effluents of each MSFW system are shown in Table 1. The normality test performed using 'Anderson Darling' test showed that pH, EC, TOC, BOD_5, COD as well as Pb, Cu and Zn at the influent were normally distributed ($p > 0.05$) except DO. Similarly, in the effluent samples, EC, BOD_5, COD, Cu and Zn concentrations at the effluents of all three wetland systems were normally distributed ($p > 0.05$). However, pH in the effluent of System 1, TOC in the effluents of Systems 01 and 02, Pb in the effluent of System 02 and DO in the effluents of System 02 and System 03 were not normally distributed ($p < 0.05$).

Table 1 Wastewater characteristics at the influent and effluents of each wetland system

Parameter	Influent		Average concentration of effluent		
	CV (%)	Average concentration	System 01	System 02	System 03
pH	3.65	7.2 ± 0.3	7.8 ± 0.3	7.9 ± 0.2	7.7 ± 0.4
EC (μS)	27.83	1.3 ± 0.4	0.8 ± 0.3	0.5 ± 0.3	1.1 ± 0.3
DO (mg/l)	135.34	0.1 ± 0.1	1.4 ± 0.6	2.7 ± 0.8	0.8 ± 0.4
TOC (mg/l)	32.52	117.5 ± 38.2	22.7 ± 17.2	9.4 ± 6.9	59.1 ± 27.7
BOD_5 (mg/l)	52.70	173.3 ± 91.4	57.6 ± 37.7	40.8 ± 30.7	79.9 ± 44.9
COD (mg/l)	34.47	465.5 ± 160.4	143.0 ± 28.8	93.5 ± 26.6	168.8 ± 31.9
Pb (mg/l)	23.25	0.28 ± 0.07	0.07 ± 0.03	0.03 ± 0.02	0.11 ± 0.04
Cu (mg/l)	25.67	0.29 ± 0.07	0.07 ± 0.04	0.03 ± 0.02	0.11 ± 0.04
Zn (mg/l)	15.98	0.38 ± 0.06	0.09 ± 0.03	0.05 ± 0.03	0.12 ± 0.04

Note System 01: inside the GH without lighting, System 02: inside the GH with lighting, System 03: outside the GH, GH: greenhouse

3.2 Pollutant Removal Efficiencies

The average removal efficiencies of BOD_5, COD, TOC, Pb, Cu and Zn in all three wetland systems are shown in Table 2. Accordingly, the System 02 (i.e. the system inside the GH with supplementary lighting) had the best overall removal performance of 77.4%, 79.1%, 97.9%, 89%, 89.3% and 87.7% for BOD_5, COD, TOC, Pb, Cu and Zn respectively. The statistical analysis carried out using 'one-way ANOVA' test at $\alpha = 0.05$ significance level confirmed this result, showing there are significant treatment differences among all three wetland systems for TOC, Pb, Cu and Zn removal ($p < 0.05$). Further, Systems 02 and 03 had a significant treatment difference for BOD_5 and COD removal and Systems 01 and 02 had significant treatment difference for COD removal.

Table 2 Removal efficiencies of wastewater parameters

Parameter	Average removal efficiency (%)		
	System 01	System 02	System 03
BOD_5	66.8	77.4	52.6
COD	66.1	79.1	59.8
TOC	94.9	97.9	86.9
Pb	76.5	89.0	61.4
Cu	75.6	89.3	59.5
Zn	76.1	87.7	59.1

Note System 01: inside the GH without lighting, System 02: inside the GH with lighting, System 03: outside the GH

Figure 4 presents the variation of removal efficiencies of BOD_5, TOC, COD, Pb, Cu and Zn over the study period. Accordingly, it is evident that the multi-stacked wetland systems kept inside the greenhouse (System 01 and 02) had higher removal efficiencies of BOD_5, TOC, COD, Pb, Cu and Zn compared to the outside system (System 03). This could be due to the effects of environmental conditions on wetland performance in the degradation of pollutants from the wastewater [10]. Further, it was noted that the System 02 had the highest overall treatment performance, for all the pollutants. This could be due to the enhancement of plant growth as a result of supplementary light observed in System 02, as increased plant growth provides more surface area for the microbial proliferation resulting in the enhanced degradation of organic pollutants [2]. Moreover, aquatic macrophytes such as *Eichhornia*

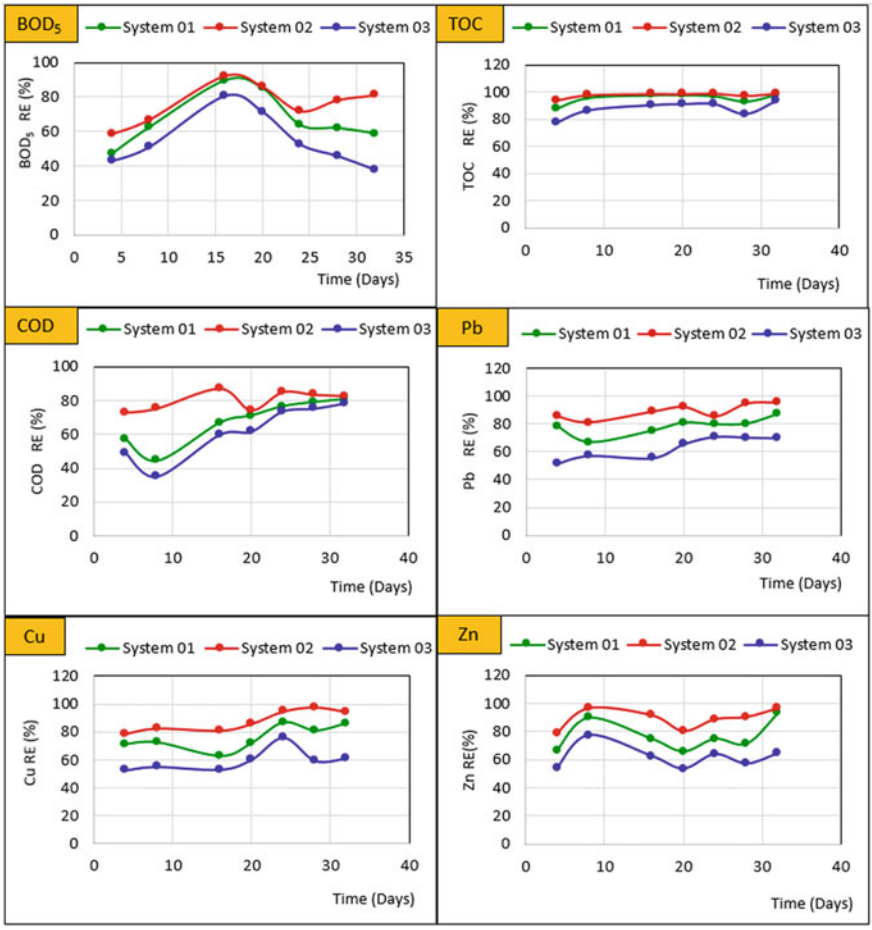

Fig. 4 Variation of BOD_5, TOC, COD, Pb, Cu and Zn removal efficiencies. *Note* System 01: inside the GH without lighting, System 02: inside the GH with lighting, System 03: outside the GH

Crassipes are known to be bio-accumulators which accumulate the contaminants in their biomass through uptake [6]. This precipitated potentially toxic metals are often taken up by the plant tissues, particularly the roots [10]. Thus, there is a positive impact of the higher rate of plant growth for pollutant removal by providing artificial lights for additional hours.

3.3 Plant Growth Performance

Results showed that System 02 (system inside the GH with supplementary lighting) had a higher average plant growth rate compared to other systems with respect to the number of leaves and wet weight of each plant. Figure 5 illustrates, the variation of RE for heavy metals with wet weight over the study period. Accordingly, it was observed that the System 02 had the highest RE compared to the other systems.

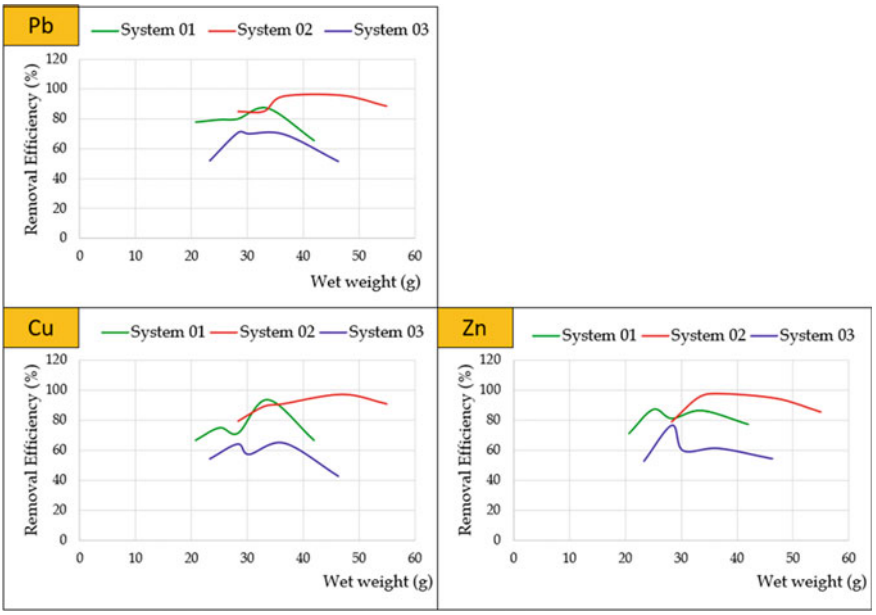

Fig. 5 Variation of Pb, Cu and Zn removal efficiencies with respect to the wet weight of plants. *Note* System 01: inside the GH without lighting, System 02: inside the GH with lighting, System 03: outside the GH

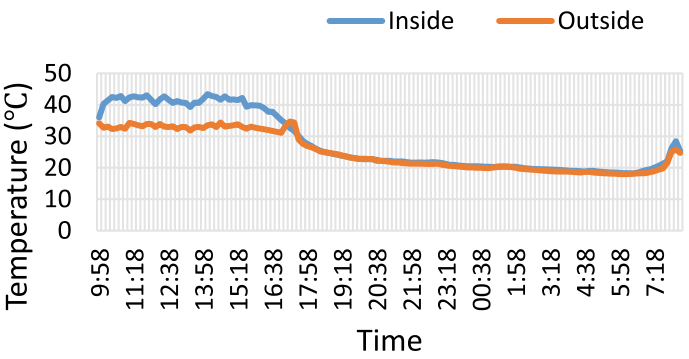

Fig. 6 Variation of temperature at the inside and outside the greenhouse for a 24-h period

3.4 Temperature Variations

The variation of the temperature inside and outside of the greenhouse were monitored during a 24-h period is shown in Fig. 6. Accordingly, it was observed that the temperature inside of the greenhouse is higher than the outside temperature, particularly during the daytime, while there is less a difference at night time. Also, it was observed that after 7.00 pm both inside and outside temperature levels were below 25 °C, which is advantageous as night temperatures above 24 °C should be avoided due to the possibility of causing serious damage to the plants [5]. Average daily temperature (ADT), which is the mathematical average of air temperatures over a 24-h period, is an important concept in greenhouse temperature management that controls the speed or rate of plant growth [5]. The ADTs inside and outside of the greenhouse was calculated to be 27.8 °C and 25.1 °C, respectively which are both between the optimal air temperature range 21–30 °C for the floating macrophyte, *Eichhornia crassipes* [3].

4 Conclusions

Results revealed that the removal efficiencies of BOD_5, COD, TOC, Pb, Cu and Zn were higher in the multi-stacked floating wetland systems kept inside the greenhouse than the system kept outside the greenhouse. Further, provision of supplementary lighting arrangement had a positive effect in removing pollutants showing the highest overall performance with average removal efficiencies of 77.4%, 79.1%, 97.9%, 89.0%, 89.3% and 87.7% for BOD_5, COD, TOC, Pb, Cu and Zn, respectively, along with the highest average plant growth. Thus, construction of multi-stacked floating wetland systems at a controlled environment such as greenhouse, and provision of an artificial lighting arrangement for additional hours can be recommended to be used

for effective treatment of leachate with reduced land area requirements at congested areas.

Acknowledgements Authors would like to acknowledge the Tokyo Cement Group and Norad WaSo Asia Project in the Department of Civil Engineering, University of Peradeniya, Sri Lanka for their financial assistance for this research.

References

1. APHA (2005) Standard methods for the examination of water and wastewater, 21st edn. American Public Health Association
2. Ashraf S, Afzal M, Naveed M, Shahid M, Zahir ZA (2018) Endophytic bacteria enhance remediation of tannery effluent in constructed wetlands vegetated with *Leptochloa fusca*. Int J Phytorem 20(2):121–128
3. Bais SS, Lawrence K, Nigam V, Engineering B (2015) Analysis of heavy metals removal by *Eichhornia crassipes* (Mart.). Solms 4(09):732–739
4. Buta E, Paulette L, Mihăiescu T, Buta M, Cantor M (2011) The influence of heavy metals on growth and development of *Eichhornia crassipes* species, cultivated in contaminated water. Notulae Botanicae Horti Agrobotanici Cluj-Napoca 39(2):135–141. https://doi.org/10.15835/nbha3926095
5. Goldammer T (2019) Greenhouse management, a guide to operations and technology
6. Mohammed RR (2012) Removal of heavy metals from waste water using black teawaste. Arab J Sci Eng 37(6):1505–1520
7. Okamoto K, Yanagi T, Takita S, Tanaka M, Higuchi T, Ushida Y, Watanabe H (1996) Development of plant growth apparatus using blue and red LED as artificial light source. Acta Hortic 111–116. https://doi.org/10.17660/ActaHortic.1996.440.20
8. Runkle E (2016) Red light and plant growth. Gpn, p 2016
9. Samuoliene G, Brazaityte A, Sirtautas R, Novičkovas A, Duchovskis P (2011) Supplementary red-LED lighting affects phytochemicals and nitrate of baby leaf lettuce. J Food Agric Environ 9(3–4):271–274
10. Shahid MJ, Arslan M, Ali S, Siddique M, Afzal M (2018) Floating wetlands: a sustainable tool for wastewater treatment. Clean Soil Air Water 46(10)
11. Soler C, Crespi R, Soler E (2019) Performance evaluation of artificial wetlands with floating macrophytes (*Lemnas*) in the treatment of urban effluents. Int J Hydrol 3(2):129–136. https://doi.org/10.15406/ijh.2019.03.00174